Transactions of the ASME®

Journal of Heat Transfer

Published Bimonthly by The American Society of Mechanical Engineers

VOLUME 123 • NUMBER 3 • JUNE 2001

Transactions of the ASME, Journal of Heat Transfer (ISSN 0022-1481) is published bi-monthly (Feb., Apr., June, Aug., Oct., Dec.) by The American Society of Mechanical Engineers, Three Park Avenue, New York, NY 10016. Periodicals postage paid at New York, NY and additional mailing offices. POSTMASTER: Send address changes to Transactions of the ASME, Journal of Heat Transfer, c/o THE AMERICAN SOCIETY OF MECHANICAL ENGINEERS, 22 Law Drive, Box 2300, Fairfield, NJ 07007-2300. **CHANGES OF ADDRESS** must be received at Society headquarters seven weeks before they are to be effective. Please send old label and new address. **STATEMENT from By-Laws.** The Society shall not be responsible for statements or opinions advanced in papers or ... printed in its publications (B7.1, Para. 3), **INDEXED** by Applied Mechanics Reviews and Engineering Information, Inc. Canadian Goods & Services Tax Registration #126148048.

TECHNICAL PAPERS

Forced Convection

417 Thermohydraulic Study of Laminar Swirl Flow Through a Circular Tube Fitted With Twisted Tapes
S. K. Saha and A. Dutta

Natural and Mixed Convection

428 Effects of a Magnetic Modulation on the Stability of a Magnetic Liquid Layer Heated From Above
Saïd Aniss, Mohamed Belhaq, and Mohamed Souhar

434 Linear Stability of Mixed Convection Flow of Two Immiscible Fluids in a Vertical Annulus
Kai-Ti R. Chang and Kang Ping Chen

441 Effect of Partition Wall on Natural Convection Heat Transfer in a Vertical Air Layer
Yoshiyuki Yamaguchi and Yutaka Asako

Radiative Transfer

450 An Efficient Method for Modeling Radiative Transfer in Multicomponent Gas Mixtures With Soot
Vladimir P. Solovjov and Brent W. Webb

458 Radiation Heat Transfer Between Fluidizing Particles and a Heat Transfer Surface in a Fluidized Bed
Jun Yamada, Yasuo Kurosaki, and Takanori Nagai

466 An Integral Formulation of Transient Radiative Transfer
Z.-M. Tan and P.-F. Hsu

Melting and Freezing

476 Phase Change in a Cylinder and a Cylindrical Shell Heated With an Axisymmetric Front Moving in the Axial Direction
C. K. Hsieh and M. Leung

Boiling and Condensation

486 A Simple Kinetic Theory Treatment of Volatile Liquid-Gas Interfaces
Dalton J. E. Harvie and David F. Fletcher

492 Flow Dynamics and Heat Transfer of Wavy Condensate Film
Akio Miyara

Heat Pipes

501 Capillary Blocking in Forced Convective Condensation in Horizontal Miniature Channels
Yuwen Zhang, A. Faghri, and M. B. Shafii

Porous Media, Particles, and Droplets

512 Effective Permeability of a Layered Porous Cavity
J. C. Leong and F. C. Lai

520 Formulation and Numerical Solution of Non-Local Thermal Equilibrium Equations for Multiple Gas/Solid Porous Metal Hydride Reactors
George M. Lloyd, A. Razani, and Kwang J. Kim

(Contents continued on inside back cover)

This journal is printed on acid-free paper, which exceeds the ANSI Z39.48-1992 specification for permanence of paper and library materials. ∞™
♻ 85% recycled content, including 10% post-consumer fibers.

Journal of Heat Transfer Volume 123, Number 3 JUNE 2001

527 Thermal Interaction at the Interface Between a Porous Medium and an Impermeable Wall
Sung Jin Kim and Duckjong Kim

534 Experimental Study of Water Sprays for the Attenuation of Fire Thermal Radiation
S. Dembele, J. X. Wen, and J.-F. Sacadura

544 Numerical Study of Spray Injection Effects on the Heat Transfer and Product Yields of FCC Riser Reactors
S. L. Chang, S. A. Lottes, C. Q. Zhou, B. J. Bowman, and M. Petrick

556 Adaptive Neurocontrol of Heat Exchangers
Gerardo Díaz, Mihir Sen, K. T. Yang, and Rodney L. McClain

563 Computation of Flow and Heat Transfer in Two-Pass Channels With 60 deg Ribs
Yong-Jun Jang, Hamn-Ching Chen, and Je-Chin Han

Heat Transfer in Manufacturing Processes

576 Modeling Dynamic Electrical Resistance During Resistance Spot Welding
S. C. Wang and P. S. Wei

586 An Experimental Investigation of Heat Affected Zone Formation and Morphology Development During Laser Processing of Metal Powder Mixtures
C. W. Buckley and T. L. Bergman

General

593 Using the Concept of Information to Optimally Design Experiments With Uncertain Parameters
A. F. Emery

TECHNICAL NOTES

601 Performance Analysis and Optimization of Annular Fin With a Step Change in Thickness
B. Kundu and P. K. Das

604 A Novel Mini Calibrator for Thermochromic Liquid Crystals
Christopher J. Elkins, John Fessler, and John K. Eaton

607 Acceleration of Anisotropic Scattering Computations Using Coupled Ordinates Method (COMET)
S. R. Mathur and J. Y. Murthy

ANNOUNCEMENTS

613 Call for Papers: Microgravity Transport Processes in Fluid, Thermal, Materials, and Biological Sciences

614 Call for Papers: Thermal Challenges in Next Generation Electronic Systems

615 Call for Papers: International Symposium on Micro/Nanoscale Energy Conversion and Transport

616 Preparing and Submitting a Manuscript for Journal Production and Publication

Thermohydraulic Study of Laminar Swirl Flow Through a Circular Tube Fitted With Twisted Tapes

S. K. Saha[1]
e-mail: sujoy_k_saha@hotmail.com

A. Dutta
e-mail: duttaa@is2.dal.ca

Department of Mechanical Engineering,
Dalhousie University,
Halifax Nova Scotia,
B3J 2X4 Canada

Heat transfer and pressure drop characteristics in a circular tube fitted with twisted tapes have been investigated experimentally. Laminar swirl flow of a large Prandtl number ($205 < Pr < 518$) viscous fluid was considered. The swirl was generated by short-length twisted-tape inserts; regularly spaced twisted-tape elements with multiple twists in the tape module and connected by thin circular rods; and smoothly varying (gradually decreasing) pitch twisted-tapes. The heat transfer test section was heated electrically imposing axially and circumferentially constant wall heat flux (UHF) boundary condition. Reynolds number, Prandtl number, twist ratio, space ratio, number of tuns in the tape module, length of the twisted-tape and smoothness of the swirling pitch govern the characteristics. Friction factor and Nusselt number are lower for short-length twisted-tape than those for full-length twisted-tape. On the basis of constant pumping power and constant heat duty, however, short-length twisted-tapes are found to perform better than full-length twisted-tapes for tighter twists. Thermohydraulic performance shows that twisted-tapes with multiple twists in the tape module is not much different from that with single twist in the tape module. Friction factor and Nusselt number are approximately 15 percent lower for twisted-tapes with smooth swirl having the average pitch same as that of the uniform pitch (throughout) twisted-tape and the twisted-tapes with gradually decreasing pitch perform worse than their uniform-pitch counterparts.
[DOI: 10.1115/1.1370500]

Keywords: Augmentation, Enhancement, Forced Convection, Laminar, Swirling

Introduction

Laminar flow heat transfer in tubes finds wide engineering applications. Heating or cooling of viscous liquids in the process industries, heating or cooling of oils, heating of circulating fluid in solar collectors, heat transfer in compact heat exchangers are few examples. Heat transfer augmentation techniques play a vital role here since heat transfer coefficients are generally low for laminar flow in plain tubes. Insertion of twisted tapes in tubes is one such augmentation technique. Tape inserts are inexpensive; they can be easily employed to improve the thermal performance of the existing systems. Also, for a given heat load, smaller heat exchangers can be made, thereby reducing capital investments. Twisted tapes reduce the dominant thermal resistance of the viscous stream and reduce the required heat transfer surface area. However, the thermal improvements are accompanied by increased pressure drop.

Ever since Whitham [1] has published his work on heat transfer enhancement by means of twisted-tape inserts, reports on the new work have been pouring in continuously. Most of the early works were concerned with turbulent flow, [2–12]. The general conclusion from these investigations is that, for turbulent flow, comparable increase in heat transfer coefficient are accompanied by pressure drop which is several orders of magnitude greater than the plain tube values.

Date and Singham [13], Date [14], and Hong and Bergles [15] investigated heat transfer enhancement in laminar, viscous liquid flows in tubes with uniform heat flux (UHF). In the numerical solutions of Date and Singham [13] and Date [14], the flow conditions were idealized for zero tape thickness but the tape twist and fin-effects were included. However, the published values of Nu in Date [14] are to be multiplied by 0.5 to get the actual values. Flow development length for swirl flow was found to be much smaller than that for straight flow. Hong and Bergles [15] observed that the circumferential temperature profile for the swirl flow is related to the tape orientation. The circumferential variation of the tube wall temperature was, however small. They have reported a correlation for predicting Nu in fully developed swirl flows, based on their experimental data for water and ethylene glycol in electrically heated tubes. Additional data for UHF conditions have been reported for laminar flows of air (Watanabe et al., [16]), oil (Bandyopadhyay et al., [17]). Du Plessis [18], van Rooyen and Kroeger [19] observed that, for laminar swirl flow heat transfer in a smooth tube subjected to axially constant tube wall temperature (UWT), the heat transfer rate increases considerably for a moderate increase in pressure drop. Marner and Bergles [20–22] have reported experimental data for laminar flows of ethylene glycol and polybutene 20 with a twisted-tape ($y = 5.39$) in an isothermal tube. Manglik and Bergles [23–25] developed generalized Nusselt number and friction factor correlations. Manglik and Bergles [26] analyzed numerically the laminar flow heat transfer in a semicircular tube with uniform wall temperature defining the lower bound of heat transfer augmentation in circular tubes with twisted-strip inserts. Carlson et al. [27] observed the favorable effect of the twisted-tape inserts for augmenting the heat transfer rate in liquid metal reactor steam generators. Du Plessis and Kroger [28–30] have presented correlations for f and Nu based on their constant property numerical solution for laminar flows. Dasmahapatra and Raja Rao [31,32] have reported experimental data for non-Newtonian liquids. Sukhatme et al. [33,34] reported as high as 44 percent of total heat transfer due to the tape-fin effect for the laminar flow of a high Pr (about 700)

[1]On leave from the Department of Mechanical Engineering Bengal Engineering College (Deemed University) Howrah 711 103, West Bengal, India

Contributed by the Heat Transfer Division for publication in the JOURNAL OF HEAT TRANSFER. Manuscript received by the Heat Transfer Division June 29, 2000; revision received January 3, 2001. Associate Editor: T. Chu.

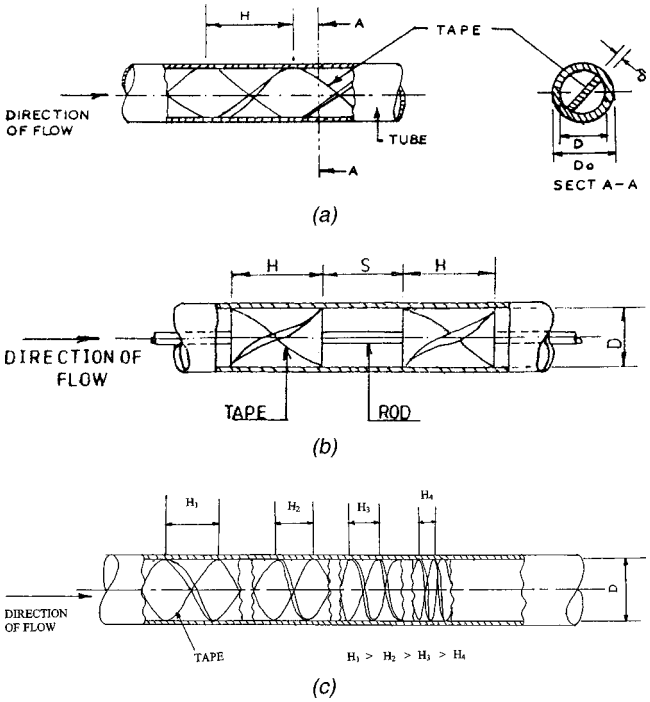

Fig. 1 (*a*) Layout of a circular tube containing a full-length twisted-tape; (*b*) layout of a circular tube containing regularly spaced twisted-tape elements; and (*c*) layout of a circular tube containing smoothly varying (gradually decreasing) pitch full-length twisted-tape.

fluid like servotherm medium oil (the trade name given to the particular variety of oil by the Indian Oil Corporation). They also observed that Nu correlation of Hong and Bergles [15] is applicable for Pr as high as 730.

Short-length twisted-tape occupies only a fraction of the entire length of the tube. Most of the early works were on turbulent flow, Colburn and King [9], Seymour [35], Kreith and Sonju [36], Klepper [37], Zozulya and Shkuratov [38], and Algifri and Bhardwaj [39]. Very recently Lokanath [40] reported experimental data on laminar flow of water through a horizontal tube under UHF and fitted with half-length twisted-tapes. He found that, from thermohydraulic point of view, half-length tapes perform better than the full-length tapes.

Saha et al. [41] have considered regularly spaced twisted-tape elements connected by thin circular rods as shown in Fig. 1(*b*). Date and Gaitande [42] developed correlations for predicting characteristics of laminar flow in a tube fitted with regularly spaced twisted-tape elements by solving momentum and energy equations by integral method taking semi-empirical approach.

Date and Saha [43] numerically solved the Navier-Stokes and energy equations in their three-dimensional parabolic form and predicted the friction and the heat transfer characteristics for laminar flow in a circular tube fitted with regularly spaced twisted-tape elements that are connected by thin circular rods.

Zozulya and Shkuratov [38] observed, for turbulent flow, a smooth decrease of swirling pitch (i.e., y), as the flow advances along the length of the tube, had no effect on heat transfer rate. No literature for such fin geometry on laminar flow was found. Figure 1(*c*) show the layout of a full-length twisted-tape with smoothly varying (decreasing) pitch inside a circular tube.

Monheit [44] evaluated the performance of tapes with surface modifications such as punched holes and plain slit edges vis-a-vis the plain tapes and it needs further study.

Al-Fahed and Chamra [45] found that the tight-tape fit gives a better performance over the loose-fit tape. Pinjala and Raja Rao [46] proposed a predictive correlation to fit well all the available laminar swirl flow heat transfer results in respect of pseudoplastic type of power law fluids under constant wall temperature condition. Shivkumar and Raja Rao [47] studied compound augmentation of laminar flow heat transfer to generalized power law fluids in spirally corrugated tubes by means of twisted-tape inserts. Isothermal and non-isothermal friction factors and mean Nusselt number for uniform wall temperature (UWT) heating and cooling of Servotherm oil ($Pr=195-375$) were experimentally determined by Agarwal and Raja Rao [48] for laminar twisted-tape-generated swirl flow in a circular tube.

The flow field in a rectangular duct behind a row of twisted-tape vortex generators was investigated by Hochdorfer et al. [49] by means of laser-Doppler anemometry (LDA) and a mass transfer photometric measuring method.

Aoyama et al. [50,51] studied the buoyancy effect on laminar heat transfer in a horizontal straight tube containing a twisted-tape swirler. They found that, when the buoyancy as well as the tape torsion is significant, the peripherally averaged Nusselt number oscillates along the tube axis in the thermally developing region and the turning pitch of the tape nearly coincides with the period of the oscillation.

Manglik and Bergles [52] made a numerical analysis of the fully developed laminar heat transfer in circular-segment ducts with uniform wall temperature and studied the two extremities of the fin effects of a straight-tape insert, i.e., 100 percent and zero fin efficiencies.

Klaczak [53] reported that short-length twisted-tape inserts perform better than their full-length counterpart when the flow is in the transition regime ($1300<Re<8000$).

In the present report, laminar flow results from experimental investigations carried out in a circular tube fitted with twisted-tapes are presented. For this, a closed loop experimental facility was made. Servotherm medium oil was used as the working fluid (giving high Pr range). Heat transfer data were obtained in an electrically heated test section giving axially and circumferentially constant wall heat flux (UHF). The phase angle (Φ) between successive tape elements is 0. The direction of twist imparted to each successive element is also the same. Both Φ and the direction of twist are parameters that do not fall under the purview of this paper.

The twisted tapes were of the following types: (*a*) short-length; (*b*) regularly spaced; and (*c*) smoothly decreasing pitch full-length.

Also, the fin effect of the tape elements is deliberately suppressed. Experiments were conducted over the following ranges of independent parameters:

Reynolds number	$45<Re<1150$
Twist ratio	$2.50\leq y\leq 10.00$
Prandtl number	$205<Pr<518$
Length of the tape	Full, half, one-third and one-fourth
Space ratio	$0\leq s\leq 5.00$

Experimental Setup

The investigations were carried out in a closed loop experimental facility as shown in Fig. 2. The loop consisted of:

1 An overhead tank (0.25 m^3 capacity located at an elevation of 2.75 meters)
2 A calming section (1.8 m long, 13 mm i.d., 20 mm o.d., PVC tube)
3 The test section (details follow)
4 An insulated mixing section i.e. exit section (13 mm i.d., 20 mm o.d., 350 mm long PVC tube)
5 A riser section with 150 mm high kink
6 A heat exchanger
7 A gear pump (1 HP)

The twisted tapes were made of 0.5 mm thick stainless steel strips, the width of the strip being 1 mm less than the inside

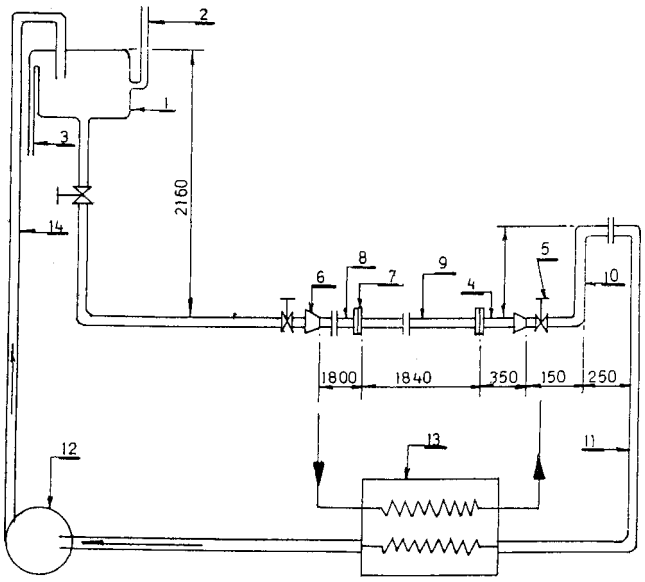

DIMENSIONS ARE IN MM

1. OVERGEAD TANK
2. LEVEL INDICATOR
3. OVER FLOW TO SUMP
4. EXIT SECTION
5. NEEDLE VALVE
6. REDUCER
7. FLANGES
8. CALMING SECTION
9. TEST SECTION
10. RISER
11. FLOW OUTLET TO H.E.
12. GEAR PUMP
13. HEAT EXCHANGER (H.E.)
14. SUPPLY TO TANK

NOT TO SCALE

Fig. 2 The experimental setup

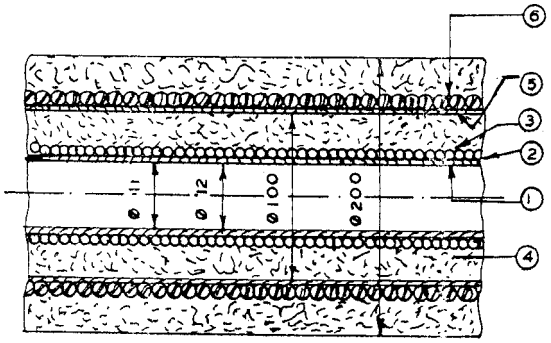

1- TEST TUBE
2-FIBERGLASS TAPE INSULATION
3-FIBERGLASS INSULATED NICHROME HEATER WIRE
4- GLASSWOOL BLANKET INSULATION
5-THIN G.I. CYLINDER
6-ASBESTOS ROPE

Fig. 3 Heat transfer test section

diameter of the test section tube. This situation closely resembles real applications where removable tapes are inserted in existing heat exchanger tubes. Twisted tapes were made separately for pressure drop tests and heat transfer tests because of different diameters of the test section. The strips were twisted on a lathe by manual rotation of the chuck. Twisted strips were heated periodically by flame to relax the stresses to prevent them from buckling and untwisting when they were removed from the lathe. Twisted tapes for heat transfer tests were covered with insulted tape to suppress the fin effect since the tape-fin effect was not studied. However, the twisted-tape would not be insulated in a real situation. Pieces of stainless steel rods of 3-mm diameter were used to make tape-rod assembly. The ends of the rods were slotted to accept the twisted-tape elements. Twisted-tape elements were spot welded to the ends of the rods.

A PVC tube of 1.85-m long, 13-mm i.d. and 20 mm o.d. was used as test section for the pressure drop tests. The pressure taps were made of 30-mm long, 3-mm i.d., 4.5-mm o.d. acrylic tube. Threads were cut on one end of the taps and drilled holes on the test section were threaded internally. The threaded portion of the taps was covered with Teflon tape before inserting them into the tapped hole to prevent leakage. Additionally, using Araldite ensured the rigidity of the taps. Flexible PVC tubing to a manometer connected the pressure taps at either end of the test section. Pressure drop was measured by means of vertical *U*-tube manometer with dibutyl phthalate (specific gravity 1.047) and mercury as the manometric fluid for lower Re and higher Re, respectively. This ensured reasonably good accuracy by producing large-scale reading with dibutyl phthalate for lower Re.

The heat transfer test section is shown in Fig. 3. It consisted of 1.84-m long, 11-mm i.d., 12-mm o.d. stainless steel (304 SS) tube. The tube was uniformly heated by passing alternating current from a stabilized three-phase source through 30 SWG fibre glass insulated nichrome wire having 16 Ω/m resistance wound around the tube. The electrical winding was made in such a way that current passed in both directions to cancel electro-magnetic field effects. Electrical resistance was measured in several sections to ensure uniform heat flux. The heater was made in three sections, each section having four parallel heaters. Autotransformers were used to regulate the heat flux supplied to the test section. To measure the outside wall temperature of the tube, 30 SWG copper-constantan thermocouples were used. The thermocouples were silver soldered and were first taken through the circumferential grooves and then radially through the heater wire turns and the insulation put on the test section. Eleven thermocouples were provided on the outside wall of the tube. The first five were placed at 15 mm, 115 mm, 225 mm, 350 mm, and 430 mm from the point where the heating started and the remaining six were placed at 525 mm, 565 mm, 627 mm, 688 mm, 738 mm, and 788 mm from the downstream end. Using polytetrafluoroethylene spacers positioned between flanges minimized axial conduction losses. Winding asbestos rope and putting a glasswool blanket of 50 mm thickness around the asbestos rope minimized the radial heat losses. The asbestos rope was wound on a GI (Galvanized Iron) cylinder (split in two halves) to protect the electrical connections. The space between the heater wire and the GI cylinder was also filled with glasswool. A precision digital multimeter measured the thermocouple output. The power input was calculated from the measured voltage and the resistance. The current was also measured to provide a crosscheck. Fluid bulk temperature measurements were made at the inlet and the exit of the test section. Saha et al. [41] and Hong and Bergles [15] have observed that the circumferential temperature variation for the swirl is very small. Accordingly, no circumferential variation of temperature was measured in the present investigation.

Twelve sets of experimental data have been generated for short-length twisted tapes with $y=10$, 7.5, 5, and 2.5. The lengths of the tapes being half, one-third and one-fourth of the test section length.

Eight sets of data have been generated with regularly spaced twisted-tape elements; for $y=5$, 2.5; $s=5$, 2.5, and $m=2$, 3.

The twisted-tapes for smooth swirling pitch were having four uniform pitches (each pitch extending up to one-fourth length of the test section), the highest pitch (y_1) being at the upstream end and the lowest pitch (y_4) being at the downstream end. The pitches were such that $y_1/y_2=y_2/y_3=y_3/y_4$. Twisted tapes with $y_1/y_4=2$, 3, and 4 were used. $y_4=2.5$ was always used in the last quarter of the tape. Thus $y_1=5$, 7.5, and 10 were used $y_2=3.97$, 5.2, and 6.3 and $y_3=3.15$, 3.6, and 3.97 were used. Y_{av}, the average twist ratio were 3.65, 4.6, and 5.69.

Operating Procedure and Data Reduction

Pressure Drop Tests. The pressure drop tests were carried out in the PVC tube. The friction factor was defined as

$$f=\tfrac{1}{2}[(\Delta P_z)(\rho U^2)](D/z), \tag{1}$$

where

$$U=\dot{m}/(\rho A_c)\ \ldots \tag{2}$$

and ΔP_z is the pressure drop over a length z.

Before the pressure drop measurements were taken, the test section was freed of air bubbles by venting them through the riser section at the end of the test section. The oil flow was taken from the overhead tank where a constant level was maintained. Typically 15 minutes were required for settling of flow after each change of mass flow rate. In addition to controlling the mass flow rate, the fluid was heated as necessary to obtain a reasonable range of laminar Reynolds number. The manometer measured pressure drop and mass flow rate was measured by collecting the fluid for a certain period and a stopwatch. Uncertainty in the mass flow rate measurement was within ± 1 percent. Mass flow rates as measured by weighing were within ± 0.5 percent of that measured by a rotameter. However, rotameter was not used since the available rotameter could not cover the entire range of the mass flow rate. Pressure drop data were obtained under isothermal conditions.

Heat Transfer Tests. The heat transfer tests were performed in the stainless steel tube. Servotherm medium oil provided substantial variation in Pr. The length averaged Nu was defined as the following:

$$\mathrm{Nu}=\frac{hD}{k}=\frac{Q}{\pi DL}\left[\int_O^L \frac{dz}{T_{wz}-T_{bz}}\right]\left(\frac{D}{k}\right), \tag{3}$$

where,

$$Q=V^2/R=\dot{m}C_p(T_{bo}-T_{bi})\ \ldots \tag{4}$$

Equation (3) was numerically integrated by Simpson's rule.

Q was measured by two methods as shown in Eq. (4). The arithmetic mean of two values was taken. Data for variation by more than 5 percent in two methods were discarded. The wall temperature T_{wz} at any z in Eq. (3) was measured directly, whereas T_{bz} was calculated by interpolation assuming linear variation of fluid bulk temperature along the length of the tube. A thermal steady state was generally reached in 60–90 minutes. The minimum and the maximum changes in the fluid viscosity from the inlet to the outlet section were 8 percent and 26 percent of the value at the inlet, respectively. Hence all fluid properties were calculated at $(T_{\mathrm{bi}}+T_{\mathrm{bo}})/2$ and functional relationships of properties with temperature available in Bandyopadhyay et al. [17] were used for this purpose. No significant improvement is expected, Hong and Bergles [15], by using the film temperature. The tube wall temperature drop was calculated by considering the steady state, one-dimensional radial heat conduction equation and this drop was applied uniformly along the length of the tube. The wall temperature and the bulk temperature were combined with the heat flux to give the axially local heat transfer coefficient and the Nusselt number. The axially averaged Nusselt number was obtained by Simpson's rule of numerical integration. The flow was hydrodynamically fully developed and with uniform temperature profile at the entrance of the test section. The inside tube diameter rather than the hydraulic diameter was used in defining Nu and Re for performance analysis and easy comparison. Since the tape inhibits free convection, the Grashof number (Gr) or Rayleigh number, important parameters in plain tube laminar flow, are unimportant in the present swirl flow; it was found that $\mathrm{Gr}/\mathrm{Re}^2<1$. Since $\mathrm{Gr}/\mathrm{Re}^2$ was less than 1 for all data, the natural convection was thought as unimportant. It this context it may be noted that the test tube diameter for Bandyopadhyay et al. [17] was double the present test section tube diameter. It is for this, Bandyopadhyay et al. [17] found natural convection important.

An uncertainty analysis conducted along the lines suggested by Kline and McClintock [54] showed that the uncertainties involved in the friction factors were within ± 10 percent whereas those involved in the estimation of Nusselt number and Reynolds number were within ± 7 percent and ± 3 percent, respectively.

Results and Discussion

Tests Conducted. The present experimental program has been carried out in two parts. Data have been generated for the following cases:

1 Friction factor
2 Nusselt number

Before the experimental data were generated, carrying out confirmatory tests validated the test setup.

Figure 4 shows the comparison of experimental friction factor data with the correlations for the full-length twisted tape ($y=5$, $s=0$), Shah and London [55]. The correlations predict the experimental data within ± 17 percent. The correlations of Manglik and Bergles [24] predict the present experimental data within ± 13 percent.

Figure 5 shows the comparison of the experimental Nusselt number data with the correlation for full-length twisted- tape ($y=5$, $s=0$) available in Hong and Bergles [15]. The correlations predict the experimental data within ± 18 percent. Correlations of Hong and Bergles [15] predict their own experimental data within ± 20 percent in the range $84<\mathrm{Pr}<192$ and later on Sukhatme et al. [33,34] reported that the correlation predicts data reasonably well upto $\mathrm{Pr}=730$. In the present investigation, for all specific

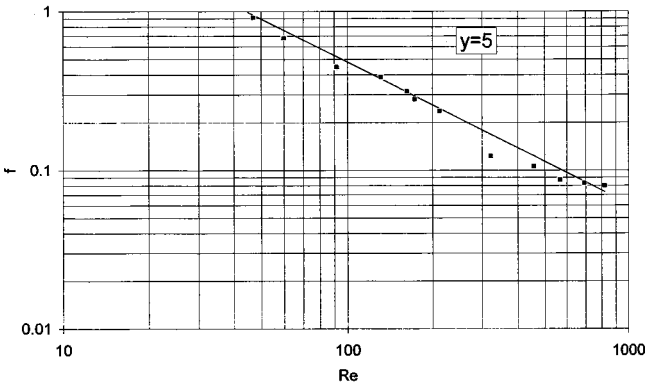

Fig. 4 Confirmatory test for pressure drop measurements

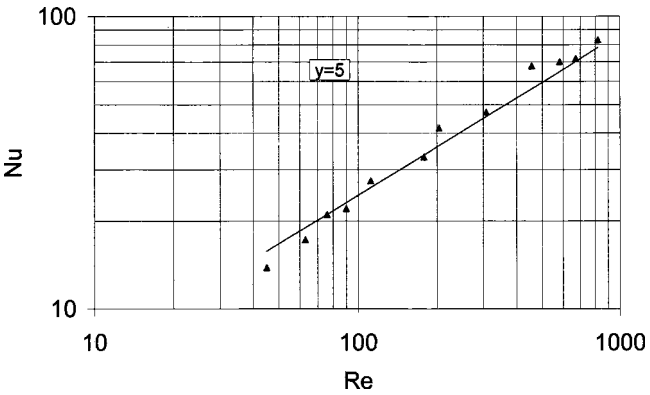

Fig. 5 Confirmatory test for heat transfer measurements

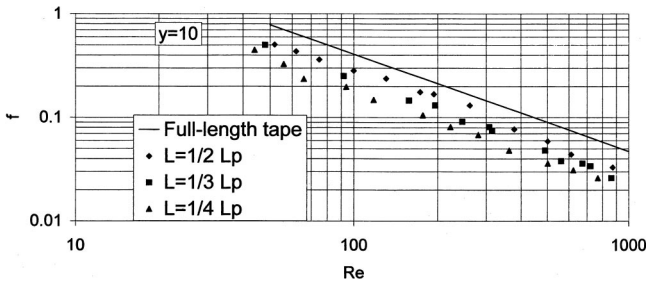

Fig. 6 Variation of friction factor with Reynolds Number for short-length twisted-tape

cases, Pr varied within the range $205<Pr<518$.
Present experimental data are reported in Part A, Part B, and Part C.

Part A: Data for Short-Length Twisted—Tapes. Only isothermal friction factor data are being reported here, as many other investigators have done. In reality, the pressure drop is affected by the heating conditions. For swirl flow, however, the correction factor for heated friction factor is much smaller compared to that for straight flow through a plain tube, Lopina and Bergles [8]. Figures 6–9 show the variation for friction factor with Re for $y=10$, 7.5, 5.0, and 2.5. The experimental data for short-length twisted tapes are compared to the correlation, Shah and London [55] for full-length twisted-tape. Friction factor reduces, as expected, for all y values. For half-length tape and $y=10$, 28 percent–30 percent reduction; for $y=7.5$, 27 percent–33 percent reduction; for $y=5$, 24 percent reduction; for $y=2.5$, 20 percent–23 percent reduction has been observed. Fore one-third length tape and $y=10$, 40 percent–50 percent reduction; for $y=7.5$, 24 percent–41 percent reduction; for $y=5$, 35 percent–55 percent reduction and for $y=2.5$, 17 percent–55 percent reduction has been observed. For one-fourth length tape and $y=10$, 50 percent–57 percent reduction; for $y=7.5$, 43 percent–45 percent reduction; for $y=5$, 42 percent–50 percent reduction, for $y=2.5$, 47 percent–50 percent reduction has been observed.

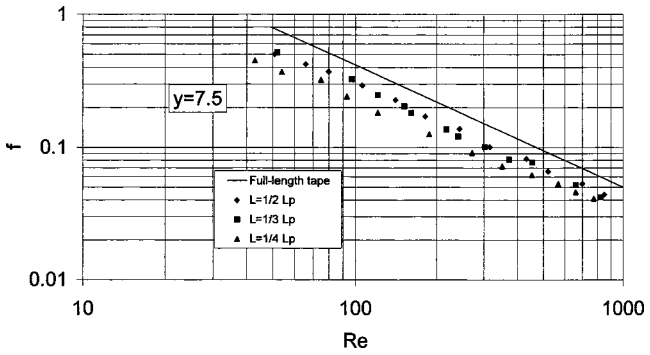

Fig. 7 Variation of friction factor with Reynolds Number for short-length twisted-tape

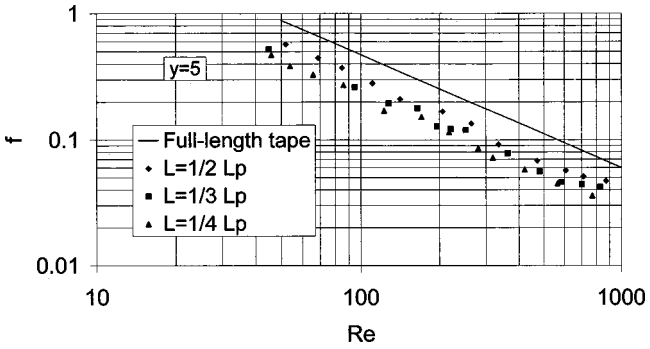

Fig. 8 Variation of friction factor with Reynolds Number for short-length twisted-tape

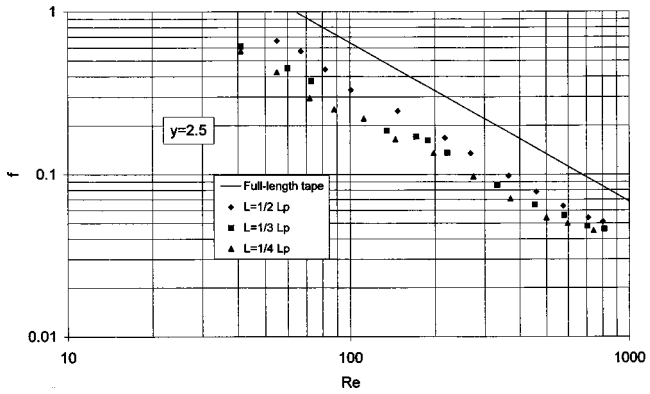

Fig. 9 Variation of friction factor with Reynolds Number for short-length twisted-tape

The swirl decays downstream of the tape and perhaps the straight flow ensues. The smaller the tape length, the larger the reduction in friction factor compared to the full-length tape. The reduction in friction factor increases with the increase in Reynolds number. For half-length tape, the lower the twist ratio, the lower the reduction in friction factor indicating the persistence of the intensity of swirl for a longer length of the tube downstream of the tape. This effect is not distinctly observed for one-third length and one-fourth length tapes due to too small length of the tapes. In the later cases swirl loses its intensity and the straight flow establishes quickly and remains so for a larger part of the tube downstream of the tape.

Figures 10–13 show the variation of Nu with Re for $y=10$, 7.5, 5.0, and 2.5. The experimental data are compared to the correlation, Hong and Bergles [15] for full-length twisted tape. The Hong and Bergles' correlation, which gives the fully developed value for full-length tape, was used since the value from the correlation would not be much different from the axially averaged value in view of small development length for twisted-tape generated swirl flow, Date [56], Hong and Bergles [15]. Nu also reduces for all y values. For half-length tape and $y=10$, 20 percent–36 percent reduction; for $y=7.5$, 26 percent–31 percent reduction; for $y=5$, 14 percent reduction; for $y=2.5$, 7 percent reduction has been observed. For one-third length tape and $y=10$, 35 percent–42 percent reduction, for $y=7.5$, 36 percent–40 percent

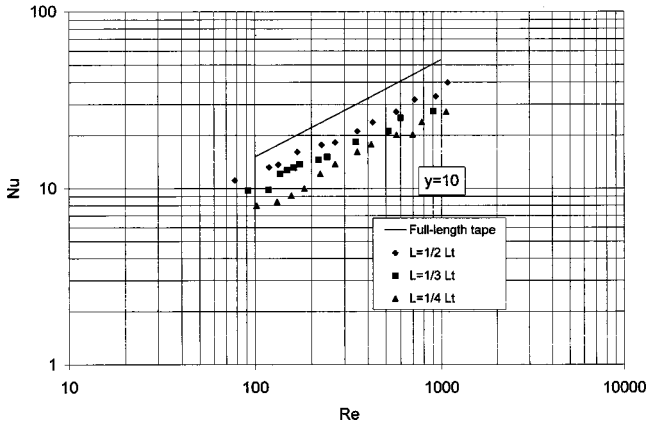

Fig. 10 Variation of Nusselt Number with Reynolds Number for short-length twisted-tape

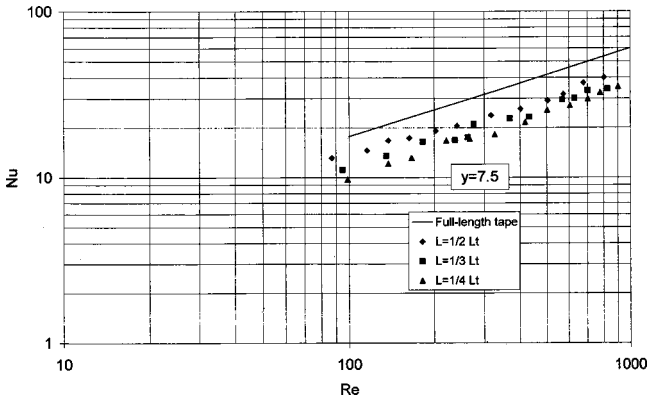

Fig. 11 Variation of Nusselt Number with Reynolds Number for short-length twisted-tape

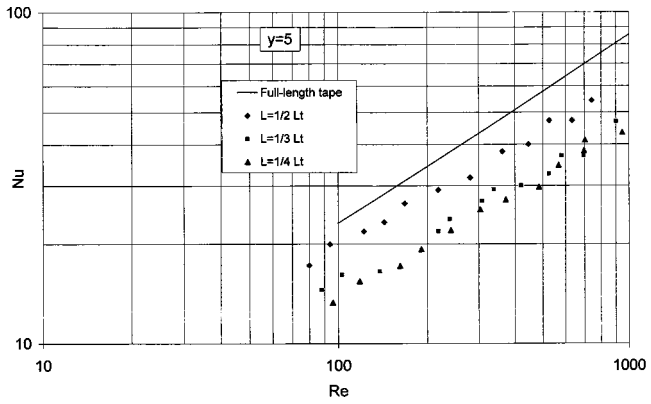

Fig. 12 Variation of Nusselt Number with Reynolds Number for short-length twisted-tape

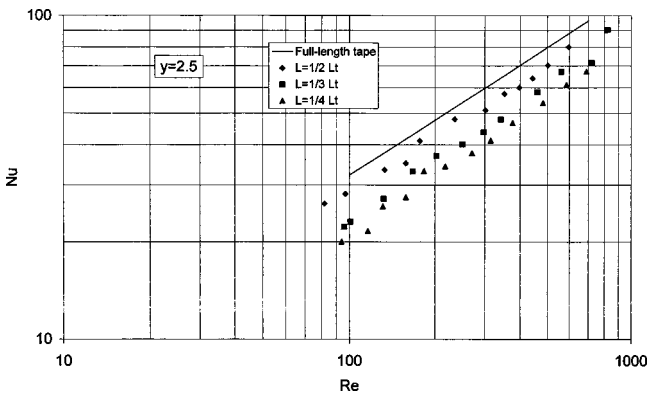

Fig. 13 Variation of Nusselt Number with Reynolds Number for short-length twisted-tape

reduction, for $y=5.0$, 33 percent reduction for $y=2.5$, 12 percent–20 percent reduction has been observed. For one-fourth length tape and $y=10$, 47 percent–50 percent reduction; for $y=7.5$, 42 percent reduction, for $y=5$, 30 percent reduction; for $y=2.5$, 36 percent reduction has been observed. The decreasing trend shown in Nusselt number for short-length tapes is similar to that shown in case of friction factor. The reduction in Nusselt number increases with the increase in Reynolds number, especially for lower twists. In contrast to friction factor results, for all tape lengths, the lower the twist ratio the lower the reduction in Nusselt number indicating the persistence of the swirl and the flatter temperature profiles for a considerable length of the tube downstream of the tape for tight twists.

Therefore, it can be concluded that the swirl loses its intensity downstream of the tape and friction factor and Nusselt number are reduced compared to the full-length tape.

Performance Evaluation

Performance of the present fin geometry has been evaluated on the basis of constant pumping power, Criterion 1 and constant heat duty, Criterion 2 as suggested by Bergles et al. [57].

Criterion 1. The performance ratio, R_1 for this criterion is given by $R_1=(\mathrm{Nu}_{\mathrm{slt}}/\mathrm{Nu}_{\mathrm{flt}})$ where the subscripts ''slt'' and ''flt'' refer to short-length tape and full-length tape. $\mathrm{Nu}_{\mathrm{flt}}$ at a given Reynolds number, $\mathrm{Re}_{\mathrm{flt}}$ is obtained from the correlation of Hong and Bergles [15] for full-length tapes. $\mathrm{Nu}_{\mathrm{slt}}$ for short-length tapes is taken at $\mathrm{Re}_{\mathrm{slt}}$ calculated from the constant pumping power consideration as: $\mathrm{Re}_{\mathrm{slt}}=[(f_{\mathrm{flt}}/f_{\mathrm{slt}})(A_{c,\mathrm{flt}}/A_{c,\mathrm{slt}})(\mathrm{Re}_{\mathrm{flt}})^3]^{1/3}$, where $A_{c,\mathrm{slt}}=[(\pi D^2-4\delta D)L+\pi D^2(L_T-L)]/4L_T$, and $A_{c,\mathrm{flt}}=\pi/4D^2-\delta D$ Subscript ''T'' refers to the test section. f_{slt} versus $\mathrm{Re}_{\mathrm{slt}}$ curves were consulted and trial and error method was adopted.

Criterion 2. The performance ratio, R_2 for this criterion is given by:

$$R_2=\frac{(f\mathrm{Re}^3A_c)_{\mathrm{slt}}}{(f\mathrm{Re}^3A_c)_{\mathrm{flt}}}.$$

For a given Reynolds number, $\mathrm{Re}_{\mathrm{flt}}$, the Nusselt number, $\mathrm{Nu}_{\mathrm{flt}}$ is obtained from the correlation. The Reynolds number, $\mathrm{Re}_{\mathrm{slt}}$ corresponding to $\mathrm{Nu}_{\mathrm{slt}}=\mathrm{Nu}_{\mathrm{flt}}$ is obtained from the curves for short-length tapes. f_{slt} corresponding to $\mathrm{Re}_{\mathrm{slt}}$ is obtained from the curves for short-length tapes.

It has been observed that, on the basis of constant pumping power, maximum 10 percent, 21 percent, and 22 percent improvement in the performance of half length, one-third length, and one-fourth length twisted tapes, respectively is possible when $y\leqslant 5$. On the basis of constant heat duty, about 15 percent, 28 percent, and 30 percent reduction in pumping power is possible for short-length (half-length, one-third length, and one-fourth length) twisted tapes when $y\leqslant 5$. Therefore, it is observed that shortening the tape-length below 33 percent of the tube length is of no practical importance.

Practical Significance

Full-length twisted tapes are used to develop new compact heat exchangers and to improve the performance of existing heat exchangers. The present experimental findings show that short-length twisted tapes (up to 33 percent of the tube length) can substantially reduce the pumping power requirements of existing heat exchangers (having full-length twisted tapes) without a reduction in heat duty. The heat transfer rating of an existing compact heat exchanger can also be improved without an increase in pumping power.

Part B: Data for Regularly Space Twisted-Tape Elements. Figures 14–17 show the variation of friction factor with Reynolds number for varied y and s and for each case with $m=2$ and $m=3$. The gap length giving $s>5$ is not enough to maintain the swirl intensity to the sufficient extent downstream of the tape. The swirl decays fast and subsequently the straight flow ensues in the gap before the fluid finds the next tape element on its way for the swirl to build up again. This yields lower Nu characteristic of the laminar flow. Therefore, s was restricted to less than or equal to five only. The experimental data are compared to the correlation of regularly spaced twisted-tape elements with single twist available in Saha et al. [41]. It is observed from the figures that f decreases for $m=2$ compared to that for $m=1$ for all y and s. For $y=5$ and $s=5$, the reduction is 20 percent–23 percent; for $y=5$

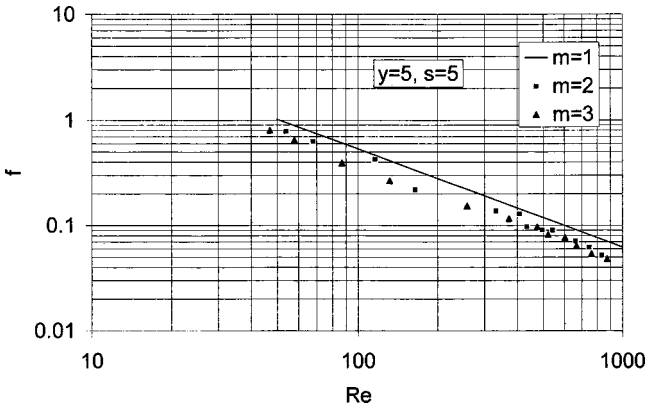

Fig. 14 Variation of friction factor with Reynolds Number for regularly spaced twisted-tape elements

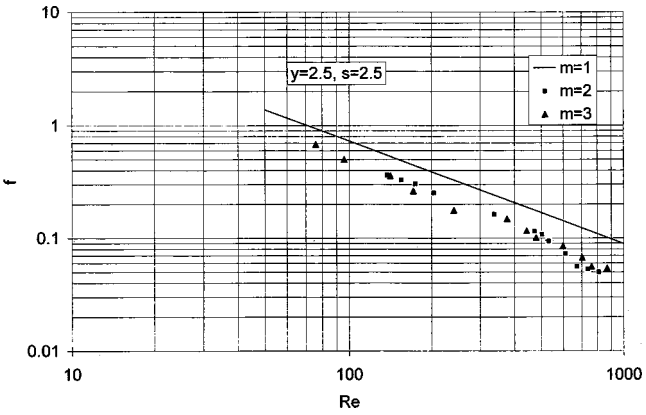

Fig. 17 Variation of friction factor with Reynolds Number for regularly spaced twisted-tape elements

and $s=2.5$, the reduction is 30 percent–35 percent, for $y=2.5$ and $s=5$, the reduction is 14 percent–47 percent and for $y=2.5$ and $s=2.5$, the reduction is 29 percent–39 percent. Saha et al. [41] have observed that some particular combinations of y and s (here $y=2.5$ and $s=5.0$) do show striking effect of Reynolds number. In fact, each combination of y and s represents particular fin geometry, which is very different from the others. The reduction in friction factor increases as the Reynolds number increases. This result compares extremely well with the prediction of Date and Saha [43], which showed a 30 percent reduction in friction factor for $m=2$ from that for $m=1$ at Re=900, $y=3.3$, and $s=2.5$. Friction factor, however, does not reduce much (<8 percent) for $m=3$ from $m=2$ for any combination of y and s and at any Re. This observation differs from the prediction which showed 22 percent reduction in friction factor from $m=2$ to $m=3$ for $y=3.3$, $s=2.5$, and Re=900. It can be conjectured that this difference is because of tape thickness, which was ignored during prediction. The tape thickness increases friction factor of the order of 5 percent to 8 percent and the effect of tape thickness is more prevalent for $m=3$ than for $m=2$ because of increased amount of the surface of the tape. The reason for decrease in friction factor from $m=1$ to $m=2$ is that for $m=1$, the pressure loss associated with the momentum change that occurs when two nonaxisymmetric velocity profiles issuing from the twisted-tape module mix in the decaying swirl section in the space module is much greater than the pressure loss that would have been encountered for $m=2$. This can be appreciated from the fact that the number of tape modules for $m=2$ is less than that for $m=1$. Also, the leading edge losses associated with twisted-tape section can be considerable. Since friction factors for decaying swirls in the entrance length are quite large, these experimental results can be expected. However, for $m=3$, additional tape-surface encountered for frictional pressure drop is comparable with the decrease in pressure drop due to less mixing phenomena in the decaying swirl section in the space module. Therefore, friction factor does not decrease much for $m=3$ compared to that for $m=2$.

Figures 18–21 show the variation of Nu with Re for $y=5$ and $s=5$, $y=5$ and $s=2.5$, $y=2.5$ and $s=5$, $y=2.5$ and $s=2.5$. The experimental data are compared with the correlation of regularly spaced twisted-tape elements with single twist available in Saha et al. [41]. It is seen from the figures that Nusselt number decreases for $m=2$ compared to that for $m=1$ for all twist ratio and space ratio. For $y=5$ and $s=5$, the reduction is 23 percent–33

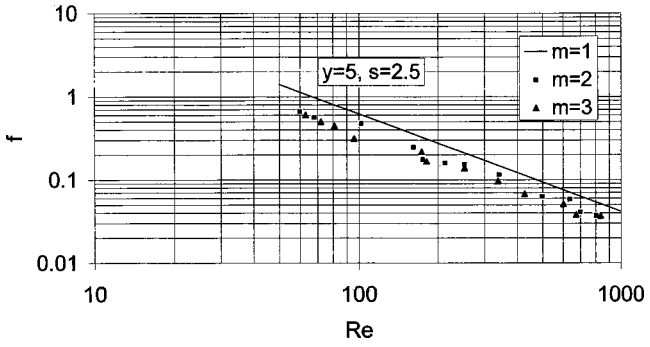

Fig. 15 Variation of friction factor with Reynolds Number for regularly spaced twisted-tape elements

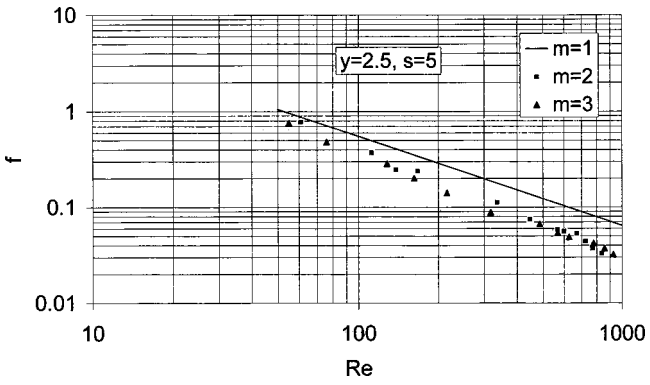

Fig. 16 Variation of friction factor with Reynolds Number for regularly spaced twisted-tape elements

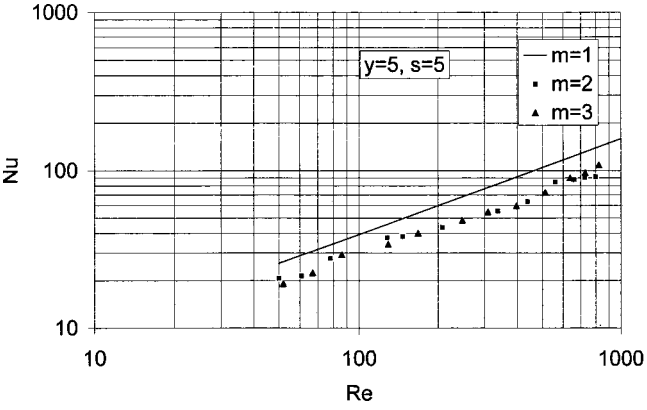

Fig. 18 Variation of Nusselt Number with Reynolds Number for regularly spaced twisted-tape elements

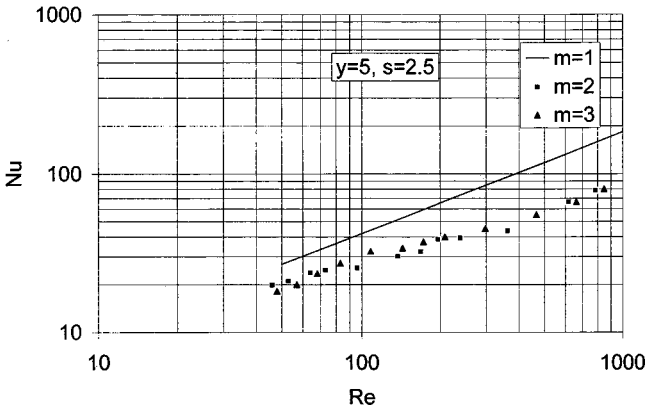

Fig. 19 Variation of Nusselt Number with Reynolds Number for regularly spaced twisted-tape elements

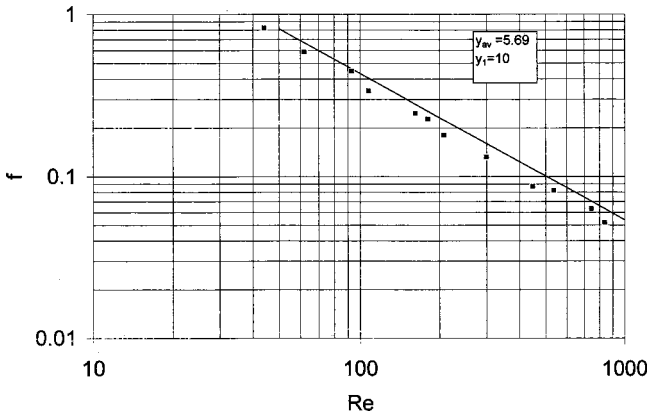

Fig. 22 Variation of friction factor with Reynolds Number for smoothly varying pitch twisted-tape

percent; for $y=5$ and $s=2.5$, the reduction is 25 percent–50 percent; for $y=2.5$ and $s=5$, the reduction is 23 percent–47 percent; and for $y=2.5$ and $s=2.5$, the reduction is 11 percent–47 percent. Reduction in the Nusselt number generally increases as the Reynolds number increases. These experimental findings are in contrast with the numerical prediction of Date and Saha [43] where a marginal increase of Nusselt number from $m=1$ to $m=2$ with $\mathrm{Pr}=50$ was observed. It was stated by Date and Saha [43] that the predicted values at higher Pr must be considered tentative because they were not checked with more refined grids during numerical analysis, which was necessary to resolve the thin boundary layers. The predicted Nusselt number is almost proportional to $\mathrm{Pr}^{0.45}$, which is also at variance with the experiments. Hong and Bergles [15] also observed this less pronounced effect of Pr on Nusselt number. However, the present findings for large Pr shows the similar trend observed experimentally in case of $4.5<\mathrm{Pr}<5.5$, Saha and Chakraborty [58]. Date and Saha [43] observed a considerable reduction in local Nusselt number at the inlet to the tape module and a sudden rise in local Nusselt number at the inlet to the space module. Because the fluid bulk mean temperature increases linearly axially, the peculiar variations in local Nusselt number are associated with the local values of tube wall temperature. This is explained as follows:

At the inlet to the space module the fluid jumps the connecting rod due to swirl. This, coupled with the tendency of the fluid to attain circumferential symmetry gives high velocity near the tube wall reducing wall temperature suddenly giving high local Nusselt number. This gives higher axially averaged Nusselt number than that in case of straight annular flow. At the inlet to the tape module, the flow enters with a weak swirl and accelerates rapidly near the axis and the fluid jumps from the rod suppressing the swirl. This reduces flow velocities near the tube wall causing higher tube wall temperature and lower local Nusselt number. Thus axially averaged Nusselt number in the tape module is substantially less than that in case of full-length tape. However, it has also been observed that the Nusselt number in the space module is higher than that in the tape module. Thus in case of $m=2$ we get lower axially averaged Nusselt number compared to $m=1$ because of increased length of the tape elements. But for $m=3$, swirl does

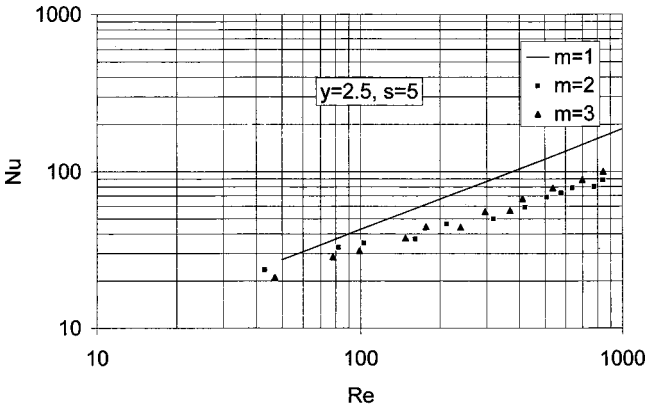

Fig. 20 Variation of Nusselt Number with Reynolds Number for regularly spaced twisted-tape elements

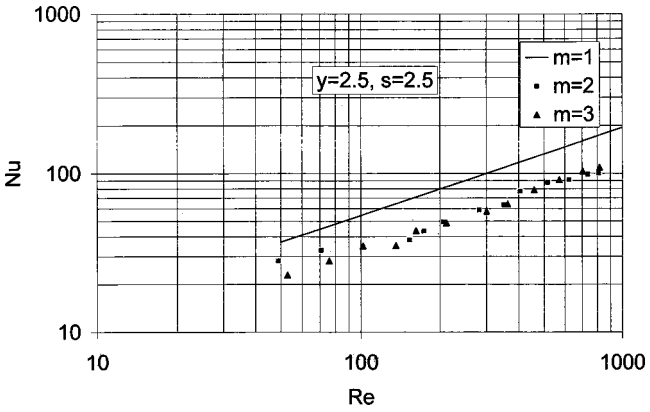

Fig. 21 Variation of Nusselt Number with Reynolds Number for regularly spaced twisted-tape elements

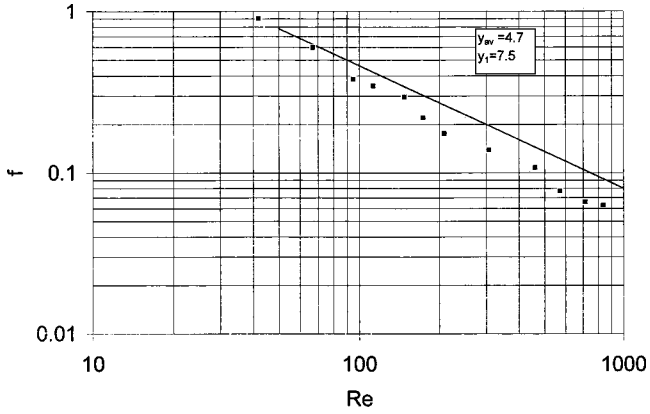

Fig. 23 Variation of friction factor with Reynolds Number for smoothly varying pitch twisted-tape

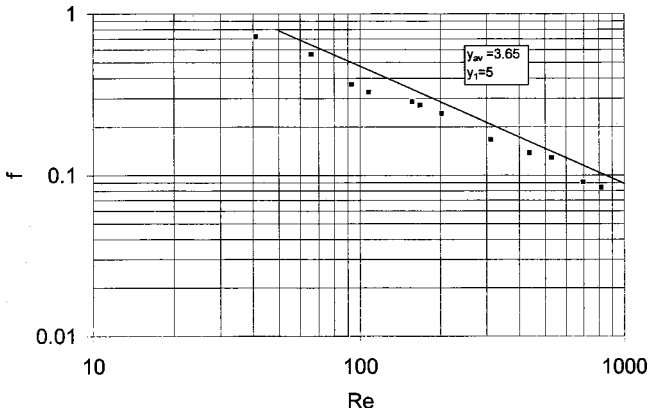

Fig. 24 Variation of friction factor with Reynolds Number for smoothly varying pitch twisted-tape

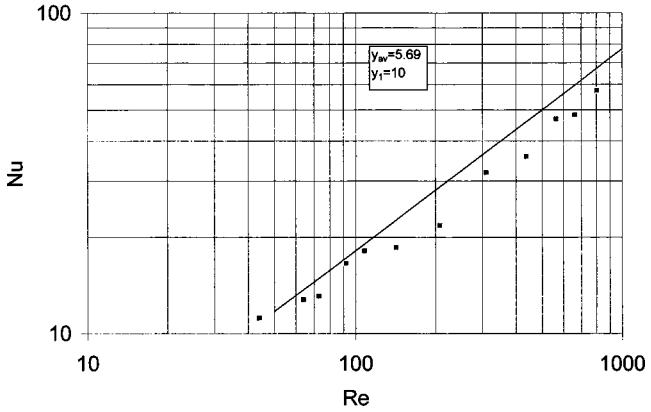

Fig. 25 Variation of Nusselt Number with Reynolds Number for smoothly varying pitch twisted-tape

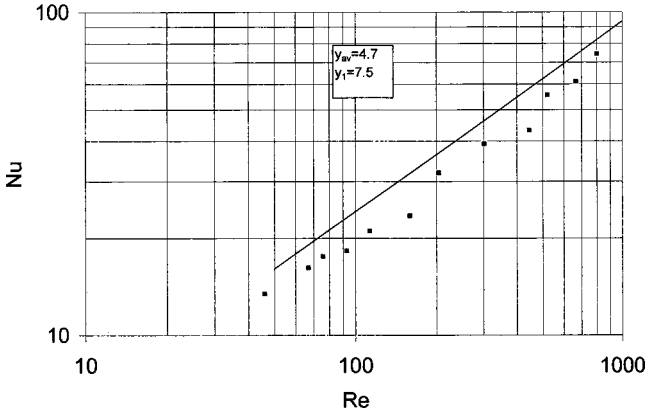

Fig. 26 Variation of Nusselt Number with Reynolds Number for smoothly varying pitch twisted-tape

not decay substantially and the swirl subsists further downstream of the tape module and the velocity and temperature profiles do not become shallower to give the still lower axially averaged Nusselt number.

Part C: Data for Smoothly Varying (Gradually Decreasing) Pitch Twisted Tapes. As mentioned earlier, this twisted-tape configuration is the full-length twisted-tape extending the whole length of the test section. The twisted-tape comprises of four

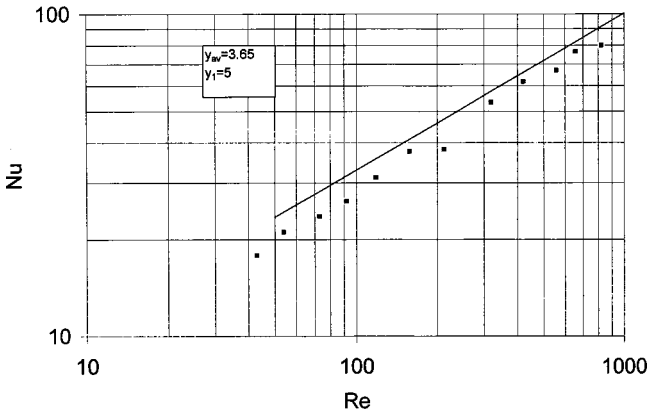

Fig. 27 Variation of Nusselt Number with Reynolds Number for smoothly varying pitch twisted-tape

equal-length pieces, each piece being welded to the adjacent one. The upstream end piece has the highest pitch and the downstream end piece has the lowest pitch.

The friction factor and the Nusselt number of the present configuration were compared to the available correlations; the base line being that evaluated at the average pitch, Fig. 22–27. As expected, f and Nu are lower for twisted-tapes with smooth swirl having the average pitch same as that of the uniform pitch (throughout) twisted-tape. On an average approximately 15 percent reduction in both friction factor and Nusselt number have been observed. The reason for reduction is that the swirl does not reach its final intensity until the flow advances to the final pitch and the downstream part of the tape with the lowest pitch plays the key role in the swirl development. The performance analysis was done following Bergles et al. [57]. This has shown that, on the basis of constant pumping power and constant heat duty, full-length twisted-tapes with gradually decreasing pitch (present fin geometry) perform worse than the full-length twisted-tapes with uniform pitch (throughout), the average pitch of the former geometry being same as that of latter.

Conclusions

Experimental data on large Prandtl number ($205 < \mathrm{Pr} < 518$) twisted-tape-generated laminar swirl flow friction factor and Nusselt number have been presented for the case of a circular tube subjected to uniform wall heat flux. Decaying swirl flow was generated by short-length twisted-tape insert. Reduction in Nusselt number for short-length twisted-tape is much less than the reduction in friction factor compared to full-length twisted-tape for tighter twists ($y \leqslant 5$). On the basis of constant pumping power and constant heat duty, short-length twisted-tapes (up to 33 percent length of the tube) is found to perform better than the full-length twisted-tapes.

It has also been observed that, for regularly spaced twisted-tape elements, there is a 14 percent–47 percent reduction in isothermal friction factor accompanied by comparable reduction in axially averaged Nusselt number for number of twist equal to two in the tape module compared to the case of single twist in the tape module. Number of twists equal to three in the tape module does not give much different thermohydraulic performance from the case with number of twists equal to two in the tape module. If reducing pumping power is of prime importance even at the cost of thermal performance, then number of twists equal to two in the tape module may be recommended.

The performance analysis has shown that the twisted-tapes with smoothly varying (gradually decreasing) pitch perform worse than the twisted-tapes with uniform pitch same as that of the average pitch of the former.

Nomenclature

A_c = flow cross-sectional area, m^2
C_p = constant pressure specific heat, J/(KgK)
D = internal diameter of the test tube, mm
D_h = hydraulic diameter of the test tube, mm
f = fully developed friction factor based on internal diameter of the tube, dimensionless
H = pitch for 180 deg rotation of twisted-tape, mm
h = heat transfer coefficient, $W/(m^2K)$
k = fluid thermal conductivity, W/(mK)
L = length of the test section, m
m = number of twists in the tape module, dimensionless
$\dot{m}$ = mass flow rate of fluid, Kg/s
Nu = axially averaged Nusselt number based on internal diameter of the tube, dimensionless
ΔP_z = pressure drop over a length z, N/m^2
Pr = fluid Prandtl number, dimensionless
Q = heat input to the test section, W
R = resistance of the heater element, Ω
s = space ratio ($=$gap length/D), dimensionless
Re = Reynolds number based on internal diameter of the tube, dimensionless
T_{bi} = inlet bulk mean temperature of the fluid, °C
T_{bo} = outlet bulk mean temperature of the fluid, °C
T_{bz} = local bulk mean temperature of the fluid, °C
T_{wz} = local tube wall temperature, °C
U = fluid mean axial velocity, m/s
y = twist ratio ($=H/D$), dimensionless
V = voltage output from the autostat, V
Z = axial length, m

Greek Symbols

δ = tape thickness, mm
μ = fluid dynamic viscosity, Kg/ms
ρ = density of the fluid, Kg/m^3

References

[1] Whitham, J. M., 1896, ''The Effects of Retarders in Fire Tubes of Steam Boilers,'' Street Railway Journal, **12**, No. 6, p. 374.
[2] Royds, R., 1921, *Heat Transmission by Radiation, Conduction and Convection*, Constable and Camp. Ltd., London, 1st ed., pp. 190–201.
[3] Cresswell, J. D., 1958, ''Mechanics of Swirling Turbulent Flow,'' M. S. thesis, Lehigh University, Bethlehem, PA.
[4] Kreith, F., and Margolis, D., 1959, ''Heat Transfer and Friction in Turbulent Vortex Flow,'' Appl. Sci. Res., Sect. A, **8**, No. 6, pp. 457–473.
[5] Thorsen, R., and Landis, F., 1968, ''Friction and Heat Transfer Characteristics in Turbulent Swirl Flow Subjected to Large Transverse Temperature Gradients,'' ASME J. Heat Transfer, **90**, No. 1, pp. 87–97.
[6] Gambill, W. R., and Bundy, R. D., 1963, ''High-Flux Heat Transfer Characteristics in Turbulent Swirl Flow Subjected to Large Transverse Temperature Gradients,'' AIChE J., **9**, No. 1, pp. 55–59.
[7] Smithberg, E., and Landis, F., 1964, ''Friction and Forced Convection Heat Transfer Characteristics in Tubes with Twisted-Tape Swirl Generators,'' ASME J. Heat Transfer, **86**, No. 1, pp. 39–49.
[8] Lopina, R. F., and Bergles, A. E., 1969, ''Heat Transfer and Pressure Drop in Tape-Generated Swirl Flow of Single-Phase Water,'' ASME J. Heat Transfer, **91**, No. 3, pp. 434–441.
[9] Colburn, A. P., and King, W. J., 1931, ''Heat Transfer and Pressure Drop in Empty, Baffled and Packed Tubes, III: Relation between Heat Transfer and Pressure Drop,'' Ind. Eng. Chem., **23**, No. 8, pp. 919–923.
[10] Seigel, L. G., 1946, ''The Effect of Turbulence Promoters on Heat Transfer Coefficients of Water Flowing in a Horizontal Tubes,'' Heat./Piping/Air Cond., **18**, No. 6, pp. 111–114.
[11] Koch, R., 1958, ''Pressure Loss and Heat Transfer for Turbulent Flow,'' VDI-Forschungsheft, **24**, No. 469, Ser. B, pp. 1–44.
[12] Backshall, R. G., and Landis, F., 1969, ''The Boundary Layer Velocity Distribution in Turbulent Swirling Pipe Flow,'' ASME J. Basic Eng., **91**, pp. 728–733.
[13] Date, A. W., and Singham, J. R., 1972, ''Numerical Prediction of Friction and Heat Transfer Characteristics of Fully Developed Laminar Flow in Tubes Containing Twisted Tapes,'' ASME Paper No. 72-HT-17.
[14] Date, A. W., 1974, ''Prediction of Fully-Developed Flow in a Tube Containing a Twisted-Tape,'' Int. J. Heat Mass Transf., **17**, No. 8, pp. 845–859.
[15] Hong, S. W., and Bergles, A. E., 1976, ''Augmentation of Laminar Flow Heat Transfer in Tubes by Means of Twisted-Tape Inserts,'' ASME J. Heat Transfer, **98**, No. 2, pp. 251–256.
[16] Watanabe, K., Taira, T., and Mori, Y., 1983, ''Heat Transfer Augmentation in Tubular Flow by Twisted Tapes at High Temperatures and Optimum Performance,'' Heat Transfer-Jpn. Res., **12**, No. 3, pp. 1–31.
[17] Bandyopadhyay, P. S., Gaitonde, U. N., and Sukhatme, S. P., 1991, ''Influence of Free Convection on Heat Transfer During Laminar Flow in Tubes with Twisted Tapes,'' Exp. Therm. Fluid Sci., **4**, No. 5, pp. 577–586.
[18] du Plessis, J. P., 1982, ''Laminar Flow and Heat Transfer in a Smooth Tube with a Twisted-Tape Insert,'' Ph.D. thesis, University of Stellenbosch, South Africa.
[19] van Rooyen, R. S., and Kroeger, D. G., 1978, ''Laminar Flow Heat Transfer in Internally Finned Tubes with Twisted-Tape Inserts,'' J. Illum. Eng. Soc., Aug 7–11, Natl Res Counc of Can.
[20] Marner, W. J., and Bergles, A. E., 1978, ''Augmentation of Tubeside Laminar Flow Heat Transfer by Means of Twisted-Tape Inserts, Static Mixer Inserts and Internally Finned Tubes,'' J. Illum. Eng. Soc., Aug. 7–11, Natl Res Counc of Can.
[21] Marner, W. J., and Bergles, A. E., 1985, ''Augmentation of Highly Viscous Laminar Tubeside Heat Transfer by Means of a Twisted-tape Insert and an Internally Finned Tube,'' ASME, HTD, **43**, pp. 19–28.
[22] Marner, W. J., and Bergles, A. E., 1989, ''Augmentation of Highly Viscous Laminar Heat Transfer Inside Tubes in Constant Wall Temperature,'' Exp. Therm. Fluid Sci., **2**, pp. 252–267.
[23] Manglik, R. M., and Bergles, A. E., 1987, ''Correlation for Laminar Flow Enhanced Heat Transfer in Uniform Wall Temperature Circular Tubes With Twisted-Tape Inserts,'' ASME HTD, **68**, pp. 19–25.
[24] Manglik, R. M., and Bergles, A. E., 1993, ''Heat Transfer and Pressure Drop Correlations for Twisted-Tape Inserts in Isothermal Tubes: Part I—Laminar Flows,'' ASME J. Heat Transfer, **115**, No. 4, pp. 881–889.
[25] Manglik, R. M., and Bergles, A. E., 1993, ''Heat Transfer and Pressure Drop Correlations for Twisted-Tape Inserts in Isothermal Tubes: Part II—Transition and Turbulent Flows,'' ASME J. Heat Transfer, **115**, No. 4, pp. 890–896.
[26] Manglik, R. M., and Bergles, A. E., 1988, ''Laminar Flow Heat Transfer in a Semi-Circular Tube With Uniform Wall Temperature,'' Int. J. Heat Mass Transf., **31**, No. 3, pp. 625–636.
[27] Carlson, R. D., France, D. M., Gabler, M. J., Kim, K., and Veljovich, W., 1986, ''Heat Transfer Augmentation in Liquid Metal Reactor Steam Generators,'' Proc. ASME/ANS Joint Nuclear Power Conf., pp. 211–217.
[28] du Plessis, J. P., and Kroeger, D. G., 1983, ''Numerical Prediction of Laminar Flow with Heat Transfer in a Tube with a Twisted Tape Insert,'' Proc. Int. Conf. Numerical Methods in Laminar and Turbulent Flow, pp. 775–785.
[29] du Plessis, J. P., and Kroger, D. G., 1984, ''Friction Factor Prediction for Fully Developed Laminar Twisted-Tape Flow,'' Int. J. Heat Mass Transf., **27**, No. 11, pp. 2095–2100.
[30] du Plessis, J. P., and Kroger, D. G., 1987, ''Heat Transfer Correlation for Thermally Developing Laminar Flow in a Smooth Tube with a Twisted-Tape Insert,'' Int. J. Heat Mass Transf., **30**, No. 3, pp. 509–515.
[31] Dasmahapatra, J. K., and Raja Rao, M., 1991, ''Augmentation of Tubeside Heat Transfer to Power Law Fluids in Laminar Flow by means of Twisted Tape Inserts,'' Proc. 2nd World Conf. on Experimental Heat Transfer, Fluid Mechanics and Thermodynamics.
[32] Dasmahapatra, J. K., and Raja Rao, M., 1991, ''Laminar Flow Heat Transfer to Generalised Power Law Fluids Inside Circular Tubes Fitted with Regularly Spaced Twisted Tape Elements for Uniform Wall Temperature Condition,'' Heat Transfer Division, HTD, **174**, ASME, pp. 51–58.
[33] Sukhatme, S. P., Gaitonde, U. N., Shidore, C. S., and Kuncolienkar, R. S., 1987, ''Forced Convection Heat Transfer to a Viscous Liquid in Laminar Flow in a Tube With a Twisted-Tape,'' Paper No. HMT-87, Part B, Proc. 9th Nat. Heat and Mass Transfer Conf., IISc, Bangalore, pp. 1–3.
[34] Sukhatme, S. P., Gaitonde, U. N., Kulkarni, S. V., and Majumdar, A., 1985, ''Laminar Convective Heat Transfer to a Thermic Fluid in a Tube With a Twisted-Tape,'' Paper No. C21-85, Proc. 8th Nat. Heat and Mass Transfer Conf., Andhra University, Vishakhapatnam, India, pp. 279–283.
[35] Seymour, E. V., 1963, ''A Note on the Improvement in Performance Obtainable from Fitting Twisted-Tape Turbulence-Promoters to Tubular Heat Exchangers,'' J. IchE, **41**, No. 4, pp. 159–162.
[36] Kreith, F., and Sonju, O. K., 1965, ''The Decay of a Turbulent Swirl Flow in a Pipe,'' J. Fluid Mech., **22**, Part 2, pp. 257–271.
[37] Klepper, O. H., 1973, ''Heat Transfer Performance of Short Twisted-Tapes,'' AIChE Symp. Ser. **69**, No. 131, pp. 87–93.
[38] Zozulya, N. V., and Shkuratov, I. Y., 1974, ''Effect of Length of a Twisted-Tape Turbulence Promoter and of its Initial Twisting Pitch of Augmenting of Heat Transfer Inside a Tube,'' Heat Transfer-Sov. Res., **6**, No. 6, pp. 98–100.
[39] Algifri, A. H., and Bhardwaj, R. K., 1985, ''Prediction of the Heat Transfer for Decaying Turbulent Swirl Flow in a Tube,'' Int. J. Heat Mass Transf., **28**, No. 9, pp. 1637–1643.
[40] Lokanath, M. S., 1997, ''Performance Evaluation of Full Length and Half Length Twisted Tape Inserts on Laminar Flow Heat Transfer in Tubes,'' Paper No. HMT-97-031, Proc. 14th Nat. Heat and Mass Transfer Conf. and 3rd ISHMT-ASME Joint Heat and Mass Transfer Conf., IIT Kanpur, India, pp. 319–324.
[41] Saha, S. K., Gaitonde, U. N., and Date, A. W., 1989, ''Heat Transfer and Pressure Drop Characteristics of Laminar Flow in a Circular Tube Fitted With Regularly Spaced Twisted-Tape Elements,'' Exp. Therm. Fluid Sci., **2**, No. 3, pp. 310–322.
[42] Date, A. W., and Gaitonde, U. N., 1990, ''Development of Correlations for Predicting Characteristics of Laminar Flow in a Tube Fitted with Regularly Spaced Twisted-Tape Elements,'' Exp. Therm. Fluid Sci., **3**, pp. 373–382.

[43] Date, A. W., and Saha, S. K., 1990, ''Numerical Prediction of Laminar Flow and Heat Transfer Characteristics in a Tube Fitted With Regularly Spaced Twisted-Tape Elements,'' Int. J. Heat Fluid Flow, **11**, No. 4, pp. 346–354.
[44] Monheit, M., 1987, ''Experimental Evaluation of the Convective Characteristics of Tubes With Twisted-Tape Inserts,'' ASME, HTD, **68**, pp. 11–18.
[45] Al-Fahed, S., and Chamra, L. M., 1998, ''Pressure Drop and Heat Transfer Comparison for Both Microfin Tube and Twisted-Tape Inserts in Laminar Flow,'' Exp. Therm. Fluid Sci., **18**, No. 4, pp. 323–333.
[46] Pinjala, V. V. Babu, and Raja Rao, M., 1991, ''Heat Transfer Correlations for Laminar Non-Newtonian Flow in Tubes with Twisted-Tape Inserts,'' ASME, HTD, **174**, pp. 59–64.
[47] Shivkumar, C., and Raja Rao, M., 1988, ''Studies on Compound Augmentation of Laminar Flow Heat Transfer to Generalised Power Law Fluids in Spirally Corrugated Tubes by Means of Twisted Tape Inserts,'' ASME, HTD, **96**, pp. 685–692.
[48] Agarwal, S. K., and Raja Rao, M., 1996, ''Heat Transfer Augmentation for the Flow of a Viscous Liquid in Circular Tubes Using Twisted-Tape Inserts,'' Int. J. Heat Mass Transf., **39**, pp. 3547–3557.
[49] Hochdorfer, E., Gschwind, P., and Kottke, V., 1995, ''Twisted Tape Vortex Generators in Duct Flow: Flow Field and Heat and Mass Transfer,'' Exp. Therm. Fluid Sci., **11**, No. 3, pp. 262–269.
[50] Aoyama, Y., Tai, Y., Mizukami, K., and Murakami, K., 1995, ''Buoyancy Effect on Laminar Heat Transfer in a Horizontal Straight Tube Containing a Twisted Tape Swirler,'' Proc. ASME/JSME Thermal Engineering Joint Conf., pp. 269–276.
[51] Aoyama, Y., Mizukami, K., Hizikata, K., and Futagami, K., 1992, ''Numerical Analysis of Laminar Heat Transfer in a Straight Tube Containing a Twisted-Tape Swirler,'' IChE Symp. Ser., **2**, No. 129, pp. 781–788.
[52] Manglik, R. M., and Bergles, A. E., 1994, ''Fully Developed Laminar Heat Transfer in Circular-Segment Ducts with Uniform Wall Temperature,'' Numerical Heat Transfer, an Int. J. Computation and Methodology; Part A: Applications, **26**, No. 5, pp. 499–519.
[53] Klaczak, A., 1996, ''Heat Transfer and Pressure Drop in Tubes With Short Turbulators,'' Heat and Mass Transfer/Waerme-und Stoffuebertragung, **31**, No. 6, pp. 399–401.
[54] Kline, S. J., and McClintock, F. A., 1953, ''Describing Uncertainties in Single Sample Experiments,'' Mech. Eng. (Am. Soc. Mech. Eng.), **75**, pp. 3–8.
[55] Shah, R. K., and London, A. L., 1978, ''Laminar Flow Forced Convection in Ducts,'' Adv. Heat Transfer, **1** Suppl. 1, T. F. Irvine, Jr., and J. P. Hartnett, eds., pp. 379–381.
[56] Date, A. W., 1972, ''Prediction of Friction and Heat Transfer Characteristics of Flow in a Tube Containing a Twisted-Tape,'' Ph.D. thesis, Imperial College, University of London.
[57] Bergles, A. E., Blumenkrantz, A. R., and Taborek, J., 1974, ''Performance Evaluation Criteria for Enhanced Heat Transfer Surfaces,'' Proc. Int. Heat and Mass Transfer Conf., **2**, pp. 239–243.
[58] Saha, S. K., and Chakraborty, D., 1997, ''Heat Transfer and Pressure Drop Characteristics of Laminar Flow through a Circular Tube Fitted with Regularly Spaced Twisted-Tape Elements with Multiple Twist,'' Proc. 14th Nat. Heat and Mass Transfer Conf. and 3rd ISHMT-ASME Joint Heat and Mass Transfer Conf., IIT Kanpur, India, pp. 313–318.

Saïd Aniss
e-mail: saniss@hotmail.com

Mohamed Belhaq

Faculté des Sciences Aïn chock,
UFR de Mécanique,
BP 5366 Maârif,
Casablanca, Marocco

Mohamed Souhar
Lemta-Ensem,
UMR 7563,
2 avenue de la Forêt de Haye,
BP 160,
Vandoeuvre 54504, France

Effects of a Magnetic Modulation on the Stability of a Magnetic Liquid Layer Heated From Above

The effect of a time-sinusoidal magnetic field on the onset of convection in a horizontal magnetic fluid layer heated from above and bounded by isothermal non magnetic boundaries is investigated. The analysis is restricted to static and linear laws of magnetization. A first order Galerkin method is performed to reduce the governing linear system to the Mathieu equation with damping term. Therefore, the Floquet theory is used to determine the convective threshold for the free-free and rigid-rigid cases. With an appropriate choice of the ratio of the magnetic and gravitational forces, we show the possibility to produce a competition between the harmonic and subharmonic modes at the onset of convection. [DOI: 10.1115/1.1370501]

Keywords: Convection, Heat Transfer, Instability, Liquid, Magnetic, Stability

1 Introduction

Several works have been devoted to describe the role of the magnetic convection in ferrofluids to control heat and transfer [1,2]. A magnetic liquid—ferrofluid —is a stable colloidal suspension of solid ferromagnetic particles (30–100 Å in size) in a carrier liquid such as water, kerosene, etc. The particles are coated with a surfactant to prevent agglomeration. In the absence of an external magnetic field, the orientations of the constant moments of particles are disordered by the thermal Brownian motion, and the magnetic moment of the unit volume (Magnetization) is equal to zero. In the presence of an ordinary magnetic field, the tendency of the dipole moments to align with the applied magnetic field is partially overcome by the thermal agitation. At very high field strengths, the particles may be completely aligned and the magnetization achieves its saturation value. Generally, the magnetization depends on the magnetic field, temperature and density. Hence, the magnetic forces depend on the thermal state of the liquid and may give rise to convection. There have been numerous studies in this area, particularly in the Rayleigh-Bénard convection. Finlayson [3] considered a magnetic liquid layer heated from below in the presence of an uniform vertical magnetic field. For free-free and rigid-rigid horizontal boundaries, a linear stability analysis was carried out to predict the critical gradient of temperature corresponding to the onset of convection when both buoyancy and magnetic forces are included. Shwab et al. [4] investigated experimentally the Finlayson's problem in the case of a strong magnetic field and detected the onset of convection by plotting the Nusselt number versus the Rayleigh number. Then, the critical Rayleigh number corresponds to a discontinuity in the slope. Later, Stiles and Kagan [5] examined the experimental problem reported by Shwab et al. [4] and generalized the Finlayson's model assuming that under a strong magnetic field, the rotational viscosity augments the shear viscosity. Rudraiah and Sekhar [6] treated the Finlayson's problem with internal heat source and showed that the variation of temperature, due to heat source, induces a variation in the magnetic field. These variations can be used to control magnetic convection. Note that the effect of the heat source is analogous to magnetocaloric effect studied earlier by Bashtovoi and Berkovsky [7].

All these works suppose the uniformity of the applied external magnetic field. Another interesting case consists of applying an external magnetic field of a constant or spatially varying gradient. Zaitsev and Shliomis [8] considered the case of a magnetic liquid confined in a cylindrical shell and submitted to a radial temperature gradient. A steady electrical current through the cylinder axis produces a radial magnetic field with a spatially varying gradient. The problem for small distance between the inner and outer cylinders was solved and a simple criterion of stability was found. Later, Polevikov and Fertman [9] studied the same problem for arbitrary gap and established a criterion of stability considering only the two-dimensional azimuthal states. The three-dimensional azimuthal state was studied recently by Zebib [10] and it was shown that this state is the most unstable one. As a variation of the theme, Berkovsky et al. [11] carried out a theoretical and experimental study of the convective heat and transfer across a vertical layer of ferrofluid heated from one side and placed in a horizontal gradient of magnetic field. A relationship was given between heat transfer and characteristic parameters. Aniss et al. [12] and Souhar et al. [13] proposed a theoretical and experimental investigation of the Rayleigh-Bénard convection in a magnetic fluid layer confined in a horizontal annular Hele-Shaw cell and submitted simultaneously to radial temperature and magnetic field gradients. With their geometrical configuration, they showed the possibility to simulate theoretically and experimentally the Rayleigh-Bénard convection and its control by an external magnetic field gradient in the absence of gravity.

In this paper, we study the case of a horizontal ferromagnetic liquid layer heated from above and submitted to a time-sinusoidal external magnetic field. In this situation, the magnetic Rayleigh number is modulated periodically in time around its mean. This magnetic modulation is similar to the gravitational one consisting on varying acceleration term in the gravitational Rayleigh number around the gravitational acceleration, i.e., by vertically oscillating a horizontal liquid layer. Gresho and Sani [14] studied the influence of the two-dimensional gravitational modulation on the convective threshold of a stable and an unstable motionless state. Biringen and Peltier [15] extended to three-dimension the linear two-dimensional problem of Gresho and Sani [14]. Clever et al. [16] investigated the effects of gravitational modulation on the two-dimensional steady, monotonic convective threshold and constructed nonlinear solutions using a Galerkin method. For a review of known results in the gravitational modulation, see Gershuni and Zhukhovitskii [17]. The magnetic modulation in ferrofluids whose Prandtl numbers are of the order of unity or larger than unity was treated by Shliomis et al. [18] in the case of a Hele-Shaw cell. However, with this configuration, Aniss et al.

Contributed by the Heat Transfer Division for publication in the JOURNAL OF HEAT TRANSFER. Manuscript received by the Heat Transfer Division December 15, 1999; revision received January 3, 2001. Associate Editor: P. S. Ayyaswamy.

[19] showed that the vertical oscillations of the cell generate parametric convective instability only for small Prandtl numbers. Consequently, using the similarity between gravitational and magnetic modulations, the parametric convective instability cannot occur in a Hele-Shaw magnetic liquid layer. Therefore, we study in this paper a two-dimensional parametric convective instability induced by an external magnetic field excitation in the case of a horizontal magnetic layer of infinite extent in the horizontal directions. Furthermore, we use some hypothesis to neglect the dynamic components in the dynamic law of magnetization and then only the static law is required. Also, we restrict our study to a linear magnetization law. The present study can serve as a theoretical support for an experimental investigation. This allows an experimental visualization of the parametric instability mechanism with an oscillating magnetic field instead of vertical vibrations in which the amplitudes and frequencies are more difficult to control.

2 Linear Formulation of the Problem

Consider a layer of incompressible ferromagnetic liquid bounded between two horizontal non-magnetic plates located at $z=-1/2d$ and $z=1/2d$ in the presence of the external magnetic field

$$\mathbf{H^{ext}}=H^a\sqrt{2}\,\sin(\omega t/2)\mathbf{k}. \tag{1}$$

The lower and upper boundaries are maintained at constant temperature T_1 and T_o, respectively, $(T_1<T_o)$. The conservation equations, in the Boussinesq approximation, are

$$\mathrm{Div}(\mathbf{V})=0 \tag{2}$$

$$\rho\frac{d\mathbf{V}}{dt}=-\nabla p+\rho\mathbf{g}+\mu_o\mathbf{M}\nabla\mathbf{H}+\mu\Delta\mathbf{V} \tag{3}$$

$$\frac{dT}{dt}=\kappa\Delta T. \tag{4}$$

The magnetic term in Eq. (3) is determined for a symmetrical model by the interaction of the continuum magnetic moment and the inhomogeneous magnetic field [20,21]. Maxwell's equations, simplified for a non-conducting fluid with non-displacement of currents, are

$$\mathrm{Div}(\mathbf{H}+\mathbf{M})=0, \tag{5a}$$

$$\mathbf{Rot}(\mathbf{H})=0 \tag{5b}$$

In the case of a time-dependent magnetic field, one uses generally the dynamic law of magnetization. The dynamic components of this law are related to the relaxation time of rotation τ_R and the one of elongation τ_B [21]. Nevertheless, for a varying magnetic field in a fixed direction the dynamic law of magnetization is independent of τ_R. Furthermore, to neglect the second dynamic component, we assume $\omega\tau_B\ll 1$, $(v/d^2)\tau_B\ll 1$ and $(\kappa/d^2)\tau_B\ll 1$. The characteristic time τ_B is of the order of 10^{-6} s. Hence, we use only the static law where the magnetization is parallel to the magnetic field and depends on both temperature and magnetic field

$$\mathbf{M}=M(T,H)\frac{\mathbf{H}}{H} \tag{6}$$

The density and magnetic equations of state are linearized about the average temperature T_a and the magnetic field H_o

$$\rho=\rho_o[1-\alpha(T-T_a)], \tag{7a}$$

$$M=M_o+\chi_r(H-H_o)-K(T-T_a). \tag{7b}$$

We restrict our analysis to a linear law of magnetization, $M=\chi H$. Hence, the vertical external magnetic field, $\mathbf{H_0^{ext}}(t)$, creates an induced field, $\mathbf{h}=-\mathbf{M}$, through the liquid layer, so that the total field in the magnetic liquid is

$$\mathbf{H_o}(t)=H_o\mathbf{k}=\frac{H^{\mathrm{ext}}(t)}{1+\chi}\mathbf{k}=\frac{\sqrt{2}H^a}{1+\chi}\sin\left(\frac{\omega t}{2}\right)\mathbf{k} \tag{8}$$

Equations (5*a*) and (6) are used to relate the magnetic field and magnetization intensities in the case of a linear law of magnetization. We obtain

$$(1+\chi)\mathrm{Div}\mathbf{H}=K\ \ \nabla T.\mathbf{e_H}, \tag{9}$$

where $\mathbf{e_H}=\mathbf{H}/H$ is the unit vector in the field direction. The basic motionless state of the system (2)–(4) is similar to that of Finlayson [3] and it is given by

$$\mathbf{V}_b=0,\quad T_b=T_a-\beta z,\quad T_a=\frac{T_1+T_o}{2},\quad \beta=\frac{T_1-T_o}{d} \tag{10}$$

$$\mathbf{H}_b=\left(H_o-\frac{K\beta z}{1+\chi}\right)\mathbf{k},\quad \mathbf{M}_b=\left(M_o+\frac{K\beta z}{1+\chi}\right)\mathbf{k}. \tag{11}$$

The linearized magnetic susceptibility about the average temperature T_a is

$$\chi(T)=\chi_o(T_a)-\gamma_a(T-T_a), \tag{12}$$

where $\chi_o=M_o/H_o$. The coefficient γ_a is analogous to that of the thermal expansion, α, in the density Eq. (7*a*) and may be estimated by the Curie-Weiss law, $\chi=C_A/T$, where C_A is the Curie constant. Thus, $\gamma_a=\chi_o/T_a$. From Eqs. (7*b*) and (12) we obtain

$$K=\gamma_a H_o. \tag{13}$$

Using the assumption [3],

$$K\beta d\ll(1+\chi_o)H_o, \tag{14}$$

which is equivalent to $\gamma_a\beta d\ll 1+\chi_o$, the basic magnetic field and magnetization can be written as follows:

$$\mathbf{H}_b=\left(H_o-\frac{\gamma_a\beta z}{1+\chi_o}H_o\right)\mathbf{k},\quad \mathbf{M}_b=\left(M_o+\frac{\gamma_a\beta z}{1+\chi_o}H_o\right)\mathbf{k}. \tag{15}$$

Now we will perform a linear stability analysis of the motionless state. Equations (6), (7*b*), (13) and (14) yield

$$\begin{aligned} H_i'+M_i'&=(1+\chi_o)H_i' \quad (i=1,2),\\ H_3'+M_3'&=(1+\chi_o)H_3'-\gamma_a H_o T', \end{aligned} \tag{16}$$

where the primes denote the perturbed quantities. Equation (5*b*) allows us to write $\mathbf{H}'=\nabla\phi'$. Scaling time by d^2/κ, the coordinates by d, the velocity field by κ/d, the temperature by (T_o-T_1) and the magnetic potential, ϕ', by $\gamma_a H_o d(T_o-T_1)/(1+\chi_o)$, we obtain the following dimensionless set of equations corresponding to a linear perturbation of the basic state:

$$Pr^{-1}\frac{\partial}{\partial t}(\Delta w)=[Rg-Rm(t)]\Delta_2 T+Rm(t)\Delta_2\left(\frac{\partial\phi}{\partial z}\right)+\Delta(\Delta w) \tag{17}$$

$$\frac{\partial T}{\partial t}=\Delta T-w \tag{18}$$

$$\Delta\phi-\frac{\partial T}{\partial z}=0. \tag{19}$$

Equation (17) represents the vertical component of the vorticity, (18) is the energy equation and the potential Eq. (19) is derived from Eqs. (5*a*) and (16). The modulated magnetic Rayleigh number is defined as follows:

$$Rm(t)=Rmo(1-\cos(\Omega t)) \tag{20}$$

Here, $Rmo=\mu_o\gamma_a^2\beta^2d^4H^{a^2}/\mu\kappa(1+\chi_o)^3$ is a static magnetic Rayleigh number and Ω is a dimensionless frequency. The boundary conditions associated to the system of Eqs. (17)–(19) and (20) are discussed in the next section.

3 Stability Analysis

Using the normal mode analysis, the component of velocity w, the temperature T, and the potential ϕ are expanded in the form

$$w=w_1(z,t)\exp(iq_x x+iq_y y),\quad T=T_1(z,t)\exp(iq_x x+iq_y y),$$
$$\phi=\phi_1(z,t)\exp(iq_x x+iq_y y). \tag{21}$$

Substituting (21) into the system (17)–(19), we obtain

$$\left[\mathrm{Pr}^{-1}\frac{\partial}{\partial t}-(D^2-q^2)\right](D^2-q^2)w_1+[Rg-Rm(t)]q^2T_1 + Rm(t)q^2D\phi_1=0 \tag{22}$$

$$\left[\frac{\partial}{\partial t}-(D^2-q^2)\right]T_1+w_1=0 \tag{23}$$

$$(D^2-q^2)\phi_1-DT_1=0, \tag{24}$$

where $D=\partial/\partial z$. Following Finlayson [3], the continuity of the normal components of the magnetic induction $\mathbf{B}=\mu_o(\mathbf{H}+\mathbf{M})$ and that of the tangential components of the magnetic field $\mathbf{H}$ across the horizontal boundaries lead to the boundary conditions on the magnetic potential

$$(1+\chi_o)D\phi_1-q\phi_1=0 \ \text{ at } \ z=-1/2,$$
$$(1+\chi_o)D\phi_1+q\phi_1=0 \ \text{ at } \ z=1/2. \tag{25}$$

The boundary conditions on the temperature and velocity are given for the free-free case by

$$w_1=D^2w_1=T_1=0 \ \text{ at } \ z=\pm 1/2 \tag{26}$$

and for the rigid-rigid case by

$$w_1=Dw_1=T_1=0 \ \text{ at } \ z=\pm 1/2. \tag{27}$$

3.1 Free-Free Case–Exact Solution. In this mathematically important case, one can derive an exact solution whose properties guide the analysis of the rigid-rigid case. Here, we consider the case of an infinite magnetic susceptibility χ_o and we neglect the deformability of the horizontal surfaces. Thus, the exact solution of the system (22)–(24) subject to the boundary conditions

$$w_1=D^2w_1=T_1=D\phi_1=0 \ \text{ at } \ z=\pm 1/2 \tag{28}$$

is written in the form

$$w_1=f(t)\cos(\pi z),\quad T_1=g(t)\cos(\pi z),\quad \phi_1=h(t)\sin(\pi z). \tag{29}$$

Substituting these functions into the system (22)–(24), the latter is reduced to the amplitude equation of temperature

$$\frac{d^2g}{dt^2}+2c_1\frac{dg}{dt}+c_2[R_o+Rg-c_3Rm(t)]g=0, \tag{30}$$

where $R_o=(\pi^2+q^2)^3/q^2$ is the gravitational Rayleigh number of the marginal stability curve related to the ordinary Rayleigh-Bénard problem. The coefficients c_1, c_2, and c_3 are given by

$$2c_1=(\mathrm{Pr}+1)(\pi^2+q^2),\quad c_2=\frac{q^2\mathrm{Pr}}{(\pi^2+q^2)},\quad c_3=\frac{q^2}{q^2+\pi^2}. \tag{31}$$

3.1.1 Stationary Onset of Convection of the Unmodulated Case. The stationary convective instability of a horizontal magnetic liquid layer heated from below in the presence of an uniform vertical magnetic field was predicted by Finlayson [3]. Here, we discuss the case of a liquid layer heated from above in the presence and absence of buoyancy force (gravity). From Eq. (30), the stationary marginal stability curve is given by

$$c_3Rm-Rg=R_o. \tag{32}$$

In this equation, we introduce the ratio of the magnetic and gravitational forces, $M_1=Rm/Rg$. Note that for large values of M_1, the marginal stability curve is given by $Rm=(\pi^2+q^2)^4/q^4$. Hence, the critical magnetic Rayleigh and wave numbers are $Rm_c=16\pi^4$ and $q_c=\pi$, respectively. For small values of M_1, we are in the presence of a stable motionless state.

3.1.2 Parametric Convective Instability. Now we proceed to the examination of the parametric instability of the motionless state using the amplitude Eq. (30) associated to Eq. (20). We obtain

$$\frac{d^2g}{dt^2}+2c_1\frac{dg}{dt}+c_2[R_o+Rg-c_3Rmo+c_3Rmo\cos(\Omega t)]g=0. \tag{33}$$

To produce a parametric resonance in Eq. (33), we introduce the change of variables inspired from the work by Gresho and Sani [14]

$$Rmo-Rg=Ra \quad Rmo=f_m\Omega^2Ra \tag{34}$$

where Ra is a positive number and f_m is an arbitrary positive constant. The ratio of the magnetic and gravitational forces is now defined by

$$M_2=Rmo/Rg=f_m\Omega^2/(f_m\Omega^2-1). \tag{35}$$

The case where Ω^2 tends to infinity corresponds to $Rg\approx Rmo$ and the one where Ω^2 tends to $1/f_m$ corresponds to $Rmo\gg Rg$. To reduce Eq. (33) to the Mathieu equation, we use the change of variables $g(t)=G(t)\exp(-c_1t)$ and $2\tau=\Omega t$ to obtain

$$\frac{d^2G}{d\tau^2}+[A-2B\cos(2\tau)]G(\tau)=0 \tag{36}$$

where

$$A=4\frac{c_2}{\Omega^2}[R_N-Ra(1+f_m\Omega^2(c_3-1))],\quad R_N=-R_o\frac{[1-\mathrm{Pr}]^2}{4\mathrm{Pr}}$$
$$B=-2c_2c_3f_mRa.$$

Using the Floquet theory, the general solution of Eq. (36) is

$$G(\tau)=P(\tau)\exp(\lambda\tau), \tag{37}$$

where λ is the Floquet exponent and $P(\tau)$ is a π-periodic or 2π-periodic function. Then, solution of Eq. (33) is written as

$$g(t)=P(t)\exp\left(\frac{\lambda\Omega}{2}-c_1\right)t \tag{38}$$

from which, the criterion of the onset of instability is

$$\frac{\lambda\Omega}{2}\geqslant c_1. \tag{39}$$

Hereafter, we focus our attention on the marginal stability condition given by

$$\frac{\lambda\Omega}{2}=c_1 \tag{40}$$

The solutions of Eq. (36) can be expressed in the form

$$G_\pi=\exp(\lambda\tau)\sum_{-\infty}^{+\infty}a_n\exp(2ni\tau), \tag{41a}$$

$$G_{2\pi}=\exp(\lambda\tau)\sum_{-\infty}^{+\infty}b_n\exp[(2n+1)i\tau]. \tag{41b}$$

The expression (41*a*) corresponds to the harmonic solutions having the same frequency that the parametric excitation while expression (41*b*) corresponds to the subharmonic ones. First, consider the harmonic solutions. Substitution of (41*a*) into Eq. (36)

leads to a homogeneous algebraic system of equations. A necessary and sufficient condition for the existence of nontrivial solutions is the vanishing of the characteristic determinant, and, hence,

$$\Delta(i\lambda)=\begin{vmatrix} . & . & . & . & . & . & . & . & . \\ . & \xi_{-2} & 1 & \xi_{-2} & 0 & 0 & 0 & 0 & . \\ . & 0 & \xi_{-1} & 1 & \xi_{-1} & 0 & 0 & 0 & . \\ . & 0 & 0 & \xi_o & 1 & \xi_o & 0 & 0 & . \\ . & 0 & 0 & 0 & \xi_1 & 1 & \xi_1 & 0 & . \\ . & 0 & 0 & 0 & 0 & \xi_2 & 1 & \xi_2 & . \\ . & . & . & . & . & . & . & . & . \end{vmatrix}=0, \tag{42}$$

where $\xi_n=B/[(2n-i\lambda)^2-A]$. The condition (42) may be written as in Morse and Feshbach [22]

$$\cosh(\lambda\pi)=1-2\Delta(0)\sin^2\left(\frac{\pi\sqrt{A}}{2}\right), \tag{43}$$

where $\Delta(0)$ is defined from (42) for $\lambda=0$. The functions $\xi_n(\lambda)$ are actually $\xi_n(0)$ and satisfy $\xi_n(0)=\xi_{-n}(0)$. The advantage of the transformation (43) is that $\Delta(0)$ can be computed in a recurrence relations between the determinants of orders differing by 2 at each step, starting with the mid-determinant [23]

$$\Delta_o=1,\quad \Delta_1=1-2\xi_o\xi_1,\quad \Delta_2=(1-2\xi_1\xi_2)^2-2\xi_o\xi_2(1-\xi_1\xi_2)$$
$$\Delta_{n+2}=(1-\xi_{n+1}\xi_{n+2})\Delta_{n+1}-\xi_{n+1}\xi_{n+2}(1-\xi_{n+1}\xi_{n+2})\Delta_n$$
$$+\xi_n^2\xi_{n+1}^3\xi_{n+2}\Delta_{n-1}.$$

Convergence of $\Delta(0)$ is rapid enough to produce data to two or three decimals in a very short time. Similarly, for subharmonic solutions, one obtains the corresponding characteristic equation

$$\cosh(\lambda\pi)=-1+2\Delta(0)\sin^2\left(\frac{\pi\sqrt{A}}{2}\right). \tag{44}$$

Equations (43) and (44) determine an eigenvalue problem of the form

$$R(\lambda,\mathrm{Pr},f_m,\Omega,Rmo,q)=0. \tag{45}$$

For the numerical analysis, we have used an alternative method to the one considered by Gresho and Sani [14]. To investigate the marginal stability curves, $Rmo(q)$, the characteristic equations are solved for prescribed values of the Prandtl numbers Pr, the dimensionless frequency Ω, and the constant f_m. For a fixed wave number q_i, we evaluate the Floquet exponent λ_i using Eq. (40), and then we determine the corresponding value $(Rmo)_i$ obeying the harmonic characteristic equation (43) or the subharmonic one (44). To display our results, we plot the critical magnetic Rayleigh number, Rmo_c, and wave number, q_c, versus the dimensionless frequency Ω. Each of these critical curves represents the minimum of the two harmonic and subharmonic solution modes in term of the critical magnetic Rayleigh number. Indeed, instability occurs at the lowest value of the critical magnetic Rayleigh number.

Figure 1 illustrates the results for $\mathrm{Pr}=7$ and $f_m=10^{-4}$. According to Eq. (35), Ω starts with values larger than $1/\sqrt{f_m}$. When Ω increases from this value, the critical magnetic Rayleigh number corresponding to the onset of harmonic solutions increases until a certain frequency at which the onset is in the form of subharmonic solutions. As Ω increases further beyond the crossover frequency $\Omega_t=134$, the critical magnetic Rayleigh number corresponding to the onset of subharmonic solutions tends to the infinity following the law $Rmo_c=648f_m\Omega^2$. We can see that close to $\Omega=1/\sqrt{f_m}$, where $Rmo\gg Rg$, the values of the critical magnetic Rayleigh number are larger than the asymptotic value of the unmodulated case, $Rm_c=16\pi^4$, corresponding to $Rm\gg Rg$. Here, we are in the presence of a stabilizing effect. The configuration where $Rg\approx Rm(M_1\approx 1)$, in the unmodulated case, corresponds to a stable motionless state and may be destabilized in subharmonic mode by the magnetic modulation for large $\Omega(Rg\approx Rmo)$.

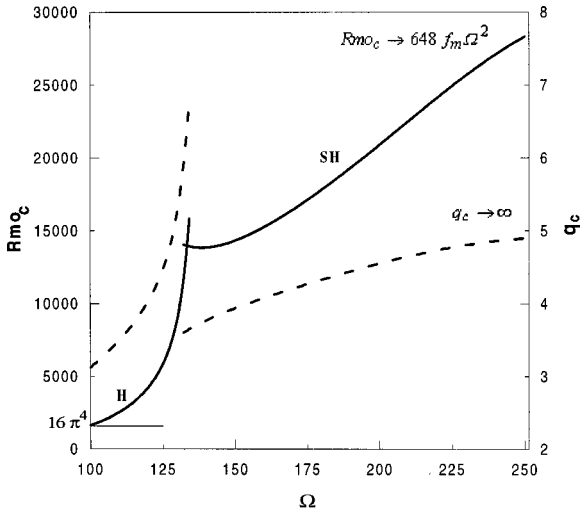

Fig. 1 Free-Free case: Critical magnetic Rayleigh number, Rmo_c, (solid line) and critical wave number, q_c, (dashed line) versus the dimensionless frequency, Ω, for $Pr=7$, $f_m=10^{-4}$ and $\chi_o=\infty$. H: harmonic solutions. SH: subharmonic solutions.

The evolution of the critical wave number q_c, as shown in Fig. 1, gives rise to a jump when crossing the value Ω_t. This jump is related to the fact that we do not continue the harmonic curve and the subharmonic one beyond their intersection. In contrast to the gravitational modulation where the critical wave number decreases in the harmonic region [14], here the wave number increases from $q_c=3.12$ at $\Omega=100$ to $q_c=6.72$ at $\Omega=134$. In the subharmonic region q_c increases from $q_c=3.65$ at Ω_t to infinity for large Ω.

3.2 Rigid-Rigid Case. To solve the system (22)–(24) associated to equation (20) and subject to the boundary conditions (27), we seek a solution by means of a first order Galerkin method

$$w_1(z,t)=f(t)Z_1(z),\quad T_1(z,t)=g(t)Z_2(z),$$
$$\phi_1(z,t)=h(t)Z_3(z). \tag{46}$$

The trial functions $Z_1(z)$, $Z_2(z)$, and $Z_3(z)$ are given by

$$Z_1(z)=\left(z^2-\frac{1}{4}\right)^2,\quad Z_2(z)=\left(z^2-\frac{1}{4}\right)\left(\frac{5}{4}-z^2\right),$$
$$Z_3(z)=z\left(1-\frac{4(6\gamma+3q)}{3(6\gamma+q)}z^2\right). \tag{47}$$

Here, $\gamma=1+\chi_o$. The chosen trial functions satisfy the boundary conditions (25)–(27) and allow to minimize the errors derived by the first order Galerkin method. Indeed, $Z_1(z)$ and $Z_2(z)$, first used by Gershuni [17] in the ordinary Rayleigh-Bénard problem, represent a good approximation to determine the convection threshold. These functions lead to the critical gravitational Rayleigh number $Rg_c=1717.98$. The exact value given by Chandrasekhar [24] is 1707.8. The function $Z_3(z)$ is written in the spirit of $Z_1(z)$ and $Z_2(z)$.

Under these assumptions and applying the Galerkin method, one obtain a parametric differential equation similar to (30). The coefficients of such equation are

$$2c_1=\frac{306}{31}+q^2+\mathrm{Pr}\frac{q^4+24q^2+504}{12+q^2},\quad c_2=\frac{121q^2\mathrm{Pr}}{124(12+q^2)}$$

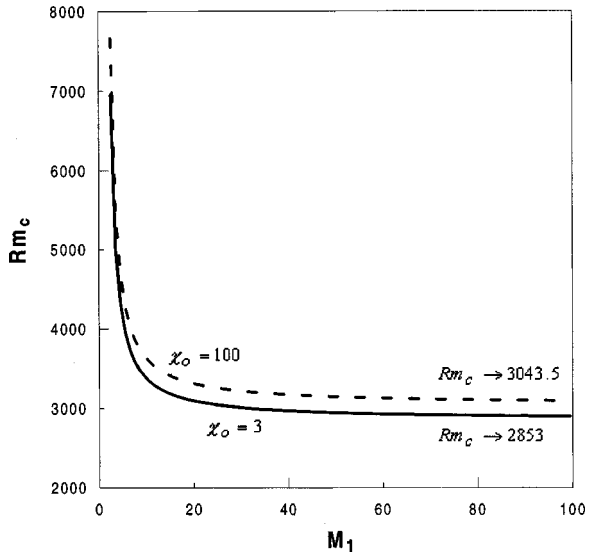

Fig. 2 Rigid-Rigid case: Stationary convection threshold of the unmodulated case: critical magnetic Rayleigh number, Rm_c, versus the ratio of the magnetic and gravitational forces, M_1. $\chi_o=3$ (solid line), $\chi_o=100$ (dashed line).

$$c_3=1-\frac{180(9\gamma+q)(34\gamma+3q)}{55[1008\gamma^2+588\gamma q+42q^2+102\gamma^2q^2+18\gamma q^3+q^4]}, \tag{48}$$

$$R_o(q)=4(504+24q^2+q^4)(306+31q^2)/121q^2.$$

The quantity $R_o(q)$ represents the gravitational Rayleigh number of the marginal stability curve for the classical Rayleigh-Bénard problem corresponding to the rigid-rigid case.

Analysis of Eq. (30), associated to the coefficients given by (48) and the ratio M_2 defined by Eqs. (34)–(35), is similar to the one detailed in the free-free case. In the present configuration, there is one more parameter to consider, i.e., the magnetic susceptibility χ_o appears in the differential Eq. (30).

3.2.1 Stationary Onset of Convection of the Unmodulated Case. In Fig. 2, we present the variation of the critical magnetic Rayleigh number Rm_c versus M_1 for $\chi_o=3$ and $\chi_o=100$. Remark that for the magnetic problem with no buoyancy ($M_1\gg1$), the critical magnetic Rayleigh and wave numbers tend to the asymptotic values: $Rm_c=2853$, $q_c=3.81$ for $\chi_o=3$ and $Rm_c=3043.5$, $q_c=3.95$ for $\chi_o=100$. For small values of M_1, the critical magnetic Rayleigh number tend to higher values and then we are in the presence of a stable equilibrium configuration.

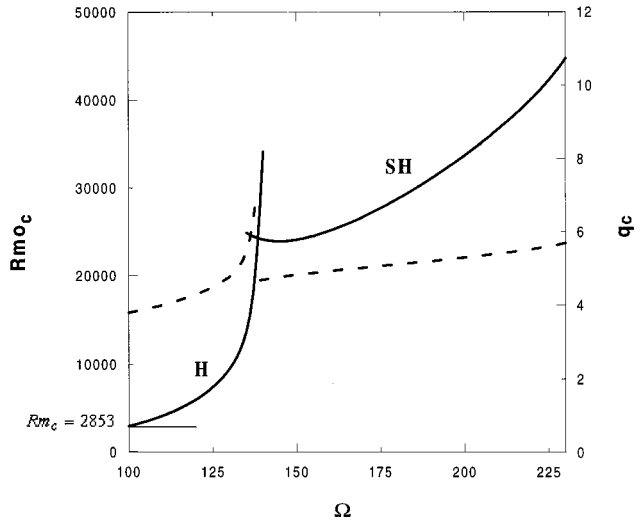

Fig. 3 Rigid-Rigid case: Critical magnetic Rayleigh number, Rmo_c, (solid line) and critical wave number, q_c, (dashed line) versus the dimensionless frequency, Ω, for $Pr=7$, $f_m=10^{-4}$ and $\chi_o=3$. *H*: harmonic solutions. SH: subharmonic solutions.

3.2.2 Parametric Convective Instability. In Fig. 3, the variation of the critical magnetic Rayleigh number and wave number is plotted for Pr=7, $\chi_o=3$, and $f_m=10^{-4}$. In this situation, the onset of convection corresponds to harmonic solutions for $\Omega<\Omega_t=139$ and subharmonic solutions for $\Omega>\Omega_t$. Near $\Omega=100$ where $Rmo\gg Rg$, the values of the critical magnetic Rayleigh number are larger than the one of the unmodulated case, $Rm_c=2853$ related to large values of $M_1=Rm/Rg$. Here, we are in the presence of a stabilizing effect. Finally, note that the stable equilibrium configuration corresponding to $M_1\approx1(Rm\approx Rg)$ in the unmodulated case may be destabilized in subharmonic mode by the magnetic modulation for large frequencies ($Rmo\approx Rg$).

Acknowledgments

The authors would like to thank the unknown referees for their remarks and suggestions which improved the work considerably.

Nomenclature

b = subscript; basic state
d = thickness of the fluid layer
$\mathbf{g}$ = gravitational acceleration
$\mathbf{H}$ = magnetic field in ferrofluid
$\mathbf{H}^{\mathbf{ext}}$ = external magnetic field
H^a = amplitude of the external magnetic field
H_o = uniform magnetic field
$\mathbf{k}$ = unit vector upward
$K=-(\partial M/\partial T)_{H_o,T_a}$ = pyromagnetic coefficient
$\mathbf{M}$ = magnetization
M_o = constant mean value of magnetization
M_1 = Rm/Rg
M_2 = Rmo/Rg
p = pressure
Pr = Prandtl number
q_x, q_y = dimensionless wave numbers on the x and y directions
q^2 = $q_x^2+q_y^2$
$Rg=-\rho_o\alpha g\beta d^4/\mu\kappa$ = gravitational Rayleigh number
Rm = magnetic Rayleigh number of the unmodulated case
$Rm(t)$ = modulated magnetic Rayleigh number
$Rmo=\dfrac{\mu_o\gamma_a^2\beta^2d^4H^{a^2}}{\mu k(1+\chi_o)^3}$ = static magnetic Rayleigh number
t = time
T = temperature
T_o = upper plate temperature
T_1 = lower plate temperature
$\mathbf{V}$ = velocity field
ν = kinematic viscosity
w = third component of the velocity
α = coefficient of thermal expansion
μ = dynamic viscosity
$\mu_o=4\pi10^{-7}$ = magnetic permeability of the vacuum
ρ = density
ρ_o = density at the ambient temperature
ϕ = scalar magnetic potential
κ = thermal diffusivity
$\chi=M/H$ = magnetic susceptibility
$\chi_r=(\partial M/\partial H)_{H_o,T_a}$ = differential magnetic susceptibility

$$\chi_o = M_o/H_o$$

ω = dimensional frequency of the magnetic field

$$\Omega = \frac{\omega d^2}{\kappa} = \text{dimensionless frequency}$$

$$\Delta = \frac{\partial^2}{\partial x^2} + \frac{\partial^2}{\partial y^2} + \frac{\partial^2}{\partial z^2}$$

$$\Delta_2 = \Delta - \frac{\partial^2}{\partial z^2}$$

References

[1] Berkovsky, B. M., 1978, *Thermomechanics of Magnetic Fluids: Theory and Applications*, Berkovsky Edition, Hemisphere, New York.

[2] Bashtovoy, V. G., Berkovsky, B. M., and Vislovich, A. N., 1988, *Introduction to Thermomechanics of Magnetic Fluids*, Berkovsky Edition, Hemisphere, New York.

[3] Finlayson, B. A., 1970, ''Convective Instability of Ferromagnetic Fluids,'' J. Fluid Mech., **40**, Part 4, pp. 753–767.

[4] Shwab, L., Hildebrandt, U., and Stierstadt, K., 1983, ''Magnetic Bénard Convection,'' J. Magn. Magn. Mater., **39**, p. 113.

[5] Stiles, P. J., and Kagan, M., 1990, ''Thermoconvective Instability of a Horizontal Layer of Ferrofluid in a Strong Vertical Magnetic Field,'' J. Magn. Magn. Mater., **85**, pp. 196–198.

[6] Rudraiah, N., and Sekhar, G. N., 1991, ''Convection on Magnetic Fluids With Internal Heat Generation,'' ASME J. Heat Transfer, **113**, pp. 122–127.

[7] Bashtovoy, V. G., and Berkovsky, B. M., 1973, ''Thermomechanics of Ferromagnetic Fluids,'' Magnitnaya Gidrodynamica, No. 3, pp. 3–14.

[8] Zaitsev, V. M., and Shliomis, M. I., 1968, ''The Hydrodynamics of a Ferromagnetic Fluid,'' J. Appl. Mech. Tech. Phys., **9**, No. 1, pp. 24–26.

[9] Polevikov, V. K., and Fertman, V. E., 1977, ''Investigation of Heat Transfer Through a Horizontal Layer of a Magnetic Liquid for the Cooling of Cylindrical Conductors With a Current,'' Magnetohydrodynamics (N.Y.), **13**, pp. 11–16.

[10] Zebib, A., 1996, ''Thermal Convection in Magnetic Fluid,'' J. Fluid Mech., **321**, pp. 121–136.

[11] Berkovsky, B. M., Fertman, V. E., Polevikov, V. K., and Isaev, S. V., 1976, ''Heat Transfer Across Vertical Ferrofluid Layers,'' Int. J. Heat Mass Transf., **19**, pp. 981–986.

[12] Aniss, S., Souhar, M., and Brancher, J. P., 1993, ''Thermal Convection In a Magnetic Fluid In an Annular Hele-Shaw Cell,'' J. Magn. Magn. Mater., **122**, pp. 319–322.

[13] Souhar, M., Aniss, S., and Brancher, J. P., 1999, ''Convection de Rayleigh-Bénard Dans les Liquides Magnétiques en Cellule de Hele-Shaw Annulaire,'' Int. J. Heat Mass Transf., **42**, pp. 61–72.

[14] Gresho, P. M., and Sani, R. L., 1970, ''The Effects of Gravity Modulation On The Stability of a Heated Fluid Layer,'' J. Fluid Mech., **40**, pp. 783–806.

[15] Biringen, S., and Peltier, L. J., 1990, ''Numerical Simulation of 3-D Bénard Convection With Gravitational Modulation,'' Phys. Fluids, **A2**, No. 5, pp. 754–764.

[16] Clever, R., Schubert, G., and Busse, F. H., 1993, ''Two-dimensional Oscillatory Convection In a Gravitationally Modulated Fluid Layer,'' J. Fluid Mech., **253**, pp. 663–680.

[17] Gershuni, G. Z., and Zhukhovitskii, E. M., 1976, *Convective Instability of Incompressible Fluid*, Keter Publisher, Jerusalem.

[18] Shliomis, M., Brancher J. P., and Souhar, M., 1995, ''Parametric Excitation in Magnetic Fluids Under a Time Periodic Magnetic Field,'' Proceeding of the Seventh conference on Magnetic Fluids, Bhavnagar, India.

[19] Aniss, S., Souhar, M., and Belhaq, M., 2000, ''Asymptotic Study of the Convective Parametric Instability in Hele-Shaw Cell,'' Phys. Fluids, **12**, (No. 2), pp. 262–268.

[20] Brancher, J. P., 1980, *Sur l'Hydrodynamique des Ferrofluides, Thèse D'état de l'INPL*, Nancy.

[21] Rosenweig, R. E., 1985, *Ferrohydrodynamics*, Cambridge University Press.

[22] Morse, P. M., and Feshbach, H., 1953, *Methods of Theoretical Physics*, Part I, Mc Graw-Hill, New York, pp. 556–563.

[23] Jordan, D. W., and Smith, P., 1987, *Non Linear Ordinary Differential Equations*, Oxford Clarendon Press, New York.

[24] Chandrasekhar S., 1961, *Hydrodynamic and Hydromagnetic Stability*, Oxford University Press, London.

Linear Stability of Mixed Convection Flow of Two Immiscible Fluids in a Vertical Annulus

Kai-Ti R. Chang
M. I. Systems,
1826 W. Broadway Rd. #B43,
Mesa, AZ 85202

Kang Ping Chen
Department of Mechanical and Aerospace Engineering,
Arizona State University,
Tempe, AZ 85287-6106

Linear stability of two immiscible liquids driven by a constant pressure gradient through a long vertical annulus in the gravitational field is investigated. If viscosity depends on temperature, it is found that thermal conductivity stratification can induce an interfacial instability, which is different from the instability identified by Yih (1986). The effect of temperature-dependent viscosity on various unstable modes and mode competitions are studied. [DOI: 10.1115/1.1370511]

Keywords: Analytical, Convection, Heat Transfer, Instability, Mixed Convection

Introduction

For multiple-fluid flows, interfacial instabilities can arise due to the difference in fluid properties such as density or viscosity. In lubricated pipelining, which is used to transport heavy crude oil by less viscous fluids, a stable interface is preferred to keep the lubrication effective. To have desirable optical and mechanical properties in the products manufactured by co-extrusion or thin film coating, interfacial instabilities have to be controlled. Better operation designs for these applications can be achieved through the understanding of interfacial instabilities.

Preziosi, Chen, and Joseph [1] investigated the linear stability of a core-annular flow (CAF) in a horizontal pipe with less viscous fluid located in an annulus surrounding the more viscous fluid. Viscosity stratification and surface tension effect were considered but gravity effect was excluded. Windows of parameters were identified for the stable core-annular flow which is free from capillary instability and shear instability. They showed that linear-stability theory can successfully predict the unstable flow regime and wavelength observed in the experiments by Charles, Grovier and Hodgson [2]. Chen, Bai, and Joseph [3] incorporated density stratification and gravity in a vertical CAF. They concluded that capillary instability can be stabilized by using heavy lubricants for down-flow and light lubricants for up-flow. Chen and Zhang [4] considered CAF of viscoelastic fluids. The inclusion of elasticity was found to have a stabilizing effect on the capillary instability at low Reynolds number. Comprehensive surveys of the stability problems for multiple fluid flows can be found in the monograph by Joseph and Renardy [5] and the review paper by Chen [6].

For lubricated pipelining, there are situations in which the temperature variation may not be ignored during the span of the operation. In the co-extrusion process, the flow can be non-isothermal. Therefore, thermal effects need to be considered. For non-isothermal multiple-fluid flows, Yih [7] first identified an interfacial instability caused by the thermal-conductivity stratification in two layers confined between inclined plates. For two-layer flows, Pinarbasi and Liakopoulos [8] considered temperature-dependent viscosity and studied the interfacial instability induced by viscosity stratification in plane Poiseuille flow. Pinarbasi and Liakopoulos [8], however, neglected temperature fluctuations. As a result, the only interfacial instability found in their work was induced by viscosity stratification, and the interfacial mode described in Yih [7] due to thermal-conductivity stratification did not appear.

In this paper, the linear stability of pressure-gradient-driven flow of two Newtonian fluids through a long vertical annulus is investigated. The temperatures of both the inner and the outer walls are fixed. When the viscosities of the fluids are considered as functions of temperature, thermal-conductivity stratification can induce an interfacial instability, which arises from the continuous shear-stress condition at the interface. This is in addition to the instability analyzed by Yih [7], which arises from the temperature continuity condition at the interface. It is also found that the stratification of the thermal expansion coefficient can induce an interfacial instability, even when the densities of the fluids are matched at the reference temperature. The effect of temperature-dependent viscosity on capillary, thermal and shear mode instabilities and mode competitions are also studied.

Formulation

Governing Equations. The non-isothermal annulus flow is modeled as incompressible and all the fluid properties, except density appearing in the gravity term in the momentum equation and viscosity, are temperature independent and are set to be constants at the reference temperature. The empirical equation used to relate viscosity and temperature is

$$\tilde{\mu}_i = A_i \tilde{\mu}_{i0} \exp(\tilde{B}_i / \tilde{T}_i). \tag{1}$$

In the gravity term, density is approximated by

$$\tilde{\rho}_i = \tilde{\rho}_{i0}(1 - \beta_i(\tilde{T}_i - \overline{T}_2)). \tag{2}$$

In Eq. (1) and (2) $i = 1,2$ are for inner and outer fluids. Surface tension σ at the interface is assumed to be a constant. The mean interface location $\tilde{R}_0$ is chosen as the length scale and the magnitude of the interfacial velocity $|\tilde{W}_{\text{int}}|$ is used as the velocity scale ($\tilde{U}_s$). $\tilde{R}_0/\tilde{U}_s$, $\tilde{\rho}_{i0}\tilde{U}_s^2$, $\tilde{\mu}_{i0}$ and $(\overline{T}_1 - \overline{T}_2)$ are the scales for time, pressure, viscosity and temperature respectively, where $\overline{T}_1$ and $\overline{T}_2$ are the inner-wall and outer-wall temperatures.

The dimensionless equations of conservation of mass, momentum and energy for both fluids in cylindrical coordinates (r, ϕ, z) are

$$\frac{\partial u}{\partial r} + \frac{u}{r} + \frac{1}{r}\frac{\partial v}{\partial \phi} + \frac{\partial w}{\partial z} = 0, \tag{3}$$

Contributed by the Heat Transfer Division for publication in the JOURNAL OF HEAT TRANSFER. Manuscript received by the Heat Transfer Division September 5, 2000; revision received January 20, 2001. Associate Editor: H. H. Bau.

$$\frac{Du}{Dt}-\frac{v^2}{r}=-\frac{\partial p}{\partial r}+\frac{\mu}{\mathrm{Re}}\left[\nabla^2 u-\frac{u}{r^2}-\frac{2}{r^2}\frac{\partial v}{\partial \phi}\right]+\frac{1}{\mathrm{Re}}\left[\frac{\partial \mu}{\partial r}\left(2\frac{\partial u}{\partial r}\right)+\frac{1}{r}\frac{\partial \mu}{\partial \phi}\left(\frac{\partial v}{\partial r}-\frac{v}{r}+\frac{1}{r}\frac{\partial u}{\partial \phi}\right)+\frac{\partial \mu}{\partial z}\left(\frac{\partial w}{\partial r}+\frac{\partial u}{\partial z}\right)\right], \quad (4)$$

$$\frac{Dv}{Dt}+\frac{uv}{r}=-\frac{1}{r}\frac{\partial p}{\partial \phi}+\frac{\mu}{\mathrm{Re}}\left[\nabla^2 v-\frac{v}{r^2}+\frac{2}{r^2}\frac{\partial u}{\partial \phi}\right]+\frac{1}{\mathrm{Re}}\left[\frac{\partial \mu}{\partial r}\left(\frac{\partial v}{\partial r}-\frac{v}{r}+\frac{1}{r}\frac{\partial u}{\partial \phi}\right)+\frac{1}{r}\frac{\partial \mu}{\partial \phi}\left(\frac{2}{r}\frac{\partial v}{\partial \phi}+\frac{2u}{r}\right)+\frac{\partial \mu}{\partial z}\left(\frac{\partial v}{\partial z}+\frac{1}{r}\frac{\partial w}{\partial \phi}\right)\right], \quad (5)$$

$$\frac{Dw}{Dt}=-\frac{\partial p}{\partial z}+\frac{\mathrm{Gr}}{\mathrm{Re}^2}\theta+\frac{\mu}{\mathrm{Re}}\nabla^2 w+\frac{1}{\mathrm{Re}}\left[\frac{\partial \mu}{\partial r}\left(\frac{\partial w}{\partial r}+\frac{\partial u}{\partial z}\right)+\frac{1}{r}\frac{\partial \mu}{\partial \phi}\left(\frac{\partial v}{\partial z}+\frac{1}{r}\frac{\partial w}{\partial \phi}\right)+\frac{\partial \mu}{\partial z}\left(2\frac{\partial w}{\partial z}\right)\right], \quad (6)$$

$$\frac{D\theta}{Dt}=\frac{1}{\mathrm{PrRe}}\nabla^2\theta, \quad (7)$$

where $\nabla^2=\partial^2/\partial r^2+(1/r)\partial/\partial r+(1/r)^2\partial^2/\partial\phi^2+\partial^2/\partial z^2$ is the Laplacian operator and D/Dt is the material derivative. At the inner and outer walls, no-slip/no-penetration and constant temperature conditions apply:

$$u_1=v_1=w_1=0, \quad \theta_1=1, \quad \text{at} \quad r=a, \quad (8a\text{–}d)$$

$$u_2=v_2=w_2=0, \quad \theta_2=0, \quad \text{at} \quad r=b. \quad (9a\text{–}d)$$

At the interface $r=R(\phi,z,t)$, the kinematic condition, continuity of velocities, balance of traction and continuity of temperature and heat flux are given by

$$u=\frac{\partial R}{\partial t}+\frac{v}{R}\frac{\partial R}{\partial \phi}+w\frac{\partial R}{\partial z}, \quad (10a)$$

$$[\![u]\!]=[\![v]\!]=[\![w]\!]=0, \quad (10b\text{–}d)$$

$$[\![\Sigma]\!]\cdot\hat{n}=\Gamma\frac{J}{\mathrm{Re}_1}\hat{n}, \quad (10e\text{–}g)$$

$$[\![\theta]\!]=0, \quad (10h)$$

$$[\![k\partial\theta/\partial n]\!]=0, \quad (10i)$$

where $[\![\ ]\!]=(\ )_1-(\ )_2$, Σ is the stress tensor, $\hat{n}$ is the unit outward normal vector pointing from fluid 1 to 2 at the interface and Γ is the mean curvature of the interface.

The Basic State. The basic state is a steady, axisymmetric and fully-developed axial flow with a perfect cylindrical interface. The system of equations for the basic state is

$$\frac{d^2\Theta}{dr^2}+\frac{1}{r}\frac{d\Theta}{dr}=0, \quad (11)$$

$$\mu_B\left[\frac{d^2W}{dr^2}+\frac{1}{r}\frac{dW}{dr}\right]+\left(\frac{d\mu_B}{dr}\right)\left(\frac{dW}{dr}\right)=\mathrm{Re}\,Q-\frac{\mathrm{Gr}}{\mathrm{Re}}\Theta, \quad (12)$$

$$\mu_B=A\exp\left[1\Big/\left(\Theta\frac{\Delta\tilde{T}}{\tilde{B}}+\frac{\tilde{T}_2}{\tilde{B}}\right)\right], \quad (13)$$

$$\Theta_1=1, \quad W_1=0, \quad \text{at} \quad r=a, \quad (14a\text{–}b)$$

$$\Theta_2=0, \quad W_2=0, \quad \text{at} \quad r=b, \quad (15a\text{–}b)$$

$$[\![W]\!]=0, \quad [\![m\mu_B dW/dr]\!]=0, \quad [\![\Theta]\!]=0, \quad [\![\kappa d\Theta/dr]\!]=0 \quad \text{at} \quad r=1, \quad (16a\text{–}d)$$

where

$$\frac{\frac{d\tilde{P}}{d\tilde{z}}+\tilde{\rho}_0 g}{\tilde{\rho}_0\tilde{U}_s^2/\tilde{R}_0}=Q, \quad (17)$$

and

$$Q_2=qQ_1. \quad (q=1 \ \text{ for } \ \tilde{\rho}_{10}=\tilde{\rho}_{20}). \quad (18)$$

Notice that Q_1, which is related to the basic-state pressure gradient, is not an independent parameter and is determined by velocity constraint.

For constant viscosity, basic state solution can be written in closed form (Chang [9]) and it is used as the starting point in the iteration process of solving the basic state.

The Linearized Disturbance Equations and the Normal Mode Equations. Three dimensional disturbances are considered in this study. Velocity, pressure, temperature, viscosity and interface position are perturbed and the disturbances are assumed infinitesimally small. Therefore, disturbance equations, boundary conditions and interfacial conditions can be linearized. For the interfacial conditions, a Taylor series expansion is carried out around $r=1$ and truncated to obtain the linearized disturbance equations.

The disturbances can be decomposed into normal modes:

$$\varphi'(r,\phi,z,t)=\hat{\varphi}(r)\exp[i\alpha(z-ct)+in\phi] \quad (19)$$

and

$$\delta'(\phi,z,t)=\hat{\delta}\exp[i\alpha(z-ct)+in\phi], \quad (20)$$

where φ' represents u, v, w, θ, p, and μ disturbances, δ' is the amplitude of the interface perturbation. The normal mode equations and the boundary conditions at the pipe walls can be obtained easily (listed in [9] but not given here due to space limit). At the interface,

$$\hat{u}=i\alpha(W-c)\hat{\delta}, \quad \text{at} \quad r=1, \quad (21)$$

$$[\![\hat{u}]\!]=[\![\hat{v}]\!]=0, \quad (22,23)$$

$$[\![\hat{w}]\!]+\left[\!\left[\frac{dW}{dr}\right]\!\right]\hat{\delta}=0, \quad (24)$$

$$-[\![m\,\mathrm{Re}\,\hat{p}]\!]+\left[\!\left[2m\mu_B\frac{d\hat{u}}{dr}\right]\!\right]=(1-\alpha^2-n^2)\frac{J}{\mathrm{Re}_1}\hat{\delta}, \quad (25)$$

$$\left[\!\left[m\left(\mu_B\left(\frac{d\hat{w}}{dr}+i\alpha\hat{u}\right)+\left(\frac{dW}{dr}\right)\hat{\mu}\right)\right]\!\right]+\left[\!\left[m\left(\mu_B\frac{d^2W}{dr^2}+\frac{d\mu_B}{dr}\frac{dW}{dr}\right)\right]\!\right]\hat{\delta}=0, \quad (26)$$

$$\left[\!\left[m\mu_B\left(\frac{d\hat{v}}{dr}-\hat{v}+in\hat{u}\right)\right]\!\right]=0, \quad (27)$$

$$[[\hat{\theta}]]+\left[\!\left[\frac{d\Theta}{dr}\right]\!\right]\hat{\delta}=0, \quad (28)$$

$$\left[\!\left[\kappa\frac{d\hat{\theta}}{dr}\right]\!\right]+\left[\!\left[\kappa\frac{d^2\Theta}{dr^2}\right]\!\right]\hat{\delta}=0. \quad (29)$$

Since viscosity is temperature-dependent, the perturbed viscosity can be related to the temperature disturbance:

$$\mu=\mu_B+\mu'=A\exp\left[1\Big/\left((\Theta+\theta')\frac{\Delta\tilde{T}}{\tilde{B}}+\frac{\tilde{T}_2}{\tilde{B}}\right)\right]. \quad (30)$$

After linearization, the viscosity change due to the temperature variation in the normal mode form becomes

$$\hat{\mu} = -\mu_B \frac{\Delta \tilde{T}}{\tilde{B}} \hat{\theta} \Bigg/ \left(\Theta \frac{\Delta \tilde{T}}{\tilde{B}} + \frac{\tilde{T}_2}{\tilde{B}} \right)^2. \tag{31}$$

In Eq. (28)

$$[\![d\Theta/dr]\!] \propto [\![k]\!] \tag{32}$$

when written in dimensional form. For temperature-dependent viscosities,

$$[\![dW/dr]\!] \propto (\mu_{1B} - m\mu_{2B}) \tag{33}$$

in Eq. (24). In Eq. (26),

$$[\![m(\mu_B d^2W/dr^2 + d\mu_B/dr dW/dr)]\!] \propto [\![\tilde{\rho}]\!] g \tag{34}$$

when written in dimensional form. Thus, stratifications in thermal conductivity, viscosity or density could cause interfacial instabilities. $[\![\tilde{\rho}]\!] \sim [\![\beta]\!]$ if the density of the fluids $\tilde{\rho}_{10}$ and $\tilde{\rho}_{20}$ are matched at the reference temperature. This implies that the discontinuity in the thermal expansion coefficient at the interface can also cause an interfacial instability even when there is no density stratification at the reference temperature. However, this mode of interfacial instability only showed little impact in Chang [9]. The jump term $[\![m\hat{\mu} dW/dr]\!]$ in Eq. (26) can bring in an additional stratification term due to the combination of thermal-conductivity stratification and variable viscosity. It is more clear when two fluids have the same temperature-dependent viscosity $\tilde{\mu}_1(\tilde{T}) = \tilde{\mu}_2(\tilde{T})$, but different thermal conductivity. From Eq. (31) and Eq. (28)

$$[\![m\hat{\mu} dW/dr]\!] \propto [\![\hat{\mu}]\!] \propto [\![\hat{\theta}]\!] \propto [\![d\Theta/dr]\!] \hat{\delta} \propto (\kappa - 1). \tag{35}$$

Therefore, thermal-conductivity stratification can induce interfacial instabilities not only through the temperature continuous condition in Eq. (28) but also through the shear-stress continuity condition in Eq. (26) when viscosity depends on temperature. Notice that this potential source of instability is not the same as the interfacial instability modified by thermal thinning/thickening of viscosity, although both originate from the temperature dependence of viscosity.

Numerical Method

Basic state temperatures Θ_1 and Θ_2 can be obtained analytically and are given as

$$\Theta_1 = (\kappa lnr - lnb)/(\kappa lna - lnb), \tag{36}$$

$$\Theta_2 = (lnr - lnb)/(\kappa lna - lnb). \tag{37}$$

After Θ_1 and Θ_2 as well as μ_{1B} and μ_{2B} are available, basic state velocities W_1 and W_2 are solved numerically with pseudospectral method employing Chebyshev polynomials as base functions ([9]).

For the normal mode equations, pseudospectral Chebyshev spectral method is applied and a generalized algebraic eigenvalue problem

$$\underline{\mathbf{A}}\ \underline{\mathbf{x}} = c\underline{\mathbf{B}}\ \underline{\mathbf{x}} \tag{38}$$

is formed. Both the Arnoldi method (Arnoldi [10] and Huang [11]) and the QZ algorithm are used to solve Eq. (38). Spurious eigenvalues appear in most of the computations and they can be identified by changing the number of collocation points for either one or both fluids, since the spurious eigenvalues do not converge. Convergence test is performed and used to determine the number of collocation points in fluid 1 and fluid 2. From the two most unstable eigenvalues displayed in Table 1 for the typical set of parameters, choosing $ncol1$ and $ncol2$ as 106 and 36 will be sufficient where $ncol1$ and $ncol2$ are the numbers of collocation points for fluid 1 and 2. Table 2 lists the thermal-physical properties of fluid 1, transformer oil, and fluid 2, water.

Table 1 Convergence test for transformer-oil/water system. ($a=0.01$, $b=1.1$, $n=0$, $\alpha=6.5$, $J=1669.6$, $\mathrm{Re}_1=350$, $\mathrm{Gr}_1/\mathrm{Re}_1=-1.25$, $\Delta\tilde{T}=-20$ K, $\tilde{T}_2=300$ K)

($ncol1$,$ncol2$)	two most unstable eigenvalues	
(76,66)	$0.471325 + 0.316069 \cdot 10^{-2} i$	$1.06847 - 0.998220 \cdot 10^{-3} i$
(96,86)	$0.471425 + 0.308834 \cdot 10^{-2} i$	$1.06847 - 0.998292 \cdot 10^{-3} i$
(116,106)	$0.471326 + 0.308287 \cdot 10^{-2} i$	$1.06847 - 0.998292 \cdot 10^{-3} i$
(106,36)	$0.471326 + 0.308358 \cdot 10^{-2} i$	$1.06847 - 0.998292 \cdot 10^{-3} i$
(106,26)	$0.471325 + 0.308364 \cdot 10^{-2} i$	$1.06847 - 0.998292 \cdot 10^{-3} i$

Table 2 Thermophysical properties of transformer oil and water from Incropera and DeWitt [14] and Vargaftik [15] (Reference temperature is chosen as 300 K and surface tension parameter $\sigma=0.045$ N/m is used).

Propertities	Transformer oil	Water
$\tilde{\mu}_0$ (N·s /m^2)	$0.15355 \cdot 10^{-1}$	$0.855 \cdot 10^{-3}$
A (1)	$0.28524 \cdot 10^{-5}$	$0.15589 \cdot 10^{-2}$
$\tilde{B}$ (K)	3830.23	1939.13
$\tilde{\rho}_0$ (Kg/m^3)	874.8	997.01
k (W/m K)	0.11017	0.613
β(K^{-1})	$0.68587 \cdot 10^{-5}$	$0.2761 \cdot 10^{-3}$
C_p (KJ/Kg K)	1.762	4.179

The results of Yao and Rogers [12] for the linear stability of non-isothermal mixed convection flow of a single fluid in a tall annulus can be used to validate the code. For a heated inner wall (Gr/Re>0) with Re=4000, Pr=0.71, $n=19$ (azimuthal wave number) and aspect ratio (defined as the ratio of inner wall radius to the gap between two walls) of 10, Yao and Rogers [12] reported that the critical condition for the onset of instability is $\alpha_c = 0.86$, $(\mathrm{Gr/Re})_c = 58.05$ and wave speed $c_r = 0.55$. The current code gives $\alpha_c = 0.8517$, $(\mathrm{Gr/Re})_c = 58.042$ and wave speed $c_r = 0.545$ when using the scalings of Yao and Rogers [12].

Yih [7] investigated the non-isothermal flow of two fluids with equal thickness down in an inclined channel. Only thermal-conductivity stratification is considered in his long-wavelength analysis which was further clarified by Smith [13]. We approximate the vertical channel using thin annulus, and our results compared favorably to the third significant digit with Yih [7] and Smith [13].

Pinarbasi and Liakopoulos [8] included the temperature-dependent viscosity in the linear stability analysis of plane Poiseuille flow with only viscosity and thermal-conductivity stratification in their transformer oil and water system. Although Pinarbasi and Liakopoulos [8] did not provide the tabulated data, neutral curves computed from our code show good agreement with Fig. 4(b) of their study ([9]).

Results

Physical parameters used in this study correspond to transformer-oil/water system. However, density of the two fluids at reference temperature is set equal to focus on the potential interfacial instability induced by viscosity and thermal conductivity stratification. The effect of density difference on vertical core-annular flow has been studied by Chen, Bai and Joseph [3]. Upflow with a length scale of $\tilde{R}_0 = 0.01m$ is investigated and the geometric parameters (a, b) are set as (0.01, 1.1) for the computations. Only thin annulus is considered in this study. In general, stability can only be achieved when the annulus is thin and less viscous (the ''thin layer effect''). In order to have a reasonable physical range for heating or cooling conditions, the dimensional quantity $\Delta\tilde{T}(K)$ is used to set up the parameters in the computations instead of assigning Gr directly.

Neutral stability curves for the most unstable capillary mode ($n=0$), thermal mode ($n=1$) and shear mode ($n=0$) are plotted in Fig. 1. The flow becomes unstable to capillary, thermal and

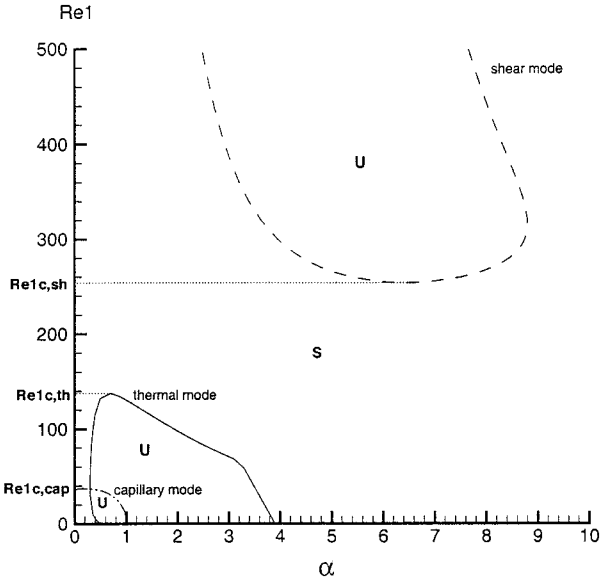

Fig. 1 Critical Re of capillary, thermal and shear modes. (*a* =0.01, *b*=1.1, transformer oil-water system with density matched, *J*=1669.6, $\Delta\tilde{T}$=20 K) *s*: stable; *u*: unstable.

shear modes when $\mathrm{Re}_1<\mathrm{Re}_{1c,cap}$, $\mathrm{Re}_1<\mathrm{Re}_{1c,th}$ and $\mathrm{Re}_1>\mathrm{Re}_{1,sh}$ respectively. $\mathrm{Re}_{1c,cap}$, $\mathrm{Re}_{1c,th}$, and $\mathrm{Re}_{1c,sh}$ are the maximum or minimum on the various branches of the neutral curves as shown in Fig. 1. The linear stability limit of the capillary mode $\mathrm{Re}_{\mathrm{cap}}$ is the critical Reynolds number $\mathrm{Re}_{1c,cap}$ for $n=0$. For thermal mode, the linear stability limit Re_{th}, is defined as

$$\mathrm{Re}_{th}=\max_n \mathrm{Re}_{1c,th},$$

and the linear stability limit of shear mode Re_{sh} is defined as

$$\mathrm{Re}_{sh}=\min_n \mathrm{Re}_{1c,sh}.$$

In the computations with this set of geometry and fluids, the axisymmetric ($n=0$) mode is found most unstable for the shear mode; $n=0$ and $n=1$ are the most unstable modes with heated inner wall ($\Delta\tilde{T}>0$) and cooled inner wall ($\Delta\tilde{T}<0$), respectively for the thermal mode.

The Effect of Temperature-Dependent Viscosity. The effect of temperature-dependent viscosity on critical Reynolds number for the capillary mode is listed in Table 3(*a*). Compared to the case of constant viscosity, the temperature dependence of viscosity shows little impact on $\mathrm{Re}_{\mathrm{cap}}$ (less than 10 percent) when the difference of the wall temperatures are $\Delta\tilde{T}=20$ K, 40 K and -20 K. However, $\mathrm{Re}_{\mathrm{cap}}$ changes substantially for $\Delta\tilde{T}=80$ K and -40 K. With cooled inner walls, the results of $\Delta\tilde{T}=-20$ K and -40 K indicate stabilization of the capillary mode when viscosity is modified from constant to temperature-dependent viscosity. With heated inner walls, temperature-dependent viscosity stabilizes the capillary mode for $\Delta\tilde{T}=20$ K and has a destabilizing effect for $\Delta\tilde{T}=40$ K and 80 K. When the temperature dependence of viscosity is considered, stronger heating of the inner wall further destabilizes the capillary mode since Re_{1c} increases as $\Delta\tilde{T}$ increases from 20 K to 40 K and 80 K. On the other hand, stronger cooling of the inner pipe wall further stabilizes the capillary mode as $\Delta\tilde{T}$ changes from -20 K to -40 K. α_c always increases when the temperature difference between pipe walls becomes larger.

For the shear mode, the effect of variable viscosity on the critical Reynolds number is displayed in Table 3(*b*). Comparisons of Re_{sh} between constant and temperature-dependent viscosity indicate that the change of Re_{sh} is less than 10 percent for $\Delta\tilde{T}=20$ K and 40 K. When $\Delta\tilde{T}=80$ K for a heated inner wall and $\Delta\tilde{T}=-20$ K for a cooled inner wall, the change of Re_{sh} is more than or equal to 10 percent and therefore this change is not negligible. For heated inner walls ($\Delta\tilde{T}>0$), decrease of viscosity with temperature destabilizes the shear mode since Re_{sh} decreases for temperature-dependent viscosity. On the other hand, increase of viscosity with temperature has a stabilizing effect on the shear mode with cooled inner wall ($\Delta\tilde{T}<0$). When the viscosity is temperature-dependent, more heating at the inner wall ($\Delta\tilde{T}>0, \Delta\tilde{T}\uparrow$) further decreases Re_{sh} while more cooling ($\Delta\tilde{T}<0, |\Delta\tilde{T}|\uparrow$) at the inner wall further increases Re_{sh}. The stabilization effect is particularly obvious when $\Delta\tilde{T}$ changes from -40 K to -80 K. The critical wave number, α_c, decreases when the temperature difference between the walls ($|\Delta\tilde{T}|$) becomes larger. This trend of decreasing α_c as $|\Delta\tilde{T}|$ increases is opposite to the capillary mode.

The influence of temperature-dependent viscosity on the critical Reynolds number for the thermal mode is given in Table 3(*c*). It is shown that when $\Delta\tilde{T}=20$ K and $\Delta\tilde{T}=-40$ K, the effect of temperature-dependent viscosity becomes important for the thermal mode. This is different from the capillary mode and the shear mode in the sense that the effect due to temperature variation of

Table 3 Effect of temperature-dependent viscosity on the capillary, shear and thermal modes (*a*=0.01, *b*=1.1, transformer oil-water system with density matched, *J*=1669.6); (*b*) shear mode ($\mathrm{Re}_{1c}=\mathrm{Re}_{sh}$); and (*c*) thermal mode ($\mathrm{Re}_{1c}=\mathrm{Re}_{th}$)

$\Delta\tilde{T}$ (K)	μ	n	α_c	Re_{1c}	Change of Re_{1c}(%)
			(a) capillary mode ($Re_{1c}=Re_{cap}$)		
20	$\mu(T)$	0	0.1586	37.221	-2.5
	constant μ		0.1270	38.191	
40	$\mu(T)$	0	0.4722	39.674	2.3
	constant μ		0.2022	38.791	
80	$\mu(T)$	0	0.5668	57.391	29
	constant μ		0.5054	44.547	
-20	$\mu(T)$	0	0.03	44.445	-0.76
	constant μ		0.03	44.785	
-40	$\mu(T)$	0	0.08923	41.521	-31
	constant μ		0.03	60.463	
			(b) shear mode ($Re_{1c}=Re_{sh}$)		
20	$\mu(T)$	0	6.354	250.80	-5.2
	constant μ		6.379	264.45	
40	$\mu(T)$	0	6.228	235.18	-8.1
	constant μ		6.367	256.02	
80	$\mu(T)$	0	5.825	212.52	-12
	constant μ		6.270	240.55	
-20	$\mu(T)$	0	6.156	311.81	10
	constant μ		6.334	282.96	
-40	$\mu(T)$	0	5.657	387.25	32
	constant μ		6.281	293.08	
-80	$\mu(T)$	0	4.614	862.28	174
	constant μ		6.133	314.96	
			(c) thermal mode ($Re_{1c}=Re_{th}$)		
20	$\mu(T)$	0	0.6623	137.94	88
	constant μ		0.9828	73.337	
40	$\mu(T)$	0	0.2072	472.34	202
	constant μ		0.5337	156.66	
-20	$\mu(T)$	1	0.3004	413.45	-1.0
	constant μ		0.3010	417.74	
-40	$\mu(T)$	1	0.1640	740.13	-14
	constant μ		0.1572	856.56	
-80	$\mu(T)$	1	0.2276	465.97	-73
	constant μ		0.08013	1731.7	

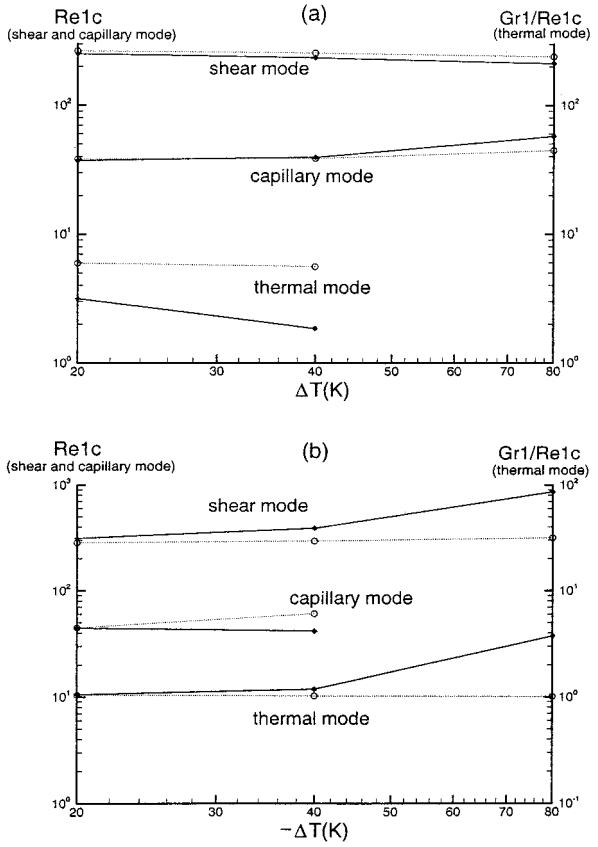

Fig. 2 Effect of temperature-dependent viscosity on the capillary, shear and thermal modes. (solid line: variable viscosity, dotted line: constant viscosity): (*a*) $\Delta\tilde{T}>0$, inner cylinder is hotter than the outer cylinder; and (*b*) $\Delta\tilde{T}<0$, inner cylinder is cooler than the outer cylinder.

viscosity is more significant for cooled inner walls ($\Delta\tilde{T}<0$) on these two modes. It is found that Re_{th} increases as stronger heating is applied to the inner wall ($\Delta\tilde{T}>0$, $\Delta\tilde{T}\uparrow$), but for a cold inner wall ($\Delta\tilde{T}<0$), Re_{th} increases and then decreases as $\Delta\tilde{T}$ changes from -20 K to -40 K and -80 K. Although the trend in the change of Re_{th} is not obvious in the case of $\Delta\tilde{T}<0$, it can be observed by using Gr/Re, the ratio of buoyancy to inertia, to analyze the thermal mode. $(\mathrm{Gr}_l/\mathrm{Re}_l)_{th}$ decreases as the heating of the inner wall intensifies ($\Delta\tilde{T}>0$, $|\Delta\tilde{T}|\uparrow$) and $|(\mathrm{Gr}_1/\mathrm{Re}_1)_{th}|$ increases as the cooling of the inner wall enhances ($\Delta\tilde{T}<0$, $|\Delta\tilde{T}|\uparrow$). Hence, the pattern of marginal stability boundary for thermal mode at $\Delta\tilde{T}<0$ is different from the pattern shown in Fig. 4 and 5 of Yao and Rogers [12] where $|(\mathrm{Gr}_1/\mathrm{Re}_1)_{th}|$ always decreases with $|\mathrm{Gr}_1|$. α_c decreases as $\Delta\tilde{T}$ changes from -20 K to -40 K and then increases as $\Delta\tilde{T}$ changes to -80 K. With $\Delta\tilde{T}>0$, α_c decreases as $\Delta\tilde{T}$ rises.

From Table 3 and Fig. 2(*a*), the effect of temperature-dependent viscosity is not negligible for the thermal, shear and capillary modes at $\Delta\tilde{T}=20$ K, 80 K, and 80 K, respectively. Therefore, the thermal mode is more sensitive to temperature-dependent viscosity than the capillary mode and the shear mode when the inner wall is heated. When the inner wall is cooled, the temperature dependence of viscosity for the shear, thermal and capillary modes is not negligible at $\Delta\tilde{T}=-20$ K, -40 K, and -40 K (Table 3 and Fig. 2(*b*)) indicating that the shear mode is more sensitive to temperature-dependent viscosity. Furthermore, when the temperature dependence of viscosity becomes important, it destabilizes/stabilizes all three modes for heated/cooled inner wall.

Table 4 Competition between the thermal mode and the capillary mode at low heating and low cooling

$\Delta\tilde{T}$ (K)	Re_{th}	Re_{cap}	Re_{L}
9	29.310	37.734	37.734
10	40.336	37.689	40.336
-4	23.704	39.179	39.179
-5	53.660	39.410	53.660

Competition Between Different Modes. Although the change of the linear stability limits Re_{th} and Re_{cap} may not be substantial enough at small $\Delta\tilde{T}$ to consider the temperature dependence of viscosity, more accurate modeling for viscosity like Eq. (1) is crucial in investigating mode competition. This is because a small change of linear stability limits by using different viscosity models can change the outcome of the dominant mode at certain flow and heating/cooling conditions.

At low Reynolds numbers, non-isothermal multi-fluid flows could become unstable to the thermal mode and/or capillary mode when Re_1 is smaller than Re_{cap} and/or Re_{th}. Because of the competition between the thermal mode and the capillary mode in non-isothermal flows, the lower bound of the linear stability limit is defined as

$$\mathrm{Re}_L=\max(\mathrm{Re}_{\mathrm{cap}},\mathrm{Re}_{th}),$$

the maximum of the linear stability limits of the capillary mode and the thermal mode. The flow is unstable to the capillary mode when $\mathrm{Re}_{th}<\mathrm{Re}_1<\mathrm{Re}_L=\mathrm{Re}_{cap}$ and becomes unstable to the thermal modes when $\mathrm{Re}_{cap}<\mathrm{Re}_1<\mathrm{Re}_L=\mathrm{Re}_{th}$. The flow is unstable to both capillary and thermal modes when $\mathrm{Re}_1<\min(\mathrm{Re}_{cap},\mathrm{Re}_{th})$, the minimum of the linear stability limits of the capillary mode and the thermal mode. Table 4 gives representative values of Re_{th}, Re_{cap} and Re_L. When $\Delta\tilde{T}=9$ K and $\Delta\tilde{T}=-4$ K, the capillary mode becomes unstable before the thermal mode as Re decreases and $\mathrm{Re}_L=\mathrm{Re}_{cap}$. However, when $\Delta\tilde{T}=10$ K and $\Delta\tilde{T}=-5$ K, thermal mode becomes unstable first and $\mathrm{Re}_L=\mathrm{Re}_{th}$. Therefore, the non-isothermal effect is important since a few degrees of cooling or heating at the inner wall, especially cooling, results in completely different physical phenomenon in which the thermal mode is dominant and cannot be neglected.

For a given $\Delta\tilde{T}$, the upper bound of the linear stability limit is the same as the linear stability limit of the shear mode, Re_{sh}. The flow is unstable to the shear mode when $\mathrm{Re}_l>\mathrm{Re}_U=\mathrm{Re}_{sh}$. In order to have stable flows which are free from the instabilities of the capillary, thermal and shear modes, Re_1 needs to be controlled so that

$$\mathrm{Re}_L<\mathrm{Re}_1<\mathrm{Re}_U. \tag{39}$$

Ideal operation conditions are searched to have complete stabilization with Eq. (39) satisfied at different heating and cooling conditions of the inner wall. When the inner wall is heated, Re_L increases and Re_U decreases as $|\Delta\tilde{T}|$ rises. From the neutral stability curves for the thermal and shear modes in Fig. 3, it is observed that the window for stable operation shrinks as $\Delta\tilde{T}=10$ K changes to $\Delta\tilde{T}=20$ K. At $\Delta\tilde{T}=40$ K and $\Delta\tilde{T}=80$ K, Eq. (39) is not satisfied and the flow becomes unstable. In Fig. 3(*d*) ($\Delta\tilde{T}=80$ K), two unstable regions representing the thermal mode and the shear mode merge. The neutral curves for the capillary mode are not displayed because $\mathrm{Re}_L=\mathrm{Re}_{th}$ except Fig. 3(*a*) in which the neutral curve for the capillary mode is also shown since Re_{cap} and Re_{th} are close ($\mathrm{Re}_{cap}<\mathrm{Re}_{th}=\mathrm{Re}_L$). When the inner wall is cooled, Re_U increases with $|\Delta\tilde{T}|$. Re_L increases as $\Delta\tilde{T}=-10$ K changes to $\Delta\tilde{T}=-20$ K and then to $\Delta\tilde{T}=-40$ K (see Fig. 4). As the inner wall is further cooled to $\Delta\tilde{T}=-80$ K, Re_L decreases. The neutral curves for the thermal mode and the shear mode show that Eq. (39) is satisfied for $\Delta\tilde{T}=-10$ K and -80 K,

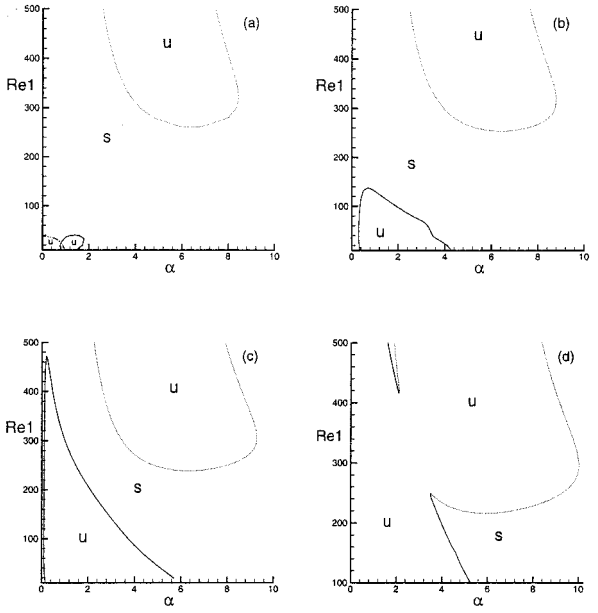

Fig. 3 Neutral curves of capillary, shear, and thermal modes with $\mu(T)$ at (*a*) $\Delta\tilde{T}=10$ K, (*b*) $\Delta\tilde{T}=20$ K, (*c*) $\Delta\tilde{T}=40$ K, and (*d*) $\Delta\tilde{T}=80$ K. (solid line: thermal mode, dotted line: shear mode, dash-dot-dot line: capillary mode; *s*: stable; *u*: unstable)

but is not satisfied for $\Delta\tilde{T}=-20$ K and -40 K. Comparing Fig. 4(*a*) and Fig. 4(*d*), the stable operation window of $\Delta\tilde{T}=-80$ K is larger than that of $\Delta\tilde{T}=-10$ K.

Therefore, there are two stable regions for a cooled inner wall ($\Delta\tilde{T}<0$) in the marginal stability boundary of the transformer oil and water system which is studied. When the inner wall is heated ($\Delta\tilde{T}>0$), there is only one completely stable operation region as shown in Yao and Rogers [12].

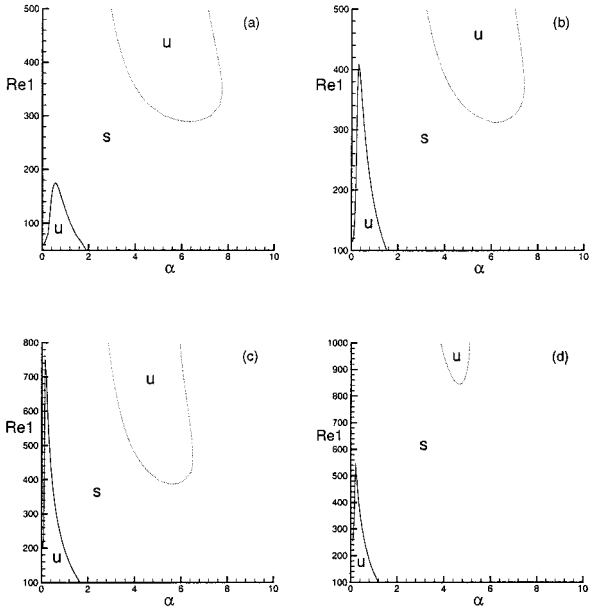

Fig. 4 Neutral curves of shear and thermal modes with $\mu(T)$ at (*a*) $\Delta\tilde{T}=-10$ K, (*b*) $\Delta\tilde{T}=-20$ K, (*c*) $\Delta\tilde{T}=-40$ K, and (*d*) $\Delta\tilde{T}=-80$ K. (solid line: thermal mode, dotted line: shear mode, *s*: stable, *u*: unstable)

Because there are many parameters and interactions involved, simple physical mechanisms for the results reported here are difficult to explain. However, physical insights can be gained by analyzing the energy budget for the disturbances. These energy analyses are given in Chang [9] and due to space limits they are not provided here.

Conclusion

For non-isothermal multiple-fluid flows, the interfacial instabilities induced by property jumps at the interface have been investigated. With temperature dependence of viscosity considered, thermal-conductivity stratification also induces an interfacial instability through shear-stress continuity condition.

From the change in the linear stability limits, temperature dependence of viscosity is not negligible for the capillary mode ($\Delta\tilde{T}=80$ K and $\Delta\tilde{T}=-40$ K), the shear mode ($\Delta\tilde{T}=80$ K and $\Delta\tilde{T}=-20$ K), and the thermal mode ($\Delta\tilde{T}=20$ K and $\Delta\tilde{T}=-40$ K). Shear mode is more sensitive to temperature-dependent viscosity than thermal and capillary modes when the inner wall is cooled. On another hand, thermal mode is more sensitive to temperature-dependent viscosity than shear and capillary modes when the inner wall is heated. As the temperature dependence of viscosity becomes important and cannot be neglected, viscosity change destabilizes all three modes when the inner wall is heated ($\Delta\tilde{T}>0$), and stabilizes all three modes when the inner wall is cooled ($\Delta\tilde{T}<0$). For temperature-dependent viscosity, the thermal mode dominates the capillary mode as long as the heating or cooling at the inner wall exceeds $|\Delta\tilde{T}|=10$ K. The neutral curves show that a region for stable operation ($\mathrm{Re}_L<\mathrm{Re}_1<\mathrm{Re}_U$) with a hot inner wall is possible at small temperature difference $\Delta\tilde{T}=10$ K and 20 K, but disappears at large temperature difference $\Delta\tilde{T}=40$ K and 80 K. For a cold inner wall, a stable region exists at -10 K but disappears at $\Delta\tilde{T}=-20$ K and -40 K. However, an ideal operating region becomes possible again at $\Delta\tilde{T}=-80$ K.

Nomenclature

$A,\tilde{B}$ = constants appeared in the empirical equation for viscosity $\tilde{\mu}=A\tilde{\mu}_0\exp[\tilde{B}/\tilde{T}]$
a = geometry parameter for inner wall $=\tilde{R}_1/\tilde{R}_0$
b = geometry parameter for outer wall $=\tilde{R}_2/\tilde{R}_0$
c = complex wave speed
Gr = Grashof number $=\beta g\tilde{R}_0^3(\overline{T_1}-\overline{T_2})/\nu_0^2$
J = Surface tension parameter $=\sigma\tilde{R}_0/\nu_{10}^2\tilde{\rho}_{10}$
m = viscosity ratio $=\tilde{\mu}_{20}/\tilde{\mu}_{10}$
n = integer azimuthal wave number
Pr = Prandtl number $=\nu/(k/\rho c_p)$
p = dimensionless pressure $=(\tilde{p}+\tilde{\rho}_0 g\tilde{z})/(\tilde{\rho}_0\tilde{U}_s^2)$
Q = $\tilde{R}_0(d\tilde{p}/d\tilde{z}+\tilde{\rho}_0 g)/(\tilde{\rho}_0\tilde{U}_s^2)$
q = Q_2/Q_1
$\tilde{R}_0$ = length scale=mean interface location
Re = Reynolds number $=\tilde{\rho}_0\tilde{U}_s\tilde{R}/\tilde{\mu}_0$
$\overline{T_2}$ = reference temperature=outer wall temperature
$\tilde{U}_s$ = velocity scale $=|\tilde{W}_{\mathrm{int}}|$ absolute interfacial velocity
u, v, w = radial, azimuthal and axial velocity

Greek Letters

α = axial wave number
β = thermal expansion coefficient
$\Delta\tilde{T}$ = basic state temperature difference between inner and outer cylinders $=\overline{T_1}-\overline{T_2}$
κ = ratio of thermal conductivity $=k_2/k_1$
$\tilde{\mu}$ = viscosity $=A\tilde{\mu}_0\exp[\tilde{B}/\tilde{T}]$
$\tilde{\rho}$ = density $=\rho_0[1-\beta(\tilde{T}-\overline{T_2})]$
σ = surface tension parameter
θ = dimensionless temperature $=(\tilde{T}-\overline{T_2})/(\overline{T_1}-\overline{T_2})$

Subscripts

0 = reference state at $\overline{T}_2$
1, 2 = inner wall/fluid and outer wall/fluid

References

[1] Preziosi, L., Chen, K., and Joseph, D. D., 1989, ''Lubricated Pipelining: Stability of Core-Annular Flow,'' J. Fluid Mech., **201**, pp. 323–356.
[2] Charles, M. E., Govier, G. W., and Hodgson, G. W., 1961, ''The Horizontal Pipeline Flow of Equal Density Oil-Water Mixtures,'' Can. J. Chem. Eng., **39**, pp. 27–36.
[3] Chen, K., Bai, R., and Joseph, D. D., 1990, ''Lubricated Pipelining. Part 3 Stability of Core-Annular Flow in Vertical Pipes,'' J. Fluid Mech., **214**, pp. 251–286.
[4] Chen, K., and Zhang, Y., 1993, ''Stability of the Interface in Co-Extrusion Flow of Two Viscoelastic Fluids through a Pipe,'' J. Fluid Mech., **247**, pp. 489–502.
[5] Joseph, D. D., and Renardy, Y., 1992, *Fundamentals of Two-Fluid Dynamics I, II*, Springer-Verlag, New York.
[6] Chen, K., 1995, ''Interfacial Instabilities in Stratified Shear Flows Involving Multiple Viscous and Viscoelastic Fluids,'' Appl. Mech. Rev., **48**, pp. 763–776.
[7] Yih, C. S., 1986, ''Instability Resulting from Stratification in Thermal Conductivity,'' Phys. Fluids, **29**, pp. 1769–1773.
[8] Pinarbasi, A., and Liakopoulos, A., 1995, ''The Effect of Variable Viscosity on the Interfacial Stability of Two-Layer Poiseuille Flow,'' Phys. Fluids, **7**, pp. 1318–1324.
[9] Chang, K.-T., 1998, ''Linear Stability Theory of Mixed Convection Flow for Two Immiscible Fluids in a Vertical Annulus,'' Ph.D. dissertation, Arizona State University, Tempe, AZ.
[10] Arnoldi, W. E., 1951, ''The Principle of Minimized Iterations in the Solution of the Matrix Eigenvalue Problem,'' Quarterly Appl. Math., **214**, pp. 17–29.
[11] Huang, A., 1993, private communication.
[12] Yao, L. S., and Rogers, B. B., 1989, ''The Linear Stability of Mixed Convection in a Vertical Annulus,'' J. Fluid Mech., **201**, pp. 279–298.
[13] Smith, M. K., 1995, ''The Long-Wave Interfacial Instability of Two Liquid Layers Stratified by Thermal Conductivity in an Inclined Channel,'' Phys. Fluids, **7**, pp. 3000–3012.
[14] Incropera, F. P., and DeWitt, D. P., 1985, *Introduction to Heat Transfer*, John Wiley & Sons, New York.
[15] Vargaftik, N. B., 1975, *Tables on the Thermophysical Physical Properties of Liquids and Gases*, 2nd ed., Hemisphere, Washington, D.C.

Effect of Partition Wall on Natural Convection Heat Transfer in a Vertical Air Layer

Yoshiyuki Yamaguchi
e-mail: yoshi@ecomp.metro-u.ac.jp

Yutaka Asako

Department of Mechanical Engineering,
Tokyo Metropolitan University,
1-1, Minami-Osawa, Hachioji,
Tokyo, 192-0397 Japan

Three-dimensional natural convection heat transfer characteristics in a vertical air layer partitioned into cubical enclosures by partition walls of finite thermal conductivity and finite thickness were obtained numerically. The air layer is differentially heated from each surface. In this work, the analyses were performed using finite thickness and finite conductivity of the partition wall for $Ra=10^4$ and 10^5, and for wide range of the thickness and the conductivity of the partition wall. The results were presented in the form of overall convection and total heat transfer coefficient. From the comparison of the results with the traditional ideal boundary conditions such as ''conduction,'' ''adiabatic,'' and ''no-thickness,'' the correlation of the heat transfer with the actual partition wall and the ideal boundary conditions were developed. After examinations of the results, it was shown that the proportion of the heat transfer quantity in the partition wall to the total heat transfer quantity from the hot wall is a function of a product of the thermal conductivity and the thickness of the partition wall. [DOI: 10.1115/1.1370515]

Keywords: Cavities, Conduction, Heat Transfer, Natural Convection, Three-dimensional

Introduction

The aim of this paper is to develop the relationship between heat conduction through a partition wall with overall heat transfer through a vertical air layer partitioned into cubical enclosures. Such an air layer is often seen in a lightweight panel for architecture, for example, a door panel and so on. Measurement of heat transfer through the lightweight panel had been reported by Cane et al. [1]. Moreover, Meyer et al. [2] measured two-dimensional natural convection heat transfer in an air layer partitioned into rectangular enclosures using a Mach-Zehnder interferometer. And Nakamura et al. [3] also measured the heat transfer using by Schlieren method. However, the Cane's experiment was on the overall heat transfer and the Meyer's and Nakamura's measurements were on the natural convection. They didn't discuss the amount of heat conduction through the partition wall, since it was difficult to measure the natural convection in the air layer and the heat conduction through the partition wall at one time. Therefore, it seems that numerical investigation is the best way to discuss the problem on the relationship between heat conduction through the partition wall and the overall heat transfer through the air layer.

A numerous numerical investigations have been conducted on two-dimensional natural convection in a rectangular enclosure. However, in many cases, the treatments of the thermal condition of the partition walls were assumed to be adiabatic or to be a good thermal conductor and thick. These thermal boundary conditions enable us to consider only the fluid domain. Ostrach [4] published an explanation on natural convection in an enclosure. But, the limitation of these ideal boundary conditions are not clear. Later, another ideal boundary condition was discussed by Asako et al. [5]. This condition is called ''no-thickness'' boundary condition and it exists when the partition wall is negligibly thin. On the other hand, some studies treated the partition walls of finite thickness and finite thermal conductivity, for examples, ElSherbiny et al. [6] and Kim et al. [7]. However, these partition walls were very thick, whose thickness was equivalent to the width of the cavity. Though ElSherbiny et al. reported that the convection heat transfer in the cavity of aspect ratio of $H/L=5$ becomes insensitive to the wall thickness when the wall thickness excesses $0.75L$, the heat transfer characteristic as the wall is thin was not described. Kim et al. carried out numerical analysis and experiment of the heat transfer on the case in which the wall of finite thickness was used in not only top and bottom but also hot and cold wall. In this paper, the case of the aspect ratio of $H/L=1$ was reported, and the wall thickness was from $0.25L$ to $0.5L$. On the other hand, an actual thermal insulation board has large cavity, and its partition walls are thin but can not be considered negligibly thin.

Another model for this problem has been used for natural convection in a two-dimensional rectangular cavity. This model was developed in an inclined air layer by Meyer et al. [8] and applied to a vertical air layer by Okada et al. [9]. This model employed an assumption that both surfaces of a partition wall are same but heat is transferred through a partition wall. Using this assumption, a single parameter of the thermal boundary condition appears as the product of the thermal conductivity and the thickness of the partition wall. However, this model needed an assumption that both surfaces of a partition wall were same but heat was transferred through a partition wall. This model is also a semi-ideal boundary condition, and the limitation of using on an actual condition is also not clear.

Lately, great progress in computer enable us to solve three-dimensional natural convection problem. Fusegi et al. [10] did numerical investigation on three-dimensional natural convection in a cubical enclosure. However, their boundary condition was used a constant thermal conductance everywhere on the side wall, and empirical value was used in the thermal conductance. The relationship between thermal conductance and thickness of actual wall was not mentioned in this paper. No three-dimensional analysis has been reported which addressed the relationship between heat conduction through a partition wall and overall heat transfer through the air layer.

Therefore, we need to know the effect of the thermal conductivity and the thickness of the partition wall on the average Nusselt number and the non-dimensional heat transfer from the hot wall to the partition wall. This is the motivation of this study.

The numerical methodology of this study was based on the

Contributed by the Heat Transfer Division for publication in the JOURNAL OF HEAT TRANSFER. Manuscript received by the Heat Transfer Division February 1, 2000; revision received January 5, 2001. Associate Editor: F. Cheung.

finite volume method. However the calculation domain includes both the air layer and the partition wall, the analyses were done in a single analytical domain. The calculations were carried out for the Rayleigh number of 10^4 and 10^5, varying the thermal conductivity and thickness of the partition wall. The effect of these three parameters on the average Nusselt number and the nondimensional heat transfer from the hot wall to the partition wall were clarified.

In this study, we discovered that the proportion of the heat transfer into the partition walls from the hot wall to the total heat transfer from the hot wall is a function of the product of the thermal conductivity and the thickness of the partition wall. This relation was valid in a wide range of the parameters. However, the effect of thermal conditions of the partition wall on the natural convection can not be expressed by a single parameter of the product of the conductivity and the thickness of the partition walls.

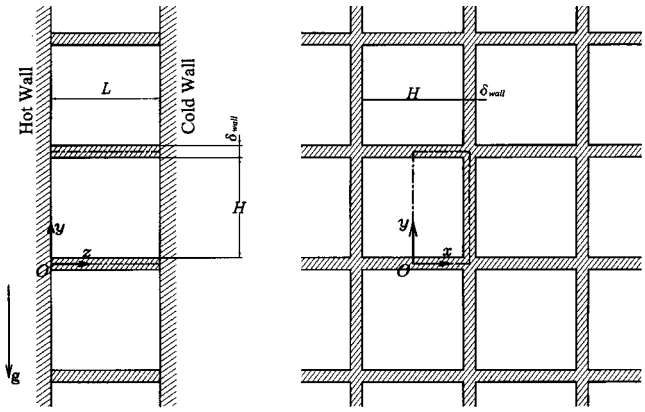

Fig. 2 The calculation domain and coordinates

Formulation

Description of the Problem. The problem considered in this study is schematically depicted in Fig. 1. It involves the determination of three-dimensional natural convection in a vertical air layer partitioned into cubical enclosures by partition walls of finite thermal conductivity and finite thickness. If the air layer is very long and wide in both vertical and horizontal directions, the velocity and temperature fields repeat themselves in successive enclosures, except at the end boundaries of the layer. Therefore, it is possible to solve the problem in only one rectangular enclosure. To investigate the velocity and temperature fields in such an enclosure, the following assumptions are made:

(i) the two end walls are kept at uniform temperatures t_H and t_C
(ii) the convection is laminar
(iii) constant thermophysical properties are assumed, except for the density in the buoyancy force term

Besides, radiation is not considered in this study.

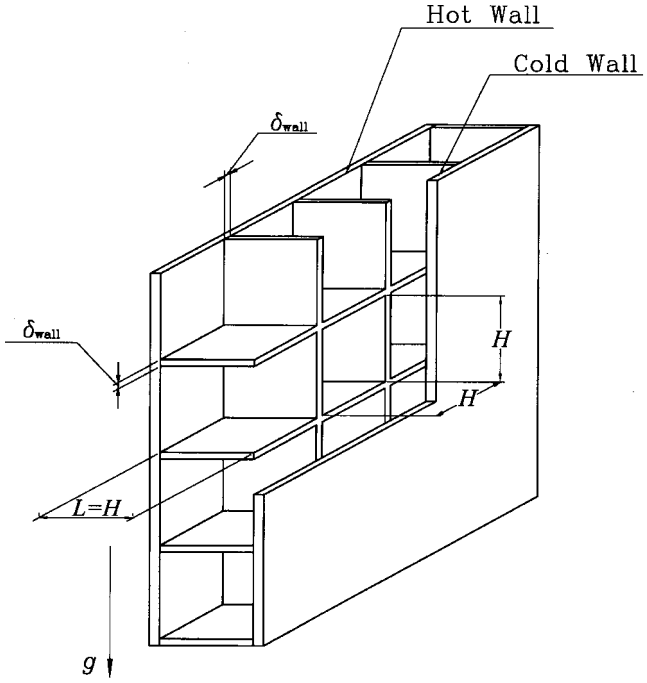

Fig. 1 Schematic diagram of a vertical air slot with a latticed partition wall

Conservation Equations. The governing equations are the continuity, momentum, and energy equations. Coordinates are defined as represented in Fig. 2. Taking the reference length to be L and the reference temperature to be $t_H - t_C$, the following dimensionless variables are used:

$$X=\frac{x}{L}, \quad Y=\frac{y}{L},$$

$$Z=\frac{z}{L}, \quad U=\frac{u}{\nu/L},$$

$$V=\frac{\nu}{\nu/L}, \quad W=\frac{w}{\nu/L}, \tag{1}$$

$$P=\frac{p}{\rho(\nu/L)^2}, \quad T=\frac{t-t_m}{t_H-t_C},$$

$$\mathrm{Ra}=\frac{g\beta L^3(t_H-t_C)}{\nu^2}, \tag{2}$$

where t_m is the average temperature of end walls and is expressed as

$$t_m=\frac{t_H+t_C}{2}. \tag{3}$$

The solution domain, with the assumption of symmetry, is confined to the right half of the enclosure. Then, upon the introduction of dimensionless variables and parameters, the governing equations for steady natural convection in the enclosure take the following forms:

$$\text{at} \quad 0<X<\frac{H}{2L} \quad \text{and} \quad \frac{\delta_{\text{wall}}}{2L}<Y<\frac{\delta_{\text{wall}}}{2L}+\frac{H}{L} \quad \text{and} \quad 0<Z<1; \tag{4}$$

$$\frac{\partial U}{\partial X}+\frac{\partial V}{\partial Y}+\frac{\partial W}{\partial Z}=0, \tag{5}$$

$$U\frac{\partial U}{\partial X}+V\frac{\partial U}{\partial Y}+W\frac{\partial U}{\partial Z}=-\frac{\partial P}{\partial X}+\nabla^2 U, \tag{6}$$

$$U\frac{\partial V}{\partial x}+V\frac{\partial V}{\partial Y}+W\frac{\partial V}{\partial Z}=-\frac{\partial P}{\partial Y}+\nabla^2 V+\frac{\mathrm{Ra}}{\mathrm{Pr}}T, \tag{7}$$

$$U\frac{\partial W}{\partial X}+V\frac{\partial W}{\partial Y}+W\frac{\partial W}{\partial Z}=-\frac{\partial P}{\partial Z}+\nabla^2 W, \tag{8}$$

$$U\frac{\partial T}{\partial X}+V\frac{\partial T}{\partial Y}+W\frac{\partial T}{\partial Z}=\frac{1}{\mathrm{Pr}}\nabla^2 T, \tag{9}$$

where

$$\nabla^2 = \frac{\partial^2}{\partial X^2} + \frac{\partial^2}{\partial Y^2} + \frac{\partial^2}{\partial Z^2}, \tag{10}$$

and

$$\mathrm{Pr} = \frac{\nu}{a}. \tag{11}$$

On the other hand, conduction is the only mechanism of heat transfer in the partition wall. Therefore the governing equations for the partition walls take the following forms:

$$\text{at} \quad \frac{H}{2L} < X < \frac{H+\delta_{\mathrm{wall}}}{2L} \quad \text{or} \quad 0 < Y < \frac{\delta_{\mathrm{wall}}}{2L} \quad \text{or}$$

$$\frac{\delta_{\mathrm{wall}}}{2L} + \frac{H}{L} < Y < \frac{\delta_{\mathrm{wall}}}{L} + \frac{H}{L}; \tag{12}$$

$$U = V = W = 0, \tag{13}$$

$$\frac{k_{\mathrm{wall}}}{k_{\mathrm{air}}} \nabla^2 T = 0. \tag{14}$$

In this study, the boundary of the solution domain is chosen at the center of the thickness of the partition wall.

Boundary Conditions. On the hot and cold walls and on the vertical symmetry plane, the boundary conditions are expressed in the following forms:

$$\text{on the hot wall:} \quad Z = 0; \quad U = V = W = 0 \quad \text{and} \quad T = 0.5. \tag{15}$$

$$\text{on the cold wall:} \quad Z = 1; \quad U = V = W = 0 \quad \text{and} \quad T = -0.5. \tag{16}$$

$$\text{on the vertical symmetry plane:} \quad X = 0;$$

$$U = \frac{\partial V}{\partial X} = \frac{\partial W}{\partial X} = 0 \quad \text{and} \quad \frac{\partial T}{\partial x} = 0. \tag{17}$$

As mentioned earlier, the temperature fields repeat themselves in successive enclosures because the air layer is assumed to be very long and wide in both vertical and horizontal directions. Therefore, the thermal boundary conditions at the top, bottom and side boundaries are expressed in the following forms:

$$\text{on the right side boundary:} \quad X = \frac{H+\delta_{\mathrm{wall}}}{2L}; \quad \frac{\partial T}{\partial X} = 0. \tag{18}$$

$$\text{on the bottom and top boundary:} \quad Y = 0 \quad \text{and} \quad Y = \frac{H+\delta_{\mathrm{wall}}}{L};$$

$$\left(\frac{\partial T}{\partial X}\right)_{Y=0} = -\left(\frac{\partial T}{\partial X}\right)_{Y=(H+\delta_{\mathrm{wall}})/L}. \tag{19}$$

Numerical Solutions. The discretization of the equations was based on the power-law scheme of Patankar [11], and the discretized equations were solved using a line-by-line method. The pressure and velocities were linked by the SIMPLE algorithm which had been developed by Patankar [12].

When a panel with partition walls is used for architecture like a door panel, the width of the panel is generally less than 30 mm. Then, in case of $L = 30 \times 10^{-3}$ m, $t_H - t_C = 40$ K and $t_m = 320$ K, the Rayleigh number of the air layer, Ra, is 10^5 (the kinetics viscosity of air, υ, is 18×10^{-3} m^2/s for $t = 300$ K and $p = 0.1$ MPa). Such structure of the panel is also seen in a body of an airplane or racing car that is required lightweight. In case of this, the width of the panel is between 5 to 10 mm, and the Ra is generally less than 10^5. If the thickness of the air layer is fixed at $L = 30$ mm, the value of δ_{wall}/L is 0.1 for $\delta_{\mathrm{wall}} = 3$ mm, and 0.01 for $\delta_{\mathrm{wall}} = 0.3$ mm. The actual parameter of δ_{wall}/L is in the range from 0.01 to 0.1. On the other hand, $k_{\mathrm{wall}}/k_{\mathrm{air}}$ is in the range from 5×10^2 to 4×10^3 for a good conductor as metal and in the range from 2 to 30 for a poor conductor as wood because the thermal conductivity of air is about 0.03 W/(m·K).

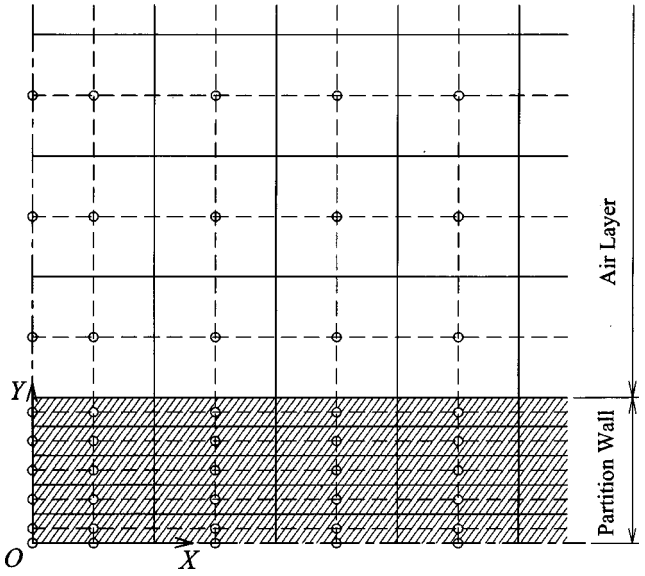

Fig. 3 Main grid points near the partition wall

Therefore, the numerical solutions were obtained for seven values of the dimensionless wall thickness ($\delta_{\mathrm{wall}}/L = 10^{-1}$, 6×10^{-2}, 2.5×10^{-2}, 10^{-2}, 6×10^{-3}, 2.5×10^{-3}, 10^{-3}) and seven values of the dimensionless wall conductivity ($k_{\mathrm{wall}}/k_{\mathrm{air}} = 1$, 3, 10, 30, 10^2, 3×10^2, 10^3). However, the Rayleigh number was limited to two values ($\mathrm{Ra} = 10^4$, 10^5), and Prandtl number, Pr and aspect ratio, H/L were fixed of $\mathrm{Pr} = 0.7$ and $H/L = 1$, in order to mainly examine the effect of thermal property of the partition wall on the heat transfer characteristic. The computations were performed with $(21 \times 40 \times 30)$ and $(21 \times 50 \times 40)$ for $\mathrm{Ra} = 10^4$ and 10^5, respectively. Inside the partition walls, five control volumes were set for the normal direction to the surfaces. Since stagger grid is employed under the SIMPLE algorithm, grid points are also placed on the surface of the solution domain. Therefore, the numbers of main grid points in the fluid region were $(14 \times 28 \times 28)$ and $(14 \times 38 \times 38)$ for $\mathrm{Ra} = 10^4$ and 10^5, respectively. This distribution of these grid points near the partition wall is depicted in Fig. 3.

Supplementary runs for $\delta_{\mathrm{wall}}/L = 10^{-2}$ and $k_{\mathrm{wall}}/k_{\mathrm{air}} = 10$ were performed to investigate the grid size effects. The comparison of the Nusselt number is listed in Table 1. The difference in Nusselt number between the coarse mesh $(17 \times 32 \times 22)$ and the fine mesh $(21 \times 40 \times 30)$ is 0.78 percent for $\mathrm{Ra} = 10^4$, and between the fine mesh $(21 \times 40 \times 30)$ and the very fine mesh $(21 \times 50 \times 40)$ is 1.46

Table 1 Effect of grid size on average Nusselt number for $\delta_{\mathrm{wall}}/L = 10^{-2}$ and for $k_{\mathrm{wall}}/k_{\mathrm{air}} = 10$

Mesh	(Grid points)	Nu_m	
		$Ra = 10^4$	$Ra = 10^5$
Coarse	$(17 \times 32 \times 22)$	1.678	3.59
Fine	$(21 \times 40 \times 30)$	1.665	3.47
Very Fine	$(21 \times 50 \times 40)$	1.658	3.42

percent for $Ra=10^5$. Thus, (21×40×30) and (21×50×40) grid points, respectively, were selected for $Ra=10^4$ and 10^5 to maintain relatively moderate computing costs.

The convergence criterion used was that the value of the mass flux residuals divided by the total mass flow in each control volume takes a value below 10^{-8}. The under-relaxation factors for velocity, pressure and temperature were set to 0.5, 0.8, and 1.0, respectively.

Heat Transfer Rate and Nusselt Number. Non-dimensional convection heat transfer rate form the hot wall, Q_{conv} is described as:

$$Q_{conv}=-2\int_{\delta_{wall}/2L}^{\delta_{wall/2L}+H/L}\int_0^{H/2L}\left(\frac{\partial T}{\partial Z}\right)dXdY. \tag{20}$$

Using the Q_{conv}, an average Nusselt number on the hot wall is defined as

$$Nu_m=\frac{Q_{conv}}{A_H}, \tag{21}$$

where

$$A_H=\left(\frac{H}{L}\right)^2. \tag{22}$$

To investigate the total heat transfer from the hot wall, non-dimensional total heat transfer rate form the hot wall, Q_{total} is calculated as below:

$$Q_{total}=-2\int_0^{(H+\delta_{wall})/L}\int_0^{(H+\delta_{wall})/2L}\overline{k}\left(\frac{\partial T}{\partial Z}\right)dXdY, \tag{23}$$

where, $\overline{k}$ is the non-dimensional thermal conductivity which is described as:

at

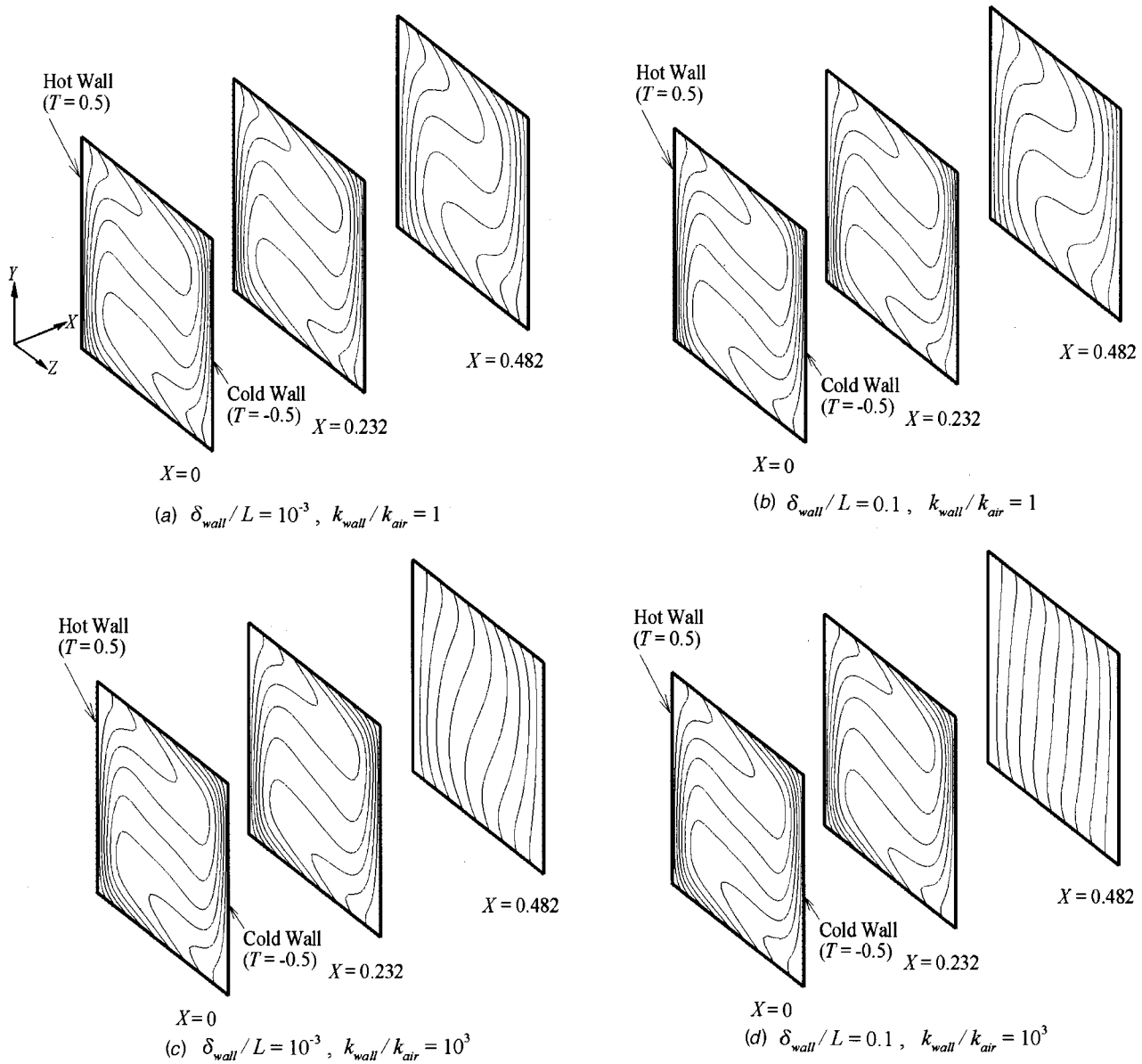

Fig. 4 Temperature Distribution in the Cell; for $Ra=10^5$; (*a*) $\delta_{wall}/L=10^{-3}$ and $k_{wall}/k_{air}=1$; (*b*) $\delta_{wall}/L=0.1$ and $k_{wall}/k_{air}=1$; (*c*) $\delta_{wall}/L=10^{-3}$ and $k_{wall}/k_{air}=10^3$; and (*d*) $\delta_{wall}/L=0.1$ and $k_{wall}/k_{air}=10^3$.

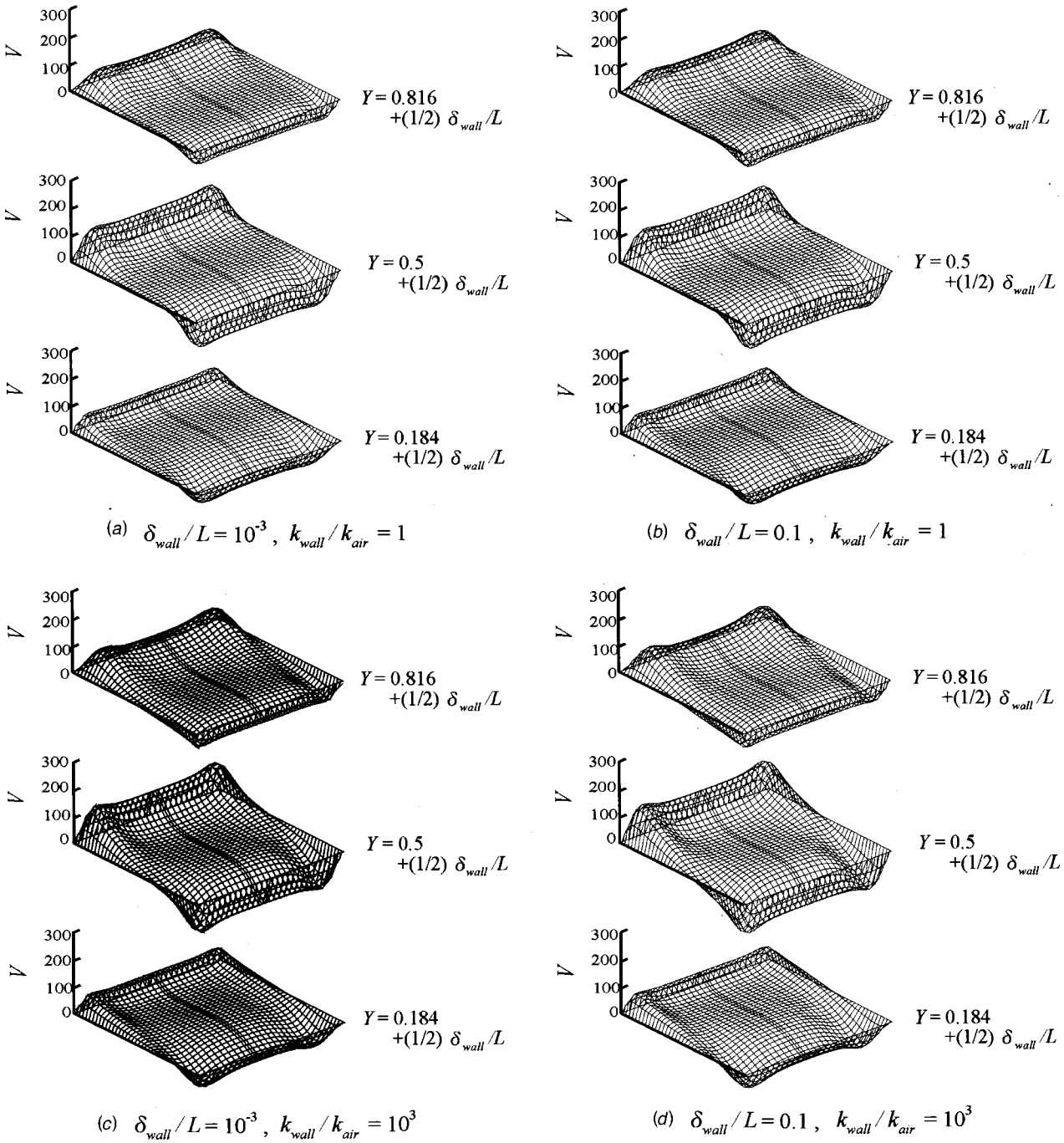

Fig. 5 Vertical velocity profiles in the Cell; for Ra=10^5; (*a*) $\delta_{wall}/L=10^{-3}$ and $k_{wall}/k_{air}=1$; (*b*) $\delta_{wall}/L=0.1$ and $k_{wall}/k_{air}=1$; (*c*) $\delta_{wall}/L=10^{-3}$ and $k_{wall}/k_{air}=10^3$; and (*d*) $\delta_{wall}/L=0.1$ and $k_{wall}/k_{air}=10^3$.

$$0<X<\frac{H}{2L} \text{ and } \frac{\delta_{wall}}{2L}<Y<\frac{\delta_{wall}}{2L}+\frac{H}{L}; \quad \bar{k}=1, \tag{24}$$

at

$$\frac{H}{2L}<X<\frac{H+\delta_{wall}}{2L} \text{ or } 0<Y<\frac{\delta_{wall}}{2L} \text{ or}$$

$$\frac{\delta_{wall}}{2L}+\frac{H}{L}<Y<\frac{\delta_{wall}}{L}+\frac{H}{L}; \quad \bar{k}=\frac{k_{wall}}{k_{air}}. \tag{25}$$

Therefore, the non-dimensional heat transfer rate into the partition wall form the hot wall, Q_{wall} is given as:

$$Q_{wall}=Q_{total}-Q_{conv} \tag{26}$$

Results and Discussion

Temperature and Velocity Profiles. The temperature distributions in the cell are presented in Fig. 4 in the form of the contours of T on Y-Z planes at $X=0$, 0.232 and 0.482. The temperatures of the hot and cold walls are $T=0.5$ and -0.5, respectively. The contours are drawn for every 0.1 of T. In addition, the vertical velocity profiles in the cell are presented in Fig. 5 on X-Z planes at $Y=0.184+(1/2)(\delta_{wall}/L)$, $0.5+(1/2)(\delta_{wall}/L)$, and $0.816+(1/2)(\delta_{wall}/L)$. Each panel of Figs. 4 and 5 shows the result for Ra=10^5 and; (a) $\delta_{wall}/L=10^{-3}$ and $k_{wall}/k_{air}=1$; (b) $\delta_{wall}/L=0.1$ and $k_{wall}/k_{air}=1$; (c) $\delta_{wall}/L=10^{-3}$ and $k_{wall}/k_{air}=10^3$; and (d) $\delta_{wall}/L=0.1$ and $k_{wall}/k_{air}=10^3$.

Natural convection makes the fluid flow from the hot wall toward the cold wall in the upper half of the cell and from the cold wall toward the hot wall in the lower half of the cell. On account of the convection, the contours of the temperature are skewed as seen in Fig. 4. Slight differences in the temperature profiles are seen at the core region ($X=0$ and 0.232) between the figures from (*a*) to (*d*), because the magnitude of convection changes as to the thermal conditions of the wall, δ_{wall}/L and $k_{\text{wall}}/k_{\text{air}}$. The effect on the natural convection by the thermal conditions of the partition wall will be discussed later.

On the other hand, the influence of the thermal conditions of the partition wall is clearly seen in temperatures near the side wall ($X=0.428$). From the comparison of Fig. 4(*a*) with (*b*), the contours of temperature on the top wall in the figure (*a*) are almost linear, but the contours in the figure (*b*) differ from linear distribution except near the hot and cold walls. It means that the contours of temperature on the top wall differ from a linear distribution when increasing the δ_{wall}/L. From the comparison of Fig. 4(*b*) with (*d*), the contours of temperature near the side wall in the figure (*b*) differ from a linear distribution except near the hot and cold walls, but the contours in the figure (*d*) are almost linear. It means that the contours of temperature near the partition walls approach a linear distribution when increasing the $k_{\text{wall}}/k_{\text{air}}$.

About the velocity profiles, slight differences in the vertical velocity profiles are seen near the four corners of each horizontal planes between the figures from Fig. 5(*a*) to (*d*). From the comparison of Fig. 5(*a*) with (*c*), the peaks of *V* near the corners in the figure 5(*c*) are clearly seen exceeding in the figure 5(*a*). Moreover, from the comparison of Fig. 5(*c*) with (*d*), the peaks of *V* near the corners in the figure 5(*d*) are clearly seen exceeding in the figure 5(*c*). Difference between Fig. 5(*a*) to (*b*) is not clearly seen. Expansion of *V* near the corners indicates magnitude of heat exchange from the side walls to fluid. Therefore, these comparisons show that the heat exchange from the side walls to fluid enlarges when the δ_{wall}/L increases. The heat exchange from the side walls also enlarges when the $k_{\text{wall}}/k_{\text{air}}$ increases, but the influence of it is dependent on the δ_{wall}/L.

Using an assumption, Okada et al. [9] discussed the effect of thermal condition of partition wall on natural convection in a two-dimensional rectangular cavity. They assumed that both surfaces of a partition wall had same temperature but heat was transferred through the partition wall. This assumption is also employed in the earlier paper by Meyer et al. [8]. In this model, the thermal boundary condition on the partition wall can be expressed by a single parameter of $(\delta_{\text{wall}}/L)\cdot(k_{\text{wall}}/k_{\text{air}})$. Using this assumption, they could solve the problem only in the fluid layer.

However, the surfaces of the partition wall do not have exactly same temperature when the partition wall has finite thickness and finite thermal conductivity. To examine suitableness of the assumption of the partition wall, the temperatures along the axis for *Z*-direction on the surfaces of the top and bottom wall are presented in Fig. 6. These temperatures are the results for $\text{Ra}=10^5$ and $(\delta_{\text{wall}}/L)\cdot(k_{\text{wall}}/k_{\text{air}})=1$. In this figure, the results for three combinations of the wall parameters are plotted by sifting origins along the vertical axis. These combinations of the wall parameters are $\delta_{\text{wall}}/L=10^{-3}$ and $k_{\text{wall}}/k_{\text{air}}=10^3$, $\delta_{\text{wall}}/L=10^{-2}$ and $k_{\text{wall}}/k_{\text{air}}=10^2$, and $\delta_{\text{wall}}/L=0.1$ and $k_{\text{wall}}/k_{\text{air}}=10$. As seen in this figure, the temperature for $\delta_{\text{wall}}/L=10^{-3}$ and $k_{\text{wall}}/k_{\text{air}}=10^3$ changes linearly from the hot wall to the cold wall, and the temperatures on the surfaces of the top and bottom wall agree with each other. When the non-dimensional wall thickness decreases, the temperature for $\delta_{\text{wall}}/L=10^{-2}$ and $k_{\text{wall}}/k_{\text{air}}=10^2$ differs from the linear distribution, but the temperatures on the surfaces of the top and bottom wall almost coincide with each other. When the non-dimensional wall thickness further decreases, the temperatures for $\delta_{\text{wall}}/L=0.1$ and $k_{\text{wall}}/k_{\text{air}}=10$ are different from the linear distribution, and the temperatures on the surfaces of the top and bottom wall do not agree with each other obviously. Even if the value of $(\delta_{\text{wall}}/L)\cdot(k_{\text{wall}}/k_{\text{air}})$ is fixed, the temperature distribution on the partition wall varies according to the combination of δ_{wall}/L and $k_{\text{wall}}/k_{\text{air}}$ as seen in this result. Therefore, the effect of thermal conditions of the partition wall can not be expressed by a single parameter of $(\delta_{\text{wall}}/L)\cdot(k_{\text{wall}}/k_{\text{air}})$.

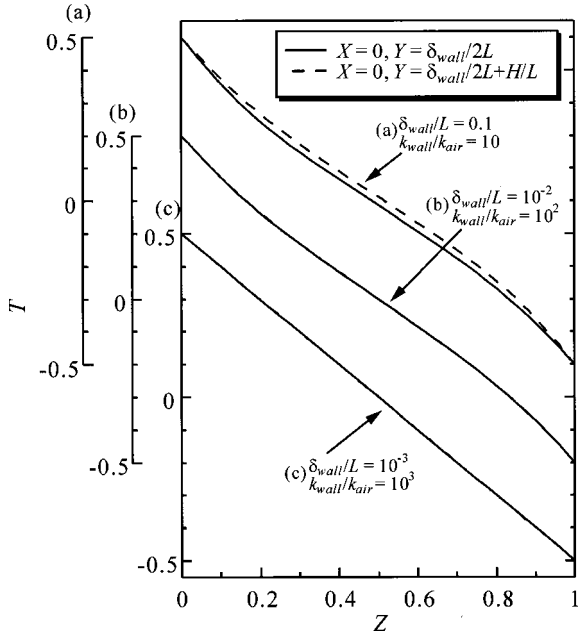

Fig. 6 Temperatures on the surfaces of the top and bottom wall; for $\text{Ra}=10^5$ and $(\delta_{\text{wall}}/L)\cdot(k_{\text{wall}}/k_{\text{air}})=1$; (*a*) $\delta_{\text{wall}}/L=0.1$ and $k_{\text{wall}}/k_{\text{air}}=10$; (*b*) $\delta_{\text{wall}}/L=10^{-2}$ and $k_{\text{wall}}/k_{\text{air}}=10^2$; and (*c*) $\delta_{\text{wall}}/L=10^{-3}$ and $k_{\text{wall}}/k_{\text{air}}=10^3$.

Average Nusselt Numbers on the Hot Wall. Figure 7 shows the contours of Nu_m as a function of δ_{wall}/L and $k_{\text{wall}}/k_{\text{air}}$. The figure 7(*a*) is the result for $\text{Ra}=10^4$ and the figure 7(*b*) is for $\text{Ra}=10^5$. The Nu_m is the average Nusselt number on the hot wall which accounts for the heat transfer of pure natural convection and dose not include the heat transfer to the partition wall from the hot wall. When $k_{\text{wall}}/k_{\text{air}}$ increases and approaches infinity, the thermal boundary condition of the cavity reaches the ''conduction'' boundary condition. On the other hand, when $k_{\text{wall}}/k_{\text{air}}$ decreases and approaches zero, the thermal boundary condition of the cavity reaches the ''adiabatic'' boundary condition. These ideal boundary conditions have been usually employed in the analysis of natural convection in a cavity. Furthermore, when the δ_{wall}/L decreases and approaches zero, the thermal boundary condition of the cavity reaches the so called ''no-thickness'' boundary condition developed by Nakamura et al. [3]. When the value of Ra is 10^4, the values of Nu_m for these ideal boundary conditions are 1.159 for ''conduction,'' 2.09 for ''adiabatic'' and 1.722 for ''no-thickness.'' If the value of Ra is 10^5, the values of Nu_m for these ideal boundary conditions are 3.21 for ''conduction,'' 4.48 for ''adiabatic'' and 3.54 for ''no-thickness.''

As seen in Fig. 7, for almost area of $0<\delta_{\text{wall}}/L\leqslant 0.1$ and $0<k_{\text{wall}}/k_{\text{air}}\leqslant 10^3$ except near the $\delta_{\text{wall}}/L=0$ and the $k_{\text{wall}}/k_{\text{air}}=0$, the Nu_m almost coincides with the value for the ''conduction'' boundary condition. This feature is seen in both results for $\text{Ra}=10^4$ and 10^5.

In order to reduce total heat transfer of the air layer with partition walls, δ_{wall}/L and $k_{\text{wall}}/k_{\text{air}}$ should decrease as small as possible. To investigate the property of Nu_m near small δ_{wall}/L and small $k_{\text{wall}}/k_{\text{air}}$ region, contours of Nu_m on log-log plots of δ_{wall}/L and $k_{\text{wall}}/k_{\text{air}}$ are presented in Fig. 8. In Fig. 8, the figure 8(*a*) is the result for $\text{Ra}=10^4$ and the figure 8(*b*) is the result for $\text{Ra}=10^5$. The areas in which Nu_m agrees with the value for the ''conduction'' or value for the ''no-thickness'' within 5 percent

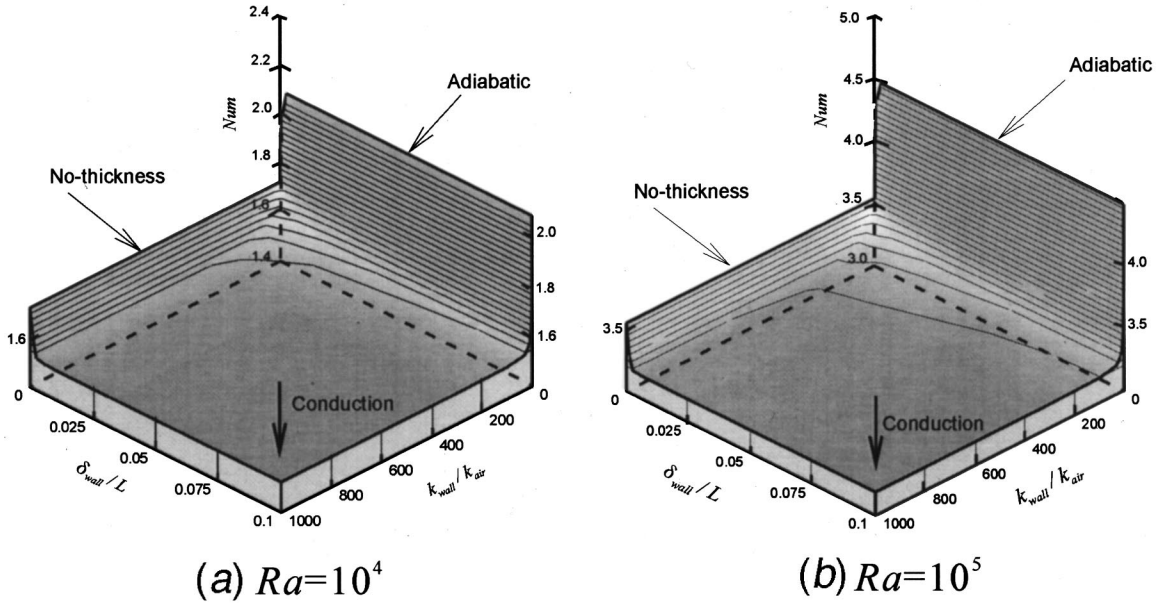

Fig. 7 Contours of *Num* as a function of δ_{wall}/L and k_{wall}/k_{air}; (*a*) Ra=10^4; (*b*) Ra=10^5.

accuracy are plotted also in Fig. 8. It is remarkable that Nu_m in the small k_{wall}/k_{air} region agrees with the value for the ''no-thickness'' even if δ_{wall}/L is large. In both figures 8(*a*) and 8(*b*), the area in which Nu_m agrees with the value for the ''adiabatic'' is not present. Of course, Nu_m increases and approaches the value of the ''adiabatic'' when k_{wall}/k_{air} decreases and approaches zero. But, the value of $k_{wall}/k_{air}<1$ means that the thermal conductivity of the partition wall is smaller than that of air. This is not a practical situation because very few materials for partition wall have so small thermal conductivity.

Heat Transfer to the Partition wall from the Hot Wall. It is interesting to investigate the proportion of the heat transfer into the partition wall from the hot wall to the total heat transfer quantity from the hot wall. The proportions of the heat transfer are presented in Fig. 9 as contours of Q_{wall}/Q_{total} on log-log plots of δ_{wall}/L and k_{wall}/k_{air}. In Fig. 9, the figure 9(*a*) is the result for Ra=10^4 and the figure 9(*b*) is the result for Ra=10^5. As seen in Fig. 9, every contour is almost straight, and parallel with each other. The inclination of the contour is as decreasing one decade of the k_{wall}/k_{air} to increasing one decade of the δ_{wall}/L. Therefore, when the product of δ_{wall}/L and k_{wall}/k_{air} is the same, the value of Q_{wall}/Q_{total} is the same.

From the comparison of the figures 9(*a*) to 9(*b*), the Q_{wall}/Q_{total} is affected by the value of Ra because natural convection increases with an increase in the Ra. When Ra is less than 10, the convection heat transfer in the cell is negligible and the Nu_m approaches 1. Then, the Q_{wall} and Q_{total} is easily solved and the equation of the Q_{wall}/Q_{total} is expressed as follows when Ra $\ll$10:

$$\frac{Q_{wall}}{Q_{total}}=\frac{(2+\delta_{wall}/L)\cdot(\delta_{wall}/L)\cdot(k_{wall}/k_{air})}{1+(2+\delta_{wall}/L)\cdot(\delta_{wall}/L)\cdot(k_{wall}/k_{air})}. \qquad (27)$$

As seen in Eq. (27), it is not strictly true that the Q_{wall}/Q_{total} is a function of the single parameter of $(\delta_{wall}/L)\cdot(k_{wall}/k_{air})$. However, if δ_{wall}/L is negligibly small as compared with 2, Q_{wall}/Q_{total} can be assumed a function of the $(\delta_{wall}/$

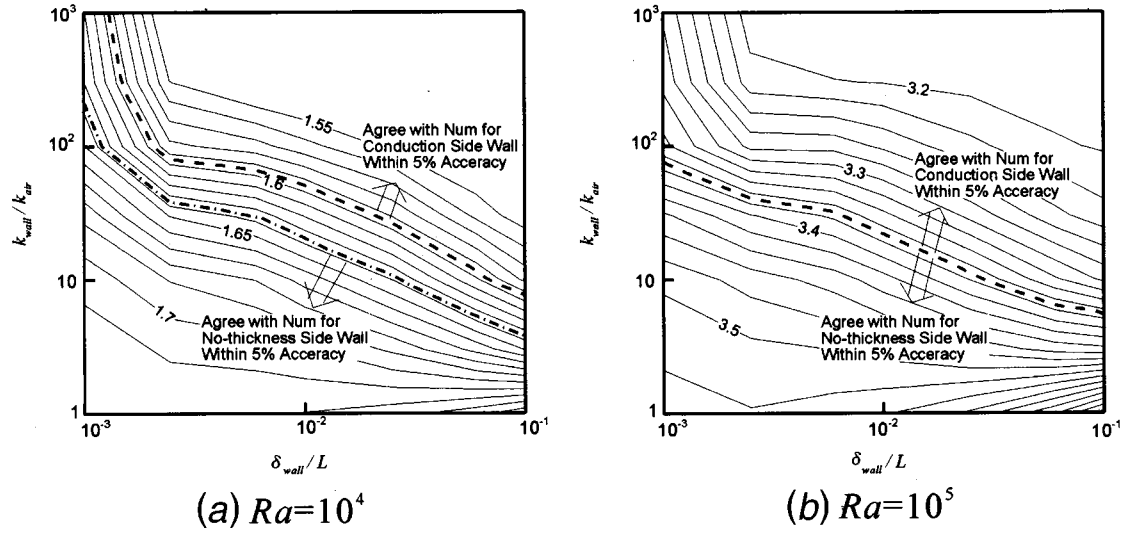

Fig. 8 Contours of *Num* on log-log plots of δ_{wall}/L and k_{wall}/k_{air}; (*a*) Ra=10^4; (*b*) Ra=10^5.

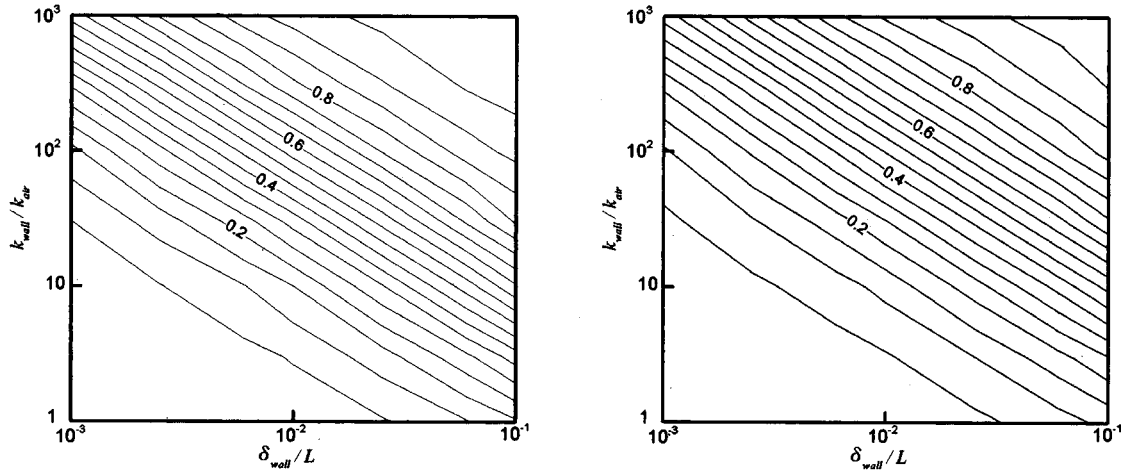

Fig. 9 Contours of Q_{wall}/Q_{total} on log-log plots of δ_{wall}/L and k_{wall}/k_{air}; (*a*) Ra$=10^4$; (*b*) Ra$=10^5$.

$L)\cdot(k_{wall}/k_{air})$ only. In this study, we consider the δ_{wall}/L to be less than 0.1, because the δ_{wall}/L should be as small as possible in order to reduce the total heat transfer.

Figure 10 shows Q_{wall}/Q_{total} as a function of $(\delta_{wall}/L)\cdot(k_{wall}/k_{air})$. In this figure, the curves are plotted from the equations obtained by the least square method. The correlation coefficient of each curve with the strict results of numerical analysis is larger than 0.999 and almost coincide with 1. Therefore, Q_{wall}/Q_{total} can be expressed as a function of $(\delta_{wall}/L)\cdot(k_{wall}/k_{air})$. As seen from Fig. 10, Q_{wall}/Q_{total} is affected by the value of Ra because natural convection increases with Ra. And as seen in Figs. 7 and 8, natural convection varies according to the combination of δ_{wall}/L and k_{wall}/k_{air}. However, it is remarkable that the proportion of the heat transfer, Q_{wall}/Q_{total} can be expressed as a function of the product of δ_{wall}/L and k_{wall}/k_{air}.

Comparison With Previous Two-Dimensional Studies. A comparison of average Nusselt number and Q_{wall}/Q_{total} with previous work is presented in Table 2. Unfortunately no other three-dimensional work that the heat transfer to the partition wall is available, these results listed in the table are the results for two-dimensional, for Ra$=10^5$ and $H/L=1$. In order to compare with the result of Okada et al. [9], we solved the two-dimensional natural convection and conduction problem for Pr$=5.68$, $(\delta_{wall}/L)\cdot(k_{wall}/k_{air})=5$ and $H/L=1$ using the present manner and the semi-ideal boundary condition of Meyer et al. [8]. On the other hand, the listed experimental results are for an air layer, therefore, the Prandtl number doesn't agree with the value for the listed numerical solutions. However, it is well known that the Prandtl number doesn't affect much on the natural convection except for a tall cavity. This was pointed out by Okada et al. [9] for the cavity of $H/L=1$ and smaller, and we also confirmed this by supplementary runs. These values of Nakamura's and Meyer's experiments were determined respectively according to the diagram by Nakamura et al. [3] and the experimental correlation by Meyer et al. [2].

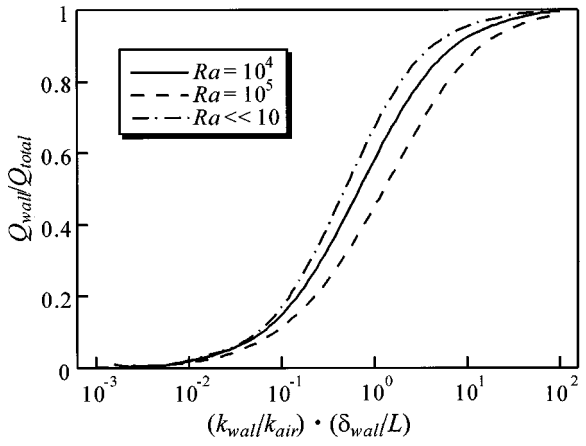

Fig. 10 Q_{wall}/Q_{total} as a function of $(\delta_{wall}/L)\cdot(k_{wall}/k_{air})$ for $H/L=1$

Comparing Q_{wall}/Q_{total} among the numerical results, the value of the present analysis doesn't agree with that of Meyer's model. The difference between the value of present analysis and that of Meyer's model is 20.3 percent. On the other hand, the value of Meyer's model doesn't agree well with Okada's result, in spite of using the same model of thermal boundary condition. Okada et al. [9] formulated the conservation equations using the stream function and discretized the equations using the upwind scheme, and solved the discretized equations using the Gauss-Seidel's method. On the contrary, our formulation based on Meyer's model was solved using the SIMPLE algorithm of Patankar [12]. This difference in the numerical methods is the reason for the difference of results. The difference between the value of Meyer's model and Okada's result is 7.6 percent. Even if the difference of Nu_m among these three results isn't large, either numerical method using the Meyer's model leads to a higher Q_{wall}/Q_{total} than that of present analysis. These comparisons show that the effect of modeling of the partition wall isn't negligible on the value of Q_{wall}/Q_{total}.

Comparing the values of Nu_m, the three numerical results agree well with each other and the value of Nakamura's experiment also

Table 2 Comparisons of Nu_m and Q_{wall}/Q_{total} with previous studies of two-dimensional rectangular enclosure for $H/L=1$ and Ra$=10^5$

	Numerical analyses for $Pr=5.68$ and $(\delta_{wall}/L)\cdot(k_{wall}/k_{air})=5$			Experiments for an air layer	
	Present Analysis*	Meyer's Model	Okada et. al. (1986)	Nakamura et. al. (1980)	Meyer et. al.** (1979)
Nu_m	3.58	3.55	3.50	3.6±0.2	3.8±0.1
Q_{wall}/Q_{total}	0.602	0.725	0.670	—	—

* The wall condition parameters are $\delta_{wall}/L=0.05$ and $k_{wall}/k_{air}=100$

** The wall condition number is $(\delta_{wall}/L)\cdot(k_{wall}/k_{air})=0.04\pm0.01$

agrees well with the numerical results. According to the paper of Nakamura et al. [3], the wall condition number $(\delta_{wall}/L)\cdot(k_{wall}/k_{air})$ of their experiment wasn't clear, but the temperatures on the partition wall changed linearly from the hot cold to the hot wall. On the other hand, slight difference is seen between the value of Meyer's experiment and other results. The reason of this may be the difference of the wall condition number, because Meyer's experiment was held for $(\delta_{wall}/L)\cdot(k_{wall}/k_{air})=0.04\pm0.01$ and the listed numerical results were performed for $(\delta_{wall}/L)\cdot(k_{wall}/k_{air})=5$. Therefore, a supplementary run for $\delta_{wall}/L=0.004$, $k_{wall}/k_{air}=10$ and $Pr=5.68$ was performed using the method of present analysis. The result was $Nu_m=3.77$, and this shows good agreement with the experiment and the present analysis.

Concluding Remarks

Three-dimensional natural convection heat transfer characteristics in a vertical air layer partitioned into cubical enclosures by partition walls of finite thermal conductivity and finite thickness were investigated numerically. The numerical solutions were obtained for $Ra=10^4$ and 10^5 and a wide range of δ_{wall}/L and k_{wall}/k_{air}. The main conclusions are as follows:

1 natural convection varies according to the combination of δ_{wall}/L and k_{wall}/k_{air}

2 for almost area of $0<\delta_{wall}/L\leqslant 0.1$ and $0<k_{wall}/k_{air}\leqslant 10^3$ except near the $\delta_{wall}/L=0$ and the $k_{wall}/k_{air}=0$, the Nu_m almost coincides with the value for the ''conduction'' boundary condition

3 Nu_m in low k_{wall}/k_{air} region agrees with the value for the ''no-thickness'' even if δ_{wall}/L is high

4 Q_{wall}/Q_{total} can be expressed as a function of $(\delta_{wall}/L)\cdot(k_{wall}/k_{air})$

Nomenclature

t = temperature
T = dimensionless temperature
δ_{wall} = thickness of the partition wall

References

[1] Cane, R. L. D., Hollands, K. G., Raithby, G. D., and Unny, T. E., 1977, ''Free Convection Heat Transfer Across Inclined Honeycomb Panels,'' ASME J. Heat Transfer, **99**, pp. 86–91.

[2] Meyer, B. A., Mitchell, J. W., and El-Wakil, M. M., 1979, ''Natural Convection Heat Transfer in Moderate Aspect Ratio Enclosures,'' ASME J. Heat Transfer, **101**, pp. 955–659.

[3] Nakamura, H., and Asako, Y., 1980, ''Heat Transfer in a Parallelogram Shaped Enclosure (1st Report, Heat Transfer by Free Convection),'' Bull. JSME, **23**, pp. 1827–1834.

[4] Ostrach, S., 1988, ''Natural Convection in Enclosures,'' ASME J. Heat Transfer, **110**, pp. 1175–1190.

[5] Asako, Y., and Nakamura, H., 1982, ''Heat Transfer in a Parallelogram Shaped Enclosure (2nd Report, Free Convection in Infinitely Stacked Parallelogram Shaped Enclosure),'' Bull. JSME, **25**, pp. 1412–1418.

[6] ElSherbiny, S. M., Hollands, K. G., and Raithby, G. D., 1982, ''Effect of Thermal Boundary Conditions on Natural Convection in Vertical and Inclined Air Layers,'' ASME J. Heat Transfer, **104**, pp. 513–520.

[7] Kim, D. M., and Viskanta, R., 1985, ''Effect of Wall Heat Conduction on Natural Convection Heat Transfer in a Square Enclosure,'' ASME J. Heat Transfer, **107**, pp. 137–146.

[8] Meyer, B. A., Mitchell, J. W., and El-Wakil, M. M., 1982, ''The Effect of Thermal Wall Properties on Natural Convection in Inclines Rectangular Cells,'' ASME J. Heat Transfer, **104**, pp. 111–117.

[9] Okada, M., and Okano, H., 1986, ''Natural Convection Heat Transfer in a Rectangular Cell Enclosed with Vertical Walls and Plate-Fins,'' Trans. Jpn. Soc. Mech. Eng., Ser. B, **52**, pp. 2158–2163.

[10] Fusegi, T., Hyun, J. M., and Kuwahara, K., 1992, ''Three-Dimensional Natural Convection in a Cubical Enclosure with Walls of Finite Conductance,'' *Natural/Forced Convection and Combustion Simulation: 2nd Int. Conf Adv Comput Method Heat Transfer*, pp. 109–126.

[11] Patankar, S. V., 1981, ''A Calculation Procedure for Two-Dimensional Elliptic Situations,'' Numer. Heat Transfer, **4**, pp. 409–425.

[12] Patankar, S. V., 1980, *Numerical Heat Transfer and Fluid Flow*, Hemisphere, Washington, DC.

An Efficient Method for Modeling Radiative Transfer in Multicomponent Gas Mixtures With Soot

Vladimir P. Solovjov

Brent W. Webb

Department of Mechanical Engineering,
Brigham Young University,
Provo, UT 84602

An efficient approach for predicting radiative transfer in high temperature multicomponent gas mixtures with soot particles is presented. The method draws on the previously published multiplication approach for handling gas mixtures in the spectral line weighted-sum-of-gray-gases (SLW) model. In this method, the gas mixture is treated as a single gas whose absorption blackbody distribution function is calculated through the distribution functions of the individual species in the mixture. The soot is, in effect, treated as another gas in the mixture. Validation of the method is performed by comparison with line-by-line solutions for radiative transfer with mixtures of water vapor, carbon dioxide, and carbon monoxide with a range of soot loadings (volume fractions). Comparison is performed also with previously published statistical narrow band and classical weighted-sum-of-gray-gases solutions. [DOI: 10.1115/1.1350824]

Keywords: Gaseous, Heat Transfer, Participating Media, Particulate, Radiation

Introduction

In a combustion environment yielding luminous flames, the combustion products are comprised not only of the mixture of combustion gases (mainly water vapor, carbon dioxide, and carbon monoxide) but also soot. Soot consists of very small carbon particles which, when unagglomerated, are primarily absorbing/emitting and non-scattering. When soot is present in the flame, the radiation transfer is significantly increased because of high values of its spectral absorption coefficient relative to that of the surrounding gases. While the prediction of radiative transfer in high temperature gas mixtures is already an imposing challenge, the added presence of soot renders the problem even more difficult because of the superposition of band radiation from the gases and the continuum radiation from the soot particles.

Historically, the simplest approach for the prediction of radiative transfer in gas/soot mixtures are simple gray models, which are computationally efficient but yield very poor accuracy [1]. The most accurate method is the line-by-line (LBL) method, in which the Radiative Transfer Equation is integrated over the detailed molecular spectrum for the gases and soot [2]. Because of the computational requirements of the line-by-line method, it is generally used only for benchmark solutions.

The statistical narrow band model (SNB) provides good accuracy in the prediction of radiative transfer in high temperature gases, but it requires a large number of bands and, therefore, is computationally expensive [3]. Often this method is used for obtaining benchmark solutions in lieu of the line-by-line approach (e.g., [4]).

The wide band model (WBM) is a simplification of the SNB method but the accuracy of this method is limited [5]. It also requires the specification of the path length in the model and spectral parameters associated with the path length. Komornicki and Tomeczek have demonstrated the use of a modified WBM for luminous flame calculation in nonhomogeneous media [6]. Modak developed a generalized code for calculating the absorptivity/emissivity of combustion gases with soot using the wide band model [7]. Taylor et al. present total emissivities of mixtures of high temperature gases and soot calculated from band models [8,9].

The Weighted-Sum-of-Gray-Gases (WSGG) model can be used with arbitrary solvers of the RTE [10]. It requires specification of the gray gas weights and absorption coefficients for any combination of gas species and soot over their expected range of concentrations, temperatures, etc. Bressloff studied the influence of soot loading on WSGG solutions to the radiative transfer equation through mixtures of gases and soot [4]. WSGG solutions were compared to SNB model predictions.

In the Spectral Line Weighted-sum-of-gray-gases (SLW) model, the weights in the classical WSGG model are determined with the help of the absorption-line blackbody distribution function, which is calculated directly from the high resolution molecular spectrum of gases [11,12]. The integration of the RTE over wavenumber (wavelength) is then replaced by an integration over absorption cross-section. The presence of soot particles in the flame has been handled previously by the hybrid SLW and k-distribution model in which the absorption line blackbody distribution function of the gas mixture was calculated using the convolution or the double integration approaches [13]. The spectral dependence of the soot absorption coefficient was accommodated by the additional subdivision of wavenumber on subintervals where the spectral properties of the soot are assumed to be constant. This approach renders the model significantly more complicated and computationally burdensome, and the SLW method loses some of its advantage for engineering radiative transfer predictions. Using this approach, Denison and Webb calculated the radiative dissipation source in water vapor with soot [13], and Denison reported predictions of the radiative dissipation source for the mixture of water vapor and carbon dioxide with soot [14].

In the present work, a new approach is proposed where the multicomponent gas mixture with soot is treated as a single gas in the SLW model. The absorption line blackbody distribution function of this single gas is calculated using the distribution functions of the individual species included in the mixture [15]. The development for the addition of soot presented here treats soot simply as another gas whose absorption distribution function is calculated from the absorption spectrum of the soot. This approach can be

Contributed by the Heat Transfer Division for publication in the JOURNAL OF HEAT TRANSFER. Manuscript received by the Heat Transfer Division September 28, 1999; revision received November 3, 2000. Associate Editor: M. P. Mengüç.

efficiently used for the mixtures of arbitrary number of gas species, and retains the engineering advantages of the SLW model.

The validation of the approach developed here is performed by the calculation of emissivity, total intensity and radiative dissipation source in the mixtures of water vapor, carbon dioxide, carbon monoxide, and soot particles, and comparison with line-by-line benchmark solutions and results previously reported. Special care is taken in comparing with line-by-line benchmark predictions to ensure that both the benchmark and the model simulations are conducted with the same spectral data base.

Radiative Transfer in Gas/Soot Mixtures

Radiation field in the absorbing, emitting and non-scattering media along a pathlength s in a direction $\hat{\Omega}$ is described by the spectral intensity of radiation $I_\eta(s,\hat{\Omega})$ the governing equation for which is the Radiative Transfer Equation (RTE) [16]:

$$\frac{dI_\eta}{ds} = -\kappa_\eta I_\eta + \kappa_\eta I_{b\eta}, \tag{1}$$

$I_{b\eta}$ is the Planck spectral distribution of blackbody intensity and κ_η is the spectral absorption coefficient of the medium. This equation does not include scattering of radiation because the characteristic size of molecules and unagglomerated soot particles is small compared to the wavelength of infrared radiation in the flames [17].

The spectral absorption coefficient κ_η is the effective absorption coefficient of the mixture of m gases with soot particles constructed from the absorption coefficients of all components included in the combustion process:

$$\kappa_\eta = \kappa_{1,\eta} + \kappa_{2,\eta} + \ldots \kappa_{m,\eta} + \kappa_\eta^{\text{soot}}, \tag{2}$$

where $\kappa_\eta^{\text{soot}}$ is the spectral absorption coefficient of soot, and $\kappa_{m,\eta}$ is the absorption coefficient of the gas m, which can be expressed through the gas absorption cross section $C_{m,\eta}$ and molar density N_m by the equation

$$\kappa_{m,\eta} = N_m C_{m,\eta}. \tag{3}$$

If N is defined as the molar density of the gas mixture, then the absorption coefficient κ_η can be expressed by the following formula:

$$\begin{aligned}
\kappa_\eta &= \kappa_{1,\eta} + \kappa_{2,\eta} + \ldots + \kappa_{m,\eta} + \kappa_\eta^{\text{soot}} \\
&= N_1 C_{1,\eta} + N_2 C_{2,\eta} + \ldots + N_m C_{m,\eta} + \kappa_\eta^{\text{soot}} \\
&= N\left(\frac{N_1}{N} C_{1,\eta} + \frac{N_2}{N} C_{2,\eta} + \ldots + \frac{N_m}{N} C_{m,\eta} + \frac{\kappa_\eta^{\text{soot}}}{N}\right) \\
&= N(Y_1 C_{1,\eta} + Y_2 C_{2,\eta} + \ldots + Y_m C_{m,\eta} + C_\eta^{\text{soot}}) \\
&= N C_\eta.
\end{aligned} \tag{4}$$

Equation (4) is an expression for the absorption coefficient for an effective single gas which is defined in terms of the individual components as

$$C_\eta = Y_1 C_{1,\eta} + Y_2 C_{2,\eta} + \ldots + Y_m C_{m,\eta} + C_\eta^{\text{soot}}. \tag{5}$$

This relationship allows the use of the traditional formulation of the SLW model for a single gas. The absorption cross-section of soot C_η^{soot} included in Eqs. (4) and (5) is artificially constructed by dividing the soot absorption coefficient by the gas molar density, which depends on the local thermodynamic properties of the gas mixture.

The SLW Model

The SLW form of the Radiative Transfer Equation obtained by the integration of Eq. (1), with respect to wavenumber, and subdivision of the absorption cross-section into gray gases, has the following form [11]:

$$\frac{dI_j}{ds} = -\kappa_j I_j + a_j \kappa_j I_b, \quad j = 0,1,\ldots,n, \tag{6}$$

where n is the number of gray gases in the model, I_j is the intensity of gray gas j. The gray gas absorption coefficient κ_j may be determined from

$$\kappa_j = N\sqrt{C_{J-1} C_j}, \tag{7}$$

where C_{j-1} and C_j are supplemental absorption cross-sections employed in the discretization of the absorption spectrum over cross-section [18]. The gray gas weight corresponding to the gray gas absorption coefficient is

$$a_j = F(C_j) - F(C_{j-1}). \tag{8}$$

In the SLW modification of the classical WSGG model the gray gas weights are calculated from the absorption line blackbody distribution function (hereafter referred to as ALBDF), determined from the detailed absorption spectrum according to

$$F(C) = \frac{\int_{\{\eta: C_\eta < C\}} E_{b\eta}(T)\, d\eta}{\sigma T^4}. \tag{9}$$

The ALBDF is defined as the fraction of the total blackbody energy for the gas mixture at temperature T corresponding to wavenumbers for which the absorption cross-section C_η is less than the specified value C [12]. Calculation of the distribution function for the mixture of gases and soot as defined by Eq. (5) will be demonstrated later.

Solving Eq. (6) for each gray gas j, one can obtain the integrated (total) intensity of radiation I by the simple summation over all gray gases:

$$I = \int_{\eta=0}^{\infty} I_\eta \, d\eta = \sum_{j=1}^{n} I_j. \tag{10}$$

For SLW modeling to be effective, values of the absorption line blackbody distribution function $F(C)$ must be calculated for any composition of the mixture at any temperature. Calculation of $F(C)$ for all possible combinations of state using the actual high resolution molecular spectra of the mixture C_η is impractical. Instead, the ALBDF's of the individual gas species, $F_m(C)$, are used. These distribution functions can be calculated and tabulated readily for each gas specie in the mixture over a range of temperature and pressure. The ALBDF of soot $F_{\text{soot}}(C)$ will be defined later. One can then use the multiplication approach developed previously for calculation of $F(C)$ in gas mixtures [15].

The multiplication approach to the calculation of the ALBDF of the mixture through the separate distribution functions of individual species is based on the assumption that the absorption cross-section sections of different species included in the mixture are statistically independent. For gas mixtures without particles this assumption is discussed in [15]. The absorption cross-section of soot is a smooth, nearly linear function of wavenumber which obviously is statistically independent of any line molecular gas spectrum. According to this approach, the ALBDF of the composite absorption cross-section $F_{C_\eta}(C)$ is obtained as a product of the distribution functions of individual contributors to this absorption cross-section

$$F_{C_\eta}(C) = F_{Y_1 C_{1,\eta}}(C) F_{Y_2 C_{2,\eta}}(C) \cdots F_{Y_m C_{m,n}}(C) F_{C_\eta^{\text{soot}}}(C), \tag{11}$$

where m is the number of species in gas mixture. As shown by Solovjov and Webb [15], the dependence of the ALBDF on the local mole fraction of the gas species allows the calculation of the ALBDF for arbitrary mole fraction through the ALBDF of the pure gas:

$$F_{Y_m C_{m,\eta}}(C) = F_{C_{m,\eta}}(C/Y_m). \tag{12}$$

Applied to Eq. (11), the relationship of Eq. (12) yields

$$F_{C_\eta}(C) = F_{C_{1,\eta}}(C/Y_1) F_{C_{2,\eta}}(C/Y_2) \cdots F_{C_{m,\eta}}(C/Y_m) F_{C_\eta^{\text{soot}}}(C). \tag{13}$$

Equation (13) provides a simple and efficient approach for calculation of the ALBDF of the gas mixture with soot particles. The absorption distribution function for soot will now be defined, and its calculation from the absorption cross-section will be explored.

Soot Absorption Distribution Function

Soot is comprised of small carbon particles produced in the fuel-rich zones of hydrocarbon flames, and is primarily responsible for flame luminosity. It is generally accepted that primary (unagglomerated) soot particles are spherical in shape and in the size range 30−65 nm [19]. Unlike combustion gases such as H_2O, CO_2, or CO, which absorb and emit only in certain wavelength bands, soot participates radiatively at all wavelengths. Therefore, the radiant energy emitted from a sooty flame may be significantly higher than for a non-luminous flame. In order to rigorously predict the radiative transfer from soot its size distribution, shape, and optical properties must be known. It is assumed here that these properties are known or can be calculated from other physical models.

In prediction of radiative transfer in practical combustion environments it is generally assumed that soot is unagglomerated. As such, the absorption coefficient can be determined from soot optical properties using the Rayleigh small particle limit by the following equation [20]:

$$\kappa_\eta = \frac{36\pi n k}{(n^2 - k^2 + 2)^2 + 4n^2 k^2} f_v \eta, \tag{14}$$

where n and k are, respectively, the real and imaginary part of the soot complex index of refraction, and f_v is the soot volume fraction, which is the ratio of soot concentration c_{soot} to the soot density ρ_{soot}:

$$f_v = c_{\text{soot}} / \rho_{\text{soot}}. \tag{15}$$

The value of soot density is near that of pure carbon (approximately 2000 kg/m^3). In the Rayleigh regime soot scattering is generally taken to be negligible relative to the absorption/emission [17]. Agglomerated soot particles also scatter appreciably, and determination of their radiative properties (absorption/emission and scattering) is more complex. For modeling soot radiation a simple engineering approximation to the dependence of the soot absorption coefficient on wavenumber was proposed by Hottel and Sarofim [21]:

$$\kappa_\eta^{\text{soot}} = c f_v \eta, \tag{16}$$

where c is a constant which was assigned a value of 7.0. Later, Siegel and Howell proposed different values of the constant c for different fuels: 6.3 for oil flames, 4.9 for propane, 4.0 for acetylene, and 3.7–7.5 for coal flames [16]. For flames, the soot volume fraction f_v varies in the range 10^{-8}–10^{-5}. A more general non-linear dependence of the soot absorption coefficient on wavenumber has also been proposed [20]

$$\kappa_\eta^{\text{soot}} = c f_v \eta^a \tag{17}$$

with the dispersion exponent a varying from 0.7 to 2.2 depending on flame conditions. In the present work, only the linear dependence of Eq. (16) will be considered. However, the method proposed here can easily accommodate the more general relationships of Eq. (14) or Eq. (17). Indeed, in theory any spectral variation of the absorption coefficient of absorbing/emitting/non-scattering particles may be accommodated by the approach.

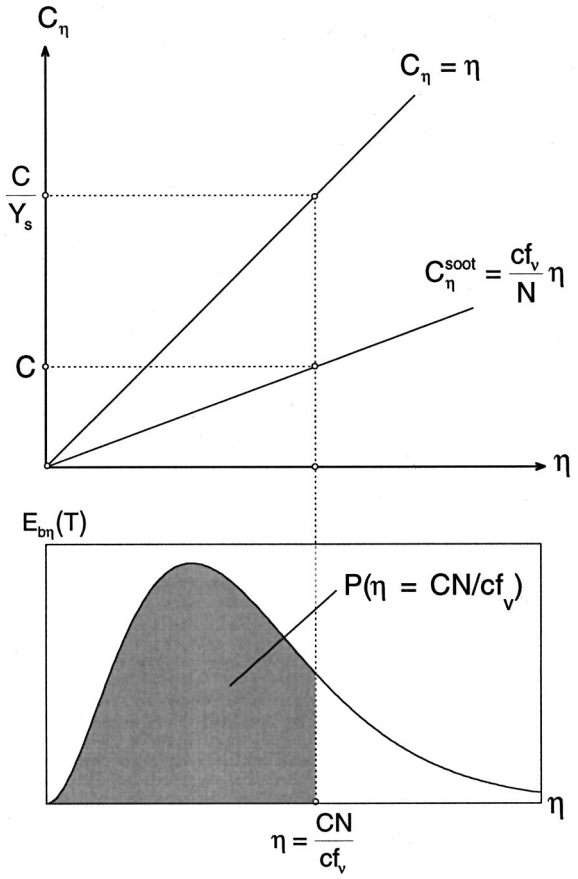

Fig. 1 Absorption blackbody radiation distribution function for soot in the gas/soot mixture

Using Eq. (16) for the soot absorption cross-section [which appears as a contributor in the expression for the absorption coefficient of the multicomponent gas/soot mixture, Eq. (4)], one obtains

$$C_\eta^{\text{soot}} = \frac{c f_v \eta}{N} = Y_s \eta, \tag{18}$$

where Y_s has the sense of soot molar ratio which depends on the local thermodynamic state of the medium.

In a similar fashion to the definition of the ALBDF for absorption cross-sections of gases, one can define an absorption blackbody radiation distribution function for soot (analogous to the absorption line blackbody distribution function for gases) as

$$F_{C_\eta^{\text{soot}}}(C) = \frac{\int_{\{\eta: C_\eta < C_\eta^{\text{soot}}\}} E_{b\eta}(T)\, d\eta}{\sigma T^4}. \tag{19}$$

Figure 1 illustrates schematically the spectral variation of soot absorption cross-section given by Eq. (18), and the Planck blackbody spectral distribution for a given temperature. As illustrated in the figure, the integration domain defined in Eq. (19) by a fixed cross-section value C and absorption cross-section C_η^{soot} is the same as for the fixed value C/Y_s and absorption cross-section $C_\eta = \eta$. The absorption blackbody radiation distribution function

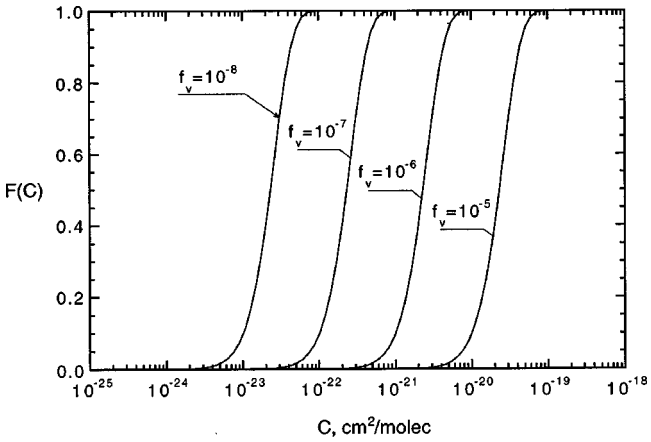

Fig. 2 Absorption blackbody radiation distribution function for soot at 1000 K

of soot $F_{C_\eta^{\text{soot}}}(C)$ can therefore be represented through the classical Planck blackbody radiation function $P(\eta)$ by the following relationship:

$$F_{C_\eta^{\text{soot}}}(C)=F_{Y_s\eta}(C)=P(C/Y_s). \tag{20}$$

As was done in this study, the Planck blackbody radiation function can be calculated by numerical integration directly from its definition [2]

$$P(\eta)=\frac{\int_0^\eta E_{b\eta}(T)d\eta}{\sigma T^4}. \tag{21}$$

Alternatively, the efficient series expansion for $P(\eta)$ presented by Chang and Rhee [22] can be employed. The result of Eq. (20) is that a special calculation of the absorption distribution function of soot is not needed. Rather, to determine the soot distribution function, one can use the classical definition of the Planck blackbody radiation function defined by Eq. (21) in which the upper limit of integration is specified as

$$\eta=\frac{CN}{cf_v}. \tag{22}$$

Indeed, textbook tabulated values for the Planck blackbody radiation function P as a function of the parameter λT may be used for determination of the soot absorption blackbody distribution function, with the Planck blackbody radiation function argument $\lambda T(=T/\eta)$ being evaluated at $\eta=CN/cf_v$ and the temperature T.

Figure 2 shows the absorption blackbody distribution function of soot calculated at 1000 K for different values of the soot volume fraction. According to Eq. (20), all curves have the same shape, shifted along cross-section axis. If instead of Eq. (16) the more general expressions for the soot spectral absorption coefficient of Eqs. (14) and (17) are used to determine the soot absorption blackbody distribution function in Eq. (21), the upper limits of integration become, respectively,

$$\eta=\left(\frac{CN}{f_v}\right)\frac{(n^2-k^2+2)^2+4n^2k^2}{36\pi nk} \tag{23}$$

and

$$\eta=\left(\frac{CN}{cf_v}\right)^{1/a}. \tag{24}$$

Applying the property defined by Eq. (20) to the multiplication relation for gas mixtures given by Eq. (13), the calculation of the ALBDF for a mixture of m gas species and soot is carried out as

$$F_{C_\eta}(C)=F_{C_{1,\eta}}(C/Y_1)F_{C_{2,\eta}}(C/Y_2)\cdots F_{C_{2,\eta}}(C/Y_m)F_\eta(C/Y_s). \tag{25}$$

The assumptions inherent in the development of the SLW model for multicomponent gas mixtures are still valid [15], and the model must be tested against benchmarks for accuracy. Equation (25) will now be used for the prediction of the radiation field in multicomponent gas mixtures with soot particles.

Model Validation

The validation of the proposed method is performed by comparison of model prediction of dissipation radiative source and total radiative intensities in the mixtures of combustion gases with soot particles with line-by-line benchmark solutions and previously published approaches. The absorption-line blackbody distribution functions for H_2O, CO_2, and CO were determined from correlations presented elsewhere [18,23–25]. The comparisons with line-by-line benchmark predictions reveal the accuracy of the model. Only emitting/absorbing (non-scattering) soot is considered in this study, as would be the case for non-agglomerated soot. This approximation is invoked in most predictions of radiative transfer in gas/soot mixtures. It should be underlined, however, that the SLW approach outlined here does not depend on the solution method of the RTE, and is easily extended to scattering media. Thus, if appropriate scattering coefficients and phase functions for agglomerated soot can be formulated, the scattering can be included in a straightforward manner, albeit at considerable additional computational expense.

Isothermal Homogeneous Medium. Consider a mixture of soot with three combustion gas species: water vapor, carbon dioxide, and carbon monoxide. A plane-parallel slab of thickness $L=1.0$ m is filled with an isothermal homogeneous mixture of these three species at 1000 K and 1 atm total pressure. The mole fractions of gas species included in the mixture are $Y_{H_2O}=0.2$, $Y_{CO_2}=0.1$, and $Y_{CO}=0.03$. It is also assumed that the boundaries of the layer are black and non-emitting. The SLW form of the RTE, Eq. (6), for gray gases can be solved analytically, and the integrated dissipation radiative source is defined by the following equation [15]:

$$Q(x)=-2\pi I_b\sum_{j=1}^{n} a_j\kappa_j[E_2(\kappa_j x)+E_2(\kappa_j x-\kappa_j L)], \tag{26}$$

where $E_2(x)$ is the exponential integral [2], and the gray gas weights a_j were determined with Eq. (8). The absorption black-

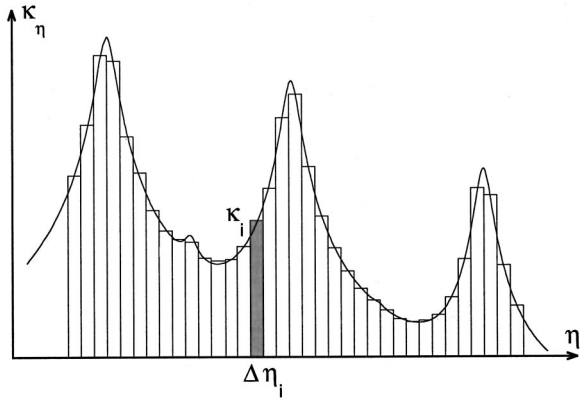

Fig. 3 Line-by-line spectrum model

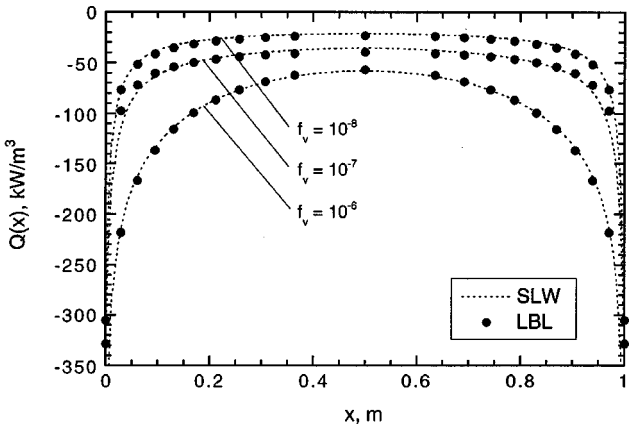

Fig. 4 Predicted local radiative dissipation source in the isothermal, homogenous gas/soot mixture with different soot loadings

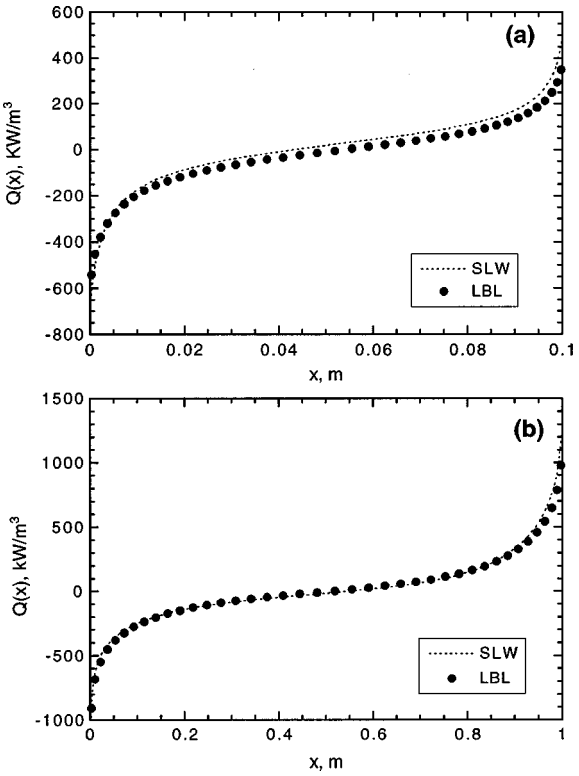

Fig. 5 Predicted local radiative dissipation source in a one-dimensional layer of gas/soot mixture between cold and hot walls for different soot volume fractions: (*a*) $L=0.1$ m, $f_v=10^{-7}$, and (*b*) $L=1.0$ m, $f_v=10^{-6}$.

body distribution function of the mixture of gases was calculated based on the multiplication approach according to Eq. (25). Twenty gray gases were taken in the SLW model calculations. The HITEMP database [26] was used for the calculation of the absorption line blackbody distribution functions for H_2O, CO_2, and CO in the model.

The benchmark prediction for this problem was obtained by the line-by-line method also using the HITEMP spectral database. In the line-by-line integration of the RTE, the high resolution absorption cross-section spectrum is divided into such narrow spectral intervals of width $\Delta\eta_i$ that the variation of absorption cross-section and spectral intensity of blackbody radiation can be neglected (Fig. 3), and they are assumed to be constant within the interval as κ_i and I_{bi}. Then the analytical solution for integrated dissipation radiative source gives

$$Q(x)=-2\pi\sum_i \kappa_i I_{bi}[E_2(\kappa_i x)+E_2(\kappa_i x-\kappa_i L)]\Delta\eta_i. \quad (27)$$

The HITEMP absorption spectrum for H_2O, CO_2, and CO contains more than 800,000 lines with intensities greater than 10^{-25} cm^2/molec at these conditions. The wavenumber interval between adjacent spectral lines was subdivided into eight subintervals. Further refinement of the spectrum yielded no appreciable change in the calculated radiative dissipation source.

Figure 4 shows the comparison of model predictions for the radiative dissipation source with the line-by-line benchmark solutions for the plane layer of gas mixture with soot particles of volume fraction in the range $10^{-8}<f_v<10^{-6}$. The deviation of the SLW solution from the line-by-line result is no greater than 4 percent for the $f_v=10^{-8}$ case, and no greater than 2 percent for $f_v=10^{-6}$. Although excellent agreement is observed in the model predictions for all values of f_v, the accuracy is seen to improve at higher values of the soot loading. Predictions made for no soot present in the layer ($f_v=0$) (not shown) are nearly identical (within 1 percent) to the $f_v=10^{-8}$ results. The predictions clearly illustrate the significant influence of soot on the radiative transfer even at low volume fractions.

The next problem considers a homogeneous layer of 40 percent H_2O/20 percent CO_2 mixture at 1250 K with soot particles bounded by emitting and diffusely reflecting walls. The walls are maintained at 400 K and 1500 K, respectively, with gray emissivity of 0.8. The line-by-line benchmark solution for this problem was obtained by Denison [14] using the discrete ordinates method. Two wall spacings, $L=0.1$ m and 1.0 m, were examined. The predictions were made with an angular resolution of 30 ordinates, and a spatial resolution of 200 and 500 grid points for the $L=0.1$ and 1.0 cases, respectively. The linear spectral variation of soot given by Eq. (16) was used in the benchmark predictions. Predictions using the modeling approach described here were carried out with 25 gray gases. The same spectral database was used both for line-by-line predictions and the generation of the SLW model parameters [23,24]. Figure 5(*a*) shows the radiative dissipation source in the layer of thickness $L=0.1$ m with moderate soot volume fraction $f_v=10^{-7}$. Comparison of the SLW model prediction with the benchmark solution shows excellent agreement even for this small layer optical thickness. Results for the case of increased wall spacing $L=1.0$ m and soot volume fraction $f_v=10^{-6}$ are shown in Fig. 5(*b*). For this case of higher optical thickness the model accuracy is further improved.

Non-Isothermal Non-Homogeneous Medium. In this section, the SLW gas/soot mixture modeling approach developed here is compared with SNB and WSGG methods previously published for situations of uniform and non-uniform properties and compositions. Bressloff explored different approximations to the spectral behavior in the solution of RTE for a binary gas mixture with soot particles [4]. Weighted-Sum-of-Gray-Gases (WSGG) predictions were made using coefficients (which depend on local thermodynamic state) of Truelove [27]. Statistical narrow band model (SNB) predictions were made as a benchmark for comparing the accuracy of WSGG model prediction.

In this study, the variation of the total radiative intensity across a one-dimensional, homogeneous gas/soot mixture is first considered under isothermal, homogeneous conditions $T=1000$ K, $Y_{H_2O}=0.16$, $Y_{CO_2}=0.08$, $L=1.0$ m, and three different soot volume fraction with values $f_v=10^{-5}$, 10^{-6}, and 10^{-7}. Figure 6 shows a comparison of SNB and WSGG predictions for local intensity reported by Bressloff [4] with SLW model solutions from this study which, for this case, is defined by the equation

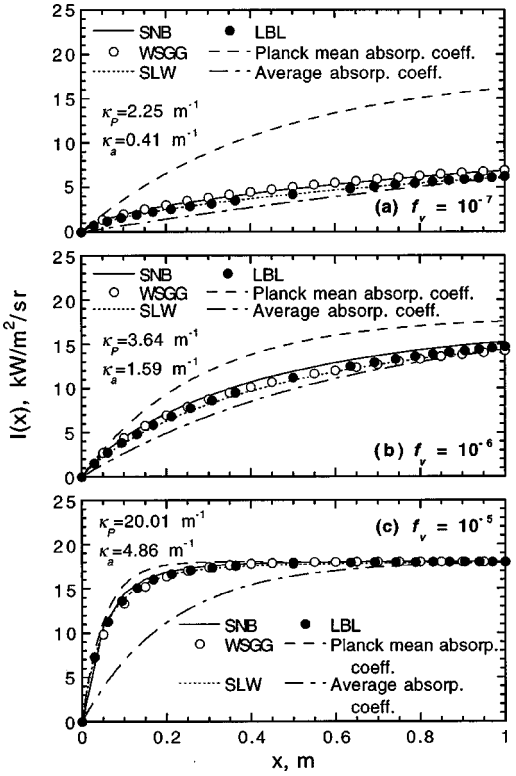

Fig. 6 Predicted local, total radiative intensity in the one-dimensional layer of gas/soot with different soot loading. The SNB and WSGG results are from Bresloff [4].

$$I(x)=I_b\sum_{j=1}^{n} a_j(1-e^{-\kappa_j x}). \tag{28}$$

A line-by-line solution was also calculated for the problem as part of this study using the HITEMP spectral database. As seen in Fig. 6, all methods give good agreement with the benchmarks, model accuracy improving with increases in soot volume fraction. The SLW solution exhibits excellent agreement with the LBL benchmark solution. There is some disagreement in both model and benchmark predictions for this study and the WSGG and SNB calculations of Bressloff. Differences between the predictions of this study and the SNB ''benchmark'' calculations of Bressloff may be explained principally by the different spectral databases and RTE solution methods used in the two studies. The most definitive validation of a radiative transfer model is one where the same spectral database is used to generate model parameters and the LBL solution, as has been done here.

The advantage of the spectral approach presented here over traditional gray calculations with averaged properties is also shown in Fig. 6. Often, an average absorption coefficient κ_a is calculated from the total emissivity ε of the layer of thickness L from Beer's law:

$$\kappa_a=\frac{1}{L}\ln(1-\varepsilon). \tag{29}$$

While different approaches may be used to determine the total emissivity ε, it can be rigorously determined by the SLW approach with a sufficiently large number of gray gases [23,24]:

$$\varepsilon=\sum_j a_j(1-e^{-\kappa_j L}). \tag{30}$$

A second averaging scheme often used in calculation of radiative properties of high temperature gases is the Planck mean κ_P, defined as [2]

$$\kappa_P=\frac{\int_0^\infty \kappa_\eta I_{b\eta}(T)d\eta}{I_b(T)}. \tag{31}$$

It has been shown that the Planck mean absorption coefficient κ_P can be rigorously calculated from the gray gas weights and corresponding gray gas absorption coefficients in the SLW model by the equation [18,25]

$$\kappa_P=\sum_j a_j\kappa_j. \tag{32}$$

The predicted local intensity of radiation using these two averaging techniques; (1) the average absorption coefficient κ_a using Eq. (30), and (2) the Planck mean absorption coefficient κ_P determined using Eq. (32) (both average coefficients calculated using 25 gray gases), is also shown in Fig. 6. The calculated values of average and Planck mean absorption coefficient are indicated in the figure for each value of soot volume fraction.

The results show that neither the simple average absorption coefficient κ_a nor the Planck mean absorption coefficient κ_P yields accurate predictions, although the Planck mean exhibits increasing accuracy as the soot loading increases. Neither averaging scheme yields desirable accuracy over the full range of soot volume fraction. Bressloff presented gray predictions for arbitrarily chosen constant values of absorption coefficient to demonstrate the increasingly gray character of solutions with increasing soot concentration [4]. However, guessing values of the absorption coefficient, or estimating values of either the average or Planck mean absorption coefficient (particularly for a non-isothermal, non-homogeneous layer) for such gray calculations would be very difficult. Although both average and Planck mean coefficients can be calculated ''exactly'' using the SLW approach outlined above, the more rigorous SLW method presented here for gas/soot mixtures yields better accuracy over the full range of soot loading.

The radiative intensity and dissipation radiative source across a one-dimensional layer of non-uniform gas/soot mixtures was calculated for the following distribution of temperatures and gas species

$$T(x)=4000x(L-x)+800,K$$

$$Y_{CO_2}(x)=0.4x(L-x)+0.06$$

$$Y_{H_2O}(x)=2Y_{CO_2}(x).$$

The spacing between walls was $L=1.0$ m, which were assumed to be radiatively black. Together with these gas temperature-species configurations, two spatially varying soot volume fraction configurations were considered

Configuration A: $f_v(x)=[40x(L-x)+6]\times10^{-7}$

Configuration B: $f_v(x)=[40x(L-x)+6]\times10^{-8}$

The SLW RTE in this case was solved using the discrete ordinates method. The detailed model procedure is described elsewhere [15]. The one-dimensional discrete ordinates solutions were carried out using 101 grid points and twelve gray gases in the SLW model for the non-homogeneous, non-isothermal mixture of three gas species and soot, requiring 3.5 s of computer time on an HP C240 workstation. An increase in resolution to 301 grid points yielded no appreciable change in the predictions. The comparison with SNB and WSGG predictions obtained by Bressloff [4] for radiative intensity and radiative dissipation source are shown in

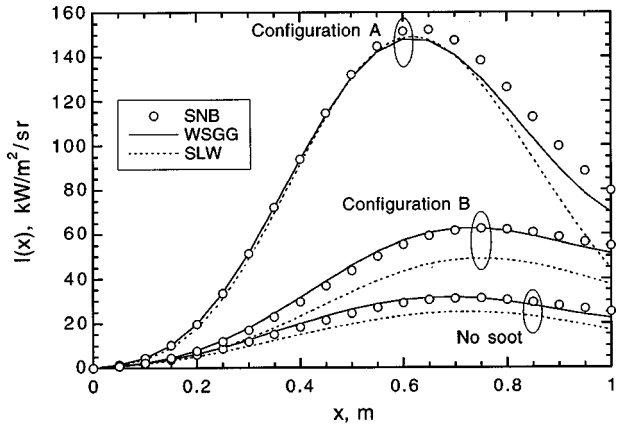

Fig. 7 Variation of the total radiative intensity with position in a non-homogeneous gas/soot mixture for different soot loadings. The SNB and WSGG results are from Bresloff [4].

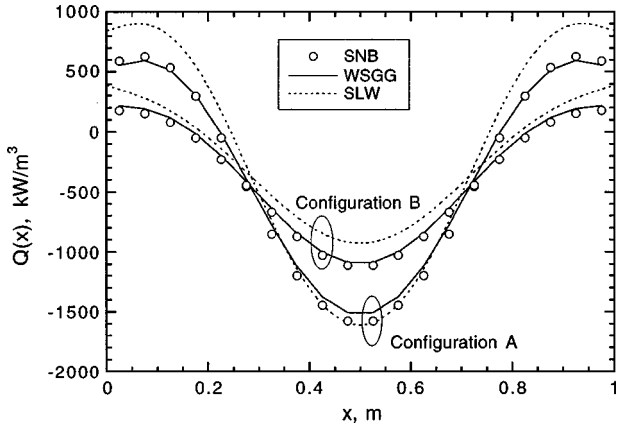

Fig. 8 Variation of the radiative dissipation source with position in a non-homogeneous gas/soot mixture for different soot loadings. The SNB and WSGG results are from Bresloff [4].

Figs. 7 and 8, respectively. Although the predictions obtained exhibit the same trend, significant disagreement is observed near the wall at $x=1.0$ m in Fig. 7. Predictions for the heavier soot loading (Configuration B) show better agreement with the SNB simulation of Bressloff. This is to be expected, since non-gray behavior of the mixture has a less dominant influence. Discrepancies in the predictions from the two studies may be the result of different solution methods for the RTE, different spectral databases used in the SNB and SLW model parameters, and/or inaccuracies in one or both models. The non-uniform temperature and species concentration distributions for this problem render generation of a line-by-line benchmark computationally prohibitive.

Conclusions

A new efficient engineering approach for predicting radiative transfer in high temperature multicomponent gas/soot mixtures has been presented. The method draws on the framework of the SLW model outlined in prior work, treating the mixture as a single non-gray gas whose absorption blackbody distribution function is calculated using the multiplication approach developed previously. Model predictions show very good agreement with line-by-line benchmark predictions generated using the same spectral database. Model accuracy improves with increasing soot loading. The model is an effective method for solution of radiation problems in combustion systems.

Acknowledgments

The authors gratefully acknowledge the assistance of Professor N. Bressloff, who kindly made his prediction data available.

Nomenclature

a = soot dispersion constant, Eq. (17)
a_j = gray gas weight j
c = constant, Eq. (16)
c_{soot} = soot concentration
C = absorption cross-section
$E_{b\eta}$ = Planck blackbody emissive power
f_v = soot volume fraction
F = absorption blackbody distribution function
I_η = spectral intensity
$I_{b\eta}$ = Planck blackbody intensity
k = imaginary part of the complex index of refraction
n = real part of the complex index of refraction
N = molar ratio
P = Planck blackbody radiation function
Q = local radiative dissipation source
T = local medium temperature
Y_i = mole fraction of species i

Greek Symbols

ε = total emissivity
η = wavenumber
κ_η = spectral absorption coefficient
κ_a = averaged absorption coefficient, Eq. (29)
κ_P = Planck mean absorption coefficient, Eq. (31)
σ = Stefan-Boltzmann constant
ρ_{soot} = soot density

References

[1] Lallemant, N., Sayre, A., and Weber, R., 1996, ''Evaluation of Emissivity Correlations for H_2O-CO_2-N_2/Air Mixtures and Coupling with Solution Methods of the Radiative Transfer Equation,'' Prog. Energy Combust. Sci., **22**, pp. 543–574.
[2] Özisik, M. N., 1973, *Radiative Transfer*, A Wiley-Interscience Publication, Wiley, New York.
[3] Goody, R. M., and Yung, Y. L., 1989, *Atmospheric Radiation*, Clarendon Press, Oxford.
[4] Bressloff, N. W., 1999, ''The Influence of Soot Loading on Weighted-Sum-of-Gray-Gases Solutions to the Radiative Transfer Equation Across Mixtures of Gases and Soot,'' Int. J. Heat Mass Transf., **42**, pp. 3469–3480.
[5] Edwards, D. K., 1976, ''Molecular Gas Band Radiation,'' Adv. Heat Transfer, **2**, pp. 116–193.
[6] Komornicki, W., and Tomeczek, J., 1992, ''Modification of the Wide-Band Gas Radiation Model for Flame Calculation,'' Int. J. Heat Mass Transf., **35**, pp. 1667–1672.
[7] Modak, A. T., 1979, ''Radiation From Products of Combustion,'' Fire Res., **1**, pp. 339–348.
[8] Taylor, P. B., and Foster, P. J., 1974, ''The Total Emissivities of Luminous and Non-Luminous Flames,'' Int. J. Heat Mass Transf., **17**, pp. 1591–1605.
[9] Taylor, P. B., and Foster, P. J., 1975, ''Some Gray Gas Weighting Coefficients for CO_2-H_2O-Soot Mixtures,'' Int. J. Heat Mass Transf., **18**, pp. 1331–1332.
[10] Modest, M. F., 1991, ''The Weighted-Sum-of-Gray-Gases Model for Arbitrary Solution Methods in Radiative Transfer,'' ASME J. Heat Transfer, **113**, pp. 650–656.
[11] Denison, M. K., and Webb, B. W., 1993, ''A Spectral Line-Based Weighted-Sum-of-Gray-Gases Model for Arbitrary RTE Solvers,'' ASME J. Heat Transfer, **115**, pp. 1004–1012.
[12] Dension, M. K., and Webb, B. W., 1996, ''The Spectral Line Weighted-Sum-of-Gray-Gases Model—A Review,'' in *Radiative Transfer-I, Proceedings of the First International Symposium on Radiation Transfer*, M. P. Mengüç, ed., Begell House, New York, pp. 193–208.
[13] Denison, M. K., and Webb, B. W., 1994, ''*k*-Distributions and Weighted-Sum-of-Gray-Gases—A Hybrid Model,'' *Heat Transfer-1994*, Hemisphere, Washington, D.C., **2**, pp. 19–24.
[14] Denison, M. K., 1994, ''A Spectral Line-Based Weighted-Sum-of-Gray-Gases Model for Arbitrary RTE Solvers,'' Ph.D. dissertation, Brigham Young University, Provo, UT.
[15] Solovjov, V. P., and Webb, B. W., 2000, ''SLW Modeling of Radiative Transfer in Multicomponent Gas Mixtures,'' J. Quant. Spectrosc. Radiat. Transf., **65**, pp. 655–672.
[16] Siegel, R., and Howell, J. R., 1992, *Thermal Radiation Heat Transfer*, Hemisphere, New York.

[17] Brewster, M. Q., 1992, *Thermal Radiative Transfer and Properties*, Wiley, New York.
[18] Solovjov, V. P., and Webb, B. W., 1998, ''Radiative Transfer Model Parameters for Carbon Monoxide at High Temperature,'' in *Proceedings of the Eleventh International Heat Transfer Conference*, Kyongju, Korea, J. S. Lee, ed., **7**, pp. 445–450.
[19] Mengüç, M. P., and Viskanta, R., 1987, ''Radiation Heat Transfer in Combustion Systems,'' Prog. Energy Combust. Sci., **13**, pp. 97–160.
[20] Modest, M. F., 1993, *Radiative Heat Transfer*, McGraw-Hill, New York.
[21] Hottel, H. C., and Sarofim, A. F., 1967, *Radiative Transfer*, McGraw-Hill, New York.
[22] Chang, S. L., and Rhee, K. T., 1984, ''Blackbody Radiation Functions,'' Int. Commun. Heat Mass Transfer, **1**, pp. 451–455.
[23] Denison, M. K., and Webb, B. W., 1993, ''An Absorption-line Blackbody Distribution Function for Efficient Calculation of Gas Radiative Transfer,'' J. Quant. Spectrosc. Radiat. Transf., **50**, pp. 499–510.
[24] Denison, M. K., and Webb, B. W., 1995, ''Development and Application of an Absorption-Line Blackbody Distribution Function for CO_2,'' Int. J. Heat Mass Transf., **38**, pp. 1813–1821.
[25] Solovjov, V. P., 1999, ''Spectral Line-Based Weighted-Sum-of-Gray-Gases Modeling of Radiative Transfer in Multicomponent Mixtures of Hot Gases,'' Ph.D. dissertation, Brigham Young University, Provo, UT.
[26] Rothman, L. S., Wattson, R. B., Gamache, R. R., Goorvitch, D., Hawkins, R. L., Selby, J. E. A., Camy-Peyret, C., Flaud, J.-M., and Schroeder, J., 2001, ''HITEMP, the High-Temperature Molecular Spectroscopic Database,'' J. Quant. Spectrosc. Radiat. Transf., (in press).
[27] Truelove, J. S., 1975, ''Zone Method for Radiative Heat Transfer Calculations,'' HTFS DR 33, AERE, Harwell, Oxon, UK.

Jun Yamada
Associate Professor
Department of Mechanical System Engineering,
Yamanashi University,
Takeda 4, Kofu,
Yamanashi 400-8511, Japan
e-mail: jyamada@ccn.yamanashi.ac.jp

Yasuo Kurosaki
Professor,
ASME Fellow
Department of Mechanical and Control Engineering,
University of Electro-Communications,

Takanori Nagai
Mitsubishi Heavy Industries,
Kan-non Shinmachi 4-6-22, Nishi,
Hiroshima, Hiroshima 733-8553,
Japan

Radiation Heat Transfer Between Fluidizing Particles and a Heat Transfer Surface in a Fluidized Bed

We have investigated the radiation heat transfer occurring in a gas-solid fluidized bed between fluidizing particles and a cooled heat transfer surface. Experimental results reveal that cooled fluidizing particles exist near the surface and suppress the radiation heat transfer between the surface and the higher temperature particles in the depth of the bed. The results also clarify the effects of fluidizing velocity, optical characteristics of particles, and particle diameter on the radiation heat transfer. Based on these results, the authors propose a model for predicting the radiation heat transfer between fluidizing particles and a heat transfer surface. [DOI: 10.1115/1.1370503]

Keywords: Fluidized Beds, Heat Transfer, Measurement Techniques, Radiation, Visualization

1 Introduction

Various research has been performed on radiation heat transfer between fluidizing particles and a heat transfer surface in a gas-solid fluidized bed because it is expected that the radiation heat transfer augments at a high temperature. As a result, a model for the radiation heat transfer in a dilute phase where the particulate concentration is low (porosity of over 0.9), as seen in the upper part of a practical fluidized bed, has been established [1–4].

On the other hand, for the radiation heat transfer in a dense phase, where the particulate concentration is high as seen in the lower part of a fluidized bed (porosity of the order of 0.5), only a rough mechanism has been understood. The radiation heat transfer model in which parameters, such as particle diameter, fluidizing velocity, etc. is constructed, has not been constructed [5]. One of the reasons for this is because the experimental results necessary to construct the model conflict among researchers. To be specific, the influence of the particle diameter, the fluidizing velocities and the radiative characteristics of particles on the radiation heat transfer, as well as the qualitative tendencies in the experimental results do not mutually correspond with each other.

In the experimental research concerning the radiation heat transfer in a gas-solid fluidized bed, where the bed temperature varies from several hundreds of degrees to over 1000°C, the radiation heat transfer is separated from the total heat transfer by a special device and measured [6–12]. The contribution of the radiation heat transfer to the total heat transfer is then evaluated from the experimental results.

In these experiments, the significant wavelength range in radiation heat transfer shortens as bed temperature increases. If the radiative characteristics of the fluidizing particles or the heat transfer surface are not gray, the non-gray effects appear in the experimental results of the radiation heat transfer. In this case, it is difficult to clarify the mechanism of the radiation heat transfer based on the radiation energy integrated over all the wavelengths.

Moreover, since the gas properties, such as kinematic viscosity and/or density, strongly depend on gas temperature, the fluidizing pattern may vary greatly with temperature. This means the radiation energies measured at much different temperatures are influenced by several parameters. Since such parameters other than the particle diameter and the fluidizing velocity influence the radiation heat transfer, differing results as mentioned before may occur even among similar experiments.

When this is taken into account, a hypothesis should not be based on experimental data measured at greatly varying temperatures. Rather, an experiment performed in a monochromatic or a narrow wavelength range is suitable in order to clarify the mechanism for the radiation heat transfer.

From this point of view, we have measured the radiation that propagates in a fluidized bed by using a visible light laser and have verified that radiation is attenuated at an extremely short distance in a dense phase. This study, which includes a corresponding numerical analysis, reveals that the particles fluidizing near the heat transfer surface are an important factor in the radiation heat transfer [13]. The temperatures of the particles fluidizing adjacent to the heat transfer surface are different from those in the middle of the bed due to cooling (or heating) by the heat transfer surface. This implies that it is important to know the temperature of the particles adjacent to the heat transfer surface or the radiation energy emitted from the particles to evaluate the radiation heat transfer between the particles and the heat transfer surface.

In a later study, we have measured the radiation energy emitted from particles fluidizing near a heated heat transfer surface in a fluidized bed, and have evaluated the radiation heat transfer between the fluidizing particles and the heat transfer surface. We have also evaluated the effects of the particle diameter, the bed emissivity and the fluidizing velocity on the radiation heat transfer [14].

However, since most practical fluidized beds are operated at a high temperature and have a cooled heat transfer surface, it is difficult to directly apply the results obtained in our previous study to such fluidized beds. This is because when the bed and surface temperatures switch, not only does the flow direction of the radiation energy reverse, but the amount of radiation energy exchanged between the surface and the bed changes as well. Moreover, in the previous study, the experimental results are not accurate enough because the temperature difference between the heat transfer surface and the fluidized bed is small.

The purposes of this study are to clarify the mechanism for the radiation heat transfer between a high temperature bed and a cooled heat transfer surface in a dense phase, and to propose a model for predicting the radiation heat transfer based on this mechanism.

Contributed by the Heat Transfer Division for publication in the JOURNAL OF HEAT TRANSFER. Manuscript received by the Heat Transfer Division May 16, 2000; revision received January 8, 2001. Associate Editor: M. Hunt.

In this study, we have made an experimental fluidized bed having a cooled heat transfer surface, and have measured the radiation energy emitted from the fluidizing particles on the heat transfer surface while varying the fluidizing velocity, optical characteristics of the particles, and the particle diameter. Based on the measured results, the effects of such parameters on the radiation heat transfer have been clarified, and a model for predicting the amounts of radiation heat transfer has been discussed.

2 Experimental Setup and Procedure

2.1 Experimental Setup. A schematic diagram of the experimental setup is shown in Fig. 1. The experimental fluidized bed has a cross section of 100 mm×100 mm and a height of 1200 mm. A cooled heat transfer surface having a diameter of 45 mm is located 60 mm above a felt sheet distributor placed on the bottom of the bed. Two cartridge heaters are equipped to control the bed temperature. One of the heaters is immersed in the bed and the other is placed below the distributor.

An IR camera (IRC-160ST, Nippon Avionics) located external to the bed is used to measure the radiation energy emitted by the fluidizing particles on the heat transfer surface without disturbing the bed fluidization. The IR camera provides not only an NTSC video signal for radiation energy distribution, but also displays a 160×100 dot image with an 8-bit gray scale that can be stored as digital data.

Since the measurements for the radiation energy are carried out through the heat transfer surface, the surface must be transparent. We have used CaF_2 windows, whose transparency is 95 percent in the camera's range of detectable wavelengths (3.0–5.4 μm).

The heat transfer surface is cooled by convection using low temperature air that is generated by an air cooler (AC-70, Tohin) applying the Joule-Thomson effect. The cooling system for the heat transfer surface is shown in Fig. 2. The system has two cavities with CaF_2 windows behind the heat transfer surface. The cooled air (less than -10°C) is blown into the inner cavity and uniformly cools the back of the heat transfer surface, and the hot dry gas is blown into the outer cavity so as to prevent condensation on the cavities' windows. Thus, this system allows measurement of only the radiation emitted from the fluidizing particles adjacent to the heat transfer surface.

The bed temperature is measured by a Chromel-Alumel (CA) thermocouple having a diameter of 0.1 mm, which is movable along the center axis of the heat transfer surface. The temperature of the heat transfer surface is measured by another CA thermocouple attached to the bed side of the surface.

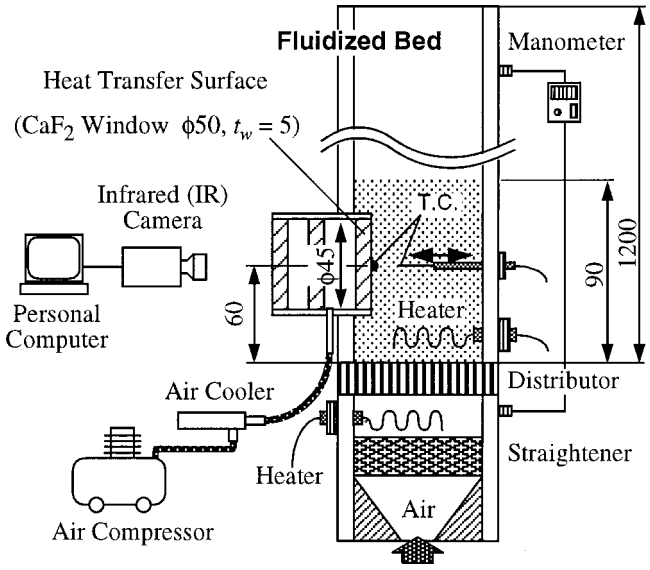

Fig. 1 Schematic diagram of the experimental setup

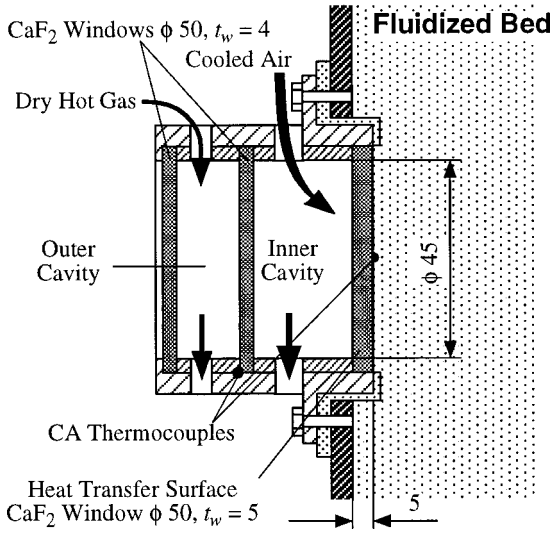

Fig. 2 Schematic diagram of the cooling system for the heat transfer surface

2.2 Experimental Conditions and Fluidizing Particles. All of the experiments, except for the bed emissivity measurement which is explained in the next section, are carried out at a surface temperature T_w of 30°C and at a bed temperature T_{bed} of 60°C. The signal output of the IR camera used in this experiment is linear when the measured radiation energy is less than the blackbody radiation of 70°C. We have allowed a margin of 10 K and have decided on 60°C for T_{bed}. T_w of 30°C is the minimum temperature that can be stably maintained by the present cooling system.

T_w is controlled by the flow rate of the air cooler. T_{bed} is the temperature outside the thermal boundary layer at the height of the heat transfer surface and is maintained constant by the two cartridge heaters. The spatial non-uniformity of the temperature in the bed is less than 3 K except near the heat transfer surface.

It has been experimentally confirmed that the CaF_2 window emits negligible radiation in the detectable wavelength region, if the window is heated up to 60°C, which is the maximum temperature in the experiment.

The static bed height is fixed at 90 mm and the fluidizing velocity U is varied between 1.2 and $4.0U_{mf}$, where U_{mf} is the minimum fluidizing velocity empirically determined by measuring the pressure drop across the bed. Under all fluidizing velocities, bubbling fluidization is observed. Table 1 presents the parameters associated with the fluidizing particles used in this study, as well as their corresponding values of U_{mf} and bed emissivity ε_{bed}, which is evaluated in the camera's range of the detectable wavelengths (3.0–5.4 μm).

2.3 Measurement of Bed Emissivity. ε_{bed} is defined as the ratio of the radiation energy emitted from the isothermal, optically thick bed to the blackbody radiation energy emitted at the bed temperature.[1] This parameter is also empirically determined as described below.

[1] ε_{bed} defined in this study is independent of the volume fraction of the bed, which varies with fluidizing velocity. This reason is as follows. The albedo and scattering phase function of a dispersed medium is constant, being independent of its void fraction under the assumption of independent scattering [15], and only the extinction coefficient is proportional to the void fraction. However, since the emissivity of an optically thick, dispersed, isothermal medium does not depend on the extinction coefficient [16], the emissivity of such medium is independent of its void fraction and is constant.

Table 1 Parameter associated with the employed fluidizing particles

Particle	Diameter [μm]	U_{mf} [m/s]	ε_{bed} (3.0-5.4 μm)
Glass Beads (Sphere)	50	0.018	0.76
	100	0.027	0.82
	200	0.042	0.88
	400	0.127	0.95
Corderite	200	0.063	0.84
SiO_2	200	0.040	0.65
Al_2O_3	200	0.109	0.59
Al_2O_3 (Sphere)	60	0.023	0.35

The experimental bed, which has been confirmed to be optically thick by transmission measurement in advance, is used for determining ε_{bed}. The bed is isothermally heated to 60°C, and the radiation energy emitted from the bed is measured by the IR camera through the heat transfer surface. During this measurement, to ensure that the fluidizing particles are not cooled by the heat transfer surface, the hot air blower is used to maintain the heat transfer surface at the same temperature. Using the IR camera, we have also measured the radiation energy emitted from a pseudo-blackbody, which is maintained at the same temperature as the bed and is placed at the same distance from the camera. The values of ε_{bed} listed in Table 1 are determined from these measurement results according to the above definition and have an uncertainty of 8.2 percent. The derivation of the uncertainty is shown in the Appendix.

However, since the radiation leaving the bed includes the reflected background radiation, such as the radiation emitted by the inner wall of the cooling cavity and the environment, it is necessary to correct the reflected background radiation. The method used to make the correction is shown in the Appendix.

In this study, because all of the radiation measurements use the IR camera, not only ε_{bed}, but other radiation parameters are also evaluated in the camera's range of detectable wavelengths. The significant wavelength range of the radiation heat transfer in practical fluidizing beds, which are usually operated at a high temperature, does not match the present range. It should be realized, however, that the results obtained here are applicable to any other fluidizing bed if the radiative parameters are replaced by those in the wavelength range of interest. The applicability to high-temperature fluidized beds will be discussed in the next section.

3 Results and Discussion

3.1 Visualization of Radiation Energy. Figure 3 shows the typical time-dependent distribution of the radiation emitted by fluidizing particles on the heat transfer surface, where the circle indicates the transparent heat transfer surface. This distribution is obtained from images recorded by a video tape recorder (VTR). The bright (red-white) region in Fig. 3(*a*), where the radiation energy is high, indicates a bubble, which represents a space where few particles exist, rising along the surface. Bubbles appear bright because high-temperature fluidizing particles can be seen through them. In the dark (black-blue) region there are low-temperature particles. They emit little radiation, and obstruct the radiation emitting from the high-temperature particles from the depth of the bed as well. This proves that cooled fluidizing particles suppress the radiation heat transfer. After the bubble is gone, the high-temperature fluidizing particles contact the heat transfer surface (Fig. 3(*b*)) and are transiently cooled by conduction during the contact period with the surface and/or by gas convection in the thermal boundary layer (Fig. 3(*c*)).

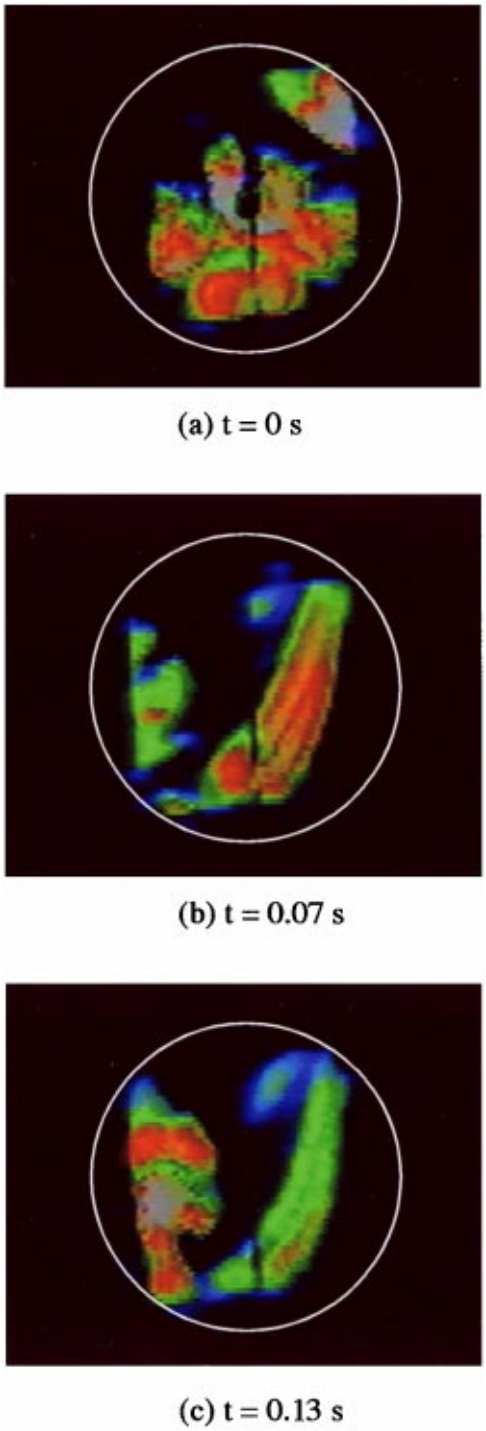

Fig. 3 Distribution of radiation energy emitted by the fluidizing particles (Glass, $d = 200\ \mu\text{m}, U/U_{mf} = 2.0$)

The radiation emitted from fluidizing particles varies because they are transiently cooled and leave the heat transfer area. Thus, for practical purposes, the time-averaged radiation energy emitted from the fluidizing particles is required to evaluate the radiation heat transfer occurring between the fluidizing particles and heat

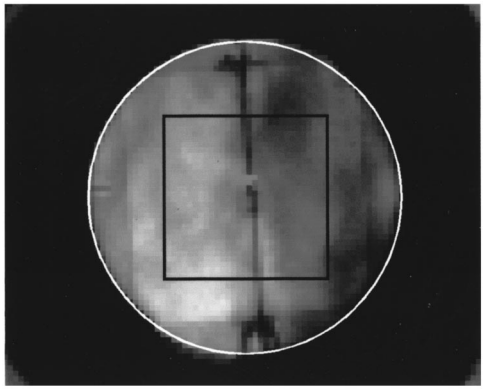

Fig. 4 Distribution of the time-averaged radiation energy emitted by the fluidizing particles (Glass, $d=200\ \mu$m, $U/U_{mf}=2.0$)

transfer surface. We have derived the time-averaged radiation energy using 270 images (27 images taken every 1/50 sec×10 sets), which are stored as digital data.

A photograph of the resultant distribution for the radiation energy is shown in Fig. 4. Since spatial non-uniformity in the distribution is evident, we use the radiation energy spatially averaged within the indicated rectangular region (30×30 dots) to evaluate the radiation heat transfer.

3.2 Effect of Several Parameters on the Radiation Heat Transfer. Figure 5 shows the dimensionless radiation energy, $E_{\text{net}}/E_b(T_{\text{bed}})$, versus the dimensionless fluidizing velocity, U/U_{mf}, of glass beads with diameters of 50, 100, 200, and 400 μm. We account for the reflected background radiation as shown in the Appendix. The error bars attached to the experimental results represent 95 percent confidence intervals. The error analysis is explained in the Appendix.

For all particles, $E_{\text{net}}/E_b(T_{\text{bed}})$ increases with increasing U/U_{mf} at comparatively low velocities. This is because the bubble frequency correspondingly increases. Obviously, as the bubble frequency increases, the total time when the heat transfer surface can detect the high temperature particles through the bubbles also increases, and so the measured radiation energy increases. Another reason is that, as the residence time of the particles near the heat transfer surface decreases, the amount of heat taken away from the particles decreases and the emitted radiation energy increases. However, this behavior appears to saturate at

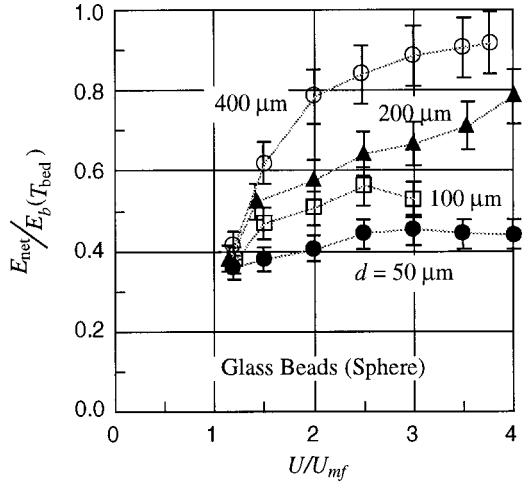

Fig. 5 Effect of the fluidizing velocity on the dimensionless radiation energy

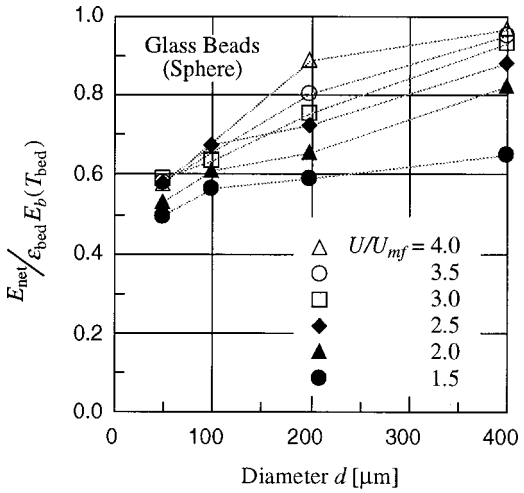

Fig. 6 Effect of the particle diameter on the dimensionless radiation energy normalized by that emitted from an isothermal fluidizing bed at 60°C

higher fluidizing velocities. This is because the particle motion does not dramatically vary with increasing fluidizing velocity.

Figure 6 shows the effect of the particle diameter, d, on the dimensionless radiation energy emitted from the fluidizing particles. Error bars are not shown in this figure. The magnitude of the 95 percent confidence interval is less than the size of the symbols. Here the radiation energy is normalized by that emitted from an isothermal fluidized bed at 60°C, which is equal to the bed temperature, T_{bed}. By doing this, we cancel out the effect of the differences in bed emissivity on the amount of measured radiation energy.

Notice that the normalized radiation energy, $E_{\text{net}}/\varepsilon_{\text{bed}}E_b(T_{\text{bed}})$, increases with increasing particle diameter. As the particle diameter increases, its heat capacity also increases, and therefore its temperature does not change easily. Also the extinction coefficient of the fluidized bed correspondingly decreases [15] and the radiation emitted at the depth of the bed can reach the heat transfer surface, thereby increasing the amount of the radiation energy.

Even if the normalized fluidizing velocities are the same between the beds having particles with different diameters, it cannot be said that the fluidized patterns are the same. Therefore, this figure may not correctly represent the effect of particle diameter on the radiation energy. However, this figure gives information regarding the effect of particle diameter because the fluidizing patterns are not very different when the normalized fluidizing velocities are the same.

Figure 7 shows the effect of bed emissivity on the radiation energy emitted from fluidizing particles at $U=2.0U_{mf}$, where the radiation energy increases with increasing bed emissivity.

The two lines indicate the limits of the emitted radiation energy from the bed, with the upper and lower line corresponding to the radiation energy emitted from an isothermal bed at T_{bed} (60°C) and T_w (30°C), respectively. Since the temperature of any fluidizing particle is between T_{bed} and T_w, the amount of radiation energy emitted from the bed must fall between the lines.

It should be noted that the radiation energy emitted from small particles, such as Al_2O_3 with $d=60\ \mu$m and glass with $d=50,100\ \mu$m, are close to the lower limit, although their bed emissivities are very different. This is because small particles cool faster than large ones, and consequently, reduce the radiation energy from the bed. This means the radiation energies from the beds having the same emissivities would be different depending on the cooling rate of the particles near the heat transfer surface.

To clarify the effect of the cooled particles on the radiation heat transfer, the radiation energy emitted from the bed to the heat transfer surface, E_{net}, is normalized as

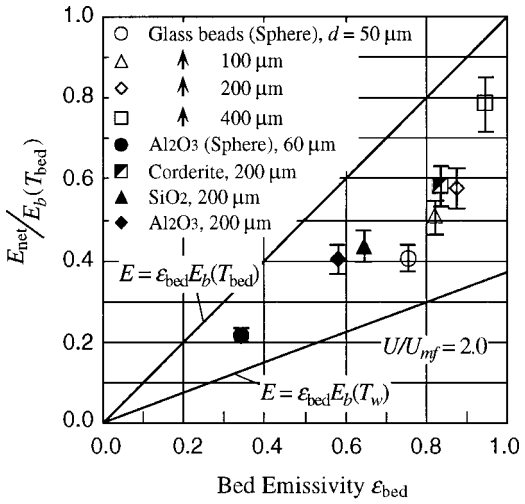

Fig. 7 Effect of the bed emissivity on the dimensionless radiation energy

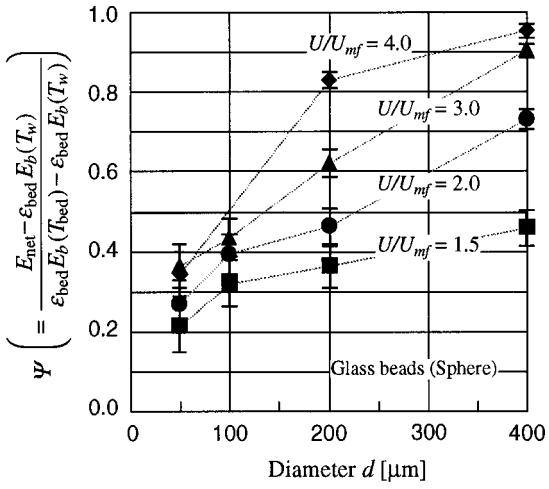

Fig. 9 Effect of the fluidizing velocity on the radiation heat transfer efficiency

$$\Psi = \frac{E_{\text{net}} - \varepsilon_{\text{bed}} E_b(T_w)}{\varepsilon_{\text{bed}} E_b(T_{\text{bed}}) - \varepsilon_{\text{bed}} E_b(T_w)} \tag{1}$$

The physical meaning of Ψ is given below.

$\Psi=0$ means that all the particles are cooled perfectly and are at T_w (the lower limit in Fig. 7), and $\Psi=1$ means they are not cooled by the cooled heat transfer surface and are at T_{bed} (the upper limit in Fig. 7). In other words, when the radiation energy is not exchanged at all, Ψ becomes zero, and when the radiation energy exchange is at a maximum, Ψ becomes unity. Thus, this dimensionless radiation energy Ψ shows the efficiency of the radiation heat transfer.

The dimensionless radiation energy from the bed, Ψ, is shown versus the diameter of the fluidizing particles in Fig. 8. This figure shows the radiation energy increases monotonically as the particle diameter increases, and, at the same time, it becomes easy for the radiation energy to be exchanged as the particle diameter increases.

From this figure, it is also found that Ψ is almost independent of ε_{bed}. This is because Ψ chiefly depends on the particle temperatures. In the present experiment, since the bed temperature is low, the radiation heat transfer would be negligible. Therefore, ε_{bed} does not affect the particle temperature, and consequently, Ψ is independent of ε_{bed}.

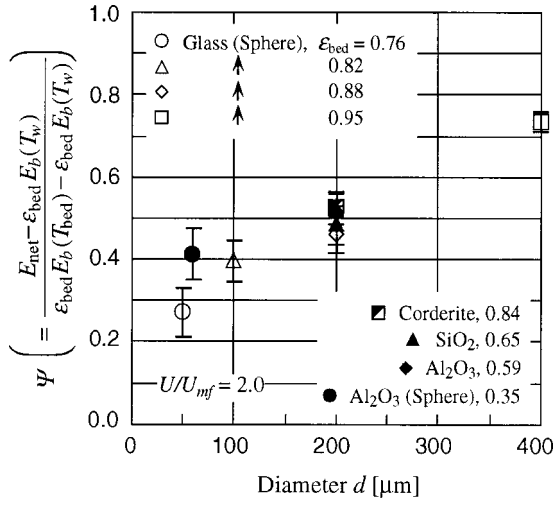

Fig. 8 Effect of the particle diameter on the radiation heat transfer efficiency

Figure 9 shows Ψ for several fluidizing velocities. It is shown that the radiation heat transfer is enhanced as the fluidizing velocity increases. As mentioned before, this is because the bubble frequency correspondingly increases, and the particles do not cool as quickly as their residence time near the heat transfer surface decreases.

3.3 Applicability to High-Temperature Fluidized Beds. All of these experiments are performed at a comparatively low temperature where the radiation heat transfer may not be significant, and the significant wavelength range in the radiation heat transfer may differ from the present range, which is the detectable range of the IR camera. However, we believe the present results are applicable to fluidized beds operating at high temperatures. The applicability of the present results to high-temperature fluidized beds is described below.

Consider a system where the radiation heat transfer is assumed to be one-dimensional. As the heat transfer surface has a spectral hemispherical emissivity of $\varepsilon_{w,\lambda}$ and the bed has an emissivity of $\varepsilon_{\text{bed},\lambda}$, the radiative flux exchanged between the surface and the bed, q_{exc} can be derived by the following equation:

$$q_{\text{exc}} = \int_0^\infty \frac{\Psi(q_{b,\lambda}(T_{\text{bed}}) - q_{b,\lambda}(T_w))}{\dfrac{1}{\varepsilon_{\text{bed},\lambda}} + \dfrac{1}{\varepsilon_{w,\lambda}} - 1} d\lambda \tag{2}$$

where the $q_{b,\lambda}(T)$ is the spectral blackbody flux. This equation is derived taking into account the multiple reflections between the heat transfer surface and the bed.

Ψ chiefly depends on the particle temperature near the heat transfer surface and the radiation propagation depth, i.e., the extinction and scattering coefficients of the fluidized bed. In the present experiment, since the absolute temperature of the bed is low, the particles near the heat transfer surface are not cooled by radiation but are cooled by conduction while in contact with the surface and /or convection in the thermal boundary layer. Therefore, the particle temperature does not depend on the wavelength. However, since the extinction and scattering coefficients depend on the size parameter, $\alpha(=\pi d/\lambda)$ [15], Ψ is a function of wavelength.

If the wavelength-dependency of Ψ is weak, the integration in Eq. (2) can be carried out and the radiation energy exchanged between the heat transfer surface and the fluidizing particles in a dense phase can be obtained by using the values of Ψ from Fig. 8

or 9, $\varepsilon_{w,\lambda}$ and $\varepsilon_{\mathrm{bed},\lambda}$. In this calculation, the temperature outside of the thermal boundary layer at the height of the heat transfer surface is taken for T_{bed} because there is a slight non-uniform distribution of temperature along the vertical position within the bed.

Basu [7] has carried out a heat transfer experiment at high temperatures using sand particles having an average diameter of 280 μm, which is similar to the glass particles used in this study. He has reported that the heat transfer coefficient of a 20–30°C surface immersed in a fluidized bed of 800–900°C is about 500 W/m^{2}K. The contribution of the radiation heat transfer is 5–10 percent when the fluidizing velocity is 0.28 m/s. If $T_{\mathrm{bed}}=900$°C, $T_w=30$°C, and the radiation contribution is 10 percent, the radiative heat flux is estimated to be about 44 W/m^2. To compare this result with the present study, we have estimated the radiative heat flux at the same condition using Eq. (2).

In the estimation, since the dependency of Ψ on wavelength is unknown, we have adopted 0.76 as the value for Ψ, which is the average value of the 200 μm and 400 μm glass particles at $U=3.0U_{mf}$ (read from Fig. 9.) Furthermore, since the emissivities of the fluidizing bed and the heat transfer surface are not given in the literature, we have adopted 0.92 as the value for $\varepsilon_{\mathrm{bed}}$ (the average value of the 200 and 400 μm glass particles shown in Table 1), and 1.0 as the value for ε_w. They are both assumed to be independent of wavelength. Under these conditions, we estimate the radiative heat flux using Eq. (2). The resultant value of the radiative heat flux is 75 W/m^2. This is much larger than Basu's result. However, in the estimation, there are many unknown parameters, such as $\varepsilon_{\mathrm{bed}}$ and ε_w. Although we have set $\varepsilon_{\mathrm{bed}}=0.92$ referring the measured values of 3.0–5.4 μm, the correct value would be smaller because the radiative energy is chiefly exchanged at shorter wavelengths at 900°C, where the emission of glass particles is lower. Moreover, the value of ε_w must be smaller than unity in the experiments by Basu. Therefore, the difference between the results for the radiative heat flux would be reduced if the correct values have been given in the estimation using Eq. (2).

Equation (2) can also be applied to the radiation heat transfer in a dilute phase. Since there are no cooled particles near the heat transfer surface, the surface detects particles being at the bed temperature. That is, $\Psi=1$.

By substituting $\Psi=1$ into Eq. (2), one can obtain the same relationship as previously reported for predicting the radiation heat transfer in the dilute phase [1–4]. This suggests a possibility that the present model can comprehensively describe the radiation heat transfer in a fluidized bed.

In this study, although the effects of particle diameter, bed emissivity and fluidizing velocity on Ψ have been evaluated, the effects of particle shape and/or its thermophysical properties are not yet fully understood. However, these effects have not been significant in this experiment. The effects are considered to be weaker than those of particle diameter, bed emissivity and fluidizing velocity.

As mentioned before, Ψ chiefly depends on the particle temperature near the heat transfer surface. If the fluidized bed operates at a realistic high temperature, the particles near the heat transfer surface would be cooled more strongly by radiation heat exchange with the heat transfer surface. Thus, the value of Ψ would be smaller than those shown in Figs. 8 and 9. In the case of small Ψ, where the particles are small and their motion is not active, high temperature particles are cooled rapidly after a bubble is gone because their heat capacities are small, and Ψ may decrease transiently. However, once the particles are cooled, radiation energy does not exchanged with the heat transfer surface, and so Ψ would be the same as the present results. Since Ψ is shown in this study as a time-averaged value, Ψ will not change significantly.

In the case of large Ψ (radiation energy is easily transferred), the particles would not cool rapidly because they are large, their motion is active and their residence time near the heat transfer surface is shorter than their thermal time constant. In such a situation, the particles would move away before they are cooled by radiation heat exchange with the heat transfer surface. Although this is not proven since the present experiment is carried out at a low temperature, it has been observed that the particles have moved away before being cooled.

Thus, in either case, the value of Ψ at a realistic high temperature is the same as the present results or slightly smaller.

4 Conclusions

To evaluate the radiation heat transfer occurring in a gas-solid fluidized bed between the fluidizing particles and a cooled heat transfer surface, we have used an infrared camera to measure the radiation energies emitted by the fluidizing particles against the heat transfer surface. It has been explained that the radiation heat transfer is enhanced by (1) using large particles, and (2) operating at a high fluidizing velocity as well as using a bed with a high emissivity. By doing so, the temperature of the particles near the heat transfer surface is not lowered, and radiation energy against the surface is kept high.

Based on these results, we have proposed a model for predicting the radiation heat transfer by obtaining its efficiency, Ψ. For the practical use of this model, the effect of the particulate concentration on Ψ must be understood. In addition to this, future research will aim to verify the ability to predict the radiation heat transfer in practical fluidized beds.

This work is supported in part by the Ministry of Education, Science and Culture of Japan under grant No. 06750197.

Nomenclature

C_1 = regression coefficient (Fig. 11)
C_2 = regression coefficient (Fig. 11), K
d = particle diameter, μm
D = system output of the measured radiation energy emitted from the fluidizing bed
D_b = system output of the measured radiation energy emitted from a blackbody
E = radiation energy emitted from the fluidizing bed, W
E_b = radiation energy emitted from a blackbody, W
E^* = dimensionless radiation energy, $E_{\mathrm{net}}/E_b(T_{\mathrm{bed}})$
q_{net} = radiative flux emitted from the fluidized bed, W/m^2
q_b = radiative flux emitted from a blackbody, W/m^2
T_{bed} = bed temperature outside the thermal boundary layer on the heat transfer surface (60°C)
T_{cav} = cavity temperature, °C
T_{env} = environment temperature, °C
T_w = temperature of the heat transfer surface (30°C)
U = fluidizing velocity, m/s
U_{mf} = minimum fluidizing velocity, m/s
σ = uncertainty
$\varepsilon_{\mathrm{bed}}$ = bed emissivity
Ψ = radiation heat transfer efficiency (Eq. (1))

Subscripts

gro = gross (including the reflected background radiation)
iso-bed = of the isothermal bed
net = net (excluding the reflected background radiation)

Appendix

A1 Correcting for the Background Radiation. The method used to correct for the background radiation is explained as follows. Suppose that the fluidized bed has a diffuse surface and its reflectivity is $1-\varepsilon_{\mathrm{bed}}$. The radiosity from the bed, q_{gro}, is given by,

$$q_{\mathrm{gro}}=q_{\mathrm{net}}+(1-\varepsilon_{\mathrm{bed}})q_{\mathrm{back}} \tag{3}$$

where q_{back} is the irradiation from the background. In this measurement system, q_{back} is

$$q_{\text{back}}=\frac{\varepsilon_2 S_2 F_{21} q_b(T_{\text{cav}})+\varepsilon_3 S_3 F_{31} q_b(T_{\text{env}})}{S_1}, \tag{4}$$

where the first term on the right hand side represents the radiation contribution coming from the inner wall of the cooling cavity shown in Fig. 10, and the second term is that from the environment, such as the room wall. $q_b(T_{\text{cav}})$ and $q_b(T_{\text{env}})$ are the blackbody radiative fluxes at the temperature of the cavity wall, T_{cav}, and the environment, T_{env}, respectively. S and F are the surface area and the view factor, respectively. It is assumed here that the emissivities of the cavity wall, ε_2, and the environment, ε_3, are equal to 1 and that the windows are transparent.

The signal output of the measurement system is proportional to the amount of measured radiation energy. Using the proportional constant C, the output for radiation energy from the bed can be expressed as

$$D_{\text{gro}}=C\varepsilon_s(q_{\text{gro}}-q_b(T_s)), \tag{5}$$

where ε_s is the sensor's emissivity and is assumed to be equivalent to the absorptivity, and T_s is the sensor temperature. Similarly, the signal output for the blackbody at the bed temperature, $D_b(T_{\text{bed}})$, is

$$D_b(T_{\text{bed}})=C\varepsilon_s(q_b(T_{\text{bed}})-q_b(T_s)). \tag{6}$$

The amount of radiation emitted from the sensor, $\varepsilon_s q_b(T_s)$, is not considered here because T_s is very low ($<$233 K). Using Eqs. (5) and (6), the following equation is derived.

$$\frac{D_{\text{gro}}}{D_b(T_{\text{bed}})}=\frac{q_{\text{gro}}}{q_b(T_{\text{bed}})}=\frac{q_{\text{net}}}{q_b(T_{\text{bed}})}+(1-\varepsilon_{\text{bed}}) \times\left\{\frac{S_2F_{21}}{S_1}\frac{q_b(T_{\text{cav}})}{q_b(T_{\text{bed}})}+\frac{S_3F_{31}}{S_1}\frac{q_b(T_{\text{env}})}{q_b(T_{\text{bed}})}\right\}. \tag{7}$$

As is evident from Eq. (6),

$$\frac{q_b(T_{\text{cav}})}{q_b(T_{\text{bed}})}=\frac{D_b(T_{\text{cav}})}{D_b(T_{\text{bed}})}, \quad \frac{q_b(T_{\text{env}})}{q_b(T_{\text{bed}})}=\frac{D_b(T_{\text{env}})}{D_b(T_{\text{bed}})}, \tag{8}$$

where $D_b(T_{\text{env}})$ and $D_b(T_{\text{cav}})$ are the signal outputs for the blackbody radiation at T_{env} and T_{cav}, respectively. Using Eq. (8), the dimensionless radiative flux emitted by the bed is given by Eq. (7) as

$$\frac{q_{\text{net}}}{q_b(T_{\text{bed}})}=\frac{D_{\text{gro}}}{D_b(T_{bed})}-(1-\varepsilon_{\text{bed}}) \times\left\{\frac{S_2F_{21}}{S_1}\frac{D_b(T_{\text{cav}})}{D_b(T_{\text{bed}})}+\frac{S_3F_{31}}{S_1}\frac{D_b(T_{\text{env}})}{D_b(T_{\text{bed}})}\right\}. \tag{9}$$

The second term on the right hand side of Eq. (9) represents the correction of the background radiation.

Since the bed and the pseudo-blackbody used in this study are the same distance from the IR camera, $E_{\text{net}}/E_b(T_{\text{bed}})$ is equal to $q_{\text{net}}/q_b(T_{\text{bed}})$, and can be evaluated by Eq. (9).

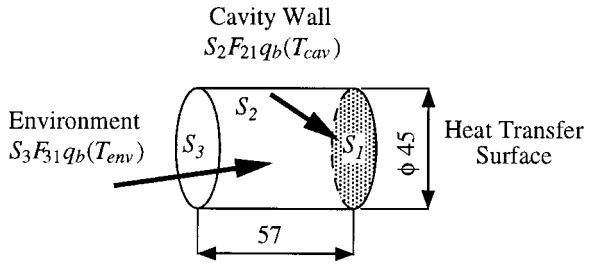

Fig. 10 Configuration for the cooling system and the background radiation

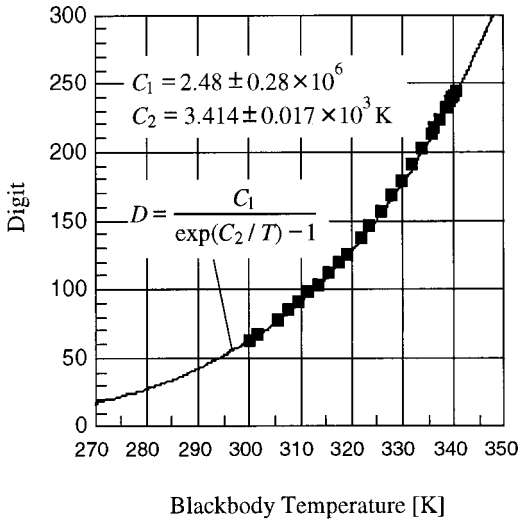

Fig. 11 System output of the IR camera versus the radiation energy emitted by a pseudo-blackbody

The radiation emitted by the bed to the heat transfer surface is observed through the three CaF_2 windows by the IR camera. Taking into account the transparency of the CaF_2 windows, which is 95 percent, we correct the values evaluated by Eq. (9) by dividing by 0.95^3. The background radiation and the transparency of the CaF_2 windows are corrected by the same manner for not only $E_{\text{net}}/E_b(T_{\text{bed}})$ in Fig. 5 but also for the other results shown in this study.

The values of $D_b(T_{\text{bed}})$, $D_b(T_{\text{env}})$, and $D_b(T_{\text{cav}})$, which are signal outputs of the IR camera for the blackbody at T_{bed}, T_{env}, and T_{cav}, respectively, are necessary to calculate $E_{\text{net}}/E_b(T_{\text{bed}})$. Using the pseudo-blackbody, we have measured the radiation emitted from the pseudo-blackbody with varying blackbody temperature. Figure 11 shows $D_b(T)$ versus the blackbody temperature. The symbols are the experimental results and the line is a regression curve, where we have chosen the regression function by taking into account the Planck blackbody function. The uncertainty for the regression coefficients, C_1 and C_2, represents 95 percent confidence intervals, which are evaluated by the literature [17]. We obtain the values of $D_b(T_{\text{bed}})$, $D_b(T_{\text{env}})$ and $D_b(T_{\text{cav}})$ by this regression function given the temperatures.

A2 Bed Emissivity. To determine ε_{bed}, the radiation energy, $E_{\text{iso-bed,gro}}$, emitted by the isothermal fluidizing bed of a temperature $T_{\text{iso-bed}}$ is measured. According to the definition of ε_{bed}, it can be written as

$$\varepsilon_{\text{bed}}=\frac{E_{\text{iso-bed,net}}}{E_b(T_{\text{iso-bed}})}. \tag{10}$$

As mentioned before,

$$\frac{E_{\text{iso-bed,net}}}{E_b(T_{\text{iso-bed}})}=\frac{q_{\text{iso-bed,net}}}{q_b(T_{\text{iso-bed}})}. \tag{11}$$

Eqs. (9), (10), and (11) yield

$$\varepsilon_{\text{bed}}=\frac{q_{\text{iso-bed,net}}}{q_b(T_{\text{iso-bed}})}=\frac{D_{\text{iso-bed,gro}}}{D_b(T_{\text{iso-bed}})}-(1-\varepsilon_{\text{bed}}) \times\left\{\frac{S_2F_{21}}{S_1}\frac{D_b(T_{\text{cav}})}{D_b(T_{\text{iso-bed}})}+\frac{S_3F_{31}}{S_1}\frac{D_b(T_{\text{env}})}{D_b(T_{\text{iso-bed}})}\right\}, \tag{12}$$

where $D_{\text{iso-bed,gro}}$ is the signal output of the IR camera for $E_{\text{iso-bed,gro}}$. Consequently, ε_{bed} is given by

$$\varepsilon_{\text{bed}}=\frac{\dfrac{D_{\text{iso-bed,gro}}}{D_b(T_{\text{iso-bed}})}-\left\{\dfrac{S_2F_{21}}{S_1}\dfrac{D_b(T_{\text{cav}})}{D_b(T_{\text{iso-bed}})}+\dfrac{S_3F_{31}}{S_1}\dfrac{D_b(T_{\text{env}})}{D_b(T_{\text{iso-bed}})}\right\}}{1-\left\{\dfrac{S_2F_{21}}{S_1}\dfrac{D_b(T_{\text{cav}})}{D_b(T_{\text{iso-bed}})}+\dfrac{S_3F_{31}}{S_1}\dfrac{D_b(T_{\text{env}})}{D_b(T_{\text{iso-bed}})}\right\}}. \tag{13}$$

A3 Error Analysis. All error bars attached to the experimental results represent 95 percent confidence intervals. The derivation for the error bar of $E_{\text{net}}/E_b(T_{\text{bed}})$ in Fig. 5 is described as follows.

The uncertainty indicated by the error bar, σ^*, is shown by,

$$\sigma^{*2}=\sigma_{\text{bias}}^2+\sigma_{\text{ran}}^2, \tag{14}$$

where σ_{bias} and σ_{ran} are the uncertainties which are caused by the bias and random errors, respectively.

$D_b(T_{\text{bed}})$ and $D_b(T_{\text{env}})$, etc. in $E_{\text{net}}/E_b(T_{\text{bed}})$ are evaluated by using the regression function. The bias error in $E_{\text{net}}/E_b(T_{\text{bed}})$ chiefly arises from the uncertainty of the regression coefficients, C_1 and C_2 in this experiment. When $E_{\text{net}}/E_b(T_{\text{bed}})$ is expressed as E^*, the bias error is given by,

$$\sigma_{\text{bias}}^2=\left(\frac{\partial E^*}{\partial C_1}\right)^2\sigma_{C1}^2+\left(\frac{\partial E^*}{\partial C_2}\right)^2\sigma_{C2}^2, \tag{15}$$

where $\partial E^*/\partial C_1$ and $\partial E^*/\partial C_2$ can be respectively expressed by,

$$\frac{\partial E^*}{\partial C_1}=\frac{\partial E^*}{\partial \varepsilon_{\text{bed}}}\frac{\partial \varepsilon_{\text{bed}}}{\partial C_1}+\frac{\partial E^*}{\partial D_b(T_{\text{bed}})}\frac{\partial D_b(T_{\text{bed}})}{\partial C_1}+\frac{\partial E^*}{\partial D_b(T_{\text{cav}})}\frac{\partial D_b(T_{\text{cav}})}{\partial C_1}+\frac{\partial E^*}{\partial D_b(T_{\text{env}})}\frac{\partial D_b(T_{\text{env}})}{\partial C_1} \tag{16}$$

$$\frac{\partial E^*}{\partial C_2}=\frac{\partial E^*}{\partial \varepsilon_{\text{bed}}}\frac{\partial \varepsilon_{\text{bed}}}{\partial C_2}+\frac{\partial E^*}{\partial D_b(T_{\text{bed}})}\frac{\partial D_b(T_{\text{bed}})}{\partial C_2}+\frac{\partial E^*}{\partial D_b(T_{\text{cav}})}\frac{\partial D_b(T_{\text{cav}})}{\partial C_2}+\frac{\partial E^*}{\partial D_b(T_{\text{env}})}\frac{\partial D_b(T_{\text{env}})}{\partial C_2}. \tag{17}$$

The derivatives in Eqs. (16) and (17) are numerically calculated by using Eqs. (9) and (13). The resultant values for $\partial E^*/\partial C_1$ and $\partial E^*/\partial C_2$ are, respectively,

$$\frac{\partial E^*}{\partial C_1}\approx -0.21\times 10^{-6}\,E^* \tag{18}$$

$$\frac{\partial E^*}{\partial C_2}\approx 3.5\times 10^{-3}\,E^*. \tag{19}$$

Consequently, the resultant bias error is

$$\sigma_{\text{bias}}\approx \pm 0.084E^*. \tag{20}$$

The random error arises from the fluctuation for the set temperature, such as T_{bed} and T_w, and/or from the noise of the IR camera, σ_D. When the temperature fluctuates, T is expressed as σ_T, the random error is given by,

$$\sigma_{\text{ran}}^2=\left(\frac{\partial E^*}{\partial T_{\text{bed}}}\right)^2\sigma_{\text{Tbed}}^2+\left(\frac{\partial E^*}{\partial T_w}\right)^2\sigma_{Tw}^2+\left(\frac{\partial E^*}{\partial T_{\text{cav}}}\right)^2\sigma_{T\text{cav}}^2+\left(\frac{\partial E^*}{\partial T_{\text{env}}}\right)^2\sigma_{\text{Tenv}}^2+\left(\frac{\partial E^*}{\partial D^+}\right)^2\sigma_D^2, \tag{21}$$

where the derivatives in Eq. (21) are also calculated by using Eqs. (9) and (13).

Since the measured results are obtained as the average values taken from many IR images, the temperature fluctuation with high frequencies and the camera noise, σ_D are negligible, and the temperature fluctuation with low frequencies causes the random error. According to our observation, the fluctuations of T_{bed}, T_w, T_{env} and T_{cav} with low frequencies are, respectively, $\sigma_{T\text{bed}}=\pm 0.2$ K, $\sigma_{Tw}=\pm 0.5$ K, $\sigma_{T\text{cav}}=\pm 0.5$ K and $\sigma_{T\text{env}}=\pm 0.2$ K. The random limit is

$$\sigma_{\text{ran}}=\pm 0.0091. \tag{22}$$

As shown by Eqs. (20) and (22), the bias limit is much larger than the random limit. The error bar shown in Fig. 5 is chiefly caused by the bias error arising from the uncertainty of the regression coefficients, σ_{C1} and σ_{C2}. This applies to the other results as well.

References

[1] Brewster, M. Q., 1986, ''Effective Absorptivity and Emissivity of Particulate Medium with Application to a Fluidized Bed,'' ASME Journal of Heat Transfer , **108**, pp. 710–713.

[2] Glicksman, L. R, 1988, ''Circulating Fluidized Bed Heat Transfer,'' *Circulating Fluidized Bed Technology-II*, P. Basu, and P. Large, eds., Pergamon Press, pp. 13–30.

[3] Basu, P., 1990, ''Heat Transfer in High Temperature Fast Fluidized Bed,'' Chem. Eng. Sci., **45**, No. 10, pp. 3123–3136.

[4] Baskakov, A. P., and Leckner, B., 1997, ''Radiative Heat Transfer in Circulating Fluidized Bed Furnaces,'' Powder Technol., **90**, pp. 213–218.

[5] Saxena, S. C., Srivastava, K. K., and Vadivel, R., 1989, ''Experimental Techniques for the Measurement of Radiative and Total Heat Transfer in Gas Fluidized Beds: A Review,'' Exp. Therm. Fluid Sci., **2**, pp. 350–364.

[6] Il'chenko, A. I., Pikashov, V. S., and Makhorin, K. E., 1968, ''Study of Radiative Heat Transfer in a Fluidized Bed,'' J. Eng. Phys., **14**, pp. 321–324.

[7] Basu, P., 1978, ''Bed-to-Wall Heat Transfer in a Fluidized Bed Coal Combustor, in Fluidization: Application to Coal Conversion Processes,'' C. Y. Wen, ed., AIChE Symp. Ser., **74**, No. 176, pp. 187–193.

[8] Vadivel, R., and Vedamurthy, V. N., 1980, ''An Investigation of the Influence of Bed Parameters on the Variation of the Local Radiative and Total Heat Transfer Coefficient Around an Embedded Horizontal Tube in a Fluidized Bed Combustor,'' *Proc. 6th Int. Conf. Fluidized Bed Combustion*, **3**, pp. 1159–1172.

[9] Ozkaynak, T. F., Chen, J. C., and Frankenfield, T. R., 1984, ''An Experimental Investigation of Radiation Heat Transfer in a High Temperature Fluidized Bed,'' *Proc. 4th Int. Conf. Fluidization*, D. Kunii and R. Toei, eds., Engineering Foundation, New York, pp. 371–378.

[10] Alavizadeh, N., Adams, R. L., Welty, J. R., and Goshayeshi, A., 1984, ''An Instrument for Local Radiative Heat Transfer Measurement in a Gas-Fluidized Bed at Elevated Temperatures,'' paper presented at the 22nd ASME/AIChE Nat. Heat Transfer Conference, Niagara Farls, August.

[11] Zhang, H., and Xie, C., 1985, ''The Radiative Heat Transfer of the Immersed Tube in a Fluidized-Bed Combustion Boiler,'' *Proc. 8th Int. Conf. Fluidized-Bed Combustion*, **1**, pp. 142–148.

[12] Mathur, A., and Saxena, S. C., 1987, ''Total and Radiaitve Heat Transfer to an Immersed Surface in a Gas-Fluidized Bed,'' AIChE J., **33**, pp. 1124–1135.

[13] Yamada, J., Kurosaki, Y., Satoh, I., and Shimada, K., 1995, ''Radiation Heat Exchange between a Fluidized Bed and Heated Surface,'' Exp. Therm. Fluid Sci., **11**, No. 2, pp. 135–142.

[14] Yamada, J., Kurosaki, Y., and Morikawa, T., 2001, ''Radiation Emitted from Fluidizing Particles Adjacent to a Heated Surface in a Fluidized Bed,'' International Journal of Thermal Sciences, **40**, pp. 104–113.

[15] Tien, C. L., 1988, ''Thermal Radiation in Packed and Fluidized Beds,'' ASME Journal of Heat Transfer , **110**, No. 4, pp. 1230–1242.

[16] Yamada, J., and Kurosaki, Y., 1997, ''Estimation for Radiative Properties of Scattering and Absorbing Media,'' Int. J. Thermophys., **18**, No. 2, pp. 547–556.

[17] Honma, H., and Kasugaya, N., 1957, *Dimensional Analysis, Method of Least Squares and Empirical Formulas*, (in Japanese), Corona Publishing Co., Tokyo, Japan, pp. 145–174.

An Integral Formulation of Transient Radiative Transfer

Z.-M. Tan[1]

P.-F. Hsu
e-mail: phsu@fit.edu

Mechanical and Aerospace
Engineering Department,
Florida Institute of Technology,
Melbourne, FL 32901

A time-dependent integral formulation is developed for modeling transient radiative transfer. The development is based on a rigorous analysis of the wave propagation process inside the participating media. The physical significance of the present integral formulation is the consideration of the time-dependent domain of computation, which is different from the domain disturbed by radiation (i.e., the wave front envelope). Numerical computations are performed for the medium that is an absorbing and isotropically scattering one-dimensional plane slab geometry. The spatial and temporal incident radiation and radiative flux distributions are presented for different boundary conditions and for uniform and nonuniform property distribution. The transient results at large time step are compared with steady-state solutions by the finite volume and quadrature methods and show excellent agreement. The solutions of reflecting boundary condition exhibit distinctive behavior from that of the non-reflecting boundary. [DOI: 10.1115/1.1371230]

Keywords: Bioengineering, Heat Transfer, Microscale, Radiation, Transient

Introduction

The motivation of the current study is to utilize the unique features of transient radiation (especially with the short pulse as the incident source) and the characteristics of their interaction with a participating medium: the scattered, reflected and transmitted signals possess the multiple scattering induced temporal signature that persists for time periods greater than the duration of the source pulse and is a function of the scattering and absorbing properties of the medium, and the location in the medium where the properties undergo changes [1]. This variation of the signal with time is an additional parameter to compare and contrast various radiative transfer models, either between themselves or with experimental data for validation. Thus the transient modeling and the examination of predictions from such models will facilitate the identification of the accuracy of various radiative transfer models, because if a model matches in the entire transient domain then it is expected to match at steady-state. This may be in contrast with steady-state modeling efforts where two models could predict very similar steady-state results, thereby creating a dilemma about which is the more accurate model, but could be differentiated through the transients where the temporal history of one may not match the experimental data.

On the other hand, most studies of radiative transfer through participating media assume the radiation transfer to be steady-state [2,3] since the time scale of the radiative transport is far smaller than the time scales of the observable properties in many engineering problems. The assumption is valid due to the large transport speed of radiation within the medium of appropriate length and time scales. However, in many emerging applications, extreme length and time scales are encountered, i.e., the physical domain may be very large or the source of disturbance is of ultrashort time interval [4,5]. Under such circumstances, the transient effect of radiative transfer must be considered.

The recent developments in microscale systems [6], pulsed laser interaction with materials [7,8], optical tomography [5,9], laser therapy [10], particle detection and sizing [11], remote sensing [12], and many other applications have indicated that transient radiative transfer is an important process that requires rigorous study. For instance, one of the critically needed advancements of optical imaging with short pulse lasers is an efficient and accurate model for forward calculation. Without good forward calculations, the inverse analysis will not provide accurate results. Besides these emerging technologies, the traditional application of transient radiative transfer can be found, for example, in astrophysical radiation hydrodynamics where a better model of the transient radiative transport is needed [13].

In the situations of dealing with extremely short time response to radiation and extremely high rate of change of radiation, the steady-state radiative transfer equation could not provide accurate representations. Since a radiation beam traveling through a participating medium in the direction of $\hat{s}$ loses energy by absorption and by out-scattering away from the direction of travel and gains energy by emission as well as by in-scattering from other directions into the direction of travel, the radiative intensity at instant t depends on the entire time history from $t'=0$ to t. Such time dependence results in a hyperbolic wave behavior in radiative transfer and is not considered in the steady-state analysis.

In the past decades, some analytical studies and numerical models of transient radiative transfer have been conducted. A review was presented by Mitra and Kumar [1] to compare various models. Several approximate models (e.g., the spherical harmonics approximation method and the commonly used diffusion approximation) and the discrete ordinates method have been used to solve the transient equation. It is shown that the predicted optical signal characteristics (magnitudes of transmitted and reflected fluxes, temporal shape and spread) are strongly dependent on the models considered. Another evident drawback of the these approximate methods is the failure to predict the correct propagation speed within the medium, or the speed can only be predicted at high order quadrature if the discrete ordinates method was used [14]. Evidently, a better numerical model is still in need to advance our understanding of the transient process. A rigorous transient model will provide the thrust to develop, improve, and apply the new technologies mentioned above.

The advantages of integral treatment of hyperbolic wave equation or time-dependent energy equation have been well recognized (see [15–17]). These prior integral treatments dealt with the thermal wave problem in the conduction media, the transient energy equation, or the convection flow. The integral treatment of the transient radiative transfer equation has not been studied, although researchers have used the steady-state integral formulation already (see the reviews by [18,19]). Among many advantages of using the integral formulation of the transient radiative transfer, the followings are the most significant: (1) There is no need of a special,

[1]Visiting scholar from Chemical Engr. Res. Inst., South China University of Tech., Guangzhou, P. R. China.

Contributed by the Heat Transfer Division for publication in the JOURNAL OF HEAT TRANSFER. Manuscript received by the Heat Transfer Division October 11, 1999; revision received June 11, 2000. Associate Editor: P. Menguc.

high order upwind difference scheme, e.g., characteristic-based scheme [20] total variation diminishing scheme-TVD [21], essentially non-oscillatory scheme-ENO [22], to handle the discontinuity at the wave front. Sometimes even the high order difference schemes cannot completely avoid the oscillation (or dispersion) errors at the wave front [23]; (2) The integral formulation provides a sound basis for physical interpretation of the problem at hand as the radiative transfer is a volumetric process; (3) Many numerical methods that have previously been developed for the steady-state integral formulation can be re-applied to treat the transient problem, for instance, the product integration method [24], YIX method [25,26], discrete exchange factor method [27], and the quadrature method [28].

In this study, an integral equation formulation is developed and used for the solution of the transient radiative transfer equation. The integral equation is a Volterra type because the domain of integral computation is time-dependent. This time-dependent zone of integration is called the domain of influence and represents the volume within which the radiation effect can reach a particular position at a specific time. An integral analysis of the transient problem can be considered with the domain of influence. If one of the boundary surfaces is reflective, additional domain of influence will arise from such boundary. The computational domain will be the superimposed multiple domains of influence. The reflected domain of influence will be different depending on whether the surface is diffuse or specular. The solution of reflective boundary condition demonstrates distinctive behavior from those of the non-reflective boundary. The wave nature of transient radiative transfer is examined and discussed. The medium under consideration is absorbing and isotropically scattering, and the radiative properties can be spatially non-uniform. The radiative properties are assumed to be independent of the strength of the intensity [29]. The steady-state radiative transfer equation can be easily obtained from the present transient analysis if the propagation speed of radiation approaches infinity.

It was pointed out by Wu [30] that a prior integral analysis by Pomraning [31] produced similar integral formulation for the transient intensity. However, the complete solution requires the specification of the domain of influence which is obtained in this study. The purposes of the numerical study are several folds: (1) to study the wave behavior of the transient radiation transport process; (2) to present a simple quadrature scheme to solve the integral formulation; and (3) to assess the validity of the transient radiative transfer equation (TRTE) and the solutions of the model by comparing the transient results at long time with the steady-state solutions by the finite volume and quadrature methods.

Theoretical Development

The equation for transient radiative transfer of the intensity in direction $\hat{s}$ is given by [32–34]

$$\frac{dI(z,\hat{s},t)}{ds}=\frac{DI(z,\hat{s},t)}{cDt}=-\kappa I(z,\hat{s},t)+aI_b(z,t)+\frac{\sigma}{4\pi}\int_{\Omega'=4\pi}I(z,\hat{s}',t)\Phi(\hat{s}',\hat{s})d\Omega', \quad (1a)$$

or

$$\frac{\partial I(z,\hat{s},t)}{c\partial t}+\frac{\partial I(z,\hat{s},t)}{\partial s}=-\kappa I(z,\hat{s},t)+aI_b(z,t)+\frac{\sigma}{4\pi}\int_{\Omega'=4\pi}I(z,\hat{s}',t)\Phi(\hat{s}',\hat{s})d\Omega', \quad (1b)$$

where the D symbol represents the substantial derivative [35]. Equation (1*a*) is the Lagrangian viewpoint and Eq. (1*b*) the Eulerian. The substantial derivative allows the expression of, in the Eulerian variable, a time derivative as one follows a specific photon. It is found that the Lagrangian viewpoint can simplify the analysis of the time-of-flight of a photon and allows for the deduction of the domain of influence. Since in the Lagrangian viewpoint the observer is moving with the wave, the dependence upon s and t could not be separated from each other. The dependence is evident from the relationship of $dt=ds/c$. Therefore, only one independent variable (either t or s) is needed in the transient analysis. When a radiation beam travels through a participating medium, it is attenuated by absorption and by out-scattering and at the same time gains energy by emission as well as by in-scattering from other directions into the direction of travel. The resulting equation is shown in Eq. (1). Once the distance ds through which the radiation travels along a certain path is given, the relative location $s+ds$ and the time interval $dt=ds/c$ (hence the instant $t'=t+ds/c$) can be determined definitely.

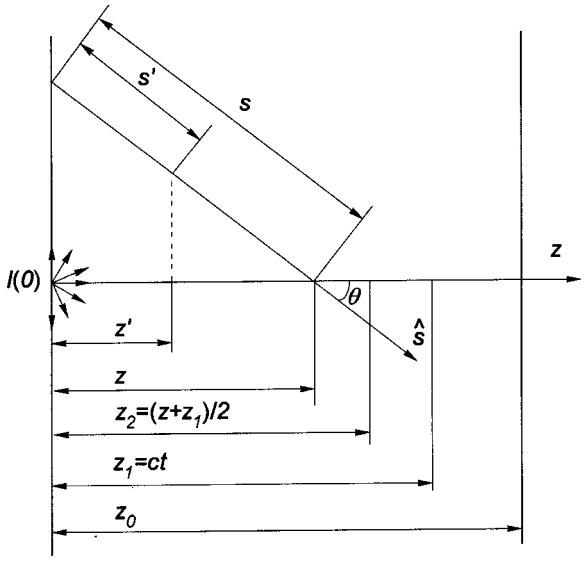

Fig. 1 Geometry and coordinate system

The physical case under consideration in this paper is a one-dimensional infinite slab of absorbing, non-emitting, and scattering medium. The non-emission assumption is valid in many situations where short pulse laser or light source is directed into a cold medium or the temperature disturbance caused by the incidence pulse in the material cannot be immediately revealed within the time scale of the radiative transport. The layer width is z_o in the z direction (see Fig. 1). The transient radiative transfer equation can be written as (Lagrangian viewpoint)

$$\frac{dI(z,\hat{s},t)}{ds}=-\kappa(z)I(z,\hat{s},t)+\frac{\sigma(z)}{4\pi}\int_{\Omega=4\pi}I(z,\hat{s}',t)\Phi(\hat{s}',\hat{s})d\Omega. \quad (2)$$

For isotropic scattering, $\Phi(\hat{s}',\hat{s})=1$. This leads to

$$\frac{dI(z,\hat{s},t)}{ds}=-\kappa(z)I(z,\hat{s},t)+\frac{\sigma(z)}{4\pi}G(z,t), \quad (3)$$

where $G(z,t)$ is the incident radiation function (or integrated intensity). Integrating Eq. (3) on both sides, one obtains

$$I(z,\hat{s},t)=I(0,\hat{s},t-s/c)e^{-\kappa s}+e^{-\kappa s}\int_{s'=0}^{s'=s}\frac{\sigma(z)}{4\pi}G(z',t')e^{\kappa s'}ds'. \quad (4)$$

When $s'=s$, the corresponding coordinate is $z'=z$ and $t'=t$, which are the location and the instant under consideration (Fig. 1). Since the time interval between $s'=0$ and $s'=s$ is $\Delta t=s/c$, therefore, at $s'=0$ the same photon can be described by $z'=0$ and $t'=t-s/c$, which is shown in Eq. (4).

In order to carry out the integration on the right side of Eq. (4), the dummy variables z' and t' of the integrated intensity G should be expressed in terms of the integrating variable s', which can easily be found (for example, see discussion leads to Eqs. (10*c*) and (10*d*)). Therefore, Eq. (4) becomes

$$I(z,\hat{s},t)=I(0,\hat{s},t-s/c)e^{-\kappa s}+\frac{1}{4\pi}\int_0^s \sigma(z')G(z-(s-s')\times\cos(\hat{s},\hat{k}),t-(s-s')/c)e^{-\kappa(s-s')}ds'. \quad (5)$$

Physically, the first term on the right-hand side of Eq. (5) is the contribution to the local intensity by the intensity entering the medium from the boundary at $s'=0$, which decays exponentially due to extinction over the optical distance κs (Fig. 2). Since it takes the photon an amount of time s/c to travel from the boundary (at $s'=0$) to the point under consideration (at $s'=s$), the boundary contribution can only come from the radiation entering the medium at an earlier instant of $t'=t-s/c$. The integrand of the second term, $\sigma(z')G(z',t')ds'/4\pi$, is the contribution from the local scattering at s', attenuated exponentially by extinction over the distance between the scattering point and the point under consideration, $s-s'$. Since the time interval between these two points is $\Delta t=(s-s')/c$, only the photons at and after the instant of $t'=t-(s-s')/c$ and in the position $z'\geqslant z-(s-s')\cos(\hat{s},\hat{k})$ contribute to the radiative intensity at the location z and the instant t, $I(z,\hat{s},t)$. The integral sums all of the contributions over the entire scattering path from $s'=0$ to $s'=s$. Equation (5) shows that the intensity in a certain direction depends on the time history along the path in that direction. Furthermore, $I(z,\hat{s},t)$ depends on the radiation emitted from the boundary at an earlier instant $t-s/c$ in the same direction and the entire time history of incident radiation along the path of travel, rather than the values at the same instant t. Thus, transient radiative transfer presents a strong time dependence, which in turn implies a path length dependence. It should be noted that after appropriate transformation and differentiation, Eq. (5) can be reduced to Eq. (1*b*).

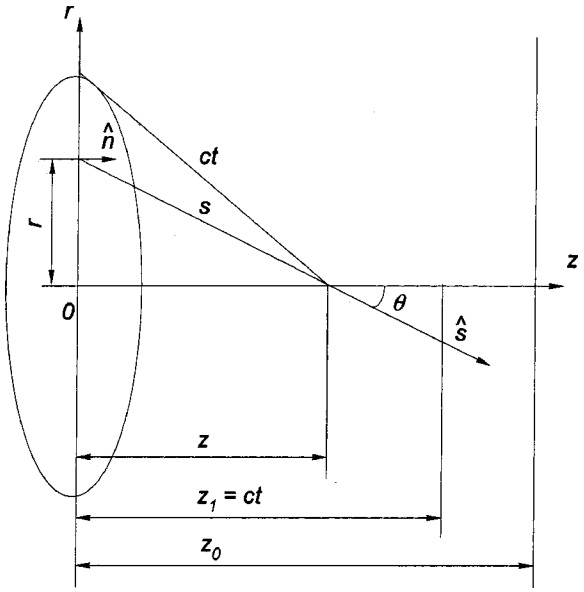

Fig. 2 Determination of the boundary integration region

Integrating Eq. (5) over all 4π solid angle gives

$$G(z,t)=\int_{4\pi} I(0,\hat{s},t-s/c)e^{-\kappa s}d\Omega+\frac{1}{4\pi}\int_{4\pi}\left[\int_0^s \sigma(z')G(z-(s-s')\cos(\hat{s},\hat{k}),t-(s-s')/c)e^{-\kappa(s-s')}ds'\right]d\Omega$$
$$=\int_A\int \frac{I(0,\hat{s},t-s/c)e^{-\kappa s}}{s^2}\cos(\hat{n},\hat{s})dA+\frac{1}{4\pi}\int\int\int_V \frac{\sigma(z')G(z-(s-s')\cos(\hat{s},\hat{k}),t-(s-s')/c)e^{-\kappa(s-s')}}{(s-s')^2}dV, \quad (6)$$

where $\hat{n}$ is the inward unit normal vector of the boundary surface. Equation (6) is a general formulation, and for problems involving explicit boundary conditions it may be reduced into a much simpler form.

The following boundary conditions are considered: one surface is black and diffusely emitting and the other is a cold and black boundary. This boundary condition is the most general case to consider since the collimated incident radiation will be a special case, which leads to simpler formulation. For the diffusive surface, the radiative intensity is independent of direction. Assuming that diffuse radiation with the intensity I_0 is suddenly emitted from the boundary at $z=0$ at the instant of $t=0$, then the boundary radiation intensity can be expressed as

$$I(0,\hat{s},t)=I_0u(t)\hat{s}, \quad (7)$$

where $u(t)$ is the Heaviside unit step function defined to be

$$u(t)=\begin{cases}0 & t<0\\ 1 & t>0\end{cases}$$

Such boundary condition has the advantage of being able to compare with steady state solutions from other models in the long time. In order to carry out the integration in Eq. (6), one needs to find the relationships among the geometrical parameters. For the surface integral, the following relationships among the geometrical parameters can be found from Fig. 2

$$s=\sqrt{z^2+r^2} \quad (8a)$$

$$\cos(\hat{n},\hat{s})=\frac{z}{s}=\frac{z}{\sqrt{z^2+r^2}} \quad (8b)$$

$$t_1'=t-s/c=t-\sqrt{z^2+r^2}/c \quad (8c)$$

$$dA=2\pi r dr. \quad (8d)$$

According to boundary condition Eq. (7) and the prior discussion (after Eq. (5)) based on the Lagrangian time-of-flight of a photon, the integration region of the boundary integral at instant t must meet the requirement $t_1'=t-s/c\geqslant 0$. Therefore, the integration region may be easily determined

$$s=\sqrt{z^2+r^2}\leqslant ct \quad \text{or} \quad r\leqslant\sqrt{(ct)^2-z^2}, \quad (9)$$

which shows that the integration region on the boundary surface is a circle and the circle radius is different for different location z even at the same instant t.

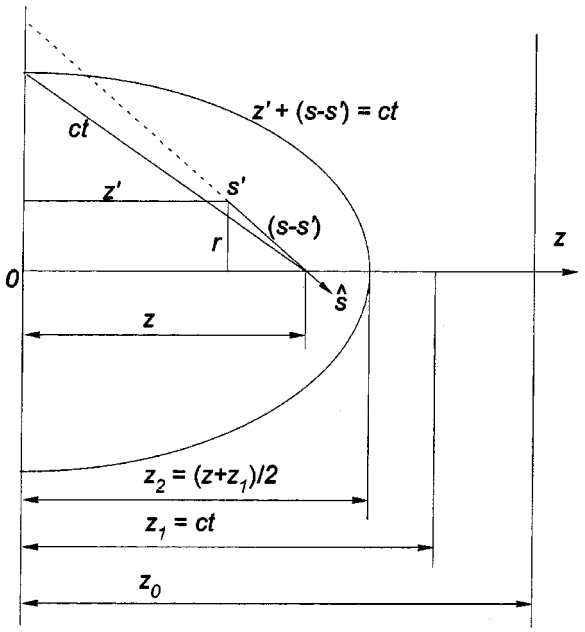

Fig. 3 Determination of the volume integration region or the domain of influence

For the volume integration in the medium, the relationships among the geometrical parameters are as follows (see Fig. 3):

$$s-s'=\sqrt{(z-z')^2+r^2} \tag{10a}$$

$$\cos(\hat{s},\hat{k})=\frac{z-z'}{s-s'}=\frac{z-z'}{\sqrt{(z-s')^2+r^2}} \tag{10b}$$

$$z'=z-(s-s')\cos(\hat{s},\hat{k}) \tag{10c}$$

$$t_2'=t-(s-s')/c=t-\sqrt{(z-z')^2+r^2}/c \tag{10d}$$

$$dV=2\pi r dr dz'. \tag{10e}$$

In order to determine volume integration region, we consider the scattering from an arbitrary location s' towards location s. As shown in Fig. 3, it takes the shortest time z'/c for the radiation emitted from the boundary to travel to location s' and then the time $(s-s')/c$ for scattering from location s' to s. Only when the total travel time is less than time t, namely, $[z'+(s-s')]/c\leqslant t$, then there is sufficient time for the single scattering of photon from location s' to s. Therefore, the volume integration region (i.e., the domain of influence due to the scattering) is found to be

$$r=0 \quad \text{to} \quad r=\sqrt{(ct-z)(ct+z-2z')} \tag{11a}$$

$$z'=0 \quad \text{to} \quad z'=z_2'=\begin{cases}(ct+z)/2 & \text{when } (ct+z)/2\leqslant z_0\\ z_0 & \text{when } (ct+z)/2>z_0\end{cases}, \tag{11b}$$

which shows that the volume integration region is also a function of location z at a certain instant t. Equation (11) shows the domain of influence is of axisymmetric shape, i.e., a paraboloid. One can see from Fig. 3 that for a certain location $z(<ct)$, the volume integration region expressed by Eqs. (11*a*) and (11*b*), namely the volume surrounded by $z'=0$ and $z'+(s-s')=ct$, is different from the region reached by the wave front, $0<z'<ct$. In the steady-state analysis, these two regions are identical.

By the application of the above conditions and geometrical relationships, the boundary and volume integrations in Eq. (6) can be carried out. Since the distance s between the location under consideration and any point on the boundary within the region from $r=\sqrt{(ct)^2-z^2}$ to $r=\infty$ is greater than ct, namely $s>ct$ or $t-s/c<0$, the unit step function $u(t-s/c)$ and hence the surface integral within this region are equal to zero. Similarly, the volume integral within the region from $r=\sqrt{(ct-z)(ct+z-2z')}$ to $r=\infty$ is also equal to zero. Therefore, Eq. (6) becomes

$$G(z,t)=2\pi z\int_{r=0}^{\sqrt{(ct)^2-z^2}}\frac{I_0 u\left(t-\frac{s}{c}\right)e^{-\kappa\sqrt{z^2+r^2}}}{(z^2+r^2)^{3/2}}rdr + \frac{1}{2}\int_{z'=0}^{z_0}\int_{r=0}^{\sqrt{(ct-z)(ct+z-2z')}} \times\frac{\sigma(z')u\left(t-\frac{z'+(s-s')}{c}\right)G(z',t_2')e^{-\kappa\sqrt{(z-z')^2+r^2}}}{(z-z')^2+r^2} \times rdrdz'. \tag{12}$$

It can be found from Fig. 2 that when the upper limit of integration for surface integral is greater then zero, $(ct)^2-z^2>0$, then $s^2=z^2+r^2<(ct)^2$ or $t-s/c>0$ and hence $u(t-s/c)=1$. When $(ct)^2-z^2<0$, then $s^2=z^2>(ct)^2$ or $t-s/c<0$ and hence $u(t-s/c)=0$. The instant $(t-z/c)$, i.e., $(ct)^2-z^2=0$, becomes a demarcation point to the Heaviside unit step function. A similar analysis may be applied to the volume integral. Therefore, the unit step functions may be taken outside of the integrands, and one obtains the following expression for integrated intensity

$$G(z,t)=2\pi z I_0 u\left(t-\frac{z}{c}\right)\int_{r=0}^{\sqrt{(ct)^2-z^2}}\frac{e^{-\kappa\sqrt{z^2+r^2}}}{(z^2+r^2)^{3/2}}rdr + \frac{1}{2}u\left(t-\frac{z}{c}\right)\int_{z'=0}^{z_2'}\int_{r=0}^{\sqrt{(ct-z)(ct+z-2z')}} \times\frac{\sigma(z')G(z',t_2')e^{-\kappa\sqrt{(z-z')^2+r^2}}}{(z-z')^2+r^2}rdrdz' = 2\pi z I_0 u\left(t-\frac{z}{c}\right)\left\{\frac{e^{-\kappa z}}{z}-\frac{e^{-\kappa ct}}{ct}-\kappa\left[\log\left(\frac{ct}{z}\right) -\kappa(ct-z)+\frac{\kappa^2(c^2t^2-z^2)}{2\cdot 2!}-\frac{\kappa^3(c^3t^3-z^3)}{3\cdot 3!}+\cdots\right]\right\} + \frac{1}{2}u\left(t-\frac{z}{c}\right)\int_{z'=0}^{z_2'}\int_{r=0}^{\sqrt{(ct-z)(ct+z-2z')}} \times\frac{\sigma(z')G(z',t_2')e^{-\kappa\sqrt{(z-z')^2+r^2}}}{(z-z')^2+r^2}rdrdz'. \tag{13}$$

Multiplying Eq. (5) by $\cos(\hat{s},\hat{k})$ and then integrating it over all 4π solid angle gives

$$q(z,t)=\int_{4\pi} I(z,\hat{s},t)\cos(\hat{s},\hat{k})d\Omega$$
$$=\pi z^2 I_0 u\left(t-\frac{z}{c}\right)\left\{\frac{(1-\kappa z)e^{-\kappa z}}{z^2}-\frac{(1-\kappa ct)e^{-\kappa ct}}{c^2t^2}\right.$$
$$-\kappa^2\left[\log\left(\frac{ct}{z}\right)-\kappa(ct-z)\right.$$
$$\left.\left.+\frac{\kappa^2(c^2t^2-z^2)}{2\cdot 2!}-\frac{\kappa^3(c^3t^3-z^3)}{3\cdot 3!}+\cdots\right]\right\}$$
$$+\frac{1}{2}u\left(t-\frac{z}{c}\right)\int_{z'=0}^{z_2'}\int_{r=0}^{\sqrt{(ct-z)(ct+z-2z')}}$$
$$\times\frac{\sigma(z')G(z',t_2')e^{-\kappa\sqrt{(z-z')^2+r^2}}}{[(z-z')^2+r^2]^{3/2}}r(z-z')drdz'. \tag{14}$$

Discussion

It's noted that Eq. (13) is a linear Volterra integral equation of the second kind [36]. The volume integral contains a singularity at $s'=s$. The resulting exponential integral in the surface integral (the first term on the right hand side of Eqs. (13) and (14)) is a monotonically decreasing series which converges rapidly to an asymptotic value when the incident radiation propagates through an optical distance at $\kappa ct \geqslant 3$ and $\kappa z \geqslant 3$. The integral $G(z',t_2')$ in the volume integral is a function of location and time. Because the values of time t_2' at any location z' in Eqs. (13) and (14) are always less than those of time t at location z (see Eq. (10*d*)), the incident radiation at the same instant but at a different location, $G(z',t)$, contributes nothing to the incident radiation $G(z,t)$. The present model demonstrates that the domains for both surface and volume integrals are time dependent due to the finite propagation speed of radiation and that the domain of volume integration (i.e., the domain of influence) is different from the domain disturbed by radiation.

Equations (13) and (14) can be applied to handle different boundary conditions, and non-homogeneous media. The concept of the domain of influence and the integral formulation can be extended to treat multi-dimensional media, anisotropically scattering phase functions, etc. This will be considered in the near future. For example, in a multi-dimensional geometry, the YIX method [26] can be used for the volume integration. In such cases, some portions of the surface and volume domains of influence can be outside the physical domain of the medium. Since the portion outside the physical domain is not considered in the integrals, the resulting domain of influence becomes irregular and needs to be treated carefully. Therefore, the multi-dimensional computation is more complicated than that of the one-dimensional case.

When the propagation speed of radiation approaches infinity, the variable t' approaches the time instant t (recall Eq. (10*d*)). In this case, the time dependence may be omitted and Eqs. (13) and (14) reduce to

$$G(z)=I_0\int\int_A\frac{e^{-\kappa s}}{s^2}\cos(\hat{n},\hat{s})dA$$
$$+\frac{1}{4\pi}\int\int\int_V\frac{\sigma(z')G(z-(s-s')\cos(\hat{s},\hat{k}))e^{-\kappa(s-s')}}{(s-s')^2}dV \tag{15}$$

and

$$q(z)=I_0\int\int_A\frac{e^{-\kappa s}}{s^2}\cos(\hat{n},\hat{s})\cos(\hat{s},\hat{k})dA$$
$$+\frac{1}{4\pi}\int\int\int_V\frac{\sigma(z')G(z-(s-s')\cos(\hat{s},\hat{k}))e^{-\kappa(s-s')}}{(s-s')^2}$$
$$\times\cos(\hat{s},\hat{k})dV, \tag{16}$$

which are the steady-state model given in the existing literature (for example, [24,37]).

To compare with experimental measurement of short pulse laser interaction with the material, it is helpful to obtain the transient reflectance and transmittance [5]. The transient reflectance and transmittance can be defined by using Eq. (14) for $z=0$ and z_0 and with half-range integration. Unlike the steady-state dimensionless reflectance and transmittance, the transient values will be half-range fluxes divided by the intensity of the boundary condition or the peak intensity of an incident temporal pulse and the resulting values are not dimensionless.

It is noteworthy that the moments of intensity (G and q) are determined directly instead of the intensity in the integro-differential treatments [1]. After solving for the G function, the intensity can be readily obtained by using Eq. (5), if needed. Computationally, the integral formulation has much smaller memory requirements than the integro-differential formulations, even lower than the Monte Carlo method in the transient transfer analysis [38]. This is because the lower dimension space variable, G, is solved instead of the intensity.

Another distinction between the integral and integro-differential formulations is the treatment of reflective boundary. As the electromagnetic wave hits a reflective surface, the domain of influence will also be reflected back and overlap with the incoming domain. In a multi-dimensional geometry with reflective boundaries, the consideration of overlapped domains of influence will not be easy although it is possible. The integro-differential formulation will not have such problem.

Numerical Computation

Example Problems. The boundary conditions and the radiative property distributions of the example problems are presented in Table 1.

Case 1. One boundary is a black surface with transient unit step function emissive power and the other boundary is cold and black or transparent.

The mathematical description for Case 1 is given in the derivation of Eqs. (13) and (14), which represent the solution. The boundary condition allows direct comparison of the transient process at long time with other steady state models.

Case 2. One boundary is a black surface with transient unit step function emissive power and the other boundary is specularly reflecting.

Reflections of radiation by a surface or an interface between dissimilar materials are crucially important in many problems where media of different refractive index are involved. The incident angle of a beam of radiation is identical to the reflection angle for the specular reflection. In this case, when the radiation emitted from one boundary travels to the reflective surface of the other boundary, the radiative energy is reflected back. The surface reflectivity is taken to be unity. The total G and q are the superposition of two components caused by both incident diffuse emission from boundary $1(z=0)$ and specular reflection from boundary $2(z=z_o)$. These two components are calculated separately according to Eqs. (13) and (14). The reflected wave component is obtained by assuming an imaginary medium in the region $z_o<z\leqslant 2z_o$ with the property distribution being the mirror image of the actual medium in the region of $0\leqslant z\leqslant z_o$ with $z=z_o$ as the plane

Table 1 Boundary and physical conditions of different case

Case	Boundary 1 $z=0$	Medium property	Boundary 2 $z=z_o$
1	diffuse emission $I_0=1$	homogeneous $\tau=1,\ \omega=0.5$	non-reflection
2	diffuse emission $I_0=1$	homogeneous $\tau=1,\ \omega=0.5$	specular reflection
3	diffuse emission $I_0=1$	nonhomogeneous $\tau=\begin{cases}1, & 0<z/z_o\le 0.4\\ 5, & 0.4<z/z_o\le 0.6\\ 1, & 0.6<z/z_o\le 1.0\end{cases}$ $\omega=0.5$	non-reflection
4	collimated radiation $I(0,\hat{s},t)=I_0u(t)\hat{k}$ and $I_0=1$	homogeneous $\tau=1,\ \omega=0.5$	non-reflection

of symmetry. The incident radiation and radiative flux in the whole region $0\leqslant z\leqslant 2z_o$ are calculated according to Eqs. (13) and (14) with the modified integration region

$$r=0 \quad \text{to} \quad r=\sqrt{(ct-z)(ct+z-2z')} \tag{17a}$$

$$z'=0 \quad \text{to} \quad z'=z_2'=\begin{cases}(ct+z)/2 & \text{when } (ct+z)/2\leqslant 2z_o\\ 2z_o & \text{when } (ct+z)/2>2z_o\end{cases}. \tag{17b}$$

The G and q in the real medium in the region $0\leqslant z\leqslant z_o$ may be obtained by the superposition, i.e.,

$$G_{\text{total}}(z,t)=G(z,t)+G(2z_o-z,t) \tag{18}$$

$$q_{\text{total}}(z,t)=q(z,t)-q(2z_o-z,t), \tag{19}$$

where location $(2z_o-z)$ is an imaginary point symmetrical to $z(0\leqslant z\leqslant z_o)$ about $z=z_o$. The superposition principle can also be used to treat a diffusely reflecting boundary. In the case where both boundary surfaces are partially reflecting and partially transmitting, it is important to distinct the effects of the multiple scattering and the multiple reflection on the reflected and transmitted output signals. The relative effect of reflective surface and multiple scattering was discussed in Hsu [38] with a Monte Carlo algorithm.

Case 3. The medium is non-homogeneous with same boundary conditions as given in Case 1.

For a nonhomogeneous medium, the extinction coefficient κ is a function of position z'. Therefore, the extinction coefficient κ in the equations should be replaced by the following expression of:

$$\kappa(z)=\frac{\int_{s'}^{s}\kappa(z')ds'}{s-s'}.$$

Similarly, the scattering coefficient σ should be replaced by $\sigma(z)$ which is determined by $\sigma(z)=\omega(z)\cdot\kappa(z)$. The $\omega(z)$ is the position-dependent scattering albedo.

Case 4. One boundary is subjected to the collimated radiation and the other is cold and black or transparent.

The radiation from boundary into medium is in a uniform direction. Considering the case that the incident radiation is normal to the boundary surface,

$$I(0,\hat{s},t)=I_0u(t)\hat{k}. \tag{20}$$

In this case, Eqs. (6) and (14) can be simplified as:

$$G(z,t)=I_0u\left(t-\frac{z}{c}\right)e^{-\kappa z}+\frac{1}{2}u\left(t-\frac{z}{c}\right)\int_{z'=0}^{z_2'}\int_{r=0}^{\sqrt{(ct-z)(ct+z-2z')}}\times\frac{\sigma(z')G(z',t_2')e^{-\kappa\sqrt{(z-z')^2r^2}}}{(z-z')^2+r^2}rdrdz' \tag{21}$$

$$q(z,t)=I_0u\left(t-\frac{z}{c}\right)e^{-\kappa z}+\frac{1}{2}u\left(t-\frac{z}{c}\right)\times\int_{z'=0}^{z_2'}\int_{r=0}^{\sqrt{(ct-z)(ct+z-2z')}}\times\frac{\sigma(z')G(z',t_2')e^{-\kappa\sqrt{(z-z')^2r^2}}}{[(z-z')^2+r^2]^{3/2}}r(z-z')drdz' \tag{22}$$

The integration region is the same as that expressed by Eq. (11).

Numerical Method

Both incident radiation $G(z,t)$ and radiative flux $q(z,t)$ at location z and the instant t depend on the entire time history from $t'=0$ to t during which the radiation field within the medium is established. The solution of the radiation temporal and spatial distribution requires the knowledge of the incident radiation in different location z' and at different instant t_2', $G(z',t_2')$. The analytical solutions to these equations are impossible except the non-scattering situation.

In this study, the medium is divided into N_{zo} equal elements Δz ($N_{zo}=100$ and $\Delta z=z_o/N_{zo}$) in the z-direction and the corresponding time interval Δt which is the amount of time the electromagnetic wave travels through the element thickness Δz, i.e., $\Delta t=\Delta z/c$. c is the propagation speed of the radiation inside the medium. It is interesting to note that the last equation is equivalent to the unity Courant number [23]. The numerical scheme is stable and guaranteed to converge. The coordinate of the volume element is $z=(N_z-0.5)\Delta z$ with $N_z=1,2,\ldots,N_{zo}$ and the time of the wave front travel after the incidence is $t=N_t\Delta t$, where N_t is the number of time interval. Since the integration domain increases with the increase of time, the radial division of the volume elements in the r-coordinate in the integration equations should be adaptive with respect to the current time and position in order to maintain sufficient accuracy. In the computation, the volume element in the r direction is divided into N_r elements,

$$N_r=N_t-N_z+10.$$

The relation shows that at a fixed location z (or at a given N_z) the number of radial elements N_r increases with the current time, i.e., the number of time intervals N_t. Because G and q depend on time history, numerical integration has to be carried out by time stepping from the beginning. Namely, one first computes the values of incident intensities $G(z,t_1)$ in the medium at instant $t_1=\Delta t$ according to the boundary conditions, then computes the values of $G(z,t_2)$ at instant $t_2=2\Delta t$ according to both the boundary conditions and the values of $G(z,t_1)$ at instant $t_1=\Delta t$. The values of $G(z,t_3)$ at instant $t_3=3\Delta t$ depends on the boundary conditions, the prior values of $G(z,t_1)$ and $G(z,t_2)$. The process continues until the value $G(z,t)$ at the desired time instant t is obtained. During the integration, the piecewise-constant interpolation within the region Δz and the time interval Δt is used.

The volume integration is conducted as follows: the domain of influence is divided into a finite number of discrete volume elements and the right hand sides of Eqs. (21) and (22), for example, are constructed as follows:

$$\int\int\int K(s-s',t)F(s-s',t)dV(s-s',t)$$
$$\approx \sum_{N_z'=1}^{2N_z}\sum_{N_r'=1}^{N_r} K(r,z',t)F(r,z',t)2\pi r\Delta r\Delta z', \qquad (23)$$

where $N_r \cdot N_z$ is the number of volume elements, $s-s'$ is the relative position vector given in Eq. (10*a*), K is the kernel of integral equation, and F is the integrand. In the one-dimensional geometry, the volume element is a ring-shape structure. To avoid the singularity at $z=z'$ and $r=0$, each volume element is divided into 2 sub-elements in the z-direction during the integration. Thus, the factor of 2 appears in the right hand side of the upper limit of the first summation sign. The division of volume elements into sub-elements also improve the integration accuracy but doesn't increase the memory usage. The piecewise constant interpolation is used across the two sub-elements.

The sole factor which influences the accuracy of integration is the grid size Δz. In order to examine the influence of the grid size on the solution accuracy, the number of volume elements is doubled (accordingly, the time interval is reduced by half) to examine the change of computation results. It is found that there is very little difference (<0.1 percent) between $N_{zo}=100$ and $N_{zo}=200$ for the Case 1 calculation. This is an indication that the grid size effect is negligible in the solutions.

Results and Discussion

The G and q functions for the boundary-driven problems listed in Table 1 are obtained by solving the one-dimensional transient radiative transfer equations according to the numerical method described above. The typical execution time, for example the Case 1, is about 30 minutes on a Pentium-Pro 200 MHz PC with $N_{zo}=100$ and the total time step is about 400.

Figure 4 shows the computation results of G and q in homogeneous medium with a diffusely emitting boundary. In this case, the radiation emitted from boundary 1 travels in the medium at a finite velocity. The wave strikes the opposite boundary 2 at and after the time $t \geqslant z_o/c$. Since boundary 2 is non-reflecting, the radiation penetrates through the boundary to the outside of the medium. Figures 4(*a*) and 4(*b*) present the G and q distributions at different instants of time inside the medium. It can be seen that a sudden diffuse emission from one boundary gives rise to a radiation wave front, which travels in the medium at a finite velocity and disappears when it strikes boundary 2. There is an undisturbed region $z_o > z > ct$ within which both G and q are zero, i.e., this happens when $t/\Delta t < z_o/\Delta z$ during the computation. The incident radiation at a certain location in the medium increases with time since both the boundary region from which the radiation can reach z and the volume region from which the in-scattering from other directions can reach z increase. Such time dependence is clearly demonstrated in the Eq. (1) and the integral equations. On the other hand, the rate of increase of incident radiation decreases with time. After the time $t/\Delta t \geqslant 3.6N_{zo}$, the G approaches the asymptotic value, i.e., the steady-state result. Since the radiative flux obtained from Eq. (14) of this work represents the net flux in the positive z-direction at a certain location, its distribution is somewhat different from the incident radiation distribution. In Fig. 4(*b*), radiative flux decreases with time near the emitting boundary due to the rapid increase of in-scattering from right-hand side region of the medium.

In order to verify the computational methodology developed in this study, the steady-state results by the finite volume and quadrature methods are compared with the transient results at large time. The steady-state results of incident radiation and radiative flux are also plotted in Figs. 4(*a*) and 4(*b*). It can be seen that the values of transient incident radiation and radiative flux at instant $t/\Delta t=360$ are very close to the steady-state values. The maximum absolute difference for incident radiation between two

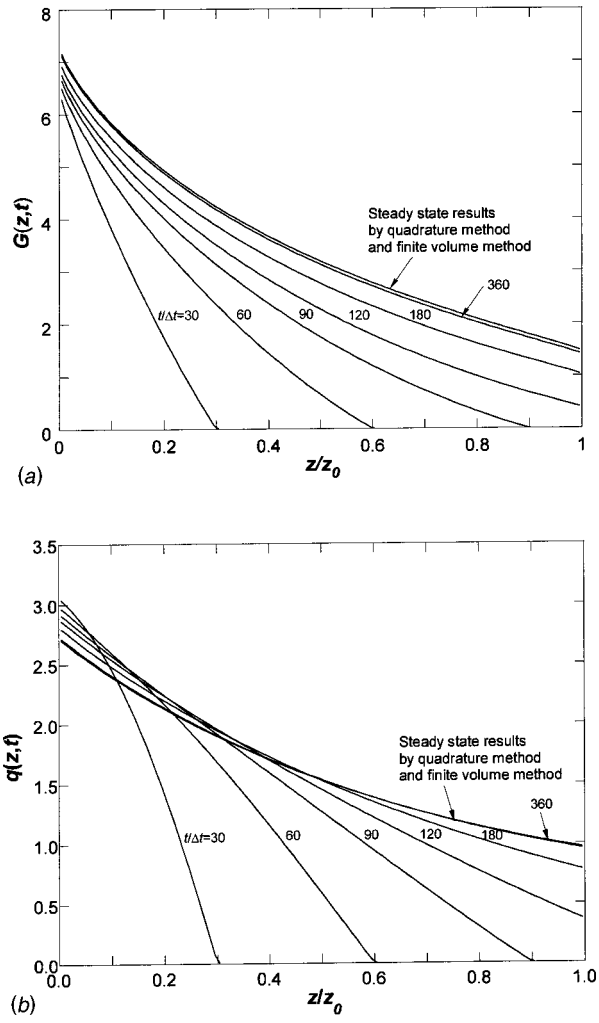

Fig. 4 Incident radiation and radiative flux in homogeneous medium with one diffusely emitting boundary: (*a*) Incident radiation distribution at different time; and (*b*) radiative flux distribution at different time

sets of values with 100 volume elements is only 0.0693 and the maximum relative difference is 4.5 percent. They are 0.0122 and 0.449 percent respectively for radiative flux results. It demonstrates that the present computation method is accurate and that radiative transfer process in the medium when time $t/\Delta t > 4N_{zo}$ may approach the steady state.

A more exhaustive verification of the integral solution will be the direct comparison with the transient solutions by other methods. Currently, the transient finite volume and discrete ordinates methods are being developed for this purpose. In a separate paper [38] the Monte Carlo method was used to compare with the integral solutions and good agreement was reported there.

Figure 5 is the Case 2 results of G and q in homogeneous medium with a diffusely emitting boundary and a specularly reflecting boundary. It can be seen from Figs. 5(*a*) and 5(*b*) that the G and q distributions are the same as those for Case 1 before the wave front strikes the specular reflection boundary 2 (see the curves for $t/\Delta t=30$, 60, and 90). When the incident wave front reaches boundary 2, the radiation is reflected back into the medium. After that, a reflected wave front can be seen which travels in the opposite direction. This reverse wave is observed at location $z/z_o=0.8$, 0.5, and 0.2 when $t/\Delta t=120$, 150, and 180, respectively. Since the incident radiation is the total intensity impinging on a point from all sides, the values of G in the reflection affected region of Case 2 are always greater than those in the

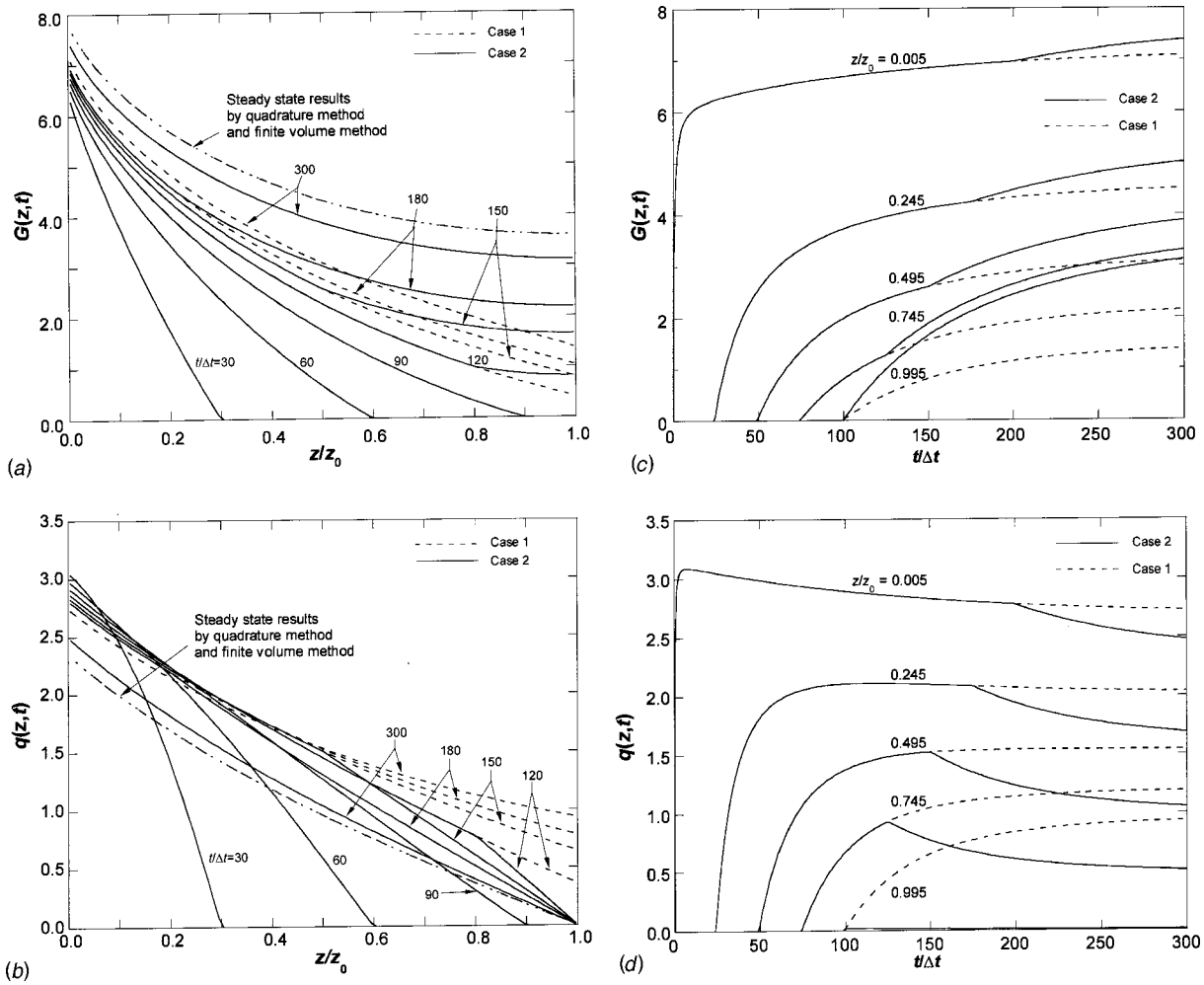

Fig. 5 Incident radiation and radiative flux in homogeneous medium with one diffusely emitting and another reflecting boundaries: (*a*) Incident radiation distribution at different time; (*b*) radiative flux distribution at different time; (*c*) incident radiation as a function of time at different location; and (*d*) radiative flux as a function of time at different location

same region without reflection of Case 1. However, the radiative flux decreases in the reflection affected region due to the increase of reversed radiative flux in opposite direction caused by the reflection. Because the radiation is fully reflected at boundary 2, there is no net radiative flux at $z/z_o=1$. As shown in Fig. 5(*b*) the radiative flux is always zero for Case 2 at the second boundary.

The wave phenomena of radiative transfer can be clearly observed if both G and q as a function of time are plotted for Cases 1 and 2 (Figs. 5(*c*) and 5(*d*)). At a given location z, both incident radiation and radiative flux are equal to zero when time t is smaller than z/c since the radiation wave front still hasn't arrived at that location. The incident radiation at those locations near the diffusely emitting boundary increases rapidly when the radiation wave front arrives and then increases slowly as the wave front passes over. The effect of sharp increase of incident radiation at the instant when the wave front arrives reduces rapidly at a larger distance of z. The temporal radiative flux distribution in Fig. 5(*d*) at location $z/z_o=0.005$ increases instantly from zero to a maximum as soon as the wave front arrives and is followed by a gradual decrease due to the increase of in-scattering from the opposite direction, i.e., the right-hand side region of the medium. For Case 2, the incident radiation at a given location increases with time (see Fig. 5(*c*)) but the radiative flux decreases significantly with time (see Fig. 5(*d*)) at the instant when the reflected wave front propagates to the same location. The branch point on the curves represents the instant when the wave front arrives at that location after reflection.

Figure 6 shows the Case 3 solutions of the G and q distributions in a nonhomogeneous medium with a larger extinction coefficient region in the middle of the one-dimensional slab. The property distribution simulates an optically less dense material embedded with an optically denser second material. The incident radiation within the optically thick region has a sudden increase near the interface, which is caused by the increase of scattering from optical thick region around that location, and then it decreases at a much faster rate than that in the optically thin region. The latter is caused by the much stronger exponential decay over the larger optical distance. By taking partial differentiation of $G(z,t)$ with respect to the extinction coefficient κ in Eq. (6), it shows that the partial differentiation of the first term on the right side of the equation is always negative and that of the second term is either positive or negative. This demonstrates that the contribution of boundary emission to the incident radiation at location s, decreases with the increase of average extinction coefficient between the boundary and the location under consideration. The contribution of scattering from a certain location s' in the medium could be either positive or negative with the increase of effective extinc-

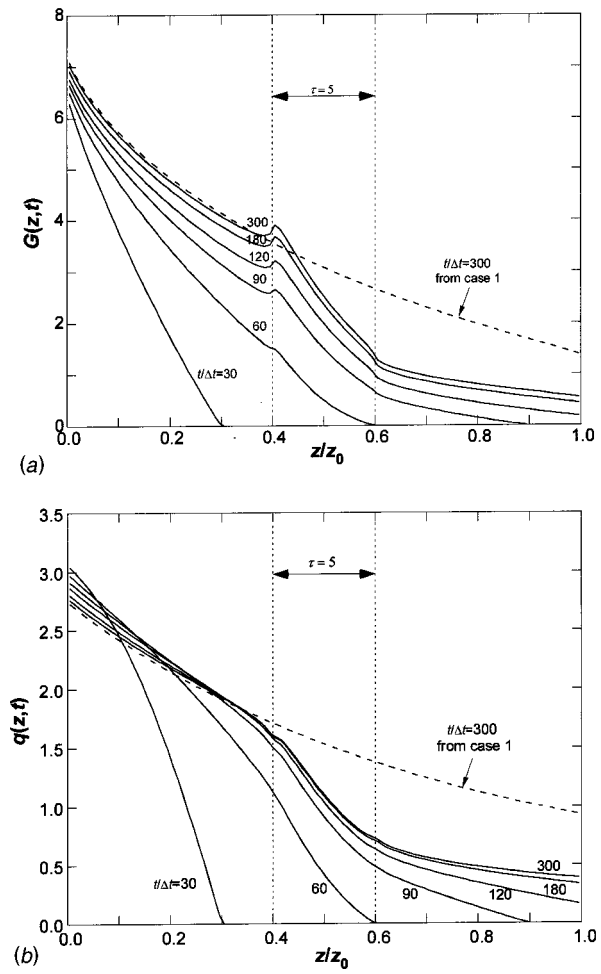

Fig. 6 Incident radiation and radiative flux in nonhomogeneous medium with one diffusely emitting boundary: (*a*) incident radiation distribution at different time; and (*b*) radiative flux distribution at different time

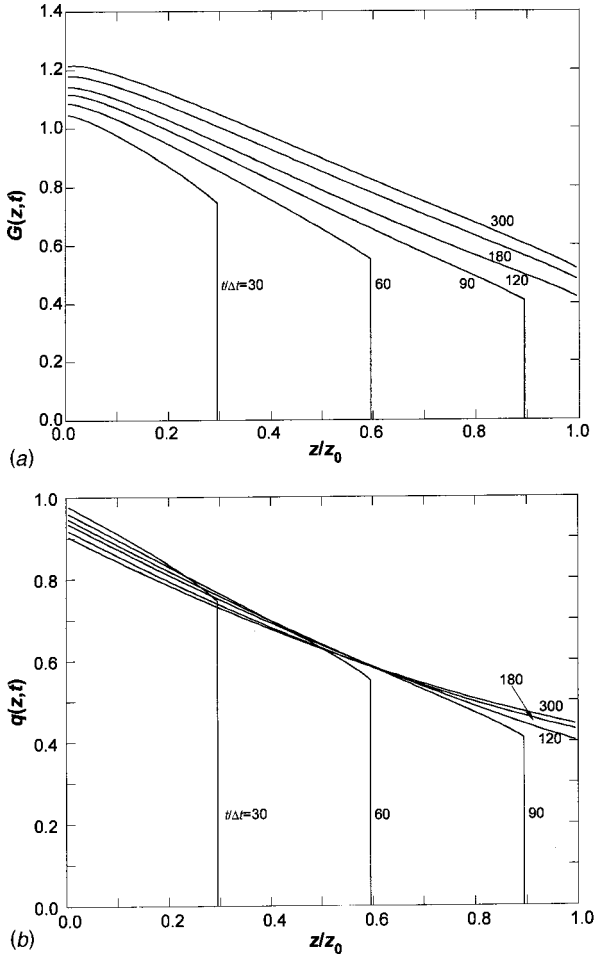

Fig. 7 Incident radiation and radiative flux in homogeneous medium with one collimated emitting boundary: (*a*) incident radiation distribution at different time; and (*b*) radiative flux distribution at different time

tion coefficient between the two points s' and s. This is because the sign of the derivative of the second term of Eq. (6) depends on the optical thickness between the two points, i.e., whether $\kappa(s-s')<1$ or >1. If the optical thickness is less than 1, the derivative has negative sign. Therefore, whether a maximum incident radiation occurs or not with the change of extinction coefficient in the nonhomogeneous medium depends on the rate of the changes of the boundary radiation and the volume in-scattering with the increase of extinction coefficient. Under the Case 3 condition, there is a local maximum G near the first interface between the different optical thickness regions. It is possible that the distinctive time responses of Case 3 will provide useful information to infer the location and extent of the nonhomogeneous region inside the medium. This will have practical applications in medical diagnostics, material property/defect determination, and remote sensing, etc.

Figure 7 is the result of a homogeneous medium subjected to the collimated radiation incidence at the boundary 1 (Case 4). In this case, the surface integration term vanishes but the contribution from the incident collimated direction remains. The contribution of boundary emission to the intensity in the medium comes from the parallel, collimated radiation which decays exponentially due to extinction over the optical distance κz. A marked difference between the results of Cases 4 and 1 is that a sharp wave front exists in the radiation wave propagation for Case 4 (see Figs. 7(*a*) and 7(*b*)). This sharp wave front advances in the medium, which clearly separates the radiation-affected zone from the unaffected zone, and disappears when it propagates into the second boundary. The integro-differential treatment of the TRTE will need a high order upwind difference scheme (e.g., TVD, ENO) to capture the discontinuity at the wave front. The problem is similar to the shock wave flows.

Conclusions

A new analytical model using integral formulation in conjunction with the domain of influence is presented to treat the space and time dependent radiative transfer within the one-dimensional medium. The domain of influence is developed by a phenomenological analysis using the Lagrangian viewpoint. The present model describes the time dependence and wave behavior of radiation propagation, which can't be treated by the steady-state radiative transfer model, and overcomes the difficulties in the existing approximate transient radiative transfer models. The integral formulation can also simulate the steady-state radiative transfer as a special case if the intensity is independent of time t. Thus, the current integral formulation is a general one. The formulation can be further extended to deal with multi-dimensional, nonhomogeneous, and high order anisotropic phase function problems.

Numerical results are obtained for incident radiation and radiative flux in the medium with different boundary conditions and property distributions. The integral formulation predicts the time dependence and wave behavior of radiation propagation in transient radiative transfer, which can't be predicted accurately with approximate models. The transient solutions have excellent agree-

ment with the steady-state finite volume and quadrature methods' solutions at large time step. The results reveal radiative wave characteristics that have not been studied before. These characteristics have important and practical applications in problems where the spatial radiative property difference can be revealed in the temporal radiative signature.

Acknowledgment

The second author would like to thank Professor Michael F. Modest of Pennsylvanian State University and Dr. Zhiqiang Tan of CFD Research Corporation for helpful comments. Mr. Fangming Li provided the finite volume method results for comparison. The work is partially supported by Sandia National Lab. with contract AW-9963.

Nomenclature

a = absorption coefficient
A = boundary surface area
c = propagation speed of radiation transport in the medium
D = substantial derivative
F = integrand function
G = incident radiation or integrated intensity
I = radiation intensity
I_0 = radiation intensity at boundary $z=0$
K = kernel function
$\hat{k}$ = unit vector in z-direction
N = number of the discretized volume element or time step
$\hat{n}$ = inward unit normal vector of boundary surface
q = radiative flux
r = radial coordinate
s = geometric path length
$\hat{s}$ = unit vector along a given direction
t = time
Δt = time of travel or time step
u = unit step function
V = volume of the medium
z = axial coordinate
z_0 = medium thickness
Δz = volume element size

Greek Symbols

κ = extinction coefficient, $\kappa=a+\sigma$
σ = scattering coefficient
τ = optical thickness of the medium, κz_0
Φ = scattering phase function
Ω = solid angle
ω = scattering albedo, $\omega=\sigma/\kappa$

Subscripts

b = black body
t = time
z = volume element

References

[1] Mitra, K., and Kumar, S., 1999, ''Development and Comparison of Models for Light-Pulse Transport through Scattering-Absorbing Media,'' Appl. Opt., **38**, No. 1, pp. 188–196.
[2] Crosbie, A. L., and Dougherty, R. L., 1982, ''Two-Dimensional Linearly Anisotropic Scattering in a Semi-Infinite Cylindrical Medium Exposed to a Laser Beam,'' J. Quant. Spectrosc. Radiat. Transf., **28**, No. 3, pp. 233–263.
[3] Menguc, M. P., and Viskanta, R., 1987, ''Radiation Heat Transfer in Combustion Systems,'' Prog. Energy Combust. Sci., **13**, pp. 97–160.
[4] Weinman, J. A., and Shipley, S. T., 1972, ''Effects of Multiple Scattering on Laser Pulses Transmitted Through Clouds,'' J. Geophys. Res., **77**, pp. 7123–7128.
[5] Yamada, Y., 1995, ''Light-Tissue Interaction and Optical Imaging in Biomedicine,'' *Annual Review of Fluid Mechanics and Heat Transfer*, C. L. Tien, ed., 6, Begell House, New York, pp. 1–59.
[6] Majumdar, A., 1998, ''Microscale Energy Transport in Solids,'' *Microscale Energy Transport*, C. L. Tien et al., eds., Begell House, New York, pp. 1–93.
[7] Longtin, J. P., and Tien, C. L., 1996, ''Saturable Absorption during High-Intensity Laser Heating of Liquids,'' ASME J. Heat Transfer **118**, pp. 924–930.
[8] Qiu, T. Q., and Tien, C. L., 1992, ''Short Pulse Laser Heating in Metals,'' Int. J. Heat Mass Transf., **35**, pp. 719–726.
[9] Liu, F., Yoo, K. M., and Alfano, R. R., 1993, ''Ultrafast Laser-Pulse Transmission and Imaging through Biological Tissues,'' Appl. Opt., **32**, No. 4, pp. 554–558.
[10] Gemert, M. J. C., and Welch, A. J., 1989, ''Clinical Use of Laser-Tissue Interaction,'' IEEE Eng. Med. Biol. Mag., **1989**, pp. 10–13.
[11] Grant, K. J., Piper, J. A., Ramsay, D. J., and Williams, K. L., 1993, ''Pulse Lasers in Particle Detection and Sizing,'' Appl. Opt., **32**, No. 4, pp. 416–417.
[12] Mitra, K., and Kumar, S., 1997, ''Application of Transient Radiative Transfer Equation to Oceanographic Lidar,'' ASME HTD-Vol. 353, pp. 359–365.
[13] Balsara, D. W., 1999, ''An Analysis of the Hyperbolic Nature of the Equations of Radiation Hydrodynamics,'' J. Quant. Spectrosc. Radiat. Transf., **61**, No. 5, pp. 617–627.
[14] Mitra, K., Lai, M.-S., and Kumar, S., 1997, ''Transient Radiation Transport in Participating Media With a Rectangular Enclosure,'' AIAA J. Thermophysics and Heat Transfer, **11**, No. 3, pp. 409–414.
[15] Wu, C.-Y., 1989, ''Hyperbolic Heat Conduction with Surface Radiation and Reflection,'' Int. J. Heat Mass Transf., **32**, No. 8, pp. 1585–1587.
[16] Frankel, J. I., 1991, ''A Nonlinear Heat Transfer Problem. Solution of Nonlinear, Weakly Singular Volterra Partial Integral Equations of the Second Kind,'' Eng. Anal. Boundary Elem., **8**, No. 5, pp. 231–238.
[17] Cotta, R. M., 1994, ''Benchmark Results in Computational Heat and Fluid Flow: the Integral Transform Method,'' Int. J. Heat Mass Transf., **37**, Suppl. 1, pp. 381–393.
[18] Ramankutty, M. A., and Crosbie, A. L., 1998, ''Modified Discrete-Ordinates Solution of Radiative Transfer in Three-Dimensional Rectangular Enclosures,'' J. Quant. Spectrosc. Radiat. Transf., **60**, No. 1, pp. 103–134.
[19] Ramankutty, M. A., and Crosbie, A. L., 1997, ''Modified Discrete-Ordinates Solution of Radiative Transfer in Two-Dimensional Rectangular Enclosures,'' J. Quant. Spectrosc. Radiat. Transf., **57**, No. 1, pp. 107–140.
[20] Roe, P. L., 1986, ''Characteristic-Based Schemes for the Euler Equation,'' Annu. Rev. Fluid Mech., **18**, pp. 337–365.
[21] Harten, A., 1983, ''High Resolution Schemes for Hyperbolic Conservation Laws,'' J. Comput. Phys., **49**, pp. 357–393.
[22] Shu, C.-W., 1988, ''Efficient Implementation of Essentially Non-oscillatory Shock-Capturing Schemes,'' J. Comput. Phys., **77**, pp. 439–471.
[23] Tannehill, J. C., Anderson, D. A., and Pletcher, R. H., 1997, *Computational Fluid Mechanics and Heat Transfer*, 2nd ed., Taylor & Francis, Washington, DC.
[24] Tan, Z., 1989, ''Radiative Heat Transfer in Multidimensional Emitting, Absorbing, and Anisotropic Scattering Media—Mathematical Formulation and Numerical Method,'' ASME J. Heat Transfer, **111**, pp. 141–146.
[25] Tan, Z., and Howell, J. R., 1990, ''A New Numerical Method for Radiation Heat Transfer in Nonhomogeneous Participating Media,'' AIAA J. Thermophysics and Heat Transfer, **4**, No. 4, pp. 419–424.
[26] Hsu, P.-F., Tan, Z., and Howell, J. R., 1993, ''Radiative Transfer by the YIX Method in a Nonhomogeneous, Scattering and Non-Gray Medium,'' AIAA J. Thermophysics and Heat Transfer, **7**, No. 3, pp. 487–495.
[27] Huan, J., and Naraghi, M. H. N., 1991, ''Source Function Approach for Radiative Heat Transfer Analysis,'' AIAA J. Thermophysics and Heat Transfer, **6**, No. 3, pp. 568–571.
[28] Wu, S.-H., Wu, C.-Y., and Hsu, P.-F., 1996, ''Solutions of Radiative Transfer in Inhomogeneous Participating Media Using the Quadrature Method,'' presented at the ASME 1996 Int. Mechanical Engineering Congress & Exposition, Atlanta, GA, November 1996, ASME HTD-Vol. 332, pp. 101–108.
[29] Penzkofer, A., 1988, ''Passive W-Switching and Mode-Locking for the Generation of Nanosecond to Femtosecond Pulses,'' Applied Physics B, **46**, pp. 43–60.
[30] Wu, C.-Y., 1999, private communication.
[31] Pomraning, G. C., 1973, *The Equations of Radiation Hydrodynamics*, Pergamon Press, New York.
[32] Ozisik, M. N., 1973, *Radiative Transfer and Interaction with Conduction and Convection*, Wiley, New York.
[33] Modest, M. F. 1993, *Radiative Heat Transfer*, McGraw-Hill, New York.
[34] Siegel, R., and Howell, J. R., 1992, *Thermal Radiative Heat Transfer*, 3rd ed., Taylor & Francis, Washington, DC.
[35] Panton, R. L., 1996, *Incompressible Flow*, 2nd ed., Wiley, New York.
[36] Linz, P., 1985, *Analytical and Numerical Methods for Volterra Equation*, SIAM.
[37] Wu, C.-Y., 1990, ''Exact Integral Formulation for Radiative Transfer in an Inhomogeneous Scattering Medium,'' AIAA J. Thermophysics and Heat Transfer, **4(4)**, pp. 425–431.
[38] Hsu, P.-F., 2000, ''Effects of Multiple Scattering and Reflective Boundary on the Transient Radiative Transfer Process,'' the 2000 National Heat Transfer Conf., paper NHTC2000-12078, Pittsburgh, PA.

Phase Change in a Cylinder and a Cylindrical Shell Heated With an Axisymmetric Front Moving in the Axial Direction

C. K. Hsieh
Fellow ASME
Professor Emeritus
Mechanical Engineering Department,
University of Florida,
Gainesville, FL 32611-6300
e-mail: doughsieh@aol.com

M. Leung
Assoc. Mem. ASME
Department of Manufacturing Engineering
and Engineering Management,
City University of Hong Kong,
Kowloon, Hong Kong
e-mail: memleung@cityu.edu.hk

A quasi-steady phase-change problem is solved for a cylindrical shell of which the inner or outer surface is heated with an axisymmetric ring heater moving at a constant velocity. The body temperature is expressed in a product solution, which leads to the derivation of a Klein-Gordon equation. A method of undetermined parameters is developed to solve this equation, and the temperatures are derived in multiple regions in the shell. The results are expressed in integral equations, which are none of the Fredholm or Volterra types. Finally, a least-squares iteration method is developed to solve for the interface positions. The four examples presented in this paper cover the phase change in cylinders and cylindrical shells. Comparisons are made between the temperatures for materials with and without phase change. [DOI: 10.1115/1.1370499]

Keywords: Analytical, Conduction, Heat Transfer, Melting, Solidification

Introduction

In the manufacturing of rotating shafts and bearings, the rubbing surfaces can be hardened by heat treatment with a circular ring of flame heaters moving at a constant velocity along the axial direction as illustrated in Fig. 1. There are two stages for the heat to transfer in a cylinder or cylindrical shell. In the first stage, the material is being heated up and the body temperature is a strong function of the initial temperature. Then, the heat transfer enters into a quasi-steady state. In this stage, the initial temperature effect damps out exponentially, and the body temperature becomes invariant with time in the moving coordinates of the heat source. In practice, the first stage occurs only briefly, while the second stage persists and dominates the effect of surface hardening.

The surface hardening of the shafts and bearings can be attributed to a diffusion-driven phase change caused by the moving heat front. The moving heat front problems have been studied by Rosenthal [1], Grosh et al. [2], Watts [3], DesRuisseaux and Zerkle [4], and Yuen [5], among others. However, no phase change has been considered in their works. The exact solutions of one-dimensional phase change due to a moving heat front have been attempted by Landau [6], Jackson [7], and Hsieh [8]. The solution of two-dimensional phase change in a thin plate subjected to a cylindrical moving heat front has been obtained by Hsieh [9]. It is noted that in the conventional method of exact solution of the phase change imposed with a stationary condition, the problem must be adaptable to a similarity transformation. This limits the problem solved to a one-dimensional semi-infinite domain imposed with a constant-temperature boundary condition. The phase change also occurs in a medium where the material properties are constant and of equal values in different phase regions [10,11].

The solutions developed by Hsieh [8,9] utilize a source-and-sink method that has virtue of deriving a singular equation for the temperature distribution in all phase regions [12,13]. This method will be extended for the solution of the phase change in solid cylinders and cylindrical shells. A method of undetermined parameters to solve a Klein–Gordon equation will be presented in this paper. The resulting temperatures can be expressed in the form of a nonlinear integral equation, which is none of the Fredholm or Volterra types. Finally, four examples are provided to illustrate the application of the analysis to phase change studies.

Analysis

It is assumed that the phase change is diffusion-driven in a medium of constant and equal property values in different phase regions. The phase change is caused by an axisymmetric heat front moving at a constant velocity, V, in the axial direction of the cylindrical shell shown in Fig. 1. The governing diffusion equation in the fixed coordinates of the shell (z',r') can be changed to the coordinates (z,r) moving with the heat front by using transformations: $z=z'-Vt$ and $r=r'$. The governing equation for heat transfer under a quasi-steady state can be expressed as

$$\nabla^2 T+\sum_{j=a,b}\frac{\varrho L_j}{k}V\delta[z-S_j(r)]+\frac{q}{2\pi R_l k}\delta(r-R_l)\delta(z)=-\frac{V}{\alpha}\frac{\partial T}{\partial z} \tag{1}$$

$$\begin{matrix}L_a\\L_b\end{matrix}=\begin{matrix}-L_1\\L_2\end{matrix};l=\begin{matrix}i\\o\end{matrix}$$

where $T(z,r)$ is the temperature for $-\infty<z<\infty$ and $R_i<r<R_o$, ρ is the density, L is the latent heat for phase change, k is the thermal conductivity, and α is the thermal diffusivity. For generality, the heat, q, can be applied either on the inside surface, R_i, or on the outside surface, R_o, as indicated in the third term on the left hand side of this equation. For an intense heat applied on a surface, two phase-change interfaces appear as shown in Fig. 1. These interfaces are represented by the summation term in Eq. (1). In this term, j equal to a refers to the interface located *a*head of the moving front, while b refers to the interface located *b*ehind the front. Using the Dirac delta function for the phase change enables the interface Stefan (flux) conditions to be incorporated into the governing equation. It is noted that, although the analysis is developed here for the cylindrical shell, it can be applied to a solid cylinder by means of general notations described later.

Under a quasi-steady state, the temperature and the interface position are invariant with time. The boundary conditions in the moving coordinates can be expressed as

$$-\frac{\partial T(z,R_i)}{\partial r}+\frac{h_i}{k}T(z,R_i)=0 \tag{2}$$

Contributed by the Heat Transfer Division for publication in the JOURNAL OF HEAT TRANSFER. Manuscript received by the Heat Transfer Division June 19, 2000; revision received November 7, 2000. Associate Editor: C. K. Hsieh.

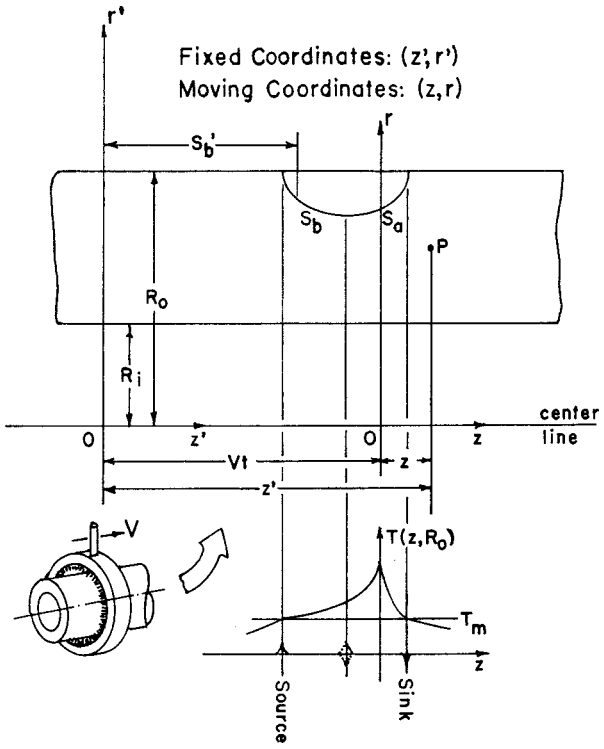

Fig. 1 Coordinate systems used for analysis and temperature profiles as a result of the presence of source and sink in a medium

$$\frac{\partial T(z,R_o)}{\partial r}+\frac{h_o}{k}T(z,R_o)=0 \tag{3}$$

$$T(-\infty,r)=\text{finite} \tag{4}$$

$$T(\infty,r)=0 \tag{5}$$

where h is the convective heat transfer coefficient to the surrounding where the temperature is zero. At the interfaces, the temperature must be continuous and reach a value for the material to change phase as

$$T[S_j(r),r]=T_m, \quad j=a,b, \tag{6}$$

where S_j denotes the positions of the interfaces and T_m is the phase-change temperature.

The quasi-steady problem above can be generalized by recasting it in a dimensionless format. The following dimensionless groups are introduced

$$x=\frac{z}{R_o}; \tag{7a}$$

$$y=\frac{r}{R_o}; \tag{7b}$$

$$u_j=\frac{S_j}{R_o}, j=a,b; \tag{7c}$$

$$Y_i=\frac{R_i}{R_o}; \tag{7d}$$

$$Z=\frac{T}{q/(2\pi R_o k)}; \tag{7e}$$

$$Z_m=\frac{T_m}{q/(2\pi R_o k)}; \tag{7f}$$

$$\mathrm{St}_j=\frac{cT_m}{L_j}, \begin{matrix} L_a \\ L_b \end{matrix} = \begin{matrix} -L_1 \\ L_2 \end{matrix}; \tag{7g}$$

$$\mathrm{Pe}=\frac{V(2R_o)}{\alpha}; \tag{7h}$$

$$\mathrm{Bi},1=\frac{h_1(2R_o)}{k}, 1=\begin{matrix} i \\ o \end{matrix}, \tag{7i}$$

where St is known as the Stefan number, Pe as the Peclet number, and Bi as the Biot number. In terms of these groups, the problem becomes

$$\nabla^2 Z+\sum_{j=a,b}\frac{\mathrm{Pe}Z_m}{2\mathrm{St}_j}\delta[x-u_j(y)]+\begin{matrix}(1/Y_i)\\1\end{matrix}\delta\left(y-\begin{matrix}Y_i\\1\end{matrix}\right)\delta(x)=-\frac{\mathrm{Pe}}{2}\frac{\partial Z}{\partial x} \tag{8}$$

$$-\frac{\partial Z(x,Y_i)}{\partial y}+\frac{\mathrm{Bi},i}{2}Z(x,Y_i)=0 \tag{9}$$

$$\frac{\partial Z(x,1)}{\partial y}+\frac{\mathrm{Bi},o}{2}Z(x,1)=0 \tag{10}$$

$$Z(-\infty,y)=\text{finite} \tag{11}$$

$$Z(\infty,y)=0 \tag{12}$$

$$Z[u_j(y),y]=Z_m, \quad j=a,b, \tag{13}$$

where $Z(x,y)$ is the dimensionless temperature for $-\infty<x<\infty$ and $Y_i<y<1$; $u_j(y)$ represents the dimensionless interface positions. The third term on the left hand side of Eq. (8) embodies two modes of heat input. The top expression is used when the shell is heated on the inside, while the bottom expression is used when the shell is heated on the outside.

The dimensionless problem derived above can be solved by assuming a product solution

$$Z(x,y)=e^{-\mathrm{Pe}(x/4)}M(x,y) \tag{14}$$

in which the $M(x,y)$ function satisfies the following governing equation, boundary and interface conditions:

$$\nabla^2 M-\left(\frac{\mathrm{Pe}}{4}\right)^2 M=-e^{\mathrm{Pe}(x/4)}\left\{\sum_{j=a,b}\frac{\mathrm{Pe}Z_m}{2\mathrm{St}_j}\delta[x-u_j(y)]+\begin{matrix}(1/Y_i)\\1\end{matrix}\delta\left(y-\begin{matrix}Y_i\\1\end{matrix}\right)\delta(x)\right\} \tag{15}$$

$$-\frac{\partial M(x,Y_i)}{\partial y}+\frac{\mathrm{Bi},i}{2}M(x,Y_i)=0 \tag{16}$$

$$\frac{\partial M(x,1)}{\partial y}+\frac{\mathrm{Bi},o}{2}M(x,1)=0 \tag{17}$$

$$M(-\infty,y)=0 \tag{18}$$

$$M(\infty,y)=0 \tag{19}$$

$$M[u_j(y),y]=Z_m e^{\mathrm{Pe}u_j(y)/4}, \quad j=a,b. \tag{20}$$

Equation (15) is a nonhomogeneous Klein–Gordon equation. A method of undetermined parameters is devised to solve this equation. In this method, the equation is first recast as

$$LM=E, \tag{21}$$

where L is an operator,

$$L=\nabla^2-\left(\frac{\mathrm{Pe}}{4}\right)^2, \tag{22}$$

and E is a function representing the nonhomogeneous term on the right hand side of Eq. (15). An auxiliary problem is then defined by means of a Helmholtz equation

Table 1 Eigenfunctions, characteristic equations, mode functions, and norm integral expressions

Geometry	$H(p_n y)$	$I(p_n)$	$1/N(p_n)$	p_n are positive roots of
Solid cylinder	$J_0(p_n y)$	$J_0(p_n)$	$\dfrac{2p_n^2}{J_0^2(p_n)\left[\left(\dfrac{Bi,o}{2}\right)^2+p_n^2\right]}$	$p_n J_1(p_n)-\dfrac{Bi,o}{2}J_0(p_n)=0$
Cylindrical shell heated inside	$KJ_0(p_n y)-QY_0(p_n y)$	$\dfrac{KJ_0(p_n Y_i)-QY_0(p_n Y_i)}{Y_i}$	$\dfrac{(\pi p_n W)^2}{2(b_o W^2-b_i Q^2)}$	$KW-QX=0$
Cylindrical shell heated outside		$KJ_0(p_n)-QY_0(p_n)$		

where

$$K=-p_n Y_1(p_n)+\frac{Bi,o}{2}Y_0(p_n)$$

$$Q=-p_n J_1(p_n)+\frac{Bi,o}{2}J_0(p_n)$$

$$W=-p_n J_1(p_n Y_i)-\frac{Bi,i}{2}J_0(p_n Y_i)$$

$$X=-p_n Y_1(p_n Y_i)-\frac{Bi,i}{2}Y_0(p_n Y_i)$$

$$b_i=\left(\frac{Bi,i}{2}\right)^2+p_n^2$$

$$b_o=\left(\frac{Bi,o}{2}\right)^2+p_n^2$$

$$\nabla^2 U+k^2 U=0, \tag{23}$$

which contains an unknown parameter k. The U function satisfies all the homogeneous boundary conditions related to M as follows:

$$-\frac{\partial U(x,Y_i)}{\partial y}+\frac{\mathrm{Bi},i}{2}U(x,Y_i)=0 \tag{24}$$

$$\frac{\partial U(x,1)}{\partial y}+\frac{\mathrm{Bi},o}{2}U(x,1)=0 \tag{25}$$

$$U(-\infty,y)=0 \tag{26}$$

$$U(\infty,y)=0. \tag{27}$$

The U function can be derived as

$$U(x,y)=[F_n(s)\cos sx+G_n(s)\sin sx]H(p_n y), \tag{28}$$

where $H(p_n y)$ represents an eigenfunction in the radial direction of the shell. This function is given together with its characteristic equation in Table 1. In this function, the eigenvalues, p_n, are discrete, while the eigenvalue, s, in Eq. (28), coming from the solution of the U function in the axial direction, is a continuum. The parameter k can be found by substituting (28) into (23); a relation between the parameter and the eigenvalues can be established as

$$k^2=p_n^2+s^2. \tag{29}$$

The U function derived above can now be used to expand the M function as

$$M(x,y)=\int_0^\infty\sum_{n=1}^\infty U(x,y)ds. \tag{30}$$

Operating L on both sides of this equation and using Eqs. (21) through (23) for simplification gives

$$E=-\int_0^\infty\sum_{n=1}^\infty\left[p_n^2+\left(\frac{\mathrm{Pe}}{4}\right)^2+s^2\right][F_n(s)\cos sx+G_n(s)\sin sx]H(p_n y)ds. \tag{31}$$

It follows that

$$\begin{Bmatrix}F_n(s)\\G_n(s)\end{Bmatrix}=-\frac{1}{p_n^2+\left(\dfrac{\mathrm{Pe}}{4}\right)^2+s^2}\frac{1}{\pi N(p_n)}\int_{Y_i}^1 y' H(p_n y')\times\int_{-\infty}^\infty E(x',y')\begin{Bmatrix}\cos sx'\\\sin sx'\end{Bmatrix}dx'dy', \tag{32}$$

where $N(p_n)$ represents the norm integral, which has been derived for the shell as listed in Table 1. As E represents the nonhomogeneous term on the right hand side of Eq. (15), one can derive the expressions of the Fourier coefficients, $F_n(s)$ and $G_n(s)$, as

$$\begin{Bmatrix}F_n(s)\\G_n(s)\end{Bmatrix}=\frac{1}{p_n^2+\left(\dfrac{\mathrm{Pe}}{4}\right)^2+s^2}\frac{1}{\pi N(p_n)}\left\{\begin{matrix}I(p_n)\\0\end{matrix}-\frac{\mathrm{Pe}Z_m}{2\mathrm{St}}\times\int_e^f\left[e^{(\mathrm{Pe}/4)u_a(y')}\begin{matrix}\cos su_a(y')\\\sin su_a(y')\end{matrix}-e^{(\mathrm{Pe}/4)u_b(y')}\begin{matrix}\cos su_b(y')\\\sin su_b(y')\end{matrix}\right]\times y' H(p_n y')dy'\right\}, \tag{33}$$

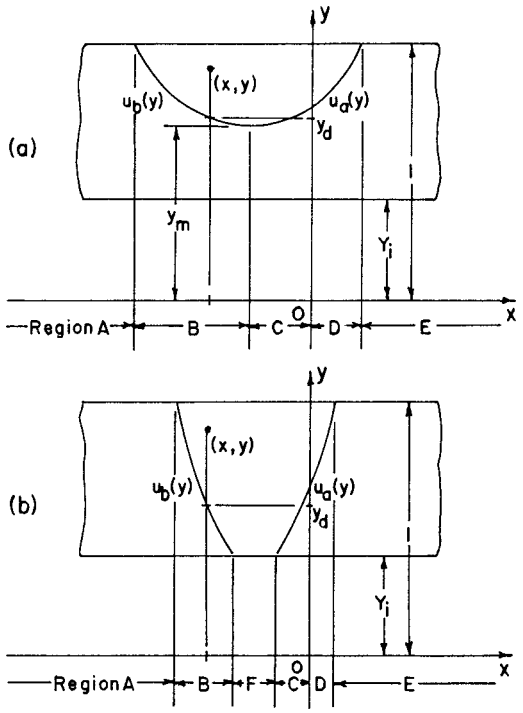

Fig. 2 Division of the domain into six regions in the moving coordinates

where $I(p_n)$ is a mode function used to characterize the specific surface that is heated on the shell. The expression of $I(p_n)$ is shown in Table 1. In Eq. (33), the Stefan number is taken to be identical in value but of different signs for the two interfaces; see Eq. (7*g*). The integration limits in Eq. (33) are taken so that e and f encompass the entire phase-change region. Thus in general, if the phase change is confined to a region close to the surface as illustrated in Fig. 2(*a*) and the shell is heated on the outside, e and f take on y_m and 1, respectively. They are changed respectively to Y_i and y_m if the shell is heated at the inside. In either case, the radius y_m refers to the maximum depth at which the material changes phase in the shell.

On the other hand, if the phase change penetrates through the entire thickness of the shell (see Fig. 2(*b*)), e and f always equal Y_i and 1, respectively, regardless of where the shell is heated. Finally, the M function can be derived, with some trigonometric manipulations, as

$$M(x,y)=\frac{1}{\pi}\sum_{n=1}^{\infty}\int_{s=0}^{\infty}\frac{1}{p_n^2+\left(\frac{\mathrm{Pe}}{4}\right)^2+s^2}\frac{1}{N(p_n)}H(p_n y)\times\left\{\cos sx I(p_n)-\frac{\mathrm{PeZ}_m}{2\mathrm{St}}\int_{y'=e}^{f}[e^{(\mathrm{Pe}/4)u_a(y')}\times\cos s(x-u_a(y'))-e^{(\mathrm{Pe}/4)u_b(y')}\times\cos s(x-u_b(y'))]y'H(p_n y')dy'\right\}ds. \quad (34)$$

The analysis developed above is general and applicable to the temperature in all phase regions in the shell. However, to derive the temperature in a specific region, one must treat the integrals in this equation with great care. The result of the s integral hinges on the sign of the argument of the cosine functions inside the braces [14]. Thus for phase change confined to the surface region as shown in Fig. 2(*a*), the temperature can be divided into five regions and derived as follows:

Region A:

$$Z(x,y)=\sum_{n=1}^{\infty}C_n\left\{e^{P_- x}I(p_n)-\frac{\mathrm{PeZ}_m}{2\mathrm{St}}\int_e^f[e^{P_-(x-u_a(y'))}-e^{P_-(x-u_b(y'))}]y'H(p_n y')dy'\right\}H(p_n y) \quad (35)$$

Region B:

$$Z(x,y)=\sum_{n=1}^{\infty}C_n\left\{e^{P_- x}I(p_n)-\frac{\mathrm{PeZ}_m}{2\mathrm{St}}\left[\int_e^f e^{P_-(x-u_a(y'))}y'H(p_n y')dy'-\int_e^{y_d(x)}e^{P_-(x-u_b(y'))}y'H(p_n y')dy'-\int_{y_d(x)}^f e^{-P_+(x-u_b(y'))}y'H(p_n y')dy'\right]\right\}H(p_n y) \quad (36)$$

Region C:

$$Z(x,y)=\sum_{n=1}^{\infty}C_n\left\{e^{P_- x}I(p_n)-\frac{\mathrm{PeZ}_m}{2\mathrm{St}}\left[\int_e^{y_d(x)}e^{-P_+(x-u_a(y'))}y'H(p_n y')dy'+\int_{y_d(x)}^f e^{P_-(x-u_a(y'))}y'H(p_n y')dy'-\int_e^f e^{-P_+(x-u_b(y'))}y'H(p_n y')dy'\right]\right\}H(p_n y) \quad (37)$$

Region D:

$$Z(x,y)=\sum_{n=1}^{\infty}C_n\left\{e^{-P_+ x}I(p_n)-\frac{\mathrm{PeZ}_m}{2\mathrm{St}}\left[\int_e^{y_d(x)}e^{-P_+(x-u_a(y'))}y'H(p_n y')dy'+\int_{y_d(x)}^f e^{P_-(x-u_a(y'))}y'H(p_n y')dy'-\int_e^f e^{-P_+(x-u_b(y'))}y'H(p_n y')dy'\right]\right\}H(p_n y) \quad (38)$$

Region E:

$$Z(x,y)=\sum_{n=1}^{\infty}C_n\left\{e^{-P_+ x}I(p_n)-\frac{\mathrm{PeZ}_m}{2\mathrm{St}}\int_e^f[e^{-P_+(x-u_a(y'))}-e^{-P_+(x-u_b(y'))}]y'H(p_n y')dy'\right\}H(p_n y) \quad (39)$$

If the phase change has penetrated through the entire thickness of the shell, a sixth region must be accounted for. This region is sandwiched in between Regions B and C as shown in Fig. 2(*b*). Calling it Region F, one can derive the temperature in this region as **Region F**:

$$Z(x,y)=\sum_{n=1}^{\infty} C_n\left\{ e^{P_- x} I(p_n) - \frac{\mathrm{PeZ}_m}{2\ \mathrm{St}}\left[\int_e^f e^{P_-(x-u_a(y'))} y' H(p_n y') dy' - \int_e^f e^{-P_+(x-u_b(y'))} y' H(p_n y') dy' \right] \right\} H(p_n y) \quad (40)$$

In Eqs. (35)–(40) derived above,

$$C_n=\frac{1}{2\left[p_n^2+\left(\frac{\mathrm{Pe}}{4}\right)^2\right]^{1/2} N(p_n)} \quad \text{and} \quad P_\pm=\left[p_n^2+\left(\frac{\mathrm{Pe}}{4}\right)^2\right]^{1/2} \pm \left(\frac{\mathrm{Pe}}{4}\right). \quad (41a,b)$$

Notice that the integration limit, y_d, in the integrals in Eqs. (36)–(38) varies with the position of x that is selected for the evaluation of temperature. This y_d is the intersection of the interface curve with a line parallel to the y axis at the selected x position (see Fig. 2) and can be determined by solving the following equation implicitly

$$u_j(y_d)=x, \quad j=a,b. \quad (42)$$

Equations (35)–(40) are six nonlinear integral equations, whose integration limits contain unknowns. They are thus none of the Fredholm or Volterra types.

The analysis developed above for the cylindrical shell can be readily adapted to the analysis of the phase change in a solid cylinder. For the solid cylinder, the heat can only be applied on its outside surface and an adiabatic condition exists at y equal to zero. Using the adiabatic condition, the eigenfunction, characteristic equation, mode function, and the norm expression can be derived as summarized in Table 1. Notice that when the surfaces of the cylinders and shells are insulated, $p_0=0$ must be included as one of the eigenvalues. When p_0 is zero, $1/N(p_0)$ is 2 for cylinders, and $2/(1-Y_i^2)$ for shells.

Verification of Solution

It is easy to show that Eqs. (35)–(40) satisfy the governing equation and boundary conditions, Eqs. (8)–(12). As will be shown later, Eq. (13) can be used to find the interface positions; satisfaction of the interface condition thus comes naturally. It is also clear that the temperatures are continuous at the interface between different regions. Furthermore, the temperatures derived in Eqs. (35)–(40) can be reduced to a special case in which the cylinders are heated but without phase change. In this case, all the integrals in these equations vanish, and the temperatures in six regions reduce to the temperatures in two regions. One is located ahead of the heat front, and the other is located behind the heat front. The resulting temperature equations are in total agreement with those derived by Watts [3] with a Hankel transform. Better yet, the temperatures in the infinite series in Eqs. (35)–(40) converge, and this is the result that each term of the series is multiplied by a convergency factor [15], a negative exponent which diminishes rapidly with the increase of the eigenvalues.

Features of the Interface Curves

The phase-change problem studied in this work possesses some distinct features. As shown in Appendix A, the change of the temperature slope in the z direction is discontinuous across a phase-change interface. This discontinuity can be expressed in terms of the dimensionless groups as follows:

$$\left(\frac{\partial Z_I}{\partial x}-\frac{\partial Z_{II}}{\partial x}\right)_{u_j}=\frac{\mathrm{PeZ}_m}{2\ \mathrm{St}}\frac{1}{1+\left(\frac{du_j}{dy}\right)^2}, \quad j=a,b, \quad (43)$$

where Z_I refers to the temperature in the medium in its initial phase state and Z_{II} refers to the medium in its changed phase state.

Equation (43) can be used to verify the continuity of the temperature slope in the axial direction at the point where the phase change makes its deepest penetration. It is expected that at this point of maximum penetration, the Dirac delta functions, representing the source and sink, line up radially and their effects cancel out [12,13]; see Fig. 1. The temperature slope must therefore be continuous in the axial direction across this point. In this case, $(du_j/dy)^{-1}$ must be zero, an outcome which is totally consistent with Eq. (43).

Examples and Results and Discussion

The interface positions must be found before the temperature in the shell can be evaluated. The interface positions can be determined by solving integral equations, which can be derived by setting Z in Eqs. (35)–(40) to Z_m and solving these equations simultaneously for the unknowns, $u_a(y)$ and $u_b(y)$. These equations are nonlinear and have additional unknowns (y_d and e or f) in their integration limits. It is practically impossible to solve them exactly. An approximate solution method is developed in this work as described in the paragraphs that follow.

In the approximate solution, the shape and the limiting position of the phase-change interface are determined by solving a special case, in which the integral terms in the temperature equations are forced to zero. This is equivalent to finding the temperature distribution when there is no phase change in the cylinders and shells. To facilitate presentation of this method, an example is provided.

A solid cylinder with an insulated surface is studied for phase change; parameters used for tests are summarized in Table 2 (see Example 1). Figure 3 gives the temperature distribution in the cylinder without phase change. As expected, the peak temperature in the cylinder is located at the point $(x,y)=(0,1)$ where the temperature has a value (4) higher than the Z_m value (1.6) given.

Table 2 Conditions tested in examples

Example	System description	Parameters tested
1	Solid cylinder, surface insulated	Bi,o=0, Pe=2, St=5, Z_m=1.6
2	Solid cylinder, surface insulated	Bi,o=0, Pe=2, St=5, Z_m=2.1
3	Cylindrical shell, surfaces insulated, heated outside	Bi,i=Bi,o=0, Y_i=0.6, Pe=2, St=10, Z_m=3.2
4	Cylindrical shell, surfaces insulated, heated outside	Bi,i=Bi,o=0, Y_i=0.6, Pe=2, St=10, Z_m=2.8

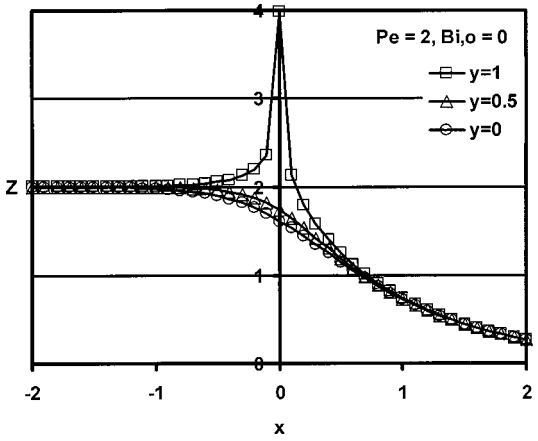

Fig. 3 Temperature curves in an insulated cylinder without phase change

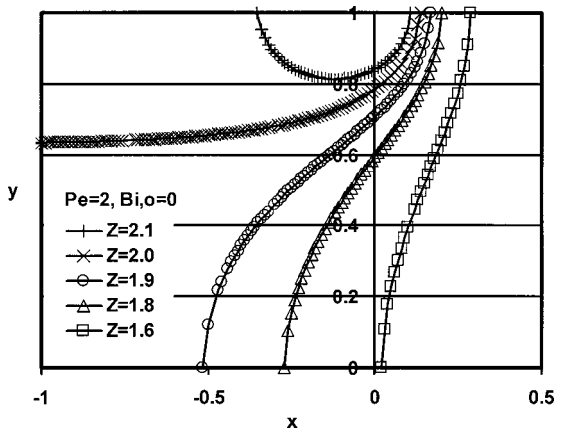

Fig. 4 Isotherms for the cylinder studied in Fig. 3

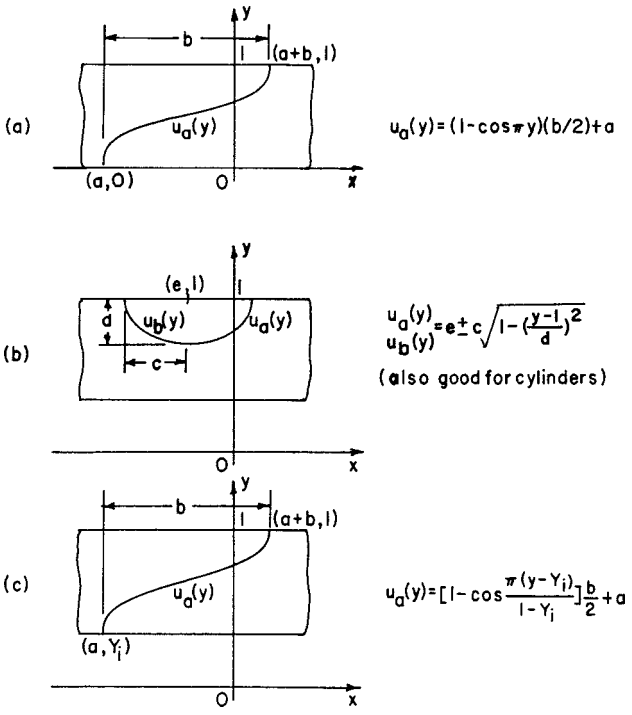

Fig. 5 Curves and equations used to model interfaces

There is thus a phase change in the cylinder. Also notice that the temperature curves behind the heat front converge to a value of 2, a result of the cylinder being insulated. Heat is trapped inside the cylinder, and the temperature in the cylinder eventually reaches an equilibrium state. This equilibrium temperature is higher than the Z_m value given. Recovery of the cylinder to its initial phase state is thus impossible.

The temperature distribution in Fig. 3 is redrawn for an isotherm plot shown in Fig. 4. Notice that a phase-change interface can be taken as an isotherm at the phase-change temperature. Since Fig. 3 is based on the solution of a special case in which the phase change has been excluded, one can consider the isotherm curves in Fig. 4 to be interface positions in the cylinder whose latent heat (or $\mathrm{PeZ}_m/\mathrm{St}$) is zero. A finite latent heat will cause a shift of the curves to the left. These isotherms can thus be taken as the limiting positions of the interfaces. Better yet, these isotherm curves provide a clue for the selection of mathematical relations to model them. For the material of Z_m equal to 1.6 as given in this example, the isotherm plot suggests the use of an inverse cosine function to model the interface as depicted in Fig. 5(a).

Equations (37) and (38) can now be used to formulate the temperature of the interface. For points (x_i, y_i) on the interface lying to the left of the y axis, Eq. (37) can be written as

$$Z(x_i,y_i)=\sum_{n=0}^{\infty} C_n\left\{ e^{P_- x_i} J_0(p_n) - \frac{\mathrm{PeZ}_m}{2\,\mathrm{St}}\left[\int_0^{y_i} e^{-P_+(x_i-u_a(y'))} y' J_0(p_n y')\,dy' + \int_{y_i}^{1} e^{P_-(x_i-u_a(y'))} y' J_0(p_n y')\,dy' \right]\right\} J_0(p_n y_i), \tag{44}$$

where $x_i \leqslant 0$. For points on the interface to the right of the y axis, Eq. (38) can be written as

$$Z(x_i,y_i)=\sum_{n=0}^{\infty} C_n\left\{ e^{-P_+ x_i} J_0(p_n) - \frac{\mathrm{PeZ}_m}{2\,\mathrm{St}}\left[\int_0^{y_i} e^{-P_+(x_i-u_a(y'))} y' J_0(p_n y')\,dy' + \int_{y_i}^{1} e^{P_-(x_i-u_a(y'))} y' J_0(p_n y')\,dy' \right]\right\} J_0(p_n y_i), \tag{45}$$

where $x_i > 0$. Residual is defined as the difference between the input Z_m and the fitted $Z(x_i, y_i)$ as follows:

$$R(x_i,y_i)=Z_m-Z(x_i,y_i). \tag{46}$$

The phase-change interface position can then be determined by a least-squares method in which the residuals are squared and summed over all fitted points. In this effort, the parameters, a and b, are varied for a best fit of the interface temperature.

The evaluated interface position is shown by the left curve in Fig. 6. Here the shift of the curve due to phase change is quite significant. In searching for this interface, six equally spaced points from tip to toe of the curve were used for fitting. In the numerical iteration, the increments of a and b were taken to be 0.01. The maximum residual found at these six points is 0.021 (or 1.3 percent of 1.6). The values of a and b found in the iteration are summarized together with other results in Table 3. The temperature distributions in the cylinder are plotted in Fig. 7. A compari-

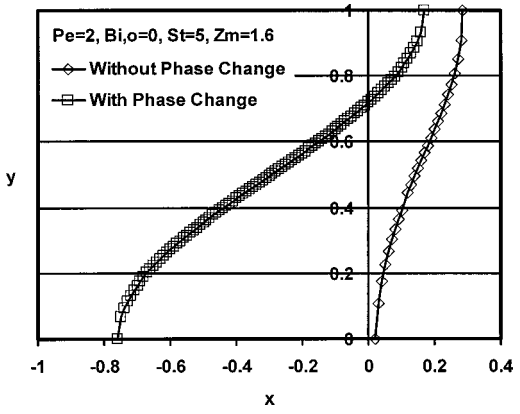

Fig. 6 Limiting position of the interface and evaluated interface position for the cylinder (Z_m=1.6) studied in Fig. 3

Table 3 Values of parameters found and errors in fitted temperatures

Example	No. of points used in least-squares	Maximum residual	Parameters found
1	6	1.3%	a = –0.76, b = 0.93
2	6	0.57%	c = 0.25, d = 0.17, e = – 0.16
3	7	0.2%	c = 0.143, d = 0.105, e = – 0.081
4	6	2.3%	a = – 0.346, b = 0.452

son of the surface temperature in this figure with that in Fig. 3 reveals that there is a marked drop of the temperature due to phase change in the cylinder.

Example 2 deals with a situation in which the phase-change interface can be modeled as a partial ellipse as shown in Fig. 5(*b*). Again, the cylinder is used for tests. As shown in Table 2, the Z_m value for this example is changed to 2.1. Equations (36)–(38) can now be used to write the interface temperature equations. Again, a least-squares method is used to determine the interface position. The results are shown in Figs. 8–10.

Figure 8 gives the evaluated interface position. With the inclusion of the phase change in the analysis, the interface curve is shown to make a left and upward shift. The interface curve now contains two sections. As illustrated in Fig. 2(*a*), u_a is the section for the material to change phase, while u_b is the section for the material to return to its initial phase. In this example, the surface temperature drop due to phase change (Fig. 9) is very small as

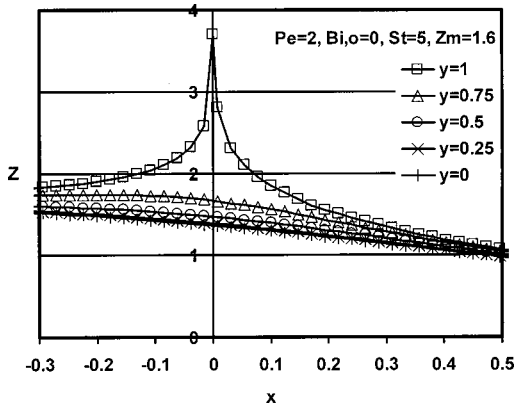

Fig. 7 Temperature distribution curves for phase change in the cylinder (Z_m=1.6) studied in Fig. 3

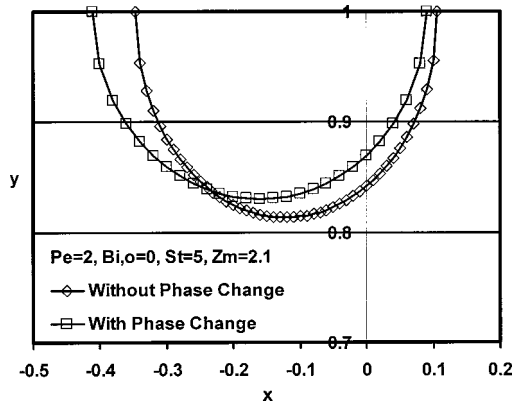

Fig. 8 Limiting position of the interface and evaluated interface position for the cylinder (Z_m=2.1) studied in Fig. 3

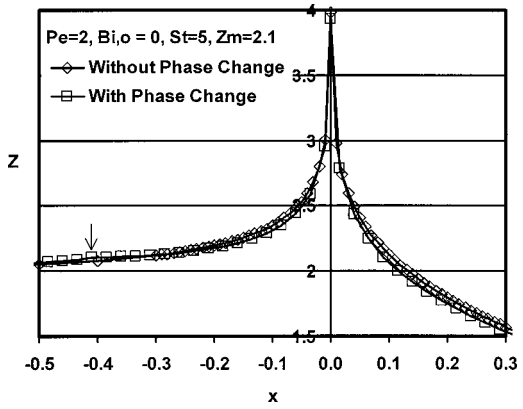

Fig. 9 Comparison of surface temperature distribution with and without phase change for the cylinder (Z_m=2.1) studied in Fig. 3

compared to that in Example 1. This can be ascribed to the fact that for the elliptic interface, the energy initially stored in phase change is recovered when the medium is returned to its initial phase state. Such a recovery of energy did not occur in Example 1 with an inverse cosine interface. The shape of the interface curve thus has a major impact on the recovery of energy and temperature distribution.

Equation (43) provides an estimation of the temperature-slope change in the axial direction across any point on the interface. It is expected that to correctly estimate this slope change using Eq. (43), one must determine the interface position with great accuracy. A slight shift of this position can have a decisive effect on the accuracy of the evaluated slope change. For the present case of elliptic interface, the slope change is in qualitative agreement with the prediction. As shown in Fig. 9, there is a noticeable change in the surface temperature slope across the data point marked by an arrow. At this point, the evaluated slope change is 0.33, which is 21 percent lower than the estimation. Given the nature of the approximate solution used here, this agreement is considered fair.

Figure 10 presents the results of the temperature distributions at various radii in the cylinder. The temperature curves far away behind the heat front converge to a value of 2. This equilibrium temperature is the same as the one found in Fig. 3, giving further indication that the heat consumed in phase change has been fully recovered. This is not so, however, for the case of the phase change without recovery as shown in Fig. 7, where the final equilibrium temperature is lower.

Example 3 repeats the tests with a cylindrical shell. Based on the isotherm plot generated (not shown), an elliptic relation (Fig.

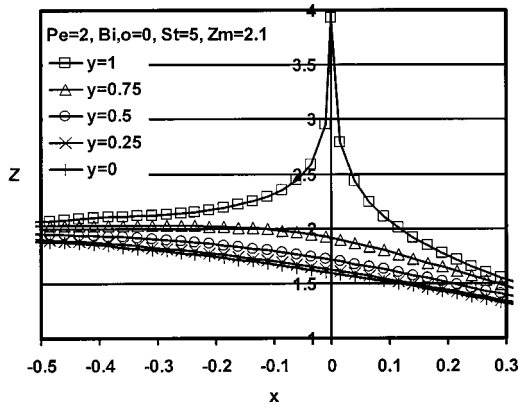

Fig. 10 Temperature distribution curves for phase change in the cylinder (Z_m=2.1) studied in Fig. 3

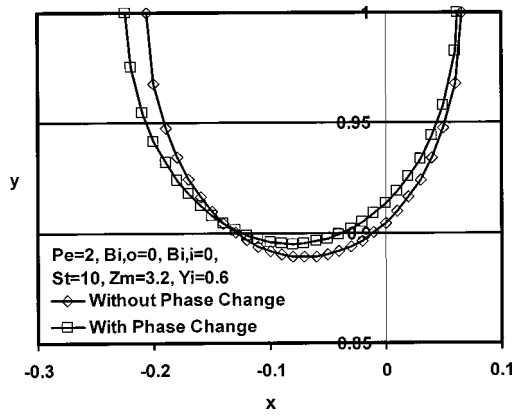

Fig. 11 Limiting position of the interface and evaluated interface position for a cylindrical shell (Z_m=3.2)

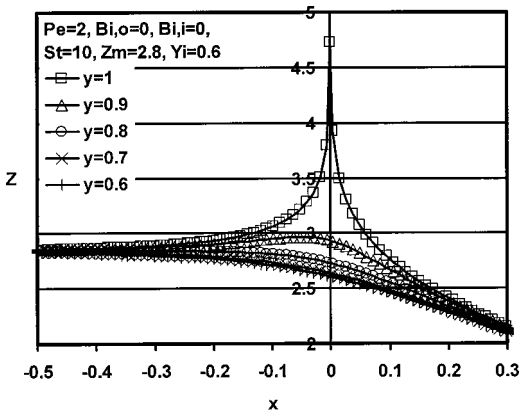

Fig. 13 Temperature distribution curves for phase change in a cylindrical shell (Z_m=2.8)

5(*b*)) can again be used to model the interface. Conditions for the tests are tabulated in Table 2, while the results in Table 3. Notice that for this example, the parameters in the elliptic interface equation were computed to third decimal place. The maximum residual is found to be 0.2 percent. The numerical data are plotted in Figs. 11 and 12. Figure 11 shows the shift of the interface position. Figure 12 shows the temperature distributions at various radii in the cylindrical shell. As in Example 2, the surface temperature drop due to phase change for the cylindrical shell is negligibly small for the elliptic interface. The change of the surface temperature slope across the trailing side of the interface cannot be visualized in Fig. 12, a result of the large St number tested here.

To complete the series of tests in this paper, Example 4 is provided. As shown in Table 2, the Z_m for this example is changed from 3.2 in Example 3 to 2.8 here; other conditions remain the same. An inverse cosine function as shown in Fig. 5(*c*) can be used to model the interface. The parameters found for this example are tabulated in Table 3, and the temperature distributions in the cylindrical shell are plotted as shown in Fig. 13. There is a marked drop of the temperatures due to energy storage in the shell.

In the absence of exact and experimental data for comparison, it is impossible to assess the temperature error in this work. Efforts have been made to improve the confidence in the results with the inclusion of the following tests. Prior to the solution of the problems in this paper, Watts' data [3] have been used to test a special case in which the cylinder was heated but without phase change. Agreement with Watts' data was good. Next following Finlayson [16], the residuals for all the examples have been evaluated as an indication of the numerical error. As listed in Table 3, the maximum residuals are small. They range from 0.2 to 2.3 percent, the errors for the elliptic interfaces being much smaller.

Finally, the equilibrium temperatures in the cylinders and shells have been checked with analysis. In this effort, Watts [3] derived the formulas for the mean temperatures in insulated cylinders and shells at $x \leqslant 0$. They can be modified to derive a general equation for the cylindrical shells as

$$Z_{\text{mean}} = \frac{4}{\text{Pe}(1-Y_i^2)}, \tag{47}$$

which can be specialized to a cylinder by taking Y_i to be zero. Derived on the basis of heat transfer without phase change, this formula can only be used to check the equilibrium temperatures where the phase changes have been fully recovered. This limits the test to bodies with an elliptic interface at points where $x<(e-c)$. Using the parameters given in Table 2, one can calculate the equilibrium temperatures for Examples 2 and 3 to be 2 and 3.125, respectively. They are in excellent agreement with the convergent values calculated by applying volumetric weights to the temperature data on the left margins in Figs. 10 and 12. Better yet, this concept can even be extended to testing the convergent temperatures in Examples 1 and 4. Realizing that the difference between these two examples and the Examples 2 and 3 is the energy stored due to phase change without recovery, one can thus use energy balance to equate $(mc\Delta T)$ to (mL) and derive

$$Z_{\text{mean,without recovery}} = Z_{\text{mean,with recovery}} - \frac{Z_{m,\text{without recovery}}}{\text{St}} \tag{48}$$

Using this relationship yields the equilibrium temperatures for Examples 1 and 4 to be 1.68 and 2.845, respectively. Again, they are in excellent agreement with the convergent values computed using the data shown in Figs. 7 and 13.

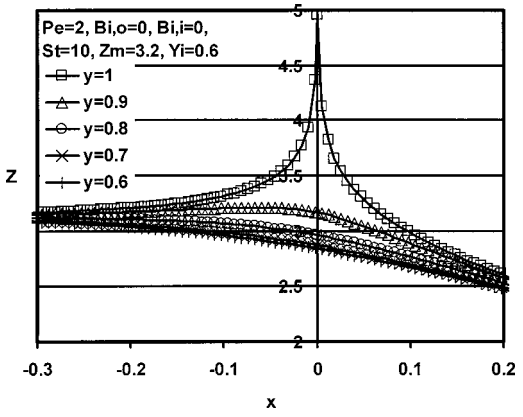

Fig. 12 Temperature distribution curves for phase change in a cylindrical shell (Z_m=3.2)

Concluding Remarks and Presentation of New Dimensionless Group

Example 4 discussed above suggests the existence of a dimensionless group, which is unique in the solution of the present problems. This group can be found by examining Eqs. (35)–(40) and (43). Here the phase change effect and the temperature-slope change in the equations are all multiplied by a dimensionless group of $\text{Pe}Z_m/\text{St}$. This group can be reduced to

$$\frac{\text{Pe}Z_m}{\text{St}} = \frac{4mL}{q} \tag{49}$$

for the cylinder and

$$\frac{\mathrm{Pe}Z_m}{\mathrm{St}}=\frac{4mL}{(1-Y_i^2)q} \tag{50}$$

for the cylindrical shell. In these two equations, m can be equated to the product of ρVA_c, which stands for the mass flow rate of the material crossing the heat front plane. Equations (49) and (50) share a common dimensionless group: mL/q. This group signifies the fraction of the heat rate applied on the surface that is consumed on phase change. A large value of this group results in a strong effect of phase change.

In the case of Example 4 discussed above, a change of the Z_m from 3.2 to 2.8 reduces the value of $\mathrm{Pe}Z_m/\mathrm{St}$ by one eighth. This lessens the phase-change effect, making the inverse cosine curve good for modeling the phase change. This group of $\mathrm{Pe}Z_m/\mathrm{St}$ has also be found by Hsieh [8,9] in the study of other phase-change problems involving a moving heat front. The utility of this group in solving such problems must not be overlooked.

In closing, it should be noted that the inverse cosine and elliptic functions given in Fig. 5 can be generalized by inclusion of more parameters so that these curves can be shifted and stretched in specific directions. They can then be used to model the interface positions when convective conditions are imposed on the surfaces. In this case, more parameters need to be solved by least-squares. The method remains unchanged.

Appendix A

Integrating Eq. (1) over a volume element consisting of a circular ring across the phase-change interface a and using the divergence theorem gives the relation

$$\int_{\Delta l}\nabla T\cdot\hat{n}dl-\frac{\rho VL}{k}\int_{\Delta r}dr=0. \tag{A1}$$

Across a differential interface element Δl, this equation takes the form

$$\Delta\left(\frac{\partial T}{\partial n}\right)\Delta l=\frac{\rho VL}{k}\Delta r. \tag{A2}$$

The relation between Δr and Δl in this equation can be established geometrically as

$$\frac{\Delta r}{\Delta l}=\frac{1}{\left[1+\left(\frac{dz}{dr}\right)^2\right]^{1/2}}. \tag{A3}$$

Equation (*A*2) follows as

$$\left(\frac{\partial T_I}{\partial n}-\frac{\partial T_{II}}{\partial n}\right)_{S_a}=\frac{\varrho VL/k}{\left[1+\left(\frac{dS_a}{dr}\right)^2\right]^{1/2}}, \tag{A4}$$

where T_I and T_{II} have been used to represent the temperatures where the medium is in the initial phase state and in the changed phase state, respectively.

Equation (*A*4) is not convenient to use because the temperature gradients in this equation are expressed in the normal direction to the interface. They need to be changed to the z direction. In this effort, the interface position is represented by an $F(z,r)$ function; the interface position in the z direction is expressed as a $S_a(r)$ function. Together, they can be expressed compactly as

$$F(z,r)=z-S_a(r)=0. \tag{A5}$$

Then,

$$\frac{\partial F}{\partial z}=1 \tag{A6a}$$

and

$$\frac{\partial F}{\partial r}=-\frac{dS_a}{dr}. \tag{A6b}$$

The $\partial T/\partial n$ in Eq. (*A*4) can be expressed in terms of the F function as

$$\frac{\partial T_i}{\partial n}=\nabla T_i\cdot\hat{n}=\nabla T_i\cdot\frac{\nabla F}{|\nabla F|},\quad i=I,II. \tag{A7}$$

At the interface, T_i is equal to T_m, a constant. The differentials of T_i and F vanish as

$$dT_i=\frac{\partial T_i}{\partial z}dz+\frac{\partial T_i}{\partial r}dr=0. \tag{A8}$$

and

$$dF=\frac{\partial F}{\partial z}dz+\frac{\partial F}{\partial r}dr=0. \tag{A9}$$

These two equations can be used to express dz/dr as

$$\frac{dz}{dr}=-\frac{\frac{\partial T_i}{\partial r}}{\frac{\partial T_i}{\partial z}}=-\frac{\frac{\partial F}{\partial r}}{\frac{\partial F}{\partial z}}. \tag{A10}$$

It follows that

$$\frac{\partial T_i}{\partial r}=\left(\frac{\partial F/\partial r}{\partial F/\partial z}\right)\frac{\partial T_i}{\partial z}. \tag{A11}$$

Equations (*A*6*a*,*b*) and (*A*11) can be used to write

$$\nabla T_i\cdot\nabla F=\frac{\partial T_i}{\partial z}\frac{\partial F}{\partial z}+\frac{\partial T_i}{\partial r}\frac{\partial F}{\partial r}=\frac{\partial T_i}{\partial z}\left[1+\left(\frac{dS_a}{dr}\right)^2\right],\quad i=I,II. \tag{A12}$$

Introducing it into (*A*7), which is, in turn, into (*A*4) yields

$$\frac{1}{|\nabla F|}\left[1+\left(\frac{dS_a}{dr}\right)^2\right]\left(\frac{\partial T_I}{\partial z}-\frac{\partial T_{II}}{\partial z}\right)_{S_a}=\frac{\varrho VL/k}{\left[1+\left(\frac{dS_a}{dr}\right)^2\right]^{1/2}}. \tag{A13}$$

It is clear from Eqs. (*A*5) and (*A*6*a*,*b*) that

$$|\nabla F|=\left[\left(\frac{\partial F}{\partial z}\right)^2+\left(\frac{\partial F}{\partial r}\right)^2\right]^{1/2}=\left[1+\left(\frac{dS_a}{dr}\right)^2\right]^{1/2}. \tag{A14}$$

Equation (*A*13) can then be simplified as

$$\left(\frac{\partial T_I}{\partial z}-\frac{\partial T_{II}}{\partial z}\right)_{S_a}=\frac{\varrho VL/k}{1+\left(\frac{dS_a}{dr}\right)^2}. \tag{A15}$$

This equation has been derived by Patel [17], Boley and Pagoda [18], and Rathjen and Jiji [19] in a stationary medium using different approaches. Equation (43) in this paper is just a dimensionless version of Eq. (*A*15).

Nomenclature

- A = cross sectional area of the cylinder or the cylindrical shell
- a = parameter in fitted inverse cosine function
- b = parameter in fitted inverse cosine function, or parameters in Table 1
- Bi = Biot number, Eq. (7)
- C = coefficient in series and integral expansions, Eq. (41)
- c = constant-pressure specific heat, or parameter in fitted ellipse
- d = parameter in fitted ellipse
- E = nonhomogeneous term in Eq. (15)

e = parameter in fitted ellipse
F = function defined as Eq. ($A5$), or coefficient in U function, Eq. (28)
G = coefficient in U function, Eq. (28)
H = eigenfunction in the radial direction, Table 1
h = convective heat transfer coefficient
I = mode function, Table 1
J = Bessel function of the first kind
K = parameter in Table 1
k = thermal conductivity, or unknown parameter in Eq. (23)
L = latent heat, or operator defined as Eq. (22)
l = interface element, Eq. ($A2$)
M = function in product solution, Eq. (14)
m = mass flow rate
N = norm integral, Table 1
n = normal direction
P = Eq. (41)
p = discrete eigenvalue
Pe = Peclet number, Eq. (7)
Q = parameter in Table 1
q = heat input rate
R = radius of the cylinder or cylindrical shell
r = radial coordinate
S = interface position
s = eigenvalue in a continuum
St = Stefan number, Eq. (7)
T = temperature
U = function governed by a Helmholtz equation, Eq. (23)
u = dimensionless interface position, Eq. (7)
V = axial velocity of heat front
W = parameter in Table 1
X = parameter in Table 1
x = dimensionless axial coordinate, Eq. (7)
Y = ratio of inner to outer radius for cylindrical shell, Eq. (7), or Bessel function of the second kind
y = dimensionless radial coordinate, Eq. (7)
Z = dimensionless temperature, Eq. (7)
z = axial coordinate

Greek Letters

α = thermal diffusivity
δ = Dirac delta function
ρ = density

Subscripts

a,b = interface located ahead and behind the heat front, respectively
c = cross section
d = refers to y position where an interface curve intersects with a line parallel to the y axis at the selected x position
i,o = inside and outside surface, respectively
m = phase-change state, or the maximum depth for phase-change penetration
n = related to discrete eigenvalue
$\pm$ = expressions for P defined as Eq. (41)
0,1 = order of Bessel function

References

[1] Rosenthal, D., 1946, ''The Theory of Moving Sources of Heat and its Applications to Metal Treatments,'' Trans. ASME, **68**, pp. 840–866.
[2] Grosh, R. J., Trabant, E. A., and Hawkins, G. A., 1955, ''Temperature Distribution in Solids of Variable Thermal Properties Heated by Moving Heat Sources,'' Quarterly Appl. Math., **13**, pp. 161–167.
[3] Watts, R. G., 1969, ''Temperature Distributions in Solid and Hollow Cylinders Due to a Moving Circumferential Ring Heat Source,'' ASME J. Heat Transfer, **91**, pp. 465–470.
[4] DesRuisseaux, N. R., and Zerkle, R. D., 1970, ''Temperature in Semi-Infinite and Cylindrical Bodies Subjected to Moving Heat Sources and Surface Cooling,'' ASME J. Heat Transfer, **92**, pp. 456–464.
[5] Yuen, W. Y. D., 1987, ''A New Formulation of Heat Transfer Between Two Moving Bodies in Contact Over a Finite Region with Different Bulk Temperatures,'' Mathematical Engineering in Industry, **1**, pp. 1–19.
[6] Landau, H. G., 1950, ''Heat Conduction in a Melting Solid,'' Quarterly Appl. Math., **8**, pp. 81–94.
[7] Jackson, F., 1965, ''Moving Heat Sources with Change of Phase,'' ASME J. Heat Transfer, **87**, pp. 329–332.
[8] Hsieh, C. K., 1995, ''Exact Solution of Stefan Problems for a Heat Front Moving at Constant Velocity in a Quasi-Steady State,'' Int. J. Heat Mass Transf., **38**, pp. 71–79.
[9] Hsieh, C. K., 1995, ''Exact Solution of Stefan Problems Related to a Moving Line Heat Source in a Quasi-Stationary State,'' ASME J. Heat Transfer, **117**, pp. 1076–1079.
[10] Crank, J., 1984, *Free and Moving Boundary Problems*, Clarendon, London.
[11] Yao, L. S., and Prusa, J., 1989, ''Melting and Freezing,'' Adv. Heat Transfer, **19**, pp. 1–95.
[12] Hsieh, C. K., and Choi, C.-Y., 1992, ''Solution of One- and Two-Phase Melting and Solidification Problems Imposed with Constant or Time-Variant Temperature and Flux Boundary Conditions,'' ASME J. Heat Transfer, **114**, pp. 524–528.
[13] Hsieh, C. K., and Choi, C.-Y., 1992, ''A General Analysis of Phase Change Energy Storage for Solar Energy Applications,'' ASME J. Sol. Energy Eng., **114**, pp. 203–211.
[14] Whittaker, E. T., and Watson, G. N., 1934, *Modern Analysis* (Fourth Edition), Cambridge University Press, London.
[15] Carslaw, H. S., 1950, *An Introduction to the Theory of Fourier's Series and Integrals* (Third Revised Edition), Dover Publications, New York.
[16] Finlayson, B. A., 1972, *The Method of Weighted Residuals and Variational Principles*, Academic Press, New York.
[17] Patel, P. D., 1968, ''Interface Condition in Heat Conduction Problems with Change of Phase,'' AIAA J., **6**, pp. 2454–2456.
[18] Boley, B. A., and Pagoda, H. P., 1969, ''The Starting Solution for Two-Dimensional Heat Conduction Problems With Change of Phase,'' Quarterly Appl. Math., **27**, pp. 223–246.
[19] Rathjen, K. A., and Jiji, L. M., 1971, ''Heat Conduction with Melting or Freezing in a Corner,'' ASME J. Heat Transfer, **93**, pp. 101–109.

Dalton J. E. Harvie

David F. Fletcher

Department of Chemical Engineering,
University of Sydney, NSW, 2006

A Simple Kinetic Theory Treatment of Volatile Liquid-Gas Interfaces

Keywords: Boiling, Evaporation, Heat Transfer, Non-Equilibrium, Vaporization

1 Introduction

The Knudsen number (Kn) is defined as the ratio of the mean free path of a gas, λ, to a dimension of an object which interacts with the gas, x,

$$\mathrm{Kn}=\frac{\lambda}{x}. \tag{1}$$

According to Rohsenow and Choi [1], when fluid velocities are small relative to the speed of sound, the dynamics of a gas can be loosely classified into four regimes, the boundaries of which are determined by characteristic Knudsen numbers.

When $\mathrm{Kn}<0.01$, the mean free path of a gas is small compared with the dimensions of the system, and the gas may be approximated as a continuous medium. This is known as the Continuum regime. At slightly higher Knudsen numbers ($0.01<\mathrm{Kn}<0.1$), the gas may be regarded as a continuum at several mean free paths distance from any adjoining medium, but near any interface, a kinetic theory treatment must be used to describe the interaction between individual gas molecules and the adjoining surface. This regime is known as the Slip regime.

The Transition regime exists at higher Knudsen number levels ($0.1<\mathrm{Kn}<3$). Here the mean free path of a gas has a length comparable with the dimensions of the system, and collisions between molecules and other molecules and collisions between molecules and the system boundaries assume equal importance in determining gas behavior. In the Free-Molecule regime ($\mathrm{Kn}>3$), the mean free path of the gas is large compared with the dimensions of the system, and collisions between molecules and other molecules occur only infrequently. Flow solutions in the free-molecule regime are performed using rarefied gas kinetic theory [2–4].

This study is concerned with determining the behavior of a gas at a volatile liquid-gas interface, within the slip flow regime. More specifically, the objective of this note is to provide simple mass, momentum, and thermal energy boundary conditions, which when used in conjunction with continuum transport equations, are able to model the molecular behavior of a gas up to a liquid-gas interface. For the transfer of tangential momentum and thermal energy, these boundary conditions take the form of effective velocity and temperature discontinuities, respectively, which occur at a liquid-gas interface.

Mass transfer at a volatile liquid-gas interface has been previously examined by researchers such as Schrage [5], Nabavian and Bromley [6], and Collier [7]. Heat and momentum transfer at a liquid-solid interface within the Slip flow regime has also been studied Loeb [2], Knudsen [4], Patterson [8], Rohsenow and Choi [1], and Chapman and Cowling [9], amongst others.

Studies of heat and momentum transfer at a liquid-gas interface are less numerous, with the previous works falling into three main categories. The simplest theories employ the Langmuir assumption [10], whereby the liquid and continuum vapor phases are assumed to be separated by a discrete molecular layer. More complex theories involve solving the Boltzmann equation in a region adjacent to the liquid phase, either by the Maxwell moment method [11], or by more direct methods [12–15]. More recently, the direct-simulation Monte-Carlo (DSMC) technique of Bird [16] has been used to determine the growth rates of droplets in supersaturated gas mixtures [17].

The approach chosen in the present study is essentially that due to Langmuir [10], but includes the Schrage correction [5] to account for molecular flow towards or away from the liquid surface. Heat and mass transfer using these methods has been previously studied to good effect by Kang [18] and Young [19] at the surface of a droplet, however, similar studies involving flat surfaces do not appear to exist. A tangential momentum transfer analysis using the Langmuir technique at a liquid-gas interface has not previously been presented.

This note is divided into four sections. In the first, a kinetic theory mass balance at the interface is performed. This analysis is largely a summary of the work accomplished Schrage [5], but repeated here for completeness. This section is followed by an examination of the tangential momentum and thermal energy transfer that occurs at a liquid-gas interface. Finally, a short discussion of the results and some applications for the theory are given.

2 Interface Mass Transfer

The theory of condensation and evaporation rates existing at a liquid-gas interface presented here is largely a summary of work performed by Schrage [5], this work being later reviewed by Collier [7].

Figure 1(*a*) illustrates the variables used in this analysis. The mass flux of molecules impacting the liquid surface is J_i, however, only a proportion of these molecules, J_c, actually condense into the liquid. The remainder of molecules, J_r, rebound from the surface without entering the liquid. The proportion of molecules which condense upon impact is specified by the Accommodation Coefficient σ_c, which is here defined as the probability that an impacting molecule will condense into the liquid upon contact with the surface. The mass flux of molecules evaporating from the surface is J_e, so the net mass flux of liquid evaporation is given by

$$J_t=J_e-J_c=J_e-\sigma_c J_i. \tag{2}$$

By assuming that the molecules which impact the liquid surface initially have a Maxwellian velocity distribution, and that the gas velocity directed away from the liquid surface is u_g, the flux of molecules impacting the liquid surface is given by [5],

$$J_i=\Gamma(a)\sqrt{\frac{M}{2\pi R}}\frac{P}{\sqrt{T_o}}, \tag{3}$$

where

Contributed by the Heat Transfer Division for publication in the JOURNAL OF HEAT TRANSFER. Manuscript received by the Heat Transfer Division May 23, 2000; revision received November 13, 2000. Associate Editor: D. Poulikakos.

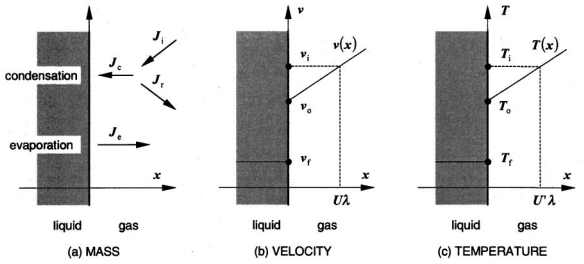

Fig. 1 Variable definition at the liquid-gas interface. Case (*a*) shows variables used in the mass transfer analysis, case (*b*) shows those used in the momentum transfer analysis, and case (*c*) shows those used in the heat transfer analysis.

$$a = u_g \sqrt{\frac{M}{2RT_o}}, \tag{4}$$

and for small values of a,

$$\Gamma(a) = 1 - a\sqrt{\pi}. \tag{5}$$

Note that Eq. (5) is an approximation to the exact solution, valid when $|a| < 0.1$ [7]. Also, the temperature used in these equations, T_o, is the average gas temperature in the vicinity of the interface, which may not be equal to the temperature of the liquid at the interface, T_f.

The velocity of gas evaporating from the liquid surface is related to the net evaporation rate via

$$u_g = \frac{J_t}{\rho_g} = \frac{J_t R T_o}{MP}, \tag{6}$$

where ρ_g is the density of the gas at the interface. Combining Eqs. (2), (3), (4), (5), and (6) gives the net evaporation flux rate at the surface as

$$J_t = \frac{2}{2-\sigma_c}\left(J_e - \sigma_c \sqrt{\frac{M}{2\pi R}} \frac{P}{\sqrt{T_o}} \right). \tag{7}$$

In order to determine J_e, we consider a liquid-gas interface which is in dynamic equilibrium. Under these conditions, the net evaporating mass flux J_t is zero, the temperature of the gas T_o is equal to the temperature of the liquid T_f, and the pressure at the interface is equal to the saturation pressure of the liquid corresponding to the temperature at the interface. Thus, Eq. (7) can be rearranged to yield the dynamic equilibrium evaporation rate as

$$J_e = \sigma_c \sqrt{\frac{M}{2\pi R}} \frac{P_{\text{sat}}(T_f)}{\sqrt{T_f}}. \tag{8}$$

A commonly used assumption in molecular condensation theories, which we will employ here, is that the evaporation mass flux is determined solely by conditions existing within the liquid at the liquid-gas interface [5,7]. Thus, the liquid evaporation mass flux is given at all times by Eq. (8), irrespective of whether the interface is in equilibrium or not, and is a function solely of the temperature of the liquid at the liquid-gas interface.

Note that the pressure within the liquid is not necessarily equal to the saturation pressure corresponding to the liquid temperature—the saturation pressure in Eq. (8) has been empirically determined to equate evaporation and condensation mass fluxes when the interface is in equilibrium. Indeed, generally when condensation or evaporation are occurring at an interface, the interface velocities are much smaller than the speed of sound in either medium, and there is no mass flux induced pressure discontinuity occurring across the interface.

Combining Eqs. (7) and (8) gives the total evaporating mass flux at a liquid-gas interface as

$$J_t = \frac{2\sigma_c}{2-\sigma_c} \sqrt{\frac{M}{2\pi R}} \left(\frac{P_{\text{sat}}(T_f)}{\sqrt{T_f}} - \frac{P}{\sqrt{T_o}} \right). \tag{9}$$

3 Interface Tangential Momentum Transfer

The objective of this section is to determine an effective tangential velocity discontinuity, which when applied using continuum equations within the body of a gas, will model the molecular behavior of the gas at a liquid-gas interface. The magnitude of this discontinuity is determined by equating the stress imposed on a molecular gas by a volatile liquid surface with the stress existing at an interface between a volatile liquid and a continuum gas.

Figure 1(*b*) shows variables used in this analysis. In the diagram, the x coordinate is directed normal to the interface, and the y coordinate tangential to the interface. Velocity in the y direction is represented by v. The tangential velocity of the liquid at the interface is v_f, the average tangential velocity of molecules impacting the liquid is v_i, and the average tangential velocity of all gas molecules at the interface is v_o. Thus, that the magnitude of the slip velocity at the interface is $v_o - v_f$.

In general, the tangential velocity of molecules impacting the liquid, v_i, is not equal to the average tangential molecular velocity at the interface, v_o, because molecules impacting the liquid experienced their last collisions at some distance to the right of the interface, and it is from these collisions that they have gained their tangential velocity. Thus, the tangential velocity of molecules impacting the liquid can be represented as,

$$v_i = v_o + U\lambda \frac{dv}{dx}, \tag{10}$$

where the distance $U\lambda$ is the characteristic distance to the right of the interface from which the impacting molecules gained their tangential velocity.

In a simple gas, molecules experience their last collision before impacting the interface at an average distance of $2/3\lambda$ from the liquid. The value of U in Eq. (10) is greater than 2/3 however, because more than a single collision is generally required to bring a molecule into equilibrium with its surroundings. A Chapman-Enskog analysis for the magnitude of U is given in Chapman and Cowling [9], where it is found that for spherical rigid molecules, $U = 0.998$, or approximately unity. For polyatomic molecules, this value represents a reasonable approximation for momentum calculations, as the average momentum of molecules tangential to an interface is not dependent on the internal molecular energy of individual molecules [9].

The average tangential velocity of molecules moving away from the interface is not in general equal to the velocity of the liquid, v_f, either. This is because molecules which are moving away from the interface may be evaporating molecules, or alternatively molecules which are rebounding from the interface without condensing. To further complicate the situation, molecules which rebound from the interface may do so in a manner varying from specularly to diffusely, depending on the molecular geometry of the interface.

Before examining further the conditions existing at a liquid-gas interface, it is necessary to examine the assumptions used by previous researchers regarding the tangential stresses existing at a solid-gas interface.

At a solid-gas interface, the stress acting on the solid due to the gas is a result of molecules which impact with the surface, and are accelerated towards the velocity of that surface as a result of the impact. Chapman and Cowling [9] and Rohsenow and Choi [1] showed that following Newton's Second Law, the magnitude of this stress is equal to

$$\tau_{xy,s} = J_i \sigma_v^* (v_i - v_f), \tag{11}$$

where they defined the Specular Reflection Coefficient for a solid-gas interface, σ_v^*, as the average proportion of the initial tangential momentum of a molecule which is transferred to the solid during an impact with the interface.

Chapman and Cowling [9] and Rohsenow and Choi [1] both assumed that the stress acting on a gas at a solid-gas interface would be equal in magnitude to the stress acting on the solid at that interface. This assumption was reasonable as no net mass transfer occurs at a solid-gas interface. Employing this assumption, and noting that the mass flux of molecules impacting a solid interface is equal to the mass flux of molecules rebounding from a solid interface, Eq. (11) is equivalent to

$$\tau_{xy,g} = J_i \sigma_v^* (v_i - v_f), \tag{12}$$

where $\tau_{xy,g}$ is the magnitude of the stress acting on a gas at a solid-gas interface.

Equation (12) is interesting in that it can be interpreted as molecules that move away from a solid-gas interface come into equilibrium with their surroundings at a location where the average tangential velocity of the gas is v_i. We will apply this concept, which is a direct result of assuming that no stress discontinuity occurs at a solid-gas interface, to molecules which move away from a liquid-gas interface in our present analysis.

The stress acting on a gas near a liquid-gas interface, $\tau_{xy,v}$, is composed of a component due to molecules evaporating from the liquid, and a component due to molecules rebounding from the interface without condensing, but after having transferred a proportion of their velocity to the liquid. Using the concepts of the previous discussion, the magnitude of this stress can be represented by

$$\tau_{xy,g} = J_e (v_i - v_f) + J_r \sigma_v (v_i - v_f). \tag{13}$$

This stress is directed against the motion of the gas. Note that we have now defined the Specular Reflection Coefficient for a volatile liquid-gas interface, σ_v, as the average proportion of the initial tangential momentum of a molecule which is transferred to the liquid, when the molecule rebounds from the interface. This coefficient is similar to the Specular Reflection Coefficient for non-volatile interfaces in that it represents the manner in which molecules rebound from an interface.

The stress on a liquid at a liquid-gas interface, $\tau_{xy,f}$, is also composed of two components. One component results from molecules which condense into the liquid upon impact, and another from molecules which rebound from the interface without condensing. In a similar fashion to the above, this stress can be represented by

$$\tau_{xy,f} = J_c (v_i - v_f) + J_r \sigma_v (v_i - v_f), \tag{14}$$

where we have again used the Specular Reflection Coefficient for a volatile liquid-gas interface, σ_v.

Equation (14) will not be used further in this analysis, however a comparison against Eq. (10) highlights some peculiarities of a liquid-gas interface within the slip regime. Firstly, if no condensation or evaporation occurs at the interface, then the tangential stress on the liquid is equal to the tangential stress on the gas. This is as expected at a solid-gas interface. Also, if the rates of evaporation and condensation are equal, as in an interface which is in dynamic equilibrium, again the stress applied to the gas phase is equal to the stress applied to the liquid phase. However, if the condensation and evaporation rates are different, then a stress discontinuity occurs at the interface, and the stresses applied to each phase are different. This phenomenon results from forces that are generated by molecules which must be accelerated to the velocity of their surroundings, and highlights one of the interesting differences between volatile and non-volatile interfaces.

In this study we are only concerned with the stress imposed on the gas at the liquid-gas interface. Using equations (2), (10), and (13), noting that the rate of molecules rebounding from the interface is given by

$$J_r = J_i - J_c, \tag{15}$$

and defining the ratio of evaporation and condensation mass fluxes as

$$\phi = \frac{J_e}{J_c}, \tag{16}$$

the shear stress imposed on the gas is given by

$$\tau_{xy,g} = J_i \{\phi\sigma_c + \sigma_v(1-\sigma_c)\}\left(v_o + U\lambda \frac{dv}{dx} - v_f\right). \tag{17}$$

To determine the magnitude of the slip velocity at the interface, we equate the value for the actual shear stress on the gas at the interface, given by Eq. (17), to the shear stress existing at a plane in a Newtonian fluid,

$$\tau_{xy} = \mu \frac{dv}{dx}. \tag{18}$$

This yields

$$\mu \frac{dv}{dx} = J_i \{\phi\sigma_c + \sigma_v(1-\sigma_c)\}\left(v_o + U\lambda \frac{dv}{dx} - v_f\right). \tag{19}$$

The mass flux of molecules impacting the interface is given by Eq. (3) of the previous section. Using Eqs. (4), (5), and (6), and expressing the flux in terms of kinetic theory variables [9], we find

$$J_i = \frac{1}{4}\rho\overline{c} - \frac{J_t}{2} = \frac{\rho\overline{c}}{4 + 2\sigma_c(\phi - 1)}, \tag{20}$$

where $\overline{c}$ is the mean molecular speed of the gas. Also, the coefficient of viscosity can be expressed in terms of kinetic theory variables [9],

$$\mu = \tfrac{1}{2} U \rho \overline{c} \lambda. \tag{21}$$

Substituting Eqs. (20) and (21) into Eq. (19) and rearranging gives the interface slip velocity as

$$v_o - v_f = \lambda U \left[\frac{1 + (1-\sigma_v)(1-\sigma_c)}{\phi\sigma_c + \sigma_v(1-\sigma_c)}\right]\frac{dv}{dx}. \tag{22}$$

As previously discussed, the Chapman-Enskog value of $U \approx 1.0$, can be employed for the majority of gases. Note that if $\sigma_c = 0$, Eq. (22) reduces to the velocity discontinuity existing at a non-volatile solid-gas interface [9].

4 Interface Heat Transfer

In a similar manner to the above momentum analysis, to model the heat transfer occurring at a liquid-gas interface using continuum equations, we assume that there exists an effective temperature discontinuity across the interface. To determine the magnitude of this discontinuity, we perform an energy balance on a thin control volume which surrounds the liquid interface, using both kinetic theory and continuum methods.

Figure 1(*c*) shows temperatures at a liquid-gas interface. In an analogous manner to the velocity slip calculation, we define the temperature of the liquid at the interface as T_f, the average temperature of molecules impacting the liquid as T_i, and the average temperature of all gas molecules at the interface as T_o. The velocity of the gas moving away from the interface is as previously defined, u_g, the velocity of liquid moving towards the interface is u_f, and the net flux of heat into the liquid is denoted by q_f.

The average temperature of molecules impacting the solid is determined using an analogous equation to the impacting tangential velocity Eq. (10). Thus,

$$T_i = T_o + U' \lambda \frac{dT}{dx}, \tag{23}$$

where $U'\lambda$ is the characteristic distance from the interface from which the molecules gained their temperature.

The characteristic temperature distance, $U'\lambda$, is not equal to the characteristic tangential velocity distance, $U\lambda$, as molecules with higher temperatures have greater translational energy than molecules with lower temperatures, and as a result can travel further between collisions. Defining f as the ratio of characteristic distances, we have

$$f=\frac{U'}{U}\approx U', \tag{24}$$

where the Chapman-Enskog value for U has been used. Results from the Chapman-Enskog analysis [9] for the transport of molecular temperature give $f=U'=5/2$ for spherical rigid molecules. Calculating the characteristic temperature distance for polyatomic molecules is more difficult, however, because molecular energy is composed of not only translation, but also internal molecular energy. Eucken's formula [9] gives an approximation for f for polyatomic molecules as

$$f=U'=\frac{9\gamma-5}{4}, \tag{25}$$

where γ is the ratio of specific heats of the gas,

$$\gamma=\frac{c_p}{c_v}. \tag{26}$$

To determine the flux of thermal energy transfer from the gas to the liquid, we define the Thermal Accommodation coefficient for a volatile liquid-gas combination, σ_t, as the average proportion of thermal energy transferred to the liquid by an impacting molecule. This coefficient is similar to the Thermal Accommodation coefficient proposed by Knudsen [4] for non-volatile surfaces, but recognizes transfer of energy from condensation as well as from simple molecular reflection.

The volatile Thermal Accommodation coefficient is composed of a component from molecular condensation, and one from molecular reflection. Thus, if we define σ_r to be the average proportion of thermal energy transferred to the liquid by a molecule which impacts the interface but rebounds, then the Thermal Accommodation coefficient can be expressed as

$$\sigma_t=\sigma_c+(1-\sigma_c)\sigma_r. \tag{27}$$

As $\sigma_r\geqslant 0$, Eq. (27) shows that $\sigma_t\geqslant\sigma_c$.

We now perform a molecular energy balance on a thin control volume which surrounds the liquid-gas interface. This gives

$$\frac{dE}{dt}=0=\sigma_c J_i U_g(T_i)-J_e U_g(T_f)+(1-\sigma_c)\sigma_r J_i(U_g(T_i)-U_g(T_f))-P(u_g-u_f)+u_f\rho_f U_f(T_f)-q_f, \tag{28}$$

where we have assumed that the thickness of the control volume is infinitely small, and as such, there is no energy contained within the volume. In equation (28) ρ_f is the density of the liquid, U_f is the internal energy of the liquid and U_g is the internal energy of the gas.

It is illustrative to outline the origins of the terms in Eq. (28). The first term on the right of this equation represents energy given to the volume from molecules condensing into the interface. These molecules have a characteristic temperature of T_i. The second term on the right represents energy lost from the control volume via molecules which evaporate from the liquid surface. The temperature of these molecules is the temperature of the liquid at the interface, T_f. The third term on the right of this equation represents energy given to the control volume as a result of molecules which impact, but do not condense into the liquid. Such molecules give a proportion of their internal energy to the control volume as a result of each reflection, as specified by the previously defined coefficient, σ_r. The third term from the right of Eq. (28) represents the flow work performed on the surroundings as gas is vaporized at the interface, while the second-last term represents the internal energy of liquid entering the control volume as liquid is vaporized at the interface. The last term represents the rate of energy conduction into the body of the liquid.

An energy balance on the same control volume, using continuum rather than kinetic theory results for the conduction of heat through the gas phase, leads to

$$\frac{dE}{dt}=0=k\frac{dT}{dx}-J_t H_{fg}(T_f)-q_f, \tag{29}$$

where k is the thermal conductivity of the gas, and $H_{fg}(T_f)$ the latent heat of vaporization of the gas evaluated at the temperature of the liquid. The first term on the right of this equation represents energy conducted from the gas into the control volume, the second the energy lost from the control volume as a net flux of molecules is vaporized from the liquid, and the last term, as in Eq. (28), the rate of energy conduction into the body of the liquid. Note that the latent heat of vaporization takes account of the flow work required when vaporizing the liquid. Equating q_f from Eqs. (28) and (29) gives

$$k\frac{dT}{dx}=\sigma_c J_i U_k(T_i)-J_e U_g(T_f)+(1-\sigma_c)\sigma_r J_i(U_g(T_i)-U_g(T_f))+J_1 H_{fg}(T_f)-P(u_g-u_f)+u_f\rho U_f(T_f). \tag{30}$$

In order to simplify Eq. (30), expressions are required to relate the kinetic theory and continuum variables. The normal velocity of the gas at the interface is specified by Eq. (6), while the normal velocity of the liquid is

$$u_f=\frac{J_t}{\rho_t}, \tag{31}$$

where ρ_f is the density of the liquid. For the simple kinetic theory gas under consideration [9], the latent heat of evaporation is given by

$$H_{fg}(T_f)=U_g(T_f)-U_f(T_f)+P\left(\frac{RT_f}{MP}-\frac{1}{\rho_f}\right), \tag{32}$$

and the internal energy of the gas by

$$U_f(T)=c_v T. \tag{33}$$

Substituting equations (6), (31), (32), and (33) into Eq. (30) gives

$$k\frac{dT}{dx}=(\sigma_c+(1-\sigma_c)\sigma_r)J_i c_v(T_i-T_f)+J_t\frac{R}{M}(T_f-T_o). \tag{34}$$

The first bracketed term on the right of this equation is the volatile Thermal Accommodation coefficient, as defined by Eq. (27). Substituting in this coefficient, and using Eq. (23) for the impacting molecule temperature, Eq. (34) becomes,

$$T_o-T_f=\frac{k-\sigma_t J_i c_v U'\lambda}{\sigma_t J_i c_v-RJ_t/M}\frac{dT}{dx}. \tag{35}$$

Recognizing that the specific heats for an ideal gas are related by

$$c_p=c_v+\frac{R}{M}, \tag{36}$$

that the kinetic theory thermal conductivity of a gas is [9]

$$k=\tfrac{1}{2}\rho c_v U'\lambda\overline{c}, \tag{37}$$

and that the mass flux of impacting molecules is given by Eq. (20), the effective temperature discontinuity at the liquid-gas interface becomes

$$T_o - T_f = \lambda U' \left[\frac{2 - \sigma_c(1-\phi) - \sigma_t}{\sigma_t + \sigma_c(1-\phi)(\gamma - 1)} \right] \frac{dT}{dx}. \quad (38)$$

As previously discussed, for most polyatomic molecules the Eucken approximation of $U' = 9\gamma - 5/4$ can be employed. Note that if there is no net mass transfer, then $\phi = 1$, and Eq. (38) yields the same magnitude of temperature discontinuity that exists at a non-volatile solid-gas interface [9].

5 Model Discussion and Applications

Equations (9), (22), and (38) completely specify conditions at a volatile liquid-gas interface. Following the restrictions placed on Eq. (5), these equations are valid when

$$|J_t| < 0.1 \sqrt{\frac{2M}{RT_o}} P. \quad (39)$$

Equations (9) and (38) are coupled through the variables ϕ, T_o, and T_f, so must be solved simultaneously. Equation (22) requires ϕ, so relies on a solution to Eq. (9).

Figure 2 shows the non-dimensional velocity and temperature discontinuities specified by Eqs. (22) and (38), plotted as a function of the evaporation to condensation ratio, ϕ. For this figure we have assumed $\sigma_c = \sigma_v = \sigma_t = 1$ and $\gamma = 5/3$. As shown, the magnitudes of the velocity and temperature discontinuities move in opposite directions as ϕ is varied. The velocity discontinuity decreases with increasing ϕ as an increased movement of molecules from the liquid into the gas causes the tangential stress resisting the movement of the gas to increase. The temperature discontinuity increases with increasing ϕ as a higher ϕ requires a higher heat flux, and consequently a steeper temperature gradient within the gas adjacent to the interface. Thus, the higher the ϕ, the higher the temperature of molecules impacting the liquid-gas interface is, and the higher the temperature discontinuity.

We have used a variation of this model in the analysis of volatile liquid droplet impacts with heated surfaces and shown that non-continuum effects become important under certain conditions [20,21]. There are other areas of heat transfer where these effects are know to be important. One of these is in the collapse of vapor layer films surrounding melt droplets in the triggering stage of vapor explosions [22]. Analysis dating back to the 1980's in three different laboratories around the world showed that in determining whether the vapor film collapsed or not following a triggering event, it was essential that the molecular behavior of the volatile interface was modeled [23–25]. However, when the mathematical treatments used in these studies were examined in detail it was noted that velocity slip was not included in some cases, and that there were differences between the thermal energy treatments used in all of them. This was the primary motivation for the first principles treatment presented here. Another application area for this theory is in the cooling of micro-chips. Although only preliminary studies have been conducted in this field, modeling coolant boiling in the narrow passages contained within these devices will require the examined non-continuum interface effects to be considered.

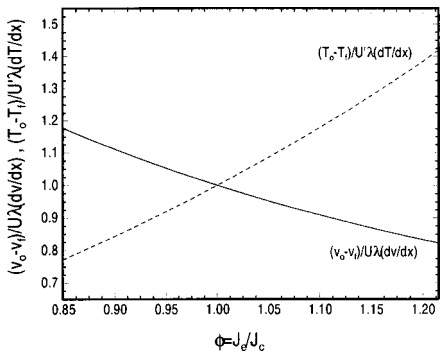

Fig. 2 Non-dimensional velocity and temperature discontinuities at a volatile liquid-gas interface, as a function of the non-dimensional evaporation rate, as given by Eqs. (22) and (38), respectively

Finally, we note that there is considerable debate as to the magnitude of the Accommodation and Specular Reflection coefficients which have been used in this analysis. Rohsenow and Choi [1] list the Specular Reflection coefficients for a number of non-volatile gas and surface combinations. Generally these coefficients are close to unity, so $\sigma_v = 1$ is probably an acceptable assumption for the majority of liquid-gas combinations.

There is some experimental data available on various volatile Accommodation coefficients [6,25–27], but consistent results between studies are yet to be established. Also, the definitions used for these coefficients are not always the same between publications. As previously noted, σ_t should be larger than σ_c, a result of energy transfer between the liquid and gas phases from molecular rebounds as well as from molecular condensation. Until more experimental investigations are conducted however, an assumption of unity for both coefficients serves as a first approximation.

Nomenclature

$\overline{c}$ = mean molecular speed [m/s]
c_v = constant volume specific heat [J/kg.K]
c_p = constant pressure specific heat [J/kg.K]
E = energy [J/m^2]
f = ratio of molecular distance coefficients
H = enthalpy [J/kg]
J = mass flux [kg/m^{2}s]
k = thermal conductivity [W/mK]
Kn = Knudsen number
M = molecular weight [kg/kmol]
P = pressure [Pa]
q = energy flux [J/m^{2}s]
R = Universal Gas Constant [J/kmol.K]
T = temperature [K]
u = velocity normal to the interface [m/s]
U = molecular tangential momentum distance coefficient
U' = molecular thermal energy distance coefficient
U = internal energy [J/kg]
v = velocity tangential to the interface [m/s]
x = coordinate normal to the interface [m]
y = coordinate tangential to the interface [m]
γ = ratio of specific heats
λ = mean free path [m]
μ = dynamic viscosity [kg/ms]
ρ = density [kg/m^3]
σ_c = Accommodation Coefficient
σ_r = Thermal Accommodation Coefficient for rebounding molecules
σ_t = Thermal Accommodation Coefficient
σ_v = Specular Reflection Coefficient
τ_{xy} = tangential stress at interface [N/m^2]
ϕ = ratio of evaporating to condensing fluxes

Subscripts

c = condensing
e = evaporating
f = liquid
g = gas
i = impacting
o = average for gas at interface
r = rebounding
s = solid
sat = saturation
t = net evaporating

References

[1] Rohsenow, W. M., and Choi, H., 1961, *Heat, Mass, and Momentum Transfer*, Prentice-Hall, Inc.
[2] Loeb, L. B., 1934, *The Kinetic Theory of Gases*, Second ed., McGraw-Hill Book Company, New York and London.
[3] Kennard, E. H., 1938, *Kinetic Theory of Gases*, McGraw-Hill Book Company, New York and London.
[4] Knudsen, M., 1950, *Kinetic Theory of Gases*, Third ed., Methuen and Co., London.
[5] Schrage, R. W., 1953, *A Theoretical Study of Interphase Mass Transfer*, Columbia University Press, New York.
[6] Nabavian, K., and Bromley, L. A., 1963, ''Condensation Coefficient of Water,'' Chem. Eng. Sci., **18**, pp. 651–660.
[7] Collier, J. G., 1981, *Convective Boiling and Condensation*, Second ed., McGraw-Hill, Berkshire, England.
[8] Patterson, G. N., 1956, *Molecular Flow of Gases*, John Wiley and Sons.
[9] Chapman, S., and Cowling, T. G., 1970, *The Mathematical Theory of Non-Uniform Gases*, Third ed., Cambridge University Press, Cambridge.
[10] Langmuir, I., 1915, ''The Dissociation of Hydrogen Into Atoms, Part II,'' J. Am. Chem. Soc., **37**, p. 417.
[11] Shankar, P. N., 1970, ''A Kinetic Theory of Steady Condensation,'' J. Fluid Mech., **40** No. 2, pp. 385–400.
[12] Pao, Y.-P., 1971, ''Application of Kinetic Theory to the Problem of Evaporation and Condensation,'' Phys. Fluids, **14**, No. 2, pp. 306–312.
[13] Pao, Y.-P., 1971, ''Temperature and Density Jumps in the Kinetic Theory of Gases and Vapors,'' Phys. Fluids, **14**, No. 7, pp. 1340–1346.
[14] Sone, Y., and Onishi, Y., 1978, ''Kinetic Theory of Evaporation and Condensation—Hydrodynamic Equation and Slip Boundary Condition,'' J. Phys. Soc. Jpn., **44**, No. 6, pp. 1981–1994.
[15] Labuntsov, D. A., and Kryukov, A. P., 1979, ''Analysis of Intensive Evaporation and Condensation,'' Int. J. Heat Mass Transf., **22**, pp. 989–1002.
[16] Bird, G. A., 1994, *Molecular Gas Dynamics and the Direct Simulation of Gas Flows*, Oxford University Press.
[17] Carey, V. P., Oyumi, S. M., and Ahmed, S., 1997, ''Post-Nucleation Growth of Water Microdroplets in Supersaturated Gas Mixtures: A Molecular Simulation Study,'' Int. J. Heat Mass Transf., **40**, No. 10, pp. 2393–2406.
[18] Kang, S.-W., 1967, ''Analysis of Condensation Droplet Growth in Rarefied and Continuum Environments,'' AIAA J., **5**, No. 7, pp. 1288–1295.
[19] Young, J. B., 1991, ''The Condensation and Evaporation of Liquid Droplets in a Pure Vapour at Arbitrary Knudsen Number,'' Int. J. Heat Mass Transf., **34**, No. 7, pp. 1649–1661.
[20] Harvie, D. J. E., and Fletcher, D. F., 2001, ''A Hydrodynamic and Thermodynamic Simulation of Droplet Impacts on Hot Surfaces, Part I: Theoretical Model,'' Int. J. Heat Mass Transf., **44**, No. 14, pp. 2633–2642.
[21] Harvie, D. J. E., and Fletcher, D. F., 2001, ''A Hydrodynamic and Thermodynamic Simulation of Droplet Impacts on Hot Surfaces, Part II: Validation and Applications,'' Int. J. Heat Mass Transf., **44**, No. 14, pp. 2643–2659.
[22] Fletcher, D. F., and Theofanous, T. G., 1997, ''Heat Transfer and Fluid Dynamic Aspects of Explosive Melt-Water Interactions,'' Adv. Heat Transfer, **29**, pp. 129–213.
[23] Inoue, A., Ganguli, A., and Bankoff, S. G., 1981, ''Destabilization of Film Boiling Due to Arrival of a Pressure Shock, Part II: Analytical,'' ASME J. Heat Transfer, **103**, pp. 465–471.
[24] Corradini, M. L., 1983, ''Modeling Film Boiling Destabilization Due to a Pressure Shock Arrival,'' Nucl. Sci. Eng., **84**, pp. 196–205.
[25] Knowles, J. B., 1985, ''A Mathematical Model of Vapour Film Destabilisation,'' Technical Report AEEW-R1933, United Kingdom Atomic Energy Authority, Winfrith, Dorchester, Dorset.
[26] Heideger, W. J., and Boudart, M., 1962, ''Interfacial Resistance to Evaporation,'' Chem. Eng. Sci., **17**, pp. 1–10.
[27] Mills, A. F., and Seban, R. A., 1967, ''The Condensation Coefficient of Water,'' Int. J. Heat Mass Transf., **10**, pp. 1815–1827.

Flow Dynamics and Heat Transfer of Wavy Condensate Film

Akio Miyara
Associate Professor,
Department of Mechanical Engineering,
Saga University,
1 Honjomachi, Saga-shi, 840-8502 Japan
e-mail: miyara@me.saga.-u.ac.jp

Wave evolution and heat transfer behavior of a wavy condensate film down a vertical wall have been investigated by a finite difference method, in which the algorithm is based on the HSMAC method, and a staggered grid fixed on a physical space is employed. For the moving interface, newly proposed methods are used. A random perturbation of the film thickness is generated near the leading edge. The perturbation quickly diminishes once and small-amplitude long waves are propagated downstream. Then the amplitude of the wave increases rapidly at a certain position, and the wave shape changes from a sinusoidal wave to a pulse-like solitary wave which is composed of a large-amplitude wave and capillary waves. A circulation flow occurs in the large wave and it affects the temperature field. The heat transfer is enhanced by space-time film thickness variation and convection effects. [DOI: 10.1115/1.1370522]

Keywords: Condensation, Numerical Methods, Thin Films, Wavy

Introduction

Many experimental studies of film condensation and evaporation show that the heat transfer is enhanced by the waves generated on the film interface. The interfacial waves are observed in the fairly low film Reynolds number region, $10<\mathrm{Re}(=\Gamma/\mu)<350$, where the flow seems to be laminar. It is often designated as a laminar wavy flow, which is addressed in the present study. Condensation heat transfer was measured by Shea and Krase [1], Slegers and Seban [2], Ratiani and Shekriladze [3], Gregorig et al. [4], and Selin [5]. Evaporation heat transfer was measured by Struve [6] and Chun and Seban [7]. From these results it is clear that the heat transfer coefficient of the laminar wave flow is 0–80 percent higher than that of the laminar flow with smooth surface. Local heat transfer correlations for the wavy films has been proposed by Kutateradze [8,9], Chun and Seban [7] and Uehara and Kinoshita [10].

Although many experimental and theoretical studies have been devoted, the enhancement mechanism of the wave has not been clarified sufficiently because of the experimental and theoretical difficulties. Accurate measurements of the velocity and temperature in such a very thin liquid film are very difficult and analytical treatment of governing equations, which have the strong nonlinearity, requires many assumptions. Hirshburg and Florschuetz [11,12] developed a wavy-film model and discussed the hydrodynamic and heat transfer characteristics. However a parabolic velocity profile and a linear temperature profile are assumed like laminar flow, which would be different from the real situation. Stuhlträger et al. [13,14] solves the wave shape, velocity and temperature fields simultaneously, but simplified force and momentum balance equations at vapor-liquid interface are used, a parabolic velocity profile is assumed near the interface, and mass conservation of the liquid film is not satisfied exactly due to simulation algorithm. For more realistic and accurate analysis, the variation of the velocity and temperature fields should be solved with a proper method and fewer assumptions.

The objectives of the present study are to simulate a two-dimensional free convection wavy condensate film on a vertical wall and to clarity the heat transfer enhancement mechanism with a numerical simulation technique. Although most applications involve internal flow, vapor shear can be ignored in its downstream region because vapor velocity decreases rapidly in its entrance region and vapor shear can be neglected. There are also many film condensations in applications, for example condensation outside of vertical tubes in vaporizers and heaters. The waves in the laminar wavy condensate flow have two-dimensional behavior because the film is very thin and the horizontal deformation of the vapor-liquid interface is much smaller than the streamwise deformation. On the other hand, strong three-dimensionality is dominant in the turbulent region, where the present simulation is not applicable. The Navier–Stokes equations and the energy equation are solved under the exact boundary conditions. The only assumption is to neglect the tangential vapor velocity on the vapor liquid interface. It, however, involves great difficulties in solving the flow field, especially in applying the exact interfacial boundary conditions, while the energy equation can be solved with conventional methods. By using a newly proposed technique for the interfacial boundary condition [15,16], the difficulties have been overcome, and the wavy condensate film flow has been simulated. The validity of the calculation method and the good agreement with experimental observations for falling film without phase change have been reported elsewhere [15–17]. The algorithm of the calculation is based on the HSMAC (highly simplified Marker and Cell) method proposed by Hirt and Cook [18]. The energy equation and the condensation rate are solved simultaneously, and detailed information about wave motion, flow dynamics, and condensation heat transfer has been obtained. Waves are generated near the leading edge by providing a random perturbation to the film thickness.

Governing Equations

Figure 1 shows the physical model and the coordinate system. Two-dimensional condensation on a vertical wall is considered. The fluid is assumed Newtonian and the tangential vapor velocity on the vapor-liquid interface, which causes shear stress and tangential momentum change due to condensation, is neglected. Because the gradient of the interface is very small, direction the vapor flow due to condensation can be assumed to be normal to the interface and the tangential vapor velocity is neglected. The wall temperature is uniform and the film surface temperature corresponds to the saturation temperature.

The governing equations are the continuity equation, the Navier–Stokes equations and the energy equation. Dimensionless equations are obtained by using the interface velocity u_0, the film thickness δ_0 and the wall and surface temperatures T'_w and T'_s. u_0 and δ_0 are values for smooth surface laminar film flow at outflow boundary at the simulation region and are calculated from the Nusselt theory.

Contributed by the Heat Transfer Division for publication in the JOURNAL OF HEAT TRANSFER. Manuscript received by the Heat Transfer Division January 11, 2000; revision received August 14, 2000. Associate Editor: T. Avedisian.

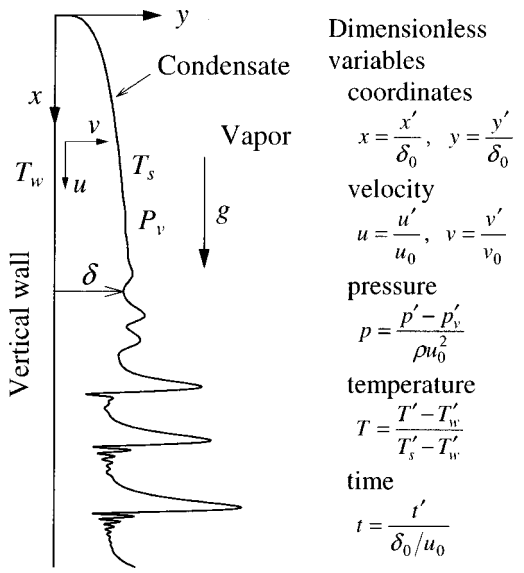

Fig. 1 Physical model and coordinates system (prime ′ means dimensional variables)

$$\frac{\partial u}{\partial x} + \frac{\partial v}{\partial y} = 0 \tag{1}$$

$$\frac{\partial u}{\partial t} + u\frac{\partial u}{\partial x} + v\frac{\partial u}{\partial y} = -\frac{\partial p}{\partial x} + \frac{1}{\mathrm{Re}_0}\left(\frac{\partial^2 u}{\partial x^2} + \frac{\partial^2 u}{\partial y^2}\right) + \frac{1}{\mathrm{Fr}_0} \tag{2}$$

$$\frac{\partial v}{\partial t} + u\frac{\partial v}{\partial x} + v\frac{\partial v}{\partial y} = -\frac{\partial p}{\partial y} + \frac{1}{\mathrm{Re}_0}\left(\frac{\partial^2 v}{\partial x^2} + \frac{\partial^2 v}{\partial y^2}\right) \tag{3}$$

$$\frac{\partial T}{\partial t} + u\frac{\partial T}{\partial x} + v\frac{\partial T}{\partial y} = \frac{1}{\mathrm{Re}_0\mathrm{Pr}}\left(\frac{\partial^2 T}{\partial x^2} + \frac{\partial^2 T}{\partial y^2}\right), \tag{4}$$

where the dimensionless parameters are defined as follows:

$$\mathrm{Re}_0 = \frac{\rho u_0 \delta_0}{\mu}, \tag{5}$$

$$\mathrm{Fr}_0 = \frac{u_0^2}{\delta_0 g}. \tag{6}$$

From the Nusselt's solution there is a relation between u_0 and δ_0 as

$$u_0 = \frac{\rho \delta_0^2 g}{2\mu}. \tag{7}$$

Therefore

$$\mathrm{Fr}_0 = \frac{1}{2}\mathrm{Re}_0 \tag{8}$$

Boundary Conditions and Initial Condition

Wall Surface. The velocity and the temperature on the wall surface are given as follows:

$$u = 0, \quad v = 0, \quad T = 0, \quad \text{at} \quad y = 0 \tag{9}$$

Boundary condition of the pressure is obtained by substituting Eq. (9) into Eq. (3).

$$\frac{\partial p}{\partial y} = \frac{1}{\mathrm{Re}_0}\frac{\partial^2 v}{\partial y^2} \tag{10}$$

Interface. The temporal variation of the dimensionless film thickness $\delta = \delta/\delta_0$ is calculated with the following kinematic boundary condition.

$$\frac{\partial \delta}{\partial t} = v - u\frac{\partial \delta}{\partial x} - m_x, \tag{11}$$

where $-m_x$ is dimensionless condensation rate per unit wall area defined as follows:

$$-m_x = \frac{-m'_x}{\rho u_0}. \tag{12}$$

The condensation rate m_x is obtained from the following equation:

$$-m_x = \frac{H}{\mathrm{Re}_0\mathrm{Pr}}\left(\left.\frac{\partial T}{\partial y}\right|_{y=\delta} - \left.\frac{\partial T}{\partial x}\right|_{y=\delta}\frac{\partial \delta}{\partial x}\right), \tag{13}$$

where H is phase change number.

$$H = \frac{c_p(T'_s - T'_w)}{L}. \tag{14}$$

On the other hand, the following equation is obtained from Eq. (1) and Eq. (11):

$$\frac{\partial}{\partial x}\int_0^\delta u\,dy + \frac{\partial \delta}{\partial t} + m_x = 0. \tag{15}$$

The temporal film thickness variation is corrected with this equation, as explained later.

Including the effects of pressure and surface tension, the force and momentum balance normal to the interface is obtained, and the pressure at the interface is calculated with the following equation.

$$p = \frac{-\partial^2\delta/\partial x^2}{\mathrm{We}_0[1 + (\partial\delta/\partial x)^2]^{3/2}} + \frac{2}{\mathrm{Re}_0[1 + (\partial\delta/\partial x)^2]}\left[\frac{\partial u}{\partial x}\left(\frac{\partial \delta}{\partial x}\right)^2 - \left(\frac{\partial u}{\partial y} + \frac{\partial v}{\partial x}\right)\frac{\partial \delta}{\partial x} + \frac{\partial v}{\partial y}\right] + \frac{m_x^2}{1 + (\partial\delta/\partial x)^2}(R - 1). \tag{16}$$

The third term of the right hand expresses momentum change caused by phase change on the interface, where it is assumed that vapor flows into the interface from the normal direction. We_0 is the Weber number and R is density ratio, defined as

$$\mathrm{We}_0 = \frac{\rho u_0^2 \delta_0}{\sigma}, \tag{17}$$

$$R = \frac{\rho}{\rho_v}. \tag{18}$$

From Eqs. (7) and (17),

$$\mathrm{We}_0 = \mathrm{Re}_0^{5/3}\left(\frac{1}{2}\,\mathrm{Ka}\right)^{1/3}, \tag{19}$$

$$\mathrm{Ka} = \frac{g\mu^4}{\rho\sigma^3}, \tag{20}$$

where Ka is Kapitza number [19]. Because Re_0 and We_0 are dependent on the wall length, the film Reynolds number Re and the Kapitza number Ka will be used in later discussion if it is needed.

By neglecting the shear stress from the vapor phase and tangential momentum change by condensation, the force and momentum balance in the tangential direction is

$$\left(\frac{\partial u}{\partial y} + \frac{\partial v}{\partial x}\right)\left[1 - \left(\frac{\partial \delta}{\partial x}\right)^2\right] - 2\frac{\partial \delta}{\partial x}\left(\frac{\partial u}{\partial x} - \frac{\partial v}{\partial y}\right) = 0. \tag{21}$$

Temperature at the interface is given as follows:

$$T = 1 \quad \text{at} \quad y = \delta. \tag{22}$$

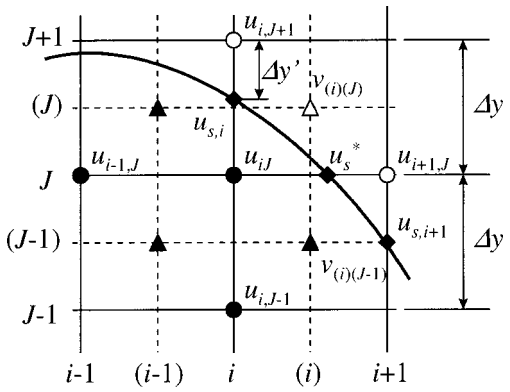

Fig. 2 Staggered grid near interface

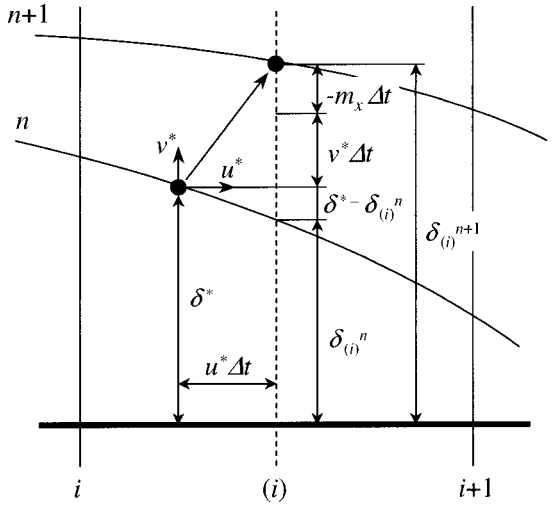

Fig. 3 Temporal variation of film thickness

Inflow Boundary. The film shape and the velocity and temperature distributions in the vicinity of the leading edge are given from the Nusselt theory. At $x=a$, zero-mean fluctuation $F(t)$ for the film thickness is superimposed on the Nusselt film thickness $\delta_{\mathrm{Nu},x=a}$ as a random noise, in similar manner to that of Chang et al. [20].

$$\delta_{x=a}=\delta_{\mathrm{Nu},x=a}+F(t). \tag{23}$$

Fourier transforming $F(t)$ in time and decomposing the Fourier coefficient into modulus and phase components

$$F(t)=\int_0^\infty \hat{F}(\omega)\exp(-i\omega t)d\omega=\int_0^\infty |\hat{F}(\omega)|\exp(i\theta(\omega)-i\omega t)d\omega, \tag{24}$$

where ω is angular frequency and $\theta(\omega)$ is the phase of the complex amplitude $\hat{F}(\omega)$. Equation (24) is approximated with M frequency units of width $\Delta\omega=\omega^*/M$ where ω^* is some high frequency cutoff.

$$F(t)=\sum_{k=1}^{M} |\hat{F}(\omega)|\exp(i\theta(\omega_k)-ik\Delta\omega t)\Delta\omega \tag{25}$$

The phase $\theta_k=\theta(\omega_k)$ is taken from a random number generator from the range $\theta_k\in[0,2\pi]$ and $|\hat{F}(\omega)|$ can be arbitrarily specified. In this paper, $\omega^*=5$, $M=1000$, and $|\hat{F}(\omega)|=0.1$ are employed.

Outflow Boundary. For the x-direcction velocity u, pressure p, and temperature T at the outflow boundary, the following conditions are employed:

$$\frac{\partial u}{\partial x}=0, \quad \frac{\partial p}{\partial x}=0, \quad \frac{\partial T}{\partial x}=0. \tag{26}$$

From the above equations, the continuity equation and the wall boundary condition, the y-direction velocity becomes $v=0$.

Initial Condition. All of the initial conditions for the film thickness, velocity, and temperature distributions are given by the Nusselt solution. As an initial pressure ambient pressure, $p=0$, is given.

Numerical Simulation Method

Wall Surface and Film Inside. Except at the interface region the algorithm of the present calculation is based on the HS-MAC method. Inside the liquid film and at the wall surface, the convection terms and the diffusion terms of the Navier-Stokes equations and the energy equations are discretized by the third-order upward scheme and the second-order central-difference scheme, respectively. Near the film surface, where the third-order upwind scheme cannot be applied, the donor cell method [21,22] is employed

Interface. At the closest grid points to the interface, the donor cell method can the second-order central-difference scheme are also employed. However, values at the grid points outside of the liquid film, which are shown as open symbols in Fig. 2, are unknown, though they are necessary. The value of $u_{i,J+1}$, at outside grid points, can be extrapolated with the following proposed scheme [16] by using the values inside of the film and the interface boundary condition, Eq. (21).

$$\begin{aligned} u_{i,J+1}&=u_{iJ}+\frac{1}{2}\left(\left.\frac{\partial u}{\partial y}\right|_J+\left.\frac{\partial u}{\partial y}\right|_{J+1}\right)\Delta y \\ &=u_{iJ}+\frac{1}{2}\left[\left.\frac{\partial u}{\partial y}\right|_J+\left.\frac{\partial u}{\partial y}\right|_\delta+\frac{\Delta y'}{3\Delta y/2-\Delta y'}\right. \\ &\quad\left.\times\left(\left.\frac{\partial u}{\partial y}\right|_\delta-\left.\frac{\partial u}{\partial y}\right|_{(J-1)}\right)\right]\Delta y, \end{aligned} \tag{27}$$

where $\partial u/\partial y|_\delta$ is calculated from Eq. (21). The x-direction surface velocity $u_{s,i}$ is obtained by interpolating from u_{iJ} and $u_{i,J+1}$. $u_{i+1,J}$ is extrapolated from u_{iJ} and u_s^*, which are calculated from $u_{s,i}$ and $u_{s,i+1}$. Validity of the proposed scheme and comparison with other extrapolation methods and experimental data have been reported elsewhere [16].

$v_{(i),(J)}$ is calculated form the continuity equation.

$$\frac{u_{i+i,J}-u_{i,J}}{\Delta x}+\frac{v_{(i),(J)}-v_{(i),(J-1)}}{\Delta y}=0 \tag{28}$$

The y-direction surface velocity $v_{s,(i)}$ is then interpolated from $v_{(i),(J)}$ and $v_{(i),(J-1)}$.

Film Thickness. The temporal film thickness variation is calculated from Eq. (11). Considering the movement of a particle which reaches a grid point (i) at new time step $n+1$ as shown in Fig. 3, Eq. (11) may be rewritten and a new film thickness at (i) may be calculated with the following equation:

$$\tilde{\delta}_{(i)}^{n+1}=\delta_{(i)}^{n}+v^*\Delta t-(\delta_{(i)}^{n}-\delta^*)-m_x\Delta t. \tag{29}$$

The calculated film thickness, however, does not satisfy mass conservation at the new time step because of the truncation error. By using Eq. (15) derived from the continuity equation, the corrected value can be obtained as follows:

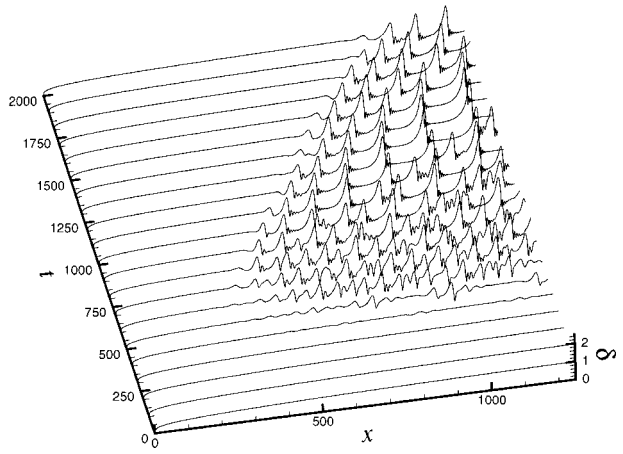

Fig. 4 Space-time evolution of the film thickness without noise near the leading edge ($Re_0=100$, $Ka=2.55\times10^{-11}$, $H=0.2$, $Pr=5$, $R=500$)

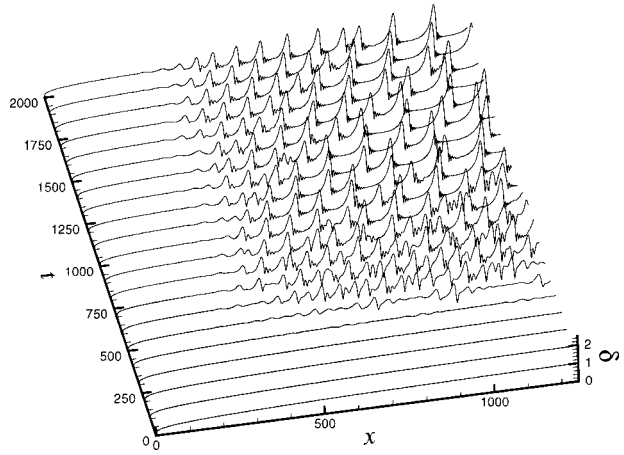

Fig. 5 Space-time evolution of the film thickness with noise near the leading edge ($Re_0=100$, $Ka=2.55\times10^{-11}$, $H=0.2$, $Pr=5$, $R=500$)

$$\Delta\delta=-(\tilde{\delta}_{(i)}^{n+1}-\delta_{(i)}^{n})-\left[\int_0^{\tilde{\delta}} udy\bigg|_{i+1}-\int_0^{\tilde{\delta}} udy\bigg|_{i}\right]\frac{\Delta t}{\Delta x}-m_x\Delta t. \tag{30}$$

Therefore, the new film thickness which satisfies mass conservation is

$$\delta_{(i)}^{n+1}=\tilde{\delta}_{(i)}^{n+1}+\Delta\delta. \tag{31}$$

Mesh Size and Time Step. Simulation results shown later have been obtained for the mesh size of $\Delta x=0.625$ and $\Delta y=0.0833$. Effects of mesh size will be discussed in the following section with simulation for a coarser and finer mesh sizes, ($\Delta x=1.00$, $\Delta y=0.0833$) and ($\Delta x=0.417$, $\Delta y=0.0556$). The time step is $\Delta t=0.02$, which is about one-tenth of a value obtained from stability analysis, in which constant velocities are assumed.

The flow field is considered convergent with the maximum residual of mass conservation in each cell is less than 10^{-4}. Convergence of the temperature field is considered when the maximum difference between the value of computed at the present and previous iterations is less than 10^{-6}. All computations were performed on a workstation, which has a 500 MHz Alpha 21264 processor. The CUP times required for a simulation were about 100–300 hours.

Simulation Results and Discussions

Figure 4 shows the temporal variation of the instantaneous film thickness distribution from the initial condition given by the Nusselt solution at the time intervals of 100. The simulation conditions are $Re_0=100$, $Ka=2.55\times10^{-11}$, $H=0.2$, $Pr=5$, and $R=500$. At $t=400$, waves are generated simultaneously in the wide simulation region of $x=300$–1250. In this case, random noise at the leading edge is not imposed. Therefore these waves are caused by spatial perturbations which are differences between the initial condition and the numerical solution. The spatial perturbations grow rapidly to irregular large amplitude waves interacting with each other. The line of the wave inception is, however, carried downstream.

A simulation result in which the random noise is introduced at $x=3.8$ is shown in Fig. 5. Other conditions are identical to those for Fig. 4. The location of the line of the wave inception fluctuates between $x=250$–300, but does not flow downstream as in Fig. 4. This wave inception is presumably caused by the random noise at the leading edge. At the initial stage of the wave growth at $x=300$–400, the wave shape is sinusoidal. The sinusoidal waves develop rapidly to pulse-like solitary waves composed of a large amplitude wave and small amplitude capillary waves. After the initial rapid growth, most of the solitary waves propagate downstream without interaction and retain similar shape. Most of the area is covered by the solitary waves and the region of the sinusoidal wave is very small as compared with the computational region.

A simulation in which the noise is provided at little more downstream, $x=35$, was also examined and the line of the wave inception fluctuated between $x=250$–300, which was identical to Fig. 5. In the case of experiments, the following situation is presumed. External noises, which are roughness of the wall, vibration of the wall, and turbulence of vapor flow, are given in the entire condensing area, from leading edge to outflow boundary, and induce the interfacial waves. The waves move downstream and grow to large waves. At a certain position, a developed wave flowing from upstream is larger than one growing in downstream region. The developed large wave moves faster than the others. It overtakes and absorbs the smaller waves in its downstream in succession. The remaining after the large wave passes becomes thin and wave generation and development are suppressed. Consequently, waves generated upstream region govern the entire condensing area. This is the reason that the noise is generated at near the leading edge in the present simulation. The absorption phenomena have been experimentally explored by Liu and Gollub [23].

Because the wave amplitude near the wave inception is very small, it is emphasized by subtracting the Nusselt film thickness from the simulation result, as shown in Fig. 6. The solid line is the

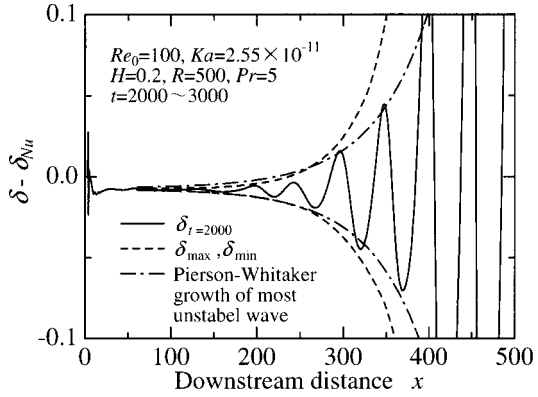

Fig. 6 Wave generation and growth behavior at upstream region

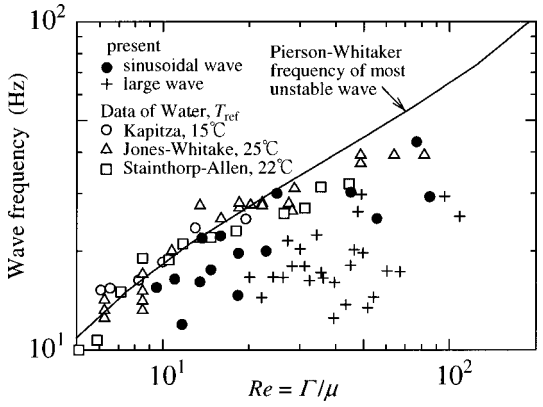

Fig. 7 Wave frequency of present simulation compared with most unstable wave and experimental data

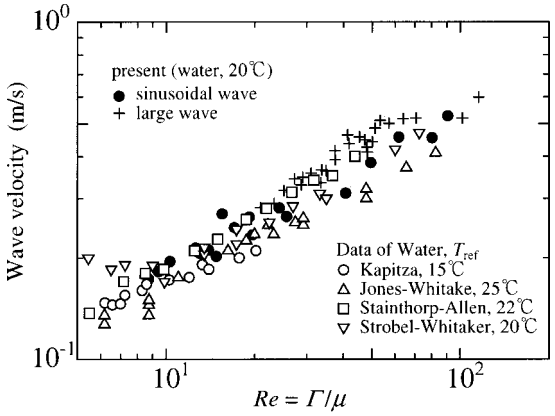

Fig. 8 Wave velocity of present simulation compared with experimental data

instantaneous film thickness distribution at $t=2000$, and dashed lines indicate the maximum and minimum film thickness distribution, δ_{max} and δ_{min}, for $t=2000-3000$. The chained lines show the spatial growth rate of a most unstable wave based on the location of Re=6.67 ($x=61.25$), which are obtained from linear stability theory [24]. The amplitude of the random noise at $x=3.8$ quickly decreases, and a very small amplitude wave is propagated downstream. The wave length of the noise becomes longer than the initial perturbation. A visible wave appears around $x=150$ and the amplitude grows rapidly. Although the wave has the regular sinusoidal shape at $t=2000$, irregular wave shapes are observed at other time steps. In the region of $x=61.25-270$, δ_{max} and δ_{min} are in good agreement with the growth rate obtained from linear stability theory. This fact implies that the initial stage of wave growth may be explained with linear stability, in which phase change is not considered, although condensation exists at the interface and the film Reynolds number increases downstream. Because the film Reynolds number increases downstream due to condensation and the wave growth rate increases with the increase of the film Reynolds number, the variation of δ_{max} and δ_{min} becomes bigger than that of the linear stability theory. According to Pierson and Whitaker [24], the spatial growth rate increases with increase of film Reynolds number in the region of Re<33.

Relations between wave frequency and film Reynolds number are shown in Fig. 7. Solid line indicates the frequency for the most unstable wave obtained from linear stability theory. Open symbols show experimental results [25–27] for water of 15–25°C by other researchers, in which there is no condensation, and the wave frequencies were measured just after the line of wave inception. The present results are shown with ● for sinusoidal waves and + for big waves, where Kapitza number corresponds to water of 20°C. The experimental results agree well to the most unstable wave. This fact indicates that waves generated at the initial stage are the most unstable wave corresponding to the film Reynolds number at the line of wave inception. The sinusoidal waves, as initial waves, of the present simulation agree at least qualitative with the most unstable wave although they are at lower frequency. The source of the disagreement is considered as follows. In the case of the condensate film, the Reynolds number increases along flow direction. The increase is especially remarkable in upstream region. Under this condition, most unstable waves generated at low Reynolds number, which have low frequency, are driven out to high film Reynolds number region. The wave frequency does not change with the increase of the film Reynolds number. Consequently, the observed sinusoidal waves are at lower frequency. The wave frequencies of the big waves are considerably lower than that of the most unstable wave. This reason may also be explained as follows. Waves generated in the upstream low film Reynolds number region propagate downstream to the high film Reynolds number region. The wave frequency at the line of wave inception agrees with the frequency of the most unstable wave corresponding to the low film Reynolds number and it is much lower than that corresponding to the high film Reynolds number in the downstream region. Furthermore, waves with higher frequency than the neutral wave diminish in the upstream region. The neutral wave frequency is lower than the most unstable wave frequency in the high Reynolds number region. Therefore, wave propagated downstream have lower frequency than the most unstable wave corresponding to the high Reynolds number.

Figure 8 shows a relation between wave velocity and the film Reynolds number. Experimental data by other researchers [25–28] are indicated with open symbol and the present simulation results are plotted with ● for sinusoidal waves and + for big waves. The wave velocity of the sinusoidal waves agrees well with the experimental results. The wave velocity of the big waves has somewhat higher velocity. It is assumed that the large wave is rolling down and accelerated by gravity.

Time averaged film thickness behavior is shown in Fig. 9. The maximum, minimum and mean film thickness distributions for $t=2000-3000$, δ_{max}, δ_{min}, and $\bar{\delta}$, and the instantaneous film thickness distribution at $t=2000$ $\delta_{t=2000}$ are shown. The Nusselt's solution δ_{Nu} is also indicated for comparison. After the rapid increase of the amplitude of $x=300-500$, the maximum increases gradually at downstream location. The minimum remains roughly constant from $x=450$ due to wall effects. The time averaged film thickness is slightly thinner than the Nusselt's solution. As shown in Fig. 9, not all the waves reach the maximum or minimum and the amplitude of the interacting waves at $x=850-950$ is smaller than other waves.

Effects of mesh size on wave behavior are examined with finer mesh and coarser mesh. Figure 10 shows instantaneous film thickness distributions at $t=3000$ for ($\Delta x=0.417$, $\Delta y=0.0556$),

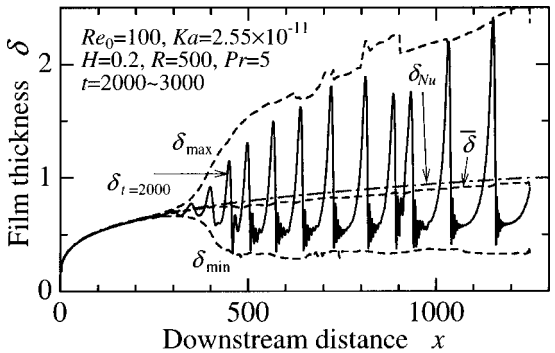

Fig. 9 Time averaged film thickness behavior

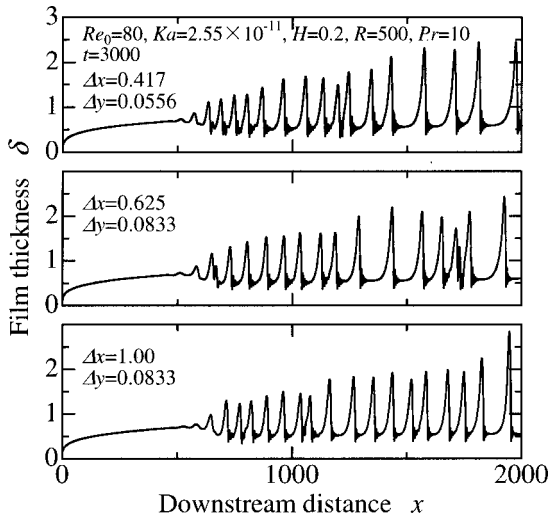

Fig. 10 Effect of mesh size on film thickness distribution

($\Delta t=0.625$, $\Delta y=0.0833$), and ($\Delta x=1.00$, $\Delta y=0.0833$). Simulation conditions are $Re_0=80$, $Ka=2.55\times10^{-11}$, $H=0.2$, $R=500$, $Pr=10$. Because the random noise is provided at different position due to different mesh size, inflow boundary conditions for each simulation change slightly. Therefore the instantaneous film thickness distributions do not agree precisely. However the wave characteristics such as wave shape, distance, and height almost agree. The maximum, minimum and mean film thickness distributions of the different mesh sizes are shown in Fig. 11. In the laminar region, $x=0$–500, where invisible waves travel, calculated film thickness agree well with the Nusselt's solution, in which the present simulation is about 0.8 percent thinner. In the wavy region, $x=500$–2000, the minimum and mean film thickness of each simulation agree well within about ±5 percent error. On the other hand, the maximum film thickness of the coarse mesh ($\Delta x=1.00$, $\Delta y=0.0833$) is about 20 percent lower than others in $x=500$–1400, and about 27 percent higher in $x>1450$. However, the differences between the results of present mesh ($\Delta x=0.625$, $\Delta y=0.833$) and finer mesh ($\Delta x=0.417$, $\Delta y=0.0556$) are very small, within ±6 percent. Therefore, grid independence of the present simulations is acceptable.

In the previous paper [17], simulation results of falling wavy liquid film on vertical and inclined wall are compared with experimental results, in which a periodic perturbation is provided at inflow boundary. Calculated wave height and velocity are agree with experimental results within ±5 percent and −5–+8 percent errors, respectively. Because wave frequency is in proportion to wave velocity, numerical uncertainty of the frequency can be estimated −5–+8 percent.

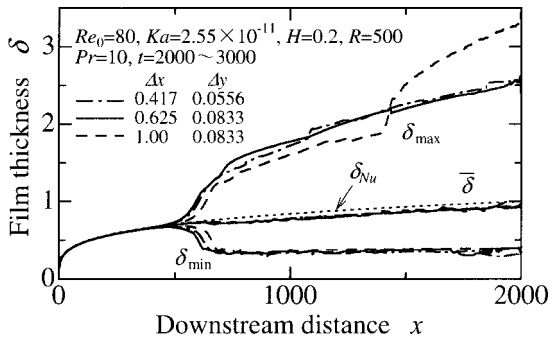

Fig. 11 Effect of mesh size on time averaged film thickness behavior

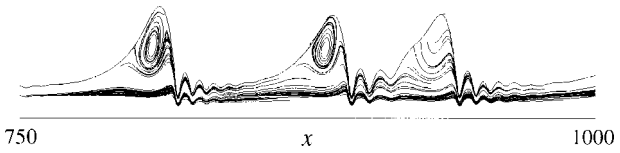

Fig. 12 Stream line

Figure 12 shows an instantaneous streamline of the waves in the region of $x=750$–1000 at $t=2000$, shown in Fig. 9. In the figure, a solitary wave without interaction and interacting waves are described. The streamline is obtained for moving coordinates with the solitary wave velocity $u_w=1.22$. In the large amplitude wave, a large recirculating flow is observed. On the other hand, the recirculating flow disappears in the downstream side wave of the interacting waves. In the capillary waves, no circulation flow is observed.

In order to investigate the heat transfer enhancement mechanism, an instantaneous temperature contour line in the condensate film, which is identical to that shown in Fig. 12, is illustrated in Fig. 13. Strong deformation of the contour lines is observed n the large amplitude wave. The deformations are obviously caused by the recirculating flow shown in Fig. 12, and it is clear that the heat transfer is enhanced by this phenomenon. The contour lines are also dense in the wave troughs. This implies that the heat transfer is enhanced by local thinning of the condensate film.

Instantaneous heat transfer coefficients at the wall and the vapor-liquid interface α_w and α_s are defined in following equations and they are calculated from instantaneous temperature gradients at the wall and the interface.

$$\alpha_w=\frac{\alpha_w'\delta_0}{\lambda}=\left.\frac{\partial T}{\partial y}\right|_{y=0} \tag{32}$$

$$\alpha_s=\frac{\alpha_s'\delta_0}{\lambda}=\left.\frac{\partial T}{\partial y}\right|_{y=\delta} \tag{33}$$

Where λ is thermal conductivity. The variations of α_w and α_s in the streamwise direction are shown in Fig. 14. The heat transfer coefficient obtained from the Nusselt theory α_{Nu} is also indicated. On the wall surface, α_w is higher than α_{Nu} in the entire wave region. On the other hand, although α_s is very high at wave

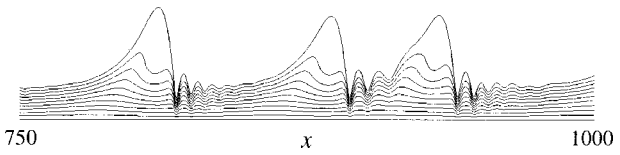

Fig. 13 Temperature contour line

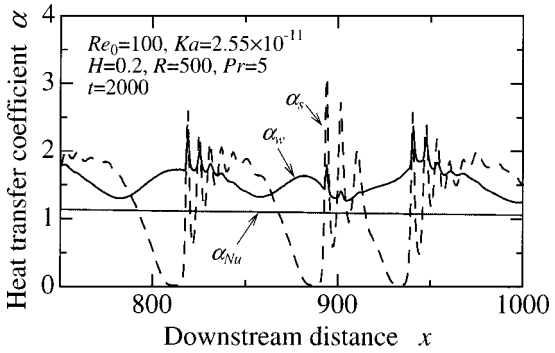

Fig. 14 Instantaneous heat transfer coefficient at the wall and the interface

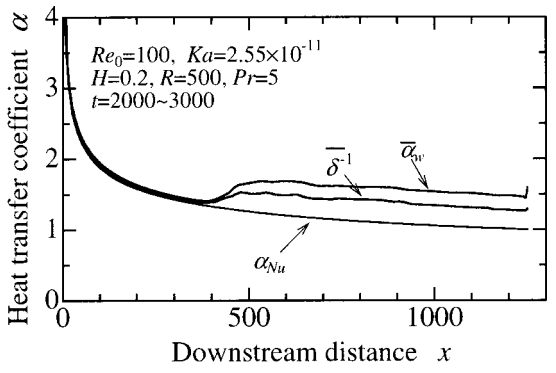

Fig. 15 Time averaged heat transfer coefficient

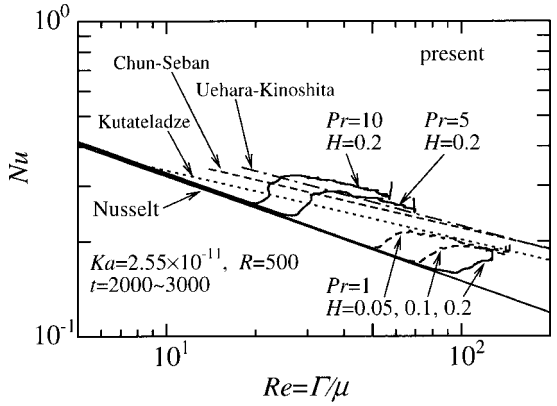

Fig. 16 Comparison of the present simulation results with the previous correlation

troughs and thin film regions between large waves, it is very low at wave crest regions. The higher value of α_s at the tail of the large wave is due to a discharge of cold liquid generated by the recirculating flow.

The ordinary condensation heat transfer coefficient is defined the time averaged heat flux at the wall, not the film surface. According to this, the time averaged dimensionless heat transfer coefficient is calculated from the time averaged temperature gradient at the wall, as follows:

$$\overline{\alpha}_w = \frac{\overline{\alpha_w'}\delta_0}{\lambda} = \left.\frac{\partial \overline{T}}{\partial y}\right|_{y=0}. \tag{34}$$

Figure 15 shows the variation of the time averaged heat transfer coefficient in the streamwise direction. For comparison, α_{Nu} and the time averaged reciprocal of the film thickness $\overline{\delta^{-1}}$, which represents the heat transfer coefficient for the case of the linear temperature distribution. $\overline{\delta^{-1}}$ also indicates the heat transfer enhancement rate caused by the local film thinning. $\overline{\alpha}_w$ includes both the effects of local film thinning and convection. As shown in the figure, $\overline{\alpha}_w$ is agree well with α_{Nu} in the region of $x<400$ where the interface is relatively smooth, and it is higher in the wavy region. Total heat transfer enhancement rate is about 45 percent. The film thinning effect is about 28 percent and the convection effect about 17 percent. An abrupt increase of $\overline{\alpha}_w$ at the outflow boundary is caused by the outflow boundary condition and this effect is limited to the vicinity of the outflow boundary.

For the wavy region, prediction equations for the local heat transfer coefficient have been proposed by Kutateladze [8,9], Chun and Seban [7], and Uehara and Kinoshita [10]. All the equations are expressed in terms of the local Nusselt number Nu as a function of the film Reynolds number Re, as follows:

$$\text{Kutateladze:} \quad \mathrm{Nu}=0.557\mathrm{Re}^{-0.22} \tag{35}$$

$$\text{Chun-Seban:} \quad \mathrm{Nu}=0.606\mathrm{Re}^{-0.22} \tag{36}$$

$$\text{Uehara-Kinoshita:} \quad \mathrm{Nu}=0.707\mathrm{Re}^{-0.25} \tag{37}$$

Where Nu and Re are defined as follows:

$$\mathrm{Nu}=\frac{\overline{\alpha_w'}}{\lambda}\left(\frac{v^2}{g}\right)^{1/3}, \tag{38}$$

$$\mathrm{Re}=\frac{\Gamma}{\mu}. \tag{39}$$

Nu of the simulation results is obtained from time averaged temperature gradient at the wall.

$$\mathrm{Nu}=(2\mathrm{Re}_0)^{-1/3}\left.\frac{\partial \overline{T}}{\partial y}\right|_{y=0}. \tag{40}$$

Figure 16 shows the comparison of the present simulation results with the previously proposed correlations and the Nusselt's solution. The simulation results are shown for the same Kapitza number, $\mathrm{Ka}=2.55\times10^{-11}$, and different Prandtl number liquids, Pr=1, 5, and 10. For Pr=1, the phase change number is varied as $H=0.05$, 0.1, and 0.2, while $H=0.2$ for Pr=5 and Pr=10. In all cases, the heat transfer is enhanced by the waves and Nu of the present simulation becomes higher than that of the Nusselt's solution. Because of limitations of the calculation scheme, the developed wavy region of Pr=1 and $H=0.2$ could not be obtained. In the high Reynolds number region, hang over of the wave occurs. This situation cannot be simulated by the present scheme. In the case of the constant phase change number, $H=0.2$, the point of departure from the Nusselt solution depends on the Prandtl number. Lower Prandlt number departs at higher Reynolds number. When the phase change number is changed for a constant Prandtl number, Pr=1, the departure point occurs at lower film Reynolds number for lower phase change number. In the fully developed wavy region, the heat transfer enhancement is higher for higher Prandtl number. The enhancement rate is about 30 percent for Pr=1, 45 percent for Pr=5, and 50 percent for Pr=10. Chun-Seban and Uehara-Konoshita equations are very close and the simulation result for Pr=5 agrees well with these equations. Because the Chun-Seban and Uehara-Kinoshita equations were derived from experimental data in the range of Pr=1.8–5.7 and Pr=4–8 respectively, the agreement is reasonable and supports the validity of the present simulation result. It is also in support of experimental observations that in the laminar wavy region waves are essentially two dimensional. In the turbulent region, however, waves deform three dimensionally and the present simulation is inapplicable. On the other hand, Kutateladze's equation agrees

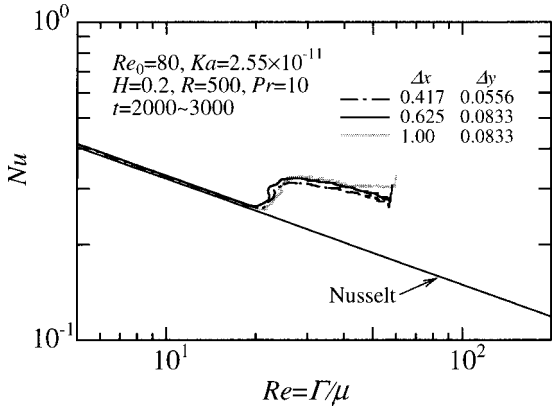

Fig. 17 Effect of mesh size on Nusselt number

with the present result of Pr=1. Since detail information about experimental data used for Eq. (35) is not given, the effect of Prandtl number could not be explained experimentally.

Figure 17 shows effects of mesh size on Nu. Because the mesh dependence is greater for larger Pr, the largest Pr in the present simulation, Pr=10, is examined. In the laminar region, Re<20, all the simulations results agree well with the Nusselt's solution, where those are about 1 percent higher. In the wavy region, there are small discrepancies. The result of present mesh size, ($\Delta x = 0.625$, $\Delta y = 0.0833$), is about 3 percent higher than that of the finer mesh, ($\Delta x = 0.417$, $\Delta y = 0.0556$). The result of coarse mesh, ($\Delta x = 1.00$, $\Delta y = 0.0833$), is closer to present result in Re=25–40 and becomes about 7 percent higher in Re>40. Although the mesh dependence is slightly appears, the error is acceptable.

Conclusions

Numerical simulations for the flow dynamics and the heat transfer of a wavy condensate film on a vertical wall have been conducted with newly proposed methods. The following conclusions are obtained.

1 Random noise introduced near the leading edge quickly diminishes, and small amplitude long wave propagates downstream. The wave amplitude increases rapidly at a certain position and grows to a pulse-like solitary wave.

2 Wave generation and the initial stage of wave growth can be explained well by the linear stability theory although increase of the film Reynolds number due to condensation should be considered in the downstream region.

3 In the big wave of the solitary wave, a large recirculating flow occurs while there is no recirculation in the capillary wave. The temperature contour lines are distorted by the recirculation. Local film thinning by the wave also produces a dense temperature contour lines.

4 The heat transfer is enhanced by two effects: the local film thinning and the convection in the film. The higher enhancement rate is obtained for higher Prandtl number.

5 In the present simulation condition, the location of wave inception depends on the Prandtl number and the phase change number. The wave inception occurs at lower film Reynolds number for higher Prandtl number, and for lower phase change number.

Acknowledgments

The author would like to acknowledge the financial support of TEPCO Research Foundation.

Nomenclature

- Fr = Froude number, $u_0^2/(\delta_0 g)$
- g = gravitational acceleration, 9.807 m/s^2
- H = phase change number, $c_p(T_s' - T_w')/L$
- Ka = Kapitza number, $g\mu^4/(\rho\sigma^3)$
- L = latent heat, kJ/kg
- $-m_x$ = dimensionless condensation rate per unit wall area, $-m_x'/(\rho u_0)$
- Nu = Nusselt number, $\overline{\alpha_w'}(v^2/g)^{1/3}/\lambda$
- p = dimensionless pressure, $(p' - p_v')/(\rho u_0^2)$
- Pr = Prandtl number, $c_p\mu/\lambda$
- R = vapor-liquid density ratio, ρ_l/ρ_v
- Re = film Reynolds number, Γ/μ
- Re$_0$ = Reynolds number, $\rho u_0^2 \delta_0/\mu$
- t = dimensionless time, $t' u_0/\delta_0$
- T = dimensionless temperature, $(T' - T_w')/(T_s' - T_w')$
- u = dimensionless streamwise velocity, u'/u_0
- u_0 = interface velocity at outflow boundary, m/s
- v = dimensinless transverse velocity, v'/u_0
- We = Weber number, $\rho u_0^2 \delta_0/\sigma$
- x = dimeionless streamwise coordinate, x'/δ_0
- y = dimensionless transverse coordinate, v'/δ_0
- α = dimensionless heat transfer coefficient, $\alpha' \delta_0/\lambda$
- Γ = mass flow rate per unit film width, kg/(m s)
- δ = dimensionless film thickness, δ'/δ_0
- δ_0 = film thickness at outflow boundary, m
- λ = thermal conductivity, kW/(m K)
- μ = dynamic viscosity, kg/(m s)
- ρ = density, kg/m^3
- σ = surface tension, N/m

Subscripts

- 0 = Nusselt solution at the outflow boundary
- l = liquid
- s = film surface
- v = vapor
- w = wall

Superscripts

- $-$ = time averaged value
- $'$ = dimensional value

Appendix

A. Condensation Rate, Eq. (13). Heat flux normal to the vapor-liquid interface which is inclined to wall by angle θ is

$$q_n' = -\lambda \frac{\partial T'}{n'} = -\lambda \left(-\sin\theta \frac{\partial T'}{\partial x'} + \cos\theta \frac{\partial T'}{\partial y'} \right) \tag{A1}$$

and condensation rate per unit area of the interfacial is

$$-m_n' = \frac{-q_n'}{L}. \tag{A2}$$

On the other hand, condensation rate per unit area of the wall is

$$-m_x' = \frac{-m_n'}{\cos\theta} = -m_n'(1+\tan^2\theta)^{0.5} = -m_n' \left[1 + \left(\frac{\partial \delta'}{\partial x'} \right)^2 \right]^{0.5}. \tag{A3}$$

Therefore, $-m_x'$ becomes

$$-m_x' = \frac{-m_n'}{\cos\theta} = \frac{\lambda}{L} \left(-\frac{\sin\theta}{\cos\theta} \frac{\partial T'}{\partial x'} + \frac{\partial T'}{\partial y'} \right)$$

$$= \frac{\lambda}{L} \left(-\frac{\partial \delta'}{\partial x'} \frac{\partial T'}{\partial x'} + \frac{\partial T'}{\partial y'} \right). \tag{A4}$$

It is rewritten in dimensionless form, which is Eq. (13), as follows:

$$-m_x = \frac{H}{\mathrm{Re}_0 \mathrm{Pr}} \left(\left. \frac{\partial T}{\partial y} \right|_{y=\delta} - \left. \frac{\partial T}{\partial x} \right|_{y=\delta} \frac{\partial \delta}{\partial x} \right). \tag{13}$$

B. Temporal Variation of Film Thickness, Eq. (15). Integrating the continuity Eq. (1) between the limit $y=0$ to $y=\delta$ gives

$$\int_0^\delta \frac{\partial u}{\partial x} dy + v_{y=\delta} = 0. \tag{A5}$$

From the differential and integral calculus,

$$\frac{\partial}{\partial x} \int_0^\delta u dy = u_{y=\delta} \frac{\partial \delta}{\partial x} + \int_0^\delta \frac{\partial u}{\partial x} dy. \tag{A6}$$

Using Eq. (A6) in Eq. (A5) and substituting in Eq. (11) give

$$\frac{\partial}{\partial x} \int_0^\delta u dy + \frac{\partial \delta}{\partial t} + m_x = 0. \tag{15}$$

C. Momentum Transport Due to Condensation, Eq. (16). An equation for the force and momentum balance normal to the vapor-liquid interface, in which phase change is not occur, is introduced in books [29–30]. Additional term for the condensation is the third term in the right hand of Eq. (16).

The normal momentum transport due to condensation is

$$-m_n'(v_{l,n}'-v_{v,n}'), \tag{A7}$$

where $v_{l,n}'$ and $v_{v,n}'$ are liquid and vapor normal velocities at vapor-liquid interface with respect to a stationary observer. Considering the moving interface with a velocity $V_{i,n}'$ and the condensation rate, $v_{l,n}'$ and $v_{v,n}'$ are expressed as follows:

$$v_{l,n}'=V_{i,n}'-\frac{-m_n'}{\rho_l} \tag{A8}$$

$$v_{v,n}'=V_{i,n}'-\frac{-m_n'}{\rho_v}. \tag{A9}$$

Substituting Eqs. (*A*8) and (*A*9) in Eq. (*A*7) gives

$$\frac{m_n'^2}{\rho_l}\left(\frac{\rho_l}{\rho_v}-1\right). \tag{A10}$$

Using Eq. (*A*3) and dividing by $\rho_l u_0^2$ for dimensionless form give

$$\frac{m_x^2}{1+(\partial\delta/\partial x)^2}(R-1), \tag{A11}$$

which is third term in the right hand of Eq. (16).

References

[1] Shea, F. L., and Krase, N. W., 1940, ''Drop-Wise and Film Condensation of Steam,'' Transactions of the American Institute Chemical Engineering, **36**, pp. 463–487.

[2] Slegers, L., and Seban, R. A., 1969, ''Nusselt Condensation of *n*-Butyl Alcohol'' Int. J. Heat Mass Transf., **12**, pp. 237–239.

[3] Ratiani, G. V., and Shekriladze, I. G., 1964, ''An Experimental Study of the Heat Exchange Process on Transition from Laminar to Turbulent Flow of the Film,'' Thermal Engineering **11**, pp. 101–103.

[4] Gregorig, R., Kern, J., and Turek, K., 1974, ''Improved Correlation of Film Condensation Data Based on a More Rigorous Application of Similarity Parameters,'' Waerme- Stoffuebertrag., **7**, pp. 1–13.

[5] Selin, G., 1961, ''Heat Transfer by Condensing Pure Vapors Outside Inclined Tubes,'' International Development in Heat Transfer, Proceedings of the Heat Transfer Conference (Part II), University of Colorado, Boulder, CO, pp. 279–289.

[6] Struve, H., 1967, ''Der Wärmeübertragang an einen verdamphenden Rieselfilm,'' DVI-Forschungsheft 534, pp. 1–36.

[7] Chun, K. R., and Seban, R. A., 1971, ''Heat Transfer to Evaporating Liquid Films,'' ASME Journal of Heat Transfer , **93**, pp. 391–396.

[8] Kutateladze, S. S., 1963, *Fundamentals of Heat Transfer*, Academic, New York.

[9] HEDH, 1983, Hemisphere Publishing Corporation, **2**.

[10] Uehara, H., and Kinoshita, E., 1994, ''Wave and Turbulent Film Condensation on a Vertical Surface (Correlation for Local Heat Transfer Coefficient),'' Trans. Jpn. Soc. Mech. Eng., **60**, pp. 3109–3116, (in Japanese).

[11] Hirshburg, R. I., and Florschuetz, L. W., 1982, ''Laminar Wavy-Film Flow: Part I—Hydrodyinamic Analysis,'' ASME Journal of Heat Transfer , **104**, pp. 452–458.

[12] Hirshburg, R. I., and Florscheutz, L. W., 1982, ''Laminar Wavy-Film Flow: Part II—Condensation and Evaporation,'' ASME Journal of Heat Tranfer **104**, pp. 459–464.

[13] StuhltrIäger, E., Naridomi, Y., Miyara, A., and Uehara, H., 1993, ''Flow Dynamics and Heat Transfer of a Condensate Film on a Vertical Wall: I—Numerical Analysis and Flow Dynamics,'' Int. J. Heat Mass Transf., **36**, No. 6, pp. 1677–1686.

[14] StuhltrIäger, E., Miyara, A., and Uehara, H., 1995, ''Flow Dynamics and Heat Transfer of a Condensate Film on a Vertical Wall: II—Flow Dynamics and Heat Transfer,'' Int. J. Heat Mass Transf. **38**, No. 15, pp. 2715–2722.

[15] Miyara, A., 1997, ''Numerical Simulation of Interfacial Waves on a Falling Liquid Film,'' *Proceedings of the 10th International Symposium on Transport Phenomena in Thermal Science and Process Engineering*, Kyoto, **3**, pp. 863–868.

[16] Miyara, A., 2000, ''A Numerical Scheme for the Simulation of Interfacial Waves on a Falling Liquid Film,'' International Journal of Transport Phenomena, **2**, pp. 241–252.

[17] Miyara, A., 2000, ''Numerical Simulation of Wavy Liquid Film Flowing Down on a Vertical and Inclined Wall,'' International Journal of Thermal Sciences, **39**, pp. 1015–1027.

[18] Hirt, C. W., and Cook, J. L., 1972, ''Calculating Three-Dimensional Flows around Structures and Over Rough Terrain,'' J. Comput. Phys., **10**, pp. 324–320.

[19] Yih, S. M., 1986, *Handbook of Heat and Mass Transfer*, **2**, N. P. Cheremisinoff, editor, Gulf Publishing Company, Houston.

[20] Chang, H. C., Demekhin, E. A., and Kalaidin, E., 1996, ''Simulation of Noise-Driven Wave Dynamics on a Falling Film,'' AIChE J. **42**, pp. 1553–1568.

[21] Gentry, R. A., Martin, R. E., and Daly, B. J., 1966, ''An Eulerian Differencing Method for Unsteady Compressible Flow Problems,'' J. Comput. Phys., **1**, pp. 87–188.

[22] Roache, P. J., 1972, *Computational Fluid Dynamics*, Hermosa Publishers, Albuquerque.

[23] Liu, J., and Gollub, J. P., 1994, ''Solitary Wave Dynamics of Film Flows,'' Phys. Fluids, **6**, No. 5, pp. 1702–1712.

[24] Pierson, F. W., and Whitaker, S., 1977, ''Some Theoretical and Experimental Observation of the Wave Structure of Falling Liquid Films,'' Industrial and Engineering Chemistry, Fundamentals, **16**, pp. 401–408.

[25] Alekseenko, S. V., Nakoryakov, V. E., and Pokusaev, B. G., 1994, *Wave Flow of Liquid Films*,, Begell House, New York.

[26] Carey, V. P., 1992, *Liquid-Vapor Phase-Change Phenomena*, Taylor & Francis, Bristol.

[27] Jones, L. O., and Whitaker, S., 1966, ''An Experimental Study of Falling Liquid Films,'' AIChE J., **12**, pp. 525–529.

[28] Kapitza, P. L., and Kapitza, S. P., 1965, *Wavy Flow of Thin Layers of Viscous Fluid*, Collected Papers of P. L. Kapitza, **2**, Pergamon, New York, pp. 662–709.

[29] Stainthorp, F. P., and Allen, J. M., 1965, ''The Development of Ripples on the Surface of a Liquid Film Flowing Inside a Vertical Tuve,'' Trans. Inst. Chem. Eng. **43**, pp. T85–T91.

[30] Strobel, W. J., and Whitaker, S., 1969, ''The Effect of Surfactants of the Flow Characteristics of Falling Liquid Films,'' AIChE J., **15**, pp. 527–532.

Capillary Blocking in Forced Convective Condensation in Horizontal Miniature Channels

Yuwen Zhang
Mem. ASME

A. Faghri
Fellow ASME

M. B. Shafii

Department of Mechanical Engineering,
University of Connecticut,
Storrs, CT 06269

Forced convective condensation in miniature channels is investigated numerically. Capillary blocking that occurs due to condensation in a horizontal miniature tube and between parallel plates is simulated by using the Volume of Fluid (VOF) method. The effects of vapor inlet velocity, saturation temperature, surface tension, and diameter on effective condensation length, film thickness, and heat transfer coefficient are investigated. The film thickness and the condensation length decrease as the hydraulic diameter or the distance between parallel plates decreases. When the total mass flow rate drops, the condensation length decreases significantly. [DOI: 10.1115/1.1351808]

Keywords: Condensation, Cooling, Forced Convection, Heat Transfer

1 Introduction

It is very important to develop new cooling strategies for electronic devices since they are becoming more compact and rejection heat flux is increasing. Demand exists for more compact heat transfer devices that are capable of removing large amounts of heat over a small temperature drop. Miniature and micro heat pipes have been and are being used in electronic cooling [1,2]. In these applications, the heat generated in the chip is transported away and rejected from the system through condensation. In order to optimize the electronic cooling system performance, it is necessary to gain a fundamental understanding of condensation in miniature tubes [3].

Flow regimes for two-phase flow in both horizontal and vertical tubes have been studied intensively in the past. However, most flow regime studies on two-phase flow were performed in large diameter tubes (>10 mm i.d.). The distinctive feature of two-phase flow in miniature tubes is that the surface tension may play a significant role in flow pattern transitions. Therefore, the flow regime maps established for conventional sized tubes [4,5] may not apply to two-phase flow in miniature tubes due to the role surface tension has on hydrodynamics. Up to now, the data regarding basic flow patterns for two-phase flow with or without heat transfer in miniature circular tubes is still very limited. Barnea et al. [6] presented flow pattern transitions for gas-liquid flow in small diameter tubes (4 to 12 mm). It was concluded that the effect of surface tension is important for stratified-slug transition in horizontal flow. It should be noted that these works dealt only with the transition of flow patterns without the effect of heat transfer and phase change.

Condensation in conventional sized circular tubes has been widely studied. A generally accepted description of forced convection two-phase flow patterns in conventional size horizontal tubes is presented by Collier and Thome [7]. Depending on orientation of the tube and the mass flow rate, both the shear stress on the liquid-vapor interface and gravitional force can play important roles on removal of condensate from the tube. Begg et al. [3] reviewed the existing works regarding flow patterns related to condensation and suggested that capillary blocking can occur in miniature tubes. Due to capillary force, capillary blocking occurs when the liquid blocks the tube cross section at some distance from the condenser entrance. Both flow visualization and an analytical solution of condensation in miniature tubes were presented. The analytical solution focused on the annular film condensation only. Therefore, the model could not predict the shape of the meniscus created complete condensation.

Numerical simulation for two-phase devices, such as heat pipes, has advanced significantly during the past decade [1,8]. In a conventional heat pipe, evaporation and condensation take place at the interface between the vapor core and the wick. In this case the location of the liquid-vapor interface is known *a priori* and the boundary condition at the interface can be easily specified. For condensation in a miniature tube, both the location of the liquid-vapor interface at the film condensation section and the length of the condensation is unknown *a priori* since they are parts of the solution. The numerical method applied in heat pipe simulation is not applicable to predict the capillary blocking in miniature tubes. The Volume of Fluid method (VOF, [9,10]) appeared to be a good candidate because it can be used to determine the location of the interface. The VOF method has been used to simulate a wide range of problems including vaporization in laser drilling processes [11,12], solidification in continuous casting [13], and bubble growth in boiling [14,15].

The objective of the present effort is to simulate two-dimensional forced convective condensation in horizontal miniature channels using the VOF method. The interphase mass transfer due to condensation will be considered as a source term in the energy equation. The effects of vapor inlet velocity, wall temperature, saturation temperature, surface tension, and hydraulic diameter on condensation in both miniature tubes and between parallel plates will also be investigated.

2 Physical Model

The physical model and geometric configuration of the condensation problem in a miniature channel is shown in Fig. 1. The miniature channel can be either a miniature circular tube with a radius of R or it can be two parallel plates $2R$ apart. The saturated vapor enters the channel with a length of L. Condensation takes place on the wall of the channel since the wall temperature, T_w, is below the saturation temperature of the working fluid, T_{sat}. The condensate fluid flows toward the positive x-direction due to the effects of shear force and surface tension. The problem of interest is condensation in the inner surface of the miniature channel with cocurrent vapor flow. It should be noted that the average vapor velocity is not constant along the x-direction since condensation occurring on the wall reduces the amount of vapor flow in the core of the tube. The following assumptions are needed in order to solve the condensation problem:

Contributed by the Heat Transfer Division for publication in the JOURNAL OF HEAT TRANSFER. Manuscript received by the Heat Transfer Division December 15, 1999; revision received November 13, 2000. Associate Editor: D. Poulikakos.

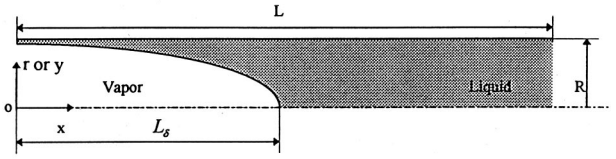

Fig. 1 Physical model of condensation in a miniature channel

1 Flow both in vapor and liquid phase is laminar and incompressible, and, therefore, the density for each phase is constant.

2 The working fluid along the liquid-vapor interface is saturated.

3 The vapor is saturated and therefore there is no temperature gradient in vapor.

4 Since the channel is horizontal and surface tension is dominant, gravitational force is negligible and the liquid film thickness is uniform along the circumferential direction. However, for the cases of Nusselt condensation and thermosyphon, which are vertical, the effect of gravity is considered.

When condensation in a conventional sized tube is investigated, the governing equations are often given in Cartesian coordinates since the thickness of the film is significantly smaller than the diameter of the tube [16–18]. For condensation in miniature tubes, however, the thickness of the liquid film is at the same order of magnitude as the diameter of the tube. The governing equations and the corresponding boundary conditions for condensation in miniature circular tubes must be given in cylindrical coordinates. Since forced convection condensation between parallel plates will also be investigated, the governing equations will be written in a generalized form which will be applicable to condensation in circular tubes as well as between parallel plates.

2.1 Governing Equations. In order to simplify the solving procedure, one set of governing equations is written for both the liquid and vapor regions. The continuity and momentum equations are

$$\frac{D\rho}{Dt}+\rho\nabla\cdot\mathbf{V}=0 \tag{1}$$

$$\frac{D(\rho\mathbf{V})}{\partial t}=-\nabla p+\nabla\cdot\tau'_{ij}+\mathbf{F}, \tag{2}$$

where

$$\tau'_{ij}=\mu\left(\frac{\partial u_i}{\partial x_j}+\frac{\partial u_j}{\partial x_i}\right)+\delta_{ij}\lambda\ \mathrm{div}\,\mathbf{V}. \tag{3}$$

F is the body force resulting from surface tension at the interface, which will be discussed later. The properties of the liquid-vapor mixture are calculated using

$$\rho=(1-\varepsilon_v)\rho_l+\varepsilon_v\rho_v \tag{4}$$

$$\mu=(1-\varepsilon_v)\mu_l+\varepsilon_v\mu_v, \tag{5}$$

where ε_v is volume fraction of vapor and its value is zero in liquid phase and unity in the vapor phase. For a control volume that includes a liquid-vapor interface, the value of ε_v is between zero and one.

The volume fraction of vapor, ε_v, satisfies the continuity equation of the vapor phase

$$\frac{D\varepsilon_v}{Dt}+\varepsilon_v\nabla\cdot\mathbf{V}=-\frac{\dot{m}'''}{\rho_v}, \tag{6}$$

where $\dot{m}'''$ represents the mass production rate of condensation.

Equation (6) can be rewritten as

$$\frac{D\varepsilon_v}{Dt}=-\frac{\dot{m}'''}{\rho_v}-\varepsilon_v\nabla\cdot\mathbf{V}=S_{\varepsilon_v} \tag{7}$$

Similarly, the volume fraction of liquid, ε_l, satisfies the following equation

$$\frac{D\varepsilon_l}{Dt}+\varepsilon_l\nabla\cdot\mathbf{V}=\frac{\dot{m}'''}{\rho_l}. \tag{8}$$

Substitute Eq. (4) into Eq. (1) and considering Eq. (6), the continuity equation is simplified

$$\nabla\cdot\mathbf{V}=-\left(\frac{1}{\rho_v}-\frac{1}{\rho_l}\right)\dot{m}'''. \tag{9}$$

Substitute Eq. (9) into Eq. (7), and obtain the VOF equation

$$\frac{D\varepsilon_v}{Dt}=-\frac{\dot{m}'''}{\rho_v}+\varepsilon_v\dot{m}'''\left(\frac{1}{\rho_v}-\frac{1}{\rho_l}\right)=S_{\varepsilon_v}. \tag{10}$$

The thermal conductivity and specific heat can be defined using a similar method by which density is defined

$$k=(1-\varepsilon_v)k_l+\varepsilon_v k_v. \tag{11}$$

The specific heat is defined using the weight fraction of liquid and vapor

$$c_p=\frac{1}{\rho}[(1-\varepsilon_v)\rho_l c_{pl}+\varepsilon_v\rho_v c_{pv}]. \tag{12}$$

The total enthalpy is defined as a weighted average of the enthalpy of the vapor and liquid phases

$$H=\frac{1}{\rho}[\rho_v\varepsilon_v(h_v+h_{fg})+(1-\varepsilon_v)\rho_l h_l]. \tag{13}$$

Equation (13) can be rearranged as

$$H=h+\Delta H, \tag{14}$$

where h and ΔH represent contributions of sensible enthalpy and latent heat on the total enthalpy, i.e.,

$$h=\frac{1}{\rho}[(1-\varepsilon_v)\rho_l h_l+\varepsilon_v\rho_v h_v] \tag{15}$$

$$\Delta H=\frac{\varepsilon_v\rho_v h_{fg}}{\rho}. \tag{16}$$

The energy equation written in terms of enthalpy and temperature is

$$\frac{D(\rho H)}{Dt}=\mathrm{div}(k\nabla T) \tag{17}$$

It should be pointed out that the effect of momentum recovery on energy balance at the liquid vapor interface is neglected because (*a*) the vapor velocity is not very high, and (*b*) the density of vapor is very low.

Substituting Eq. (16) into Eq. (17), one can obtain

$$\frac{D(\rho h)}{Dt}=\mathrm{div}(k\nabla T)+S_{\Delta H}, \tag{18}$$

where

$$S_{\Delta H}=-\left[\frac{\partial}{\partial t}\rho\Delta H+\nabla\cdot(\rho\Delta HV)\right]. \tag{19}$$

It can be seen that an additional term appears on the right hand side of Eq. (18). This term accounts for the effect of condensation in the energy equation.

Substituting Eq. (15) into Eq. (19) leads to

$$S_{\Delta H}=-\left[\frac{D(\varepsilon_v\rho_v h_{fg})}{Dt}+\varepsilon_v\rho_v h_{fg}\nabla\cdot\mathbf{V}\right]. \tag{20}$$

For incompressible flow, the density of vapor is a constant, and Eq. (20) is simplified

$$S_{\Delta H} = -\rho_v h_{fg}\left(\frac{D\varepsilon_v}{Dt} + \varepsilon_v \nabla \cdot \mathbf{V}\right). \tag{21}$$

Compare Eq. (6) and Eq. (21); the mass production rate due to condensation, $\dot{m}'''$, is related to the source term in the energy equation, $S_{\Delta H}$, using

$$\dot{m}''' = \frac{S_{\Delta H}}{h_{fg}} \tag{22}$$

2.2 Boundary Conditions. The inlet condition for both the circular tube and parallel plates can be written as

$$u = \begin{cases} u_{\text{in},v} & 0 < r < R - \delta, \quad x = 0 \\ u_{\text{in},l} & R - \delta < r < R, \quad x = 0 \end{cases} \tag{23}$$

$$v = 0, \quad x = 0 \tag{24}$$

$$T = T_{\text{sat}}, \quad x = 0. \tag{25}$$

The boundary conditions at the wall are

$$u = v = 0, \quad r = R(\text{tube}) \text{ or } y = R(\text{parallel plates}) \tag{26}$$

$$T = T_w, \quad r = R(\text{tube}) \text{ or } y = R(\text{parallel plates}). \tag{27}$$

The boundary condition at exit of the computational domain can be written in a generalized form: $\partial\phi/\partial x = 0$ at $x = L$, where ϕ can be u, v, or T. The boundary conditions along the line of symmetry can be expressed as $\partial\phi/\partial r = 0$ at $r = 0$ for circular tube, or $\partial\phi/\partial y = 0$ at $y = 0$ for parallel plates.

2.3 Consideration of Liquid-Vapor Interface. The conservation of normal and tangential momentum for the control volumes at the solid-liquid interface is automatically satisfied due to the fact that the governing equations were written for the entire computational domain, including liquid and vapor. The pressure jump conditions at the liquid vapor interface due to surface tension need to be taken into account. The effect of surface tension on pressure is modeled using the continuous surface tension model. The model interprets surface tension as a continuous, three-dimensional effect across the interface rather than a boundary condition on the interface [19]. Forces resulting from the pressure jump at the interface can be expressed as volume force using the divergence theorem

$$\mathbf{F} = 2\sigma K \varepsilon_l \nabla \varepsilon_l, \tag{28}$$

where curvature of the interface, K, is given by [19]

$$K = \frac{1}{|\mathbf{n}|}\left[\left(\frac{\mathbf{n}}{|\mathbf{n}|} \cdot \nabla\right)|\mathbf{n}| - (\nabla \cdot \mathbf{n})\right]. \tag{29}$$

The normal direction of the liquid-vapor interface toward vapor phase is **n**. It can be seen that the body force, **F**, will be zero everywhere except for the control volume that includes the interface. The body force, **F**, obtained by Eq. (28) is substituted into the momentum Eq. (2) to solve for the velocities in the liquid and vapor phases.

Liquid and vapor temperatures are continuous at the interface. Therefore, the temperature at the liquid-vapor interface is expressed as

$$T = T_{\text{sat}}, \tag{30}$$

where T_{sat} is the saturation temperature.

The energy balance at the liquid vapor interface also needs to be satisfied. Since liquid and vapor regions are treated as one domain, the energy balance at the liquid vapor interface is satisfied when the converged solution for the entire domain is obtained.

3 A Numerical Technique to Determine the Source Terms

3.1 Determination of S_ε. At the liquid-vapor interface, the temperature is equal to the saturation temperature as stated in Eq. (30). The enthalpy corresponding to the above interface temperature is

$$h = c_p(T_{\text{sat}} - T_{\text{ref}}), \tag{31}$$

where T_{ref} is the reference temperature which is defined as the temperature at which the enthalpy is zero.

In order to set the temperature and enthalpy at the interface to the above values, the following source term is introduced into the enthalpy equation

$$S_{\Delta H} = A + Bh \tag{32}$$

with $A = 10^{10} c_p(T_{\text{sat}} - T_{\text{ref}})$ and $B = 10^{10}$ for the cells with ε between 0 and 1. By doing this, the numerical solution will yield Eqs. (30)–(31). This is a numerical technique to set the value of temperature and enthalpy values at the interface.

After the temperature at the interface is set to T_{sat} by the above technique, Eq. (18) is used to determine the $S_{\Delta H}$

$$S_{\Delta H} = \frac{D(\rho h)}{Dt} - \text{div}(k \nabla T). \tag{33}$$

The mass source $\dot{m}'''$ for VOF equation and continuity equation is then determined using Eq. (22).

4 Numerical Solution Procedure

Here, only the steady state solution of the condensation problem is investigated. It is impossible to solve the steady state problem directly, because the donor-acceptor model used in the VOF method works only for transient state problems. A false transient method [20] is employed. With this methodology, the false transient terms are included in the governing equations and a steady state is obtained when the condensation length does not vary with the false time. In order to accelerate convergence, the initial VOF distribution in the channel for a specific case can be set as the converged VOF distribution for a similar case. Numerical experiments on the effect of initial VOF distribution on the final results are performed for several cases. It is found that the final results are the same for different initial VOF distributions which proves that the final results are not influenced by initial conditions. The overall numerical solution procedure for a particular time step is outlined below:

1 Assume a value for the mass production rate, $\dot{m}'''$, and compute the source term for the VOF Eq. (10) and the continuity Eq. (9).
2 Solve the VOF Eq. (10).
3 Solve the continuity equation and the momentum equations.
4 Solve for the temperature distribution from Eq. (18). For the control volumes including the interface, the temperature is set to the saturation temperature and Eq. (22) is used to determine the mass production rate, $\dot{m}'''$.
5 Compute the source term for the VOF Eq. (10) and the continuity Eq. (9).
6 Go back to step 2 until the relative residuals for the pressure correction equation, momentum equations, and enthalpy equation are within the limit.

After the solution for the current time step is obtained, the computation for the next time step is performed. The above numerical procedure is implemented in a commercial package [21]. Although the VOF method has been employed in Fluent to simulate multiphase flow with a free surface, the interphase mass transfer model was not available. Therefore, the evaporation and condensation phenomena cannot be simulated directly using Fluent. To simulate condensation in miniature channels using Fluent, the

interface mass transfer is modeled using a customized user defined code. This code is compiled and linked with the remaining Fluent objects code to create a new customized executable file.

5 Results and Discussion

5.1 Verification. To verify the numerical method and code, Nusselt condensation of steam vapor on a vertical flat plate is solved. The vapor is assumed to be at the saturation temperature (363 K) and the wall temperature is 340 K. The effect of gravity is included in the model since it is dominant for the vertical plate. The comparison of liquid film thickness obtained by the present model versus the Nusselt analysis is presented in Fig. 2. It can be seen that the interface obtained by the present method is not very smooth, which is due to the limitation of the donor-acceptor method used to solve the VOF equation [15]. However, the overall agreement between the present result and the Nusselt analysis is still very good.

Forced film condensation on a horizontal flat plate (Fig. 3(*a*)) is then solved. The working fluid is R-113, and the velocity and saturation temperature of vapor at infinity are assumed to be 0.3 m/s and 320.57 K. The temperature at the surface of the plate is chosen to be 310.56 K. Fig. 3(*b*) shows the comparison of the film thicknesses obtained by the present numerical solution and the approximate solution by Shekriladze and Gomelauri [22]. The agreement between the present results and that of Shekriladze and Gomelauri [22] is fairly good up to 1 cm from leading edge. The discrepancy between the present results and those of Ref. [22] for larger x can be explained using the shear stress model used by Shekriladze and Gomelauri [22]. The shear stress at the liquid vapor interface is calculated using

$$\tau_0 = j(U_\infty - U_s), \tag{34}$$

where j is mass flow rate of vapor at the liquid-vapor surface due to condensation, and U_s is velocity at the liquid vapor interface. The shear stress caused by the gradient of the horizontal velocity was neglected, and the shear stress on the liquid-vapor interface was assumed to be dependent on the momentum change due to suction at the interface. This becomes more accurate when the film thickness is very small and the condensation rate is very high. As the film thickness increases, the rate of condensation decreases, and consequently the momentum transferred by the suction mass at the interface decreases. Eventually the momentum transferred by the suction mass is no longer significant. The shear stress on the liquid-vapor interface depends on the momentum changes due to the velocity gradient and the suction due to condensation. Therefore the approximate solution in Ref. [22] overestimates the film thickness for larger x.

Another verification of the numerical method was performed by simulating the condensation in a condenser section of a thermosyphon [16]. The geometric configuration of the problem is similar to Fig. 1, except that the tube is closed at $x=0$ and the effect of gravity must be taken into account. The tube is vertical, and the gravity acts in the positive x-direction. Vapor flows toward the negative x-direction, but the liquid flows toward the positive x-direction due to the effect of gravity. For the complete problem description see Ref. [16]. The radius and the length of the circular tube are $R=1.21$ mm and $L=4.0$ cm, respectively. The working fluid is methanol with a saturation temperature of 336 K and a wall temperature of 310.8 K. The numerical results are compared with the analytical results of Seban and Faghri [16], and the present results are shown in Table 1. The vapor phase Reynolds numbers is defined as

$$\mathrm{Re}_v = \frac{u_{\mathrm{in},v} D}{\nu_v}, \tag{35a}$$

where $u_{\mathrm{in},v}$ is the vapor velocity at the inlet of the condenser section of the thermosyphon. The liquid phase Reynolds number is defined as

$$\mathrm{Re}_v = \frac{u_l \delta|_{x=L}}{\nu_l}, \tag{35b}$$

where u_l and $\delta|_{x=L}$ are liquid outlet velocity and liquid film thickness at the inlet of the condenser section of the thermosyphon, respectively. The average Nusselt number in the condenser section is

$$\overline{\mathrm{Nu}} = \frac{\overline{h} D}{k_l}, \tag{35c}$$

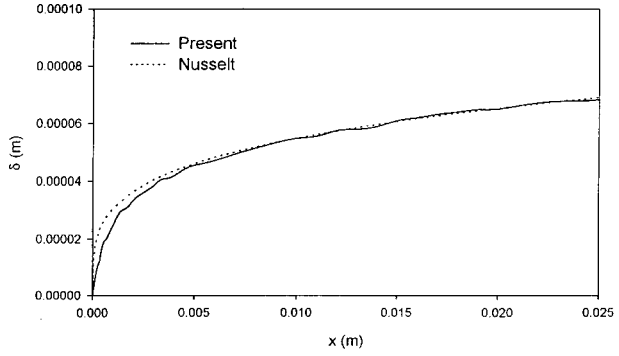

Fig. 2 Comparison of liquid film thickness for Nusselt Condensation

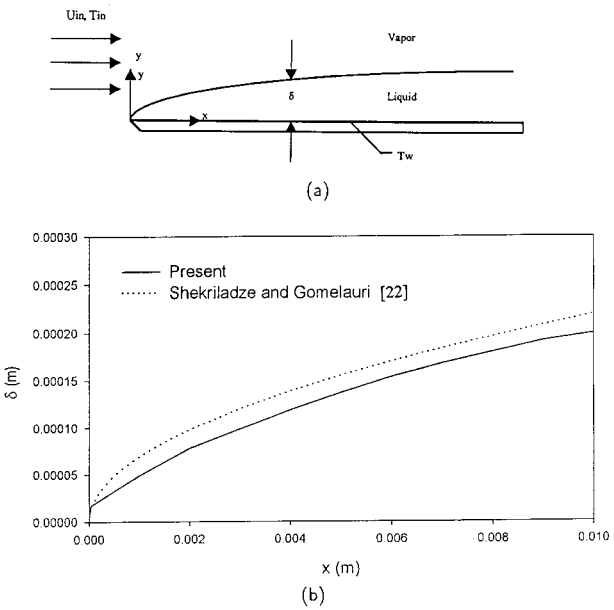

Fig. 3 Forced convection film condensation: (*a*) physical model; (*b*) comparison with Shekriladze and Gomelauri [22]

Table 1 Comparison of present results with the results of Seban and Faghri [16]

	Re_v	Re_l	$\delta\|_{x=L}$	$\overline{Nu}$
Nusselt Analysis				18.1
Seban and Faghri (1984)	495	3.3	2.78×10^{-4}	38.4
Present (without surface tension)	510	3.42	2.69×10^{-4}	39.6
Present (with surface tension)	530	3.51	2.60×10^{-4}	41.1

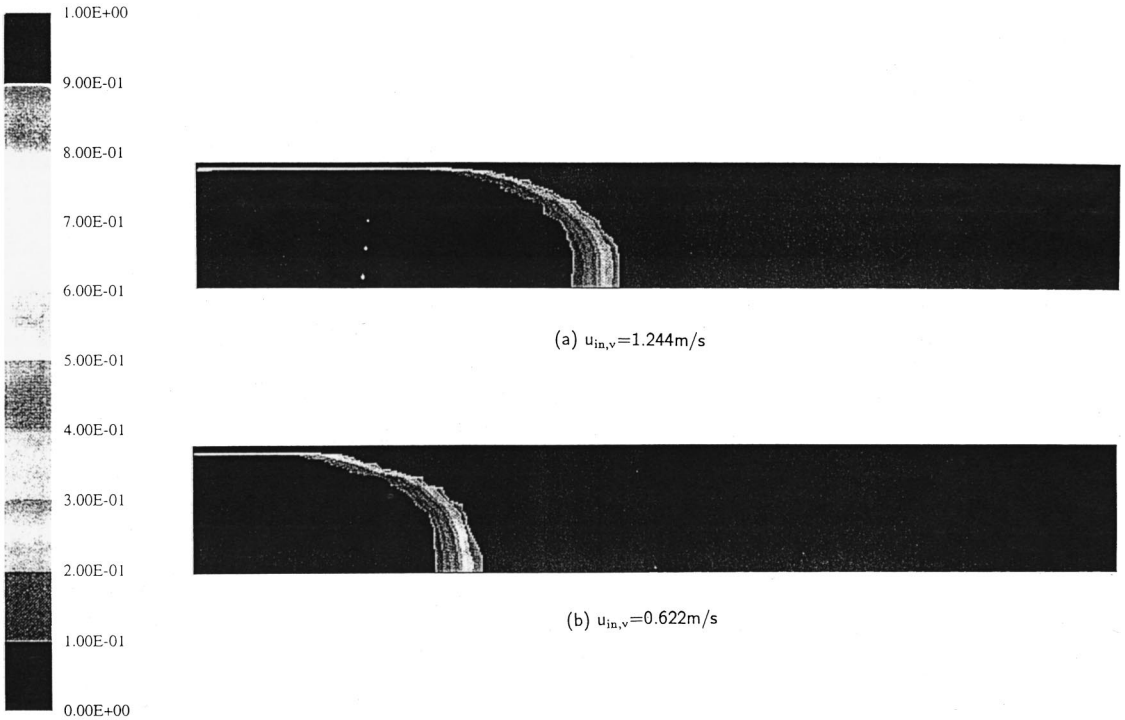

Fig. 4 Contour of vapor VOF at different vapor inlet velocities ($\dot{m}_t = 10^{-5}$ kg/s, $T_{sat} = 363$ K, $T_w = 340$ K)

where $\bar{h}$ is the average heat transfer coefficient at the condenser section.

The agreement between the present results and Ref. [16] is very good. Also evident from Table 1 is that the effect of surface tension is not significant for this case, because the process is mainly dominated by gravity.

5.2 Condensation in a Miniature Circular Tube. The condensation in horizontal miniature tubes as shown in Fig. 1 is then investigated. The radius and the length of the tube is $R = 1.5$ mm and $L = 2$ cm, respectively. The working fluid is water with a saturation temperature of 363 K or 323 K. The inlet temperature is always equal to the saturation temperature. The difference between the wall temperature and saturation temperature is 23 K for all cases. Thermal properties of the working fluid can be found in Ref. [1] and will not be repeated here. After the grid size and the time step test, the problem is solved using a non-uniform grid of $42(x) \times 32(r)$. The grid near the wall is very fine in order to simulate fluid flow in the liquid layer. The grid at small x is very fine in order to simulate the closed condensation phenomena. After several numerical tests, the false time step used in the computation is $\Delta t = 10^{-6}$ s.

Figure 4 shows the volume fraction of water at different vapor inlet velocities. The dark area in the figure is vapor and the gray area is liquid. The light area that exists between the liquid and vapor region is the liquid-vapor interface. Total mass flow rate of liquid and vapor for both cases is $\dot{m}_t = 10^{-5}$ kg/s, and the liquid film thickness at the entrance of the tube is 0.08 mm [3]. In both cases the capillary blocking phenomenon occurs. For the case with vapor inlet velocity of 1.244 m/s, the condensation length measured at the center of the tube is 4.7 mm. When the vapor inlet velocity is reduced by half, the condensation length is reduced to 3.1 mm.

Figure 5 shows the VOF for water when the saturation temperature is reduced to 323 K. The mass flow rate of vapor in Fig. 5(*a*) and (*b*) is the same as the mass flow rate of vapor in Fig. 4(*a*) and (*b*). Since the density of vapor at 323 K is significantly lower than that at 363 K, the vapor inlet velocities in Fig. 5 are significantly higher than those for Fig. 4. As shown in Fig. 5, the liquid film is not smooth due to the shear force induced by the high vapor velocity. The condensation lengths for two cases are 4.6 mm and 2.7 mm respectively. Compared with the condensation length in Fig. 4, the condensation length is not strongly affected by the saturation temperature. For the same mass flow rate of vapor, the condensation lengths at different saturation temperatures are very close. The effect of vapor inlet velocity on the condensation length for a saturation temperature of 323 K is shown in Fig. 6. The total mass flow rate remains at $\dot{m}_t = 10^{-5}$ kg/s for different vapor inlet velocities. The condensation length increases sharply when the vapor inlet velocity is small. The condensation length, however, becomes a linear function of vapor inlet velocity after the vapor inlet velocity is greater than 2.5 m/s.

The velocity vectors corresponding to the case in Fig. 4(*a*) and Fig. 5(*a*) are shown in Fig. 7(*a*) and (*b*). As mentioned before, the mass flow rates for Fig. 7(*a*) and (*b*) are the same although the vapor inlet velocities are different. Since condensation occurs on the wall, the vapor velocity vectors near the wall point towards the wall. The mean vapor velocity decreases with x, due to condensation.

Figure 8(*a*) shows the variation of liquid film thickness for the cases in Fig. 4(*a*) and (*b*). It can be seen that the behavior of liquid film thickness is different for different vapor inlet velocities. When the vapor inlet velocity is low, the film thickness is almost constant before it increases sharply to block the tube. When the vapor inlet velocity is higher, the film thickness along most of the effective condensation length is constant. However, there is a film thickness decrease before the sharp increase, which agrees with Begg et al. [3]. The heat transfer coefficient based on the difference between saturation temperature and wall temperature corresponding to Fig. 8(*a*) is shown in Fig. 8(*b*). It can also be noted that the heat transfer coefficient along the condensation length is very high but decreases sharply when capillary blocking occurs. For the case of high vapor inlet velocity, the heat transfer coefficient before capillary blocking is very high since the liquid film is thinner at this location.

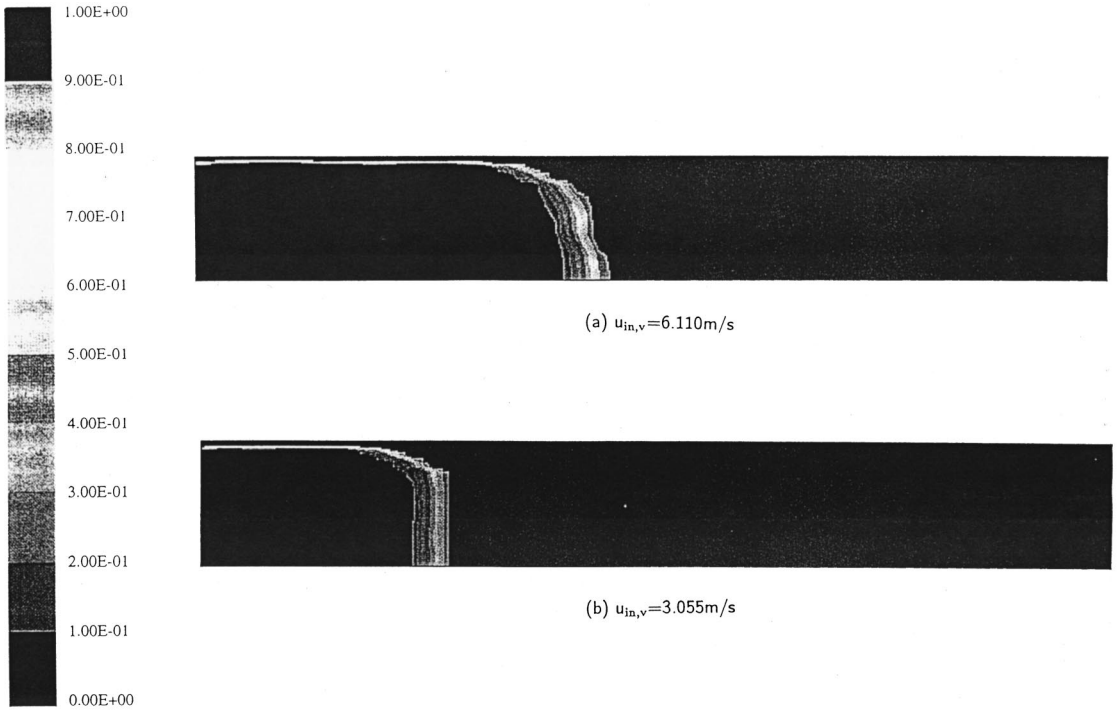

Fig. 5 Contour of vapor VOF at different vapor inlet velocities ($\dot{m}_t = 10^{-5}$ kg/s, $T_{sat} = 323$ K, $T_w = 300$ K)

The variations of liquid film thickness corresponding to the cases in Fig. 5(*a*) and (*b*) are shown in Fig. 9(*a*). The liquid film thickness at first decreases but then increases. Before capillary blocking occurs in the tube, there is a decrease in liquid film thickness. This wavy shape of liquid film shown is due to the shear force caused by high vapor velocity. The heat transfer coefficients corresponding to Fig. 9(*a*) are shown in Fig. 9(*b*). It is also noted that the heat transfer coefficients in the condensation length show wavy shapes due to variation in liquid film thickness.

The effect of surface tension on the liquid film thickness and condensation length for the vapor inlet velocity of 1.244 m/s is shown in Fig. 10(*a*). In addition to the result for surface tension at its normal value, σ_0, two curves with changed surface tension but with identical mass flow rates are also plotted in Fig. 10(*a*) for comparison. It can be seen that the condensation length decreases with an increase in the surface tension, which is in agreement with Ref. [3]. Increasing the surface tension thins the liquid film thickness, and therefore the condensation rate within the condensation length increases. Consequently, the condensation length required to condense the same amount of vapor decreases. The reason that film thickness thins with increasing surface tension is that the condensation phenomenon always tends to minimize the surface energy at the interface. Increasing the surface tension increases this energy. In order to reduce this energy, the radii of curvature has to be increased which means liquid film thickness also has to be decreased. Fig. 10(*b*) shows the heat transfer coefficient along the tube for varying surface tension. The maximum heat transfer coefficient value within the condensation length is obtained from the case with the highest surface tension. In this case, the average heat transfer coefficient is greater than the others. This is consistent with the expectation that a higher total average heat transfer coefficient leads to a shorter condensation length.

The effect of the radius of the miniature tube on film thickness and the heat transfer coefficient is shown in Fig. 11. The inlet velocities of both liquid and vapor for three cases presented in Fig. 11 are the same, and therefore the total mass flow rate for a smaller diameter tube is lower. As can be seen from Fig. 11(*a*), the liquid film thickness decreases with decreasing tube diameter, because surface tension plays a more important role. The condensation length also decreases with decreasing tube diameter, since the total mass flow rate decreases with decreasing tube diameter. Fig. 11(*b*) shows the effect of tube diameter on the heat transfer coefficient. It is noticed that the heat transfer coefficient within the condensation length is significantly higher for smaller diameter tubes because the liquid film is thinner.

The effect of the total mass flow rate on condensation in circular miniature tubes is also investigated and the results are shown in Fig. 12. In addition to the reference case ($\dot{m}_t = 10^{-5}$ kg/s), the results for the reduced total mass flow rate are shown in Fig. 12. It can be seen from Fig. 12(*a*) that the film thickness is significantly increased and the condensation length is significantly reduced with a decreasing total mass flow rate. Consequently, the heat transfer coefficient is significantly decreased when the total mass flow rate is reduced by one order of magnitude.

5.3 Condensation Between Parallel Plates. Condensation phenomena in miniature channels formed by two parallel plates

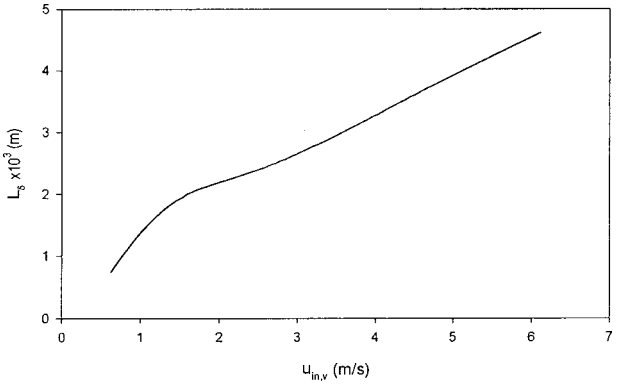

Fig. 6 Effect of vapor inlet velocity on the condensation length ($\dot{m}_t = 10^{-5}$ kg/s, $T_{sat} = 323$ K, $T_w = 300$ K)

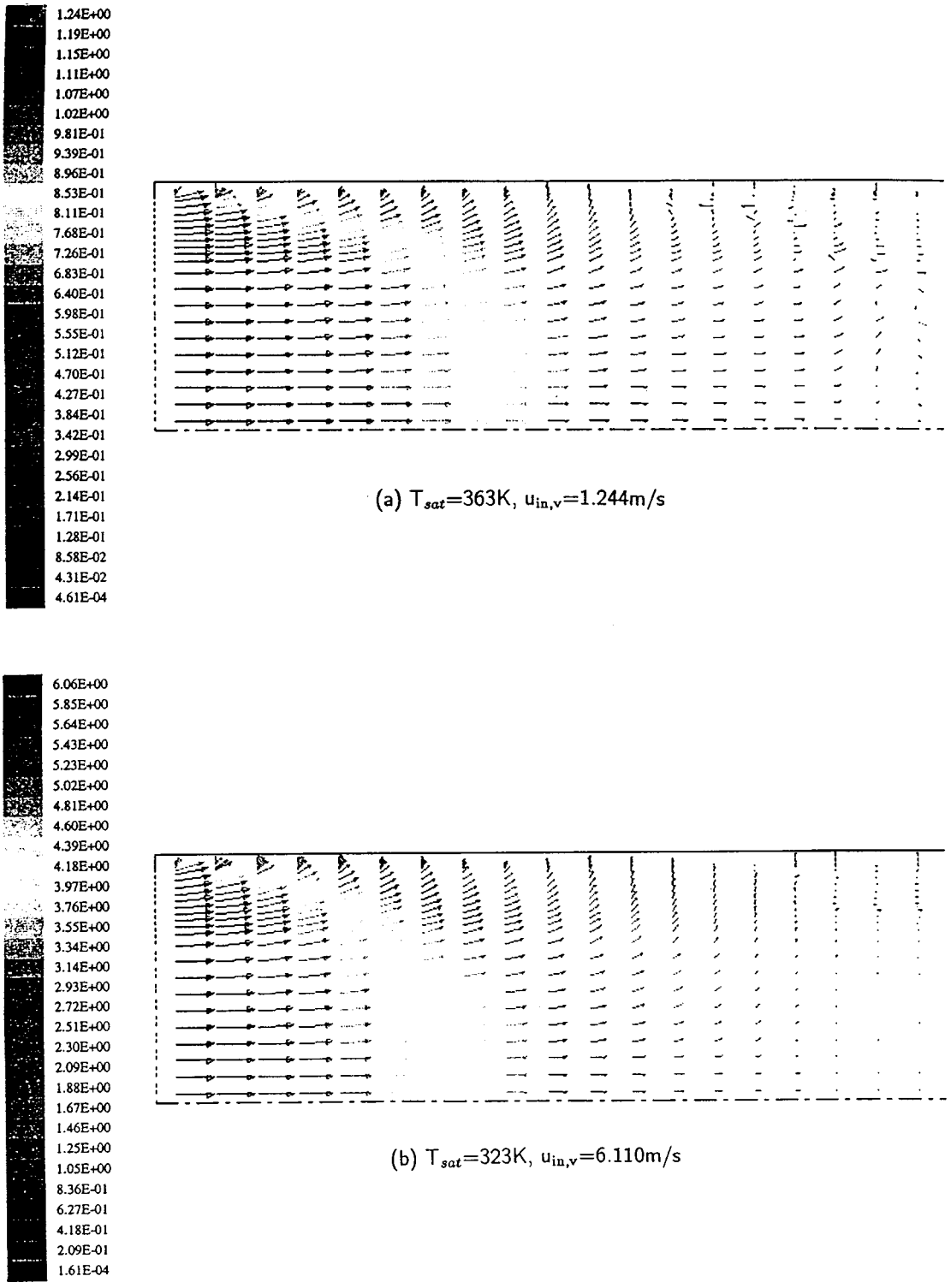

Fig. 7 Velocity vectors at different saturation temperature for miniature tube

are also investigated. The distance between plates and the length of the channel are: $2R=3$ mm and $L=2$ cm, respectively. The effect of gravity is neglected and therefore this is an axisymmetric problem about $y=0$. Only half of the domain ($0<y<R$) is solved. A non-uniform grid of $42(x)\times 32(y)$ with a time step of $\Delta t=10^{-6}$ is used to solve this problem. Fig. 13(*a*) shows the variation of liquid film thickness along the horizontal parallel plates for different vapor inlet velocities. The total mass flow rates of liquid and vapor for both cases are $\dot{m}_t=8.3\times 10^{-4}$ kg/(ms). It is seen that the condensate film thins close to the blocking point for both high ($u_{\text{in},v}=0.62$ m/s) and low ($u_{\text{in},v}=0.2$ m/s) vapor inlet velocities. The variation of the liquid film thickness is different for two distinct velocities. For the lower vapor inlet velocity, film thickness decreases in the positive *x*-direction up to the blocking point due to shear stress and surface tension at the blocking point where the curvature of the interface is large. For higher vapor inlet velocities, the film is thin and tends to be wavy due to the higher shear stresses. These variations of liquid film thickness

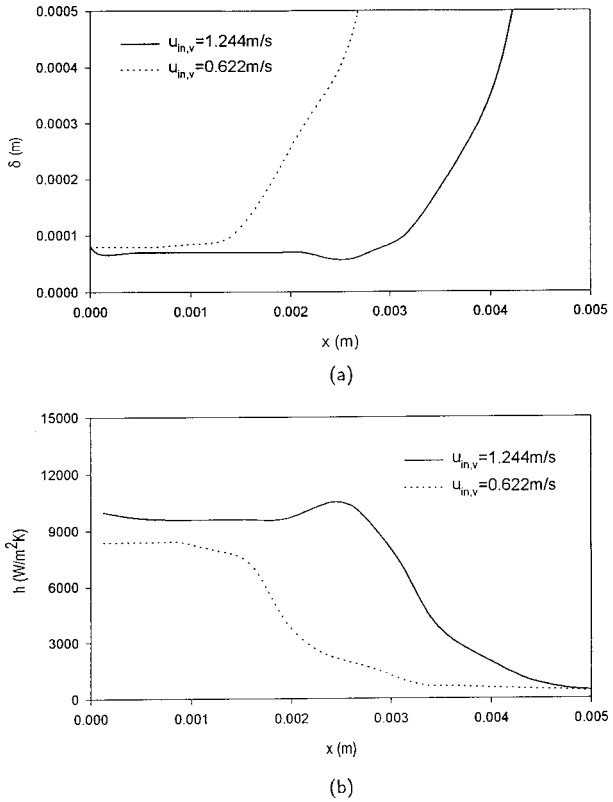

Fig. 8 Effect of vapor inlet velocity on condensation in miniature tubes ($\dot{m}_t = 10^{-5}$ kg/s, $T_{sat} = 363$ K, $T_w = 340$ K): (*a*) film thickness; (*b*) heat transfer coefficient

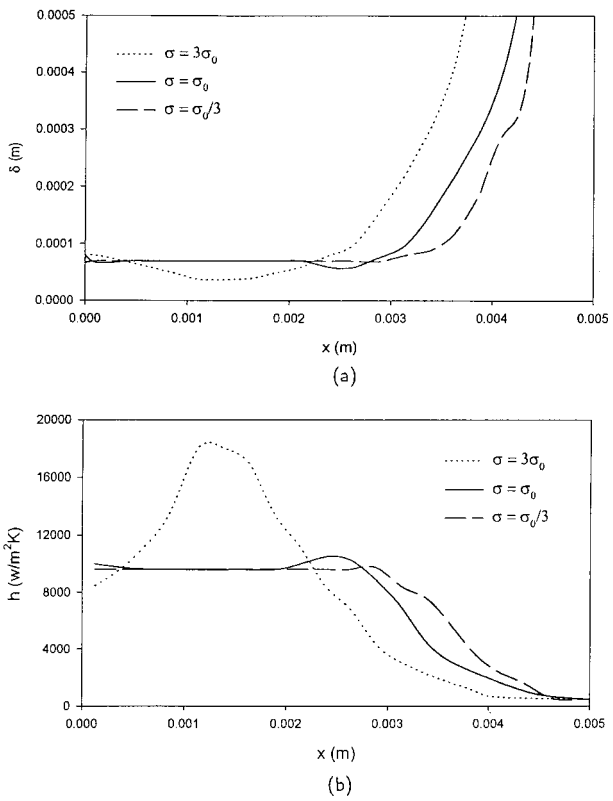

Fig. 10 Effect of surface tension on condensation in miniature tubes ($\dot{m}_t = 10^{-5}$ kg/s, $u_{in,v} = 1.244$ m/s, $T_{sat} = 363$ K, $T_w = 340$ K): (*a*) film thickness; (*b*) heat transfer coefficient

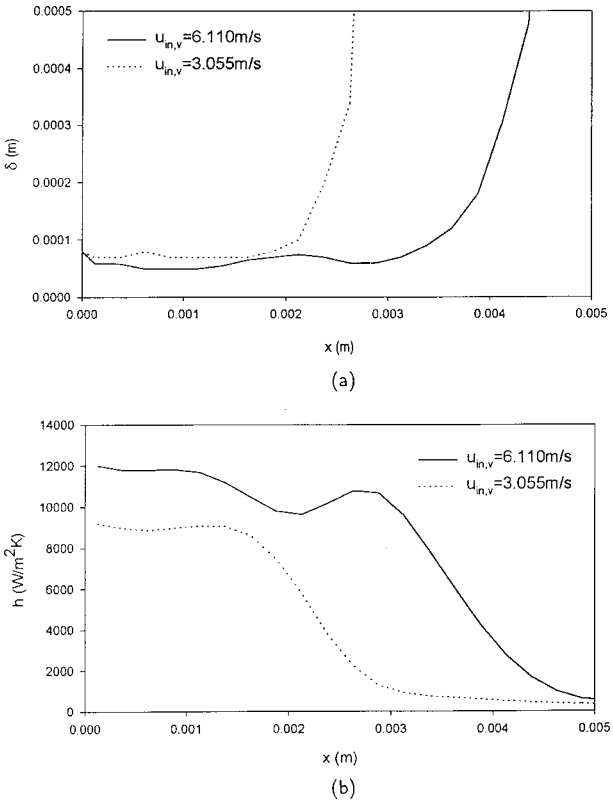

Fig. 9 Effect of vapor inlet velocity on condensation in miniature tubes ($\dot{m}_t = 10^{-5}$ kg/s, $T_{sat} = 323$ K, $T_w = 300$ K): (*a*) film thickness; (*b*) heat transfer coefficient

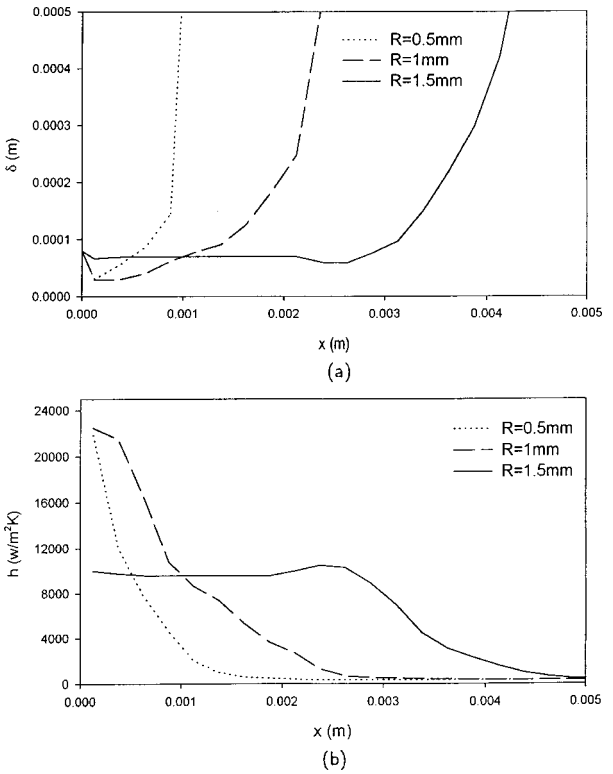

Fig. 11 Effect of diameter on the condensation in miniature tubes ($u_{in,v} = 1.244$ m/s, $T_{sat} = 363$ K, $T_w = 340$ K): (*a*) film thickness; (*b*) heat transfer coefficient

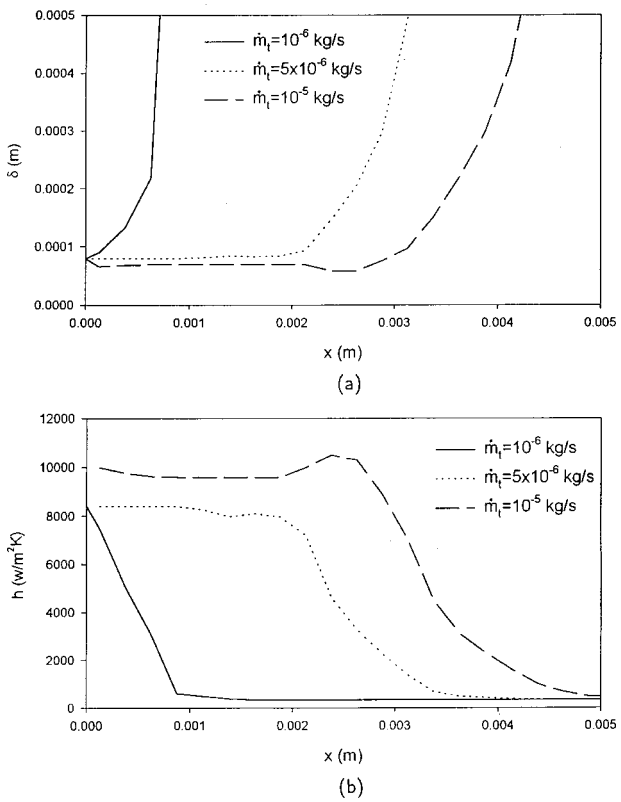

Fig. 12 Effect of total mass flow rate on the condensation in miniature tubes (R=1.5 mm, T_{sat}=363 K, T_w=340 K): (*a*) film thickness; (*b*) heat transfer coefficient

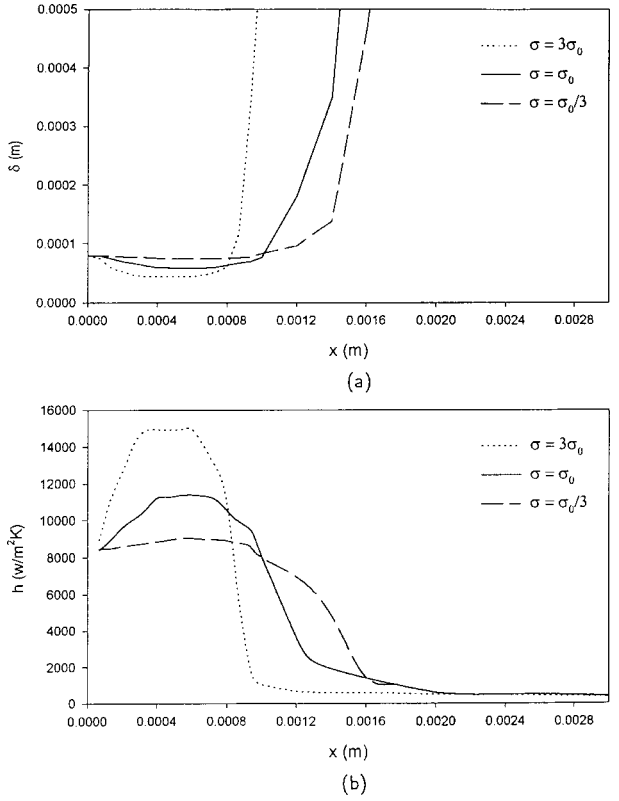

Fig. 14 Effect of surface tension on condensation between parallel plates ($\dot{m}_t$=8.3×10^{-4} kg/ms, $u_{in,v}$=0.2 m/s, T_{sat}=363 K, T_w=340 K): (*a*) film thickness; (*b*) heat transfer coefficient

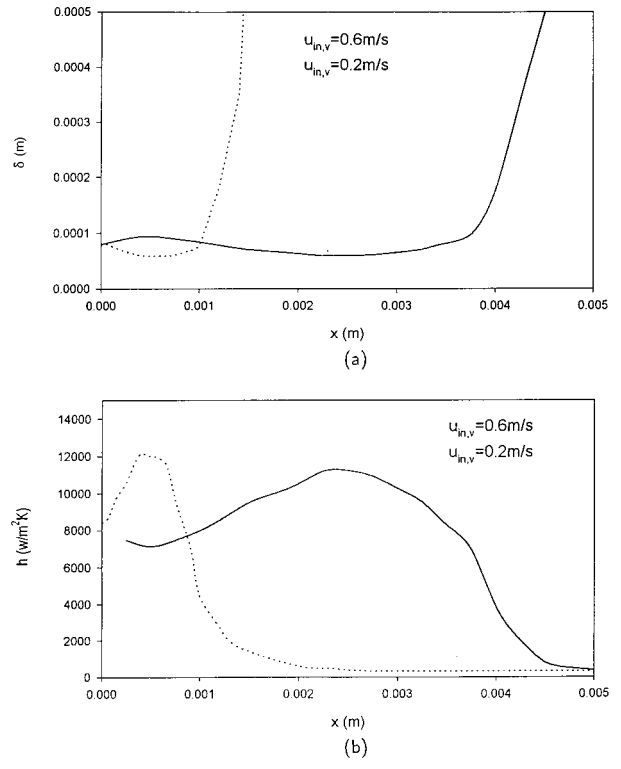

Fig. 13 Effect of vapor inlet velocity on condensation between parallel plates ($\dot{m}_t$=8.3×10^{-4} kg/ms, T_{sat}=363 K, T_w=340 K): (*a*) film thickness; (*b*) heat transfer coefficient

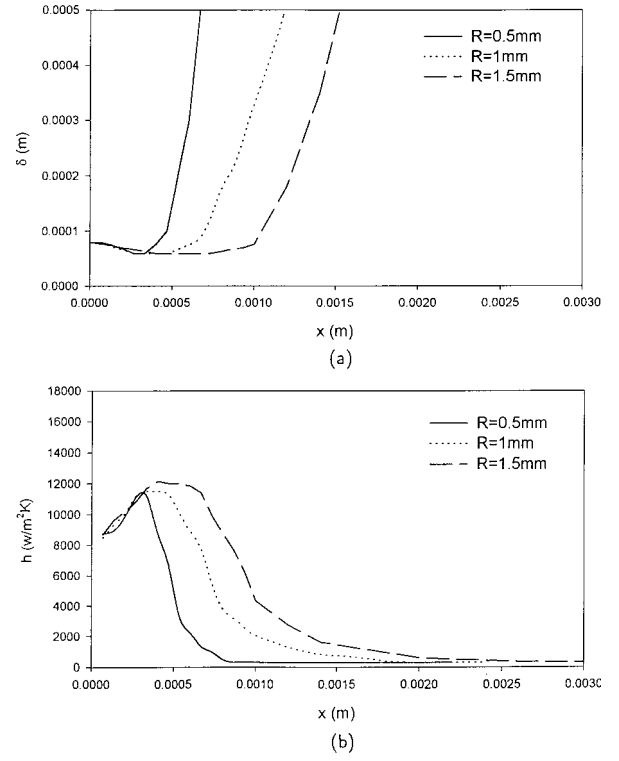

Fig. 15 Effect of the distance between parallel plates on condensation (T_{sat}=363 K, T_w=340 K): (*a*) film thickness; (*b*) heat transfer coefficient

were not observed for the circular tube since the surface tension resulting from the curvature of the tube radius can suppress the wave in the tube. The heat transfer coefficients for the cases corresponding to Fig. 13(*a*) are shown in Fig. 13(*b*). The heat transfer coefficients are highest before the blocking point, where the rate of condensation is the greatest.

The effect of surface tension on film thickness and the condensation length is shown in Fig. 14(*a*). The vapor inlet velocity for all three cases is 0.2 m/s. As can be seen from Fig. 14(*a*), the condensation length decreases with the increasing surface tension. When the surface tension increases, the liquid film thickness becomes thinner at the locations closest to the blocking point. The heat transfer coefficients along the plates for different values of surface tension are shown in Fig. 14(*b*). It is observed that the total average heat transfer coefficient for all cases is the same, because the vapor inlet velocities are the same.

Figure 15 shows the effect of distance between parallel plates on condensation. The inlet velocities of liquid and vapor for different distances are the same, which means that the total mass flow rate for smaller distances between parallel plates is lower. It can be seen from Fig. 15(*a*) that the liquid film thickness slightly decreases when the distance between parallel plates is reduced. This is different from the behavior in circular tubes because surface tension is less important for condensation between parallel plates. The condensation length is reduced with decreasing distance between parallel plates, since the total mass flow rate is lower for smaller distances between parallel plates.

6 Conclusion

Numerical simulation for condensation in horizontal miniature circular tubes and between parallel plates with capillary blocking is performed using the VOF method. The effects of various physical and geometric parameters on liquid film thickness, condensation length, and heat transfer coefficients for both circular tube and parallel plates are investigated. The results show that the condensation length increases sharply with increasing vapor inlet velocity when the vapor velocity is small. When the inlet vapor velocity is higher, the condensation length is a linear function of inlet vapor velocity. The condensation lengths for different saturation temperatures are very close for the same mass flow rate of vapor. The liquid film thickness is smooth for lower vapor velocities. The wavy shape of the liquid film was observed for the cases with high vapor velocity. When the surface tension increases, the liquid film thickness up to the blocking point decreases and the condensation length decreases for both tubes and parallel plates. The liquid film thickness and the condensation length decrease with decreasing channel size. When the total mass flow rate decreases, the liquid film thickness increases and the condensation length decreases.

Acknowledgments

Funding for this work was provided by NASA Grant NAG3-1870 and NSF Grant CTS 9706706.

Nomenclature

c_p = specific heat, J/kgK
$\mathbf{F}$ = body force, N
g = gravitional acceleration, m^2/s
h = sensible enthalpy, J/kg
H = total enthalpy, J/kg
h_c = heat transfer coefficient, W/m^2K
h_{fg} = latent heat, J/kg
$\mathbf{i}$, $\mathbf{j}$ = unit vector in x, r, (or y) directions
k = thermal conductivity, W/mK
L = length of the tube, m
L_δ = condensation length, m
$\dot{m}''$ = mass flux at the interface, kg/m^2s
$\dot{m}'''$ = mass source, kg/m^3s
$\dot{m}_t$ = total mass flow rate, kg/s
p = pressure, Pa
R = radius of the tube or one half of the distance between parallel plates, m
r = radial coordinate, m
t = time, s
T = temperature, K
u = axial velocity, m/s
v = radial velocity or velocity in y direction, m/s
$\mathbf{V}$ = velocity vector, $u\mathbf{i}+v\mathbf{j}$, m/s
x = axial coordinate, m
y = vertical coordinate for parallel plate, m

Greek Symbols

δ = liquid film thickness, m
ε = volume fraction of vapor
μ = dynamic viscosity, kg/ms
ρ = density, kg/m^3
σ = surface tension, N/m
σ_0 = normal value of surface tension, N/m
∇ = gradient operator, $\mathbf{i}(\partial/\partial x)+(\mathbf{j}\partial/\partial y)$

Subscripts

in = inlet
l = liquid
sat = saturation
v = vapor
w = wall

References

[1] Faghri, A., 1995, *Heat Pipe Science and Technology*, Taylor and Francis, Washington, D.C.
[2] Faghri, A., 1999, ''Recent Advances and Challenges in Micro/Miniature Heat Pipes,'' *Procs. of 11th International Heat Pipe Conference*, Tokyo, Japan, Sep. 12–15, 1999.
[3] Begg, E., Khrustalev, D., and Faghri, A., 1999, ''Complete Condensation of Forced Convection Two-Phase Flow in a Miniature Tube,'' ASME J. Heat Transfer, **121**, No. 4, pp. 904–915.
[4] Mandhane, J. M., Gregory, G. A., and Aziz, K., 1974, ''A Flow Pattern Map for Gas-Liquid Flow in Horizontal Pipes,'' Int. J. Multiphase Flow, **1**, pp. 537–553.
[5] Taitel, Y., and Dukler, A. E., 1976, ''A Model for Predicting Flow Regime Transitions in Horizontal and Near Horizontal Gas-Liquid Flow,'' AIChE J., **22**, pp. 47–55.
[6] Barnea, D., Luninski, Y., and Taitel, Y., 1983, ''Flow Pattern in Horizontal and Vertical Two Phase Flow in Small Diameter Pipes,'' Can. J. Chem. Eng., **61**, pp. 617–620.
[7] Collier, J. G., and Thome, J. R., 1994, *Convective Boiling and Condensation*, 3rd Ed., Oxford University Press, New York.
[8] Faghri, A., 1996, ''Heat Pipe Simulation, From Promise to Reality,'' *Procs. of 5th International Heat Pipe Symposium*, Melbourne, Australia, Nov. 17–20, 1996, pp. 1–21.
[9] Hirt, C. W., and Nichols, B. D., 1981, ''Volume of Fluid (VOF) Method for the Dynamics of Free Boundaries,'' J. Comput. Phys., **39**, pp. 201–225.
[10] Nichols, B. D., Hirt, C. W., and Hotchkiss, R. S., 1980, *SOLA-VOF: A Solution Algorithm for Transient Fluid Flow with Multiple Free Boundary*, Los Alamos Scientific Laboratory, LA-8355.
[11] Ganesh, R. K., Faghri, A., and Hahn, Y., 1997, ''A Generalized Thermal Modeling for Laser Drilling Process: Part I—Mathematical Modeling and Numerical Methodology,'' Int. J. Heat Mass Transf., **40**, pp. 3351–3360.
[12] Ganesh, R. K., Faghri, A., and Hahn, Y., 1997, ''A Generalized Thermal Modeling for Laser Drilling Process: Part II—Numerical Simulation and Results,'' Int. J. Heat Mass Transf., **40**, pp. 3361–3373.
[13] Takata, Y., Shirakawa, H., Sasaki, H., Kuroki, T., and Ito, T., 1999, ''Numerical Analysis of Rapid Solidification in a Single Roller Process,'' *Heat Transfer—Asian Research*, **28**, pp. 34–49.
[14] Takata, Y., Shirakawa, H., Kuroki, T., and Ito, T., 1998, ''Numerical Analysis of Single Bubble Departure from a Heated Surface,'' *Heat Transfer 1998, Proceedings of 11th International Heat Transfer Conference*, **4**, pp. 355–360.
[15] Takata, Y., Shirakawa, H., Kuroki, T., and Ito, T., 1999, ''An Improved VOF Method and Its Application to Phase Change Problems,'' *Proceedings of the 5th ASME/JSME Joint Thermal Engineering Conference*, March 15–19, 1999, San Diego, CA.
[16] Seban, R. A., and Faghri, A., 1984, ''Film Condensation in a Vertical Tube with a Closed Top,'' Int. J. Heat Mass Transf., **27**, pp. 944–948.
[17] Harley, C., and Faghri, A., 1994, ''Complete Transient Two-Dimensional Analysis of Two-Phase Closed Thermosyphons Including the Falling Condensate Film,'' ASME J. Heat Transfer, **116**, pp. 418–426.

[18] Narain, A., Yu, G., and Liu, Q., 1997, ''Interfacial Shear Models and Their Required Asymptotic for Annular/Stratified Film Condensation Flows in Inclined Channels and Vertical Pipes,'' Int. J. Heat Mass Transf., **40**, pp. 3559–3575.
[19] Brackbill, J. U., Kothe, D. B., and Zemach, C., 1992, ''A Continuum Method for Modeling Surface Tension,'' J. Comput. Phys., **100**, pp. 335–354.
[20] Basu, B., and Srinivasan, J., 1988, ''Numerical Study of Steady State Laser Melting Problem,'' Int. J. Heat Mass Transf., **31**, pp. 2331–2338.
[21] *Fluent 4.5, User's Guide*, Fluent Inc., 1998, Lebanon, NH.
[22] Shekriladze, I. G., and Gomelauri, V. I., 1966, ''Theoretical Study of Laminar Film Condensation of Flowing Vapor,'' Int. J. Heat Mass Transf., **9**, pp. 581–591.

Effective Permeability of a Layered Porous Cavity

J. C. Leong
Graduate Student

F. C. Lai
Assoc. Professor
e-mail: flai@ou.edu

School of Aerospace and Mechanical Engineering,
University of Oklahoma,
Norman, OK 73019

The feasibility of using a lumped system approach in the heat transfer analysis of a layered porous cavity is numerically investigated in this paper. Two layered cavities are considered; in one case the sublayers are perpendicular to the imposed temperature gradient while in the other case they are parallel to the imposed temperature gradient. Numerical calculations have covered a wide range of parameters (i.e., $10 \leqslant Ra_1 \leqslant 1000$, $0.01 \leqslant K_1/K_2 \leqslant 100$, and $L_1/L(H_1/H) = 0.25$, 0.5 and 0.75). The results are presented in term of the effective Rayleigh number which is defined based on the effective permeability. Two averaging techniques are used for the evaluation of the effective permeability; one is arithmetic average and the other is harmonic average. The results show that the lumped system approach can provide a fairly accurate prediction in heat transfer if the permeability is correctly characterized. Also found is that the effective permeability of a layered porous cavity is strongly dependent on the orientation of sublayers and the primary heat flow direction. [DOI: 10.1115/1.1351164]

Keywords: Finite Difference, Heat Transfer, Natural Convection, Porous Media

Introduction

Over the years, heat transfer in saturated porous media has received considerable attention because of its important applications in geophysics and energy related engineering problems. Although layered porous media are frequently encountered in many applications mentioned above, they have received relatively little attention as compared with homogeneous porous media. To authors' knowledge, there is no correlation available for convective heat transfer in layered porous media. As a result, for applications involving layered porous media, a simple lumped-system approach is usually employed to expedite the heat transfer calculation, instead of a detailed analysis of energy transport in each sublayer. Clearly, the feasibility of lumped-system approach is largely dependent on a successful characterization of the average properties of the system. Among the thermophysical properties involved, permeability is one of the most important properties to be characterized for a layered system. In this study, an attempt has been made to characterize the effective permeability of a layered porous cavity subject to differential heating from the vertical walls. Based on the results obtained, the feasibility of lumped-system approach is evaluated. To this end, a detailed numerical analysis is performed over a wide range of parameters (i.e., $10 \leqslant \mathrm{Ra}_1 \leqslant 10^3$ and $10^{-2} \leqslant K_1/K_2 \leqslant 10^2$) for various sublayer thickness ratios, $H_1/H(L_1/L) = 1/4$, 1/2, and 3/4.

Formulation and Numerical Method

The geometry considered is a square porous cavity comprising two sublayers (Fig. 1). While the vertical walls are maintained respectively at constant temperatures T_h and $T_c (T_h > T_c)$, the horizontal walls are insulated. The sublayers have a distinct permeability and are saturated with the same fluid. Two layered cavities are considered in this study. For the cavity with vertical sublayers, the layer interface is perpendicular to the temperature gradient imposed (Fig. 1(*a*)) while it is parallel to the temperature gradient for the cavity with horizontal sublayers (Fig. 1(*b*)). The governing equations based on the Darcy's law are given by [1,2]

$$\frac{\partial u_i}{\partial x} + \frac{\partial v_i}{\partial y} = 0, \tag{1}$$

$$u_i = -\frac{K_i}{\mu}\frac{\partial P_i}{\partial x}, \tag{2}$$

$$v_i = -\frac{K_i}{\mu}\left(\frac{\partial P_i}{\partial y} + \rho g\right), \tag{3}$$

$$u_i\frac{\partial T_i}{\partial x} + v_i\frac{\partial T_i}{\partial y} = \alpha_i\left(\frac{\partial^2 T_i}{\partial x^2} + \frac{\partial^2 T_i}{\partial y^2}\right), \tag{4}$$

where the subscript $i(=1,2)$ denotes the sublayers. The corresponding boundary and interface conditions are

(*a*) Vertical Layers

$$x = 0, \quad u_1 = 0, \quad T_1 = T_h, \tag{5a}$$

$$x = L, \quad u_2 = 0, \quad T_2 = T_c, \tag{5b}$$

$$y = 0,\ x < L_1, \quad v_1 = 0, \quad \frac{\partial T_1}{\partial y} = 0,$$

$$x > L_1, \quad v_2 = 0, \quad \frac{\partial T_2}{\partial y} = 0, \tag{5c}$$

$$y = H,\ x < L_1, \quad v_1 = 0, \quad \frac{\partial T_1}{\partial y} = 0,$$

$$x > L_1, \quad v_2 = 0, \quad \frac{\partial T_2}{\partial y} = 0, \tag{5d}$$

$$x = L_1, \quad u_1 = u_2, \quad p_1 = p_2,$$

$$T_1 = T_2, \quad k_1\frac{\partial T_1}{\partial x} = k_2\frac{\partial T_2}{\partial x}, \tag{5e}$$

(*b*) Horizontal Layers

$$x = 0,\ y < H - H_1, \quad u_1 = 0, \quad T_1 = T_h,$$

$$y > H - H_1, \quad u_2 = 0, \quad T_2 = T_h, \tag{6a}$$

$$x = L,\ y < H - H_1, \quad u_1 = 0, \quad T_1 = T_c,$$

$$y > H - H_1, \quad u_2 = 0, \quad T_2 = T_c, \tag{6b}$$

$$y = 0, \quad v_1 = 0, \quad \frac{\partial T_1}{\partial y} = 0, \tag{6c}$$

Contributed by the Heat Transfer Division for publication in the JOURNAL OF HEAT TRANSFER. Manuscript received by the Heat Transfer Division April 7, 1999; revision received October 6, 2000. Associate Editor: M. Hunt.

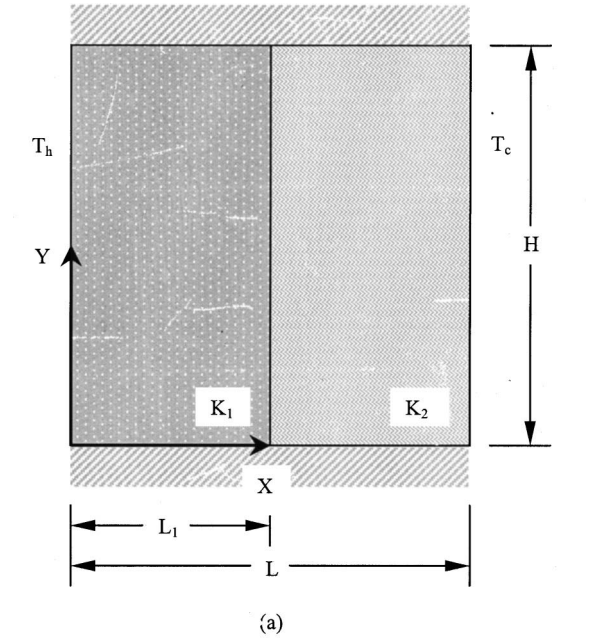

(a)

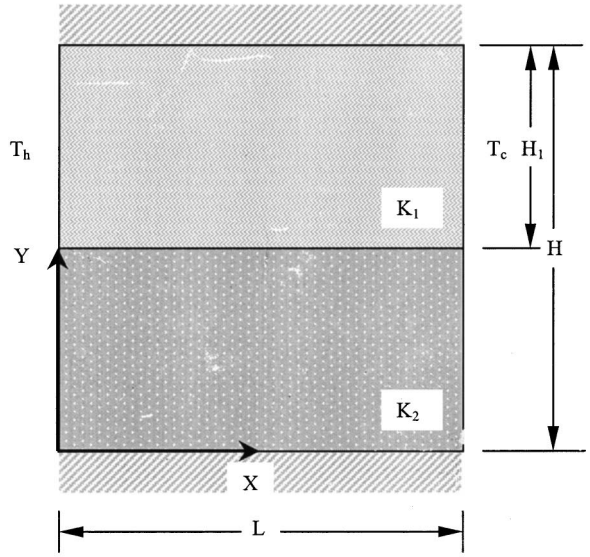

(b)

Fig. 1 A layered porous cavity subject to differential heating from vertical walls: (*a*) vertical sublayers; (*b*) horizontal sublayers.

$$y=H, \quad v_2=0, \quad \frac{\partial T_2}{\partial y}=0, \tag{6d}$$

$$y=H-H_1, \quad v_1=v_2, \quad p_1=p_2,$$

$$T_1=T_2, \quad k_1\frac{\partial T_1}{\partial y}=k_2\frac{\partial T_2}{\partial y}, \tag{6e}$$

The interface conditions, Eqs. (5*e*) and (6*e*), are formulated based on the continuity requirements for mass flow, pressure, temperature, and heat flux. The justification of these boundary conditions has been given by Rana et al. [3] as well as McKibbin and O'Sullivan [4].

After invoking Boussinesq's approximation for the body force term, the dimensionless governing equations in terms of stream function are given by

$$\frac{\partial^2\Psi_i}{\partial X^2}+\frac{\partial^2\Psi_i}{\partial Y^2}=-\mathrm{Ra}_i\frac{\partial\theta_i}{\partial X}, \tag{7}$$

$$\frac{\partial\Psi_i}{\partial Y}\frac{\partial\theta_i}{\partial X}+\frac{\partial\Psi_i}{\partial X}\frac{\partial\theta_i}{\partial Y}=\frac{\partial^2\theta_i}{\partial X^2}+\frac{\partial^2\theta_i}{\partial Y^2}, \tag{8}$$

whereas the boundary and interface conditions are expressed as

(*a*) Vertical Layers

$$X=0, \quad \Psi_1=0, \quad \theta_1=1, \tag{9a}$$

$$X=1, \quad \Psi_2=0, \quad \theta_2=1, \tag{9b}$$

$$Y=0, \quad X<\frac{L_1}{L}, \quad \Psi_1=0, \quad \frac{\partial\theta_1}{\partial Y}=0,$$

$$X>\frac{L_1}{L}, \quad \Psi_2=0, \quad \frac{\partial\theta_2}{\partial Y}=0, \tag{9c}$$

$$Y=1, \quad X<\frac{L_1}{L}, \quad \Psi_1=0, \quad \frac{\partial\theta_1}{\partial Y}=0,$$

$$X>\frac{L_1}{L}, \quad \Psi_2=0, \quad \frac{\partial\theta_2}{\partial Y}=0, \tag{9d}$$

$$X=\frac{L_1}{L}, \quad \Psi_1=\frac{\alpha_2}{\alpha_1}\Psi_2, \quad \frac{\partial\Psi_1}{\partial X}=\frac{K_1}{K_2}\frac{\alpha_2}{\alpha_1}\frac{\partial\Psi_2}{\partial X},$$

$$\theta_1=\theta_2, \quad \frac{\partial\theta_1}{\partial X}=\frac{k_2}{k_1}\frac{\partial\theta_2}{\partial X}. \tag{9e}$$

(*b*) Horizontal Layers

$$X=0, \quad Y<-\frac{H_1}{H}, \quad \Psi_1=0, \quad \theta_1=1,$$

$$Y>1-\frac{H_1}{H}, \quad \Psi_2=0, \quad \theta_2=1, \tag{10a}$$

$$X=1, \quad Y<1-\frac{H_1}{H}, \quad \Psi_1=0, \quad \theta_1=1,$$

$$Y>1-\frac{H_1}{H}, \quad \Psi_2=0, \quad \theta_2=1, \tag{10b}$$

$$Y=0, \quad \Psi_1=0, \quad \frac{\partial\theta_1}{\partial Y}=0, \tag{10c}$$

$$Y=1, \quad \Psi_2=0, \quad \frac{\partial\theta_2}{\partial Y}=0, \tag{10d}$$

$$Y=1-\frac{H_1}{H}, \quad \Psi_1=\frac{\alpha_2}{\alpha_1}\Psi_2, \quad \frac{\partial\Psi_1}{\partial Y}=\frac{K_1}{K_2}\frac{\alpha_2}{\alpha_1}\frac{\partial\Psi_2}{\partial Y},$$

$$\theta_1=\theta_2, \quad \frac{\partial\theta_1}{\partial Y}=\frac{k_2}{k_1}\frac{\partial\theta_2}{\partial Y}. \tag{10e}$$

Since both sublayers are saturated with the same fluid, it is important to note that $\alpha_1/\alpha_2=k_1/k_2$. The interface conditions have been implemented in the same way as described by Rana at al. [3]. Using the imaginary nodal points, Eqs. (9*e*) and (10*e*) can be discretized to give

(*a*) Vertical Layers

$$\Psi^1_{N,j}=\frac{1}{4}\Bigg[\Psi^1_{N,j-1}+\Psi^1_{N,j+1}+\frac{2K_2/K_1}{1+K_2/K_1}\Psi^1_{N-1,j}+\frac{2\alpha_2/\alpha_1}{1+K_2/K_1}\Psi^2_{N+1,j}+\frac{K_2/K_1}{1+K_2/K_1}\mathrm{Ra}_1(\theta^1_{N-2,j}-4\theta^1_{N-1,j}+4\theta^2_{N+1,j}-\theta^2_{N+2,j})\frac{\Delta X}{2}\Bigg] \tag{11a}$$

$$\theta^1_{N,j}=\frac{4\left(\theta^2_{N+1,j}+\frac{\alpha_1}{\alpha_2}\theta^1_{N-1,j}\right)-\left(\theta^2_{N-2,j}+\frac{\alpha_1}{\alpha_2}\theta^1_{N+2,j}\right)}{3\left(1+\frac{\alpha_1}{\alpha_2}\right)}. \tag{11b}$$

(*b*) Horizontal Layers

$$\Psi^1_{i,N}=\frac{1}{4}\Bigg[\Psi^1_{i+1,N}+\Psi^1_{i-1,N}+\frac{2K_2/K_1}{1+K_2/K_1}\Psi^1_{i,N-1}+\frac{2\alpha_2/\alpha_1}{1+K_2/K_1}\Psi^2_{i,N+1}+\frac{K_2/K_1}{1+K_2/K_1}\mathrm{Ra}_1(\theta^1_{i-2,N}-4\theta^1_{i-1,N}+4\theta^2_{i+1,N}-\theta^2_{i+2,N})\frac{\Delta X}{2}\Bigg] \tag{12a}$$

$$\theta^1_{i,N}=\frac{4\left(\theta^2_{i,N+1}+\frac{\alpha_1}{\alpha_2}\theta^1_{i,N-1}\right)-\left(\theta^2_{i,N-2}+\frac{\alpha_1}{\alpha_2}\theta^1_{i,N+2}\right)}{3\left(1+\frac{\alpha_1}{\alpha_2}\right)}, \tag{12b}$$

where the superscript denotes the sublayer and N is the nodal number at the interface.

The governing equations and boundary conditions are solved using a finite difference method which has been successfully employed by the author [1,2]. Gauss-Seidel iterative scheme has been employed in the solution procedure with a convergence criterion set to be 10^{-4} for the primary variables between two successive iterations. Uniform grids, 51×51, are used for most calculations in the present study while finer grids (81×81 and 101×101) are necessary for a few cases (primarily at $K_1/K_2=0.01$) to obtain converged solutions. It should be noted that once solutions converged using the grids specified above, further grid refinement does not produce any significant improvement in the calculated Nusselt numbers. As an additional check on the accuracy of the computational results, an overall energy balance has been performed after each calculation. For the present study, the energy balance for most calculations is satisfied within one percent (only a few cases are three percent). All computations in the present study have been performed on the Digital Alpha workstation. The required CPU time ranges from a few minutes to more than an hour, depending on the base Rayleigh number and sublayer permeability ratio. To validate the numerical code, the solutions thus obtained have been compared with those reported in the literature for the case of a homogeneous cavity by setting K_1/K_2 and α_1/α_2 to unity. The agreement is very good as shown in Fig. 2.

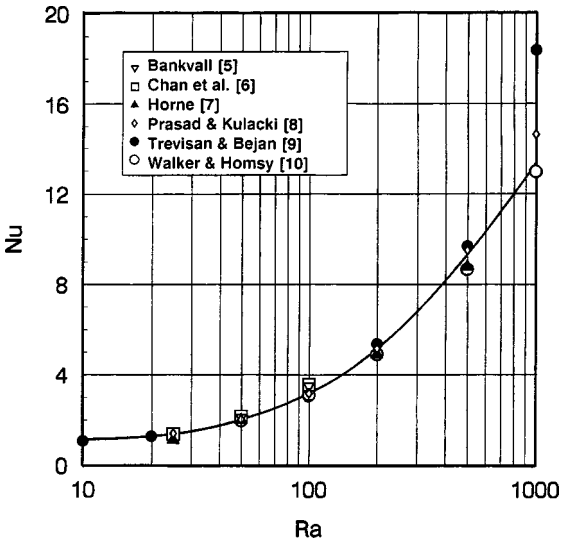

Fig. 2 Validation of numerical code ($K_1/K_2=1$); the result from the present study is represented by the solid line.

Results and Discussion

For a layered porous cavity, the flow and temperature profiles are very different from those of a homogeneous one due to the step change in permeability. In addition, the orientation and location of the layer interface have a significant impact on the flow and temperature fields as will be discussed separately in the following sections.

(*a*) Vertical Sublayers. When the sublayers are perpendicular to the primary heat flow direction, the results obtained are very similar to those reported earlier by Lai and Kulacki [2]. At a small base Rayleigh number Ra_1, convection starts in the layer with a higher permeability with the layer of lower permeability remaining in the conduction mode. With an increase in the base Rayleigh number, convective flow begins to penetrate the less permeable sublayer (Fig. 3). However, it should be noted that the mass transfer by convective flow across the interface is minimal for $K_1/K_2=100$. For a layered cavity of $K_1/K_2\gg1$, the second sublayer behaves like an impermeable layer and the convective flow is almost completely confined to the first sublayer. The heat transfer mechanism in each sublayer can be easily identified from Fig. 4. It is clear that convection is always the dominant heat transfer mode for a layered cavity of $K_1/K_2<1$ and it becomes the dominant mode for a layered cavity of $K_1/K_2>1$ only when the Rayleigh number is sufficiently large. For the latter case, the nearly

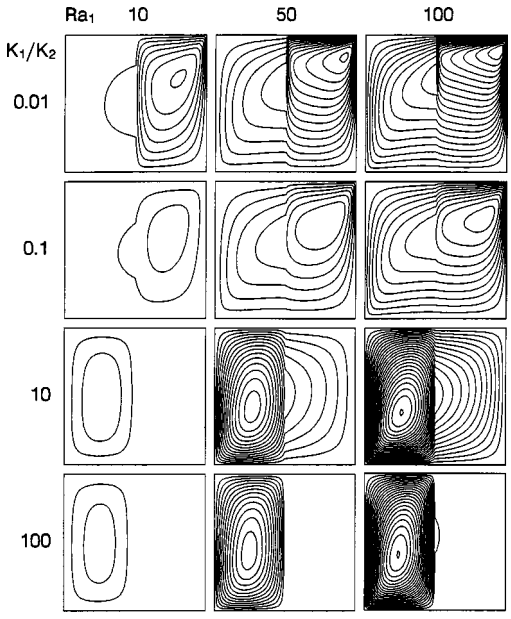

Fig. 3 Flow fields in a porous cavity with vertical sublayers ($L_1/L=0.5$, $\Delta\Psi=1$ for $K_1/K_2<1$ and $\Delta\Psi=0.1$ for $K_1/K_2>1$)

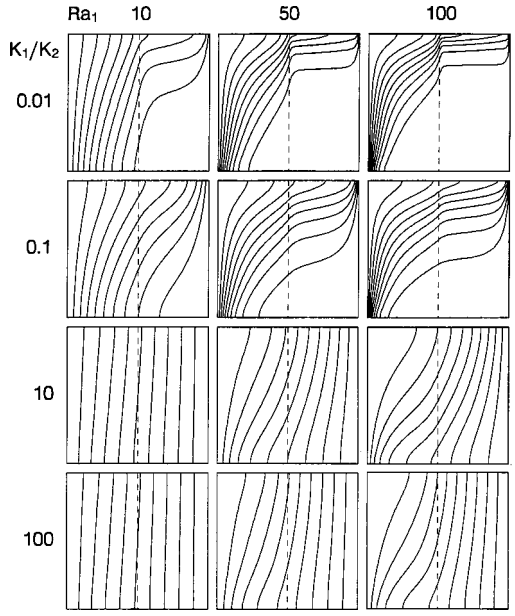

Fig. 4 Temperature fields in a porous cavity with two vertical sublayers ($L_1/L=0.5$, $\Delta\theta=0.1$)

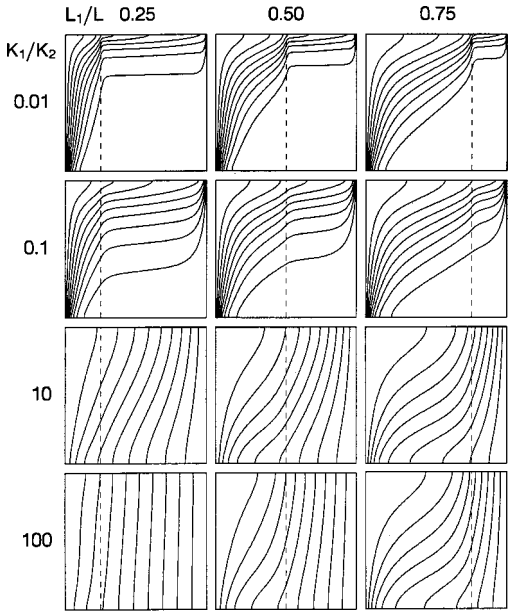

Fig. 6 Temperature fields in a porous cavity with two vertical sublayers ($Ra_1=100$, $\Delta\theta=0.1$)

vertical isotherms in the second sublayer indicate that conduction is the primary heat transfer mode in the less permeable layer.

For a fixed Rayleigh number, it is observed that the strength (in terms of the values of stream function) of convective cell increases with the thickness ratio L_1/L for $K_1/K_2>1$, and decreases for $K_1/K_2<1$ (Fig. 5). For $K_1/K_2<1$, a smaller thickness ratio leads to a small temperature gradient across the first layer and a higher gradient in the second layer (Fig. 6). This has consequently initiated a stronger convective cell in the second layer. With an increase in the thickness ratio, the temperature gradient across the first layer increases while it decreases in the second layer. Because of the permeability contrast, the result of this change is a slight increase in the strength of the convective cell in the first layer, but a significant reduction in the second layer. For $K_1/K_2>1$, the situation is just reversed to what has been described for $K_1/K_2<1$.

(***b***) **Horizontal Sublayers** When the sublayers are parallel to the primary heat flow direction, the results obtained on the other hand bear some similarities from those reported by Lai and Kulacki [1] for a layered porous cavity heated from below. Same as the previous case, convection also starts in the sublayer with a higher permeability (Fig. 7). With an increase in the base Rayleigh number Ra_1, convective flow begins to penetrate the less permeable sublayer. For $K_1/K_2=100$, the second (bottom) sublayer behaves like an impermeable wall and the flow field in the

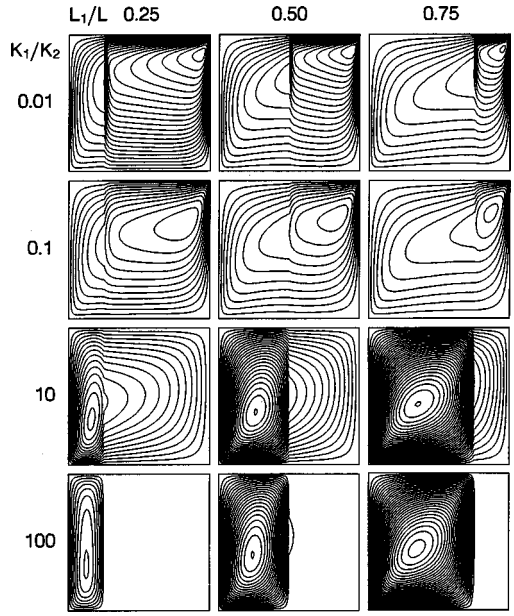

Fig. 5 Flow fields in a porous cavity with two vertical sublayers ($Ra_1=100$, $\Delta\Psi=0.1$ for $K_1/K_2<1$ and $\Delta\Psi=0.1$ for $K_1/K_2>1$)

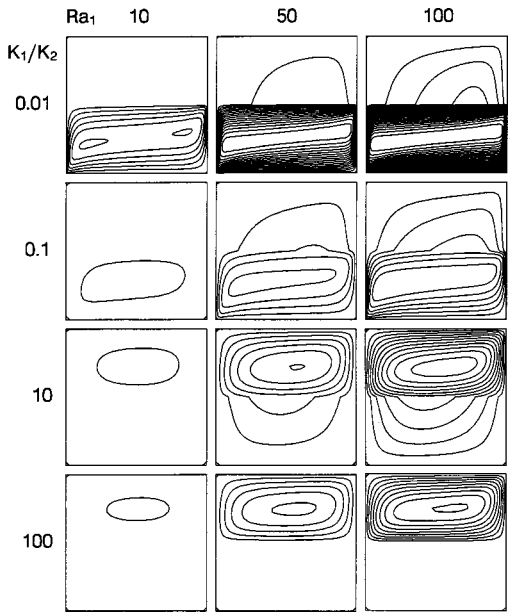

Fig. 7 Flow fields in a porous cavity with two horizontal sublayers ($H_1/H=0.5$, $\Delta\Psi=2$ for $K_1/K_2<1$ and $\Delta\Psi=0.25$ for $K_1/K_2>1$)

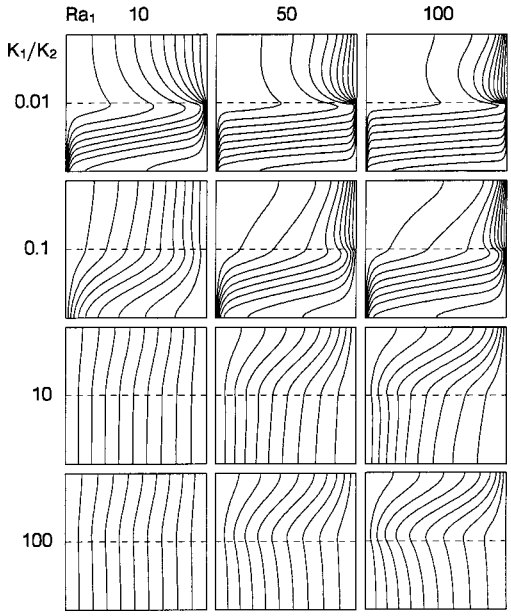

Fig. 8 Temperature fields in a porous cavity with horizontal sublayers ($H_1/H=0.5$, $\Delta\theta=0.1$)

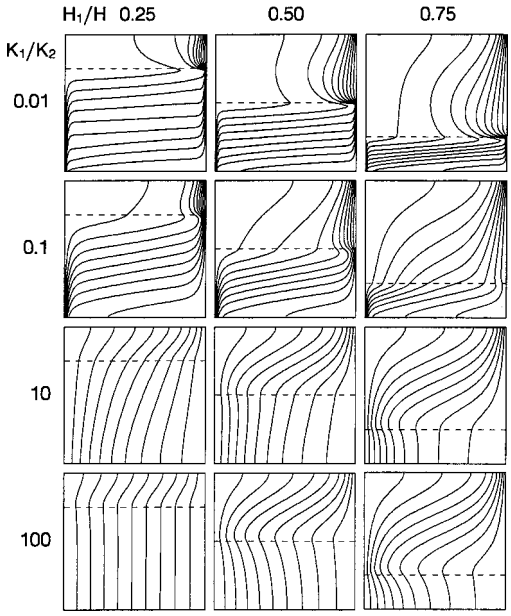

Fig. 10 Temperature fields in a porous cavity with horizontal sublayers ($Ra_1=100$, $\Delta\theta=0.1$)

first sublayer looks almost identical to that of a rectangular enclosure with an aspect ratio of 0.5 (Prasad and Kulacki, [8]). The difference in the heat transfer mode involved in each sublayer is particularly clear in the present case (Fig. 8). For $K_1/K_2<1$, heat transfer is primarily by conduction in the less permeable (upper) layer, thus the temperature field is characterized by near evenly spaced isotherms. For $K_1/K_2>1$, on the other hand, heat transfer is always by convection in the layer with a higher permeability and the temperature field becomes stratified as the Rayleigh number increases.

For a given base Rayleigh number Ra_1, it is observed that the strength of convective cell increases with the thickness ratio H_1/H for $K_1/K_2>1$, and decreases for $K_1/K_2<1$ (Fig. 9). Also noticed is that the penetration of convective flow increases with the thickness ratio for $K_1/K_2<1$ and decreases for $K_1/K_2>1$. It is also clear from Fig. 10 that the flow penetration to the less permeable layer is enhanced by the additional heat transfer from the interface. For $K_1/K_2<1$, the contribution to total heat transfer by conduction from the less permeable layer increases as the thickness ratio increases, which is evident from the isotherms displayed in Fig. 10. On the other hand, for $K_1/K_2>1$, the contribution by convection from the more permeable layer increases as the thickness ratio increases.

For the present study, the total heat transfer from the cavity is of the greatest interest and is given in terms of the Nusselt number,

$$\mathrm{Nu}=-\int_0^1 \frac{\partial\theta}{\partial X}\,dY. \tag{13}$$

Physically, this represents the total heat fluxes from the cavity wall.

It is observed that the Nusselt number for a layered cavity of $K_1/K_2<1$ is always greater than that of a homogeneous one while it is constantly less for a system with $K_1/K_2>1$. In addition, it is observed that, at a given base Rayleigh number Ra_1, the

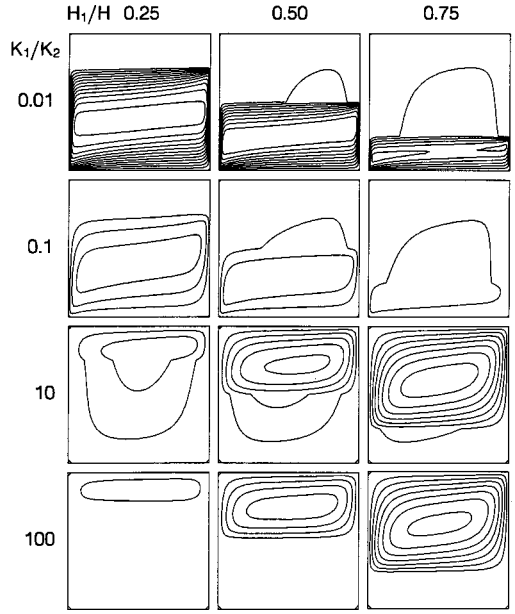

Fig. 9 Flow fields in a porous cavity with horizontal sublayers ($Ra_1=100$, $\Delta\Psi=5$ for $K_1/K_2<1$ and $\Delta\Psi=0.5$ for $K_1/K_2>1$)

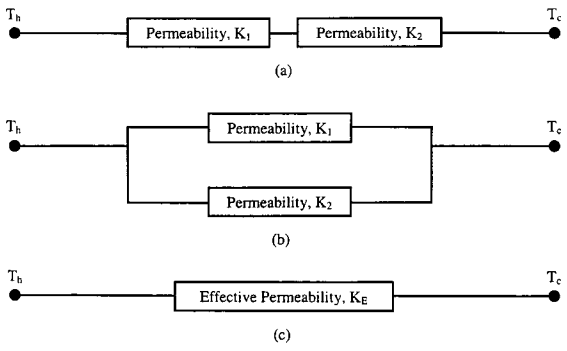

Fig. 11 Electric circuit analogy for natural convection in a layered porous cavity: (*a*) vertical sublayers; (*b*) horizontal sublayers; (*c*) an equivalent homogeneous layer.

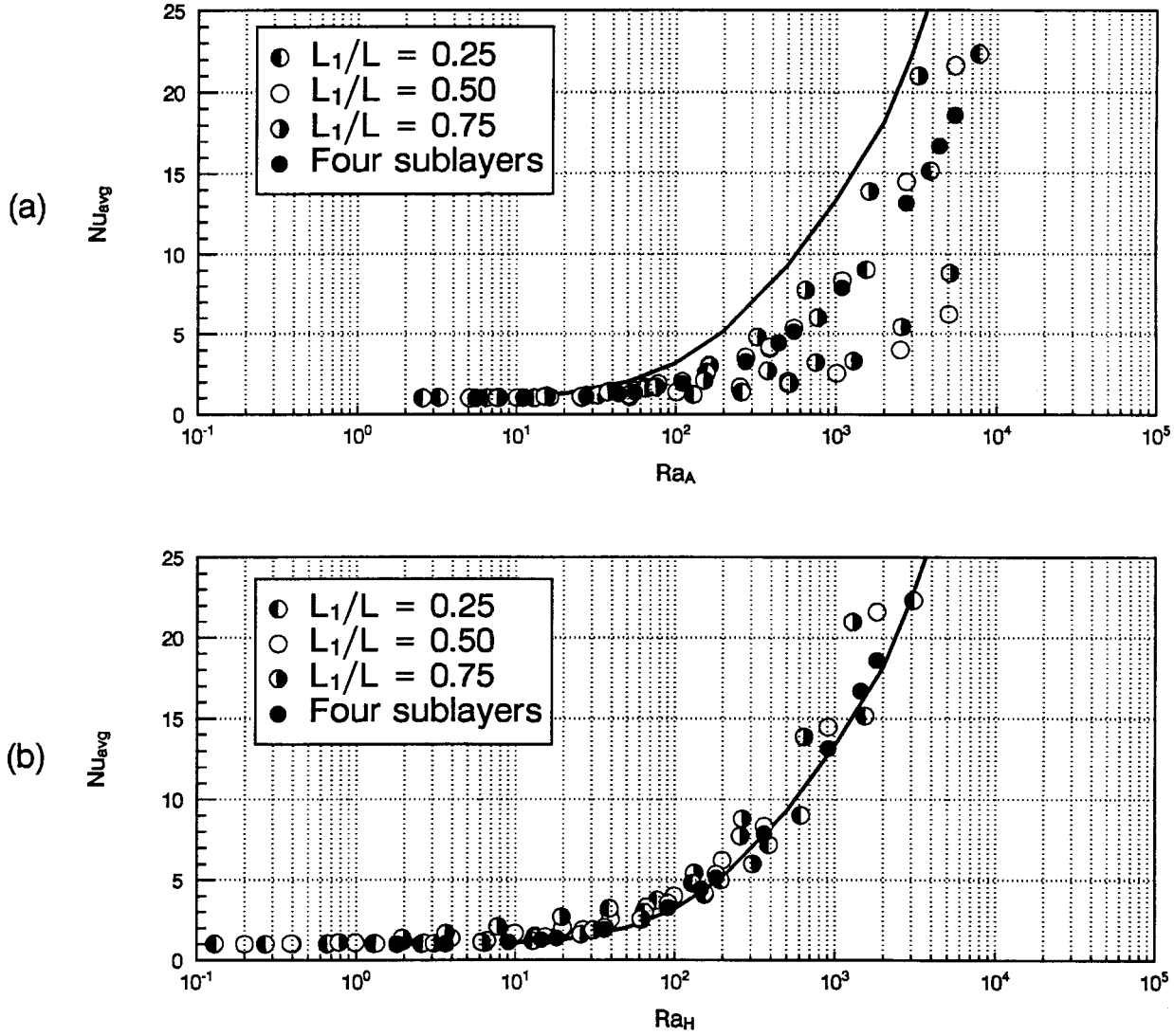

Fig. 12 Heat transfer results for a porous cavity with vertical sublayers: (*a*) arithmetic mean; (*b*) harmonic mean.

heat transfer rate is higher for a horizontally layered cavity than that for a vertically layered cavity. As is clear from the temperature profiles (Figs. 8 and 10), for a horizontal layered cavity, the upper sublayer is not only subject to a differential heating from vertical walls, but also subject to a non-uniform heating from below due to a non-uniform temperature distribution along the interface. As a result, a horizontally layered cavity transfers more heat than a vertically layered cavity at a given temperature difference across the cavity.

As mentioned earlier, it is desirable to use a lumped system analysis for problems involving a layered system. Here, two averaging schemes are examined for their appropriateness in defining an effective permeability for such a system. One is based on the arithmetic average while the other is based on the harmonic average. The expressions for these averaging techniques are given below.

(*a*) Vertical Layers

$$\overline{K}_A = \frac{L_1}{L} K_1 + \left(1 - \frac{L_1}{L}\right) K_2 \tag{14a}$$

$$\frac{1}{\overline{K}_H} = \frac{L_1/L}{K_1} + \frac{(1 - L_1/L)}{K_2} \tag{14b}$$

(*b*) Horizontal Layers

$$\overline{K}_A = \frac{H_1}{H} K_1 + \left(1 - \frac{H_1}{H}\right) K_2 \tag{15a}$$

$$\frac{1}{\overline{K}_H} = \frac{H_1/H}{K_1} + \frac{(1 - H_1/H)}{K_2} \tag{15b}$$

For flows in porous media, the flow resistance is inversely proportional to the permeability. Observing the similarity between the present problem and that of electric current in a resistance circuit, one would attempt to define the effective permeability in the same manner as that of the equivalent resistance of an electric circuit. Based on the analogy of electric circuit (Fig. 11), it is expected that the effective permeability defined by arithmetic average should work well for a system in which heat flows in parallel (e.g., a horizontally layered cavity) and the one by harmonic average would be appropriate for a system in which heat flows in series (e.g., a vertically layered cavity).

The heat transfer results are summarized in Figs. 12 and 13 as a function of the effective Rayleigh number which is defined using the effective permeability given in Eqs. (14) and (15). Also shown in these figures is the numerical result obtained from a homogeneous cavity [11], which can be adequately correlated by

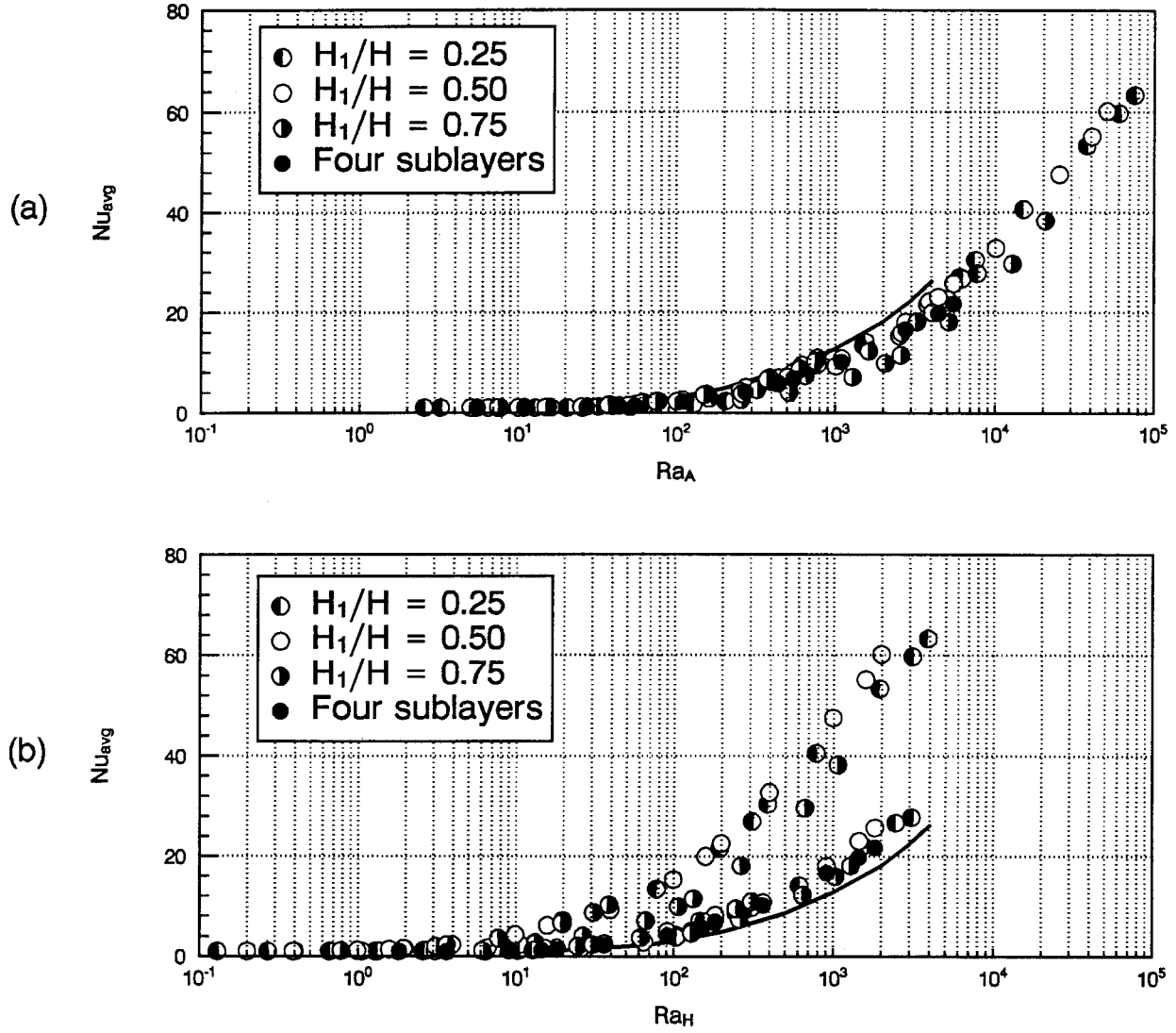

Fig. 13 Heat transfer results for a porous cavity with horizontal sublayers: (*a*) arithmetic mean; (*b*) harmonic mean.

$$Nu = 0.137\,Ra^{0.704}, \quad \text{for } Ra > 100. \tag{16}$$

Since heat transfer is mainly by conduction at a small Rayleigh number, the results obtained from the two effective permeabilities defined above do not differ much from each other. However, when convection becomes dominant at a large Rayleigh number, the discrepancy between these two results begins to widen up. For a vertically layered system, despite some scattering, the results obtained from using the harmonic-average permeability do provide a better agreement with the correlation (Eq. (16)) than those using the arithmetic average. On the other hand, for a horizontally layered system, the results based on the arithmetic-average permeability conform better to the correlation than those by the harmonic average. To further confirm the results obtained above, additional computations have been performed by Leong [12]. For these additional cases, the cavity is evenly divided to four sublayers with alternate permeabilities (i.e., $K_1 = K_3$ and $K_2 = K_4$). From the results obtained, the success of using the lumped system approach has been further demonstrated. Clearly, using this approach can greatly simplify the problem. However, there is one major drawback of this approach, that is, it completely ignores the differences in the layer structure. For example, if a cavity has two sublayers of the same thickness, one would obtain the same effective permeability even if the sublayers were interchanged. Although the heat transfer results for these two cases might be the same (if the lumped system approach were employed), the flow and temperature profiles inside the cavity would be very different from each other.

Conclusions

Heat transfer across a layered porous cavity has been numerically examined. Based on the results obtained, the feasibility of using lumped-system approach is the heat transfer analysis of a layered system is evaluated. It is found that a lumped-system approach is applicable as long as the effective permeability is correctly characterized. Employing the analogy of electric circuit, one can define the effective permeability using two averaging techniques. As to which effective permeability to use in the analysis, it is strongly dependent on the layer structure and the primary heat flow direction. When the sublayers are parallel to the primary heat flow direction, it is found that the effective permeability defined by the arithmetic average produces very good results. On the other hand, when the sublayers are perpendicular to the primary heat flow, the results based on the harmonic mean permeability have better agreement with the numerical prediction. While the

present study has explored a fundamental heat transfer problem in a layered porous cavity, the study has primarily focused on the effect of permeability contrast. Effects of other thermophysical properties on the applicability of lumped system analysis to a layered system await further study.

Nomenclature

H = height of the porous cavity, [m]
K = permeability, [m^2]
L = width of the porous cavity, [m]
Ra_i = sublayer Rayleigh number, $K_i g\beta(T_h-T_c)L/\alpha_i v$
Ra_1 = Rayleigh number based on the first sublayer properties, $K_1 g\beta(T_h-T_c)L/\alpha_1 v$
Ra_A = Rayleigh number based on the arithmetic average permeability, $\overline{K}_A g\beta(T_h-T_c)L/\alpha_1 v$
Ra_H = Rayleigh number based on the harmonic average permeability, $\overline{K}_H g\beta(T_h-T_c)L/\alpha_1 v$
U_i = dimensionless velocity in the x-direction, $U_i=\partial\Psi_i/\partial Y$
u_i = Darcy velocity in the x-direction, $u_i=\alpha_1 U_i/L$, [m/s]
V_i = dimensionless velocity in the y-direction, $V_i=-\partial\Psi_i/\partial X$
v_i = Darcy velocity in the y-direction, $v_i=\alpha_1 V_i/L$, [m/s]
α = thermal diffusivity of porous medium, $k/(\rho c_p)_f$, [m^2/s]
θ = dimensionless temperature, $(T-T_c)/(T_h-T_c)$
Ψ = dimensionless stream function

Subscript

f = fluid
i = index for sublayer ($i=1,2,3,4$)

References

[1] Lai, F. C., and Kulacki, F. A., 1987, ''Natural Convection in Layered Porous Media Partially Heated from Below,'' *Heat Transfer in Geophysical and Geothermal System*, K. Vafai et al., eds., ASME, New York, **HTD-Vol. 76**, pp. 27–36.
[2] Lai, F. C., and Kulacki, F. A., 1988, ''Natural Convection across a Vertical Layered Porous Cavity,'' *Int. J. Heat Mass Transf.*, **31**, pp. 1247–1260.
[3] Rana, R., Horne, R. N., and Cheng, P., 1979, ''Natural Convection in a Multi-Layered Geothermal Reservoir,'' ASME J. Heat Transfer , **101**, pp. 411–416.
[4] McKibbin, R., and O'Sullivan, M. J., 1981, ''Heat Transfer in a Layered Porous Medium Heated from Below,'' J. Fluid Mech., **111**, pp. 141–173.
[5] Bankvall, C. G., 1974, ''Natural Convection in Vertical Permeable Space,'' *Warme-und Stoffubertragune*, **7**, pp. 22–30.
[6] Chan, B. K. C., Ivey, C. M., and Barry, J. M., 1970, ''Natural Convection in Enclosed Porous Media with Rectangular Boundaries,'' ASME J. Heat Transfer, **92**, pp. 21–27.
[7] Horne, R., 1975, ''Transient Effects in Geothermal Convective Systems,'' Ph.D. thesis, University of Auckland, New Zealand.
[8] Prasad, V., and Kulacki, F. A., 1984, ''Convective Heat Transfer in a Rectangular Porous Cavity—Effect of Aspect Ratio on Flow Structure and Heat Transfer,'' ASME J. Heat Transfer , **106**, pp. 158–165.
[9] Trevisan, O. V., and Bejan, A., 1985, ''Natural Convection with Combined Heat and Mass Transfer Buoyancy Effects in a Porous Medium,'' *Int. J. Heat Mass Transf.*, **28**, pp. 1597–1611.
[10] Walker, K. L., and Homsy, G. M., 1978, ''Convection in a Porous Cavity,'' J. Fluid Mech., **97**, pp. 449–474.
[11] Prasad, V., and Kulacki, F. A., 1984, ''Natural Convection in a Rectangular Porous Cavity with Constant Heat Flux on One Vertical Wall,'' ASME J. Heat Transfer , **106**, pp. 152–157.
[12] Leong, J. K., 1999, ''Natural Convection in Layered Porous Cavities,'' M.S. thesis, University of Oklahoma, Norman, OK.

Formulation and Numerical Solution of Non-Local Thermal Equilibrium Equations for Multiple Gas/Solid Porous Metal Hydride Reactors

George M. Lloyd
Mem. ASME
Postdoctoral Associate
Department of Civil and Materials Engineering,
University of Illinois at Chicago,
842 West Taylor Street,
Chicago, IL 60607
e-mail: lloydg@asme.org/glloyd@uic.edu

A. Razani
Professor
Department of Mechanical Engineering,
University of New Mexico,
Albuquerque, NM 87106

Kwang J. Kim
Research Professor
Department of Mechanical Engineering,
University of New Mexico,
Albuquerque, NM 87106

The assumption of local thermal equilibrium (LTE) is very common in the study of reacting flows in porous media. The assumption simplifies the structure of the solutions and places fewer constraints on computational methods for the domain and boundary conditions. However, in certain systems, such as gas/solid metal hydride reactors, the boundary conditions may impose high energy transfer rates which produce slowly evolving phase change fronts coupled with rapid kinetics. Overall performance of the systems is proportional to the release or absorption of hydrogen, and this is sensitively related to temperature. Thus, capturing local departures from LTE is required. This paper directly evaluates the influence of these effects by solving an NLTE (non-local thermal equilibrium) formulation for coupled reactors as a function of the interphase heat transfer coefficient, h_{sf}. *The reactor dynamics and overall energy balances are compared to solutions previously obtained from LTE calculations. The results appear to be the first NLTE results for coupled reactors. They confirm the existence of NLTE effects and suggest the magnitude of* h_{sf} *for which they can be minimized.* [DOI: 10.1115/1.1370521]

Keywords: Heat Transfer, Phase Change, Porous Media, Sorption Heat Pump, Two-Phase Flow

Introduction

A large literature describing computational studies of heat pumps based upon metal hydride gas/solid reactors has evolved during the last twenty years [1]. These heat pumps utilize the enthalpy change ΔH associated with certain metal hydride/hydrogen reactions, such as the following:

$$\mathrm{LaNi_5H}_{x_{\alpha_{\max}}} + \left(\frac{x_{\beta_{\min}} - x_{\alpha_{\max}}}{2}\right)\mathrm{H_2} \overset{p}{\underset{T}{\rightleftharpoons}} \underset{\substack{\text{metal hydride}\\ \text{phase}}}{\mathrm{LaNi_5H}_{x_{\beta_{\min}}}} + \left(\frac{x_{\beta_{\min}} - x_{\alpha_{\max}}}{2}\right)\Delta H \qquad (1)$$

for heat transformation [2]. The purpose of the aforementioned studies has been to understand the influence of the many reacting and non-reacting subsystems upon different measures of performance. Models of varying complexity have been formulated for this purpose. One assumption nearly always used is $T^s \approx T^f$-typically refered to as *local thermal equilibrium*.

While this assumption greatly simplifies analysis, and may be reasonable for certain problems, there exists neither theory nor sufficient experimental heat transfer data for powder metal hydride compacts on which to universally adopt the LTE assumption [3]. Indeed, scrutiny of the reactor dynamics in the vicinity of high temperature reactor boundaries has shown high energy fluxes promote the slow evolution of spatially confined phase change fronts, as a result of large values of ΔH [4]. The injection of hydrogen at depressed or elevated temperatures was also observed to induce the same phenomenon [5]. Such spatially concentrated non-equilibrium behavior constitutes an important reason to study the limitations of the LTE assumption in the analysis of metal hydride heat pumps.

There is a well established literature on the heat and mass transfer characteristics of non-equilibrium packed-beds and porous structures for catalytic operations, reacting columns, and for widespread heat and mass absorption operations [6,7,8]. However, there have been only a few studies of this type for metal hydride heat pumps, such as depicted in Fig. 1. Jemni and Nasrallah [9] studied two-dimensional, two phase-temperature desorption for a single reactor. They concluded that the difference between the solid phase and fluid phase was important near the reactor wall boundary. Mhimid [10] applied this work to a zeolite-water reactor during desorption for very long desorption times, with similar findings. Kuznetsov and Vafai [11] began with a general set of mass and energy equations (again, for a single reactor) based on the volume-averaging technique and sought to develop criteria to distinguish among several simplifying assumptions. In the inlet region during desorption, they concluded that non-local thermal equilibrium effects could be predicted using the dimensionless parameter, $\rho_{H_2} v c_{p_{H_2}} / (L_R h_{sf} dA_{sf}/dV_{(c)})$, where L_R refers to the reactor length.

The extension of these conclusions to predictive statements on heat pump performance is not straightforward since the fraction of the hydrogen inventory transferred within the finite time period of an imposed cycle is strongly coupled to transient factors affecting the local reaction rate through an Arrenhius type expression:

$$\left.\frac{\partial x(\underline{r},t)}{\partial t}\right)_{\underline{r}} = \mathrm{A}e^{-E_a/\bar{R}T(\underline{r},t)} f[p_{H_2}(\underline{r},t), p_{eq_{H_2}}(x)]. \qquad (2)$$

This observation initiated the formulation and solution of a system of NLTE (non-LTE) equations in order to study the influence of

Contributed by the Heat Transfer Division for publication in the JOURNAL OF HEAT TRANSFER. Manuscript received by the Heat Transfer Division October 25, 1999; revision received December 6, 2000. Associate Editor: C. Beckermann.

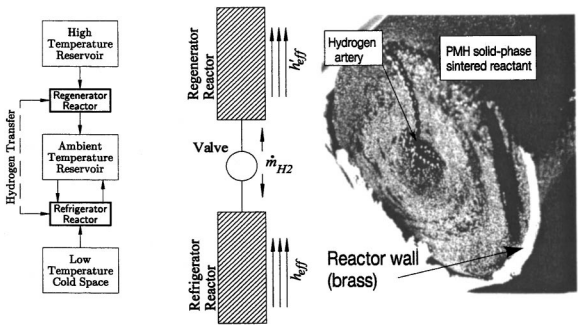

Fig. 1 Block diagram of the heat pump system studied in the paper (left and middle). Two reactors exchange hydrogen during a cycle, and each communicates with three thermal reservoirs (right) photograph of experimental reactor.

two-temperature effects on the reactor dynamics and overall performance of a heat-driven cycle previously investigated from the LTE framework.

Formulation

The heat pump system model consists of two reactors coupled by a thin tube. The reactors are filled with a porous metal hydride reactant. The configuration for the system and experimental characterization of the reactors are described elsewhere [4,2]. The model of the heat and mass transfer processes at the microscopic level in the reactor matrix are developed using the representative equivalent volume (REV) approach which, when restricted to one dimension in cylindrical coordinates, become [12] the continuity equation,

$$\left(\frac{K\gamma}{\bar{R}\mu}\right)\left\{p\frac{\partial^2 p}{\partial r^2}+\frac{\partial p}{\partial r}\left[\frac{p}{r}+\frac{\partial p}{\partial r}-\frac{p}{\overset{f}{T}}\frac{\partial \overset{f}{T}}{\partial r}\right]\right\}+\dot{\varphi}\overset{f}{T}=\left(\frac{\phi\gamma}{\bar{R}}\right)\left[\frac{\partial p}{\partial t}-\frac{p}{\overset{f}{T}}\frac{\partial \overset{f}{T}}{\partial t}\right] \tag{3}$$

a *solid* phase energy equation,

$$(\overset{f}{T}-\overset{s}{T})h_{sf}\frac{dA_{sf}}{dV_{(c)}}+(1-\phi)k_s\left[\frac{1}{r}\frac{\partial \overset{s}{T}}{\partial r}+\frac{\partial^2 \overset{s}{T}}{\partial r^2}\right]+g-c_{pf}\dot{\varphi}\begin{cases}0, & \dot{\varphi}>0,\ \text{desorp.}\\ \overset{f}{T}-\overset{s}{T}, & \dot{\varphi}<0,\ \text{absorp.}\end{cases}=(1-\phi)\rho_s c_{v_s}\frac{\partial \overset{s}{T}}{\partial t},\ (W/m^3_{(c)}) \tag{4}$$

and a *fluid* phase energy equation (assuming hydrogen is ideal),

$$(\overset{s}{T}-\overset{f}{T})h_{sf}\frac{dA_{sf}}{dV_{(c)}}+\phi k_f\left[\frac{1}{r}\frac{\partial \overset{f}{T}}{\partial r}+\frac{\partial^2 \overset{f}{T}}{\partial r^2}\right]+\frac{c_{pf}\gamma K}{\bar{R}_\mu}\left[\frac{p}{r}\frac{\partial p}{\partial r}+\left(\frac{\partial p}{\partial r}\right)^2+p\frac{\partial^2 p}{\partial r^2}\right]+c_{pf}\dot{\varphi}\begin{cases}\overset{s}{T}-\overset{f}{T}, & \dot{\varphi}>0,\text{desorp.}\\ 0, & \dot{\varphi}<0,\text{absorp.}\end{cases}=\left(\frac{\phi c_{v_f}\gamma}{\bar{R}}\right)\frac{\partial p}{\partial t},\ (W/m^3_{(c)}). \tag{5}$$

The parameter h_{sf} is an empirical parameter typically called the *interstitial convection heat transfer coefficient*. A standard correlation for h_{sf} (for spherical particles) is available [[13], pg. 403] $\mathrm{Nu}_D=h_{sf}D/k_f=2+1.1\,\mathrm{Re}_D^{0.6}\mathrm{Pr}^{1/3}$. Fukuda [14] derive a similar relationship $\mathrm{Nu}=f(\mathrm{Re})$ for a larger class of porous materials. In any case, the contribution from the second term is ignored in this work due to the small values of Re_D (or $\mathrm{Re}_{\sqrt{K}}$) [15].

The parameter dA_{sf}/dV is the specific surface area; values for cohesive materials (sintered spherical copper powders) are reported to depend quite sensitively on porosity, densification history, applied tractions, internal stress history, and other factors [16]. The product of these two has been referred to as the volumetric heat transfer coefficient α_v [14]. Variants of Eq. (4) and Eq. (5) are customarily referred to as the continuous solid model [[13], p. 402]. The difficulty in rigorously treating interphase enthalpy transport is not resolved in most treatments; it is handled here heuristically through the interphase transport of sensible heat. The source terms g and $\dot{\varphi}$ are functions of the hydride particle density $\wp$, and the local reaction rate Eq. (2) [4].

An order-of-magnitude prediction for NLTE effects can be obtained from these correlations and the solid-phase energy equation, Eq. (4), using values for D in the range 10 to 100 (μm):

$$\left|\overset{f}{T}-\overset{s}{T}\right|\sim\frac{|g|}{h_{sf}dA_{sf}/dV}=\frac{5\times10^7(\mathrm{W/m^3\cdot K})}{10^3(\mathrm{W/m^2\cdot K})10^4(\mathrm{m^2/m^3})}=5(\mathrm{K}). \tag{6}$$

Estimates for g were taken from regions of intense absorption or desorption in the LTE calculations.

Boundary Conditions

The NLTE model assumes (''assumption one'') that *the sensible energy resulting from transpiration from one reactor and injection into the other* is deposited within a macroscopically thin boundary layer on the injection side, as depicted in Fig. 2 [17]. The degree to which energy is transferred between the incoming phase and the resident phases can be expected to depend upon a characteristic time which is a function of the injection velocity and the resident matrix constituents and their thermodynamic state. For sintered porous metal compacts it is reasonable to conjecture that the boundary energy transfer is dominated by processes confined within a microscopically significant entrance depth δr (''assumption two''). A value of $\delta r=0.1$ (mm) was used, corresponding roughly to 3–5 times the characteristic diameter of the starting powder size (Fig. 1).

From assumption one, the transport of sensible heat is represented as a boundary heat flux between fluid phases. Phenomenologically this approach assumes the dominant mechanism of energy transport is from one fluid phase to the other. This avoids the problem of introducing a ''boundary'' surface convection coefficient [8]. Assumptions one and two lead to:

$$-(c_{p_f}\rho_f v_f)[\overset{f}{T}(r_0,t)-\overset{f}{T}(r_{0'},t)]A_0=-k_{f'}\frac{\partial \overset{f}{T}(r_{0'},t)}{\partial r}A_{0'} \tag{7a}$$

$$h_{sf'}\frac{dA_{sf'}}{dV_{(c)'}}[\overset{f}{T}(r_{0'},t)-\overset{s}{T}(r_{0'},t)]V_{0'}=-k_{s'}\frac{\partial \overset{s}{T}(r_{0'},t)}{\partial r}A_{0'}. \tag{7b}$$

In Eq. (7*b*) $V_{0'}=\pi[(r_{0'}+\delta r)^2-r_{0'}^2]L'$ denotes the deposition volume. Equation (7) uses nomenclature consistent for transpiration *from* the refrigerator *to* the regenerator. Equation (7*a*) and Eq. (7*b*) apply to the *regenerator*. The remaining two boundary conditions for the transpiring refrigerator are constraints on the phase temperature gradients—i.e., the adiabatic approximations,

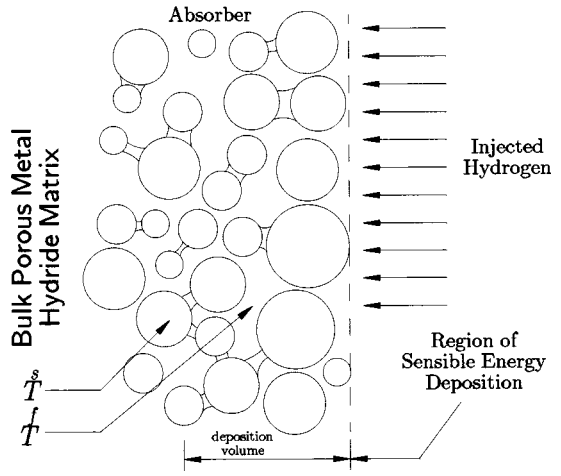

Fig. 2 Boundary region at $r_{0'}, t$. Hydrogen at $\overset{f}{T}(r_0, t)$ is injected into the reactor with interface phase temperatures $\overset{f}{T}(r_{0'}, t)$ and $\overset{s}{T}(r_{0'}, t)$

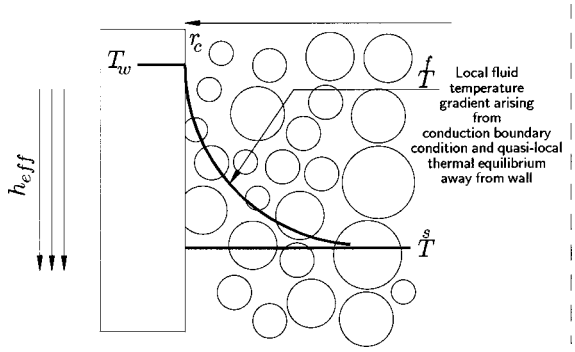

Fig. 3 Schematic diagram of conditions existing at the microscopic level dictating idealizations made for interface boundary conditions

$$\frac{\partial \overset{s}{T}(r_0,t)}{\partial r} = 0 \tag{8a}$$

$$\frac{\partial \overset{f}{T}(r_0,t)}{\partial r} = 0 \tag{8b}$$

since there is no thermal connection of the boundary to the regenerator. When the reactors are coupled the mechanical driving potentials must be equal:

$$p(r_{0'},t) = p(r_0,t). \tag{9}$$

Finally, the steady-state mass flow condition,

$$\left(\frac{K'}{K}\right)\frac{1}{T(r_{0'},t)}\frac{\partial p(r_{0'},t)}{\partial r}\frac{A_{0'}}{A_0} = -\frac{1}{T(r_0,t)}\frac{\partial p(r_0,t)}{\partial r} \tag{10}$$

must be satisfied. There are six unknowns: p, p', $\overset{f}{T}$, $\overset{f}{T'}$, $\overset{s}{T}$, and $\overset{s}{T'}$ Equation (7*a*) and, Eq. (7*b*), Eq. (8*a*), Eq. (8*b*), Eq. (9), and Eq. (10) provide the required boundary conditions at the core.

From a physical and computational perspective, the reactor wall boundary conditions are more difficult to treat adequately than the coupling boundary conditions. The basic reason is illustrated in Fig. 3, which depicts the temperature gradients expected to exist in the local region of the reactor-wall boundary. In a one dimensional geometry there is no tangential component to the hydrogen motion. Therefore, heat transfer between the wall and fluid phase must occur entirely through conduction,

$$T_w(t) = \overset{f}{T}(r_c,t). \tag{11}$$

As with the LTE model, the gradient of the solid-phase temperature is postulated to depend upon a solid-solid contact conductance, $h_{c_{sw}} (= 1000\,(\mathrm{W/m^2 \cdot K}))$:

$$-k_s \frac{\partial \overset{s}{T}(r_c,t)}{\partial r}(1-\phi)A_c = h_{c_{sw}}[\overset{s}{T}(r_c,t) - T_w(t)](1-\phi)A_c. \tag{12}$$

Eq. (11) and Eq. (12) are reasonable approximations for the macroscopic boundary conditions.

Numerical difficulties are introduced, however, by Eq. (11). Near the boundary, the use of a single, spatially homogeneous wall temperature in Eq. (11) implies the existence of a large temperature gradient in the fluid phase due to the condition $\overset{f}{T} \to \overset{s}{T}$, as shown in Fig. 3. For the most part, the gradients are also confined in time. For this reason, and because of the low thermal conductivity of hydrogen, the gradient of the fluid phase temperature was approximated using the same form as Eq. (12):

$$-k_f \frac{\partial \overset{f}{T}(r_c,t)}{\partial r}\phi A_c = h_{c_{fw}}[\overset{f}{T}(r_c,t) - T_w(t)]\phi A_c. \tag{13}$$

A value of $h_{c_{fw}} = 50\,(\mathrm{W/m^2 \cdot K})$ was used, selected in order to match the ratios $k_f/h_{c_{fw}}$ and $k_s/h_{c_{sw}}$, where $k_s = 5\,(\mathrm{W/m \cdot K})$—a value consistent with measurements [3] and previously shown to be an optimum choice [15]. Equation (12) and Eq. (13) are the wall boundary conditions for the NLTE model, in conjunction with the following energy balance on the reactor wall:

$$\frac{d(c_w \rho_w V_w T_w)}{dt} = h_{c_{sw}}[\overset{s}{T}(r_c,t) - T_w(t)](1-\phi)A_c + h_{c_{sf}}[\overset{f}{T}(r_c,t) - T_w(t)]\phi A_c - h_\infty A_f (T_w(t) - T_{\mathrm{res}}). \tag{14}$$

These equations complete the boundary conditions for the NLTE formulation.

Numerical Validation Methodology

The governing equations with p, $\overset{f}{T}$, $\overset{s}{T}$, and x as dependent variables were discretized using a centered-space approach with an explicit time integrator [12]. The approach is second order [18]. Double-precision arithmetic was used exclusively and bench-marked against extended-precision arithmetic; roundoff error was insignificant with this approach [19]. The discretization can be shown by standard methods to be consistent [12]. In a linear system the Lax-Equivalence Theorem ensures that the demonstration of consistency of the finite-difference scheme in conjunction with demonstration of stability is sufficient for the scheme to converge [20]. While the Lax-Equivalence Theorem does not apply to the problem here, the requirement of stability remains a necessary condition for convergence. In the method adopted here the following stability criterion;

$$\Delta t \leqslant \lambda \left(\frac{\min\limits_i \phi \cdot \mu \cdot (\min\limits_i \Delta r)^2}{2 \cdot \max\limits_i K \cdot \max\limits_i \rho} \right), \quad i \in [1,N] \cup [1',N'] \tag{15}$$

for the explicit scheme used was derived from a linearization of the gas flow equation [21], a procedure applied previously to models of thermal plasmas [22]. The parameter λ in Eq. (15) was included as a heuristic factor less than unity chosen to ensure

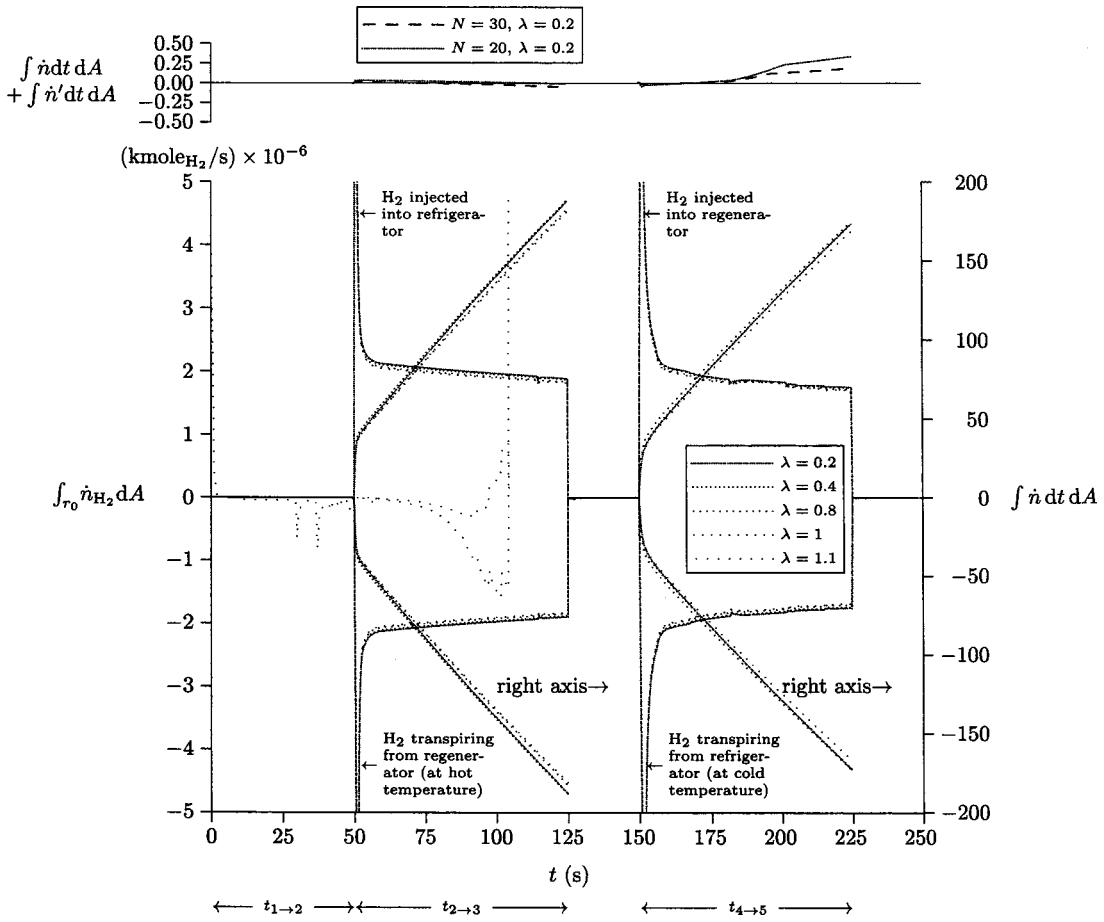

Fig. 4 Stability and convergence study of numerical method. Bottom plot: Effect of λ on boundary transport of H_2, for varying λ and constant zone size of $\Delta r = 0.40$ (mm). Top plot: variation in integral error for two grid sizes.

global stability. The applicability of Eq. (15) as a stability criterion was investigated by running a number of LTE test problems in which the grid size and stability parameter λ were varied. Two important results from these studies are summarized in Fig. 4.

The bottom strip plot of Fig. 4 shows the instantaneous and integral boundary transport of hydrogen (i.e., intra-reactor flow calculated at r_0 or $r_{0'}$) over a complete cycle using several values of λ. One result of this suite of calculations is that $\lambda \sim 1$ is sufficient for global stability including the boundary conditions. A second result is that for the grid size associated with $N=20$ convergence is shown as λ is decreased from unity. A value of $\lambda = 0.2$ appears reasonable (the value used throughout this work).

The top strip plot shows the residual integral error in the H_2 transferred between the two reactors for two grid spacings, at constant λ. Although many possible comparative parameters can be used to gage effects of generalized mesh refinements [23], $\int \dot{n}$ is used here in view of its fundamental importance to P and COP. An analysis of the enthalpy balance for the system was also examined in [5] in order to verify energy conservation.

Computational Results

A direct comparison between the LTE and NLTE cases was achieved by running two NLTE calculations with $h_{sf} = 100\,(\mathrm{W/m^2 \cdot K})$ and $h_{sf} = 1000\,(\mathrm{W/m^2 \cdot K})$. The basic parameters of the heat pump consisted of a temperature lift of $\Delta T = 20\,(\mathrm{C})$ in a refrigeration configuration, with an ambient reservoir at a temperature of 20 (C), a cold bath temperature of 0 (C), and a heat bath at 150 (C). These choices are appropriate for the two metal hydrides, $MmNi_{4.15}Fe_{0.85}$ and $LaNi_{4.3}Al_{0.7}$, for which equilibrium data was gathered from the literature and curved fitted [4]. These model parameters corresponded to a heat pump consisting of two optimized reactors in the sense of the optimization parameter Π_2 [4,15],

$$\Pi_2 = \frac{\text{energy transfered from the reactor}}{\text{thermal energy stored by the reactor}} = (A_w)\left(\frac{\Delta T}{R_r}\right)\left(\frac{t_{\text{cycle}}}{\Delta H_R}\right) = 0.74, \tag{16}$$

where A_w is the area of the heat transfer boundary. The heat pump cycle was identical for all calculations, and consisted of five subcycles, as follows: $t_{1\to2}$ is the pre-heating phase. Waste heat is transferred to the regenerator reactor through a thermal resistance R_r which incorporates convection and contact resistances. The reactors are uncoupled. $t_{2\to3}$ is the *charging* phase: the reactors are coupled and waste heat continues to be transferred to the regenerator, which desorbs hydrogen for absorption in the refrigerator reactor. The enthalpy of absorption is rejected. $t_{3\to4}$ is the first *equilibration* phase. Both reactors (uncoupled) are connected to the ambient heat bath. $t_{4\to5}$ is the active *cooling* phase. The reactors are again coupled. Desorption of hydrogen in the refrigerator causes heat to be absorbed from the cold space. Hydrogen is absorbed in the regenerator; the enthalpy of absorption is rejected. $t_{5\to6}$ is the second *equilibration* phase. The reactors are connected to the ambient heat bath and returned to the initial state.

An overall summary of the two NLTE calculations with the baseline LTE calculation is given in Table 1. From a system-optimization standpoint the NLTE calculations do not differ sub-

Table 1 Calculation summary

h_{sf} (W/m^2·K)	$Q_{preheat}$ (J)	Q_{charge} (J)	Q_{spol} (J)	COP	P (W/kg$_h$)
100 (NLTE1a)	5215.5	3941.4	2498.0	0.273	606.6
1000 (NLTE2)	5219.1	3825.4	2501.5	0.277	608.6
[a]∞	5253.9	4253.5	2784.5	0.293	672.6

[a] i.e., LTE calculation, $R_r = 0.00150$ (m^2·K/W).

stantially in predicted performance from the LTE calculation. *The essential conclusion is that for a reasonable lower bound of* $h_{sf} \cdot dA_{sf}/dV = 10^6$ (W/$m^3_{(c)}$·K) *for powder metal hydride compacts, power and efficiency may be predicted using the LTE formulation*. The conclusion is parenthetically restricted to the system optimized in the sense of $\Pi_2 = 0.74$ [4], the heat-driven cycle, and the present kinetic model.

Integral performance is not necessarily indicative of the presence or absence of NLTE behavior. Perhaps the most straightforward means of depicting this is through Figs. 5 and 6, which show the phase temperature difference fields $\overset{f}{T} - \overset{s}{T}$ for the two values of h_{sf} used. Fig. 5, ($h_{sf} = 100$), clearly shows that LTE is violated: phase temperature differences of ± 10 (K) are observed in the regenerator. Here, departures from LTE are widespread through the majority of the reacting matrix, and are particularly evident in regions where reaction fronts form. These NLTE regions are outlined with dashed rectangles in Fig. 5. The phase temperature differences in the refrigerator are smaller and more localized. Figure 6 ($h_{sf} = 1000$) shows phase temperature differences of the order ± 1 (K). In both calculations the magnitudes of the phase temperature differences are in agreement with Eq. (6).

Figure 7 is a field plot for $h_{sf} = 100$ of the mass source term $\dot{\varphi}$, which is directly proportional to the rate of absorption or desorption (Eq. (2)). In conjunction with Fig. 5 it shows that in regions of desorption, $\overset{f}{T} < \overset{s}{T}$; regions of absorption are primarily characterized by $\overset{f}{T} > \overset{s}{T}$. The former effect is due to the much greater solid-phase thermal conductivity. The phase change fronts deduced from the $\dot{\varphi}$ fields are qualitatively similar to those from the LTE calculation.

An overall assessment of differences is presented in the concentration field plot in Fig. 8, again for the case of $h_{sf} = 100$. In particular, the dashed contours in Fig. 8 are calculated from the LTE calculation and have been overlain on the solid NLTE contours. There are few notable differences. The core absorption front during $t_{4\to5}$(150–225 (s)) does advance further in the LTE case.

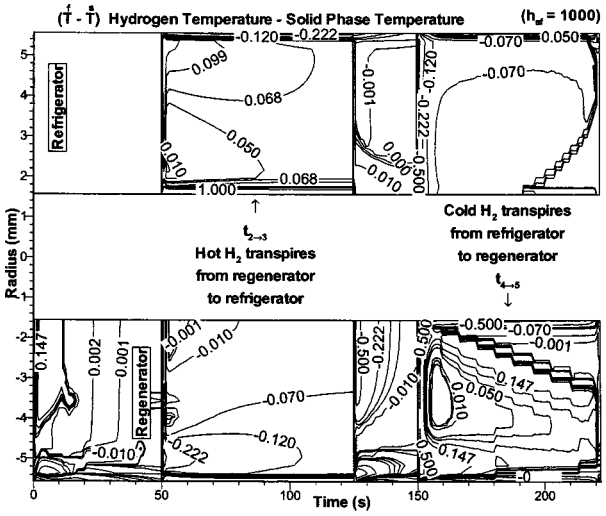

Fig. 6 Temperature difference, $\overset{T}{T} - \overset{s}{T}$, field for $h_{sf} = 1000$ (W/m^2·K). Dashed lines demarcate regions of significant NLTE effects.

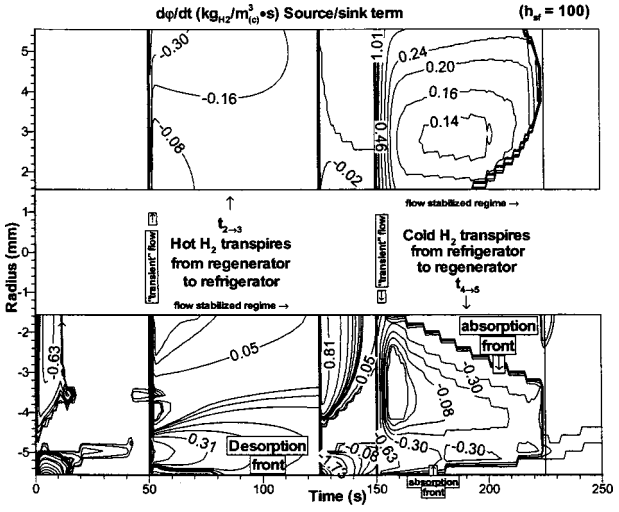

Fig. 7 Hydrogen desorption rate, $\dot{\varphi}$ for $h_{sf} = 100$ (W/m^2·K)

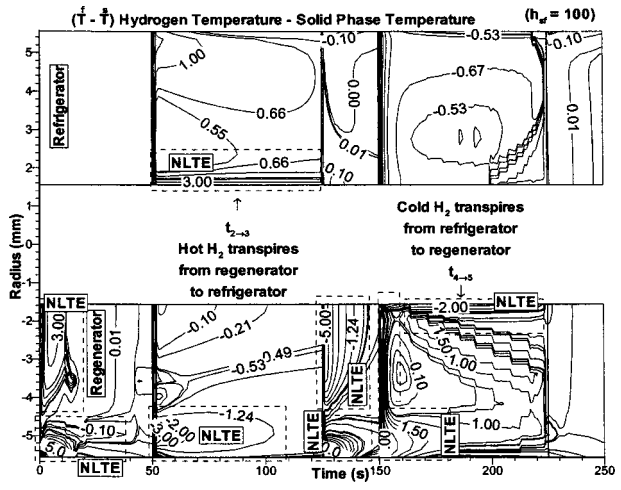

Fig. 5 Temperature difference, $\overset{T}{T} - \overset{s}{T}$, field for $h_{sf} = 100$ (W/m^2·K)

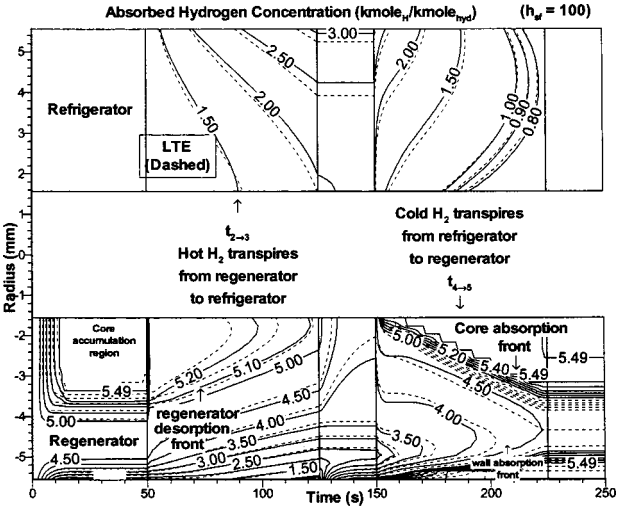

Fig. 8 Overlay of hydrogen concentration, x for $h_{sf} = 100$ (W/m^2·K) (solid) with LTE (dashed)

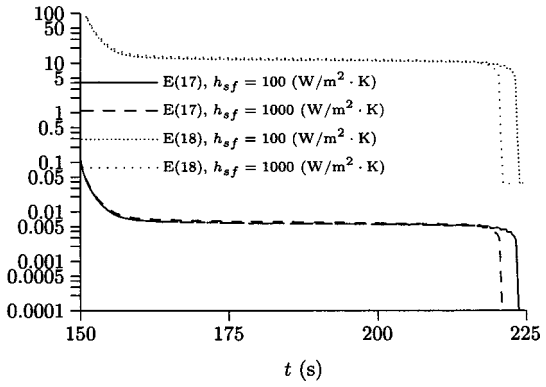

Fig. 9 Comparison of two dimensionless criteria for local thermal equilibrium near the regenerator injection boundary

However, it is difficult to separate boundary condition effects due to Eq. (7) from intrinsic differences due to the governing equations.

This information can be used to shed further light on criteria for LTE. For high energy density reactors, it might be supposed at least two such criteria exist—one applicable at boundaries, and one dependent upon bulk material parameters and conditions. The dimensionless inlet condition arrived at in Kuznetsov and Vafai [11] can be written,

$$\frac{\rho v c_{p_{H_2}}}{L_R \alpha_v} \ll 1. \tag{17}$$

This is a criterion of the boundary condition type. The physical interpretation is a rate of advection of sensible heat scaled to the fluid residence time in the reactor, compared with the rate of bulk heat transfer.

By forming the ratio of dimensionless heat fluxes in the boundary region using Eq. (7), one can define the following dimensionless parameter:

$$\mathrm{Lr}_b \overset{\text{def}}{=} \frac{k_s c_{pf} \rho_f v_f}{k_f \delta \alpha_v}, \tag{18}$$

where δ denotes the depth of the NLTE region. A comparison of the two parameters is shown in Fig. 9. An initial flow-stabilization transient is followed by a long period of quasi-static hydrogen transfer between reactors. (The final cutoff is due to depletion of hydrogen in the refrigerator reactor, and is not pertinent.) The quantity Lr_b may be useful for gaging local thermal equilibrium in the injection region, as well as for estimating δ.

Conclusions

A NLTE model for two coupled reactors was formulated and solved for a complete heat pump cycle, using two different values of h_{sf}. The solutions were compared to previous LTE results using integral heat pump measures, such as COP and average thermal power, as well as through field plots which illustrate the differences in reactor dynamics.

For the parameters investigated—which correspond to a moderately optimized reactor in the sense of Π_2—it was found that NLTE effects are present, but are predominately confined to the regenerator reactor, and to the injection boundary and the reactor wall regions. These NLTE effects do not substantially alter the coefficient of performance or average cooling power predicted for the heat pump (<10 percent). For the particular heat pump examined, it may be concluded that LTE models are sufficient for the prediction of both heat pump performance and the reactor dynamics.

Nomenclature

A = reaction prefactor, ($\mathrm{kmole_H/kmole_h \cdot s}$)
COP = coefficient of performance
c = heat capacity, ($\mathrm{W \cdot s/kg \cdot K}$)
E_a = activation energy, ($\mathrm{J/kmole_{H_2}}$)
g = heat generation term, ($\mathrm{J/s \cdot m^3_{(c)}}$)
h_∞ = exterior heat transfer coefficient, ($\mathrm{W/m^2 \cdot C}$)
$h_{c_{sw}}$ = solid-phase/wall heat transfer coefficient
$h_{c_{fw}}$ = fluid-phase/wall heat transfer coefficient
h_{sf} = interstitial heat transfer coefficient
k_{eff} = stagnant (or effective) thermal conductivity, ($\mathrm{W/m \cdot K}$)
k_f = thermal conductivity H_2, 10^{-1}($\mathrm{W/m \cdot K}$)
K = permeability, ($\mathrm{m^2}$)
Lr_b = dimensionless parameter defined in paper
LTE = local thermal equilibrium
NLTE = nonlocal thermal equilibrium
Nu_D = interstitial Nusselt number based upon particle diameter, $h_{sf}D/k_f$
P = average cooling power, ($\mathrm{W/kg_h}$)
$p_{eq_{H_2}}$ = equilibrium hydride pressure, ($\mathrm{N/m^2}$)
Q_{useful} = useful thermal energy, (J)
Q_{hot} = thermal energy from source at T_{hot}, (J)
r = radial space coordinate, (m)
R = perfect gas constant, 8314 ($\mathrm{J/kmole \cdot K}$)
R_r = thermal containment resistance, ($\mathrm{m^2 \cdot K/W}$) or ($\mathrm{K/W}$)
REV = representative equivalent volume
t = time coordinate, (s)
$T(r,t)$ = temperature, (K)
$\overset{s}{T}$ = temperature function for solid phase, (K)
$\overset{f}{T}$ = temperature function for fluid phase, (K)
$T_w(t)$ = average wall temperature, (K)
T_{cold} = temperature of cold reservoir, (C)
T_{hot} = temperature of hot reservoir, (C)
T_{cycle} = characteristic cycle time
v = Darcy filtration velocity, (m/s)
x = absorbed hydrogen concentration, ($\mathrm{kmole_H/kmole_h}$)
$x_{\alpha_{\max}}$ to $x_{\beta_{\min}}$ = plateau region of the metal hydride
ΔH = $\alpha-\beta$ phase transition enthalpy change, ($\mathrm{J/kmole_{H_2}}$)
Δr = mesh size
ΔS = entropy change, ($\mathrm{J/kmole \cdot K}$)
$\Delta x_{\max}$ = theoretical hydrogen, ($\mathrm{kmole_H/kmole_h}$)
$\Delta_{\max}$ = reactor hydrogen inventory, ($\mathrm{kmole_{H_2}}$)
δr = energy deposition depth, (m)
$dA_{sf}/dV_{(c)}$ = specific surface area, ($\mathrm{m^2/m^3_{(c)}}$)
α_v = volumetric heat transfer coefficient, ($\mathrm{W/m^3 \cdot K}$)
μ = viscosity ($\mathrm{Pa \cdot s}$)
γ = molecular weight, (kg/kmole)
ϕ = porosity, ($\mathrm{m^3_{pore}/m^3_{(c)}}$)
$\dot{\varphi}$ = field source term for hydrogen, ($\mathrm{kg_{H_2}/m^3_{(c)} \cdot s}$)
$\wp$ = hydride particle density, ($\mathrm{particles_h/m^3_{(c)}}$)
λ = time step limiter
Π_2 = reactor optimization parameter; $E(16)$

Superscripts and Accents

$'$ = refers to regenerator property
^{i} = pertaining to the i-phase

Subscript

(c) = refers to continuum
H_2 = hydrogen
R = reactor

w = reactor wall
h = hydride
H = atomic hydrogen

References

[1] Dantzer, P., 1997, ''Metal-Hydride Technology: A Critical Review,'' in *Hydrogen in Metals III. Properties and Applications*, H. Wipf, ed., Top. Appl. Phys., **73**, Springer-Verlag, New York, pp. 279–340.

[2] Kim, K. J., Feldman, K. T., Lloyd, G., Razani, A., and Shanahan, K. L., 1998, ''Performance of High Power Metal Hydride Reactors,'' Int. J. Hydrogen Energy, **23** (5), pp. 355–362.

[3] Lloyd, G., Kim, K. J., Razani, A., and Feldman, K. T., Jr., 1998, ''Thermal Conductivity Measurements of Metal Hydride Compacts Developed for High Power Reactors,'' J. Thermophys. Heat Transfer, **12** (1), pp. 132–137.

[4] Lloyd, G., Razani, A., and Feldman, K. T., Jr., 1998, ''Transitional Reactor Dynamics Affecting Optimization of a Heat-Driven Metal Hydride Refrigerator,'' Int. J. Heat Mass Transf., **41** (3), pp. 513–427.

[5] Lloyd, G., Razani, A., and Kim, K. J., 1998, ''Performance Characteristics of a Compressor-Driven Metal Hydride Refrigerator,'' J. Energy Resour. Technol., **120** (4), pp. 305–313.

[6] Kuznetsov, A. V., 1997, ''Optimal Control of the Heat Storage in a Porous Slab,'' Int. J. Heat Mass Transf., **40** (7), pp. 1720–1723.

[7] Kuznetsov, A. V., 1996, ''Investigation of a Non-Thermal Equilibrium Flow of an Incompressible Fluid in a Cylindrical Tube Filled with Porous Media,'' Zeitschrift für Angewandte Mathematik und Mechanik, **76**(6), pp. 411–418.

[8] Vu Dang, C., and Delcambre, B., 1987, ''Etude Expérimentale et Modélisation d'un Stockage Thermique de Longue Durée en Lit de Cailloux Enterré, Couplé à des Capteurs Solaires à Air,'' Rev. Phys. Appl., **22**, pp. 487–503.

[9] Jemni, A., and Nasrallah, S. B., 1995, ''Study of Two-Dimensional Heat and Mass Transfer During Desorption in a Metal-Hydrogen Reactor,'' Int. J. Hydrogen Energy, **20** (11), pp. 881–891.

[10] Mhimid, A., 1998, ''Theoretical Study of Heat and Mass Transfer in a Zeolite Bed During Water Desorption: Validity of Local Thermodynamic Equilibrium Assumption,'' Int. J. Heat Mass Transf., **41**, pp. 2967–2977.

[11] Kuznetsov, A. V., and Vafai, K., 1995, ''Analytical Comparison and Criteria for Heat and Mass Transfer Models in Metal Hydride Packed Beds,'' Int. J. Heat Mass Transf., **38** (15), pp. 2873–2884.

[12] Lloyd, G. M., 1998, ''Optimization of Heat and Mass Transfer in Metal Hydride Systems.'' Ph.D. thesis, University of New Mexico, Albuquerque, NM.

[13] Kaviany, M., 1995, *Principles of Heat Transfer in Porous Media*, 2nd ed., Springer-Verlag, New York.

[14] Fukuda, K., Tetsuya, K., and Haseqawa, S., 1992, ''Similarity Rule Between Heat Transfer and Pressure Drop of Porous Material,'' AIChE J., **38** (11), pp. 1840–1842.

[15] Lloyd, G., Razani, A., and Feldman, K. T., 1995, ''Fundamental Issues Involved in a Theoretical Description of the Heat and Hydrogen Transfer Occurring in Coupled Porous Metal Hydride Reactors,'' *Proceedings of the ASME Int. Mech. Eng. Cong. & Exp., San Francisco*, **HTD-Vol. 321/FED-Vol. 233**, pp. 671–681.

[16] Reid, C. R., and Oakberg, R. G., 1990, ''A Continuum Theory for the Mechanical Response of Materials to the Thermodynamic Stress of Sintering,'' Mech. Mater., **10**, pp. 203–213.

[17] White, F. M., 1991, *Viscous Fluid Flow*, 2nd ed., McGraw-Hill Inc., p. 50.

[18] Strikwerda, J. C., 1989, *Finite Difference Schemes and Partial Differential Equations*, Chapman & Hall, Ltd., London.

[19] Lloyd, G. M., 1994, ''Transient Heat/Mass Transfer Modeling of Metal Hydride Cycles,'' M.S. thesis, University of New Mexico, Albuquerque, NM.

[20] Ames, W. F., 1992, Numerical Methods for Partial Differential Equations, 3rd ed., Academic Press Inc., San Diego, CA, p. 73.

[21] Nobles, M. A., 1974, *Using the Computer to Solve Petroleum Engineering Problems*, Gulf Publishing Company, Houston, CA, p. 405.

[22] Ramshaw, J. D., and Chang, C. H., 1992, ''Computational Fluid Dynamics Modeling of Multicomponent Thermal Plasmas,'' Plasma Chem. Plasma Process., **12** (3), pp. 299–325.

[23] Roache, P. J., 1993, ''A Method for Uniform Reporting of Grid Refinement Studies,'' *Quantification of Uncertainty in Computational Fluid Dynamics*, I. Celik, ed., *American Society of Mechanical Engineers, Fluids Engineering Division*, **FED-158**, pp. 109–120.

Thermal Interaction at the Interface Between a Porous Medium and an Impermeable Wall

Sung Jin Kim

Duckjong Kim

Department of Mechanical Engineering,
Korea Advanced Institute of Science and Technology,
Taejon, 305-701, Korea

The present work investigates a heat transfer phenomenon at the interface between a porous medium and an impermeable wall subject to a constant heat flux at the bottom. Currently, two possible thermal boundary conditions (which are called the First Approach and the Second Approach) at the interface are used interchangeably for the thermal analysis of convection in a channel filled with a porous medium. The focus of this paper is to determine which of these thermal boundary conditions is more appropriate in accurately predicting the heat transfer characteristics in a porous channel. To this end, we numerically examine the heat transfer at the interface between a microchannel heat sink (an ideally organized porous medium) and a finite-thickness substrate. From the examination, it is clarified that the heat flux distribution at the interface is not uniform for an impermeable wall with finite thickness. This means that a non-uniform distribution of the heat flux (First Approach) is physically reasonable. When the First Approach is applied to the thermal boundary condition, an additional boundary condition based on the local thermal equilibrium assumption at the interface is used. This additional boundary condition is applicable except in the case of a very thin impermeable wall. Hence, for practical situations, the First Approach with a local thermal equilibrium assumption at the interface is suggested as an appropriate thermal boundary condition. In order to confirm our suggestion, convective flows both in a microchannel heat sink and in a sintered porous channel subject to a constant heat flux condition are analyzed by using the two Approaches separately as a thermal boundary condition at the interface. The analytically obtained thermal resistance of the microchannel heat sink and the numerically obtained overall Nusselt number for the sintered porous channel are shown to be in close agreement with available experimental results when our suggestion for the thermal boundary condition at the interface is applied. [DOI: 10.1115/1.1370504]

Keywords: *Heat Transfer, Interface, Microscale, Packed Beds, Porous Media*

1 Introduction

The present work investigates a heat transfer phenomenon at the interface between a porous medium and an impermeable wall. In general, a porous medium has many tortuous fluid passages. As a result, by using the porous medium as a transport medium, the heat exchange between the solid matrix and the fluid phase flowing through the porous medium is significantly enhanced due to the large heat transfer area and the thermal dispersion effect. Therefore, utilization of porous insertions is a promising means of augmenting heat transfer in high heat flux applications. However, the actual mechanism of heat and fluid flow in the porous medium has not been completely clarified because of the complex structure of the porous medium. Above all, since the thermal interaction at the interface between the porous medium and the impermeable wall is frequently encountered in engineering applications, understanding the mechanism of the heat and fluid flow at this interface is necessary to predict accurately the thermal performance of packed bed heat exchangers, heat pipes, porous heat sinks, and insulating materials, etc. (Fig. 1).

Much relevant research has been conducted. At first, the prime issue was, under the local thermal equilibrium assumption, whether the temperature profile at the interface is continuous or discontinuous. Sahraoui and Kaviany [1,2] showed that the phase distribution nonuniformities near bounding surfaces result in anisotropy and nonuniformity of the effective thermal conductivity tensor for a circular cylinder-packed structure. The temperature profile at the interface is continuous as it should be if the effective thermal conductivity of the porous medium is a function of the location, while the temperature profile is no longer continuous if the effective thermal conductivity is treated as a constant. Since the mid 90's, due to the temperature difference between the fluid and solid phases of the porous medium, many research projects using the two-equation model for heat transfer, which treats the fluid and solid regions separately, have been conducted. Hence, how the heat that flows from the impermeable wall to the porous medium is distributed along the interface between the solid matrix and the fluid phase became a new issue. Amiri et al. [3] proposed two Approaches for the heat transfer at the interface. The First Approach is based on the assumption that the heat flux is divided between the solid matrix and the fluid phase depending on the physical values of their effective conductivities. The mathematical expression for the First Approach is as follows:

$$q'' = -k_s^* \left.\frac{\partial \langle T\rangle_s}{\partial y}\right|_{\text{wall}} - k_f^* \left.\frac{\partial \langle T\rangle_f}{\partial y}\right|_{\text{wall}}. \tag{1}$$

The Second Approach is to assume that each of the individual phases at the interface between the porous medium and the impermeable wall receives an equal amount of the heat flux and the corresponding mathematical expression is as follows:

Contributed by the Heat Transfer Division for publication in the JOURNAL OF HEAT TRANSFER. Manuscript received by the Heat Transfer Division June 26, 2000; revision received January 1, 2001. Associate Editor: M. Faghri.

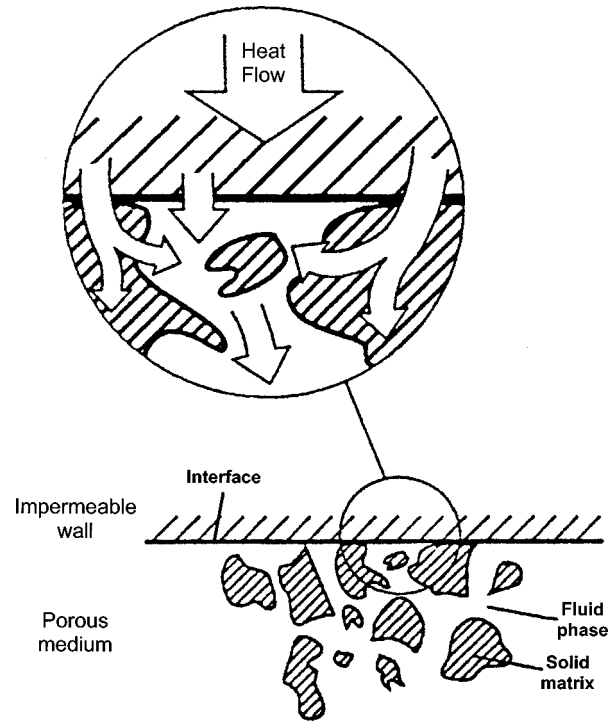

Fig. 1 Heat transfer at the interface between the porous medium and the impermeable wall [1]

$$q'' = -k_s \left.\frac{\partial \langle T \rangle_s}{\partial y}\right|_{\text{wall}} = -k_f \left.\frac{\partial \langle T \rangle_f}{\partial y}\right|_{\text{wall}}. \tag{2}$$

Amiri et al. [3] numerically obtained the wall temperature and the heat transfer coefficient of the packed bed by applying the Second Approach to the thermal boundary condition and they showed that their numerical results agreed with available experimental results. On the other hand, Hwang et al. [4] used the First Approach in the thermal analysis of the sintered porous channel and they showed that their numerical results agreed with their experimental results. As the two research endeavors stated above show, the heat transfer mechanism at the interface between the porous medium and the impermeable wall remains to be clarified. Since the boundary condition affects the final solution significantly, determination of the appropriate boundary condition at the interface is very important in the thermal analysis of the porous medium.

The purpose of the present study is to determine which of the two Approaches better describes the heat transfer phenomena at the interface. When a constant heat flux is applied to an impermeable wall, the wall is typically modeled as having zero-thickness, even though in reality it has finite thickness. Hence, in Section 2, to have an insight into the heat transfer mechanism at the interface on a microscopic level, direct numerical simulations for the forced-convection heat transfer in a microchannel heat sink (an ideally organized porous medium) with a finite-thickness substrate subject to a constant heat flux at the bottom are performed. Effects of the conductivity ratio, the substrate thickness, and the porosity on the heat flux distribution and the temperature difference between the fluid and solid phases at the porous/solid interface are examined. The results of this examination yield the answer to the question as to which interface boundary condition is more appropriate for heat transfer study in porous media. In order to confirm the findings in Section 2, the macroscopic heat and fluid flow in a microchannel heat sink (Section 3) and in a sintered porous channel (Section 4) are analyzed by applying the two Approaches separately as a thermal boundary condition at the interface between the porous medium and the impermeable wall which is modeled as having zero-thickness. The analytical results for the thermal resistance and the numerical results for the overall Nusselt number are compared with the available experimental data in Section 3 and Section 4, respectively. Through this comparison, the boundary conditions proven appropriate in Section 2 are validated and suggested for use in future investigations.

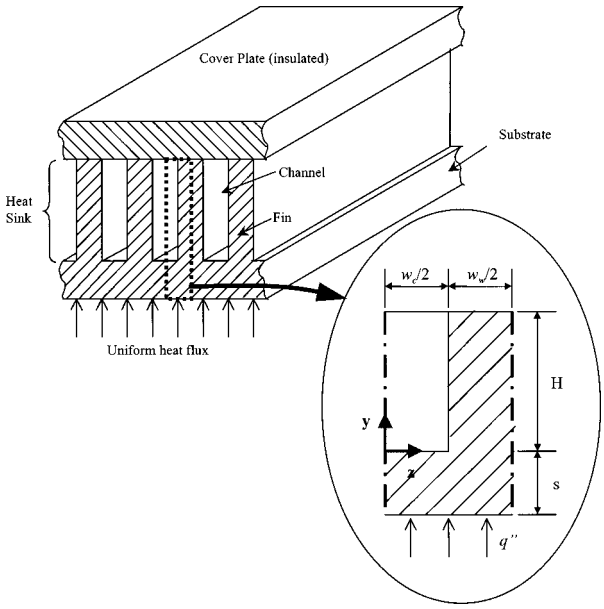

Fig. 2 Microchannel heat sink

2 Heat Transfer at the Microchannel Heat Sink/Substrate Interface

Since a porous medium has a complex structure, it is difficult to investigate the microscopic heat and fluid flow in the porous medium. Koh and Colony [5] pointed out that the heat and fluid flow in a microchannel heat sink is similar to that in a porous medium in view of the small dimensions of channels and fins. Hence, by performing the numerical simulation for the heat transfer at the interface between the microchannel heat sink and the substrate, we investigate the heat transfer mechanism at the interface between the porous medium and the impermeable wall and suggest appropriate thermal boundary conditions at the interface.

The problem under consideration in this Section concerns the forced convective flow through a microchannel heat sink, as shown in Fig. 2. The top surface is insulated and the bottom surface of the substrate is uniformly heated. Water passes through the microchannel and takes heat away from a heat-dissipating component attached at the bottom of the substrate. In general, the substrate has finite thickness and thermally interacts with the heat sink. Therefore, the heat sink and the substrate are included in the calculation domain as shown in the enlarged picture in Fig. 2. In analyzing the conjugate heat transfer problem, the flow is assumed to be hydrodynamically and thermally fully developed laminar and all physical properties are assumed to be constant. The velocity distribution in the rectangular duct has already been published by Shah and London [6] and this is transformed according to the coordinates shown in Fig. 2 as follows:

$$u(y,z) = -\frac{4(dp/dx)w_c^2}{\mu_f \pi^3} \sum_{n=1,3,\ldots}^{\infty} \frac{1}{n^3}(-1)^{(n-1)/2} \times \left[1 - \frac{\cosh\left(\frac{n\pi}{w_c}\left(y - \frac{H}{2}\right)\right)}{\cosh\left(\frac{n\pi H}{2w_c}\right)}\right] \cos\left(\frac{n\pi}{w_c} z\right). \tag{3}$$

The energy equation and boundary conditions are as follows:

$$k\frac{\partial^2 T}{\partial y^2}+k\frac{\partial^2 T}{\partial z^2}=\rho_f c_f u\frac{\partial T}{\partial x} \tag{4}$$

$$\left.\frac{\partial T}{\partial z}\right|_{z=0}=\left.\frac{\partial T}{\partial z}\right|_{z=(w_c+w_w)/2}=0 \tag{5a}$$

$$-k\left.\frac{\partial T}{\partial y}\right|_{y=-s}=q'' \tag{5b}$$

$$\left.\frac{\partial T}{\partial y}\right|_{y=H}=0. \tag{5c}$$

To obtain the temperature distribution, the energy equation (4) with boundary conditions (5a)–(5c) is solved by using the control-volume-based finite difference method for the domain including the fluid and solid phases [7]. The thermal conductivity is determined according to the physical property of the phase at the location and the thermal conductivity at the interface between the two phases is determined by the harmonic mean formulation. In order to predict the flow and temperature fields accurately, a fine grid is used near the interface. A grid size of $40\times 90\,(z\times y)$ is selected, above which the overall Nusselt number of the microchannel heat sink changes less than 1 percent. From the numerical solution for the temperature distribution near the interface, we can calculate the heat flux distribution at the interface between the microchannel heat sink and the substrate. This heat flux distribution will clearly indicate which boundary condition is physically appropriate at the interface.

If the substrate has zero-thickness, the uniform heat flux boundary condition at the bottom of the substrate can be directly applied to the interface. In this case the Second Approach can appropriately describe the heat transfer phenomena at the interface. However, the substrate in reality has finite thickness and the heat flux distribution at the interface is by no means uniform for a practical range of parameters as shown in Fig. 3. This means that the Second Approach is not applicable to practical problems. On the other hand, the First Approach, based on the energy balance for the representative elementary volume in the porous medium, is physically reasonable.

If the First Approach is to be applied as the thermal boundary condition, an additional boundary condition is required because the energy equation is a second order differential equation. Previous studies [4,8,9] based on the First Approach used an additional condition that the volume-averaged temperature of the solid phase is identical to that of the fluid phase at the interface. To check the validity of the additional condition, the nondimensionalized temperature difference between the two phases at the interface, Δ_T, is defined as follows:

$$\Delta_T=\left.\frac{\langle T\rangle_f-\langle T\rangle_s}{T_w-T_b}\right|_{\text{interface}}. \tag{6}$$

Figure 4 shows effects of the thermal conductivity, the thickness of the substrate, and the width ratio (porosity) of the microchannel heat sink $(w_c/(w_c+w_w))$ on Δ_T. As shown in Fig.'s 4(*a*) and (*c*), effects of the thermal conductivity and the width ratio are not significant at all. On the other hand, Fig. 4(*b*) shows that the temperature difference at the interface remains almost constant for $s/H>0.1$ but increases with decreasing s/H for $s/H<0.1$. This implies that there is a limit for s/H below which the First Approach in combination with the local thermal equilibrium assumption at the interface may not be applicable as the thermal boundary condition at the interface. However, most applications of the porous medium use impermeable walls which fall under the category of $s/H\geqslant 0.1$.

Therefore, for practical situations, appropriate thermal boundary conditions at the interface between the porous medium and the impermeable wall are as follows:

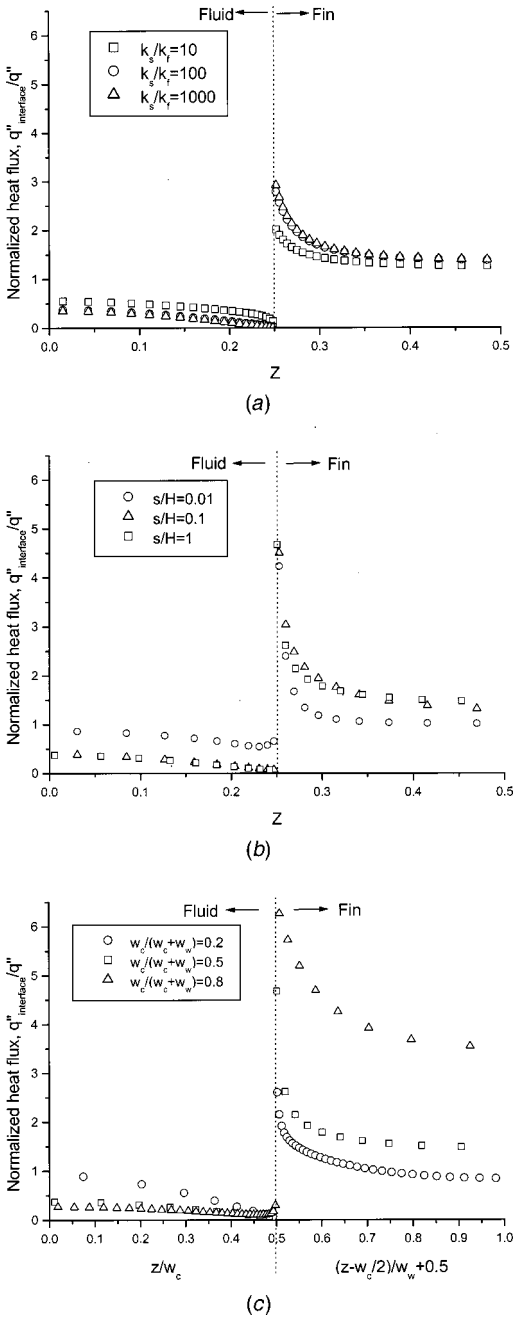

Fig. 3 Effects of parameters on the heat flux distribution at the interface: (*a*) thermal conductivity ($s/H=1$, $w_c/(w_c+w_w)=0.5$); (*b*) thickness of the substrate ($k_s/k_f=100$, $w_c/(w_c+w_w)=0.5$); and (*c*) width ratio of the microchannel heat sink ($k_s/k_f=100$, $s/H=1$) [$\alpha_s=2$, $H=100\,(\mu\text{m})$, $k_f=0.59\,(\text{W/m°C})$].

$$q''=-k_f^*\left.\frac{\partial\langle T\rangle_f}{\partial y}\right|_{\text{wall}}-k_s^*\left.\frac{\partial\langle T\rangle_s}{\partial y}\right|_{\text{wall}} \tag{7a}$$

$$\langle T\rangle_f|_{\text{wall}}=\langle T\rangle_s|_{\text{wall}}. \tag{7b}$$

3 Thermal Resistance of Microchannel Heat Sink

In Section 2, appropriate thermal boundary conditions at the interface between the porous medium and the impermeable wall are suggested. In this Section, the microchannel heat sink shown in Fig. 2 is treated as a porous medium and analytical results of the thermal resistance obtained by using the two Approaches separately as a boundary condition at the interface are compared

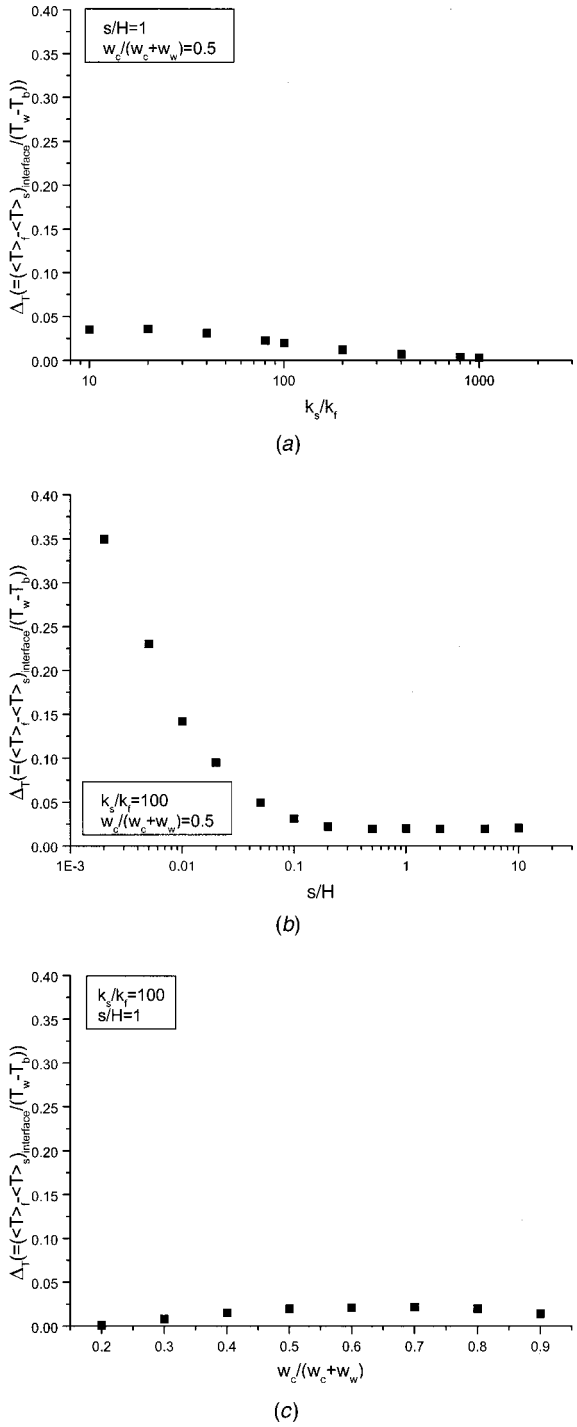

Fig. 4 Effects of parameters on Δ_T; (*a*) thermal conductivity; (*b*) thickness of the substrate; and (*c*) width ratio of the microchannel heat sink [$\alpha_s=2$, $H=100$ (μm), $k_f=0.59$ (W/m°C)].

with the available experimental data of Tuckerman and Pease [10]. It is shown that the thermal resistance from the First Approach is in good agreement with the experimental data, in contrast with the Second Approach, thus validating our findings in Section 2.

Research which treats the microchannel heat sink as a porous medium has been conducted by Kim and his coworkers [8,9]. In this study, the methodology introduced by them for obtaining analytical solutions for velocity and temperature distributions is used. However, in order to apply the heat flux boundary condition properly, nondimensionalization of the temperature is changed as follows:

$$\theta_s=\frac{\langle T\rangle_s}{\dfrac{q''H}{(1-\varepsilon)k_s}},\qquad \theta_f=\frac{\langle T\rangle_f}{\dfrac{q''H}{(1-\varepsilon)k_s}}. \tag{8}$$

Nondimensionalized governing equations and boundary conditions are as follows:

The momentum equation:

$$U=Da\,\frac{d^2U}{dY^2}-P. \tag{9}$$

The energy equation for the solid region:

$$\frac{d^2\theta_s}{dY^2}=\mathrm{Bi}(\theta_s-\theta_f). \tag{10}$$

The energy equation for the fluid region:

$$U=\mathrm{Bi}(\theta_s-\theta_f)+C\,\frac{d^2\theta_f}{dY^2}. \tag{11}$$

Boundary conditions at $Y=0$:

$$U=0$$

$$1=-C\,\frac{\partial\theta_f}{\partial Y}-\frac{\partial\theta_s}{\partial Y},\quad \theta_f=\theta_s \quad \text{for First approach}$$

$$1=-\frac{k_f}{(1-\varepsilon)k_s}\frac{\partial\theta_f}{\partial Y}=-\frac{1}{(1-\varepsilon)}\frac{\partial\theta_s}{\partial Y} \quad \text{for Second approach} \tag{12}$$

Boundary conditions at $Y=1$:

$$U=0$$

$$\frac{d\theta_s}{dY}=\frac{d\theta_f}{dY}=0. \tag{13}$$

Analytical solutions for velocity and temperature distributions can be obtained by solving governing Eqs. (9)–(11) with boundary conditions (12), (13). The analytical solution for the velocity distribution is:

$$U=P\left\{\cosh\left(\sqrt{\frac{1}{\mathrm{Da}}}Y\right)+\frac{1-\cosh\left(\sqrt{\dfrac{1}{\mathrm{Da}}}\right)}{\sinh\left(\sqrt{\dfrac{1}{\mathrm{Da}}}\right)}\times\sinh\left(\sqrt{\frac{1}{\mathrm{Da}}}Y\right)-1\right\} \tag{14}$$

where

$$P=\frac{\sinh\left(\sqrt{\dfrac{1}{\mathrm{Da}}}\right)}{2\sqrt{\mathrm{Da}}\left\{\cosh\left(\sqrt{\dfrac{1}{\mathrm{Da}}}\right)-1\right\}-\sinh\left(\sqrt{\dfrac{1}{\mathrm{Da}}}\right)}. \tag{15}$$

Analytical solutions for temperature distributions are

$$\theta_f=\frac{P}{1+C}\left[-\frac{1}{2}Y^2+C_1'Y+C_2'+C_3'\left\{\cosh\left(\sqrt{\frac{1}{\mathrm{Da}}}Y\right)+\frac{1-\cosh\left(\sqrt{\frac{1}{\mathrm{Da}}}\right)}{\sinh\left(\sqrt{\frac{1}{\mathrm{Da}}}\right)}\sinh\left(\sqrt{\frac{1}{\mathrm{Da}}}Y\right)\right\}+C_4'\cosh\left(\sqrt{\frac{\mathrm{Bi}(1+C)}{C}}Y\right)+C_5'\sinh\left(\sqrt{\frac{\mathrm{Bi}(1+C)}{C}}Y\right)\right] \tag{16}$$

$$\theta_s=P\left[-\frac{1}{2}Y^2+C_1Y+C_2+\mathrm{Da}\left\{\cosh\left(\sqrt{\frac{1}{\mathrm{Da}}}Y\right)+\frac{1-\cosh\left(\sqrt{\frac{1}{\mathrm{Da}}}\right)}{\sinh\left(\sqrt{\frac{1}{\mathrm{Da}}}\right)}\sinh\left(\sqrt{\frac{1}{\mathrm{Da}}}Y\right)\right\}\right]-C\theta_f, \tag{17}$$

where

$$C_1=1-\sqrt{\mathrm{Da}}\,\frac{\cosh\left(\sqrt{\frac{1}{\mathrm{Da}}}\right)-1}{\sinh\left(\sqrt{\frac{1}{\mathrm{Da}}}\right)}$$

$$C_4=\left[-C_3\sqrt{\frac{\mathrm{Bi}(1+C)}{C}}\sinh\left(\sqrt{\frac{\mathrm{Bi}(1+C)}{C}}\right)-\frac{P}{\sqrt{\mathrm{Da}}\left(\mathrm{Bi}(1+C)-\frac{C}{\mathrm{Da}}\right)}\left\{\sinh\left(\sqrt{\frac{1}{\mathrm{Da}}}\right)+\frac{1-\cosh\left(\sqrt{\frac{1}{\mathrm{Da}}}\right)}{\sinh\left(\sqrt{\frac{1}{\mathrm{Da}}}\right)}\cosh\left(\sqrt{\frac{1}{\mathrm{Da}}}\right)\right\}\right]\Bigg/\sqrt{\frac{\mathrm{Bi}(1+C)}{C}}\cosh\left(\sqrt{\frac{\mathrm{Bi}(1+C)}{C}}\right)$$

$$C_1'=C_1$$

$$C_2'=C_2+\frac{1}{\mathrm{Bi}(1+C)}$$

$$C_3'=\mathrm{Da}-\frac{1}{\mathrm{Bi}(1+C)-\frac{C}{\mathrm{Da}}}$$

$$C_4'=-\frac{C_3}{P}$$

$$C_5'=-\frac{C_4}{P}.$$

Analytical solutions for temperature distributions have a unique form regardless of the Approach that is applied to the thermal boundary condition at the interface. The coefficient C_3 changes according to the Approach. In the case of the First Approach,

$$C_3=\frac{-\frac{C}{\mathrm{Da}}P}{\mathrm{Bi}(1+C)\left\{\mathrm{Bi}(1+C)-\frac{\mathrm{Bi}}{\mathrm{Da}}\right\}}.$$

In the case of the Second Approach,

$$C_3=-\left[P\cosh\left(\sqrt{\frac{\mathrm{Bi}(1+C)}{C}}\right)\left\{\frac{\varepsilon(1+C)}{CP}-C_1'-C_3'\sqrt{\frac{1}{\mathrm{Da}}}\,\frac{1-\cosh\left(\sqrt{\frac{1}{\mathrm{Da}}}\right)}{\sinh\left(\sqrt{\frac{1}{\mathrm{Da}}}\right)}\right\}-\frac{P}{\sqrt{\mathrm{Da}}\left(\mathrm{Bi}(1+C)-\frac{C}{\mathrm{Da}}\right)}\left\{\sinh\left(\sqrt{\frac{1}{\mathrm{Da}}}\right)+\frac{1-\cosh\left(\sqrt{\frac{1}{\mathrm{Da}}}\right)}{\sinh\left(\sqrt{\frac{1}{\mathrm{Da}}}\right)}\cosh\left(\sqrt{\frac{1}{\mathrm{Da}}}\right)\right\}\right]\div\left\{\sqrt{\frac{\mathrm{Bi}(1+C)}{C}}\sinh\left(\sqrt{\frac{\mathrm{Bi}(1+C)}{C}}\right)\right\}.$$

Since boundary conditions of Neumann type are used, the constant term C_2 remains undetermined and a unique temperature distribution for each phase cannot be obtained. Therefore, to eliminate the constant term, the thermal resistance, which is a function of the temperature difference, is obtained (Eqs. (27)–(29) in [8]) and this is compared with the experimental results of Tuckerman and Pease [10]. Tuckerman and Pease used three different microchannel heat sinks whose substrates come within the category of $s/H \geqslant 0.1$ ($s/H=0.25, 0.394, 0.325$), for which boundary conditions (7*a*) and (7*b*) based on the First Approach are applicable. As shown in Fig. 5, the thermal resistance from the First Approach is in good agreement with the experimental results, in contrast with the Second Approach.

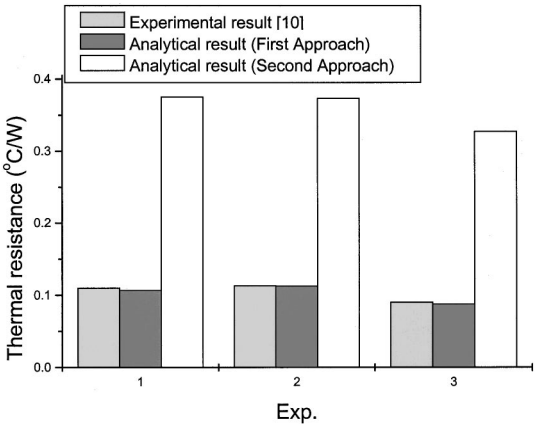

Fig. 5 Comparison with the experimental results for thermal resistance of the microchannel heat sink

4 Overall Nusselt Number of Sintered Porous Channel

In Section 3, thermal boundary conditions suggested through direct numerical simulations in Section 2 are shown to be valid for theoretical analysis of the forced convection in the microchannel heat sink through the comparison with the available experimental data. In this Section, we demonstrate that the First Approach is a physically appropriate boundary condition for investigating forced convection not only in an ideally organized porous medium with an impermeable wall like the microchannel heat sink, but also in the complexly structured sintered porous channel with an impermeable wall.

Figure 6 shows the heat transfer problem in the porous channel. The top surface is insulated and the bottom surface of the impermeable wall is uniformly heated. Air passes through the porous channel and takes heat away from a heat-dissipating component attached at the bottom of the impermeable wall. For the heat transfer problem shown in Fig. 6, Hwang and Chao [11] published their numerical and experimental results for the wall temperature distribution and the overall Nusselt number of the porous channel. In this study, we conduct numerical simulations for the porous channel as Hwang and Chao did. However, we use different thermal boundary conditions at the bottom surface of the porous channel by applying the two Approaches. We numerically obtain the overall Nusselt number of the porous channel and compare it with the experimental results of Hwang and Chao. New thermal boundary conditions from the two Approaches are as follows:

in the case of the First Approach:

$$1 = -\frac{k_f^*}{k_s^*}\frac{1}{\mathrm{Bi}}\frac{\partial\theta_f}{\partial Y}\bigg|_{Y=0} - \frac{1}{\mathrm{Bi}}\frac{\partial\theta_s}{\partial Y}\bigg|_{Y=0} \tag{18a}$$

$$\theta_f|_{Y=0} = \theta_s|_{Y=0} \tag{18b}$$

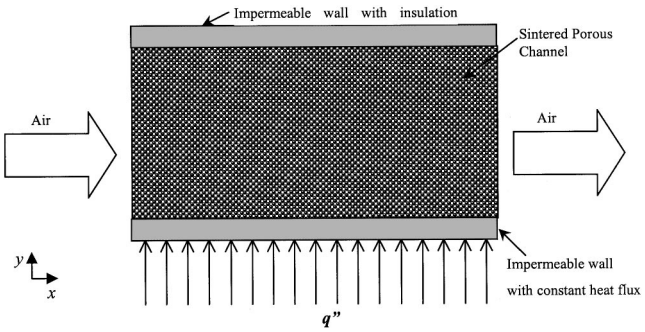

Fig. 6 Sintered porous channel

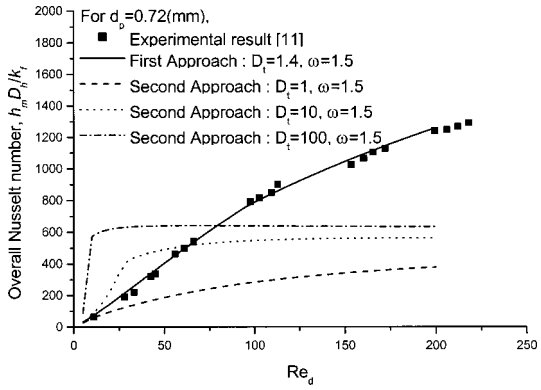

Fig. 7 Overall Nusselt number of the sintered porous channel

in the case of the Second Approach:

$$1 = -\frac{k_f}{k_s^*}\frac{1}{\mathrm{Bi}}\frac{\partial\theta_f}{\partial Y}\bigg|_{Y=0} = -\frac{k_s}{k_s^*}\frac{1}{\mathrm{Bi}}\frac{\partial\theta_s}{\partial Y}\bigg|_{Y=0}. \tag{19}$$

The effective thermal conductivity of the fluid, k_f^*, includes the thermal dispersion effect. To calculate the thermal dispersion effect, the Van Driest type of wall function is used as follows [11]:

$$k_f^* = \varepsilon(k_f + D_t\rho_f c_f d_p u \mathrm{l}) \tag{20}$$

where

$$\mathrm{l} = \begin{cases} 1-\exp[-y/(\omega d_p)] & \text{for } 0 \leqslant y \leqslant \frac{1}{2}H \\ 1-\exp[-(H-y)/(\omega d_p)] & \text{for } \frac{1}{2}H \leqslant y \leqslant H. \end{cases}$$

Hwang and Chao proposed appropriate values of D_t, ω as 0.375, 1.5 for which their numerical results are in good agreement with their experimental results in their paper. However, Kim and Kim [12] pointed out that the numerical simulation of Hwang and Chao is in error and newly suggested 1.4, 1.5 as appropriate values of D_t, ω. In this study, $D_t = 1.4$ and $\omega = 1.5$ are used in the numerical simulation and the resultant overall Nusselt number of the porous channel is compared with the available experimental results. As in Section 3, the impermeable wall used by Hwang and Chao is thicker than 0.1 times the channel height ($s/H = 0.2$). Figure 7 shows the comparison between numerical results and experimental results for the overall Nusselt number. In the case of the First Approach, numerical results are in good agreement with experimental results when $D_t = 1.4$ and $\omega = 1.5$, while in the case of the Second Approach, numerical results deviate from experimental results significantly for any values of D_t, ω. Consequently, it is verified that the First Approach in combination with the local thermal equilibrium assumption at the interface can appropriately describe the heat transfer phenomenon at the interface for practical situations such as the microchannel heat sink and the sintered porous channel.

5 Conclusion

In this work, a heat transfer phenomenon at the interface between a porous medium and an impermeable wall subject to a constant heat flux at the bottom is investigated. To this end, we numerically examine the heat transfer at the interface between a microchannel heat sink (an ideally organized porous medium) and a finite-thickness substrate. From the examination, it is clarified that the heat flux distribution at the interface is not uniform for the impermeable wall with finite thickness. This means that the First Approach is physically reasonable. When the First Approach is applied to the thermal boundary condition, an additional boundary condition based on the local thermal equilibrium assumption at the interface is used. This additional boundary condition is applicable except in the case of a very thin impermeable wall. Hence,

for practical situations, appropriate thermal boundary conditions at the interface between the porous medium and the impermeable wall are formulated as Eqs. (7*a*) and (7*b*). In order to validate our suggestion, convective flows both in a microchannel heat sink and in a sintered porous channel are analyzed by using the two Approaches separately as a thermal boundary condition at the interface. The analytically obtained thermal resistance of the microchannel heat sink and the numerically obtained overall Nusselt number for the sintered porous channel are shown to be in close agreement with available experimental results when our suggestion for the thermal boundary condition at the interface is applied.

Acknowledgments

This work was supported by KISTEP (Korea Institute of Science and Technology Evaluation and Planning) under grant number 2-578 through the National Research Lab Program.

Nomenclature

c = specific heat
C = effective conductivity ratio, $(=\varepsilon k_f/(1-\varepsilon)k_s)$
dp/dx = pressure drop
Bi = equivalent Biot number, $(=h_l a H^2/k_s^*)$
d_p = average bead diameter
Da = Darcy number, $(=K/\varepsilon H^2)$
D_h = hydraulic diameter of the sintered porous channel
D_t = empirical constant of the Van Driest model
h_m = heat transfer coefficient based on the bulk mean temperature
H = channel height
k = thermal conductivity
k_f^* = effective thermal conductivity of the fluid
k_s^* = effective thermal conductivity of the solid
K = permeability
$\mathrm{Nu}_{\infty,0}$ = overall Nusselt number, $(=2Hh_m/\varepsilon k_f)$
P = dimensionless pressure drop, $(=K(dp/dx)/\varepsilon\mu_f u_m)$
q'' = heat flux
Re = Reynolds number, $(=\varepsilon\rho_f u_m d_p/\mu_f)$
s = substrate thickness
T = temperature
T_b = bulk mean temperature
T_w = wall temperature
u = fluid velocity
u_m = mean velocity of the fluid
U = dimensionless fluid velocity, $(=u/u_m)$
ω = empirical constant of the Van Driest model
w_c = channel width
w_w = thickness of the fin
x,y,z = Cartesian coordinate system
Y = dimensionless y-coordinate, $(=y/H)$
Z = dimensionless z-coordinate, $(=z/H)$
α_s = aspect ratio, $(=H/w_c)$
ε = porosity
μ = viscous coefficient
θ = dimensionless temperature
ρ = density
Δ_T = nondimensionalized temperature difference between the two phases at the interface
$\langle\ \rangle_f$ = volume-averaged value over the fluid region
$\langle\ \rangle_s$ = volume-averaged value over the solid region

Subscripts

f = fluid
s = solid

References

[1] Sahraoui, M., and Kaviany, M., 1993, ''Slip and No-Slip Temperature Boundary Conditions at Interface of Porous, Plain Media: Conduction,'' Int. J. Heat Mass Transf., **36**, pp. 1019–1033.
[2] Sahraoui, M., and Kaviany, M., 1994, ''Slip and No-Slip Temperature Boundary Conditions at the Interface of Porous, Plain Media: Convection,'' Int. J. Heat Mass Transf., **37**, pp. 1029–1044.
[3] Amiri, A., Vafai, K., and Kuzay, T. M., 1995, ''Effects of Boundary Conditions on Non-Darcian Heat Transfer Through Porous Media and Experimental Comparisons,'' Numer. Heat Transfer, Part A, **27**, pp. 651–664.
[4] Hwang, G. J., Wu, C. C., and Chao, C. H., 1995, ''Investigation of Non-Darcian Forced Convection in an Asymmetrically Heated Sintered Porous Channel,'' ASME J. Heat Transfer, **117**, pp. 725–732.
[5] Koh, J. C. Y., and Colony, R., 1986, ''Heat Transfer of Microstructures for Integrated Circuits,'' Int. Commun. Heat Mass Transfer, **13**, pp. 89–98.
[6] Shah, R. K., and London, A. L., 1978, *Laminar Flow Forced Convection in Ducts*, Academic, New York.
[7] Patankar, S. V., 1980, *Numerical Heat Transfer and Fluid Flow*, McGraw-Hill, New York.
[8] Kim, S. J., and Kim, D., 1999, ''Forced Convection in Microstructures for Electronic Equipment Cooling,'' ASME J. Heat Transfer, **121**, pp. 639–645.
[9] Kim, S. J., Kim, D., and Lee, D. Y., 2000, ''On the Local Thermal Equilibrium in Microchannel Heat Sinks,'' Int. J. Heat Mass Transf., **43**, pp. 1735–1748.
[10] Tuckerman, D. B., and Pease, R. F. W., 1981, ''High-Performance Heat Sinking for VLSI,'' IEEE Electron Device Lett., **2**, pp. 126–129.
[11] Hwang, G. J., and Chao, C. H., 1994, ''Heat Transfer Measurement and Analysis for Sintered Porous Channels,'' ASME J. Heat Transfer, **116**, pp. 456–464.
[12] Kim, S. J., and Kim, D., 2000, ''Discussion on Heat Transfer Measurement and Analysis for Sintered Porous Channels,'' ASME J. Heat Transfer, **122**, pp. 632–633.

S. Dembele
E-mail: s.dembele@kingston.ac.uk

J. X. Wen

Combustion and Fire Modelling Group,
School of Mechanical, Aeronautical, and
Production Engineering,
Kingston University,
Roehampton Vale, Friars Avenue,
London SW15 3DW, England

J.-F. Sacadura
Centre de Thermique de Lyon (CETHIL),
Bâtiment 404, 20 avenue Albert Einstein,
69621 Villeurbanne Cedex, France

Experimental Study of Water Sprays for the Attenuation of Fire Thermal Radiation

A laboratory experimental work is carried out to investigate the attenuation ability of water sprays subjected to thermal radiation. The objective is to analyze the key parameters involved in the mitigation properties of this fire protection technique. The spectral transmittances of two types of sprayers, TG03 and TG05, are measured with a Fourier infrared spectrometer under various conditions. The wavelength range varies from 1.5 to 12 μm. The influence on the transmittance of both the flow rate and the pressure ranging from 1 to 7 bars, as well as the effect of the number of spray nozzles are considered. The results clearly show the advantage of small drops with high concentration. An investigation on the multi-ramp curtain configuration also provides valuable information on the mitigation behavior of the whole spray. Key guidelines are provided for fire protection engineering. [DOI: 10.1115/1.1371921]

Keywords: Droplet, Experimental, Heat Transfer, Radiation, Sprays

1 Introduction

Over years, many studies have been carried out to find the most effective methods of protection for storage tanks, distribution systems and other sensitive areas against the risk of fire. In the technology of safety that has evolved, a most important part is played by water sprays, which can be used in fixed protection systems in at least three distinct ways. First they can be used alone for the direct extinction of fires. Secondly, water sprays can be used for surface cooling, to inhibit the spread of fire. Finally, they can be used to provide a water curtain (i.e., series of spray nozzles) that will present a continuous barrier to obstruct the passage of flame and thermal heat. This last application of water sprays (Fig. 1) for fire radiation attenuation was investigated through the European research project ASTRRE (1994–1997). Most of the past works on the use of water sprays in fire protection are theoretically based. Among others, Thomas [1], Ravigururajan and Beltran [2], and Coppalle et al. [3]. Water spray is a two-phase participating medium composed of polydisperse droplets and water vapor. A spray curtain attenuates thermal radiation by the combined absorption and scattering mechanisms due to water droplets, as well as by water vapor absorption mainly. Theoretical analyses have helped understanding the main parameters controlling the attenuation efficiency of a spray (Dembele et al. [4]; Dembele [5]). However few experimental studies have supported the theoretical works. The main purpose of the experimental work presented here is to fully analyze the optical behavior of water sprays when subjected to thermal radiation. We investigate the influence on the attenuation ability of many parameters such as the droplet size and distribution, the spray nozzle type, feeding pressure and flow rate. Series of similar sprayers as well as mixed water sprays are analyzed. Useful information is provided regarding the mitigation power of these arrangements. The wavelength dependency of the spray attenuation properties is also clearly shown through the results. This study is probably among the first to deeply investigate experimentally the spectral attenuation features of water sprays. Key guidelines are suggested for fire protection engineers using water sprays.

Contributed by the Heat Transfer Division for publication in the JOURNAL OF HEAT TRANSFER. Manuscript received by the Heat Transfer Division November 8, 1999; revision received November 15, 2000. Associate Editor: J. Gore.

2 Experimental Water Spray Facility

Facility Description. Figure 2 presents the experimental facility used to analyze the attenuation performance of water sprays by measuring the fraction of the infrared collimated radiation transmitted through the spray, i.e., transmittance. It is composed of three main parts: the Fourier spectrometer, the water spray and the detection system. The spectrometer FTS 60 A, manufactured by Bio-Rad Inc., is based on Fourier transform spectroscopy and the wavelength range considered here varies from 1.5 to 12 μm. The source of radiation is a tungsten filament inside a silica tube. Its emission spectrum is close to that of a blackbody at 1300°C. The solid angle of the collimated beam reaching the spray is determined by selecting one of the four movable holes (1.2, 2.7, 4, and 7 mm diameter) of the entrance slit, Fig. 3. The spectrometer uses the Michelson interferometer principle and the exit infrared beam is measured by a detector as a function of path difference between the fixed and movable mirrors. The detection system, Fig. 3, is composed of a spherical mirror collecting the beams and concentrating them on a quantic detector HgCdTe. This system is mounted on a rotating arm for off-incidence measurements, i.e., scattering effect quantification. The spectrometer and the detection system are connected to a central computer for monitoring and data processing. Spray nozzles, movable in the vertical direction (y in Fig. 2), are fed with water at a pressure ranging from 1 to 7 bars. These nozzles generate the water spray. The pressure difference at the nozzle exit breaks up the liquid mass and pro-

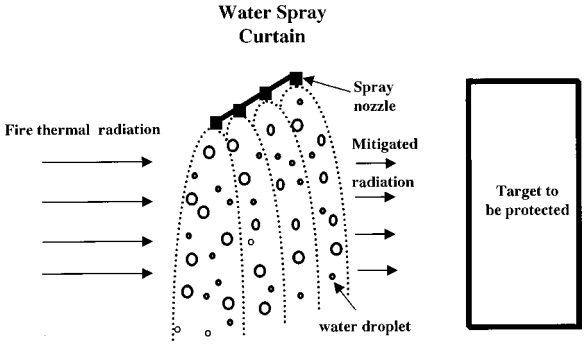

Fig. 1 Protecting plants with water sprays technique

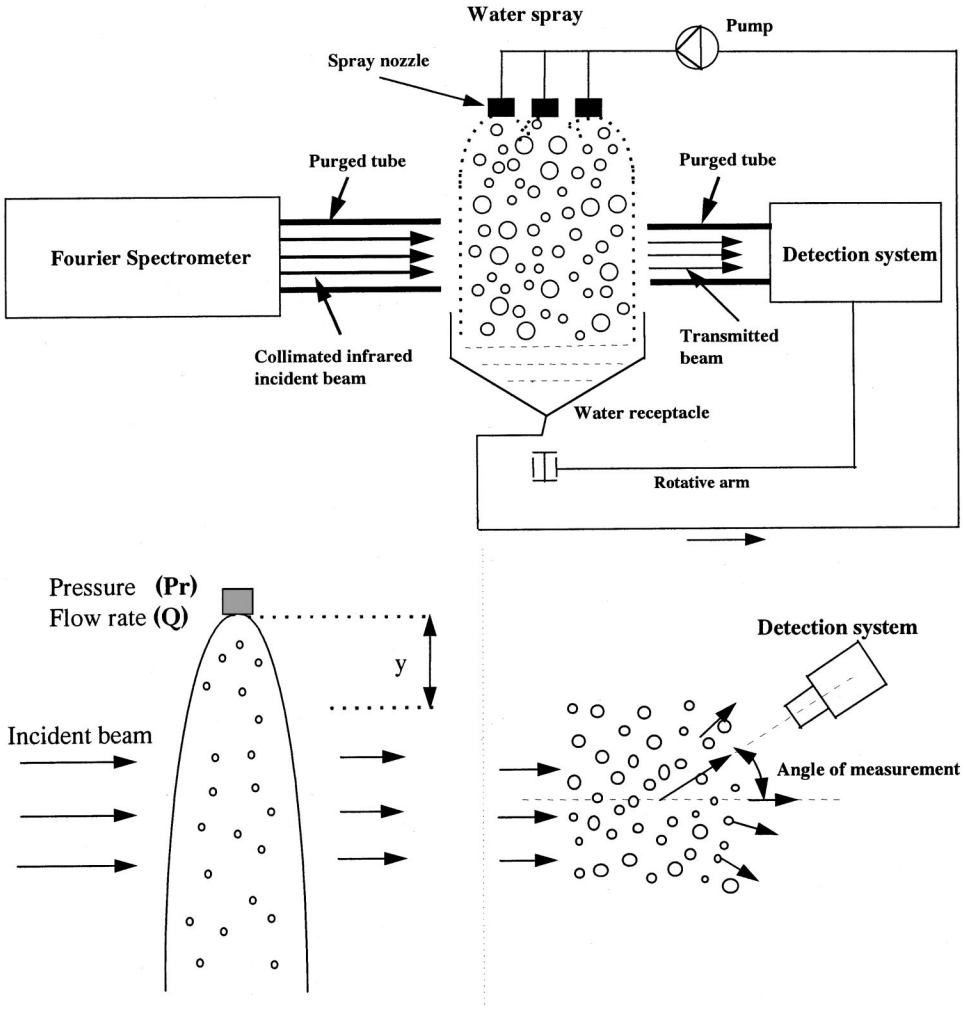

Fig. 2 Laboratory experimental water spray facility and measurement parameters

FOURIER SPECTROMETER

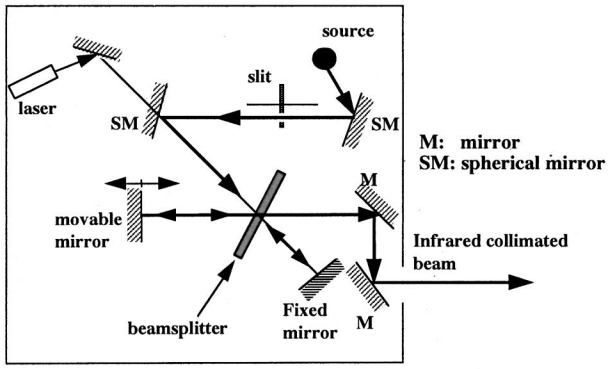

DETECTION SYSTEM

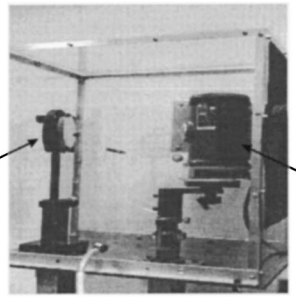

Fig. 3 The Fourier spectrometer and the detection system

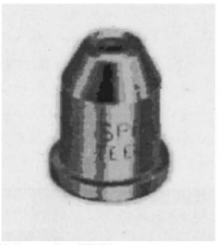

Nozzle TG

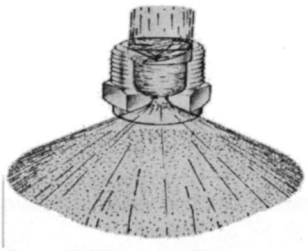

Spray TG03 & TG05 pattern

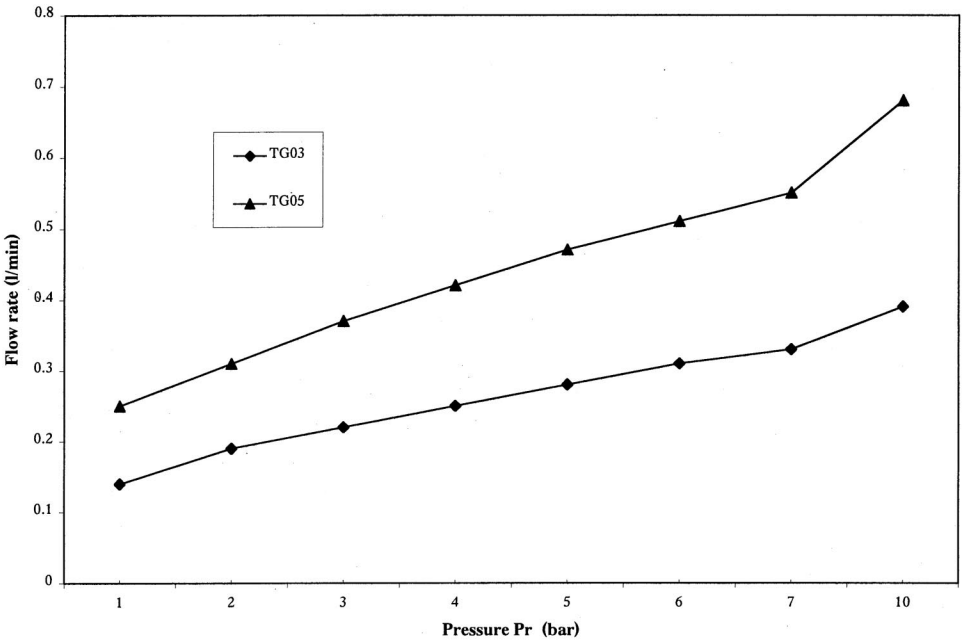

Fig. 4 Characteristics of the spray nozzles tested

duce droplets characterized by their size and distribution. Two tubes purged by dry air are used on both the spectrometer and detection sides to prevent any absorption by ambient air. Therefore only the spray gases absorption and droplets extinction are considered in the transmittance spectra. An optical alignment procedure of the whole system is carried out by using both the spectrometer and an external mirror laser beams.

Spray Nozzles. Spray nozzles differ according to their spray pattern, flow capacity, spray angle, the velocity and impact of the sprays and the size and distribution of the liquid particles (droplets). In our investigation, the nozzles were chosen according to some practical considerations related to the available measurement environment. Sprayers with low volume flow rates were chosen to avoid important splashes on the water receptacle that can affect the spectrometer's components. Also the sprayers selected provide small drops. It is important to recall that small droplets at high concentration should achieve a better attenuation efficiency. Round pattern spray nozzles have been chosen because of their axisymetric property leading to major simplifications in the hydrodynamic modelling (St. Georges [6]). Even if hydrodynamic modelling was not part of our work, others modellers could easily use the radiation measurements presented here when there is a need to couple the radiative and hydrodynamic behaviors. Two classes of industrial round pattern nozzles, so-called TG03 and TG05, all manufactured by Spraying Systems Co. are investigated here. The exit diameters of the nozzles TG03 and TG05 are respectively 0.41 mm and 0.51 mm. Figure 4 presents a photography of the nozzle and the pressure-flow rate curves for each sprayer. These curves were determined experimentally prior to each set of tests, and compared with that provided by the manufacturer to detect any nozzle defect. The flow number FN (ratio of the volume flow rate to the square root of the pressure) is a constant characteristic parameter for each nozzle and has the values of $6.698\,10^{-9}$ and $1.123\,10^{-8}\,\mathrm{m^3/s}\sqrt{Pa}$, respectively for TG03 and TG05.

Measurement Procedure. The water spray transmittance is measured with the experimental facility, Fig. 2, by two steps. In a first step, a measurement of the infrared signal is carried out without the water spray; this signal is known as the ''background.'' In the second step, the nozzle is fed with water (spray on) and only the transmitted beam through the spray is measured by the detection system. The ratio of the signal measured with the spray activated to the ''background'' signal provides the transmittance of

the spray. Transmittance measurements are functions of many parameters. Only the following four parameters are considered here: the nozzle pressure (Pr) or flow rate (Q), the vertical position (y) measured from the nozzle exit, the angle of measurement (incident or off-normal directions) and the spectrometer spectral resolution.

3 Experimental Results and Discussion

A triangular instrument line shape (ILS) is chosen for the spectrometer. A spectral resolution of 25 cm^{-1} of the spectrometer is also taken for reasonable measurement time. This time is to be multiplied by five for measurements at 2 cm^{-1}. A lower value of the resolution, i.e., higher spectral resolution involves enormous measurement time since the displacement of the movable mirror (Fig. 3) is larger and an important number of data points is required. Each single transmittance spectrum measured by the spectrometer is the average of 200 co-added measurements. This averaging process is performed by the spectrometer and improved the ratio signal/noise of the interferogram. For a fixed set of the experiment parameters, each single spectrum recorded by the spectrometer was measured 15 times in similar conditions and then averaged. The uncertainties due to random errors are assessed through the standard deviation, which is the measure of the dispersion. The standard deviation, function of the measurement parameters is defined as $\sigma=\sqrt{1/n-1\Sigma_{i=1}^{n}(T_n-T_r)^2}$, where $\overline{T_r}$ is the mean value of the n measurements.

The 95 percent confidence interval limits are given by $\pm 2\sigma$. Figure 5 presents the confidence interval limit 2σ for a sprayer TG03 at the position $y=200$ mm from the spray nozzle, in the incident or normal direction. The values are spectrally dependent. The precision limit on the spectral transmittance is less than ± 1.2 percent at 7 bars, ± 0.6 percent at 5 bars and ± 0.5 percent at 1 bar. The bias limit with the spectrometer was found to be about ± 0.2 on transmittance values. The maximum of the spectral overall uncertainty would therefore be about ± 1.21 at 7 bars. For the sprayer TG05, the standard deviation curves show the same features as those presented for the sprayer TG03.

3.1 Effect of the Vertical Position on the Attenuation For a given nozzle and pressure, the vertical position, y in Fig. 2, is varied and the transmittances spectra measured in the incident direction. The objectives of these measurements are to quantify the effect of this vertical position on the attenuation, to select a position for all data set record and also to identify the position from which the transmittances do not vary. The relative pressure was varied from 1 to 5 bars and three vertical positions selected: $y=200$, 300, and 350 mm. Figure 6 presents the experimental curves for the nozzle TG03 at the pressures of 1 and 5 bars. At a given pressure, the curves show that the transmittances are very close, independently of the vertical position. At 1 bar (three curves located around 90 percent transmittance), the relative differences between spectral transmittances, taking values at 200 mm as reference do not exceed 2 percent for 300 and 350 mm. At 5 bars, the three curves close to 70 percent transmittance, the same differences do not exceed 7 percent and there is not a major difference between the results. Similar conclusions are found for the nozzle TG05. The major conclusion from these results on the effect of the vertical position is that for the sprayers TG03 and TG05, the droplet distribution as well as the spray pattern are nearly stable over 200 mm. This stabilization corresponds, from the hydrodynamics point of view, to a balance between the competing effects of air entrainment and radially outbound droplet motion. These conclusions are valid for more other industrial sprayers. Even if the numerical values of the stabilization position may vary from one nozzle to another, there does exist a position for which the spray properties are stable. Afterwards in this paper, results will be shown only for the vertical position of 200 mm.

3.2 Effect of the Pressure on the Attenuation of a Single Nozzle Water Spray. In this section, we analyze the influence of the pressure on the attenuation ability of the water spray provided by a single sprayer TG03 and TG05. Figures 7 and 8 show the transmittance spectra respectively for the nozzle TG03 and TG05 in the incident direction at 200 mm. Values of the total transmittance (Trtot) are calculated by integrating the spectral transmittances. These curves reveal two types of zones in the attenuation spectrum of a water spray:

- Continuous zones corresponding to the wavelength range where the spray attenuation is mainly due to absorption and scattering by liquid droplets (liquid phase). The gas contribution is negligible in these regions.
- Zones presenting the absorption bands of the gas [centred at

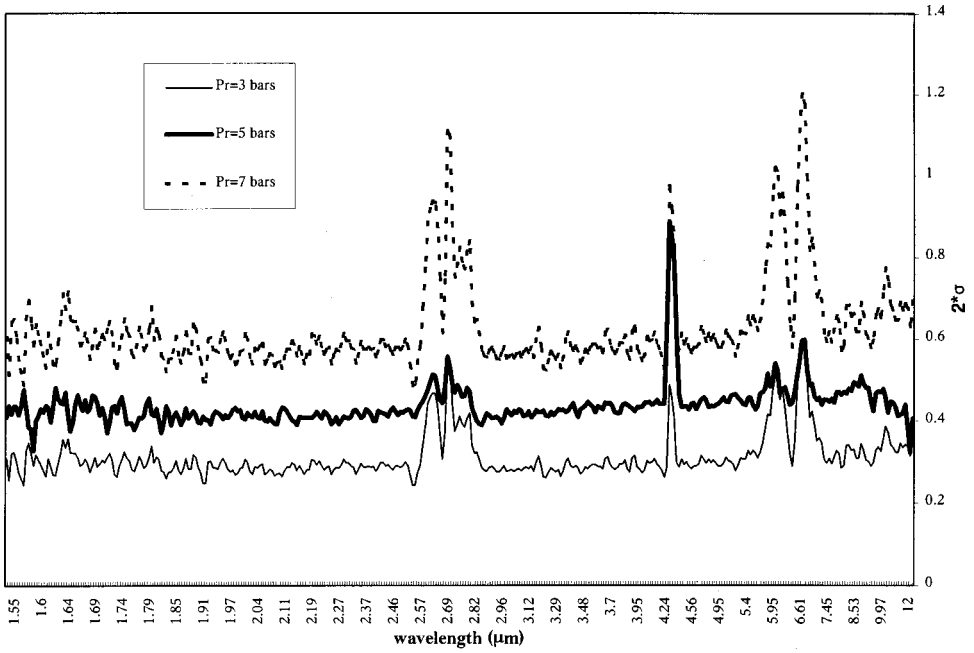

Fig. 5 Standard deviation curves for the spray nozzle TG03

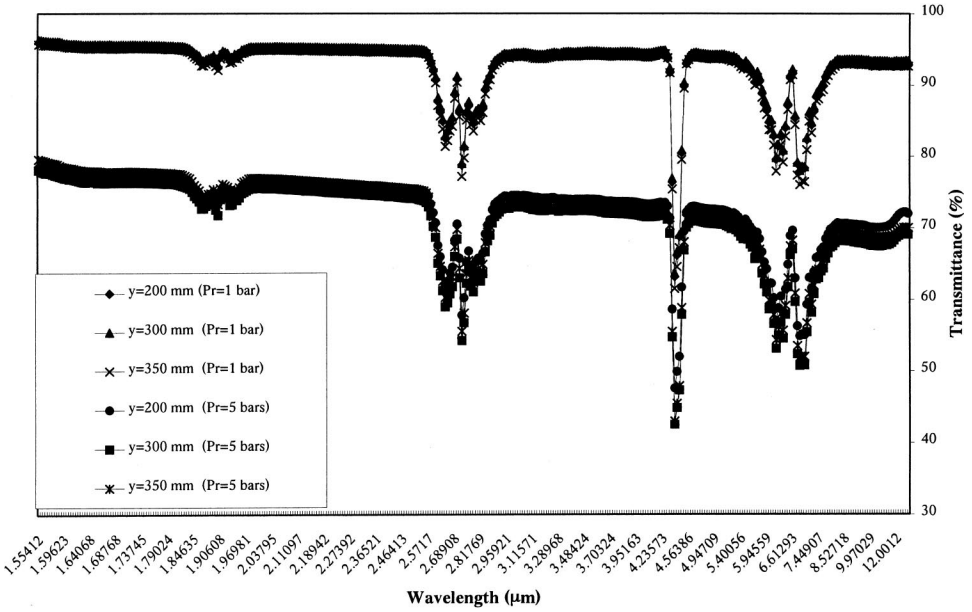

Fig. 6 Influence of the vertical position on the transmittance spectra of a single sprayer TG03

1.9, 2.7, and 6.3 μm for H_2O and 4.3 μm for CO_2]. Both the liquid and gaseous phases of the spray attenuate simultaneously radiation in these bands.

The total transmittance of a single sprayer TG03 (Fig. 7) varies from 90 percent at 1 bar (0.14 l/min) to 66 percent at 7 bars (0.33 l/min). An attenuation value of about 35 percent can be achieved with this type of sprayer in the absence of important evaporation. The width of the spray TG03 is of about 240 mm and its relative humidity measured by a hygrometer is of 80 percent. Figure 8 shows the results for the nozzle TG05. Similar attenuation values are obtained for a given pressure, compared to TG03, but with flow rates 1.5 times greater. In the light of these curves, the clear tendency is that, for each spray nozzle, an increase in pressure (and flow rate) leads to higher attenuation power (i.e., lower transmittance values). This fact can be explained by the combined effects of the following two parameters controlling the droplets (liquid phase) attenuation: their size and number density or concentration. The concentration C (kg/m^3) is related to the number of particles per unit volume (N) by $C=(\varrho\pi d^3N)/6$, where d is the droplet diameter and ϱ the liquid density (water). An increase in pressure and flow rate leads to finer drops and greater number density (N) and concentration. All these will result in higher attenuation efficiency. For a deeper understanding of these experimental results, Fig. 9 presents the volumetric fraction distribution at the position $y=200$ mm obtained by phase-Doppler anemometry for a nozzle TG03 at the Von Karman Institute. The laser anemometer called the Phase Doppler Particle Analyser of Aerometric Inc., measures the diameter and the velocity of a droplet

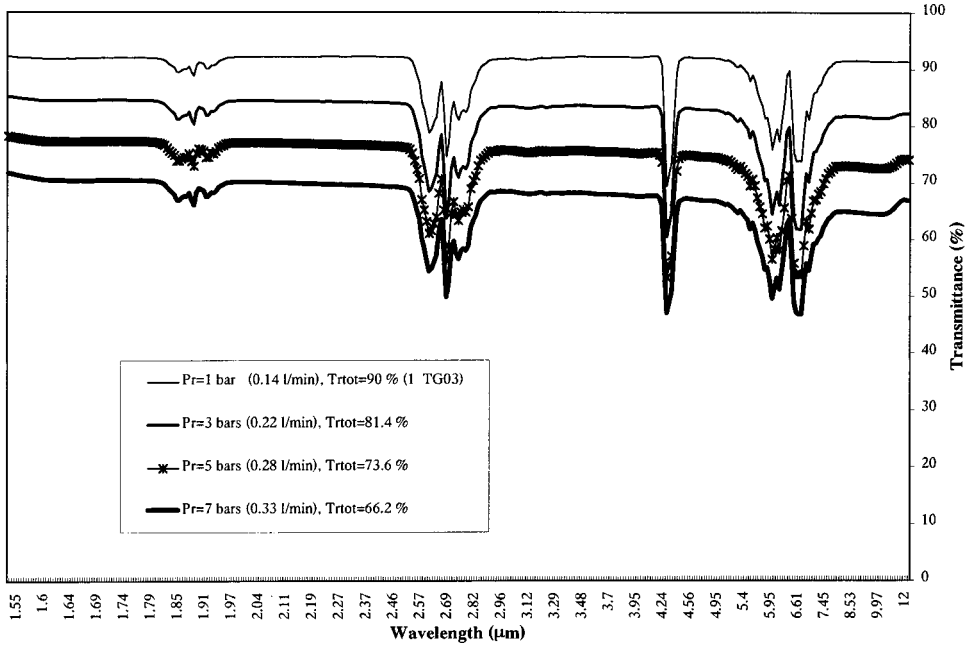

Fig. 7 Influence of the pressure on the transmittance of a single spray TG03

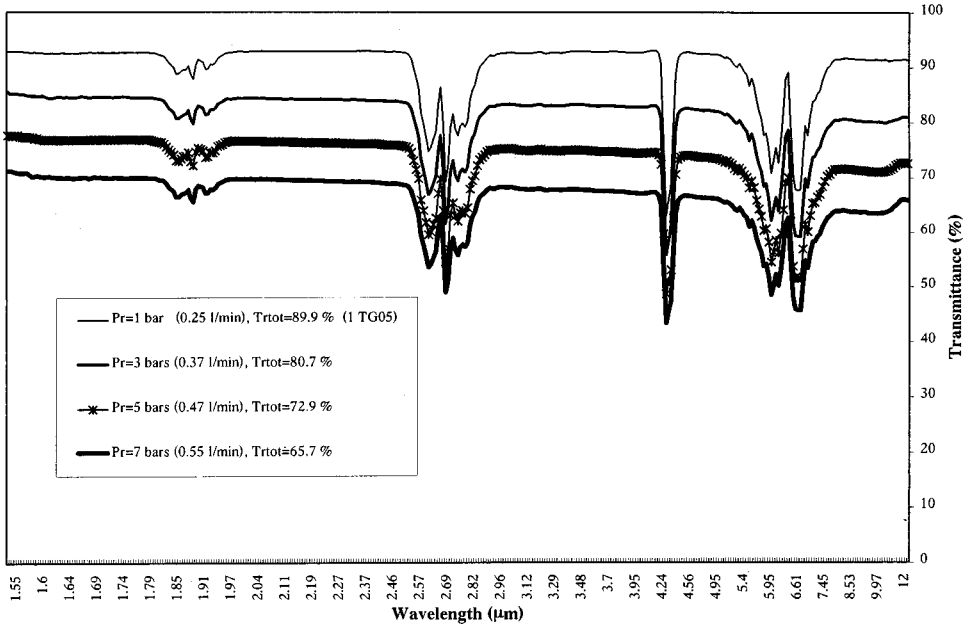

Fig. 8 Influence of the pressure on the transmittance of a single spray TG05

located at the intersection of two laser beams. The results show that in general an increase in the pressure from 1 to 7 bars, results in a displacement of the distribution pattern towards smaller drops with higher volumetric fraction. In Fig. 7, the mean Rosin-Rammler diameters (MRD) are 187, 135, 115, and 104 μm respectively for the pressures of 1, 3, 5, and 7 bars. The mean volumetric diameters (MVD) for the nozzle TG05 are respectively 550, 375, 300, and 220 μm for the same pressures. The higher attenuation obtained with small droplets can be theoretically explained. For a monodispersion of droplets characterized by a diameter (d) and concentration (C), the extinction coefficient in m^{-1} unit (sum of the scattering and absorption coefficients) is given by $K_{ext}=3Q_{ext}C/2\varrho d$, where Q_{ext} is the extinction efficiency factor obtained by the Mie theory in general.

This equation suggests in a straightforward manner that a simultaneous increase in the concentration of drops and decrease in their diameters will lead to a higher extinction coefficient. Moreover, to fully analyze theoretically the scattering mechanism, Figure 10 shows the spectral scattering phase functions (obtained by Mie theory, Dembele et al. [4]) for three droplets diameters (10, 100, 300 μm) at 10 μm wavelength. The phase function describes the angular distribution of scattered radiation. It is highly peaked

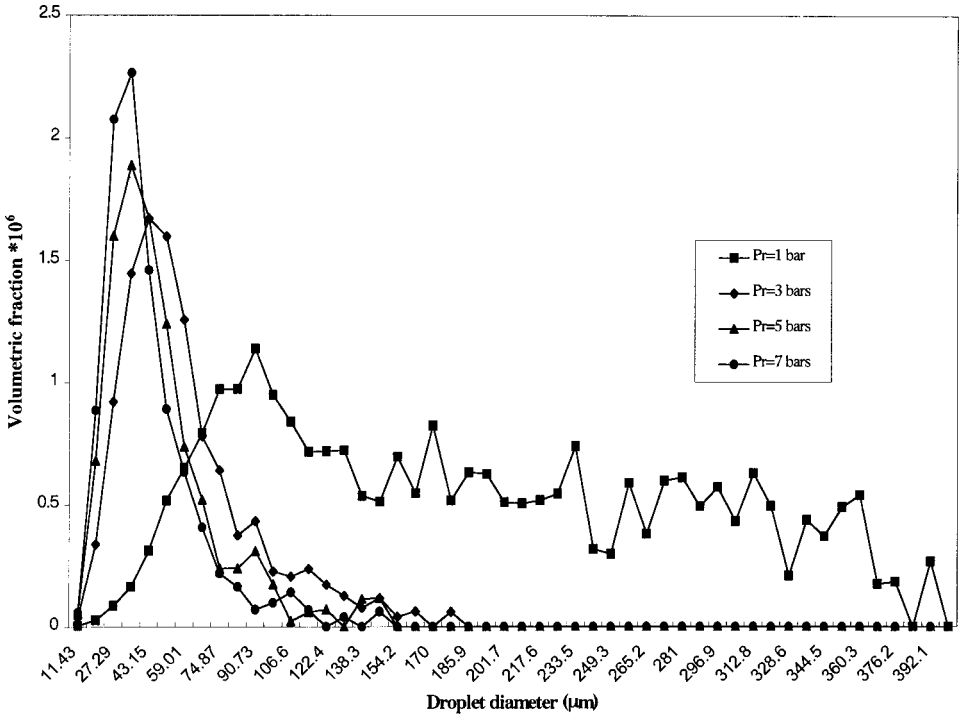

Fig. 9 Droplets volumetric fraction distribution of a sprayer TG03

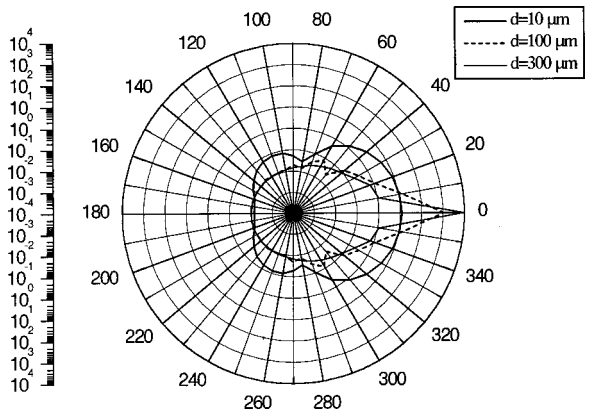

Fig. 10 Mie phase function of a water droplet at the wavelength $\lambda = 10\ \mu$m

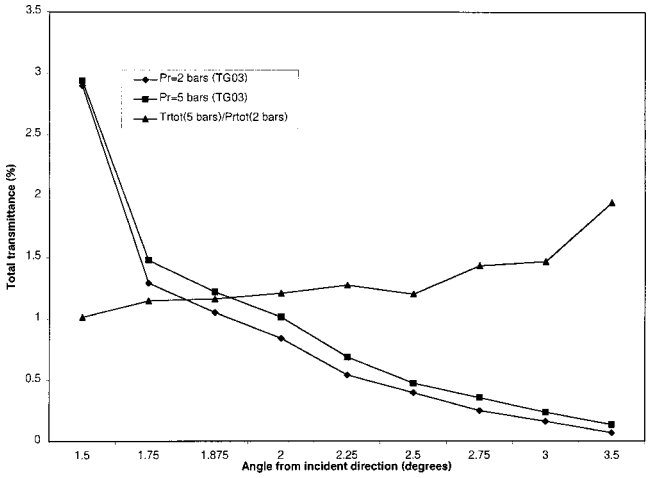

Fig. 11 Angular distribution of scattered radiation for a sprayer TG03

forward (i.e., concentrated in incident or normal directions 180 $\rightarrow$0) for $d = 300$ and 100 μm because of light diffraction occurring in directions close to the incident one. For the diameter $d = 10\ \mu$m, the scattered radiation distribution is more uniform in off-normal directions, with some backscattered fraction (angles between 0 and 180 deg). Therefore in terms of attenuation by scattering, smaller droplets are more efficient than larger ones since they scatter in off-normal directions with some backscattering. These theoretical analyses also support the experimental results shown in Figs. 7 and 8.

3.3 Quantification of Scattered Radiation. Measurements of scattered radiation have been carried out for both types of sprayers TG03 and TG05, by rotating the movable arm supporting the detection system (Fig. 2). The objective of these off-normal transmittance measurements is to quantify the angular distribution of the scattered energy. Figure 11 presents typical results obtained with the sprayer TG03 (similar to those obtained with TG05) at 2 and 5 bars. The major scattering region is between 1.5 and 3.5 degrees. This confirms that for the droplet distribution pattern encountered here (MRD of 160 μm at 2 bars, MRD$=$115 μm at 5 bars) the scattering is mainly in directions close to the incident or normal direction (i.e., perpendicular and co-planar to the spray axis). At a given angle, the energy transmitted in off-normal directions is greater at 5 bars compared to 2 bars because of the effect of small drops. The ratio of transmittances reaches 2 at 3.5 deg. At 5 bars, the number of these finer drops is more important. Above 3.5 deg, the measured transmittance is low ($<$0.1 percent) and the noises of measurements are important. These experimental results are in good agreement with the phase function diagram shown in Fig. 10. Moreover, as expected an increase in pressure strengthen the scattering in off-normal directions. Because of the small droplets at high concentration, scattering occurs mainly in these off-normal directions. The ratio between total transmittances at 5 and 2 bars is always greater than 1 (Fig. 11).

3.4 Transmittance Spectra of a Series of Similar Nozzles A water curtain is in practice formed by a series of nozzles arranged on a ramp (Fig. 1 shows a single or mono-ramp curtain). The investigation in this section is carried out for a series of nozzles (aligned in the direction of the incident beam, Fig. 2). The

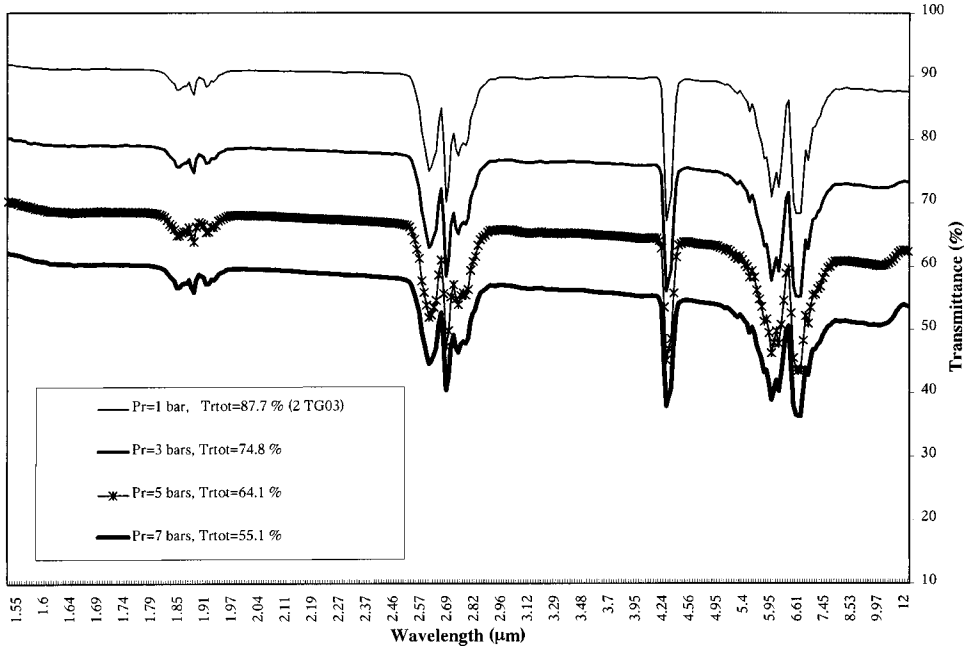

Fig. 12 Influence of the pressure on the transmittance of 2 sprayers TG03 in series. Spacing between nozzles 50 mm.

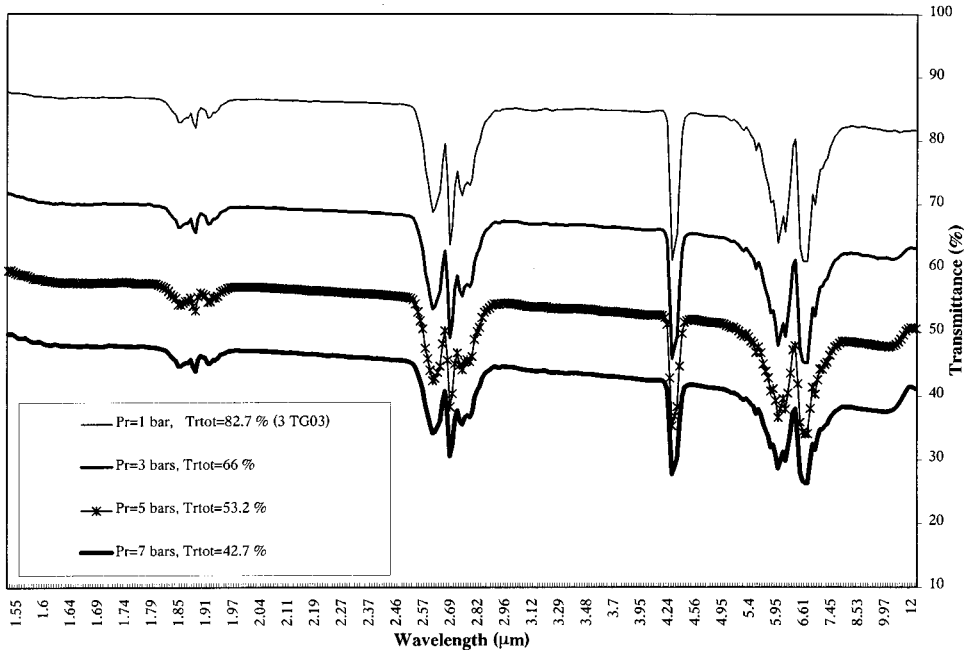

Fig. 13 Influence of the pressure on the transmittance of 3 sprayers TG03 in series

objective is to quantify and analyze the influence of this arrangement, i.e., bi and tri-ramp curtain, on the attenuation behavior. The spacing between two successive nozzles is 50 mm and measurements are carried out for the incident direction. Figures 12 and 13 present the influence of the pressure on the transmittance, respectively for 2 nozzles (bi-ramp, double flow rate) and 3 nozzles (tri-ramp, triple flow rate) in series. The width of the spray at 7 bars is 240 mm for a single sprayer TG03. For 2 and 3 nozzles, this width is 290 and 340 mm respectively. At 7 bars (maximum attenuation for the pressure range presented), the total transmittance which was 66 percent for a single sprayer TG03, falls to 55 percent and 43 percent respectively for 2 and 3 nozzles. For the sprayer TG05, the total transmittance (curves not presented here) at 7 bars varies from 66 percent (1 nozzle) to 59 percent (2 nozzles) and 47 percent (3 nozzles). These curves clearly show, as expected that an increase in the number of ramp (i.e., nozzles) improves the attenuation but at the price of higher flow rate. To further analyze this effect, the variation of the optical path ($\tau = -\ln(Tr_{tot})$) is shown in Figs. 14 and 15 respectively for nozzles TG03 and TG05. We note that at the lowest pressure of 1 bar, the optical thickness varies slightly linearly with the number of nozzles (i.e., flow rate). For higher pressures (3, 5, and 7 bars), the optical thickness does not increase proportionally with the flow rate and the attenuation is smaller than what we should expect by adding single optical thicknesses. This important behavior of multi-ramp spray could be explained by the hydrodynamic interaction between sprays provided by each nozzle. In the region where two adjacent sprays interact, droplet coalescence occurs, increasing the droplet sizes. As a result of larger drop sizes with lower number density, the attenuation efficiency will be lower than expected by adding the effects of the two sprays. Then an increase in the spacing between nozzles (achieved here by decreasing the pressure) improves the attenuation since the coalescence effects become negligible.

3.5 Investigation of the Flow Rate Effect on the Attenuation. For a given spray nozzle, the results have shown that an increase in both pressure and flow rate improves the attenuation. The drops size and distribution as well as the liquid quantity play a role. The aim of this part is to assess the contribution to the mitigation power, due on one hand to the drops size and concen-

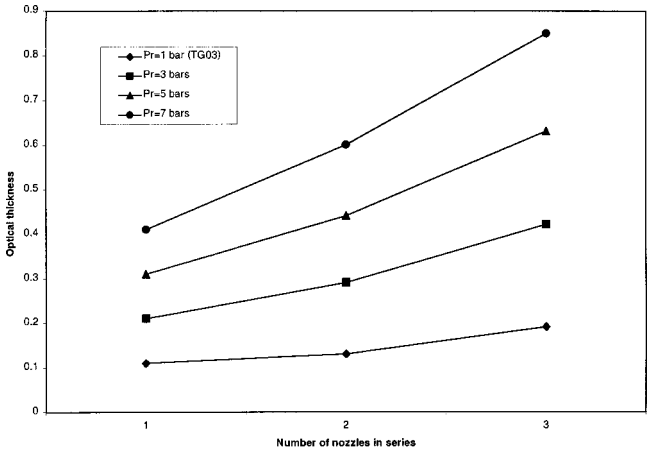

Fig. 14 Influence of the number of nozzles on the optical thickness of the sprayer TG03

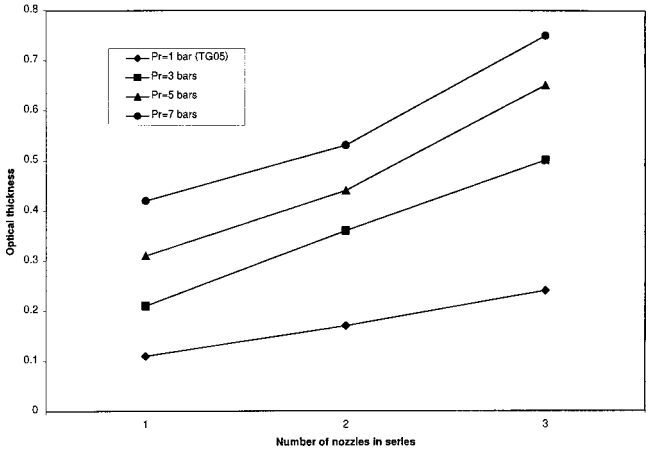

Fig. 15 Influence of the number of nozzles on the optical thickness of the sprayer TG05

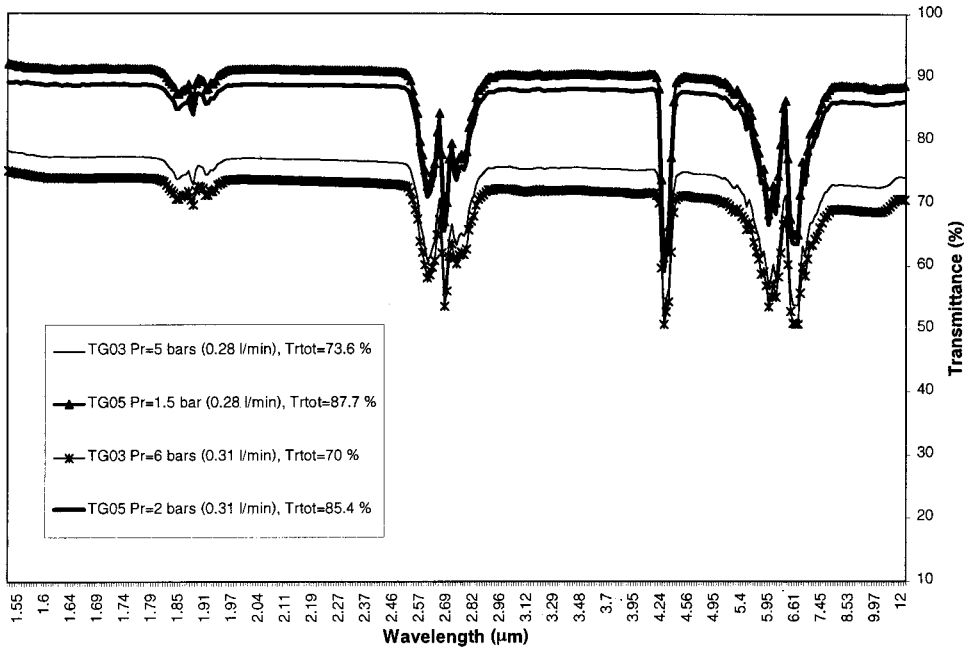

Fig. 16 Effect of the flow rate on the transmittance spectra of the sprayers TG03 and TG05

tration, and on another hand to the quantity of liquid used. The influence of the flow rate is investigated here by comparing the transmittance spectra of water sprays provided by nozzles TG03 and TG05, for the same flow rate. Figure 16 presents the results for identical flow rates of 0.28 l/min and 0.31 l/min. At 0.28 l/min, the total transmittance is 73.6 percent for the sprayer TG03 (Pr=5 bars) and 87.7 percent for the TG05 one. The same transmittances at 0.31 l/min are respectively 70 percent and 85.4 percent for TG03 and TG05. These results clearly show that for the same flow rate, the attenuation is better with the sprayer TG03 than TG05, because of the finer drops at higher concentration obtained with the former. An important conclusion can be underlined from these experimental results: as far as the attenuation ability of a water spray is concerned, the most important thing is rather the way water is distributed into droplets than the quantity of water used.

3.6 Investigation of the Attenuation Efficiency of Mixed Sprayers. The idea behind the results presented in this section is linked to the practical use of water spray curtain in industrial environment. The previous results have clearly shown that small droplets at high concentration can achieve good attenuation performance. However in a large scale environment, this type of spray could be blown by a strong wind, contrary to spray of large drops (less efficient in terms of attenuation) which are more

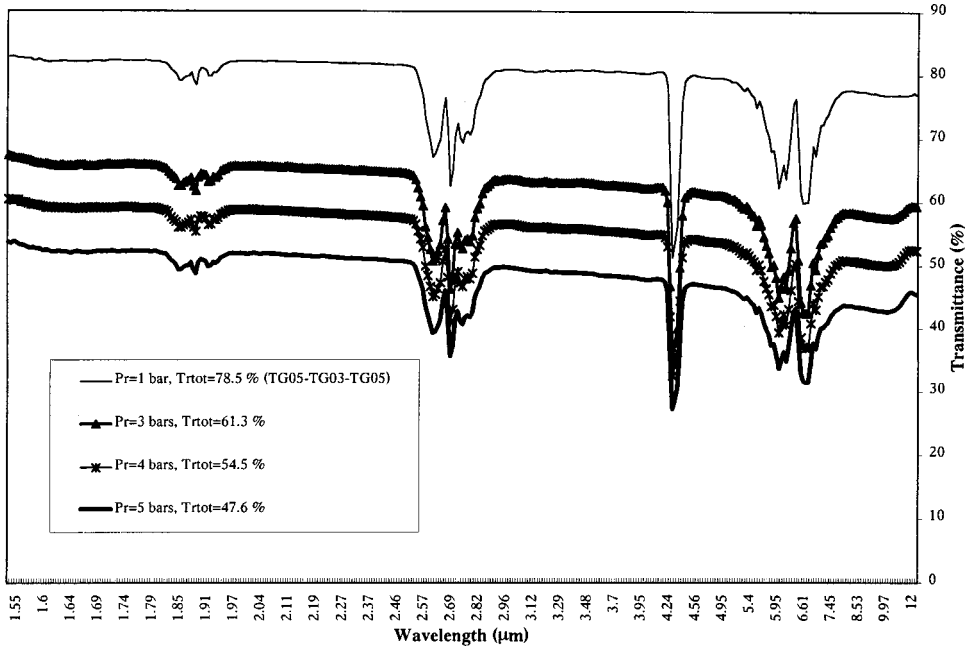

Fig. 17 Influence of the pressure on the transmittance of a mixed water spray: TG05-TG03-TG05. Spacing between 2 successive nozzles 50 mm.

stable. A practical suggestion is to use mixed sprayers on a multi-ramp configuration. For example on a tri-ramp water curtain, the two boundary ramps will use sprayers of large drops for more stability while the central one will use nozzles with finer drops for higher attenuation. This configuration is reproduced in laboratory by using three sprayers in series: two TG05 providing larger drops on boundaries and one TG03 (finer drops) in the middle. The spacing between two successive nozzles is 50 mm. Figure 17 presents the transmittance results obtained for the pressures of 1, 3, 4, and 5 bars. Logically, because of the finer drops provided by TG03 nozzle, the attenuation should be higher (transmittance lower) than that obtained with three sprayers TG05. With three sprayers TG05 in series, the total transmittance values are 78.9 percent, 60.4 percent, 52.2 percent, and 47.2 percent respectively for the pressures of 1, 3, 4, and 5 bars. At 1 bar, the transmittances are slightly identical. However for the pressures of 3, 4, and 5 bars, despite the contribution of TG03, the attenuation obtained with the mixed sprayers is lower than that with 3 nozzles TG05. One explanation to this key behavior of mixed water sprays is related to the hydrodynamics of the whole spray. The finer drops (TG03) in the central zone of the mixed spray are accelerated (high velocities) in the spray, dragged by the large drops from neighboring sprays. The number density of these small drops will therefore decrease in the spray, leading to a lower attenuation value. Thus these small drops, expected to the attenuation, will has a low number density in the spray and not contribute to the mitigation. Thus in the practical use of mixed sprayers in industry, special consideration should be given to the hydrodynamic mechanisms involved.

4 Conclusions

The experimental work presented in this paper has provided useful and valuable information about the attenuation parameters of a water spray subjected to thermal radiation. The spectral transmittances curves have clearly shown that the attenuation spectrum of a water spray comprises a continuous zone (attenuation due to water droplets) and zones where both the gases (water vapor and carbon dioxide) and the droplets mitigate radiation. A theoretical analysis on the water vapor contribution in the total attenuation power of a spray is presented in Dembele et al. [4]. The experimental results have also shown that for a given sprayer, an increase in pressure and flow rate improves the attenuation because of the finer drops in high concentration. Through the transmittance curves of the spray TG03 and TG05, we have identified the key parameters controlling the attenuation of a water spray curtain: the size and concentration of the droplets, the molar fraction of the gases, and the width of the curtain. An analysis of the influence of the flow rate has proved that for the same quantity of water, the sprayer TG03 with finer drops achieves higher attenuation than the TG05 type, which provides larger drops. Therefore to improve the efficiency of a water spray curtain, the key element is the way that water is sprayed into droplets, rather than the quantity of water delivered. An investigation of series of similar nozzles and mixed sprayers has also shown that the hydrodynamic interaction between the sprays of each single nozzle can deeply modify the attenuation ability of the whole curtain. Information provided in this study can be used as practical guidelines for fire protection engineers in the choice of spray nozzles. It can also serve as a validation database for water spray modellers.

References

[1] Thomas, P. H., 1952, ''Absorption and Scattering of Radiation by Water Sprays of Large Drops,'' Br. J. Appl. Phys., **3**, pp. 385–393.

[2] Ravigururajan, T. S., and Beltan, M. R., 1989, ''A Model for Attenuation of Fire Radiation Through Water Droplets,'' Fire Saf. J., **15**, pp. 171–181.

[3] Coppalle, A., Nedelka, D., and Bauer, B., 1993, ''Fire Protection: Water Curtains,'' Fire Saf. J., **20**, pp. 241–255.

[4] Dembele, S., Delmas, A., and Sacadura, J.-F., 1997, ''A Method for Modeling the Mitigation of Hazardous Fire Thermal Radiation by Water Spray Curtains,'' ASME J. Heat Transfer, **119**, pp. 746–753.

[5] Dembele, S., 1998, ''Mitigation of Hydrocarbon Fires Radiation by Water Spray Curtains: Modelling and Experimental Validations,'' Ph.D. dissertation (French), INSA Lyon, No. 98 ISAL 0043, Lyon, France.

[6] St. Georges, M., 1993, ''Hydrodynamic Study of Water Spray Curtains,'' Ph.D. dissertation (French), University Claude Bernard, Lyon, France.

S. L. Chang
ASME Mem.
e-mail: SLChang@anl.gov

S. A. Lottes

Argonne National Laboratory,
9700 South Cass Avenue,
Argonne, IL 60439

C. Q. Zhou

B. J. Bowman

Purdue University Calumet,
Hammond, IN 46323

M. Petrick
Argonne National Laboratory,
9700 South Cass Avenue,
Argonne, IL 60439

Numerical Study of Spray Injection Effects on the Heat Transfer and Product Yields of FCC Riser Reactors

A three-phase reacting flow computational fluid dynamics (CFD) computer code was used to study the major effects of spray injection parameters on mixing, heat transfer, vaporization, and reaction product yields in fluidized catalytic cracking (FCC) riser reactors. The CFD code was validated using experimental or field data. A number of computations were performed with varied injection parameters, including injection velocity, injection angle, and droplet size. Local optimum operating windows for spray injection parameters were identified, and the sensitivity of local optima to variation in spray parameters was also investigated. [DOI: 10.1115/1.1370509]

Keywords: Computational, CFD, FCC, Heat Transfer, Modeling, Multi-Phase, Sprays

Introduction

The rapid advance in the performance of computers has made possible a concurrent advance in computational approaches to simulate complex multiphase reacting flows. In many reacting flow systems of practical interest, the multiphase fluid dynamics and interaction between phases have a significant impact on heat transfer, flow development, and chemical kinetics because relevant flow properties, such as temperature, particle/droplet concentration, and gaseous mixture composition, change from point to point throughout the flowfield. The fluid catalytic cracking (FCC) process developed in the 1940s is a typical example. The FCC process using heated catalyst particles to vaporize liquid oil and crack the heavy oil vapor into lighter products is extensively used in the modern refinery industry. Currently, FCC operating capacity is estimated at 12,800,000 barrels per day worldwide and 4,400,000 barrels per day in the U.S. The FCC units in U.S. refineries produce about 40 percent of the nation's gasoline pool. It is also estimated that the U.S. will need about 200,000 barrels per day of additional capacity in the next few years. Over the years, refineries have greatly improved the FCC process to compete in the global markets and meet more stringent environmental regulations. In the past, the development of catalysts had the most significant impact on the improvement of FCC technology. Recently, refiners have become interested in the advancement of the feed injection system. Detailed knowledge of the relationships between process operating parameters and conditions within the system is needed to facilitate and speed up the development of new and/or upgraded FCC systems. Bienstock et al. [1] suggested that such knowledge can be obtained by using computer simulations.

Computer simulation of an FCC system began with kinetic calculation. Weekman and Nace [2] developed a three-lump cracking model to study gasoline production of an FCC unit. Later, Dave et al. [3] improved the model by adding the deactivation effect of coke on cracking reactions. Recently, Nigam and Klein [4] and Quann and Jaffe [5] developed ways to approach chemical kinetics computation and model building for cracking reaction systems with thousands of oil species. These kinetic computations are all based on simplified or assumed flow fields. In the last decade, with the advancement of computational techniques and computer hardware, computational fluid dynamics (CFD) codes were used to simulate FCC flows. The solid/gas flow hydrodynamics of risers has been modeled by a number of research groups. Sinclair and Jackson applied a granular flow model and demonstrated the lateral segregation of solids observed in experiments [6]. Pita and Sundaresan investigated effects of different inlet configuration on the flow pattern development [7]. Neri and Gidaspow compared modeling results with experimental data with a reasonable agreement and described the most significant features of the two-phase flow riser hydrodynamics, including the time-averaged core-annular flow regimes and the radial and axial nonhomogeneity of the flow [8]. Theologos and Markatos [9] used a commercial CFD code to study two-phase (gas/solid) reacting flow in FCC riser reactors. Weekman and Nace's kinetic model was used to account for the cracking reactions of the oil species in the FCC flow. Both gas and solid phases were treated as continua (Eulerian approach) in the flow. Empirical drag and heat transfer correlations were used for the phase interaction processes. A calibrated friction factor was used to predict pressure drop and total void fraction. Later, Theologos et al. [10] extended the riser flow simulation with a ten-lump kinetic model developed by Jacob et al. [11]. Gao et al. [12] used a three-dimensional two-phase flow-reaction CFD code to predict the performance of FCC riser reactors. The CFD code used a 13-lump kinetic model for cracking reactions. Again, an Eulerian approach was employed for the formulation of both gas and solid phase flows. An additional solid turbulent kinetic energy equation was added to the $k-\varepsilon$ turbulent model to account for particle diffusion. Both CFD codes were validated with some experimental data but have yet to include a spray vaporization model for the feed injection process, which is very important for commercial-scale risers.

Since 1994, Argonne National Laboratory (ANL) has been working with refining industry partners to develop a validated, three-dimensional, three-phase (gas/droplet/particle), reacting flow CFD code for the simulation of FCC riser reactors. The computer code was originally a general CFD code for two-phase flows (gas/liquid or gas/solid). It had been successfully validated [13] and used to predict characteristics of two-phase reacting flows in coal-fired combustors [14], air-breathing jet engines [15],

Contriibuted by the Heat Transfer Division for publication in the Journal of Heat Transfer. Manuscript received by the Heat Transfer Division September 26, 2000; revision received February 2, 2001. Associate Editor: J. P. Gore.

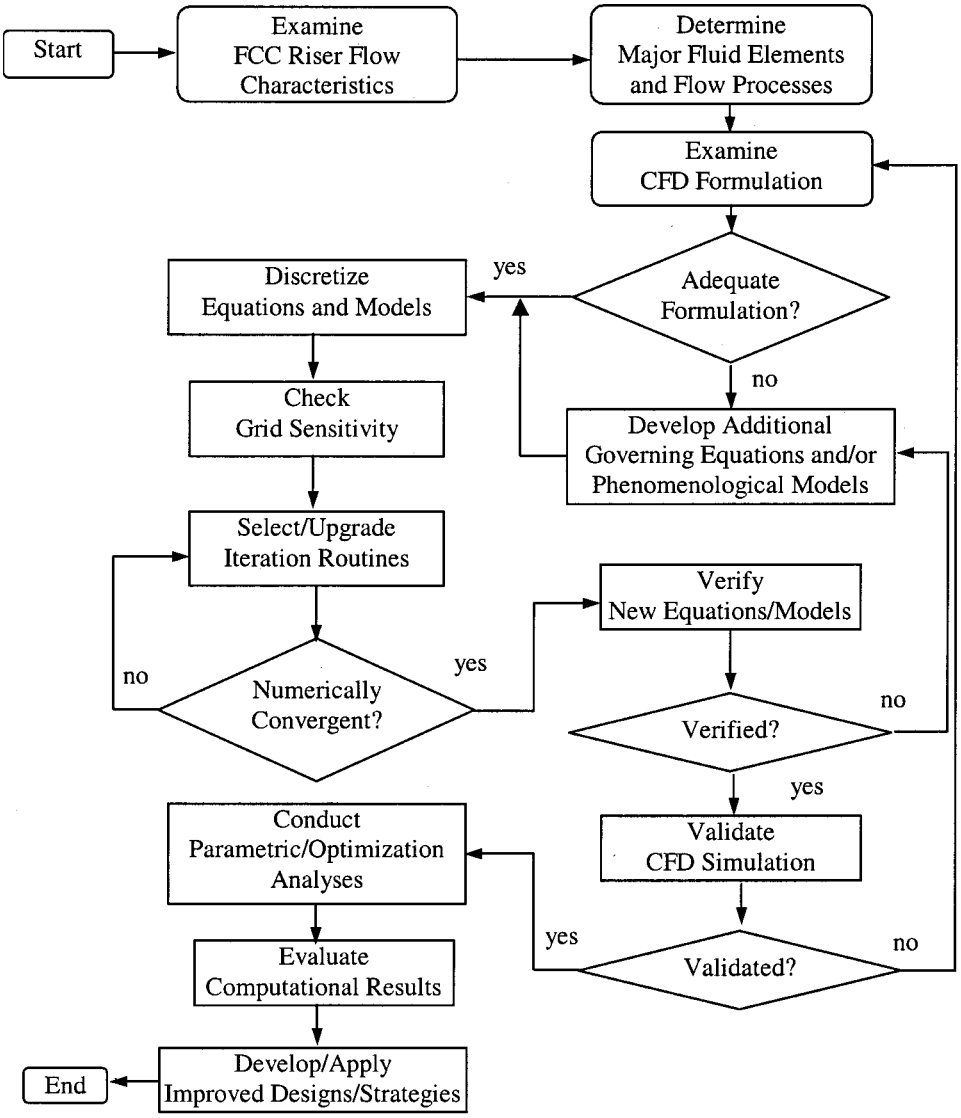

Fig. 1 Development of CFD simulation for FCC riser units

and internal combustion engines [16]. The code was greatly enhanced for the simulation of FCC riser flows. First, the two-phase flow simulation was expanded to three-phase. Then, additional models relevant to the FCC process were developed and added to the code. Among them are spray vaporization, particle-solid interactions, particle-droplet heat transfer, general lumped kinetics, and coke transport models. The complexity of the three-phase FCC riser flow also makes numerical calculations difficult. Several useful numerical techniques were developed for the computation. Among them are the sectional approach and the blocked cells technique for complex geometries, the kinetic-flow decoupling approach for the calculation of a large number of reacting species, and the improved exit boundary conditions for enhanced numerical convergence. The code was validated with experimental/test data from the literature and with data obtained from pilot and commercial-scale FCC units. The validated code was used to perform parametric studies to evaluate the effects of the design and operating conditions on the FCC product yields. Based on the needs and interest of industrial partners, the spray injection effects on the performance of a commercial-scale FCC riser unit were investigated. This paper presents the results of the study.

Technical Approach

Figure 1 shows a simple flow chart of the technical approach for this study. First, the research staff of ANL and the industrial partners jointly selected an FCC riser unit, examined the flow characteristics, and determined the major fluid elements and flow processes to be modeled. Next, an ANL CFD code was selected and modified for the FCC riser flow simulation. After checking the numerical convergence of the CFD simulation, the modified code and its new models were validated with available test data. Then the validated code, called ICRKFLO, was used to conduct a parametric and optimization study, and the results were evaluated to develop improved FCC riser designs and better operating strategies.

FCC Riser Flow. An FCC unit converts heavy oils to lighter products by catalytic and thermal cracking processes. The inputs for an FCC unit are gas oils with high boiling temperatures (above 620K or 650°F), as well as the heaviest portion of crude oil. The oil products and catalyst particles are separated at the end of the riser in a separator. Most of the products can be blended into distillate (such as diesel fuel), gasoline, or liquid propane gas. The

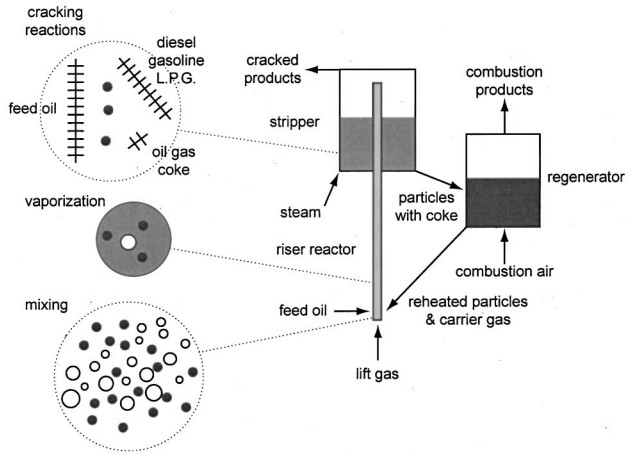

Fig. 2 A typical FCC unit

remainder forms light gases (used for refinery fuel to power furnaces) and coke (a solid which is deposited on the catalyst during the reaction). Coke is a solid by-product of feedstock cracking reactions on acid sites of the FCC catalyst that adheres to the catalyst surface, reducing the active catalyst surface area and thus the effectiveness of the catalyst in cracking the feedstock. Therefore, the catalyst must be regenerated before being used again in the reactor. This is done by burning off the coke with air in another part of the FCC unit, called the regenerator. The hot regenerated catalyst provides the heat for vaporization and the endothermic cracking reactions of crude oil in the riser. A typical FCC unit consisting of riser reactor, stripper/separator, and regenerator is shown in Fig. 2. In this study, the focus is on the riser reactor.

A typical pilot-scale FCC riser and its mixing, vaporization, and cracking processes are also illustrated in Fig. 2. The catalyst stream of regenerated hot catalyst particles and a small amount of carrier gas steam enter from the lower right side of the riser. The inert lift gas stream of nitrogen enters the riser from the bottom to lift the catalyst particles up the riser before the hot particles are mixed with the feed oil. The feed oil stream is injected from the lower left side of the riser, forming a spray of droplets in the riser.

The mixing process includes the combined effects of interfacial interactions (momentum, heat, and mass transfer between phases), flow convection, and turbulent diffusion of gas, oil droplets (solid circles), and catalyst particles (hollow circles). During the mixing process, the heat carried by the catalyst particles is transferred to the gas and the oil droplets. Under typical operating conditions of an FCC riser reactor, the catalyst temperature is much higher than the boiling point of the feed oil. Consequently, the vaporization process is dominated and characterized by the heat transfer rate to oil droplets.

During the vaporization process, a liquid oil droplet (dark colored circle) is releasing oil vapor (light colored ellipse) in the presence of a hot catalyst particle. Following the vaporization process, the cracking process takes place. In general, the product yields are represented by lumped species, which are defined by boiling ranges or hydrocarbon types [9,10,12]. The selection of the oil species lumps is arbitrary and depends heavily on the application. Four lumps, including feed oil, gasoline (or light oil), dry gas, and coke, are shown in Fig. 2. Feed oil vapor (larger ellipse) contacts a catalyst particle, and the cracking reactions on the catalyst surface convert the feed oil vapor to light oil vapor and dry gas (smaller ellipses). Coke (dark circle) is a by-product of the process. Interfacial drag, heat transfer, and droplet vaporization processes have an impact on the performance of a riser reactor. This impact becomes very large for commercial-scale risers.

Governing Equations. FCC riser flow includes three phases: catalyst particles, feed oil droplets, and gaseous species. To evaluate the impacts of injection parameters, i.e., injection velocity and droplet size, on the product yields of an FCC riser, a CFD simulation needs to include all three phases.

The gas phase includes the lift and carrier gases and oil vapor. The lift and carrier gases are generally steam and nitrogen respectively. The number of oil vapor species can be thousands [4]. Due to the limitation of computer speed and memory space, and the severe problem of numerical instability, a CFD simulation usually only includes a few lumped species. ICRKFLO uses a hybrid approach to include tens of oil lumps and avoid numerical instability problems. The approach includes two computational steps. In the first step, three oil lumps (feed oil, light oil, and dry gas), a lift gas, a carrier gas, and catalyst particles are included in a fully coupled CFD calculation. In the second step, transport and reaction of tens of oil lumps (or subspecies) are computed based on the flow field calculated in the first step. The feed oil lump includes the oil species of boiling temperature higher than 494 K (or 430°F); the light oil lump includes those of boiling temperature between room temperature and 494 K (or 430°F); and the dry gas includes those of boiling temperature below room temperature. Similarly, the subspecies can be defined based on boiling ranges that depend on the number of subspecies to be considered.

In this study, the main purpose of the simulations is to determine concentrations of various oil species (feed oil vapor, light oil vapor, dry gas, nitrogen, or steam) in an FCC unit, especially at the riser exit. Since species concentrations depend on other gas, droplet, and particle properties, the CFD code needs to solve for the flow properties of all three phases.

In the gas phase calculations, gas properties, including pressure p, density ρ, velocity components $(u_i,\ i=1,2,3)$, temperature T, enthalpy h, and species concentrations (f_n), are governing by equations of state, and the conservation equations *of mass, momentum*, and *energy*. Equation (1) is the ideal gas law that correlates pressure with temperature, density, and species compositions. Equation (2) is the caloric equation that relates enthalpy and temperature. The conservation equations for mass (species), momentum, and energy are expressed as elliptic-type partial differential equations. For convenience in numerical formulation, the gas phase conservation equations are put in a common form, Eq. (3).

$$p=\rho RT\sum_n\ (f_n/M_n) \tag{1}$$

$$h=\sum_n\ f_nCp_n(T-T_o) \tag{2}$$

$$\sum_{i=1}^{3}\ \frac{\partial}{\partial x_i}\left(\theta\rho u_i\xi-\Gamma_\xi\frac{\partial\xi}{\partial x_i}\right)=S_\xi \tag{3}$$

In the above equations, M_i and Cp_i are molecular weight and specific heat of a gas species n, respectively, R is the universal gas constant, T_o is the reference temperature, ξ is a general flow property that represents scalar, velocity components, or enthalpy, x_i, $i=1-3$, are coordinates, θ is gas volume fraction, u_i are velocity components, Γ is effective (turbulent and laminar) diffusivity, and S_ξ is the sum of source terms. A multiphase k-ε model was used to calculate turbulent diffusivity, and other phenomenological models were developed to determine the source terms.

The solid phase is very dense in the riser. Its volume fraction ranges from 2 to 40 percent. The liquid phase is also dense near the injection location. ICRKFLO uses an Eulerian approach for the particle/droplet phase formulation by dividing droplets/particles into size groups. Figure 3 shows a typical droplet number density distribution versus size at the injection location in which droplets are divided into five size groups, represented by the dashed line rectangles. The arrows indicate the effects of the va-

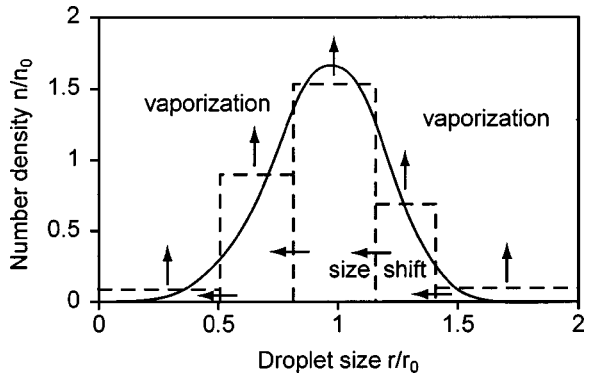

Fig. 3 Droplet number density distribution function

porization process. Vaporization causes droplets to shift from larger to smaller size groups at a computed rate and also results in transfer of vapor from the droplets into the gas phase. For each size group, the Eulerian approach treats the particles/droplets as a continuum (having the same fluid properties). Droplet/particle properties, including number density, velocity components, temperature, and coke concentration (for particles only), are governed by the conservation equations *of mass*, *momentum*, and *energy*.

Similar to the gas phase formulation, the governing transport equations for the liquid and particle phases are put in a common form. Eq. (4) shows the equations for the k^{th} size group.

$$\sum_{i=1}^{3} \frac{\partial}{\partial x_i}\left(n_k u_{i,k}\xi - T_\xi \frac{\partial n_k \xi}{\partial x_i}\right) = S_\xi \tag{4}$$

in which n_k is the droplet or particle number density, $u_{i,k}$, $i=1-3$, droplet or particle velocity components, Γ is droplet or particle diffusivity, and S_ξ is the sum of source terms. The formulation and computer code allow for a size distribution of both droplets and particles; however, in this study only one size group of particles was used, although a size distribution of five droplet size groups was used. A size distribution of five droplet size groups was used because a droplet size distribution is a required component of the vaporization model, which shifts the distribution toward the smaller droplet sizes in order to balance mass in the vaporization mass transfer between the droplet and gas phases. Again, phenomenological models were needed to determine the source terms.

Phenomenological Models. Phenomenological models are used to define the diffusivity and source terms of the governing equations. ICRKFLO uses six major phenomenological models: a lumped integral (as opposed to differential) reaction model, a coke interphase transfer and transport model, a two-parameter turbulence model modified for multiphase flows, an interfacial drag and heat transfer model, a droplet/particle turbulent dispersion model, and a droplet vaporization model. The primary interfacial transfer models for momentum, heat, and mass that greatly influence development of flow patterns and cracking processes in an FCC riser are presented in the following sections.

Interfacial Drag Model. Empirical equations are commonly used to correlate the drag force with the slip velocity (the velocity difference between the gas and solid phases, with components $u_{\delta i}$). Drag force is a vector defined by three orthogonal components in three spatial directions (x_i), which have similar formulations. For a single droplet or particle in the gas, the x_i-direction drag force ($F_{d,x}$) of gas exerted on the droplet or particle can be expressed as Eq. (5).

$$F_{d,x} = \tfrac{1}{2}\rho |u_{1,k}| u_{1,k} \pi r^2 C_d \tag{5}$$

The empirical drag coefficient, C_d, is given in Eq. (6). It includes two major effects, one is viscous, based on a correlation using the Reynolds number based on slip velocity, Re_δ, and the other is the vaporization effect represented by a transfer number B. In Eq. (7), L is the latent heat of a droplet and T_b is the phase change temperature of a droplet [18].

$$C_d = \frac{24}{\mathrm{Re}_\delta}\frac{(1+0.15\,\mathrm{Re}_\delta^{0.687})}{1+B} \tag{6}$$

$$\mathrm{Re}_\delta = \frac{2\rho|u_\delta|}{\mu} \quad \text{and} \quad B = \begin{cases} Cp(T-T_b)/L & \text{vaporization} \\ 0 & \text{otherwise} \end{cases} \tag{7}$$

Interfacial Heat Transfer Model. Empirical equations are also used to correlate the interfacial heat transfer with the slip velocity. For a single particle or droplet in the gas, the heat transfer between the gas and the particle or droplet, when droplets are not vaporizing, is expressed as

$$q_c = 2\pi r \lambda \mathrm{Nu}_\delta (T - T_k)\,\delta(T_b) \tag{8}$$

in which λ is thermal conductivity of the gas; Nu_δ is an empirical Nusselt formula, Eq. (9); T_k is the droplet/particle temperature; and $\delta(T_b)$ is a step function, which changes from one to zero when a droplet or particle reaches its phase change temperature [18]. In Eq. (9), *Sc* is the Schmidt number, and *D* is the mass diffusivity of a species. After the droplet temperature reaches the boiling temperature, further heat transfer from the gas to particles goes into droplet vaporization. In this case, the step function $\delta(T_b)$ makes q_c zero for T_k equal to T_b.

$$\mathrm{Nu}_\delta = \begin{cases} 2+0.552\,\mathrm{Re}_\delta^{1/2} Sc^{1/3} & \text{vaporization} \\ 2+0.654\,\mathrm{Re}_\delta^{1/2} Sc^{1/3} & \text{otherwise} \end{cases} \quad \text{and} \quad Sc = \frac{\mu}{\rho D} \tag{9}$$

Droplet Vaporization Model. The source term in the gas continuity equation is the vaporization rate of the droplets per unit volume. The droplet vaporization model is based on the fundamental physics of stationary single droplet vaporization and then modified for large groups of droplets in a convective environment using correlations. Direct interactions between droplets (collisions) are not significant and not modeled; however, droplets do interact with each other indirectly through their effects on the gas phase, and a collision heat transfer model between droplets and catalyst particles is included [17]. Because gas phase properties, such as specific heat, heat transfer coefficients, etc., may be functions of local gas phase properties, different size droplets will respond differently to varying local conditions. The basic vaporization model is characterized briefly as follows. Williams gave the classical solution of the droplet vaporization rate for a single stationary droplet [18]. A correction for the convection effect, sometimes referred to as the Ranz-Marshall model [19], can be applied to the stationary solution to yield an empirical correlation for vaporization in a flow, Eq. (10). The correction adds a Nusselt number, Nu_δ, to the stationary solution.

$$\frac{dm}{dt} = 4\pi r(\lambda/Cp)\ln(1+B)\mathrm{Nu}_\delta \tag{10}$$

The total vaporization rate at a point per unit volume of physical space is determined by integrating the product of single droplet vaporization rate and the spray distribution function over the droplet size distribution.

Lumped Integral Reaction Model. In the FCC reacting flow calculations, ICRKFLO uses a lumped cracking reaction model, based on lumped kinetics modeling work by Weekman and Nace [2] and by Dave et al. [3] and a new integral reacting-flow time-scale-conversion method [13], for the simulation of FCC riser flows. The model considers four lumped oil components in two cracking reactions. The four lumps include feed oil with a higher boiling point, light oil with a lower boiling point, dry gas (includ-

ing oil vapor of carbon number C_5 and below), and coke as a by-product of the cracking reaction. The cut-off boiling temperature between feed and light oil lumps is chosen according to the feed stock and riser operating conditions. Two cracking reactions include (a) one that converts feed oil to light oil, dry gas, and coke, and (b) another that converts light oil to dry gas and coke. Reaction rates of these reactions are expressed respectively in Arrhenius' formula.

Many reacting flow calculations suffer severe numerical stiffness problems due to the difference of the flow and the reaction time scales. A time scale bridging integral as opposed to a differential approach was developed to overcome these numerical problems. The integral approach converts the reaction time scale used in the above formulation to the flow time scale of the hydrodynamic calculations [20].

Subspecies Formation and Transport Computation. The major gaseous species in the flow calculation include feed oil, light oil, dry gas, and inert gas. However, within these species lumps exist a very large number of oil species produced from numerous kinetic reactions in the riser. These species are not included in the flow calculation because of numerical stiffness problems. The formation and transport of the oil species have a strong impact on the flow field because of the significant density changes between feed oil and products. This density change effect is represented by the 4-lump model in the flow calculation. Assuming the 4-lump flow field solution is adequate to account for the density change effect, one can decouple the solution routines of the transport equations of individual species or large numbers of groups of lumped species from the flow calculation and solve the transport equations on a pre-determined flow field. This second stage of reaction and transport computation is referred to as a subspecies computation. Free from the interactions of the pressure and velocity fluctuations, the calculation of the decoupled species transport equations becomes very stable numerically. This technique is the essence of the hybrid approach to solving governing equations for a complex multiphase reacting flow field combined with solving for the local reaction kinetics and transport equations of a large number of subspecies or lumped subspecies groups, simply called lumps. The details are described in Chang et al. [21].

Numerical Scheme

Computational Grid and Numerical Convergence. The CFD code uses a control volume approach to convert the governing equations to algebraic equations on a discretized grid system. The grid system is staggered and consists of four grids: three staggered x_i-momentum grids, one for each spatial direction, and a scalar grid for all the other equations. The algebraic equations are solved iteratively with the boundary conditions. There are two major iteration routines in the multiphase reacting flow simulation. The first is for the gas flow calculation, and the second is for the droplet and particle flow calculation. In the calculations, Patankar's SIMPLER computational scheme is used to solve the pressure linked momentum equations [22].

In order to conserve computational time and still provide adequately accurate results, grid sensitivity studies were conducted to choose final grids that gave grid-independent numerical results to three significant decimal digits upon further grid refinement. An important feature of the control volume approach used in the computational scheme is that it is conservative in terms of mass, energy, species, and all variables solved for via the transport equations, both locally and globally, to a very high degree regardless of grid size. This feature helps to ensure that results are physically realistic regardless of grid size and that trends in parametric studies are relatively independent of grid size even for relatively coarse grids. For the purposes of the current study, little would be gained from attempting to refine the grid to make results grid-independent to more than three significant digits.

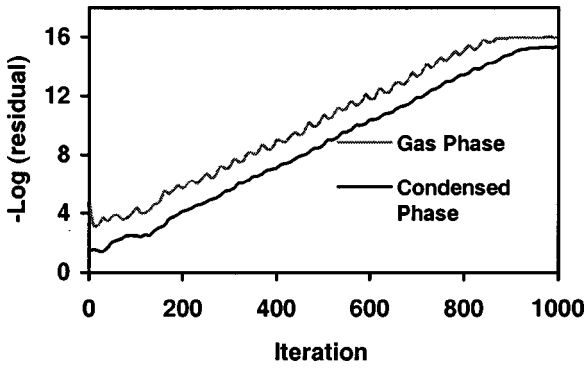

Fig. 4 Typical convergence history

The simulated FCC reactor flow includes four gas species, five droplet size groups, a single particle size group, and a coke species carried by particles. In the ICRKFLO code, a calculation is considered to have converged if the local and global mass balances of the three phases are smaller than a set of predetermined criteria. For this simulation, convergence criteria, defined by average mass residual of all computational cells, are 10^{-10} (in dimensionless form, normalized by the inlet mass flow rate) for the gas phase and 10^{-8} for both the liquid and solid phases. Most computations in the current study, except those near physical operating limits, were robust enough to drive the residuals down to the level of double precision round-off error of one to three low order digits, as shown in Fig. 4. Generally in this application, with reasonable boundary conditions (e.g., inlet flow rates, etc.), a converged solution can be obtained in about 1000 global iterations. Each global iteration includes ten gas phase iterations and three liquid and solid phase iterations. On a Pentium™III 600 computer with 256 megabytes of random access memory, using a 32-bit FORTRAN compiler, this computation takes four to eight hours on a 110-by-26-by-26 cell grid.

Results and Discussion

The FCC process is used to convert feed oil into more valuable light products. Many interacting phenomena occur in the mixing zone, including those affecting the crude oil mass distribution, droplet heating, onset of vaporization, and subsequent cracking reactions. Achieving an understanding of these complex local interactions as they relate to reactor performance is a very difficult undertaking. Simulation provides a tool that can generate an enormous amount of data on conditions and system-state evolution as a multiphase mixture flows through the riser reactor, and also can provide insight into these processes.

Code Validation. The CFD code has been validated by comparison between computational results and experimental data obtained by an industrial member of a cooperative research agreement. Both pilot-scale and commercial-scale experimental data have been used. A methodology for extracting kinetic constants based on experimental data has been developed [23]. The detailed validation strategies will be elaborated in a separate paper. Comparison of computational results with data in the open literature has also been done whenever possible. The predicted product yields, pressure, temperature, and other flow properties showed good agreement with experimental data [20,21,24]. An example of one of many graphs that generically compares computed data against measured data is shown in Fig. 5.

Riser Flow Patterns. Numerical simulations were performed for various FCC riser flows. Typical flow patterns in an FCC riser are presented in Figs. 6(*a*), 6(*b*), and 6(*c*). A grayscale key is plotted on the right side of the property figure indicating the corresponding shade for the property value. Riser dimensions are

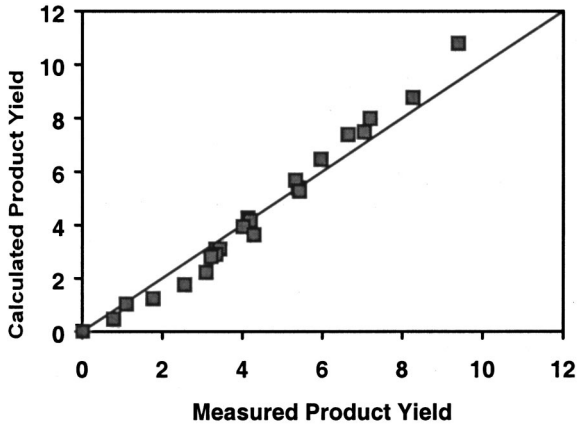

Fig. 5 Comparison of calculated and measured product yields

proprietary information of a petroleum company and will not be discussed here. All the numbers are normalized. In this riser configuration, the catalyst is introduced from the right side near the bottom and the feed oil is injected from the bottom around the centerline. The regions where most of the catalyst and feed oil mixing and interaction take place are called mixing zones. The lower 1/5 section of the riser is shown in these figures to provide a more detailed picture of mixing zones. The gas velocity, temperature, density, pressure, and particle number density are shown in Fig. 6(*a*). The velocity field is plotted as velocity vectors. The vector length is proportional to velocity magnitude. The gas velocity field in the mixing zone of the riser is highly influenced by the addition of new mass in the gas phase from vaporizing oil droplets. The vaporizing droplets cause expansion of the gas and therefore an increase in gas velocity. The patterns of the gas temperature and density distributions correspond to the patterns of droplet and particle number distributions in the mixing zone. In the locations where particle number density is higher, the gas temperature is higher due to heat transfer between the hot particles and gas. In the locations where droplet number density is higher, the gas temperature is lower due to vaporization. The catalyst particles are injected from the right side near the bottom of the riser. Some of them are accumulated in the left corner and some of them are pushed by the oil vapor to the right side along the riser.

Figure 6(*b*) shows the droplet number density with five different droplet sizes. It is clear that almost all the droplets are vaporized in the mixing zone. The droplets with smaller size react more quickly to drag effects and tend to follow the gas flow. They are also dispersed more rapidly by turbulence in the gas phase and therefore spread more across the riser while the larger droplets are pushed to the left side of the riser through interaction with the catalyst/gas mixture flow near its inlet. As shown in Fig. 6(*c*), a large amount of vaporization occurs in the left corner because of the large droplet number density. Once the feed oil is vaporized, cracking reactions take place to convert feed oil into light oil and dry gas. Coke is produced during cracking. All these figures show that the flow pattern in strongly affected by the interactions of multiphase hydrodynamics, droplet vaporization, and chemical kinetics in FCC riser reactors.

Effects of Droplet Vaporization on Flow Patterns. The flow patterns in Figure 6 indicate strong effects of the droplet distribution in the riser. These effects are further demonstrated in Figs. 7 and 8, which include the distributions of mid-size droplet number density, particle number density, and gas temperatures. The riser dimension and input conditions are the same, and there is no cracking reaction for both figures. The only difference is that droplets are not vaporized in Fig. 7 but are vaporized in Fig. 8. Mass entering the gas phase from vaporizing droplets dramatically changes flow patterns, resulting in significant differences in catalyst particle and temperature distributions. Consequently, cold flow parametric mixing studies with no vaporization (no mass transfer from liquid to gas phase) cannot be used as a basis to predict the flow in an FCC riser and the efficiency of FCC cracking reactions.

Some aspects of the interaction of the vaporization process with the general flow hydrodynamics and heat transfer are seen more clearly when a computational experiment is conducted where only mono-sized droplets of the largest size are injected at the droplet/lift gas inlet. In this case smaller droplets do not enter the system at the inlet, but exist in the system only as a result of droplet shrinkage during the vaporization process. Some of the primary results of such a computation for reacting flow in a pilot-scale riser are shown in Fig. 9. The lower 1/5 of the riser is shown in the figure. Several observations can be made about the interrelations between the feed oil droplet and catalyst flow and the vaporization process. The initial catalyst distribution is asymmetric over the cross-section because catalyst particles come in from one side only. However, in a pilot-scale system the cross-section distribution of catalyst tends to even out fairly quickly due to the dispersion of particles through interaction with the gas phase turbulence, as indicated in Fig. 9(*a*). Large droplets are less affected by drag than either smaller droplets or the smaller catalyst particles, and therefore once the cross-section distribution of large droplets is established, it tends to persist as large droplets travel up the riser, as shown in Fig. 9(*b*). Momentum exchange between large numbers of catalyst particles and lift gas and feed oil vapor induces a gas flow to the left, which is also transferred to large droplets and causes a high concentration of large droplets on the left side of the tube. Nearly all the large droplets vaporize before reaching about 1/7 of the tube length. As seen in Fig. 9(*c*) no droplets of the smallest size group exist at the bottom of the riser tube. First, there is a preheating delay before the large droplets injected at the droplet inlet begin to vaporize, and then there is a delay time while the large droplets vaporize and shrink into the smallest size group before any significant number of small droplets appear in Fig. 9(*c*). The smallest droplets are more affected by drag and turbulent dispersion through interaction with the gas phase. Therefore, although there is a higher concentration of small droplets on the left side of the riser, as expected from the distribution of larger droplets from which they come, turbulent dispersion makes their cross-section distribution much more uniform than that of the largest droplets.

It is worth noting that the smallest droplet group has a number density maximum located at about 1/10 the distance up the riser. Two factors cause number densities in the smallest group to drop after this region of maximum number density. First, the smallest droplets disappear because they vaporize completely. Second, as feed oil vapor is deposited into the gas phase due to vaporization, the acceleration caused by this expansion also accelerates and spreads out the droplets, causing the number density to drop. Finally, it should be noted that a few percent of the original feed oil mass injected still exists in the presence of small droplets as far as 2/3 up the length of the riser tube (not shown in the figure). Therefore, reaction models for the feed oil vapor must either explicitly or implicitly take into account the vaporization delay of the feed oil.

Parametric Effects on FCC Product Yields. In this research, the effects of spray injection parameters, including feed oil injection velocity, droplet size, and injection angle, on the product yields of a commercial-scale FCC riser were investigated; the computational results are presented in the following sections. In this riser, the catalyst particles are introduced from the bottom of the riser and the feed oil is injected from the side walls of the riser at a small distance above the bottom of the riser. To demonstrate the parametric effects, gasoline yield as a mass fraction, which is a very important product, will be used as one of the examples.

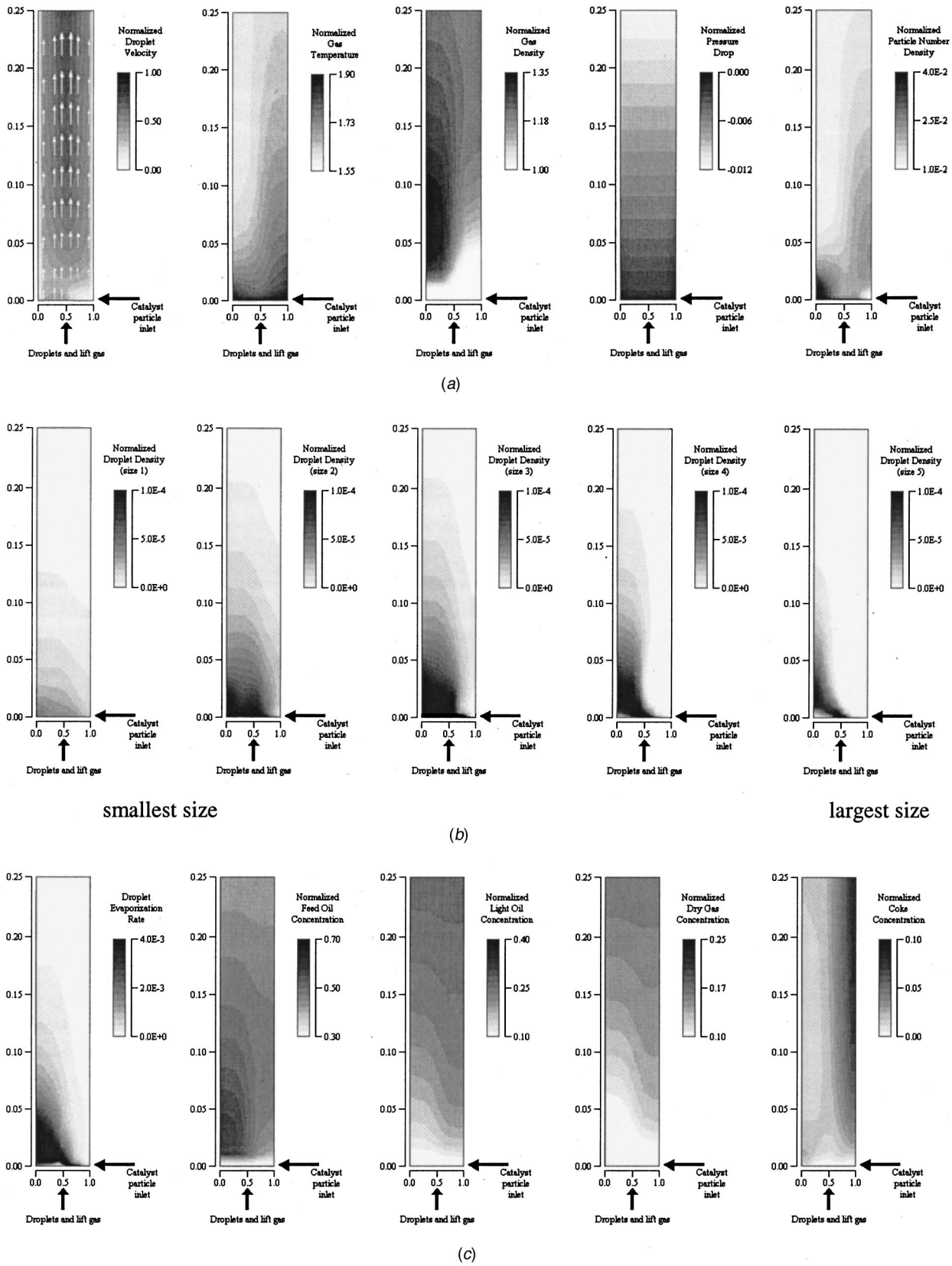

Fig. 6 (*a*) **FCC riser flow pattern;** (*b*) **FCC riser flow pattern;** (*c*) **FCC riser flow pattern**

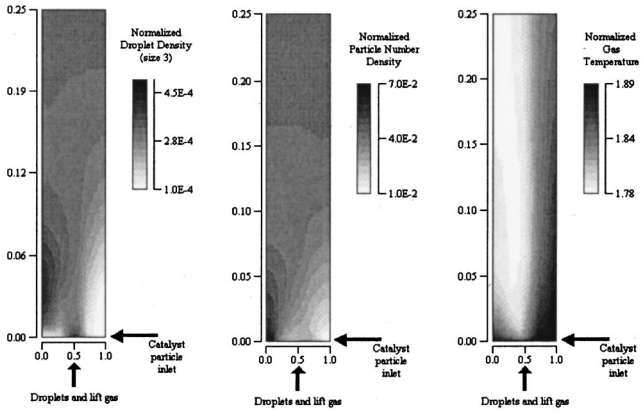

Fig. 7 FCC riser flow without droplet vaporization and cracking reactions

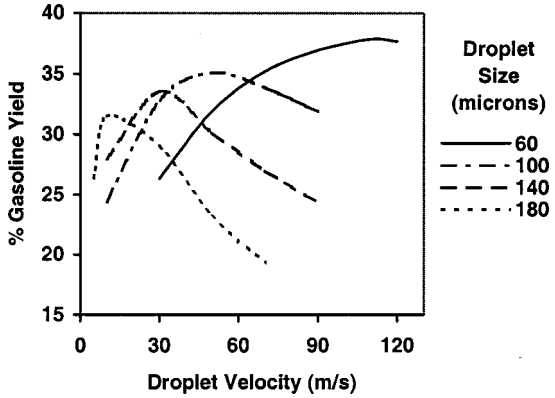

Fig. 10 Effects of droplet injection velocity on gasoline yield for four mean droplet diameters

Effect of Feed Oil Injection Velocity. Figure 10 shows the percent of gasoline yield as a function of feed droplet injection velocity. High gasoline yield is, in general, considered desirable, although a similar study could be used to look for optima in yields of diesel fuel or heating oil if those or other products were considered to be of prime importance due to changes in seasonal market demand. Yield curves are shown over a wide spray injection velocity range for four cases of different inlet mass mean droplet sizes. The spray injection velocities cannot be related directly to flow velocities in a nozzle because the spray injection velocity is a device-level simulation parameter that specifies a mean spray velocity after the spray has already formed. In a real device, this velocity would vary greatly depending on the measurement point in relation to the nozzle outlet. Thus, these velocities are in the range that would be encountered in actual equipment, but they are not nozzle velocities; their significance is to show trends. The trends shown in the gasoline yield curves reveal a number of characteristics and relationships that are both important and physically reasonable.

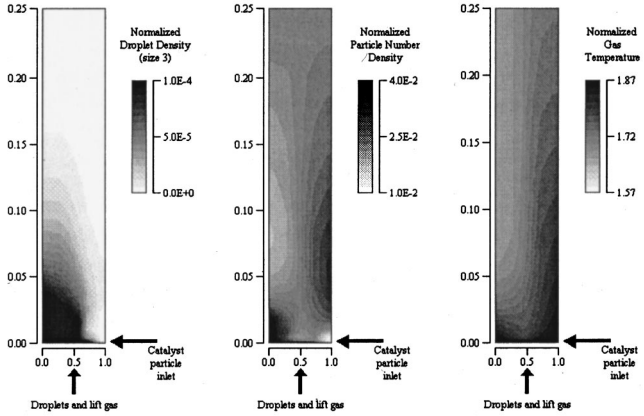

Fig. 8 FCC riser flow with droplet vaporization and without cracking reactions

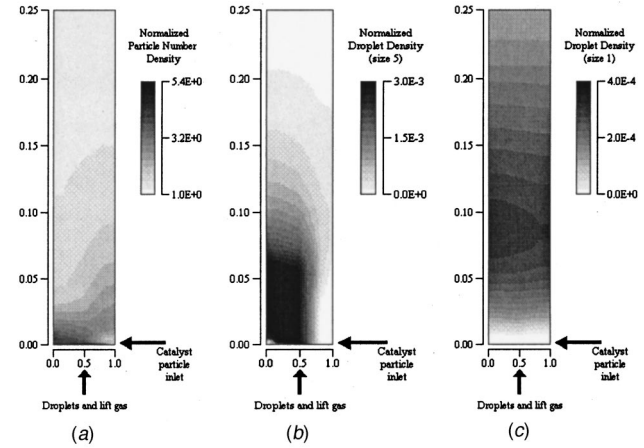

Fig. 9 Catalyst particle and droplet distributions for monosized large droplet injection: (*a*) catalyst; (*b*) largest droplets; (*c*) smallest droplets

First, there is an injection velocity that is optimal for gasoline yield for each mean droplet size. Reasons for the existence of these optima were presented previously. Second, the optimum spray injection velocity increases with decreasing mean droplet size. Optimal performance should reasonably be expected to require that the spray penetrate to the center of the reactor and be fairly evenly distributed over the reactor cross-section. Droplet drag reduces cross-stream droplet velocities more rapidly for smaller droplets than for larger ones, thus requiring higher velocities for smaller droplets to reach the reactor center. Finally, the breadth of the optimum increases as the mean droplet size of the droplet size distribution decreases within the range of droplet sizes tested. A combination of reasons may account for this characteristic. Because the spray consists of a size distribution, larger droplets, which can carry a substantial percent of the total droplet mass of the spray, do exist in sprays with the smaller mean droplet sizes. Therefore, each spray will have a range of penetration depths into the cross-section, based on its size distribution. Because small droplets carry much less mass (order r^3), the size distribution must consist of a much larger portion of droplets that are small or have relatively low velocities in order to achieve a fairly even coverage of crude oil vapor over the cross-section during the vaporization process. Once cross stream slip is reduced to near zero and droplets are turned into the downstream, further mixing of droplet number density over the cross-section is primarily due to interaction with gas phase turbulence, which is a slow process compared to the convective cross-stream transport resulting from spray momentum.

The broadening of the gasoline yield and crude conversion optima for smaller mean droplet sizes in the tested cases is very significant. This finding indicates that a droplet size distribution with the smallest mean droplet size that still allows sufficient numbers of droplets to reach the centerline of the reactor under normal operating conditions will be the least sensitive to yield or conversion reductions when operating at slightly off-optimum conditions. A note of caution, however, is in order regarding the apparent relation between the breadth of the injection velocity optimum and the mean droplet size. This particular characteristic

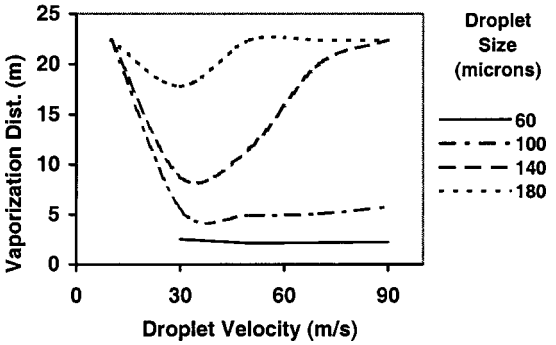

Fig. 11 Vaporization distance as a function of feed oil spray inlet velocity

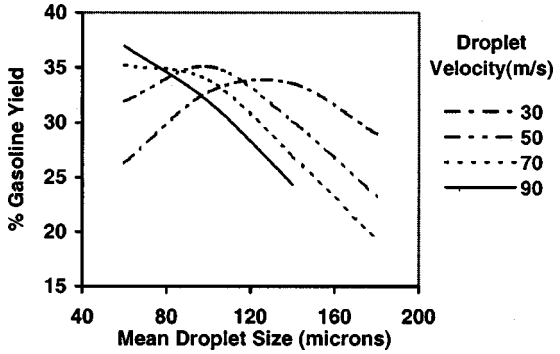

Fig. 12 Effects of droplet size on gasoline yield

has been tested only for a normal size distribution of droplets in the spray. Further study is required for a variety of size distributions to determine the effect of the size distribution on the breadth of the injection velocity optimum in relation to mean droplet size.

Another way of evaluating the effectiveness of the spray operating conditions is to determine the distance from the spray injectors for a given percentage of the spray mass to vaporize. In a simulation, the amount of unvaporized droplet mass crossing a plane of grid cells at any downstream location is easy to calculate. The downstream distance traveled by the droplets from the injector entry to a point where 99 percent of the spray mass is vaporized is shown in Fig. 11, which depicts curves plotted as a function of droplet injection velocity. For the larger droplet sizes, these curves correlate very well (in the inverse) with the curves for gasoline yield. This correspondence for the larger droplet sizes means that those factors relating to the spray distribution over the cross-section of the reactor that prolong the vaporization process are apparently the primary factors that limit the extent of the crude oil cracking reactions, which are endothermic. For example, local high concentrations of droplet number density in some regions can rapidly use up the locally available heat from near-field hot catalyst particles, extending vaporization time and limiting the heat available for cracking reactions during the residence time in the reactor.

This observation does not hold for the smallest mean droplet diameter spray of 60 microns. For the smallest mean droplet diameter spray, the vaporization distance is nearly constant over the velocity injection range. Smaller droplets reach vaporization temperature faster and vaporize faster (the spray mass has a much higher surface-to-volume ratio for small droplets). Vertically conveyed heat carrier catalyst particles tend to form a characteristic slightly *U*-shaped number density distribution, which means that somewhat more heat sources are available at shallow penetration depths. This heat is sufficient for vaporization in a fairly short and uniform distance, but it is not sufficient to drive the endothermic cracking reactions to the same level of completeness for the shallower penetration depths of the bulk of the droplet mass at lower injection velocities. As shown in Fig. 10, gasoline yields drop off at lower injection velocities for the smallest mean droplet size, even though the vaporization distance is nearly constant over this range. This characteristic is also a consequence of the relatively slow cross-stream turbulent mixing process relative to initial spray penetration and the short reactor residence time (on the order of 1 second with a travel distance on the order of 10 diameters downstream, which is insufficient to achieve a well developed flow).

Effects of Mean Droplet Diameter. Another view of the data presented above can be obtained by plotting gasoline yield and vaporization distance against the mean droplet diameter, for the most reasonable injection velocities of the representative commercial-scale FCC riser that were determined previously. This view of the data poses an important question about the sensitivity of local optima in mean droplet size to variations in mean droplet size. Figure 12 shows that local optima occur only for the 30 m/s and 50 m/s injection velocities, and that the optimum size increases as the injection velocity decreases. This inverse relationship is again a consequence of the requirement to have droplets penetrate to the center to achieve good performance, as well as the relationship between the effects of droplet drag force and droplet inertia. Note, however, that the highest gasoline yields occur for small droplets at high injection velocities.

For all but the 30 m/s injection velocity, Fig. 12 shows a fairly rapid decrease from the maximum in gasoline yield as the mean droplet diameter increases. This characteristic appears to be a consequence of a poor distribution of droplet mass due to overpenetration of the spray. The effect can also be seen clearly in Fig. 13, which indicates that the vaporization distance increases very rapidly for mean droplet diameters over 100 microns and for the 70 and 90 m/s injection velocities. For 30 m/s and 50 m/s injection velocities, the vaporization distance increases more slowly, although these curves still have a slope that increases with mean droplet size.

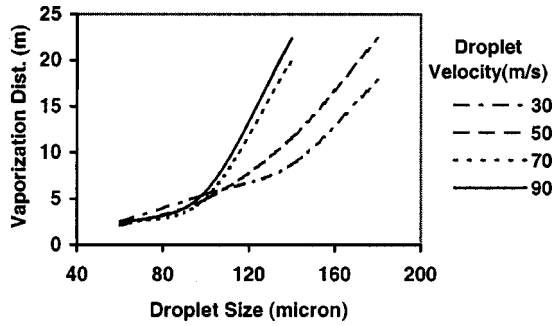

Fig. 13 Effect of droplet size on vaporization

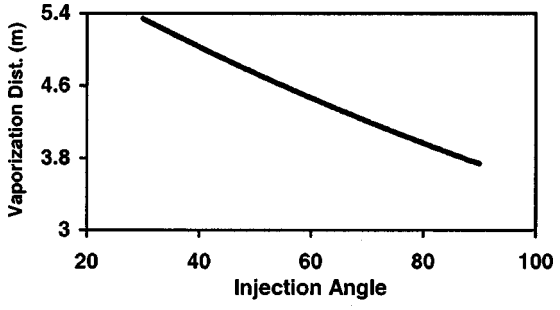

Fig. 14 Injection angle effect on vaporization for 100 micron mean diameter and 50 m/s injection velocity

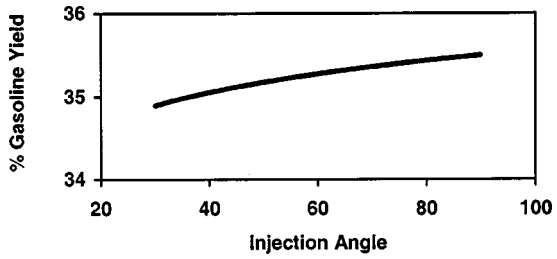

Fig. 15 Injection angle effect on gasoline yield for 100 micron mean diameter and 50 m/s injection velocity

Effects of Injection Angle. For a constant spray mass flow rate, the injection angle measured from the vertical essentially changes the path length and consequent travel time to the center of the reactor. Effects of injection angle are presented in Fig. 14 for sprays of 100 micron mean diameter at the optimum injection velocity (50 m/s). It shows a significant decrease in the vaporization distance as the injection angle is increased to 90 degrees (perpendicular to the stream-wise direction). Figure 15, which presents the gasoline yields with the injection angles, indicates that there is a small increase in gasoline yield as the injection angle is increased to 90 deg. The difference over the entire injection angle range of 30 to 90 deg is less than 2 percent in gasoline yield. Such an increase, though small, may be considered significant when large quantities of crude oil are processed. However, realizing such an increase in an actual unit, rather than in a tightly controlled simulation, could require tighter than feasible controls on the operating conditions of the real unit to keep it near optimum conditions. This possible control difficulty arises because the angled injection with longer path lengths to the reactor center allows higher velocity injection (more mass flow from a given nozzle type) with a smaller cross-stream velocity component. In this case, more overall production per day may possibly be obtained from the unit without significant loss in gasoline yield due to over-penetration of the sprays. Therefore, the optimum operating conditions for spray angle may depend on whether the goal is to optimize the production rate of the FCC unit or to optimize the percent of gasoline or other product yields.

Effect of Poor Distribution of Spray over Reactor Cross-Section.. When spray parameters are set to achieve a relatively even mass distribution of droplets over the reactor cross-section, measures of performance for the reactor tend to be near the optimum, and other factors may have a more controlling influence on deviations of performance about the optimum. Spray conditions that poorly distribute droplet number density over the reactor cross-section, however, have a major negative impact on vaporization and product yields. Figure 16 shows the development of normalized droplet mass deviation about the mean over a reactor cross-section from the spray injection point to a little over one meter downstream, where vaporization is well underway. The

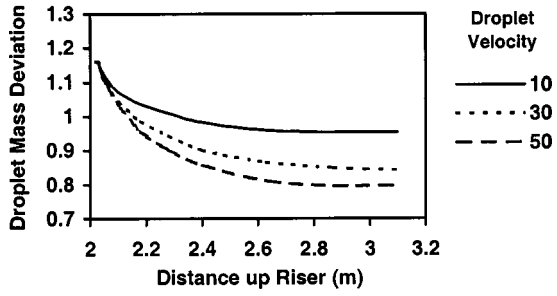

Fig. 16 Droplet mass deviation over cross-section for 100 micron mean diameter droplets

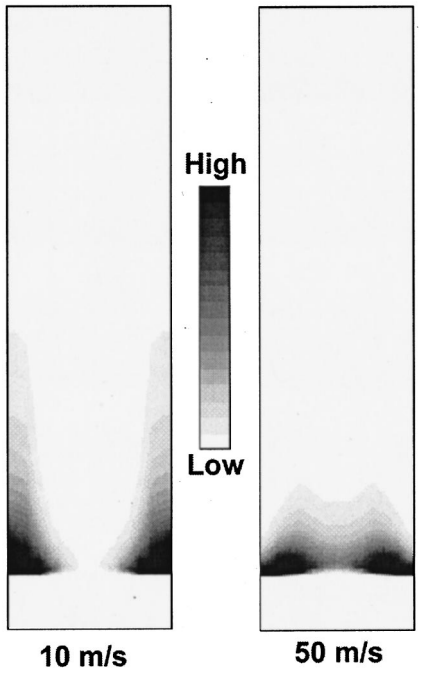

Fig. 17 Droplet number density for two injection velocities

cases shown are for 100 micron mean diameter droplets at three nominal injection velocities: 10, 30, and 50 m/s. Near the injectors, the spray is penetrating into the riser interior, so the droplet mass is not evenly distributed. As the spray penetrates, the deviation drops off until it levels out about a meter downstream. The droplet mass deviation for the 10 m/s injection velocity levels out at about 15 percent higher than the deviation for the 50 m/s injection velocity. At the lower injection velocity, the gasoline yield drops over 25 percent (see Fig. 10). These results show that conditions producing more uniform feed oil mass distributions over

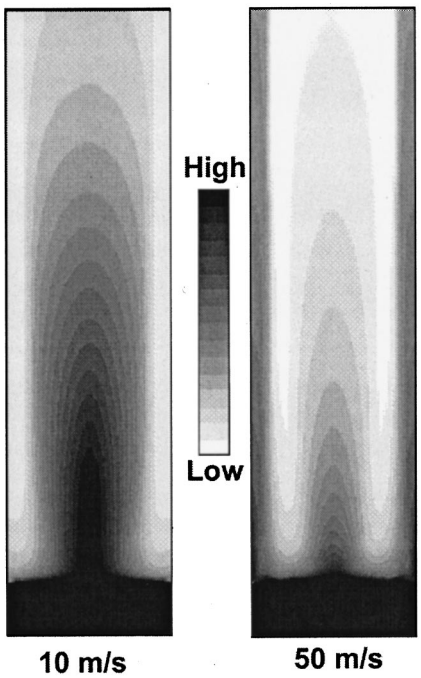

Fig. 18 Temperature distribution for two injection velocities

the reactor cross-section normal to the primary flow direction are directly related to significantly higher gasoline yields.

Figures 17 and 18 graphically illustrate two conditions in the reactor interior that, in part, account for this drastic change in performance. Figure 17 shows a two-dimensional grayscale plot of droplet number density for the lowest and highest injection velocity cases. This figure illustrates that droplets do not penetrate evenly over the cross-section for the low injection velocity case; turbulent mixing does not bring droplets into the middle to any significant degree; and, being concentrated near the riser walls, the droplets will rapidly use the heat available in this region to heat up and vaporize, thus slowing the vaporization process and allowing droplets to persist significantly farther downstream.

Figure 18 shows the effect of a poor droplet distribution on the temperature field. In the 10 m/s case, the temperature in the outer region drops to a low value very close to the injectors and remains relatively high in the central region over most of the reactor length. The energy available in this hotter central region is not effectively used for cracking reactions because most of the crude oil vapor is deposited in the near-wall region and does not mix rapidly enough into the center during the short reactor residence time. The 50 m/s injection case, however, has a well distributed crude oil droplet mass, and locally available heat from the catalyst goes into droplet heating, vaporization, and subsequent cracking reactions fairly evenly over the cross-section. This process yields a much more uniform temperature profile for most of the length of the reactor and near optimum product yields for this mean droplet size.

Conclusions

Argonne National Laboratory has developed a copyrighted CFD code, ICRKFLO, for analysis and development of advanced multiphase reacting flow systems. It employs a hybrid hydrodynamic-chemical kinetic coupling technique and has been successfully applied to the simulation of petroleum fluid catalytic cracking risers. Governing equations are solved for flow properties of all three phases (gas, liquid, and solid) locally in an FCC riser flow, with models governing the transport of catalyst particles and feed oil droplets, the vaporization of the feed oil droplets, the cracking of the oil vapor, and the formation and deposition of coke on particles. The code was validated by comparing computational results with experimental data for various cases.

The validated code was used to study the interactions of multiphase hydrodynamics, droplet vaporization, and chemical kinetics in a pilot-scale FCC riser reactor. Results of this study showed that the hydrodynamics of mixing among the phases and interphase exchange rates in the entry region (or mixing zone) of the riser play an important role in the initial development of the flow and cracking processes within the riser. The mixing zone performance becomes even more important on commercial scale units because of the change in aspect ratio of the riser, with consequent large changes in internal flow patterns. Decreasing the residence time in a riser also magnifies the effects of mixing on performance. In the parametric studies, local optimum operating windows for spray injection parameters, including spray injection velocity, droplet size, and injection angle, were identified, and the sensitivity of local optima to variation in these parameters was also investigated. The CFD code developed in this research can be a very useful tool to use in optimizing riser performance for specific operating conditions and performance goals, such as maximizing valuable product yields.

Acknowledgments

This work was supported by BP-Amoco. This work was also supported by the U.S. Department of Energy, Assistant Secretary for Energy Efficiency and Renewable Energy, under Contract W-31-109-ENG-38. B. Golchert of ANL participated in the validation of the code. His contribution is greatly appreciated. Special thanks are extended to George Hoekstra, Winni Torres-Ordonez, and Massimo Sangalli of BP-Amoco for their support and consultation.

Nomenclature

C = coke species
C_d = drag coefficient
C_p = specific heat (J/kg K)
F = drag force (N)
m = droplet mass (kg)
M = molecular weight (kg)
n_k = droplet or particle number density (number of droplets/m^3)
r = droplet radius (m)
R = gas constant (J/kmol-K)
S = source term of a governing equation
T = temperature (K)
t = time (s)
u_i = velocity component in the x_i-direction (m/s)
x_i = ith coordinate (m)

Greek Symbols

Γ = effective diffusivity (pa-s)
θ = gas void fraction
ρ = gas density (kg/m^3)
ξ = general variable for 1, u, v, h, f, k, or ε
μ = dynamic viscosity (kg/m·s)

Subscripts

o = reference value
d = droplet
i = coordinate direction
k = size group k of droplets or particles
δ = slip property
ξ = general variable for 1, u, v, h, f, k, or ε

References

[1] Bienstock, M. G., Draemel, D. C., Ladwig, P. K., Patel, R. D., and Maher, P. H., 1993, ''A History of FCC Process Improvement through Technology Development and Application,'' AIChE Spring National Meeting, Houston, TX.
[2] Weekman, V. W., and Nace, D. M., 1970, ''Kinetics of Catalytic Cracking Selectivity in Fixed, Moving, and Fluid Bed Reactors,'' AIChE J., **16**(3), pp. 397–404.
[3] Dave, N. C., Duffy, G. J., and Udaja, P., 1993, ''A Four-Lump Kinetic Model for the Cracking/Coking of Recycled Heavy Oil,'' Fuel, **72**(9), pp. 1331–1334.
[4] Nigam, A., and Klein, M. T., 1993, ''A Mechanism-Oriented Lumping Strategy for Heavy Hydrocarbon Pyrolysis: Imposition of Quantitative Structure-Reactivity Relationships for Pure Components,'' Ind. Eng. Chem. Res., **32**, pp. 1297–1303.
[5] Quann, R. J., and Jaffee, S. B., 1996, ''Building Useful Models of Complex Reaction Systems in Petroleum Refining,'' Chem. Eng. Sci., **51**(10), pp. 1615–1635.
[6] Sinclair, J. L., and Jackson, R., 1989, ''Gas-Particle Flow in a Vertical Pipe with Particle-Particle Interactions,'' AIChE J., **35**(9), pp. 1473–1486.
[7] Pita, J. A., and Sundaresan, S., 1993, ''Developing Flow of a Gas-Particle Mixture in a Vertical Riser,'' AIChE J., **39**(4), pp. 541–552.
[8] Nuri, A., and Gidaspow, D., 2000, ''Riser Hydrodynamics: Simulation Using Kinetic Theory,'' AIChE J., **46**(1), pp. 52–67.
[9] Theologos, K. N., and Markatos, N. C., 1993, ''Advanced Modeling of Fluid Catalytic Cracking Riser-Type Reactors,'' AIChE J., **39**(6), pp. 1007–1017.
[10] Theologos, K. N., Nikou, I. D., Lygeros, A. I., and Markatos, N. C., 1997, ''Simulation and Design of Fluid Catalytic-Cracking Riser-Type Reactors,'' AIChE J., **43**(2), pp. 486–494.
[11] Jacob, S. I., Gross, B., Voltz, S. E., and Weekman, V. W., 1976, ''A Lumping and Reaction Scheme for Catalytic Cracking,'' AIChE J., **22**(4), pp. 701–713.
[12] Gao, J., Xu, C., Lin, S., Yang, G., and Guo, Y., 1999, ''Advanced Model for Turbulent Gas-Solid Flow and Reaction in FCC Riser Reactors,'' AIChE J., **45**(5), pp. 1095–1113.
[13] Chang, S. L., and Lottes, S. A., 1993, ''Integral Combustion Simulation of a Turbulent Reacting Flow in a Channel With Cross-Stream Injection,'' Numer. Heat Transfer, Part A, **24**(1), pp. 25–43.
[14] Chang, S. L., and Lottes, S. A., 1995, ''Characteristic of Multiphase Flow with Particle Vaporization in a Combustor with Counter-Flow Injection,'' Energy Convers. Manage., **36**(11), pp. 1031–1045.
[15] Zhou, X. Q., and Chiu, H. H., 1983, ''Spray Group Combustion Processes in Air Breathing Propulsion Combustors,'' AIAA/SAE/ASME 19th Joint Propulsion Conference, Seattle, Washington, AIAA-83-1323.

[16] Chang, S. L., and Wang, C. S., 1987, ''Thermal Radiation and Spray Group Combustion in Diesel Engines,'' ASME Winter Annual Meeting, Boston, Mass., HTD-81:25-34 (December 13–18, 1987).
[17] Chang, S. L., Zhou, C. Q., Lottes, S. A., and Petrick, M., 1999, ''Modeling of Heating and Vaporization of Larger Feed Droplets in Fluidized Catalytic Cracking Risers,'' *Proceedings of the Second Asia-Pacific Conference on Combustion*, the Combustion Institute, pp. 553–557, Tainan, Taiwan, ROC (May 9–12, 1999).
[18] Williams, F. A., 1985, *Combustion Theory*, The Benjamin/Cummings Publishing Company, Inc.
[19] Aggarwal, S. K., Tong, A. Y., and Sirignano, W. A., 1984, ''A Comparison of Vaporization Models in Spray Calculations,'' AIAA J., **22**(10), pp. 1448–1457.
[20] Chang, S. L., Lottes, S. A., Zhou, C. Q., and Petrick, M., 1996, ''Evaluation of Multiphase Heat Transfer and Droplet Evaporation in Petroleum Cracking Flows,'' HTD-Vol. 335, Proceedings of the ASME Heat Transfer Division 4:17–27, International Mechanical Engineering Congress and Exposition, Atlanta, GA (November 17–22, 1996).
[21] Chang, S. L., Lottes, S. A., Zhou, C. Q., and Petrick, M., 1997, ''A Hybrid Technique for Coupling Chemical Kinetics and Hydrodynamics Computations in Multiphase Reacting Flow Systems,'' HTD-Vol. 352, Proceedings of the ASME Heat Transfer Division 2:149-157, International Mechanical Engineering Congress and Exposition, Dallas, TX (November 16–21, 1997).
[22] Patankar, S. V., 1980, *Numerical Heat Transfer and Fluid Flow*, Hemisphere, Washington, D.C.
[23] Chang, S. L., Lottes, S. A., and Zhou, C. Q., 2000, ''Methodology for Extracting Local Constants from Petroleum Cracking Flows,'' ANL Invention Report, ANL-IN-97-074, U.S. Patent No. 6,013,172 (January 11, 2000).
[24] Chang, S. L., Lottes, S. A., and Petrick M., 1995, ''Development of a Three-Phase Reacting Flow Computer Model for Analysis of Petroleum Cracking,'' Proceedings of 1995 Mid-America Chinese Professional Annual Convention, Itasca, III., pp. 281–288 (June 23–25, 1995).

Adaptive Neurocontrol of Heat Exchangers

Gerardo Díaz[1]

Mihir Sen
Fellow ASME

K. T. Yang
Fellow ASME

Rodney L. McClain

Hydronics Laboratory,
Department of Aerospace and
Mechanical Engineering,
University of Notre Dame,
Notre Dame, IN 46556

This paper investigates the use of adaptive artificial neural networks (ANNs) to control the exit air temperature of a compact heat exchanger. The controllers, based on an internal model control scheme, can be adapted on-line on the basis of different performance criteria. By numerical simulation a methodology by which the weights and biases of the neural network are modified according to these criteria was developed. An ANN controller for an air-water compact heat exchanger in an experimental facility is then implemented. The parameters of the neural net are modified using three criteria: minimization of target error, stabilization of the closed-loop performance of the controller, and minimization of a performance index that we have taken to be the energy consumption. It is shown that the neural network is able to control the air exit temperature in the heat exchanger. The neurocontroller is able to adapt to major structural changes in the system as well as to simultaneously minimize the amount of energy used.
[DOI: 10.1115/1.1370512]

Keywords: Artificial Intelligence, Control, Heat Transfer, Heat Exchangers, Systems

1 Introduction

Most thermal systems present nonlinear dynamical characteristics that make them difficult to control. Heat exchangers (HXs) are one of these thermal components that present nonlinear behavior mainly due to complicated hydrodynamics and temperature dependence of fluid properties [1]. Because of these complexities the dynamics of HXs are difficult to model using first principles. This is not because the individual phenomena that play a role in the dynamics are not understood, but when they are all combined, the result is a complex system that is not easy to compute numerically [2]. For this reason, much of the information available about specific HXs is in the form of correlations that predict the steady state heat transfer [3]. On the other hand, even though numerical simulations based on simplifying assumptions may be possible [4], they are slow and thus not suitable for real-time control purposes. There is also need for a model that can adjust to the changes in the thermal system that occur over time, such as the those due to fouling in HXs.

The application of artificial neural networks (ANNs) to the simulation and control of thermal systems is currently of great research interest. This is a powerful technique to predict the response of physical systems that are too complex to be modeled from first principle analysis. They have been used to model the steady state [2] and dynamic [5] behaviors of HXs. They have also been applied to thermal systems for control purposes. Marwah et al. [6] address issues involved in the modeling of electronic manufacturing processes for optimization and control using artificial neural networks. Blazina and Bolf [7] used ANNs as a feedforward control for a two-stage heat exchange process; Ayoubi [8] used dynamic multilayer perceptron networks as the predictive model in model-based predictive control of a water-steam HX; Nahas et al. [9] used internal model control and ANNs to control the models of a continuous stirred tank reactor and a pH neutralization process; Chen et al. [10] used an adaptive single neuron to control a nonlinear and open-loop unstable model of a continuous stirred tank reactor. In this work, we deal mainly with the dynamics and control of thermal processes using ANNs. The interested readers are referred to Haykin [11] for further information about steady-state simulations and learning algorithms for ANNs.

It has been shown [12] that a trained ANN, even though its steady-state predictions may be accurate, may be unstable when used as part of a control system. Since we are interested in the on-line adaptation of an ANN controller, we will train it not only to minimize the target error but also to increase the stability of the resulting controller. In addition, in order to handle any optimal condition or conditions that may be imposed on the control, we will minimize a third criterion that in general can be user-defined. As a specific example that may be useful in certain applications, we will minimize the use of energy in the thermal system, though any other criterion can be used instead. The experimental facility in which the control system is installed uses a single-row fin-tube heat exchanger with water and air as the in-tube and over-tube fluids, respectively.

2 Neurocontrol

There are several control schemes that use ANNs as the dynamic model and/or the controller of a physical system [13]. Here, we have chosen to use the internal model control (IMC) approach because of its good characteristics of adaptation, robustness, and stability. The main objective of this paper is to show the excellent adaptive characteristics of neurocontrollers applied to thermal systems. We refer the reader to Díaz et al. [5] for details on the implementation of neuro-controllers for temperature control in heat exchangers, and to Díaz et al. [12] for the stabilization of their closed-loop performance during training. The ANNs in the previous work were all trained off-line before use; the present work is directed towards on-line adaptation of the ANN for optimum performance. The ANN is trained while it is performing its control function.

2.1 Internal Model Control. The idea behind IMC, shown diagrammatically in Fig. 1, is to have a model of a plant, indicated as ANN_1, in parallel with a real system. The difference between the output of the real system and the model is used as the feedback for a controller, shown as ANN_2, that is located in the forward path of the control scheme. In this case, ANN_1 and ANN_2 are neural networks. We first train ANN_1 to learn the dynamics of the plant. ANN_2 is then trained to learn its inverse dynamics in order to be used as a nonlinear controller. In the experiments, we trained ANN_1 and ANN_2 with information of the exit air tempera-

[1]Currently at Modine Manufacturing Co., Racine, WI 53403, g.c.diaz@modine.com

Contributed by the Heat Transfer Division for publication in the JOURNAL OF HEAT TRANSFER. Manuscript received by the Heat Transfer Division March 20, 2000; revision received January 8, 2001. Associate Editor: A. Bejan.

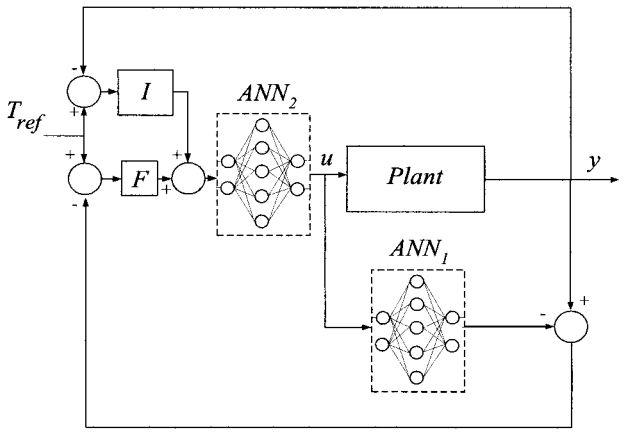

Fig. 1 IMC with integral control

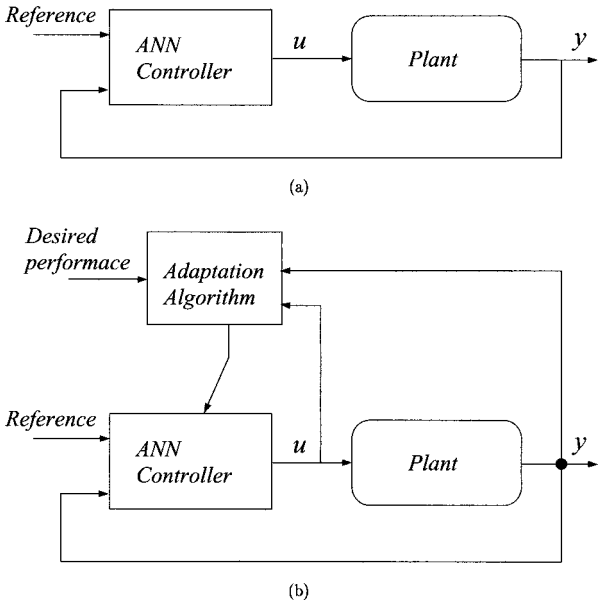

Fig. 2 Controllers: (*a*) non-adaptive, (*b*) adaptive

ture from the heat exchanger, T^a_{out}, and the air speed, v_a, while keeping the inlet air and water temperatures and the water flow rate constant. These data were obtained by making measurements of the system subject to small increments in the set target point temperature. As we are working with a model of the plant, and since ANNs provide only an approximation to the behavior of the real system, we use a one-parameter filter, *F*, preceding the controller in the forward path which accounts for plant-model mismatch. An integral control structure, *I*, was also added in parallel with the action of *F* to help to obtain an offset-free controlling action. The filter *F* and the integral control *I* help the system to reach the actual setpoint temperature even with the destabilizing action of the noise embedded in the experimental measurements.

2.2 Adaptive Control. Adaptive control consists of automatically adjusting in real time the parameters of a controller so that a desired level of performance of a control system is achieved when the parameters of the process being controlled are unknown or vary with respect to time. The way to evaluate the performance of a control system is by selecting an index that will be compared with its desired value, the difference being fed back to activate the process of adaptation. The difference between conventional and adaptive control schemes is that the former reacts to disturbances acting upon the controlled variables and the latter to disturbances acting upon the parameters of the process [14]. Figure 2(*a*) shows the schematic of a non-adaptive controller compared to an adaptive controller shown in Fig. 2(*b*). In the present case, the adaptation is achieved by modifying the weights and biases of the two neural networks ANN_1 and ANN_2. It is done by carrying out single additional training cycles until the performance criteria are satisfied.

There are some issues relating to the different time scales involved in the problem that have to be addressed here. For instance, the plant has its own time scale for changes in its variables, and possibly more than one. On the other hand, the controller acts on actuators that have their own particular reaction time. Finally, if we want to implement an adaptive control system, we need to know how long ANN_1 and ANN_2 take to finish the adaptation process. Thus, if the adaptation period is long enough so that the physical system deviates from the desired set point in a significant way, we need a back-up controller that will keep the system as close as possible to the set point until adaptation is completed. In the experiments, the time scale of the adaptation process is the largest, that of the physical system intermediate, and the reaction time of the actuator smallest. Thus, we use a PID controller to keep the system under control until the ANNs adapt to the new operating characteristics of the plant. Because the plant may have a very different behavior due to its new characteristics, the PID controller keeps the system close to the set point. The constants of the PID controller are chosen, and kept fixed, for a certain behavior of the plant which may not be suitable for the system after the disturbance is applied; we only use it until the ANN controller has learned the new behavior.

2.3 Simultaneous Minimization Criteria. One of the purposes of training an ANN is to minimize the target error between some known output and the prediction of the ANN with respect to a certain input. Since this ANN, if used as a controller within a closed-loop control system, may produce a dynamically unstable behavior, we must continuously check the stability of the closed loop system when training the ANN. For stability purposes, the closed-loop controller was treated as a nonlinear map that is iterated in time [12]. Its stability is checked by obtaining the spectral radius, *r*, of the Jacobian matrix of the map; $r<1$ indicates stability. As we modify the parameters of the ANN with respect to the target error and the spectral radius, we can also simultaneously consider other optimality criteria. For instance, we can use an index corresponding to the energy consumption for the particular plant and drive the system to an operating point where we achieve the desired temperature, obtain at the same time a stable controller, and also use the minimum rate of energy. If there are other functions that are needed to be minimized or maximized simultaneously, they can be treated in the same way.

3 Development of a Neurocontroller

The techniques and methodology for adaptive training of the ANN will be developed and shown here first using numerical simulations on examples with known analytic dynamic models. Different adaptation criteria will be considered. The results applied to a real heat exchanger test facility and its dynamic control will be shown in a later section.

3.1 Single Adaptation Criterion. We start with a simple example in which we track the behavior of a nonlinear dynamical system described by $\dot{y}+ay^3=x(t)$, where $x(t)$ is a forcing function taken to be $x(t)=\sin(t)$, and *a* is a parameter. We take $a=1$ for $t\in[0,25]$ and $a=4$ for $t\in(25,50]$. This represents a sudden change in system characteristics. A 2-5-1 ANN, i.e. one with an input layer with two input nodes, a hidden layer with five nodes and an output layer with one output node, is used to learn the behavior of the dynamical system. At $t=25$ the parameter *a* of the system is modified and the ANN is expected to adapt until it

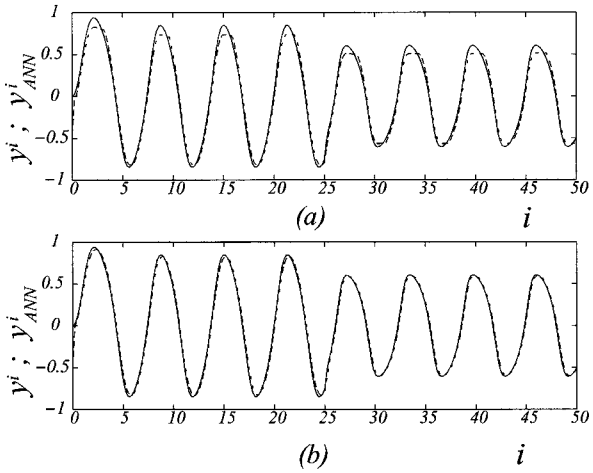

Fig. 3 Tracking of a dynamical system by an ANN; (*a*) adaptation for target error ⩾5 percent; (*b*) adaptation for target error ⩾1 percent; — numerical solution; –– ANN prediction

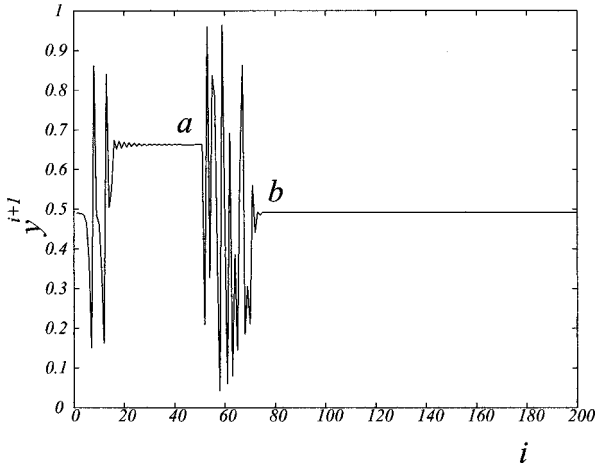

Fig. 4 Result of using a 2-4-1 ANN as an iterated map; *i* is the time index and y^{i+1} is the output

learns the new behavior of the system. The inputs to the ANN are y^i and x^i and the output is y^{i+1}, where i is a discrete time index.

Figures 3(*a*) and (*b*) show the results of tracking the output y^i compared with the numerical solution. In Fig. 3(*a*) the adaptation process is turned on for errors larger than five percent. It is seen that the overall behavior of the system is captured by the ANN, but there are still some discrepancies close to maximum values of the function. In Fig. 3(*b*) the ANN is adapted for errors larger than one percent. It is seen that the prediction is much closer to the numerical, but the program takes 20 percent longer to run. Thus, if we are performing an on-line adaptation there is a compromise between the error obtained and the length of the adaptation period.

3.2 Two Adaptation Criteria. We now examine the adaptation of ANNs using two criteria: one for accuracy in prediction and the other for stability. In this example we train a 2-4-1 neural network to learn the fixed point of the differential equation $\dot{y}+y=x^2$, where x^2 is a constant, and $y(0)$ is the same constant. This can be implemented with an ANN by providing only one set of values as the training data, i.e., inputs $y^i=0.49$, $x^i=0.7$ and output $y^{i+1}=0.49$. First we train the ANN for reduction of target error, and once this is less than 10^{-3}, we train it for stability.

From the stability perspective, we view the ANN as an iterated map, i.e., we supply the input values x^i and y^i and we obtain an output. This output becomes the input for the next iteration of the map. The value of x^i remains constant and the values of y^i iterate. The spectral radius of the Jacobian matrix of the map, r, is calculated to determine the stability.

We first train the ANN to make sure that $r>1$ with a target error less than 10^{-3}, and then we use the ANN as a dynamical system. As we expect, the system is unstable. In order to stabilize it at the correct fixed point, we modify the weights and biases of the ANN until r is sufficiently less than unity (we chose $r<0.9$ as a sufficiency criterion). We use a gradient descent method to modify the weights and biases of the ANN. As the target error might increase due to the fact that we are training in the direction of decreasing r, we need to retrain the ANN to reduce the target error again. Thus there is an alternating process of training with respect to the two different criteria until we obtain the desired value of the target error with $r<1$. Figure 4 shows the behavior of the dynamical system during this training process. The parameters of the ANN chosen make $r=4.7$ so that it is unstable to the iterative process. The system goes from the $y^i=0.49$ at $i=0$ for which the error was zero to the point a at $i=50$. This fixed point is stable with $r<1$, but is not the state that is desired. So we turn on the adaptation routine for the reduction of r to below unity along with reduction of error to bring the system back to point b where $y^i=0.49$. This occurs at about $i=77$. Thus it takes about 27 iterations for the system to stabilize at the desired fixed point.

There is a need for a back-up controller that will keep the system close to the set point when either the controller or the model of the plant is going through the adaptation process with respect to any of the chosen criteria. The process described in this section can also be used to modify the parameters (biases and weights) of the ANN controller with respect to several adaptation criteria.

3.3 Adaptation Criteria With Optimization. We now develop a third example showing the use of adaptive rules for driving a dynamical system composed by an ANN to a desired fixed point. We train an ANN with the function $y=1/x$ with $x\in[0.1,10]$. Each point of this curve is a fixed point of the ANN. The inputs of the ANN are y^i and x^i and the output is y^{i+1}. We select an initial condition within the given range of the variables. We check the stability of the system and the target error, but we want at the same time to drive the system to the maximum of the unrelated function $z=x(1-x)y(1-y)$. For this purpose we apply a gradient ascend method to modify the current values of x^i and y^i so that the dynamical system maximizes z. Figure 5 shows the behavior of the system during this process in (x,y,z) space. It moves from the initial condition along the given curve until it finds the maximum of the function z. Figure 6 shows the values of

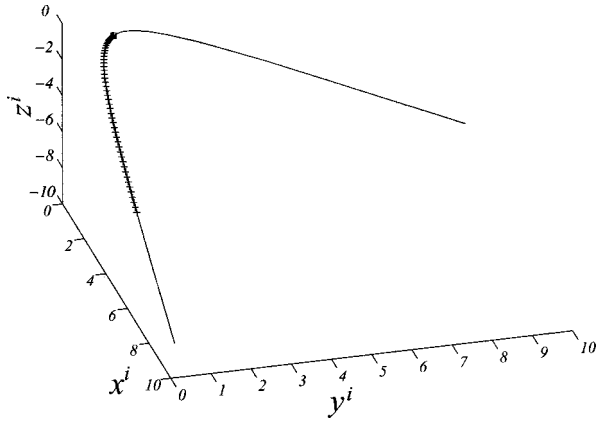

Fig. 5 Simultaneous optimization criteria; training curve is continuous line, path of dynamical system is shown with +

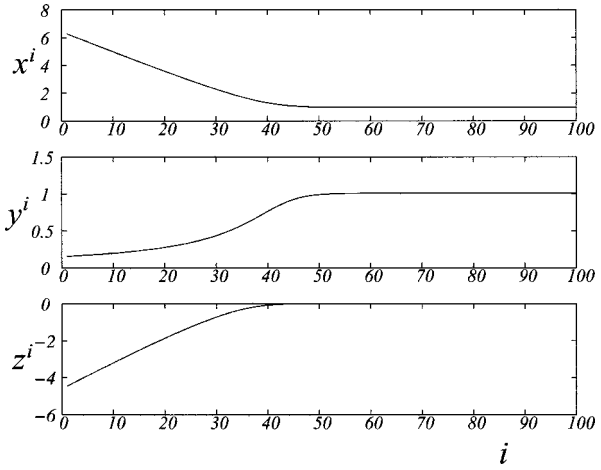

Fig. 6 ***x*, *y*, and *z* versus discrete time index**

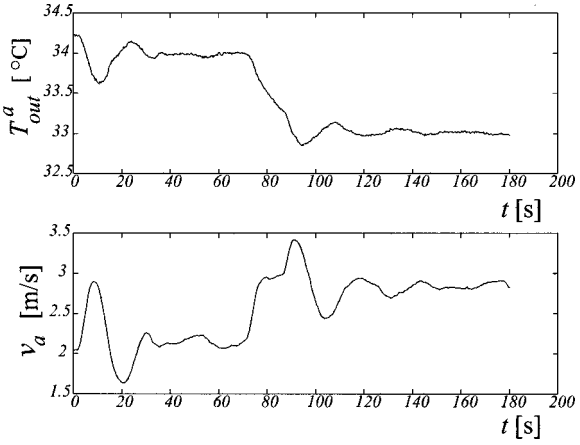

Fig. 8 Response to change in the T^a_{out} set point

x, *y*, and *z* at each iteration *i*. It is observed that since the spectral radius of the system was kept below unity, the maximum value of *z* is also a stable fixed point of the system.

4 Experimental Verification

We will now use the ANN training technique described above to control the exit air temperature of a heat exchanger. The experimental setup consists of a variable speed wind tunnel facility, shown in Fig. 7, with a water-to-air fin-tube heat exchanger as described by Zhao [15]. Thermocouples are used to measure the inlet and outlet temperature of the air and water side. The motion of the air in the tunnel is due to a blower that is controlled by a variable speed drive that can be operated manually or automatically from a personal computer. The air speed can be controlled within a certain range and is measured using a Pitot tube located upstream of the heat exchanger. The calibration of the air flow measurements was performed using average air velocities based on ASHRAE test codes. A single-point temperature measurement is used upstream of the heat exchanger and five thermocouples connected in parallel are used to obtain the T^a_{out} measurement. Information about inlet and outlet temperatures of both the air and water side, T^a_{in} and T^w_{in} respectively, the mass flow rate of water, $\dot{m}_w$, the air speed, v_a, and the time t at which the measurements were taken are sent to the PC that also serves as a controller. T^w_{in} is varied by using a heater with a PID-controlled electrical resistance. $\dot{m}_w$ is modified by an electronic valve so that the percentage of opening can be controlled as desired from the PC. The data acquisition board used can obtain measurements of up to 16 different channels, simultaneously. LabVIEW is used to acquire and send data to the experimental system and a program written in C interfaces with it to perform the desired control action.

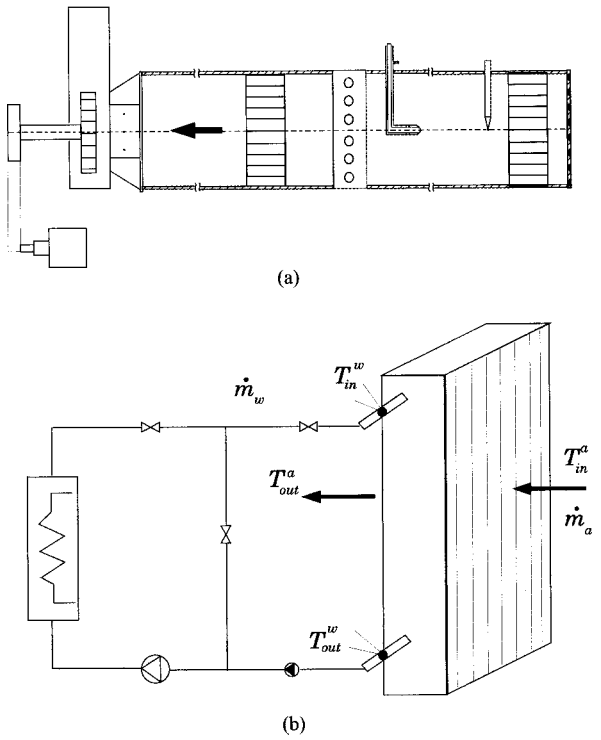

Fig. 7 Schematic of test facility: (*a*) wind tunnel; (*b*) heat exchanger connections

4.1 Change in the Set Point. The first test corresponds to a sudden change in the set point of T^a_{out}. Figure 8 shows a typical result of this experiment. The curve on the top shows the values of T^a_{out} and that on the bottom shows the values of the control variable v_a. The experiment consists on turning on the controller at an outlet air temperature close to 34°C. The volumetric flow rate of water in the system was kept constant at 2.71×10^{-4} m^3/s. If the adaptation criteria are not matched, i.e., stability and target error, then the controller starts the adaptation process to let a PID controller keep the physical plant as close as possible to the set point temperature until the adaptation criteria are satisfied. It is possible to see that, during approximately the first 30 seconds of the test, the controller is adapting and then it stabilizes the plant at the desired set point temperature. At $t=70$ s, we change the set point to 33°C. The controller detects an abrupt change in target error and starts another adaptation process. During this adaptation period, the PID controller takes over again and tries to keep the system close to the set point. At approximately $t=90$ s the controller regains control of the system and stabilizes it at the new set point. It is observed that v_a increases by approximately 50 percent.

4.2 Disturbance Rejection. The response of the controller to four different kinds of disturbances were determined.

(a) Water-Side Disturbance. The testing procedure is similar to the case of change in the set point. We turn on the controller and it adapts until the adaptation criteria are matched. The initial oscillations are mainly due to the action of a PID controller that controls the system while the neurocontroller adapts. It reacts to an arbitrary initial condition of the system that might not be exactly at the set point temperature. The neurocontroller then keeps the system close to $T^a_{\text{out}}=34$°C, at which point we apply a distur-

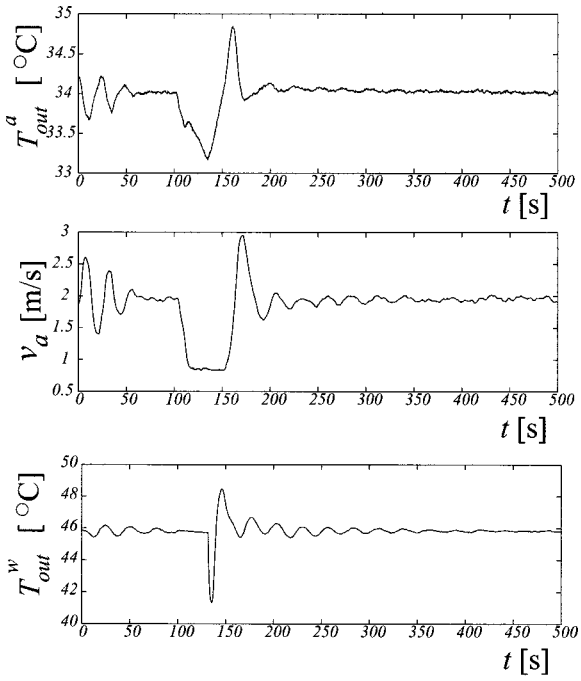

Fig. 9 Response to water-side disturbance

bance which consists of shutting off the water. Figure 9 shows the results of this experiment. The first 50 s is under the action of PID control, after which the neurocontroller takes over. At $t=100$ s we shut the water flow rate for a period of 30 s. The neurocontroller works until $t=110$ s at which point it hands the control action to PID while it is itself adapting. At $t=130$ s the water flow resumes. Meanwhile, the PID has tried to keep the reference temperature by reducing v_a to its minimum possible value but is unable to maintain T^a_{out} without the water flow. Adaptation of the neurocontroller is complete around $t=170$ s after which it takes over the control action. The graph also shows the water outlet temperature T^w_{out} during the same period. Between $t=100$ s and $t=130$ s there is no water flow so that the water outlet temperature remains constant. When water flow is resumed the cold water that was stagnant inside the HX flows past the thermocouple followed by the hot water that was stagnant in the heater; the resulting blip in T^w_{out} can be seen. The temperature oscillations are due to these portions of cold and hot water repeatedly passing by the thermocouple while circulating within the closed loop. It is observed that v_a has a similar oscillatory behavior.

(b) Air-Side Disturbance. We now perform perhaps the most difficult test for the controller by reducing the inlet air area of the wind tunnel representing a structural change in the thermal system. We do this in two ways, once gradually and then suddenly.

Figure 10 shows the results of the gradual reduction. The first 30 s is under PID control, and the neurocontroller gains control of the system at that point. From $t=100$ s until $t=220$ s we gradually block the inlet area until there is only one-half of the initial area left. As this happens, the neurocontroller increases v_a to keep the system at 34°C. There is a point at approximately $t=190$ s where the ANN model is not able to characterize the system and an adaptation process begins; the neurocontroller adapts until about $t=260$ s. After it has learned, the new relation between T^a_{out} and v_a takes over the control action to stabilize the system. It is observed that there are some oscillations of the temperature between $t=330$ s and $t=390$ s but T^a_{out} finally settles down to the set point.

To further test the adaptive ability of the controller, the previous experiment is repeated but with suddenly blocking one-half the inlet air area. We let the controller keep the system stable at $T^a_{\text{out}}=34$°C and then block the inlet. The controller adapts until it is able to return the system to the same outlet air temperature. Figure 11 shows the results obtained for this test. For the first 50 s the controller adapts until it learns the behavior of the system and then it keeps it stable at 34°C. At $t=150$ s, the inlet area is blocked and we let the controller adapt until it learns the new characteristics of the system. It is seen that v_a increases approximately 50 percent. Finally at about $t=240$ s, the neurocontroller regains the control of the plant and stabilizes the system at the set point.

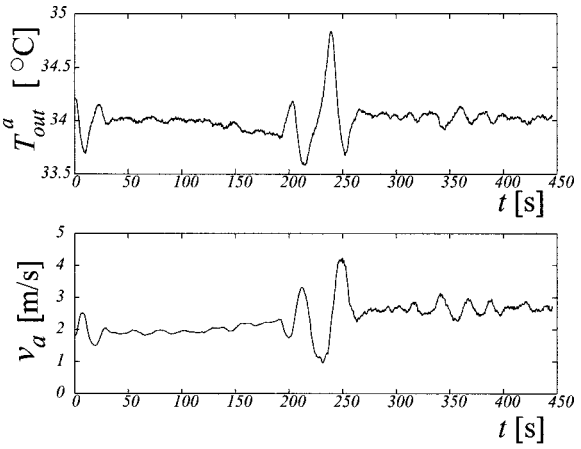

Fig. 10 Response to air-side disturbance; gradual reduction of the inlet air area

4.3 Energy Consumption. In order to minimize the energy consumption of the system, the main components that consume energy in the experimental facility need to be identified, and they are the hydraulic pump, the fan and the electric heater. Measurements of the voltage and current for these three components were made and the amount of energy consumed by each one of them could be determined. Different operating points of $\dot{m}_w$ and $\dot{m}_a$ were chosen for taking the measurements and the results indicated that the electric heater was the thermal component that consumed the most energy. Thus, we use the measurements taken from this component to develop a surface with $E=E(\dot{m}_w,\dot{m}_a)$, where E is the power consumed. Figure 12 shows the corresponding surface. As expected, the lower $\dot{m}_w$ and $\dot{m}_a$, the lower is the use of energy.

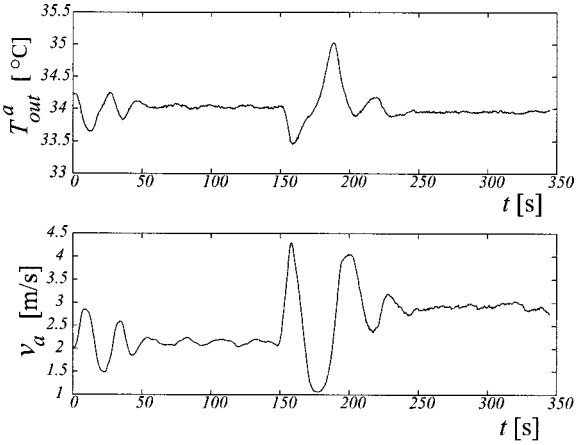

Fig. 11 Response to air-side disturbance; sudden reduction of the inlet air area

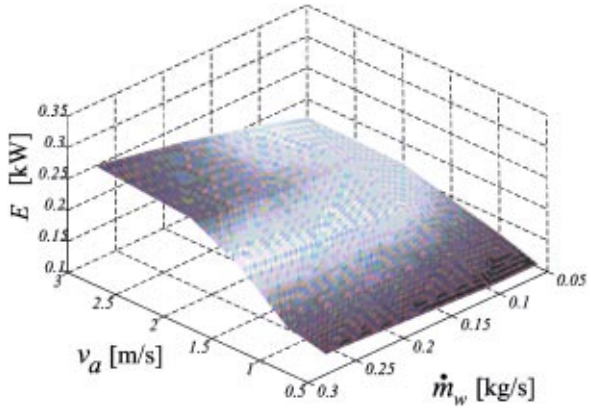

Fig. 12 Energy consumption surface $E(v_a, \dot{m}_w)$

We use this surface now to find the value of the energy for each sampled measurement during the operation of the system and to determine the direction of minimal use of energy. We let the controller drive the system in this direction. If the controller senses that the system is behaving in a different way, it will adapt to the new characteristics of the system.

In addition to the two previous adaptation criteria for the weights and biases of the ANNs, i.e., low target error and stable operation, we added the third which is the minimization of energy consumption. We let the controller stabilize the system at $T^a_{\text{out}} = 34°\text{C}$ and then turn on the training using the third criterion. Figure 13 shows the results obtained. The controller is supposed to keep the system stable at the same T^a_{out}. The minimization of energy routine reduces the $\dot{m}_w$ so that the controller has to reduce $\dot{m}_a$. The disturbance is not strong enough to make the controller detect a change in the system characteristics so no adaptation is needed, and the system is successfully kept at the set point.

It is noted that in the present study, there is essentially one controlled parameter (exit air temperature) and one controlling parameter (air flow), and several other operating parameters remain constant. This is however not a limitation of the adaptive neurocontroller strategy. As already shown in the case where a disturbance in the water flow is introduced (Fig. 9), the additional training due to the changed water flow and its effect on the exit air temperature provides the needed modulation of the neurocontroller. However, it is true that for general multiple controlling and controlled-parameter problems, the control strategy does become more complex and requires further study.

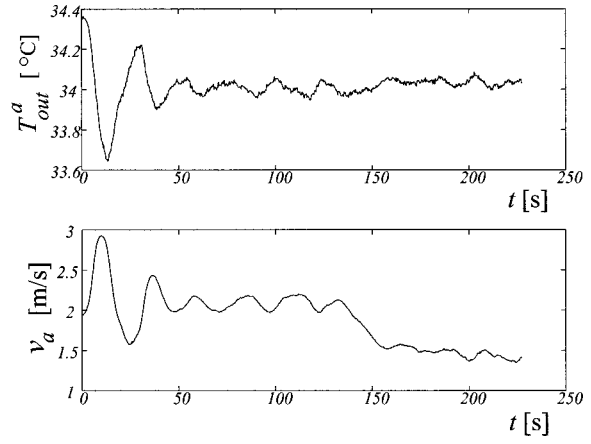

Fig. 13 Application of energy minimization routine. $\dot{m}_w$ is reduced to consume less energy and as a consequence, $\dot{m}_a$ is also reduced.

5 Conclusions

It has been previously shown that ANNs are a powerful technique to model and control nonlinear systems. They can be trained to give small errors in prediction and a stable closed-loop feedback control operation. However, one of the main advantages of ANNs is that they are easy to adapt such that their parameters can be modified on-line. We have shown how this can be done in also minimizing some other index, such as energy consumption, at the same time. The neurocontroller was able to control the experimental facility and adapt to its new conditions for disturbances in the air and water flow rates. It was also able to learn and control the plant behavior for a change in the set point of the temperature. The methodology is fairly general; the same procedure can be used, for example, for the adaptive and stable control of other thermal systems while at the same time minimizing the energy used. The results of this study suggest that ANNs are useful for the control of thermal systems that may change over time.

Acknowledgments

We gratefully acknowledge the support of Mr. D. K. Dorini of BRDG-TNDR for this and related projects in the Hydronics Laboratory. G. D. also thanks the Organization of American States for a PRA Fellowship.

Nomenclature

a = parameter of the analytical model
E = power consumed [kW]
F = filter for control scheme
I = integral control
i = discrete time index
$\dot{m}$ = mass flow rate [kg/s]
r = spectral radius of Jacobian matrix
T = temperature [°C]
T_{ref} = reference temperature [°C]
t = time [s]
u = control action
v = air speed [m/s]
x = control variable
y = controlled variable
z = optimization variable

Subscripts and Superscripts

a = air side
in = inlet
out = outlet
w = water side

References

[1] Sen, M., and Yang, K. T., 2000, ''Applications of Artificial Neural Networks and Genetic Algorithms in Thermal Engineering,'' *CRC Handbook of Thermal Engineering*, section 4.24, F. Kreith, ed., pp. 620–661.
[2] Díaz, G., Sen, M., Yang, K. T., and McClain, R. L., 1999, ''Simulation of Heat Exchanger Performance by Artificial Neural Networks,'' HVAC&R Research Journal, **5**, No. 3, pp. 195–208.
[3] Kays, W. M., and London, A. L., 1984, *Compact Heat Exchangers*, 3rd ed., McGraw-Hill, New York.
[4] Sundén, B., and Faghri, M., (eds.), 1998, *Computer Simulations in Compact Heat Exchangers*, Computational Mechanics Publications, Boston, MA.
[5] Díaz, G., Sen, M., Yang, K. T., and McClain, R. L., 2001, ''Dynamic Prediction and Control of Heat Exchangers Using Artificial Neural Networks,'' International Journal of Heat and Mass Transfer, **44**, pp. 1671–1679.
[6] Marwah, M., Li, Y., and Mahajan, R. L., 1996, ''Integrated Neural Network Modeling for Electronic Manufacturing,'' J. Electron. Manuf., **6**, No. 2, pp. 79–91.
[7] Blazina, A., and Bolf, N., 1997, ''Neural Network-Based Feedforward Control of Two-Stage Heat Exchange Process,'' *Proceedings of the IEEE International Conference on Systems, Man and Cybernetics*, **1**, pp. 25–29.
[8] Ayoubi. M. 1997, ''Dynamic Multi-Layer Perceptron Networks: Application to the Nonlinear Identification and Predictive Control of a Heat Exchanger,''

Applications of Neural Adaptive Control Technology, World Scientific Series in Robotics and Intelligent Systems, **17**, pp. 205–230.
[9] Nahas, E. P., Henson, M. A., and Seborg, D. E., 1992, ''Nonlinear Internal Model Control Strategy for Neural Network Models,'' Comput. Chem. Eng., **16**, No. 12, pp. 1039–1057.
[10] Chen, C. T., Hwu, J., and Chang, W. D., 1999, ''Nonlinear Process Control Based on Using an Adaptive Single Neuron,'' J. Chin. Inst. Chem. Eng., **30**, No. 2, pp. 141–149.
[11] Haykin, S., 1994, *Neural Networks, A Comprehensive Foundation*, Macmillan College Publ. Co., New York.
[12] Díaz, G., Sen, M., Yang, K. T., and McClain, R. L., 2001, ''Stabilization of Thermal Neurocontrollers,'' International Journal of Heat and Mass Transfer, in press.
[13] Hunt, K. J., Sbarbaro, D., Zbikowski, R., and Gawthrop, P. J., 1992, ''Neural Networks for Control Systems—A Survey,'' Automatica, **28**, No. 6, pp. 1083–1112.
[14] Landau, I. D., Lozano, R., and M'Saad, M., 1998, *Adaptive Control*, Springer-Verlag, London.
[15] Zhao, X., 1995, ''Performance of a Single-Row Heat Exchanger at Low In-Tube Flow Rates,'' M.S. thesis, Department of Aerospace and Mechanical Engineering, University of Notre Dame, IN.

Computation of Flow and Heat Transfer in Two-Pass Channels With 60 deg Ribs

Yong-Jun Jang
Ph.D. Student
Turbine Heat Transfer Laboratory,
Department of Mechanical Engineering,
Texas A&M University,
College Station, TX 77843-3123

Hamn-Ching Chen
Associate Professor
Ocean Engineering Program,
Department of Civil Engineering,
Texas A&M University,
College Station, TX 77843-3136

Je-Chin Han
HTRI Professor
Turbine Heat Transfer Laboratory,
Department of Mechanical Engineering,
Texas A&M University,
College Station, TX 77843-3123

Numerical predictions of three-dimensional flow and heat transfer are presented for a two-pass square channel with and without 60 deg angled parallel ribs. Square sectioned ribs were employed along one side surface. The rib height-to-hydraulic diameter ratio (e/D_h) is 0.125 and the rib pitch-to-height ratio (P/e) is 10. The computation results were compared with the experimental data of Ekkad and Han [1] at a Reynolds number (Re) of 30,000. A multi-block numerical method was used with a chimera domain decomposition technique. The finite analytic method solved the Reynolds-Averaged Navier Stokes equation in conjunction with a near-wall second-order Reynolds stress (second-moment) closure model, and a two-layer k-ε isotropic eddy viscosity model. Comparing the second-moment and two-layer calculations with the experimental data clearly demonstrated that the angled rib turbulators and the 180 deg sharp turn of the channel produced strong non-isotropic turbulence and heat fluxes, which significantly affected the flow fields and heat transfer coefficients. The near-wall second-moment closure model provides an improved heat transfer prediction in comparison with the k-ε model.
[DOI: 10.1115/1.1371931]

Keywords: Computational, Cooling, Heat Transfer Enhancement, Turbines, Turbulence

Introduction

Advanced gas turbine blades are designed to operate with a high inlet temperature that is far above the allowable metal temperature. Sophisticated cooling techniques such as film cooling and convective internal cooling are essential for maintaining acceptable blade life. For the internal cooling of the blades, the heat transfer augmentation is achieved by using repeated ribs as turbulence promoters. The presence of the ribs leads to a complex flow field such as flow separation and reattachment between the ribs, which produces a high turbulence level that leads to high heat transfer coefficients. Detailed information about the flow and heat transfer characteristics in a ribbed channel is very important in designing gas turbine engines.

Han and Park [2] performed experimental studies on heat transfer characteristics in channels with 30 deg, 45 deg, 60 deg angled ribs and normal ribs. Bonhoff et al. [3] and Schabacker et al. [4] studied the flow characteristics in square channels with 45 deg angled ribs. Tse and Steuber [5] investigated flow characteristics in a serpentine coolant passage with angled ribs (45 deg) using LDV. Wagner et al. [6] and Johnson et al. [7] studied surface heat transfer coefficients in a multi-pass square channel with normal and 45 deg angled ribs, respectively. The recent experimental work of Ekkad and Han [1] provided the most detailed heat transfer coefficient distribution in two-pass square channels with and without rib turbulators using a liquid crystal transient technique. Their study motivated further numerical investigation and so was used as the basis for the verification of the present calculation.

The earlier computational studies on internal coolant passages with ribs have mostly been restricted to two-dimensional flows. In recent years, some researchers have reported three-dimensional studies. Prakash and Zerkle [8] performed the calculation of flow and heat transfer in a ribbed rectangular duct (only one rib-pitch was investigated). Turbulence was modeled with the k-ε model in conjunction with the wall function. They concluded the low Reynolds number model was necessary to get better results and Reynolds stress model was required to capture the anisotropic effects around the ribs. Stephens and Shih [9] investigated three-dimensional flow and heat transfer in a rectangular duct (one pass) in which one wall was roughened with five equally-spaced 90 deg square ribs. They used a low-Reynolds number k-ω turbulence model. Rigby et al. [10] presented the numerical results for flow and heat transfer in a straight channel (one pass) with 90 deg parallel ribs using a k-ω turbulence model. They compared their data with Ekkad and Han [1] experimental data. The heat transfer coefficient between the ribs showed good agreement with the experimental data. However, the heat transfer coefficient on the top of the ribs was underestimated by this model. Stephens et al. [11] investigated flow and heat transfer characteristics in a straight duct (one pass) with inclined, 45 deg rounded ribs on two opposite walls using a low-Reynolds number k-ω turbulence model and provided important features for inclined rib ducts. Iacovides [12] calculated the periodic flow and heat transfer through the square-cross-sectioned duct (one pass) with rib-roughened walls. He employed two turbulence models; a k-ε with a one-equation model of a k transport across the near-wall region and a low-Re differential stress model (DSM). He concluded that the DSM thermal computations were clearly superior to those of the k-ε/one-equation model, even though the heat transfer coefficient results were not as close to the experimental data as the flow prediction.

Bonhoff et al. [13] presented the heat transfer predictions for U-shaped coolant channels with 45 deg angled ribs. The Reynolds stress model (RSM) in FLUENT was used for the calculation. Rigby [14] presented a numerical prediction of flow and heat transfer in a ribbed (90 deg rib) coolant passage with a 180 deg turn. The computation was performed using a k-ω turbulence model, and the heat transfer coefficient was overpredicted for the stationary case and underpredicted for the rotating case compared to experimental data. Iacovides and Raisee [15] explored turbulence modeling issues related to the computation of flow and heat transfer in internal cooling passages of turbine blades with normal ribs (90 deg). They tested four turbulence models: zonal k-ε, a low-Re k-ε, a zonal differential stress model (DSM), and a low-Re DSM. They found that zonal models underpredict surface heat transfer coefficients because they ignored the effects of transport on the near-wall turbulence scale. The low-Re closures were

Contributed by the Heat Transfer Division for publication in the JOURNAL OF HEAT TRANSFER. Manuscript received by the Heat Transfer Division March 2, 2000; revision received February 1, 2001. Associate Editor: B. Chung.

found to be able to reproduce the correct surface heat transfer coefficients. In their results, they found that the low-Re DSM model reproduced the turbulence field more faithfully than the k-ε model.

There are three main reasons why extensive numerical studies of the flow and heat transfer in ribbed ducts with sharp 180 deg turn have not been possible to date. First, detailed experimental data around/on the ribs was not available. The second, as indicated in Iacovides and Raisee [15] and Stephen et al. [11], wall function approach was inappropriate when there were flow separations. Moreover, the simple isotropic eddy viscosity model could not capture the physically reasonable flow and heat transfer behavior induced by the anisotropic characteristic of turbulent flow around the ribs and the 180 deg sharp turn region. Third, for flows within a strong curvature, which cause flow separation, it has been necessary to employ high order schemes for the discretization of convective transport.

However, recent computational work by Chen et al. [16,17] demonstrated the superiority of the second-order Reynolds stress closure over simpler k-ε isotropic eddy viscosity models using the finite analytic method in rotating two-pass square channels with smooth walls. Encouraged by this successful result, this model has been used to predict the flow and heat transfer in ribbed channels. This paper presents the prediction of flow and heat transfer characteristic in a two-pass square channel, with and without 60 deg angled parallel ribs, that was experimentally investigated by Ekkad and Han [1]. The computation was performed by a two-layer k-ε eddy viscosity model and also a near-wall second-moment turbulence closure model in order to assess its effectiveness. The governing equations for this model were described in detail in Chen et al. [16] and will not be repeated here. For completeness, we will briefly summarize the numerical method in the following section.

Chimera Rans Method

In the present study, the chimera RANS method of Chen [18,19] and Chen, Jang and Han [16] was employed for the calculation of fluid flow and heat transfer in stationary ribbed channels. The present method solved the mean flow and turbulence quantities in arbitrary combinations of embedded, overlapped, or matched grids using a chimera domain decomposition approach. In this approach, the solution domain was first decomposed into a number of smaller blocks to facilitate efficient adaptation of different block geometries, flow solvers, and boundary conditions for calculations involving complex configurations and flow conditions. Within each computational block, the finite-analytic numerical method of Chen and Chen [20] and Chen, Patel, and Ju [21] was employed to solve the unsteady RANS equations on a general curvilinear, body-fitted coordinate system. The coupling between the pressure and velocity was accomplished using a hybrid PISO/SIMPLER algorithm given by Chen and Patel [22] and Chen and Korpus [23]. The method satisfied continuity of mass by requiring the contravariant velocities to have a vanishing divergence at each time step. Pressure was solved by using the concept of pseudo-velocities and, when combined with the finite-analytic discretization gives the Poisson equation for pressure. To ensure the proper conservation of mass and momentum between the linking grid blocks, the grid-interface conservation techniques of Hubbard and Chen [24] and Chen and Chen [20] were employed to eliminate the unphysical mass source resulting from the interpolation errors between the chimera grid blocks. More detailed descriptions of the chimera RANS method were given in Chen and Chen [20] and Chen and Liu [25].

Results and Discussion

Calculations were performed for the two-pass square channel with angled (60 deg) ribbed wall as tested by Ekkad and Han [1].

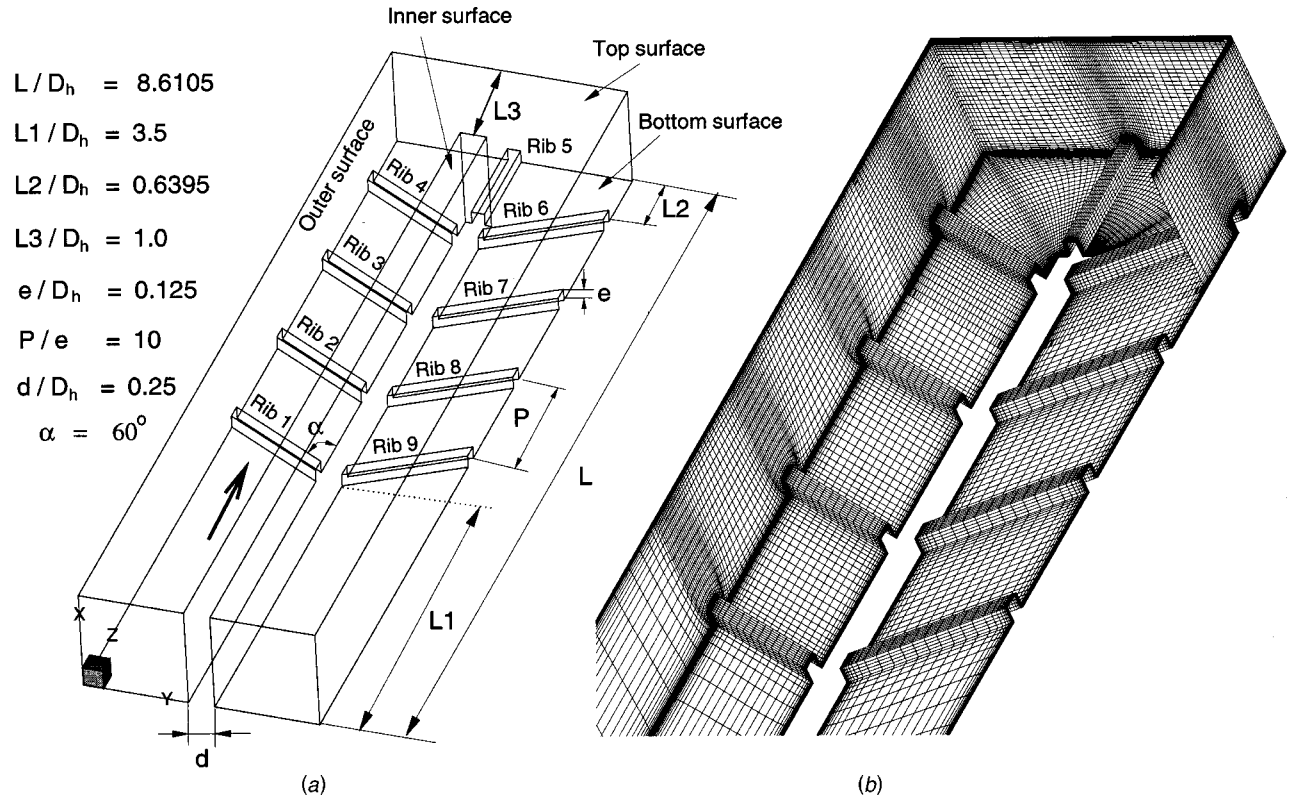

Fig. 1 Geometry and numerical grid

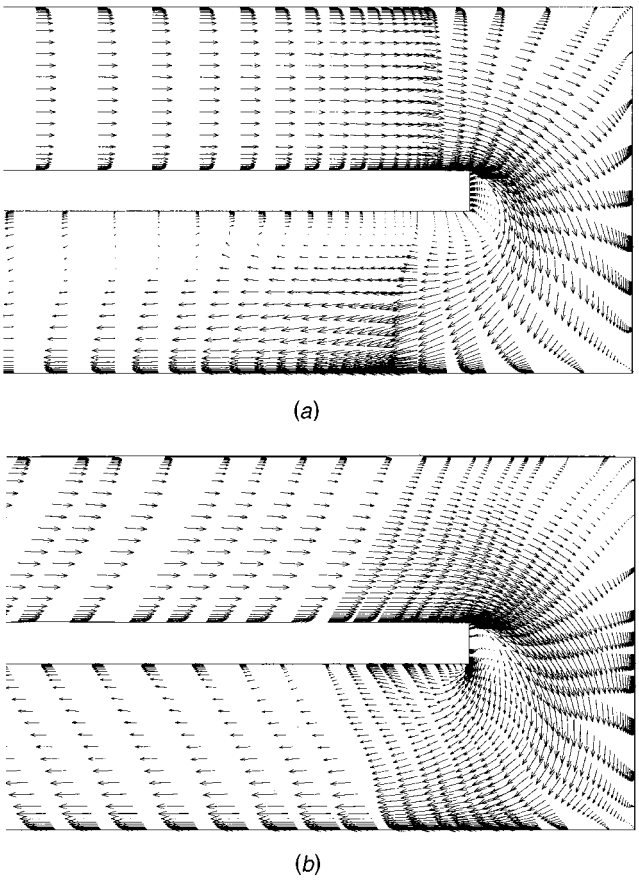

Fig. 2 Streamwise velocity vector midway between the top and bottom surface: (*a*) smooth duct; and (*b*) 60 deg angled ribbed duct.

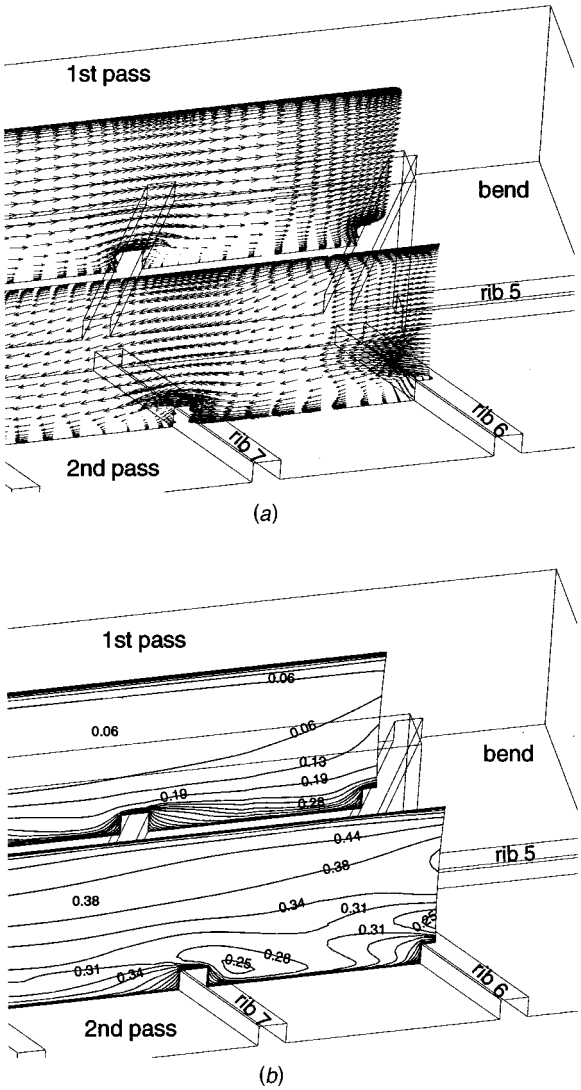

Fig. 3 Streamwise velocity and temperature fields midway between the inner and outer surfaces for 60 deg angled ribbed duct

Figure 1 shows the geometry and the numerical grids for the one side ribbed channels. The ribbed side wall was denoted as the bottom surface and the opposite side wall was denoted as the top surface. The other two side walls were denoted as the inner and outer surfaces. A total of nine ribs were simulated. Four ribs in the first passage were angled away from the divider wall and four ribs in the second passage were angled toward the divider wall. There was a 90 deg rib in the turn region. All ribs were inclined, with respect to the flow, at an angle (α) of 60 deg except for the rib in the bend.

The length of the duct was $8.6105D_h$. The length from the inlet to the first rib (L_1) was $3.5D_h$ and the length from the last rib in the first passage to the outer surface in the bend (L_2) was $0.6395D_h$. The length from the divider wall tip to the outer surface in the bend (L_3) was $1D_h$. The divider wall thickness (d) was $0.25D_h$. The rib height-to-hydraulic diameter ratio (e/D_h) was 0.125 and the rib pitch-to-height ratio (P/e) was 10. The arc length (S) was measured from the middle of the turn. Positive S indicated the second passage and negative S indicated the first passage.

A fully developed turbulent boundary layer profile was used at the inlet of the duct in the present calculations. Since the fully developed profiles for mean flow and turbulence quantities were not known analytically, a separate calculation was performed for a straight duct to provide the inlet conditions at the duct entrance. The flow was assumed to be parabolic at the exit of the duct with zero-gradient boundary conditions for mean velocity and all turbulence quantities, while linear extrapolation was used for the pressure field. All walls including the rib surfaces were heated to a constant temperature. The coolant fluid at the entrance of the duct was air, at a uniform temperature, T_o (i.e., $\theta=(T-T_o)/(T_w-T_o)=0$) and the wall temperature, including the ribs, was kept constant at $T=T_w$ ($\theta=1$).

The Nusselt numbers presented herein were normalized with a smooth tube correlation (Kays and Crawford [26]) for fully developed, non-rotating, turbulent flow

$$\mathrm{Nu}_o = 0.0176\,\mathrm{Re}^{0.8}.$$

The present numerical grid was generated using an interactive gridding code GRIDGEN developed by Steinbrenner et al. [27] It was then reblocked into several interlocked computational blocks to facilitate the implementation of near-wall turbulence models and specification of boundary conditions. To provide adequate resolutions of the viscous sublayer and buffer layer adjacent to a solid surface, the minimum grid spacing in the near-wall region was maintained at 10^{-4} of the body length which corresponded to a wall coordinate y^+ of the order of 0.1. In all calculations, the root-mean-square (rms) and maximum absolute errors for both the mean flow and turbulence quantities were monitored for each computational block to ensure complete convergence of the numerical solutions. A convergence criterion of 10^{-5} was used for the maximum rms error in all computational blocks.

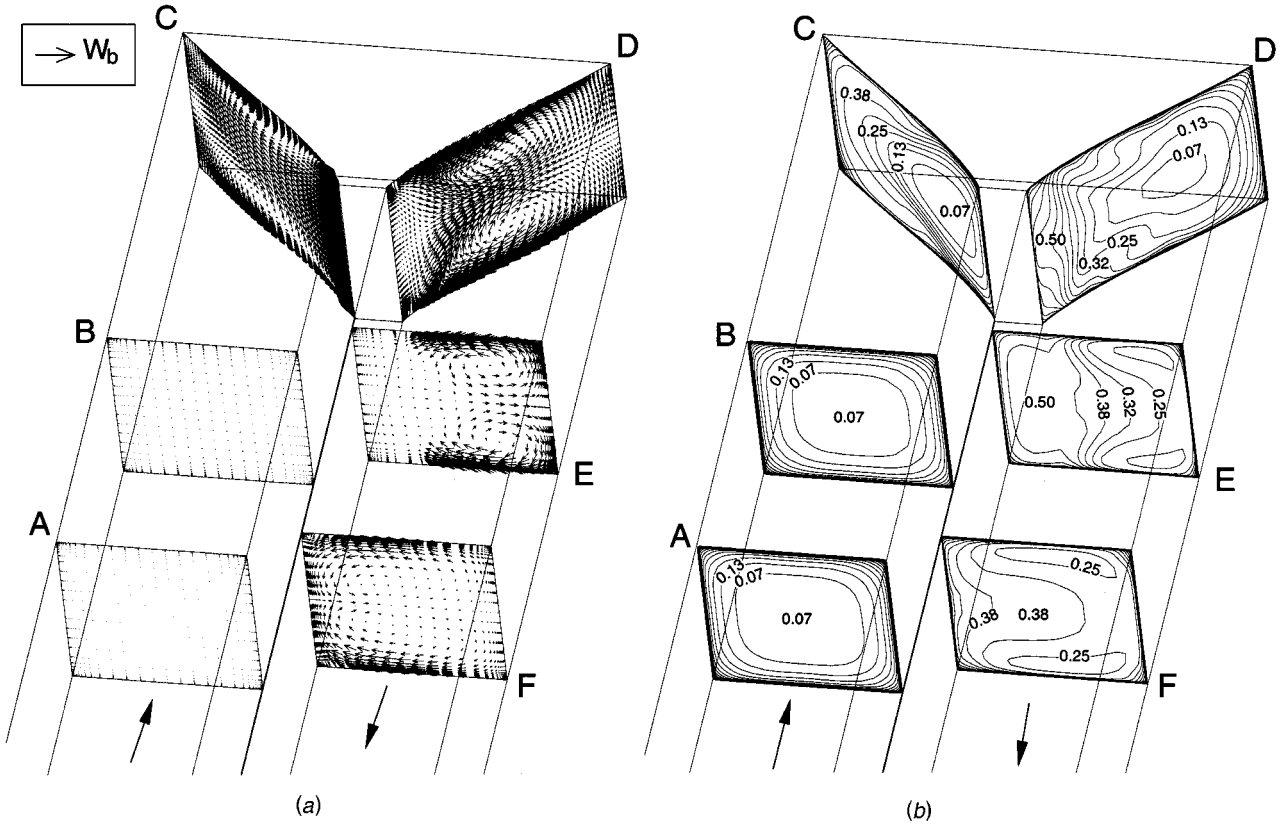

Fig. 4 Secondary flows and temperature fields ($\theta=(T-T_o)/(T_w-T_o)$) for smooth duct

A grid-refinement study was performed using four different grid distributions. In the first test, three grid systems $21\times21\times416$, $41\times41\times416$, $61\times61\times416$ (416 in the streamwise direction and 21, 41, and 61 in each of the two cross-stream directions) were evaluated. The maximum improvement in the spanwise averaged Nusselt number ratio was about 40 percent when the numerical grid was refined from $21\times21\times416$ to $41\times41\times416$. Further grid refinement to $61\times61\times416$ produced only 4 percent improvement in the straight regions and 10 percent improvement in the bend for the predicted spanwise averaged Nusselt number ratio. In the second test, two grid systems of $41\times41\times208$ and $41\times41\times416$ were examined to determine the grid resolution in the axial direction. The Nusselt number ratio was improved by 5 percent with $41\times41\times416$ compared to $41\times41\times208$. As indicated in Stephens et al. [11], the Nusselt number is more sensitive to the grid spacing in the cross-stream direction than in the streamwise direction. The findings from this investigation showed that the grid system $41\times41\times261$ for the straight regions and $61\times61\times155$ for the bend regions was nearly grid independent. All the results in the following discussions were based on the $41\times41\times261$ for the straight regions and $61\times61\times155$ distributions for the bend regions using the Chimera method. The grid was divided into five computational blocks with a total grid point of approximately 1,020,000 points.

Mean Velocity and Temperature Fields. The three-dimensional mean flow and temperature fields for a two-pass square channels with and without 60 deg angled parallel ribs are presented in this section. For the sake of brevity, we will only present the details of the flow and temperature fields for the second-moment solutions, since the second-order Reynolds stress model produced more accurate results for all test cases. The two-layer $k-\varepsilon$ results will be discussed only in the comparison of Nusselt number ratio distributions to quantify the effects of Reynolds stress anisotropy.

The velocity vector distributions in the planes midway between the top and bottom surfaces are shown in Fig. 2. For the smooth channel case (Fig. 2(*a*)), the velocity profiles were flat before the turn. As the fluids approached the bend region, the flow showed an acceleration near the inner surface and a deceleration near the outer surface. This phenomenon was caused by the favorable and adverse pressure gradients along the inner and outer surface, respectively. Due to the inability of the flow to follow the sharp turn, a large separation bubble existed near the tip of the divider wall. Immediately downstream of the sharp turn, the pressure distributions along the inner and outer surfaces were completely opposite of those in the first passage. Thus, the acceleration was now occurring near the outer surface and deceleration occurred near the inner surface as shown in Fig. 2(*a*). The separation bubble occurring in the bend still existed along the inner surface after bend. The reattachment length was about $1.8D_h$ away from the divider wall tip which is consistent with Liou and Tzeng [28] experimental data. For the 60 deg angled ribbed duct case, velocity vector distribution midway between the top and bottom surface are shown in Fig. 2(*b*). Unlike the smooth duct case, separation bubbles did not exist near the divider wall tip in the bend region. Even immediately downstream of the bend, there were no separation bubble. This phenomenon was caused by two factors. First, it is attributed to the effect of the rib-induced secondary flow upstream of the bend, which pushed the fluid in the core toward the divider wall and thus, weakened the development of the curvature-induced radial velocity component in the bend. Second, the centrifugal effect was reduced due to the presence of the ribs in the bend. Figure 3 shows the streamwise velocity and temperature profiles at both the first and second passages in the planes midway between the inner and outer surfaces. The reversal flow occurred immediately downstream of the ribs. In the first passage, the reattachment length was about 3.1 times the rib height, which was consistent with the Ekkad and Han [1] data. Immediately

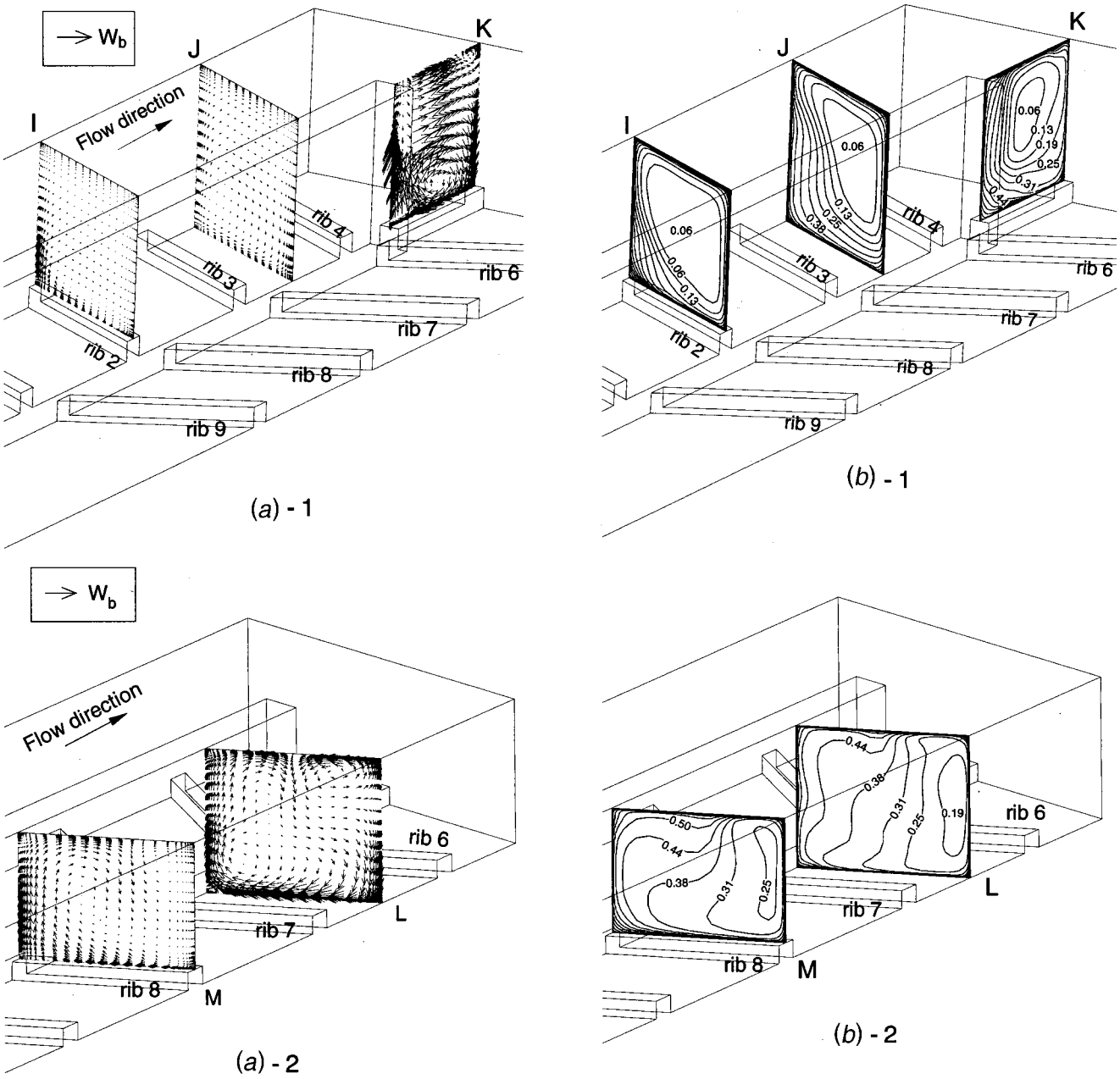

Fig. 5 Secondary flow and temperature fields ($\theta=(T-T_o)/(T_w-T_o)$) for 60 deg angled ribbed duct: (*a*) secondary flow; (*b*) temperature.

upstream of the ribs, however, there was no separation, such as that generally found in a 90 deg normal ribbed channel case (Fig. 3(*a*)). After the bend, a strong flow impingement occurred on the bottom surface between ribs 6 and 7, which was due to the bend effect. Temperature fields on the bottom surface were disturbed by the presence of the ribs (Fig. 3(*b*)). The periodic ribs broke the laminar sublayer and created local wall turbulence due to the flow separation and reattachment between the ribs. This caused thinner thermal boundary layer on the bottom surface (Fig. 3(*b*)). After the bend, much higher temperature gradient could be seen on the bottom surface due to the centrifugal effect in the bend.

In order to facilitate a more detailed understanding of the three-dimensional flow field, the secondary flow and temperature fields are also presented. Figure 4 shows the cross-stream velocity vectors and isothermal contours for a smooth channel at selected planes of $2.7D_h$ and $1.2D_h$ (sections A and B) away from the divider wall tip in the first passage, 45 deg and 135 deg cross section (sections C and D) in the bend, and $1D_h$ and $2.5D_h$ (sections E and F) away from the divider wall tip in the second passage. In the first passage, at sections A and B in Fig. 4(*a*), four corner vortices were generated as a result of the Reynolds stress anisotropy in the straight duct. The magnitude of those vortices was less than $0.02W_b$. Thus, it cannot be clearly seen in this figure. In the bend, the centrifugal forces and the associated pressure gradients (low pressure near the inner surface, high pressure near the outer surface) produced two counter-rotating vortices as shown in Fig. 4(*a*)-sections C and D, which transported fluid from the core toward the outer surface. After the turn, the counter-rotating vortex pair was pushed toward the outer surface as shown in Fig. 4(*a*)-section E and was limited to half of the cross-section by the separating bubble mentioned earlier. Down stream of the separation bubble (Fig. 4(*a*)-section F), the counter-rotating vor-

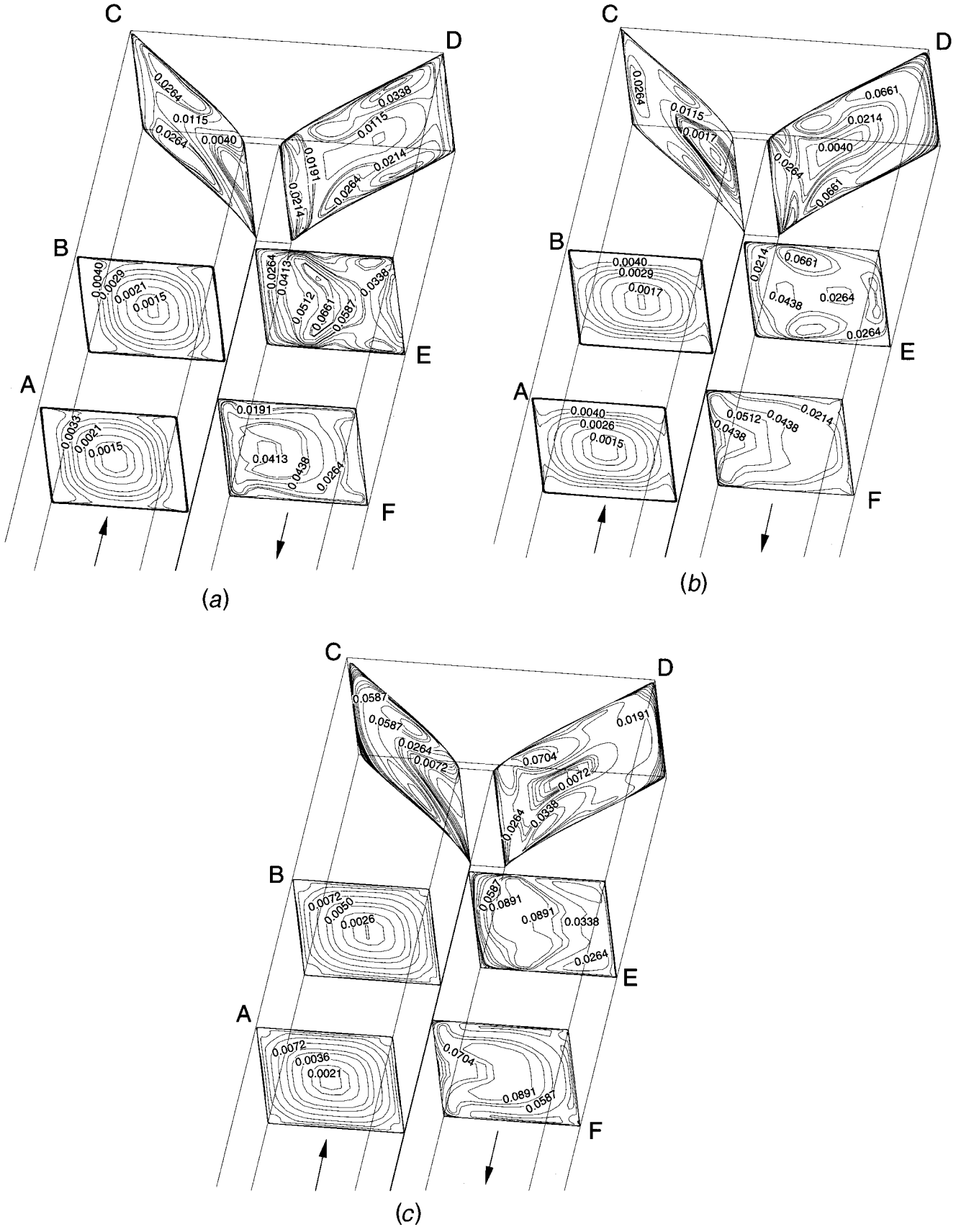

Fig. 6 Reynolds stress components at selected cross section for smooth duct: (*a*) $\overline{uu}/W_b^2$; (*b*) $\overline{vv}/W_b^2$; and (*c*) $\overline{ww}/W_b^2$

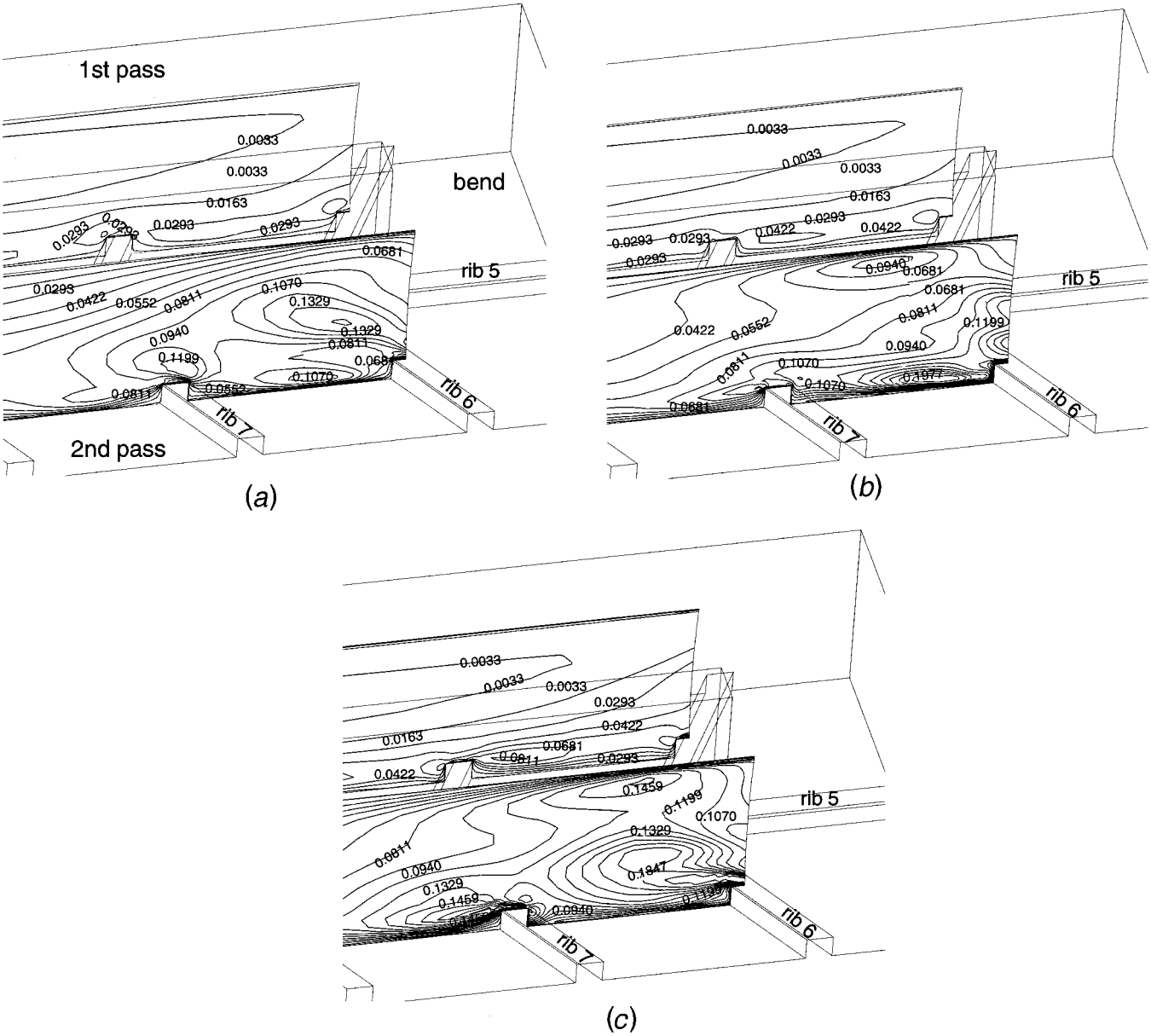

Fig. 7 Reynolds stress components midway between the inner and outer surface for 60 deg angled ribbed duct: (*a*) $\overline{uu}/W_b^2$; (*b*) $\overline{vv}/W_b^2$; and (*c*) $\overline{ww}/W_b^2$.

tex pair was again pushed toward the inner surface because the pressure gradient was recovered on the inner surface. Temperature fields were presented at the same locations as shown in Fig. 4(*b*). It was observed that the temperature fields were dependent on the secondary flow patterns. Thus, in the bend, the core fluid was pushed toward the outer surface due to the two counter-rotating vortices and generated a high temperature gradient near the outer surface. After the bend, high temperature gradients still remained near the outer surface (section E). Farther downstream (section F), it was seen that temperature distributions were mixed.

Figure 5 shows the cross-stream velocity vectors and the isothermal contour for the 60 deg angled ribbed channel at selected planes. Section I is on the top of rib 2 and section J is on the midway between ribs 3 and 4 in the first passage. Section K is on the top of rib 5 in the center of the bend. Section L is on the midway between ribs 6 and 7 and section M is on the top of rib 8 in the second passage. Sections I and J in Fig. 5(*a*)-1 show that the 60 deg angled one-side ribbed channel produced one large vortex in the first passage. These figures also show that the angled ribs induced the fast flow near the bottom surface between the ribs, which impinged on the outer surface and then returned along the top surface. Instead of the two counter-rotating vortices in the bend as was observed in the smooth channel, one strong vortex was generated near the top of rib 5 due to the combined effect of centrifugal induced vortex in the bend and rib-induced vortex upstream. Figure 5(*a*)-2 shows the secondary flow pattern in the second passage. It was more complicated due to the bend effect. In section L between ribs 6 and 7, three vortices were generated. It can be seen velocity magnitude was very high near all four surfaces. Farther downstream (section M in Fig. 5(*a*)-2), rib-induced secondary flow tried to overcome the bend effect. Thus, one large vortex started to appear and simultaneously the other vortices began to disappear. The secondary flow structure generated in the first passage transported the cooler fluid from the core toward the top and inner surfaces. This led to steep temperature gradients as shown in Fig. 5(*b*)-1. In the bend the cooler fluid was pushed toward the outer surface due to the secondary flow char-

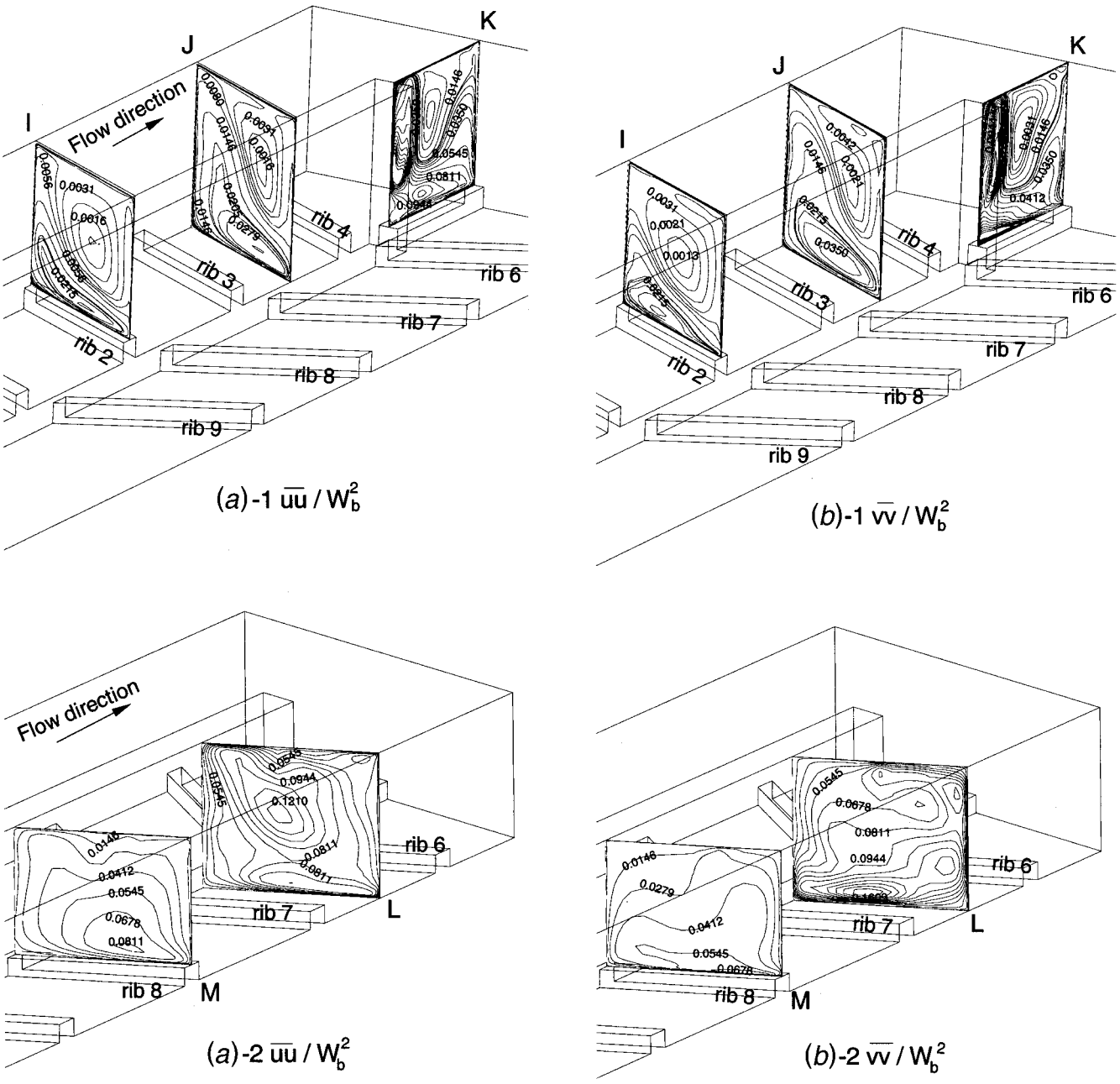

Fig. 8 Reynolds stress components at selected cross section for 60 deg angled ribbed duct: (*a*) $\overline{uu}/W_b^2$; (*b*) $\overline{vv}/W_b^2$; and (*c*) $\overline{ww}/W_b^2$.

acteristic in this region. In the second passage, the secondary flows pushed the cooler fluid toward the outer surface, which was opposite to that seen in the first passage.

Reynolds Stresses. The calculated Reynolds stress normal components are presented in Figs. 6–8. Figure 6 shows the Reynolds stress components for the smooth channel at selected cross sections (A, B, C, D, E, F are the same locations as defined in Fig. 4). In the first passage, the levels of turbulence intensity ($\sqrt{\overline{ww}}/W_b$, $\sqrt{\overline{vv}}/W_b$, and $\sqrt{\overline{uu}}/W_b$) were about 5 percent–10 percent near the wall and diminished gradually toward the core region of the duct. Near the wall, a higher degree of anisotropy ($2 \leq \overline{ww}/\overline{uu} \leq 3$) occurred compared to the of core region ($\overline{ww}/\overline{vv} \sim 1.6$) in the first passage. This anisotropic turbulent structure caused four pairs of counter-rotating corner vortices at the straight duct (Chen et al. [17]). In the bend, the patterns of Reynolds stresses were dramatically changed. This was clearly caused by the pressure-driven cross-stream flow with the presence of two strong counter-rotating vortices. Relatively high levels of turbulence intensity (15 percent–25 percent) arose near the outer surface, whereas lower values (8 percent–15 percent) were observed near the inner surface. However, the degree of anisotropy ($\overline{ww}/\overline{vv}$) near the inner surface was as high as 4.2 at a 45 deg cross section in the bend. In the second passage, the turning geometry-induced separating recirculation flow and the reattachment of separating shear flow contributed to the increase of the turbulence level. The peak turbulence intensity ($\sqrt{\overline{ww}}/W_b \approx 30$ percent) occurred around the shear layer bounding the recirculation zone as shown in Fig. 6(*c*)-section E. The degree of anisotropy ($1 \leq \overline{ww}/\overline{vv}$ or $\overline{ww}/\overline{uu} \leq 3$) in the second passage was not much higher than that of the bend region.

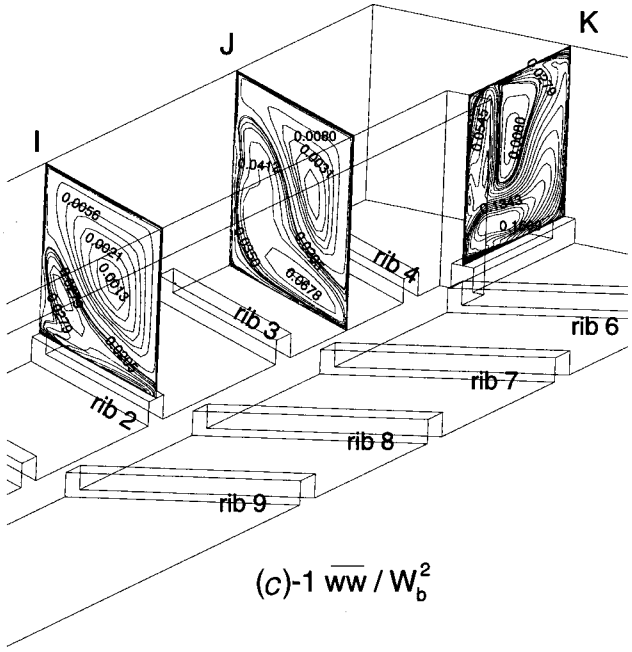

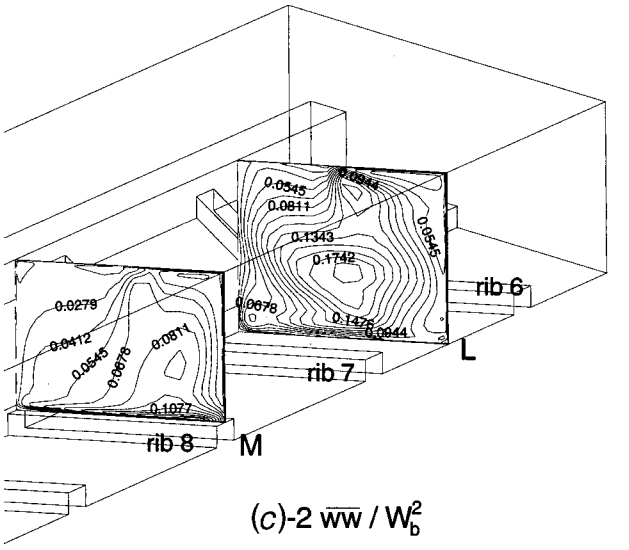

Fig. 8 (*Continued.*)

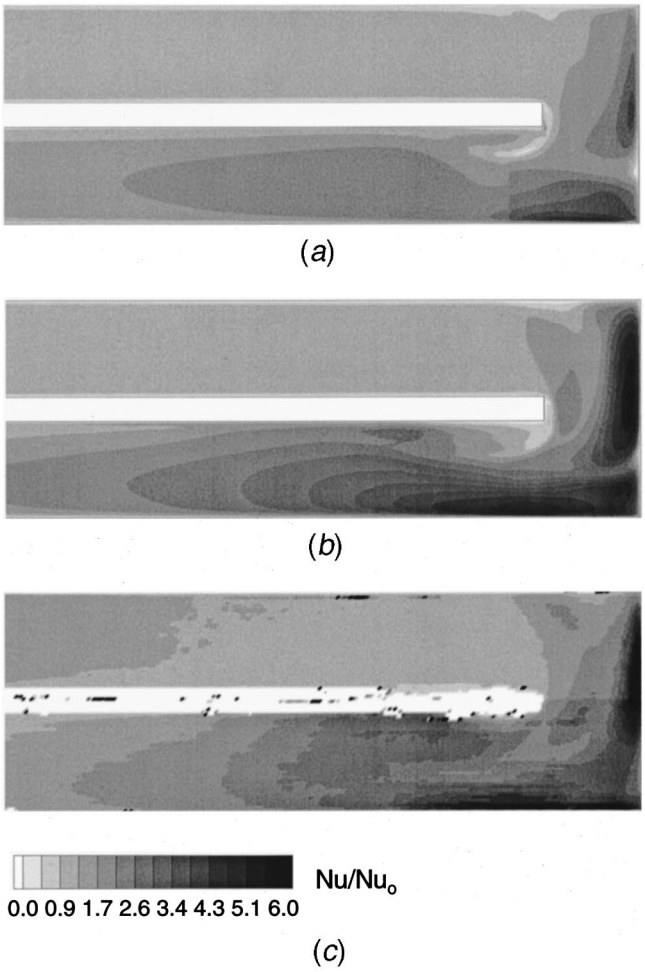

Fig. 9 Detailed Nusselt number ratio distributions for smooth duct: (*a*) two-layer model (k-ε); (*b*) second-moment model; and (*c*) Ekkad and Han [1].

Figure 7 shows the Reynolds stress normal components midway between the inner and outer surfaces in the first and second passage for a 60 deg angled ribbed channel. A close examination of the overall Reynolds stresses characteristics in the ribbed channel indicated that the ribs produced a high level of turbulence with enhanced heat transfer. In the first passage, turbulence intensity ($\sqrt{\overline{ww}}/W_b$) was as high as 29 percent immediately downstream of the ribs and diminished gradually toward the smooth top surface, ($\sqrt{\overline{ww}}/W_b \sim 6$ percent). A high degree of anisotropy ($2.3 \leqslant \overline{ww}/\overline{uu}$ or $\overline{ww}/\overline{vv} \leqslant 3$) was also observed downstream of each rib. In the second passage, the level of turbulence intensity increased due to the bend effect. $\sqrt{\overline{ww}}/W_b$, $\sqrt{\overline{vv}}/W_b$, and $\sqrt{\overline{uu}}/W_b$ were about 27 percent–43 percent in the region between ribs 6 and 7. The high turbulence intensity for $\sqrt{\overline{ww}}/W_b$ occurred immediately on the top of rib 6 and was transported downstream (Fig. 7(*c*)). However, the high turbulence intensity for $\sqrt{\overline{vv}}/W_b$ occurred near the bottom surface, in the region between ribs 6 and 7 due to the rib-induced fast flow between the ribs (Fig. 7(*b*)). Farther downstream in the second passage, turbulence intensity level decreased to 16 percent–37 percent. The degree of the anisotropy was similar to that of the first passage. Figure 8 shows the Reynolds stress components for a 60 deg angled ribbed channel at selected cross sections (I, J, K, L, M are the same locations as those defined in Fig. 5). In the first passage, high turbulence intensities (15 percent–26 percent) occurred on the top of the ribs and in the regions of reattachment between the ribs. These Reynolds stresses were transported toward the outer surface and then to the top surface due to the rib-induced secondary flow patterns in the first passage. Thus, the turbulence level was relatively high near the bottom and outer surfaces and low near the top and inner surfaces. In the first passage, the degree of anisotropy was about $1 \leqslant \overline{ww}/\overline{uu}$ or $\overline{ww}/\overline{vv} \leqslant 2.4$. In the bend, turbulence level was still high on the top of rib: where the turbulence intensity was about 30 percent–41 percent. The secondary flow in the bend transported the high Reynolds stresses toward the inner and top surfaces. In the second passage, the peak turbulence intensity (~42 percent) for $\sqrt{\overline{ww}}/W_b$ occurred around the core region in section L (between ribs 6 and 7), (Fig. 8(*c*)-2). The reason for this is high shear layer in that location, which was caused by the bend effect. For the $\sqrt{\overline{vv}}/W_b$ case, high turbulence intensity (40 percent) occurred near the bottom surface due to the rib-induced secondary flow between the ribs. Farther downstream, the general turbulence level

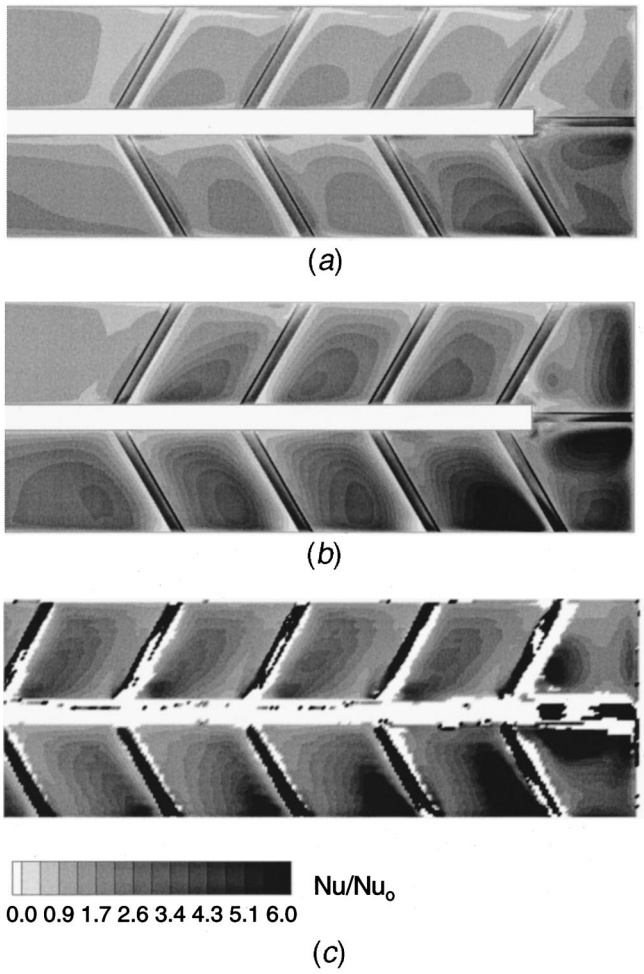

Fig. 10 Detailed Nusselt number ratio distributions for 60 deg angled ribbed duct: (*a*) two-layer model (k-ε); (*b*) second-moment model; and (*c*) Ekkad and Han [1].

was down to about 10 percent–30 percent. The degree of the anisotropy ($\overline{ww}/\overline{uu}$ or $\overline{ww}/\overline{vv}$) in the second passage was about $1\sim2$.

Surface Heat Transfer. Figure 9 shows the Nusselt number ratio contour plots on the bottom surfaces in a two-pass smooth channel at Re=30,000. The entrance and exit regions were cut off to focus on the bend effect. As the flow approached the 180 deg turn, the Nusselt number ratio reached the fully developed flow Nusselt number (Nu_o) for a smooth circular tube. In the bend, the turn effect was attributed to the secondary flows induced by the centrifugal forces. Thus, high heat transfer was observed near the outer surface in the bend due to the flow impingement. As the flow entered the second passage, another flow impingement was observed near the outer surface caused by the centrifugal force created by the 180 deg sharp turn. Farther downstream in the second passage, the Nusselt number ratios decreased as the effect of the turn reduced. Two-layer calculations predicted well the heat transfer behavior in the first passage, while it underpredicted the Nusselt number ratio in the bend and second passage. Whereas, the second-moment calculation results were in good agreement with the Ekkad and Han [1] data. Figure 10 shows the detailed Nusselt number ratio distributions in a two-pass channel with 60 deg parallel ribs. The highest Nusselt number ratios were obtained on the top of ribs in both passages of the channel. Heat transfer distribution between the ribs in the first passage was periodic in Ekkad and Han [1]. However, the calculation results did not show the periodic Nusselt number distributions in the first passage. The reason was that the flow in the passage with 60 deg parallel ribs arrangement required at least eight ribs to achieve a fully developed flow conditions because the angled rib-induced secondary flow was developed and became stronger along the channel, as indicated by Han and Park [2]. For this reason, the heat transfer results, even for the second-moment calculations showed slightly lower values and the reattachment point between the ribs was a little farther away from the ribs compared to Ekkad and Han [1] data. In the second passage, the Nusselt number ratios were higher near the outer surface and decreased toward the inner surface.

Figure 11 presents an enlarged view of the detailed Nusselt number ratio distributions on all four surfaces around ribs 1, 2, and 3 in the first passage and ribs 7, 8, and 9 in the second passage in a two-pass channel with 60 deg parallel ribs. The highest heat transfer coefficients in the first passage took place on the front side of the rib due to flow impingement (Fig. 11(*a*)). It can be clearly seen that there was a flow separation and reattachment on the top of the rib (Fig. 11(*a*)). In the regions between the ribs, the heat transfer was higher next to the inner surface because the flow reattachment took place there, so that the thermal boundary layer was thinner (Fig. 11(*a*)). Due to the rib-induced secondary flow characteristics of this configuration, the heat transfer decreased diagonally downstream of the rib leading edge to upstream of the next rib trailing edge. Another high heat transfer spot was seen on the outer surface next to the bottom surface, which was caused by the impingement of secondary flow (Fig. 5(*a*)-1). Heat transfer on the top surface was lower than the inner and outer surface (Fig. 11(*b*)).

In the second passage, due to the centrifugal force in the bend, the Nusselt number ratio increased over all four surfaces. The Nusselt number ratios on the inner and bottom surfaces are higher than that of the first passage due to the strong flow impingement and reattachment. High heat transfer was observed even on the top surface caused by flow impingement due to the turn effect.

Spanwise-Averaged and Regional-Averaged Heat Transfer Distribution. The spanwise average Nusselt number ratios on the bottom surfaces for a two-pass smooth channel is shown in Fig. 12(*a*). Comparisons were made between the calculations and the experimental data of Ekkad and Han [1]. The numerical results obtained from both the second-moment closure model and the two-layer eddy viscosity models were presented to facilitate a detailed assessment of the effect of the Reynolds stress anisotropy. In the first passage, the heat transfer coefficient decreased and approached the fully developed value. The heat transfer in the bend and the second passage was high because of the secondary flows induced by the centrifugal force in the bend. Figure 12(*b*) shows the spanwise average and regional average Nusselt number ratios on the bottom surface (ribbed surface) for a two-pass channel with 60 deg parallel ribs. The Ekkad and Han [1] regional-averaged data were also plotted for comparisons. The spanwise-averaged Nusselt number distributions on the ribbed surface show the periodic spikes, where the higher ones were caused by the flow impingement on the ribs and the smaller ones were caused by the flow reattachment between the ribs. The Nusselt number ratios were low immediately upstream and downstream of the ribs. In the bend and second passage, the Nusselt number ratios increased due to the turning effect.

The predicted Nusselt number ratios by the second-moment closure model were close to the Ekkad and Han [1] data. As a conclusion from Figures 9, 10, and 12, the heat transfer prediction by a two-layer model was good just for the first passage in a smooth channel. However, the two-layer model failed to capture the steep increases of the heat transfer in the bend and second passage for the smooth channel, and in the ribbed channel. On the other hand, the near-wall second-moment solutions were in considerably better agreement with the experimental data for both cases. Since both the two-layer and second-moment calculations were performed using the same numerical method and grids, the

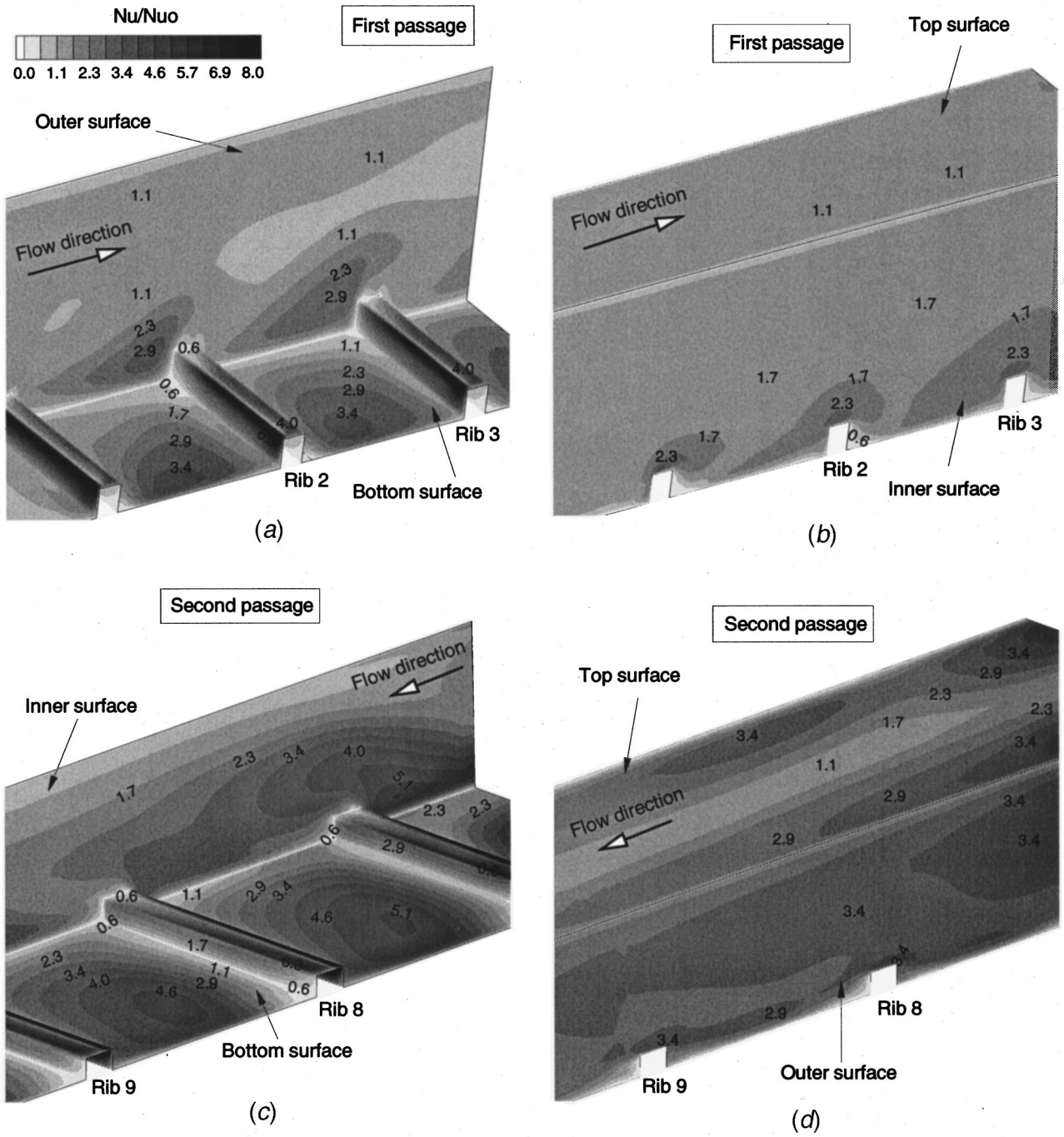

Fig. 11 Enlarged view of detailed Nusselt number ratio distributions for 60 deg angled ribbed duct

improved prediction could clearly be attributed to the inclusion of the Reynolds stress anisotropy in the present second-order Reynolds stress closure model.

Conclusions

Numerical prediction of flow and heat transfer are presented for a two-pass square channel with a 60 deg angled ribbed wall. The method solved Reynolds-Averaged Navier-Stokes equations in conjunction with a near-wall second-order Reynolds stress closure model for accurate resolution of the turbulent flow and thermal fields produced by angled ribs and 180 deg sharp turn. Calculations were also performed using a two-layer isotropic eddy viscosity model to facilitate a detailed assessment of the second-order effects due to the Reynolds stress anisotropy.

The obtained numerical results clearly demonstrate the superiority of the present second-order Reynolds stress closure models over simpler isotropic eddy viscosity models. In general, the second-moment solutions exhibit a significant level of anisotropy in the normal components of a Reynolds stress tensor. For the ribbed two-pass square channels considered here, the angled ribs with a high blockage ratio and a 180 deg sharp turn produced strong non-isotropic turbulence that significantly influence the development of momentum and thermal boundary layers along the duct. Specially, in the bend, the higher level of anisotropy of Reynolds stresses occurred in all of the regions which rendered

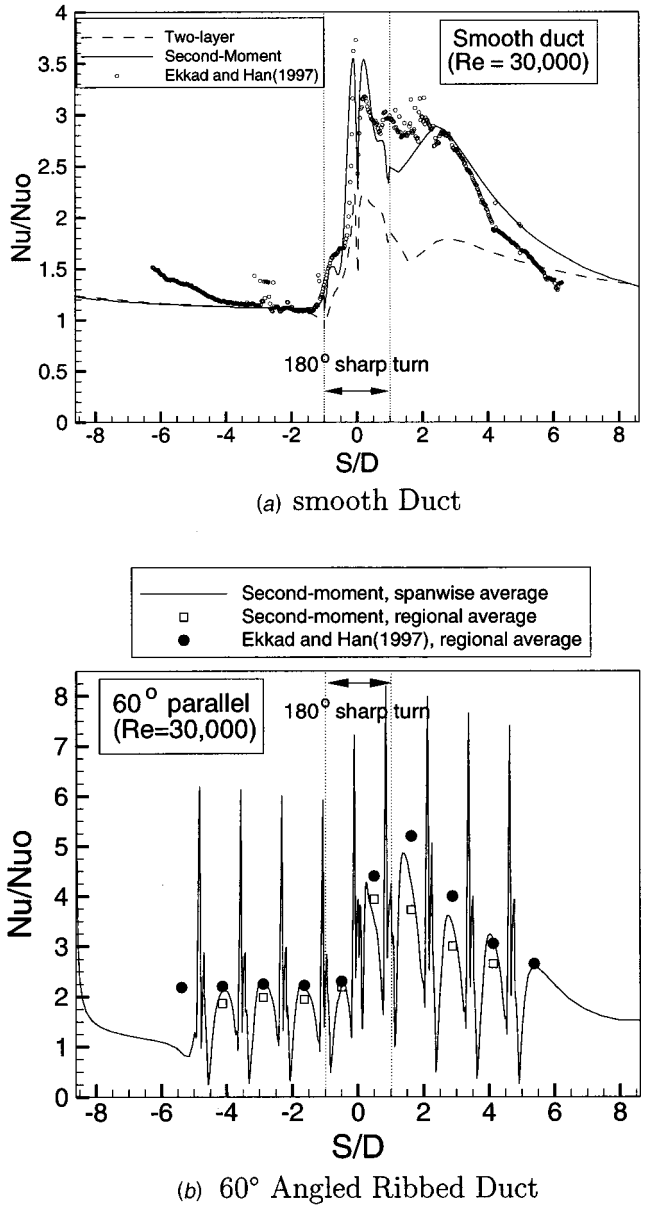

Fig. 12 Calculated and measured Nusselt number ratios: (*a*) smooth duct; and (*b*) 60 deg angled ribbed duct.

the isotropic eddy viscosity model failed to predict the complex flow behaviors. Therefore, it is important to employ second-moment closure models that solve each individual Reynolds stress component directly from their respective transport equations. The present near-wall second-moment closure model accurately predicts the complex three-dimensional flow and heat transfer characteristics resulting from the angled ribs and strong wall curvatures. It provides the most reliable numerical predictions, which are in good agreement with the experimental data of Ekkad and Han [1].

Acknowledgments

This work was supported by the Texas Higher Education Coordinating Board-Advanced Technology Program under grant number 999903-165. The computations were performed on the Cray J90 at the Texas A&M Supercomputer Center under a supercomputer research grant, and the Cray C90 at Cray Research Inc. in Eagen, Minnesota under the sponsorship of Frank Kampe. Their support is greatly appreciated.

Nomenclature

d = divider wall thickness
D_h, D = hydraulic diameter
e = rib height
P = rib pitch
H = heat transfer coefficient
K = thermal conductivity of coolant
L = length of the duct
L_1 = length from the inlet to the first rib
L_2 = length from the last rib in the first passage to the outer surface in the bend
L_3 = length from the divider wall tip to the outer surface in the bend
Nu = local Nusselt number, hD_h/K
Nu_o = Nusselt number in fully-developed turbulent non-rotating tube flow
Pr = Prandtl number
Re = Reynolds number, $\rho W_b D_h/\mu$
S = streamwise distance
T = local coolant temperature
T_o = coolant temperature at inlet
T_w = wall temperature
W_b = bulk velocity in streamwise direction
α = rib angle
ρ = density of coolant
$\Delta\rho/\rho$ = coolant-to-wall density ratio, $(T_w - T_o)/T_w$
θ = dimensionless temperature, $(T - T_o)/(T_w - T_o)$
μ = dynamic viscosity of coolant

References

[1] Ekkad, S. V., and Han, J. C., 1997, ''Detailed Heat Transfer Distributions in Two-Pass Square Channels with Rib Turbulators,'' Int. J. Heat Mass Transf., **40**, No. 11, pp. 2525–2537.
[2] Han, J. C., and Park, J. S., 1988, ''Developing Heat Transfer in Rectangular Channel with Rib Turbulators,'' Int. J. Heat Mass Transf., **31**, No. 1, pp. 183–195.
[3] Bonhoff, B., Parneix, S., Leusch, J., Johnson, B. V., Schabacker, J., and Bolcs, A., 1999, ''Experimental and Numerical Study of Developed Flow and Heat Transfer in Coolant Channels with 45deg Ribs,'' Int. J. Heat Fluid Flow, **20**, pp. 311–319.
[4] Schabacker, J., Boelcs, A., and Johnson, B. V., 1999, ''PIV Investigation of the Flow Characteristics in an Internal Coolant Passage with 45deg Rib Arrangement,'' ASME Paper 99-GT-120.
[5] Tse, D. G. N., and Steuber G. D., 1997, ''Flow in a Rotating Square Serpentine Coolant Passage with Skewed Trips,'' ASME Paper 97-GT-529.
[6] Wagner, J. H., Johnson, B. V., Graziani, R. A., and Yeh, F. C., 1992, ''Heat Transfer in Rotating Serpentine Passages with Trips Normal to the Flow,'' ASME J. Turbomach., **114**, pp. 847–857.
[7] Johnson, B. V., Wagner, J. H., Steuber, G. D., and Yeh, F. C., 1994, ''Heat Transfer in Rotating serpentine Passage with Trips Skewed to the Flow,'' ASME J. Turbomach., **116**, pp. 113–123.
[8] Prakash, C., and Zerkle, R., 1995, ''Prediction of Turbulent Flow and Heat Transfer in a Ribbed Rectangular Duct With and Without Rotation,'' ASME J. Turbomach., **177**, pp. 255–264.
[9] Stephens, M. A., Shih, T. I-P., and Civinskas, K. C., 1995, ''Computation of Flow Heat Transfer in a Rectangular Channel with Ribs,'' AIAA Paper 95-0180.
[10] Rigby, D. L., Steinthorsson, E., and Ameri, A. A., 1997, ''Numerical Prediction of Heat Transfer in a Channel with Ribs and Bleed,'' ASME Paper 97-GT-431.
[11] Stephens, M. A., Chyu, M. K., and Shih, T. I-P., 1996, ''Computation of Convective Heat Transfer in a Square Duct with Inclined Ribs of Rounded Cross Section,'' ASME Paper 96-WA/HT-12.
[12] Iacovides, H., 1998, ''Computation of Flow and Heat Transfer Through Rotating Ribbed Passage,'' Int. J. Heat Fluid Flow, **19**, pp. 393–400.
[13] Bonhoff, B., Tomm, U., Johnson, B. V., and Jennions, I., 1997, ''Heat Transfer Predictions for Rotating *U*-Shaped Coolant Channels with Skewed Ribs and With Smooth Walls,'' ASME Paper 97-GT-162.
[14] Rigby, D. L., 1998, ''Prediction of Heat Mass Transfer in a Rotating Ribbed Coolant Passage with a 180 Degree Turn,'' ASME Paper 98-GT-329.

[15] Iacovides, H., and Raisee, M., 1999, ''Recent Progress in the Computation of Flow and Heat Transfer in Internal Cooling passages of Turbine Blades,'' Int. J. Heat Fluid Flow, **20**, pp. 320–328.
[16] Chen, H. C., Jang, Y. J., and Han, J. C., 2000, ''Computation of Heat Transfer in Rotating Two-Pass Square Channels by a Second-Moment Closure Model,'' Int. J. Heat Mass Transf., **43**, pp. 1603–1616.
[17] Chen, H. C., Jang, Y. J., and Han, J. C., 2000, ''Near-Wall Second-Moment Closure for Rotating Multiple-Pass Cooling Channels,'' J. Thermophys. Heat Transfer, **14**, No. 2, pp. 201–209.
[18] Chen, H. C., 1995, ''Assessment of a Reynolds Stress Closure Model for Appendage-Hull Junction Flows,'' ASME J. Fluids Eng., **117**, No. 4, pp. 557–563.
[19] Chen, H. C., 1995, ''Submarine Flows Studied by Second-Moment Closure,'' J. Eng. Mech., **121**, No. 10, pp. 1136–1146.
[20] Chen, H. C., and Chen, M., 1998, ''Chimera RANS Simulation of a Berthing DDG-51 Ship in Translation and Rotational Motions,'' Int. J. Offshore Polar Eng., **8**, No. 3, pp. 182–191.
[21] Chen, H. C., Patel, V. C., and Ju, S., 1990, ''Solutions of Reynolds-Averaged Navier-Stokes Equations for Three-Dimensional Incompressible Flows,'' J. Comput. Phys., **88**, No. 2, pp. 305–336.
[22] Chen, H. C. and Patel, V. C., 1989, ''The Flow Around Wing-Body Junctions,'' Proceedings of the 4th Symposium on Numerical and Physical Aspects of Aerodynamic Flows, Long Beach, CA.
[23] Chen, H. C., and Korpus, R., 1993, ''Multi-Block Finite-Analytic Reynolds-Averaged Navier-Stokes Method for 3D Incompressible Flows,'' ASME Fluids Engineering Conference, FED-Vol. 150, pp. 113–121.
[24] Hubbard, B. J., and Chen, H. C., 1994, ''A Chimera Scheme for Incompressible Viscous Flows with Applications to Submarine Hydrodynamics,'' AIAA Paper 94-2210, 25th AIAA Fluid Dynamics Conference, Colorado Springs, CO.
[25] Chen, H. C., and Liu, T., 1999, ''Turbulent Flow Induced by a Full-Scale Ship in Harbor,'' J. Eng. Mech., **125**, No. 7, pp. 827–835.
[26] Kays, W. M., and Crawford, M. E., 1993, *Convective Heat and Mass Transfer*, Third edition, McGraw Hill, New York.
[27] Steinbrenner, J. P., Chawner, J. R., and Fouts, C. L., 1990, ''The GRIDGEN 3D Multiple Block Grid Generation System,'' Vols. I & II, WRDC-TR-90-3022, Wright Patterson AFB, OH.
[28] Liou, T. M., Tzeng, Y. Y., and Chen, C. C., 1998, ''Fluid Flow in a 180deg Sharp Turning Duct With Different Divider Thicknesses,'' ASME Paper 98-GT-189.

Modeling Dynamic Electrical Resistance During Resistance Spot Welding

S. C. Wang
Graduate Student

P. S. Wei
Professor, Fellow ASME
e-mail: pswei@mail.nsysu.edu.tw

Department of Mechanical and Electro-Mechanical Engineering,
National Sun Yat-Sen University,
Kaohsiung, Taiwan
Republic of China

Dynamic electrical resistance during resistance spot welding has been quantitatively modeled and analyzed in this work. A determination of dynamic resistance is necessary for predicting the transport processes and monitoring the weld quality during resistance spot welding. In this study, dynamic resistance is obtained by taking the sum of temperature-dependent bulk resistance of the workpieces and contact resistances at the faying surface and electrode-workpiece interface within an effective area corresponding to the electrode tip where welding current primarily flows. A contact resistance is composed of constriction and film resistances, which are functions of hardness, temperature, electrode force, and surface conditions. The temperature is determined from the previous study in predicting unsteady, axisymmetric mass, momentum, heat, species transport, and magnetic field intensity with a mushy-zone phase change in workpieces, and temperature and magnetic fields in the electrodes of different geometries. The predicted nugget thickness and dynamic resistance versus time show quite good agreement with available experimental data. Excluding expulsion, the dynamic resistance curve can be divided into four stages. A rapid decrease of dynamic resistance in stage 1 is attributed to decreases in contact resistances at the faying surface and electrode-workpiece interface. In stage 2, the increase in dynamic resistance results from the primary increase of bulk resistance in the workpieces and an increase of the sum of contact resistances at the faying surface and electrode-workpiece interface. Dynamic resistance in stage 3 decreases, because increasing rate of bulk resistance in the workpieces and contact resistances decrease. In stage 4 the decrease of dynamic resistance is mainly due to the formation of the molten nugget at the faying surface. The molten nugget is found to occur in stage 4 rather than stage 2 or 3 as qualitatively proposed in the literature. The effects of different parameters on the dynamic resistance curve are also presented. [DOI: 10.1115/1.1370502]

Keywords: Contact Resistance, Electric Fields, Heat Transfer, Manufacturing

Introduction

Resistance spot welding has been widely used in joining thin workpieces due to its light weight and easy manufacturing. Water-cooled copper electrodes apply a load to squeeze the workpieces. In addition to produce an intimate contact between workpieces to allow the current to flow, the electrode force also serves to break up any surface oxides or films on the faying surface. A voltage is applied across the ends of electrodes. In view of the induced current flow, electrical contact resistance at the faying surface results in the greatest heat generation and temperature near the interface. Melting begins either in the center of the contact patch at the faying surface or near the periphery between the electrode and workpiece. The molten nugget grows until current flow is terminated. The electrode force continues to be applied until cooling has been finished.

Evidently, electrical resistance is the most important factor affecting resistance spot welding. A rigorous study of electrical resistance is necessary not only for an understanding but also for a monitoring of the process to obtain good weld quality [1,2]. Aside from studying static electrical resistance affected by different electrode forces and workpieces in different thicknesses, Roberts [3] experimentally found that dynamic resistance cannot be considered as a constant during resistance spot welding. The dynamic resistance was equal to the sum of the bulk resistance of the two workpieces, and contact resistances at the faying surface and two electrode-workpiece interfaces. An initial drop of dynamic resistance was attributed to the rupture of the surface film. After the initial breakdown of contact resistance, the resistance increased slightly with time in welding aluminum using cleaned electrode tips, while the resistance tended to decrease in welding stainless steel and aluminum with contaminated electrodes. Dynamic resistance curves for welding low-carbon steel showed an increase and subsequent decrease after the breakdown of contact resistance. The rise in dynamic resistance after the breakdown of contact resistance was proposed to be due to the heating of the workpiece, and the subsequent fall after the maximum resistance has been reached may be attributed to two causes; the growth of the nugget diameter and the increasing penetration of the electrodes into the workpiece. Both produced increasing current carrying areas. At a given instant, the greater the welding current, the lower the resistance.

Bhattacharya and Andrews [4] obtained the similar dynamic resistance curve to monitor the quality of spot welds in mild steel, stainless steel and aluminum. In general, a contact resistance must experience (*a*) fritting or electrical breakdown of contact insulation, (*b*) softening, and (*c*) melting. In welding mild steel, the initial steep fall was followed by a trough and a distinct peak. Neither aluminum nor stainless steel showed this peak. Dynamic resistance can be divided into three stages. The decrease of dynamic resistance in Region I was due to the breakdown of contact insulation or fritting; in Region II the increase of dynamic resistance was attributed to the temperature coefficient of constriction resistance [5,6]; the diminishing dynamic resistance in Region III resulted from the growth of fused metallic bond. They proposed a detailed interpretation by using concepts of softening and melting voltages. In contrast to stainless steel and aluminum alloy and

Contributed by the Heat Transfer Division for publication in the JOURNAL OF HEAT TRANSFER. Manuscript received by the Heat Transfer Division May 10, 2000; revision received November 28, 2000. Associate Editor: F. Cheung.

many other materials, the dynamic resistance curve for mild steel permitted correlation with nugget growth and offered a means of monitoring weld quality.

Savage et al. [7] extensively measured dynamic resistance curves for different welding currents, electrode forces, and material combinations of uncoated and galvanized auto-body steels with degreased or pickled surface conditions. The shape of the dynamic resistance curve differed markedly with the surface conditions and different material combinations. The typical dynamic resistance curves of steel-to-steel welds made from as-received stock agreed with the curves presented by Roberts [3]. Expulsion was found to occur for high welding current and time. If the nugget grows to a size such that it can no longer be contained by the surrounding solid metal under the compressive electrode force, expulsion will occur. The dynamic resistance curve of the plain carbon AK material interpreted by Dickinson et al. [8] can also be divided into five stages. Stage I reflects the breakdown of insulating layers or fritting. The contacts then become workpiece-workpiece contacts. In Stage II, contact resistance at the faying surface decreases due to the competition between the softening of contact spots and increases of bulk resistances in the surface film and workpieces with temperature. The increase of dynamic resistance in Stage III results from an increase of resistivity with temperature. The end of this stage corresponds to the local melting beginning to occur at the contact spots. Dynamic resistance in Stage IV results from a competition between the increased resistivity of bulk workpieces and decreased contact resistance at the faying surface from additional melting and softening. Stage V shows that contact resistance at the faying surface decreases due to the growth of the molten nugget and mechanical collapse. Variables including current level, electrode force, and material being welded can cause significant variations in the shape of the dynamic resistance curve.

Dynamic resistance is usually calculated by dividing the weld voltage by current. Most investigations measured the dynamic impedance rather than resistance, because a phase shift existed between voltage and current. At a small phase shift which is a function of resistance of the load and inductance, the impedance and resistance are nearly equivalent. To avoid the error induced by inductance, only one data point of dynamic resistance is available per half cycle. Applying a method to reduce the discrepancy, Gedeon and Eagar [9] and Gedeon et al. [10] found that the generalized dynamic resistance curve can be divided into four, six or eight stages depending on if the steels were uncoated, galvannealed, or hot-dipped. Weld quality thus can be more successfully monitored by using multiple sensors simultaneously measuring dynamic resistance, voltage, current, and electrode displacement.

A number of experimental studies have been carried out to quantify electrical contact resistance of sheet steels [11–14]. The contact resistance was found to decrease both with electrode force and temperature. It has been unclear if the contact resistance at the faying surface was greater than that at the electrode-workpiece interface, as discussed by Vogler and Sheppard [15]. Contact resistances at the faying surface and electrode-workpiece interface in welding aluminum alloys can cover a very wide range in magnitude as measured by Thornton et al. [16]. The decrease in contact resistance which usually occurs with an increase in electrode force may not occur with aluminum alloys. James et al. [17] measured contact resistances at the faying surface and electrode-workpiece interface in welding pre-treated and abraded aluminum alloy strip with different geometries of electrodes. With conventional domed electrodes, the contact resistance was much larger at the faying surface than that at the electrode-workpiece interface. When the coating was removed the difference between the faying surface and electrode-workpiece interface became much smaller.

Evidently, a quantitative and theoretical interpretation of the complicated dynamic resistance curve is needed to clarify the observed results. Holm [18] first pointed out that a constriction resistance will arise when current flows from one conductor of infinite extent to another through a finite area of perfect electrical contact. For a clean metal contact the contact resistance is simply a constriction resistance. If a film is present, the contact resistance consists of the constriction and film resistance. Greenwood [19] derived a general equation to find the constriction resistance of a cluster of contact spots. It was shown that the resistance may be regarded as the sum of the parallel resistance of contact spots. Although the theoretical analysis has been provided for a long time, a rigorous determination associated with experimental validification during resistance spot welding has not been found yet. This becomes the objective in this work.

In this study, a model including constriction and film resistances to determine dynamic resistance affected by hardness, temperature, electrode force, and surface conditions during resistance spot welding is proposed. The effects of rupture, softening, heating and melting of surface films at the faying surface and electrode-workpiece interface, as well as the heating and melting of bulk workpieces on dynamic resistance are accounted. The predicted results with the temperature obtained from the previous study [6] are compared with available experimental data. The significance and mechanism of dynamic resistance together with bulk and contact resistances therefore are revealed.

System Model and Analysis

Resistance spot welding is accomplished by the heat generated from temperature-dependent electrical contact resistance at the faying surface. Temperatures are obtained by solving axisymmetric, unsteady equations of mass, momentum, energy, species, and magnetic field intensity in the workpieces and electrodes [6]. Modeling electrical contact resistance is described as follows:

Electrical Contact Resistance. A local electrical contact resistance at the faying surface or electrode-workpiece interface can be simulated by

$$\tilde{R}_c = \frac{1}{2a\tilde{\sigma}} + \frac{\tilde{s}}{\pi a^2 \tilde{\sigma}_f}, \tag{1}$$

where the first and last terms on the right-hand side represent constriction and film resistances, respectively [18]. Each contact spot is considered as a circle with an effective radius

$$a = \sqrt{\frac{W}{\pi n \tilde{H}_v}}, \tag{2}$$

which shows that the size of a contact spot is a function of electrode force, hardness, and the total number of contact spots [18,19,20]. Temperature-dependent hardness indicates that contact area increases with time. In view of temperature-dependent electrical properties and hardness, the model presented by Eqs. (1) and (2) involves transient coupling between thermal-mechanical effects. In this work, the distribution of contact spots is considered to be uniform and the number of contact spots remains the same during the welding process. Considering a load $W=3000$ N, hardness $\tilde{H}_v = 5\times10^9$ N/m^2 and choosing the number of contact spots $n_1 = 10$ implying the total number of contact spots $n = 14940$, Eq. (2) leads to an effective radius $a = 3.6\times10^{-6}$ m as a reasonable comparison to the electrode radius of $r_o = 3.05\times10^{-3}$ m. Substituting Eq. (2) into Eq. (1), local contact resistance in a dimensionless form becomes

$$R_c = R_1 \frac{\sqrt{nH_v}}{\sigma} + R_2 \frac{snH_v}{\sigma_f}, \tag{3}$$

where dimensionless parameters governing constriction and film resistances are, respectively, defined as

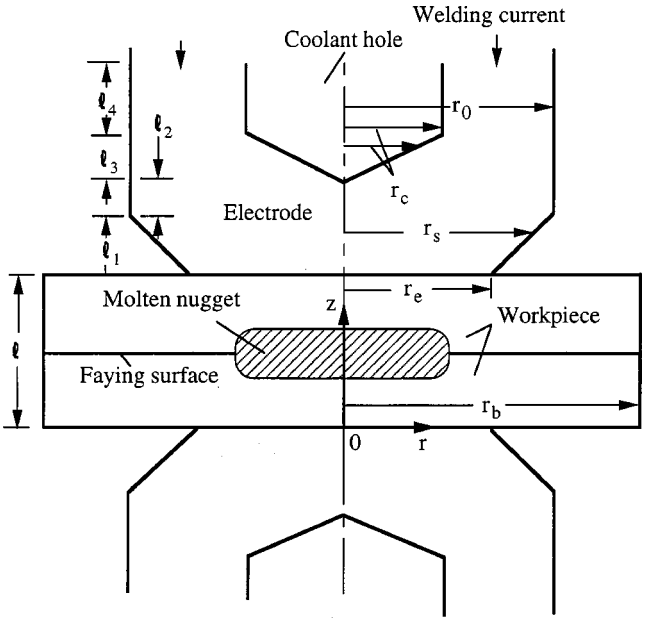

Fig. 1 Sketch for resistance spot welding and coordinate system

$$R_1 \equiv \frac{1}{2\tilde{R}_0\tilde{\sigma}_{\text{liq}}}\sqrt{\frac{\pi\tilde{H}_{v0}}{W}}, \quad R_2 \equiv \frac{r_0\tilde{H}_{v0}}{W\tilde{R}_0\tilde{\sigma}_{\text{liq}}}. \tag{4}$$

In Eq. (3) temperature-dependent electrical conductivities of workpieces and surface film and hardness can be found by curve-fitting experimental data provided by Ono et al. [21], Boyer and Gall [22], Touloukian [23], and Grange et al. [24], respectively. A local equivalent contact electrical conductivity related to contact resistance from Eq. (3) yields

$$\sigma_c = \frac{E_f}{E^* R_c A_c}, \tag{5}$$

where A_c is a local area through which electric current flows.

Numerical Simulation. Resistance spot welding is analyzed by setting a cylindrical coordinate system with the origin on the intersection of the axisymmetric axis and bottom electrode-workpiece interface, as illustrated in Fig. 1. Except for proposing more relevant and accurate electrical resistances to replace film resistance decreasing linearly with increasing temperature [25–28], the major assumptions made are the same as those proposed by Wei et al. [6]. They are that the mushy zone is a porous medium in a local thermal and phase equilibrium. Mean values of properties within the temperature range considered are chosen and allowed to be distinct between phases. Solid solutal diffusion is neglected.

Governing Equations and Boundary Conditions in Workpieces. With the above assumptions, the dimensionless continuity, momentum, energy, species, magnetic field intensity equations [6,29,30], respectively, become

$$\frac{\partial\rho}{\partial\tau} + \nabla.(\rho\mathbf{V}_m) = 0 \tag{6}$$

$$\frac{\partial\rho u_m}{\partial\tau} + \nabla.(\rho\mathbf{V}_m u_m) = \text{Pr}\nabla.(\rho\nabla u_m) - \frac{\text{Pr}}{\text{Da}}\frac{\rho(1-g_l)^2}{g_l^3}u_m - \frac{\partial p}{\partial z} + \text{Pr}^2\text{Gr}[\theta_0(T-T_{\text{sol}}) + F_0(f_l^\alpha - f_{l,T_{\text{sol}}}^\alpha)] - \frac{\text{Lo}}{\pi^2}\mu_r H\frac{\partial H}{\partial z} \tag{7}$$

$$\frac{\partial\rho v_m}{\partial\tau} + \nabla.(\rho\mathbf{V}_m v_m) = \text{Pr}\nabla.(\rho\nabla v_m) - \frac{\text{Pr}}{\text{Da}}\frac{\rho(1-g_l)^2}{g_l^3}v_m - \frac{\partial p}{\partial r} - \frac{\text{Lo}}{\pi^2}\frac{\mu_r}{r}H\frac{\partial}{\partial r}(rH) \tag{8}$$

$$\frac{\partial\rho h_m}{\partial\tau} + \nabla.(\rho\mathbf{V}_m h_m) = C\nabla.(K\nabla h_m) + C\nabla.[K\nabla(h_s - h_m)] - \nabla.[\rho(h_l - h_m)\mathbf{V}_m] + \frac{\text{Lo}\Sigma}{\pi^2}\left(\frac{1}{\sigma_c} + \frac{1}{\sigma}\right) \times \left[\left(\frac{1}{r}\frac{\partial rH}{\partial r}\right)^2 + \left(\frac{\partial H}{\partial z}\right)^2\right] \tag{9}$$

$$\frac{\partial\rho f_m^\alpha}{\partial\tau} + \nabla.(\rho\mathbf{V}_m f_m^\alpha) = \frac{\text{Pr}}{\text{Sc}}\nabla.(\rho f_l\nabla f_m^\alpha) + \frac{\text{Pr}}{\text{Sc}}\nabla.[\rho f_l\nabla(f_l^\alpha - f_m^\alpha)] - \nabla.[\rho(f_l^\alpha - f_m^\alpha)\mathbf{V}_m] \tag{10}$$

$$\frac{\partial\mu_r H}{\partial\tau} + \nabla.(\mu_r\mathbf{V}_m H) = \text{Pr}_m\nabla.\left(\frac{1}{\sigma}\nabla H\right) + \text{Pr}_m\left[\frac{H}{r}\frac{\partial}{\partial r}\left(\frac{1}{\sigma}\right) - \frac{H}{\sigma r^2}\right] + \frac{\mu_r v_m H}{r}, \tag{11}$$

where dimensionless parameters are defined as

$$\text{Pr} = \frac{\tilde{\nu}_l}{\tilde{\alpha}_l}, \quad \text{Da} = \frac{K_0}{r_0^2}, \quad \text{Gr} = \frac{g\beta_T(\tilde{T}_{\text{sol}} - \tilde{T}_e)r_0^3}{\tilde{\nu}_l^2},$$
$$\theta_0 = \frac{\tilde{T}_0}{\tilde{T}_{\text{sol}} - \tilde{T}_e}, \quad F_0 = \frac{\beta_s\hat{f}_{m,0}^\alpha}{\beta_T(\tilde{T}_{\text{sol}} - \tilde{T}_e)}, \tag{12}$$
$$\text{Lo} = \frac{I^2\mu_0\mu_{rl}}{\tilde{\rho}_l\tilde{\alpha}_l^2}, \quad C = \frac{\tilde{c}_l}{\tilde{c}_s}, \quad \Sigma = \frac{\tilde{\alpha}_l\tilde{\eta}_l}{r_0^2 h_f}, \quad \text{Sc} = \frac{\tilde{\nu}_l}{D_l^\alpha}.$$

All the lengths in Eqs. (6)–(11) are nondimensionalized by the maximum radius of the electrode r_0. The last term on the right-hand side of Eq. (9) combines heat generation at contact surfaces and in bulk workpieces. Boundary conditions are the same as the previous work [6] and described briefly as follow:

(a) The Electrode-Workpiece Interface, $z=0$, $\boldsymbol{l}$, $0 \leqslant r \leqslant r_e$. Boundary conditions are

$$u_m = v_m = \frac{\partial f_m^\alpha}{\partial z} = 0 \tag{13}$$

$$K\frac{\partial T}{\partial z} = k_s k_E\frac{\partial T_E}{\partial z} \mp \frac{\text{Lo}E_f\Sigma}{\pi^2 RC\sigma_{cE}}\left[\left(\frac{1}{r}\frac{\partial rH}{\partial r}\right)^2 + \left(\frac{\partial H}{\partial z}\right)^2\right] \tag{14}$$

$$\pm K\frac{\partial T}{\partial z} = k_s\,\text{Bi}_E(T - T_E) \tag{15}$$

$$\frac{\sigma_E}{\sigma}\frac{\partial H}{\partial z} = \frac{\partial H_E}{\partial z} \tag{16}$$

$$H = H_E, \tag{17}$$

where Eq. (13) allows for the molten region possibly occurring on the interface. The last term on the right-hand side of Eq. (14)

represents the heat generated due to contact resistance. Eq. (15) reflects a discontinuity of temperatures across the interface. Continuities of tangential electric and magnetic field intensities across the interface are governed by Eqs. (16) and (17), respectively [31,32].

(b) The Surfaces Between Workpieces and Surroundings, $z=0$, l, $r_e<r\leqslant r_b$.

$$u_m=\frac{\partial v_m}{\partial z}=\frac{\partial f_m^\alpha}{\partial z}=0 \tag{18}$$

$$\pm K\frac{\partial T}{\partial z}=\mathrm{Bi}_0 k_s(T-1) \tag{19}$$

$$H=-\frac{1}{2r} \tag{20}$$

Eq. (18) also accounts for the molten region possibly occurring near the surfaces between workpieces and surroundings. Eq. (20) is a result of negligible electric current escaped to the surroundings.

(c) The Workpiece Surface $0\leqslant z\leqslant l$, $r=r_b$.

$$u_m=v_m=0,\quad f_m^\alpha=1,\quad H=-\frac{1}{2r_b} \tag{21}$$

$$-K\frac{\partial T}{\partial r}=k_s\mathrm{Bi}_0(T-1) \tag{22}$$

(d) The Axisymmetric Axis, $0\leqslant z\leqslant l$, $r=0$.

$$\frac{\partial}{\partial r}(u_m,v_m,h_m,f_m^\alpha)=0,\quad H=0 \tag{23}$$

Magnetic field intensity must vanish at the axisymmetric axis to avoid infinite electric currents.

Supplementary Relationships. In Eq. (10) the fraction of solute α in the solid or liquid is found by

$$f_s^\alpha=\frac{k_p f_m^\alpha}{1+f_s(k_p-1)},\quad f_l^\alpha=\frac{f_m^\alpha}{1+f_s(k_p-1)} \tag{24}$$

where equilibrium partition coefficient k_p represents the ratio of solute contents in the solid and liquid at the same temperature. Determinations of distinct regions of the mushy zone, full liquid and solid have been presented in details by Bennon and Incropera [29,30].

Governing Equations and Boundary Conditions in Electrode. Since the electrode is irregular in shape, an immobilization transformation can be effectively used for facilitating numerical computation. Energy and magnetic field intensity equations of the upper electrode, respectively, yield

$$\frac{\partial T_E}{\partial\tau}=\frac{k_E k_s RC}{\rho_E R_E}\left[\frac{\partial^2 T_E}{\partial\xi^2}+\left(\frac{1}{N^2}+M^2\right)\frac{\partial^2 T_E}{\partial\xi^2}+2M\frac{\partial^2 T_E}{\partial\xi\partial\zeta}+\left(\frac{1}{\xi N+r_c}-2M\frac{dN}{d\zeta}\right)\frac{1}{N}\frac{\partial T_E}{\partial\xi}\right]+\frac{\mathrm{Lo}\Sigma}{\pi^2\rho_E R_E\sigma_E}\times\left[\left(M\frac{\partial H_E}{\partial\xi}+\frac{\partial H_E}{\partial\zeta}\right)^2+\left(\frac{H_E}{\xi N+r_c}+\frac{1}{N}\frac{\partial H_E}{\partial\xi}\right)^2\right] \tag{25}$$

$$\frac{\partial H_E}{\partial\tau}=\mathrm{Pr}_m\eta_E\left[\frac{\partial^2 H_E}{\partial\xi^2}+\left(\frac{1}{N^2}+M^2\right)\frac{\partial^2 H_E}{\partial\xi^2}+2M\frac{\partial^2 H_E}{\partial\xi\partial\zeta}+\left(\frac{1}{\xi N+r_c}-2M\frac{dN}{d\zeta}\right)\frac{1}{N}\frac{\partial H_E}{\partial\xi}-\frac{H_E}{(\xi N+r_c)^2}\right]. \tag{26}$$

Independent variables in Eqs. (25) and (26) are chosen to be

$$\xi=\frac{r-r_c(z)}{r_s(z)-r_c(z)},\quad \zeta=z-l, \tag{27}$$

which implies $r_s=1$ for $\zeta\geqslant l_1$, $r_c=0$ for $0\leqslant\zeta\leqslant l_1+l_2$. Boundary conditions are as follows:

(a) The Top Surface of the Upper Electrode, $\zeta=l_1+l_2+l_3+l_4$, $0\leqslant\xi\leqslant 1$.

$$-\frac{\partial T_E}{\partial\zeta}=\mathrm{Bi}_{0E}(T_E-1) \tag{28}$$

$$H_E=\frac{-1}{2(1+r_c)}\frac{\xi^2(1-r_c)+2r_c\xi}{\xi(1-r_c)+r_c}, \tag{29}$$

where Eq. (29) is obtained by assuming uniform current across the top surface. Magnetic field intensity $H_E=0$ at $\xi=0$ is satisfied because of negligible currents in the coolant hole.

(b) Boundaries $l_1+l_2+l_3\leqslant\zeta\leqslant l_1+l_2+l_3+l_4$. At the inner and outer surfaces of the upper electrode boundary conditions yield

$$\frac{1}{N}\frac{\partial T_E}{\partial\xi}=\mathrm{Bi}_w(T_E-T_w),\quad H=0\quad\text{at}\quad\xi=0 \tag{30}$$

$$-\frac{1}{N}\frac{\partial T_E}{\partial\xi}=\mathrm{Bi}_{0E}(T_E-1),\quad H=-\frac{1}{2}\quad\text{at}\quad\xi=1 \tag{31}$$

(c) Boundaries $l_1+l_2\leqslant\zeta\leqslant l_1+l_2+l_3$. At the surface of the coolant hole energy balance yields

$$\frac{1}{N}\frac{\partial T_E}{\partial\xi}\cos\tan^{-1}\left(\frac{r_c}{l_3}\right)-\left(M\frac{\partial T_E}{\partial\xi}+\frac{\partial T_E}{\partial\zeta}\right)\sin\tan^{-1}\left(\frac{r_c}{l_3}\right)=\mathrm{Bi}_w(T_E-T_w),\qquad H=0\quad\text{at}\quad\xi=0, \tag{32}$$

where r_c is evaluated at $\zeta=l_1+l_2+l_3$. Boundary conditions at the outer surface of the electrode are the same as Eq. (31).

(d) The Boundary $l_1\leqslant\zeta\leqslant l_1+l_2$.

$$\frac{\partial T_E}{\partial\xi}=0,\quad H=0\quad\text{at}\quad\xi=0 \tag{33}$$

Other conditions are the same as Eq. (31).

(e) The Boundary $0\leqslant\zeta\leqslant l_1$.

$$-\frac{1}{N}\frac{\partial T_E}{\partial\xi}\cos\tan^{-1}\frac{1-r_e}{l_1}+\left(M\frac{\partial T_E}{\partial\xi}+\frac{\partial T_E}{\partial\zeta}\right)\sin\tan^{-1}\frac{1-r_e}{l_1}=\mathrm{Bi}_{0E}(T_E-1),\qquad H=-\frac{1}{2r_s}\quad\text{at}\quad\xi=1, \tag{34}$$

while other conditions are the same as Eq. (33).

Initial conditions are $u_m=v_m=H=H_E=0$, $f_m^\alpha=1$, $h_m=R$, $T_E=1$ at $t=0$.

Solution Methodology. Each of conservation Eqs. (6)–(11), (25), and (26) can be cast in the form

$$\frac{\partial\rho\phi}{\partial\tau}+\nabla.(\rho\mathbf{V}_m\phi)=\nabla.(\Gamma_\phi\nabla\phi)+S_\phi. \tag{35}$$

The control-volume, implicit finite-difference scheme with staggered grids [33] was used. A grid system 50×53 in workpieces and 27×72 in the electrode were selected. The axial direction is divided into uniform spaces while the spacing ratio in the radial direction is 0.95. A dimensionless uniform time step was 2×10^{-5}. A test of grid refinement is shown in Table 1. The maxi-

Table 1 Test of convergence

Time	Resistance		Relative error
	50x53	72x75	
0.001	4.4233	4.4348	0.26%
0.01	1.8777	1.8872	0.51%
0.05	2.5916	2.6050	0.52%
0.1	2.7848	2.7847	0.004%

mum deviation of the computed resistances by using grid systems of 50×53 and 72×75 is less than 1 percent. Solution procedure is described in the following paragraph.

Temperature and magnetic field intensity in the electrodes are determined from Eqs. (25) and (26) subject to boundary conditions (14)–(17), while the continuity, momentum, energy, species and magnetic field intensity transport governed by Eqs. (6)–(11) in the workpieces were solved by satisfying other boundary conditions. The convergence tolerances for global energy and velocity components and enthalpy, concentration, and magnetic intensity fields were 10^{-2} and 10^{-3}, respectively. Otherwise, equations for the electrode were solved again and the process was repeated. If solutions converged, temperature distributions were used to calculate resistances. Computations then proceeded to the next time. Number of iterations at each time were around 100. The global energy balance was that heat generation in the workpieces and electrodes should be equal to the total internal energy rise and heat convected to the electrodes, coolant hole, and surroundings. Considering 1500 time steps, the execution time by using an IBM RS6000 computer was about 4 hours.

Results and Discussion

In this study, the unsteady variation of electrical resistance during resistance spot welding is quantitatively determined by incorporating in the previous work [6] predicting axisymmetric unsteady mass, momentum, energy, species and magnetic field intensity transport in the workpieces and electrodes. Electrical resistivity of the insulating surface film on a contact surface is much greater than that of the workpieces. An increase of temperature results in electrical resistivity of the surface film to decrease while bulk resistivity of the workpieces to increase. Hardness decreases with increasing temperature. The size of a contact spot on the contact surface is a function of the electrode force, total number of contact spots, and hardness. Interactions between these factors affecting the change of electrical resistance during spot welding (see Eq. (3)) are therefore studied in the present work.

This model is confirmed from a good agreement with a measured relationship between nugget thickness and time provided by Gould [25] in welding AISI 1008, as shown in Fig. 2. In this case, solute concentration $\hat{f}^{\alpha}_{m,0}=0.32$ wt percent of Mn in a Fe-Mn alloy, total thickness of the two workpieces $l=0.715$, electrode tip radius $r_e=0.9$, dimensionless parameter governing welding current (or Lorentz force) $\mathrm{Lo}=6.17\times10^{8}$, and constriction and film resistance parameters $R_1=100$ and $R_2=50$. Temperature-dependent electrical conductivities and hardness are presented in Appendix. This work shows a better agreement with the experimental result than the one-dimensional prediction from Gould [25], and three-dimensional prediction from Wei et al. [6]. The former neglected heat transfer in the radial direction so that thicknesses of the nugget are overestimated. The latter assumed an inaccurate electrical resistance, where the film resistance decreases linearly with increasing temperature and bulk resistivity of the workpieces remains constant.

Figure 3 shows that the predicted dimensionless dynamic resistance curve agrees quite well with the experimental result from Savage et al. [7] in welding uncleaned steels by choosing work-

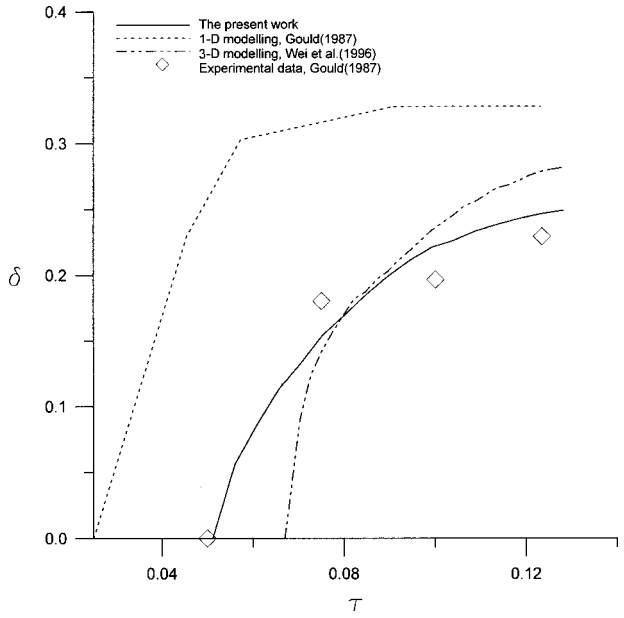

Fig. 2 Comparisons of dimensionless nugget thickness versus time in welding AISI 1008 steel between one and three-dimensional predictions from Gould [25], Wei et al. [6] and this work, and measurement from Gould [25]

piece thickness of 0.89 mm, the number of contact points $n_1=10$, and $r_0=2.78$ mm, $\mathrm{Lo}=4.67\times10^{8}$, $I=8700A$, $R_1=40$, and $R_2=30$. The trend of the dynamic resistance curve also agrees with that presented by, for example, Roberts [3], Bhattacharya and Andrews [4], and Dickinson et al. [8]. In this work, the dynamic resistance represents the total electrical resistance, which is the sum of bulk resistance in the workpieces, contact resistance at the faying surface and two times of contact resistance at the electrode-workpiece interface. After taking a sum of local resistances of grid points in series along the axial direction between the elec-

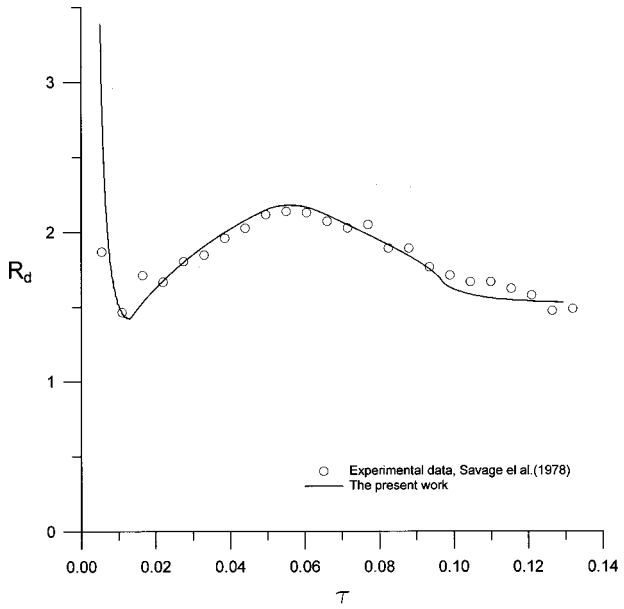

Fig. 3 A comparison of dimensionless dynamic resistance versus time between the measurement from Savage et al. [7] and prediction from this work in welding not cleaned steels with welding current of 8700 amps

Table 2 Typical values of dimensionless parameters

Biot numbers, Bi_{0E}, Bi_E, Bi_w	3.8×10^{-4}, 2.0, 3.0
Darcy number, Da	6.17×10^{-6}
Constriction resistance parameter, R_1	30.0
Film resistance parameter, R_2	30.0
Electrical contact resistance, E^*	0.56
Thickness of surface film, E_f	10^{-3}
Effective thickness of heat source at contact surface, s	3.28×10^{-7}
Electrode thermal conductivity, k_E	11.4
Solid-to-liquid thermal conductivity ratio, k_s	1.0
Parameter governing welding current, Lo	3×10^{7}
Lengths for electrode, ℓ_2, ℓ_3, ℓ_4	0.5, 0.5, 1
Slope parameter of liquidus and solidus lines, m_{liq} , m_{sol}	4.0, 3.0
Magnetic Prandtl number Pr_m	3×10^{4}
Maximum radius of coolant hole, r_c	0.5
Electrode enthalpy parameter, R_E	0.59
Curie temperature, T_c	3.5
Eutectic and melting temperatures, T_e , T_m	5.0, 6.0
Solid-to-liquid permeability ratio, μ_{rs} / $\mu_{r\ell}$	3500
Electrode density, ρ_E	1.28
Thermal-to-electrical property parameter, Σ	2.5×10^{-5}
Electrical conductivity ratios, σ_{sol} , σ_E	1.05, 6.5

trode tips for any given radius less than the electrode tip radius through which electric current primarily flows, the resulting resistances for all radii were added in parallel to give the total bulk resistance. The total contact resistance at the faying surface or electrode-workpiece interface was obtained by summing local contact resistances in parallel for all radii less than the electrode tip radius.

Typical values of dimensionless parameters estimated from pure iron and manganese and its alloy are listed in Table 2. The variations of dimensionless bulk resistance in workpieces, contact resistances at the faying surface and electrode-workpiece interface, and the resulting dynamic resistance with time are shown in Fig. 4. It can be seen that contact resistance at the faying surface decreases rapidly in an early stage until the minimum value at a dimensionless time 0.02 is reached. Contact resistance then increases and reaches a local maximum value at a dimensionless time of 0.05. Thereafter, it decreases gradually and finds an inflection point at a dimensionless time of 0.125. As can be seen from Eq. (3), contact resistance is composed of constriction and film resistances. The latter overrides the former in the early stage of welding. Because both electrical resistivity and hardness of the surface film on the contact surface decrease with increasing temperature, film resistance decreases in the early stage. The drop of contact resistance in the early stage therefore is a result of rapid decrease in film resistance. Since electrical resistivity of workpieces increases and hardness decreases with increasing temperature, constriction resistance or contact resistance at the faying surface exhibits a local maximum within a certain range of temperature in an intermediate stage. The inflection point of contact resistance at the faying surface at dimensionless time of 0.125 is due to an initiation of the molten nugget. A similar trend can be seen for the contact resistance at the electrode-workpiece interface. As welding time is large, contact resistance at the faying surface becomes lower than that at the electrode-workpiece interface. This is attributed to a more marked softening and earlier melting at the faying surface. It is also found that bulk resistance of the workpieces increases while the increasing rate decreases with increasing time or temperature.

The resulting dynamic resistance curve therefore can be divided into four regions. In the first stage, the rapid drop of dynamic resistance results from decreases in film resistances at the faying

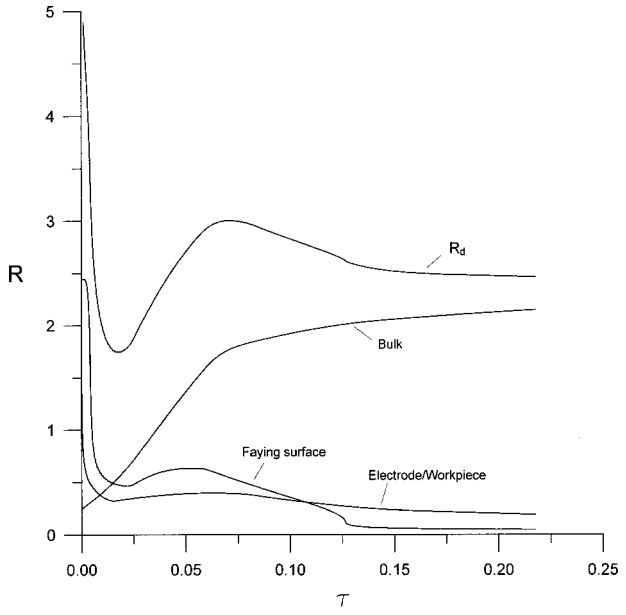

Fig. 4 Unsteady variations of dimensionless dynamic resistance, bulk resistance, and contact resistances at the faying surface and electrode-workpiece interface

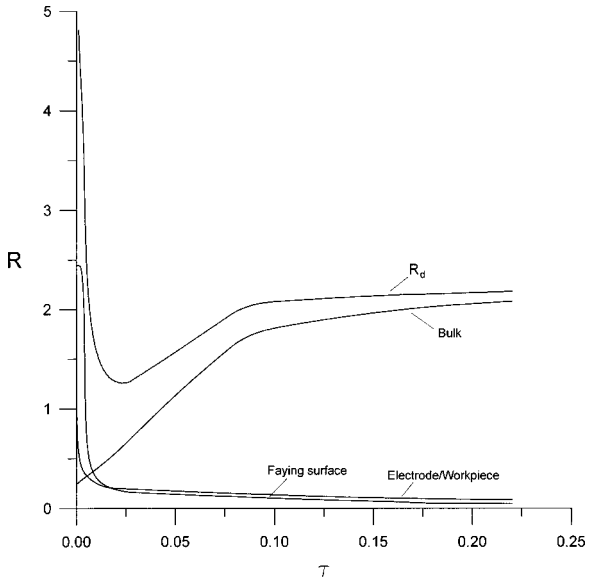

Fig. 5 Unsteady variations of dimensionless dynamic resistance, bulk resistance, and contact resistances at the faying surface and electrode-workpiece interface, $\sigma_s = \sigma_s(20°C)$.

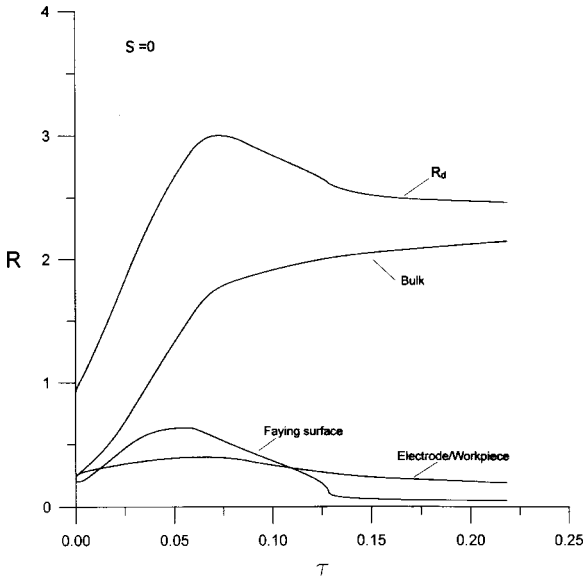

Fig. 6 Unsteady variations of dimensionless dynamic resistance, bulk resistance, and contact resistances at the faying surface and electrode-workpiece interface for vanished film resistance

surface and electrode-workpiece interface. In the second stage, dynamic resistance increases with time. High increasing rate of dynamic resistance at the beginning of this stage is a result of increases in bulk resistance and contact resistances at the faying surface and electrode-workpiece interface. Near the end of this stage the reduction of increasing rate of contact resistance at the faying surface decreases the increase of dynamic resistance until the maximum is reached. In the third stage, dynamic resistance decreases as time proceeds. This is because the decreases in contact resistance at the faying surface and electrode-workpiece interface are greater than the increase in bulk resistivity. Decreases in contact resistances are due to an incessant increase in the soften area. The fourth stage starts from a marked drop accompanying with an inflection at a dimensionless time of 0.125, where the molten nugget initiates. It should be noted that the molten nugget takes place in this stage rather than the second region, as proposed by Dickinson et al. [8]. As time further increases, expulsion will take place. In view of mechanical collapse, expulsion cannot be treated in the present work.

Provided that bulk resistivity of the workpieces is a constant at the ambient temperature (namely, $\sigma = \sigma(20°C)$), the predicted variations of dynamic resistance, bulk resistance in workpieces and resistances at contact surfaces with time are shown in Fig. 5. Instead of a local maximum within an intermediate stage as shown in previous figure (Fig. 4), contact resistances at the faying surface and electrode-workpiece interface monotonically decrease with time. This is due to the ignorance of the increase in bulk resistivity with temperature in constriction resistance. Contact resistances decrease solely from the reduction of hardness. Therefore, the local maximum of the dynamic resistance curve disappears and dynamic resistance becomes rather flat in the intermediate stage of welding time. Temperature-dependent bulk resistivity of the workpieces exhibits a significant effect on the shape of the dynamic resistance curve.

The surface contaminant and oxide layer can be removed by alkaline degreasing or acid pickling. In the case of a vanished film resistance or film thickness $s = 0$, rapid decreases of contact resistances and dynamic resistance in the early stage disappears, as shown in Fig. 6. Contact resistances at the faying surface and electrode-workpiece interface thus increase and then decrease with increasing time. The corresponding dynamic resistance curve increases with time until the maximum value is reached. Referring to Fig. 4, contact resistance at the faying surface exhibits a more pronounced rise. The effects of the parameter governing constriction resistance on the dynamic resistance curve are shown in Fig. 7. It can also be considered that contact resistance decreases as electrode force increases. A decrease in the parameter governing constriction resistance decreases dynamic resistance and its variation, which imply a delay of the formation of the molten nugget.

Comparing to Fig. 4 ($Pr_m = 3 \times 10^4$), Figure 8 shows that a decrease in magnetic Prandtl number ($Pr_m = 10^4$) reduces the increase of constriction resistance. This is attributed to low temperatures at the faying surface. Wei et al. [6] found that a decrease of magnetic Prandtl number induces a highly concentrated current density near the periphery between the electrode and workpiece surface. Different patterns of electrical currents result in different dynamic resistance curves.

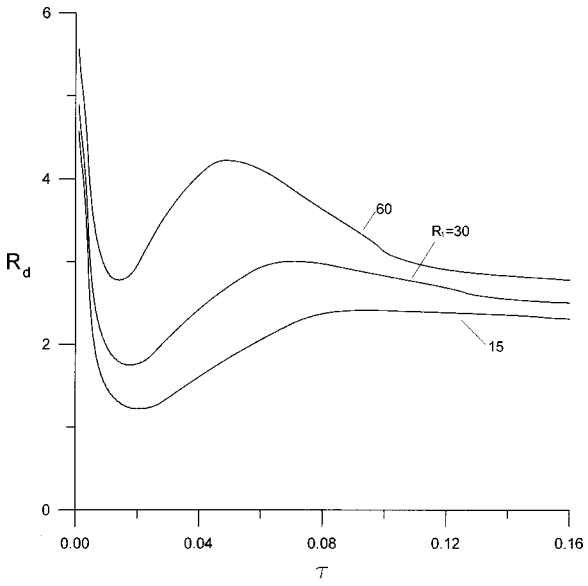

Fig. 7 Dimensionless dynamic resistance curve for different values of dimensionless constriction resistance parameter

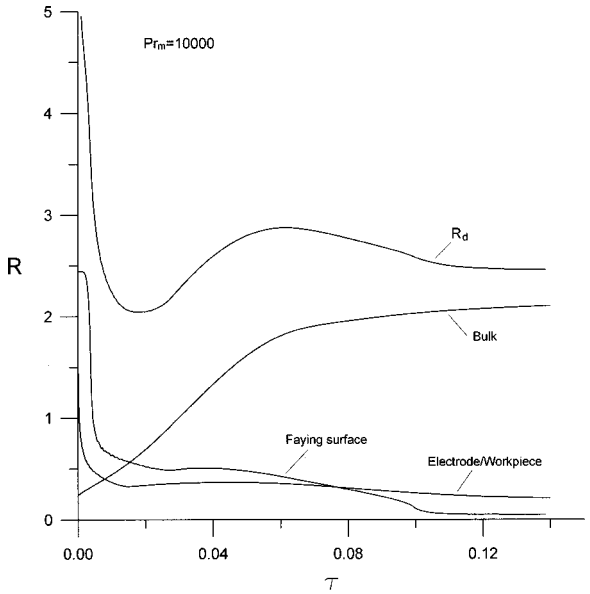

Fig. 8 Unsteady variations of dimensionless dynamic resistance, bulk resistance, and contact resistances at the faying surface and electrode-workpiece interface by decreasing magnetic Prandtl number from $Pr_m = 3 \times 10^4$ (see Fig. 4) to 10^4

Figure 9 shows that a decrease in the number of contact spots increases dynamic resistance and its variation with time and decreases the time for the minimal value to occur. In Fig. 10, it shows that as welding current increases or the parameter governing welding current increases to 4×10^7, dynamic resistance shifts to left as a result of a rapid increase of temperature. Moreover, the variations of dynamic resistance with time increase with the parameter governing welding current. No weld forms within the range of welding time considered in this figure in the case of the parameter governing welding current $Lo = 2 \times 10^7$.

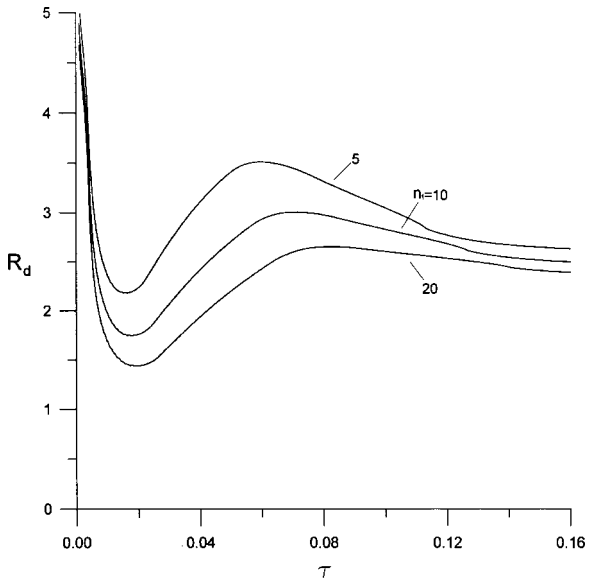

Fig. 9 Dimensionless dynamic resistance curve for different numbers of contact spots at the faying surface

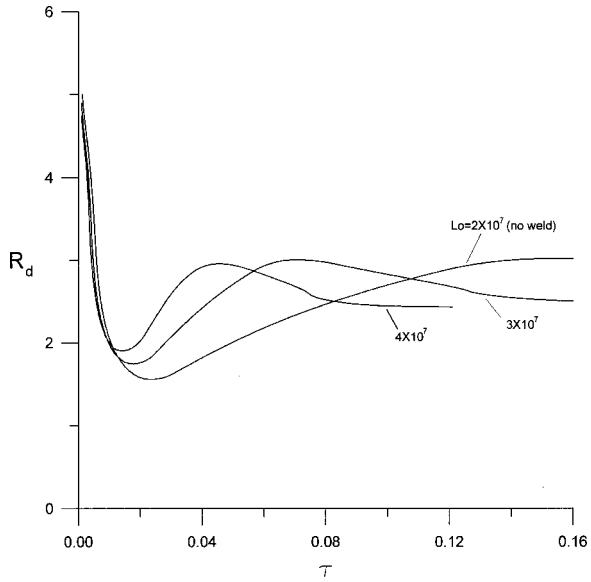

Fig. 10 Dimensionless dynamic resistance curve for different values of dimensionless parameter governing welding current

Conclusions

In this study, dynamic electrical resistance affected by hardness, temperature, electrode force and surface conditions during resistance spot welding has been quantitatively modeled and analyzed. The temperature is obtained from the previous study predicting axisymmetric, unsteady transport processes in the workpieces and electrodes during resistance spot welding. The conclusions drawn are the following:

1 The predicted nugget thickness and dynamic resistance versus time agree quite well with available experimental data. Dynamic resistance is defined by taking the sum of the total bulk resistance in the workpieces and contact resistances at the faying surface and two electrode-workpiece interfaces within an effective area corresponding to the electrode tip where welding current primarily flows. The total bulk resistance is obtained by adding temperature-dependent resistance at each grid point in series for any given radius less than the electrode tip radius and then summing the resulting resistances of all radial locations in parallel. The total contact resistance at the faying surface or electrode-workpiece interface is determined by adding all local contact resistances in parallel within the electrode tip radius.

2 This model considers electrical resistivity of the insulating surface film to be much greater than that of the workpieces. An increase of temperature decreases and increases resistivities of the surface film and workpieces, respectively. Hardness decreases with increasing temperature. The size of a contact spot on a contact surface is a function of electrode force, hardness, and total number of contact spots.

3 Contact resistance at the faying surface or electrode-workpiece interface is determined by taking the sum of constriction and film resistances. A rapid drop of contact resistances in an early stage results from the decrease of film resistance, where both resistivity and hardness decrease as temperature increases. Contact resistance exhibits a local maximum in an intermediate stage, since constriction resistance can be increased or decreased by competing increased resistivity and decreased hardness with increasing temperature. The increasing rate of resistivity in workpieces gradually reduces as time or temperature becomes high.

4 Without film resistance the rapid decrease of contact resistance in the early stage disappears. Provided that resistivity of workpieces is independent of temperature, the local maximum of contact resistance disappears. Even though contact resistance at

the faying surface is higher than that at the electrode-workpiece interface in the early stage, the opposite result is found in the range of large welding time. The distribution of electric current affects contact resistance at the faying surface. A decrease in magnetic Prandtl number enhances current density near the outer edge between the electrode and workpiece. This leads to lower temperature and contact resistance at the faying surface.

5 Excluding expulsion, dynamic resistance versus time can be divided into four stages: Stage 1 is the decrease of dynamic resistance due to decreases in contact resistances at the faying surface and electrode-workpiece interface; an increase in dynamic resistance in stage 2 results from the primary increase of bulk resistance in the workpieces and an increase in the sum of contact resistances at the faying surface and electrode-workpiece interface; dynamic resistance in stage 3 decreases because the increasing rate of bulk resistance of workpieces and contact resistances decrease; in stage 4 the decrease of dynamic resistance is mainly due to a formation of the molten nugget at the faying surface. The molten nugget is initiated in stage 4 in contrast to stage 2 or 3 as qualitatively proposed in the literature.

6 The rapid drop of the dynamic resistance curve in the early stage is absent if film resistance is ignored. The local maximum of the dynamic resistance curve disappears if electrical resistivity of constriction resistance is independent of temperature. Dynamic resistance and its variation with time increase while the time at which the minimum value occurs decreases with increasing the parameters governing constriction resistance and decreasing the number of contact spots. The variation of dynamic resistance with time decreases with welding current.

7 This resistance model can also be used for a simulation of transport phenomena involving high electric current passing through the contact surface between two workpieces.

Appendix

Curve-fitting dimensionless temperature-dependent electrical conductivities and hardness from experimental data are as follows:

(a) Electrical conductivity of workpiece AISI 1008
Solid [22]

$$\sigma_s=\frac{1}{0.11+0.275(T-1)} \quad \text{for } 1\leqslant T\leqslant 3.5 \tag{A1}$$

$$\sigma_s=\frac{1}{\dfrac{1}{\sigma_{\text{sol}}}+0.07147(T-T_{\text{sol}})} \quad \text{for } 3.5\leqslant T\leqslant T_{\text{sol}} \tag{A2}$$

Liquid [21]

$$\sigma_l=\frac{1}{1+0.034(T-T_{\text{liq}})} \quad \text{for } T\geqslant T_{\text{liq}} \tag{A3}$$

while electrical conductivity in the mushy zone $\sigma=g_s\sigma_{\text{sol}}+g_l$ for $T_{\text{sol}}<T<T_{\text{liq}}$.

(b) Film electrical resistivity of iron oxide [23]

$$\frac{1}{\sigma_f}=175483e^{-2.64301\,T} \tag{A4}$$

(c) Hardness of workpieces AISI 1026 [24]

$$H_v=2.0657e^{-0.610487\,T}-0.065 \tag{A5}$$

Nomenclature

Bi_{0E} = $\tilde{h}_{0E}r_0/\tilde{k}_E$
Bi_E = $\tilde{h}_E r_0/\tilde{k}_S$
Bi_w = $\tilde{h}_w r_0/\tilde{k}_E$
Bi_0 = $\tilde{h}_0 r_0/\tilde{k}_S$
C = specific heat ratio, as defined in Eq. (12)
Da = Darcy number
E^* = $r_0\tilde{R}_0\tilde{\sigma}_{\text{liq}}$
E_f = ε_f/r_0
f = mass fraction of liquid or solid
F_0 = dimensionless parameter, as defined in Eq. (12)
f^α = solute mass fraction $=\hat{f}^\alpha/\hat{f}^\alpha_{m,0}$
$\hat{f}^\alpha$ = solute mass fraction
$\hat{f}^\alpha_{m,0}$ = initial solute content
g = volume fraction or gravitational acceleration
h = enthalpy, $h=\tilde{h}/h_f$, or heat transfer coefficient
H = magnetic field intensity in θ direction, $H=\tilde{H}\pi r_0/I$
H_v = hardness
h_f = fusion latent heat at eutectic point, J/kg
h_l = $RCT+R(1-C)T_e+1$
h_s = RT
I,j = welding current, amp, electric current density, $j=\tilde{j}\pi r_0^2/I$
K = $g_l+g_s k_s$
k_E = thermal conductivity ratio $=\tilde{k}_E/\tilde{k}_s$
k_s = thermal conductivity ratio $=\tilde{k}_s/\tilde{k}_l$
k_p = equilibrium partition coefficient
K_0 = permeability constant, m^2
l = distance between electrodes
l_1,l_2,l_3,l_4 = length, as illustrated in Fig. 1
Lo = dimensionless parameter, as defined in Eq. (12)
M = $-(dr_c/d\zeta+\xi dN/d\zeta)/N$
N = $r_s(\zeta)-r_c(\zeta)$
n = total number of contact spots
n_1 = number of contact spots in the first control volume near axisymmetric axis
Pr_m = magnetic Prandtl number $=\tilde{\eta}_l/\tilde{\alpha}_l$
R = $\tilde{c}_s\tilde{T}_0/h_f$ or resistance
R_d = dynamic resistance, $R_d=\tilde{R}_d/\tilde{R}_0$
R_E = $\tilde{c}_E\tilde{T}_0/h_f$
r_0 = dimensional electrode radius, as illustrated in Fig. 1
$\tilde{R}_0$ = electrical contact resistance at faying surface at T_0
s = film thickness
T = temperature $=\tilde{T}/\tilde{T}_0$
T_e = eutectic temperature
u,v = axial and radial velocity, $u=\tilde{u}r_0/\tilde{\alpha}_l$, $v=\tilde{v}r_0/\tilde{\alpha}_l$
$\mathbf{V}$ = velocity vector
W = electrode force
β_S,β_T = solutal and thermal expansion coefficient
δ = nugget thickness
$\varepsilon_f,\varepsilon_{fE}$ = effective thickness of heat source at faying surface and electrode-workpiece interface, m
$\tilde{\eta}_l$ = magnetic diffusivity of liquid $=1/\tilde{\sigma}_{\text{liq}}\mu_0\mu_{rl}$
η_E = $\tilde{\eta}_E/\tilde{\eta}_l$, where $\tilde{\eta}_E=1/\sigma_E\mu_0\mu_{rE}$
θ_0 = dimensionless temperature ratio, as defined in Eq. (12)
μ_r = relative magnetic permeability, $\mu_r=g_l+g_s\mu_{rs}/\mu_{rl}$
μ_0 = free magnetic permeability, N/amp^2
ρ = dimensional and dimensionless density, $\rho=\tilde{\rho}/\tilde{\rho}_l$
σ = electrical conductivity, $\sigma=\tilde{\sigma}/\tilde{\sigma}_{\text{liq}}=g_s\sigma_{\text{sol}}+g_l$, mho/m
Σ = dimensionless parameter, as defined in Eq. (12)
τ = dimensionless time, $\tau=t\tilde{\alpha}_l/r_0^2$

Superscript

α = solute
$\sim$ = dimensional quantity

Subscript

E = electrode
l, liq = liquid and liquidus
m = mixture
s, sol = solid and solidus
w = water or coolant
0 = ambient

References

[1] Nied, H. A., 1984, ''The Finite Element Modelling of the Resistance Spot Welding Process,'' Weld. J. (Miami), **63**, pp. 123s–132s.
[2] Tsai, C. L., Jammal, O. A., Papritan, J. C., and Dickinson, D. W., 1992, ''Modeling of Resistance Spot Weld Nugget Growth,'' Weld. J. (Miami), **71**, pp. 47s–54s.
[3] Roberts, W. L., 1951, ''Resistance Variations During Spot Welding,'' Weld. J. (Miami), **30**, pp. 1004–1019.
[4] Bhattacharya, S., and Andrews, D. R., 1974, ''Significance of Dynamic Resistance Curves in the Theory and Practice of Spot Welding,'' Welding and Metal Fabrication, **42**, pp. 296–301.
[5] Greenwood, J. A., and Williamson, J. B. P., 1958, ''Electrical Conduction in Solids. II. Theory of Temperature-Dependent Conductors,'' Proc. R. Soc. London, **246**, pp. 13–31.
[6] Wei, P. S., Wang, S. C., and Lin, M. S., 1996, ''Transport Phenomena During Resistance Spot Welding,'' ASME J. Heat Transfer, **118**, pp. 762–773.
[7] Savage, W. F., Nippes, E. F., and Wassell, F. A., 1978, ''Dynamic Contact Resistance of Series Spot Welds,'' Weld. J. (Miami), **57**, pp. 43s–50s.
[8] Dickinson, D. W., Franklin, J. E., and Stanya, A., 1980, ''Characterization of Spot Welding Behavior by Dynamic Electrical Parameter Monitoring,'' Weld. J. (Miami), **59**, pp. 170s–176s.
[9] Gedeon, S. A., and Eagar, T. W., 1986, ''Resistance Spot Welding of Galvanized Steel: Part II—Mechanisms of Spot Weld Nugget Formation,'' Metall. Trans. B, **17B**, pp. 887–901.
[10] Gedeon, S. A., Sorensen, C. D., Ulrich, K. T., and Eagar, T. W., 1987, ''Measurement of Dynamic Electrical and Mechanical Properties of Resistance Spot Welds,'' Weld. J. (Miami), **66**, pp. 378s–385s.
[11] Studer, F. J., 1939, ''Contact Resistance in Spot Welding,'' Weld. J. (Miami), **18**, pp. 374s–380s.
[12] Kouwenhoven, W. B., and Tampico, J., 1941, ''Surface Polish and Contact Resistance,'' Weld. J. (Miami), **20**, pp. 468s–471s.
[13] Tylecote, R. F., 1941, ''Spot Welding, Part III: Contact Resistance,'' Weld. J. (Miami), **20**, pp. 591s–602s.
[14] Kaiser, J. G., Dunn, G. J., and Eagar, T. W., 1982, ''The Effect of Electrical Resistance on Nugget Formation during Spot Welding,'' Weld. J. (Miami), **61**, pp. 167s–174s.
[15] Vogler, M., and Sheppard, S., 1993, ''Electrical Contact Resistance under High Loads and Elevated Temperatures,'' Weld. J. (Miami), **72**, pp. 231s–238s.
[16] Thornton, P. H., Krause, A. R., and Davies, R. G., 1996, ''Contact Resistances in Spot Welding,'' Weld. J. (Miami), **75**, pp. 402s–412s.
[17] James, P. S., Chandler, H. W., Evans, J. T., Wen, J., Browne, D. J., and Newton, C. J., 1997, ''The Effect of Mechanical Loading on the Contact Resistance of Coated Aluminum,'' Mater. Sci. Eng., A, **A230**, pp. 194–201.
[18] Holm, R., 1967, *Electric Contacts, Theory and Application*, 4th edition, Springer-Verlag, New York.
[19] Greenwood, J. A., 1966, ''Constriction Resistance and the Real Area of Contact,'' British J. Applied Physics, **17**, pp. 1621–1632.
[20] Crinon, E., and Evans, J. T., 1998, ''The Effect of Surface Roughness, Oxide Film Thickness and Interfacial Sliding on the Electrical Contact Resistance of Aluminum,'' Mater. Sci. Eng., A, **A242**, pp. 121–128.
[21] Ono, Y., Hirayama, K., and Furukawa, K., 1974, ''Electric Resistivity of Molten Fe-C, Fe-Si, and Fe-C-Si Alloys,'' Tetsu to Hagane, **60**, pp. 2110–2118.
[22] Boyer, H. E., and Gall, T. L., 1984, *Metals Handbook*, Desk Edition, ASM.
[23] Touloukian, Y. S., editor, 1967, *Thermophysical Properties of High Temperature Solid Materials, Vol. 4: Oxides and Their Solutions and Mixtures*, Macmillan Co, New York, pp. 214.
[24] Grange, R. A., Hribal, C. R., and Porter, L. F., 1977, ''Hardness of Tempered Martensite in Carbon and Low-Alloy Steels,'' Metall. Trans. A, **8A**, pp. 1775–1785.
[25] Gould, J. F., 1987, ''An Examination of Nugget Development During Spot Welding, Using Both Experimental and Analytical Techniques,'' Weld. J. (Miami), **66**, pp. 1s–10s.
[26] Wei, P. S., and Ho, C. Y., 1990, ''Axisymmetric Nugget Growth During Resistance Spot Welding,'' ASME J. Heat Transfer, **112**, pp. 309–316.
[27] Wei, P. S., and Yeh, F. B., 1991, ''Factors Affecting Nugget Growth with Mushy-Zone Phase Change during Resistance Spot Welding,'' ASME J. Heat Transfer, **113**, pp. 643–649.
[28] Khan, J. A., Broach, K., and Arefin Kabir, A. A. S., 2000, ''Numerical Thermal Model of Resistance Spot Welding in Aluminum,'' J. Thermophys. Heat Transfer, **14**, pp. 88–95.
[29] Bennon, W. D., and Incropera, F. P., 1987, ''A Continuum Model for Momentum, Heat and Species Transport in Binary Solid-Liquid Phase Change Systems—I. Model Formulation,'' Int. J. Heat Mass Transf., **30**, pp. 2161–2170.
[30] Bennon, W. D., and Incropera, F. P., 1988, ''Numerical Analysis of Binary Solid-Liquid Phase Change Using a Continuum Model,'' Numer. Heat Transfer, **13**, pp. 277–296.
[31] Cramer, K. R., and Pai, S.-I., 1973, *Magnetofluid Dynamics for Engineers and Applied Physicists*, Scripta Publishing, Washington, D.C., pp. 42–45.
[32] Modest, M. F., 1993, *Radiative Heat Transfer*, McGraw-Hill, New York, pp. 52–53.
[33] Patankar, S. V., 1980, *Numerical Heat Transfer and Fluid Flow*, chap. 5 and 6, Hemisphere Publishing Corp., New York.

An Experimental Investigation of Heat Affected Zone Formation and Morphology Development During Laser Processing of Metal Powder Mixtures

C. W. Buckley
ASME Mem.
e-mail: jandb@neca.com

T. L. Bergman
ASME Fellow
e-mail: tberg@engr.uconn.edu

Department of Mechanical Engineering,
The University of Connecticut,
Storrs, CT 06268

Laser-induced melting and subsequent resolidification of a metal powder mixture consisting of low and high melting temperature materials was experimentally examined. First, the onset of melting for the low melting point material was determined and correlated with dimensionless parameters. Next, the morphologies of the heat affected zones were categorized and finally, a process map for use in rapid prototyping technology was developed. The results indicate a strong dependence of the system behavior on the laser-material coupling efficiency and in turn, the ratio of the laser beam radius to particle size.
[DOI: 10.1115/1.1370508]

Introduction

Melting and resolidification within a porous medium that is composed of multiple solid materials possessing different melting temperatures is relevant to nuclear reactor design [1], soil engineering [2], the manufacture of composite materials [3] and rapid prototyping methods [4,5].

In this study, attention is given to the case where heating is achieved with a scanning laser beam delivered to the top surface of a powder layer. Hence, the study is pertinent to Selective Laser Sintering (SLS) which is a net shape, rapid prototyping technology. Details of the SLS process have been discussed elsewhere [6] and will not be repeated here.

In SLS, objects are fabricated by first irradiating the top surface of loose powder with a scanning laser beam, forming a slender heat affected zone (HAZ) of bonded material. The laser-fabricated HAZ's are formed adjacent to one another to eventually form a thin (fractions of mm) layer of solid material. Individual layers are fabricated, one atop another, until a three-dimensional object is built (ideally of full density and to net shape.) Ultimately, both the dimensions and properties of the fabricated object are governed by (a) the bulk properties of the raw material, (b) the morphology of each HAZ, (c) the manner in which the HAZ's are interconnected within a layer, and (d) the layer-to-layer bonding characteristics. The first step in developing a predictive capability to relate the part properties and finish to the processing conditions is the ability to *predict* or *correlate* the formation and evolution of individual HAZ's.

Considerable progress has been made recently regarding the thermal aspects of HAZ formation in laser-irradiated polymer powders based upon development of unique models for net shape evolution during non-isothermal heating of polymer powder regions [7–9]. The focus of the present study is to evaluate HAZ formation in *metal* powder systems. When metal parts are fabricated using SLS, a mixture of melting and non-melting material is typically used [10]. As will become evident, use of mixtures of metal powders results in HAZ morphologies that are fundamentally different than those that evolve in single component powders. The heat transfer and fluid flow phenomena are extremely complex and include effects ranging from laser-material coupling in non-stationary, multiphase (solid, liquid and gas) systems to capillary-induced flow in a non-stationary porous matrix that is *itself* undergoing solid-liquid phase change. The entire phase change history (melting through resolidification) may occur in fractions of a second. Details of the heat transfer and fluid mechanics phenomena that drive HAZ formation in laser-irradiated metal powders have been investigated to a limited extent [11].

The objective of this study is to experimentally investigate HAZ development in laser-irradiated metal powder mixtures. The onset of HAZ formation is correlated with dimensionless parameters, as is the ultimate HAZ morphology that evolves in response to laser heating, material melting, flow of the molten as well as the entrained solid material, and resolidification.

Experiments

To produce HAZ's using laser irradiation for net shape manufacturing purposes, it is desirable to utilize powder mixtures that consist of low- and high-melting temperature metals because when single material powders are melted, randomly-shaped HAZ's (and in turn, poor part dimensional tolerance and surface finish) typically are formed. For similar reasons, it is a requirement that the low melting point material readily infiltrate into the non-melting skeletal structure that is formed by the second, high melting point material. Hence, the molten phase must wet the non-melting material, and possess a relatively low viscosity. Because of these restrictions, a rather small set of material pairs can, unfortunately, be used [10].

In this study, a mixture of nickel braze (Nicrobraz LM manufactured by Wall Colmonoy Corp., $T_m = 1273\,\mathrm{K}$) and AISI 1018 carbon steel ($T_m = 1795\,\mathrm{K}$) was used. Micrographs of the unprocessed powders are shown in Fig. 1 and the powder properties are listed in Table 1 [12–18].

The experimental apparatus is discussed elsewhere [8,11] and consists of a CW, 50 W (max.) CO2 laser (Synrad 48-5) operating at a wavelength of 10.6 microns. The gaussian beam is focussed onto the powder by a set of infrared lenses and computer-controlled scanning mirrors (a Synrad SH marking head) so that the scanning speed and the minimum spot size ($r_{\min} = 1.27\lambda f / r_{\max}$) [19] can be varied. The laser beam spot size could be enlarged by changing the working distance between the material and the focal point of the lens system.

The powder mixture was held within a $25\,\mathrm{mm} \times 50\,\mathrm{mm}$

Contributed by the Heat Transfer Division for publication in the Journal of Heat Transfer. Manuscript received by the Heat Transfer Division June 26, 2000; revision received December 14, 2000. Associate Editor: T. Avedisian.

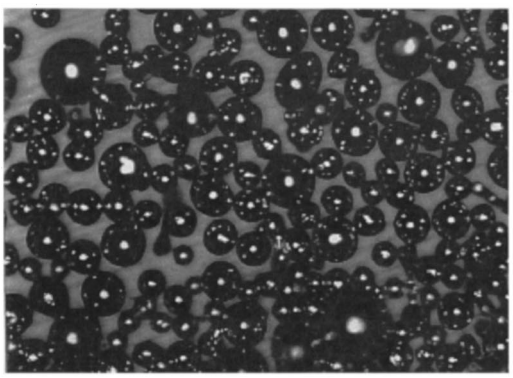

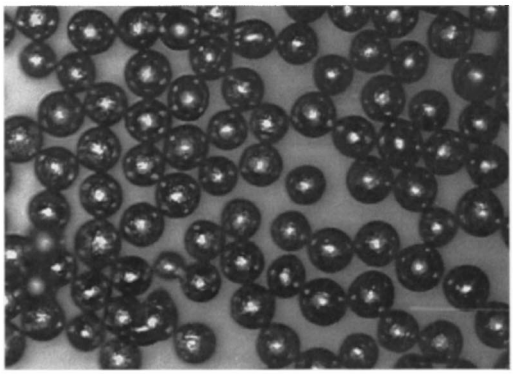

Fig. 1 Micrographs of the nickel braze powder (top) and AISI 1018 carbon steel powder (bottom)

$\times 10$ mm pocket milled into a steel block. The pre-mixed powder (without a wetting agent or flux) was poured into the pocket and carefully leveled with a straight edge. The powder was irradiated, the HAZ (if formed) was photographed within the surrounding loose powder and was subsequently removed from the loose powder and archived. The onset of melting (and hence HAZ formation) for a particular scanning speed and beam size was determined by gradually increasing the laser power (allowing the powder to cool to room temperature between experiments) until a very fine and porous HAZ could be removed from the loose powder. The initial temperature for each experiment was uniform at approximately 300 K.

Table 1 Properties (at 600 K)

Property	Nickel Braze	AISI 1018	Air
α	0.05[13]	0.05[13]	
ρ (kg/m³)	7675*	8124*	0.58[14]
c (J/kgK)	410[15]	560[14]	1050[14]
k(W/mK)	19[15]	48[14]	0.047[14]
μ (kg/ms)	0.005[16]	-	-
λ (kJ/kg)	298[17]	-	-
T_m (K)	1273[18]	1798[17]	-
η	0.5[12]	0.5[12]	-
σ (N/m)	2.28[27]	-	-
dσ/dT (N/mK)	4.9[27]	-	-
d (μm)	45*	68*	-

*measured data

Table 2 Ranges of processing parameters

P_{min} = 0.88 W	P_{max} = 44.4 W
r_{min} = 0.13 mm	r_{max} = 4.08 mm
U_{min} = 0.32 mm/s	U_{max} = 33 mm/s
X_{min} = 0.30	X_{max} = 1.0

Experiments were performed using a range of processing parameters and powder mixtures, as shown in Table 2. The powder mixtures were characterized by $X=0.30$, 0.50, 0.65, 0.70, and unity. The effective specific heat and effective density of the porous medium were estimated by volume-averaging the properties of the nickel braze, the 1018 steel, and atmospheric pressure air. Properties were evaluated at 600 K, which is approximately midway between the initial temperature and melting temperature of the nickel braze. The effective thermal conductivity was calculated based upon a series resistance approximation for the powder morphology [20]. The series resistance approximation yields reasonable predictions for the measured effective thermal conductivity of metal powders [21] although other models for the effective thermal conductivity could be used as well. The effective viscosity of the mixture was determined by $\mu_{eff}=\mu[1-V/V_{crit}]^{-2}$ (for $V<V_{crit}$) and $\mu_{eff}\rightarrow\infty$ (for $V>V_{crit}$) where $V_{crit}=0.62$ [22].

Results

A series of preliminary experiments was performed under (a) atmospheric (b) modest vacuum ($P\cong 0.05$ atm) conditions by placing the powder in a vacuum chamber fabricated of infrared-transparent Zn-Se windows, and (*c*) under conditions with a 1 atm nitrogen wash. Little sensitivity to the atmospheric conditions was observed for the formation of a single HAZ. Figure 2 includes a micrograph of a typical cross section of a HAZ formed in atmospheric conditions. The HAZ morphology is extremely complex with regions of very high (dark) and very low porosity. It is evident that the molten nickel braze wets the solid steel particles (see the marked area on the lower right) and has infiltrated certain regions of the non-melting matrix to form zones of full density (lower left). The ability of the molten braze to wet and infiltrate the non-melting phase to form a single HAZ is not apparently affected by oxidation, although the top surfaces of the HAZ's were oxidized and (using our experimental apparatus) good layer-to-layer bonding could not be readily achieved.

HAZ Formation. Analytical solutions of the heat equation can be used to predict the thermal response of materials to scanning laser irradiation. In particular, Cline and Anthony [23], Lax [24] and Nissim et al. [25] provide solutions for the local maximum temperatures that evolve during laser irradiation of a semi-infinite medium (neglecting surface heat losses due to convection and radiation).

For the experiments associated with the formation of the HAZ, the maximum local temperatures will correspond to the melting temperature of the nickel braze. The results of Nissim et al. [25] can be used to predict the dimensionless laser power (Bi) and dimensionless laser scanning velocity (Pe) associated with the onset of melting where

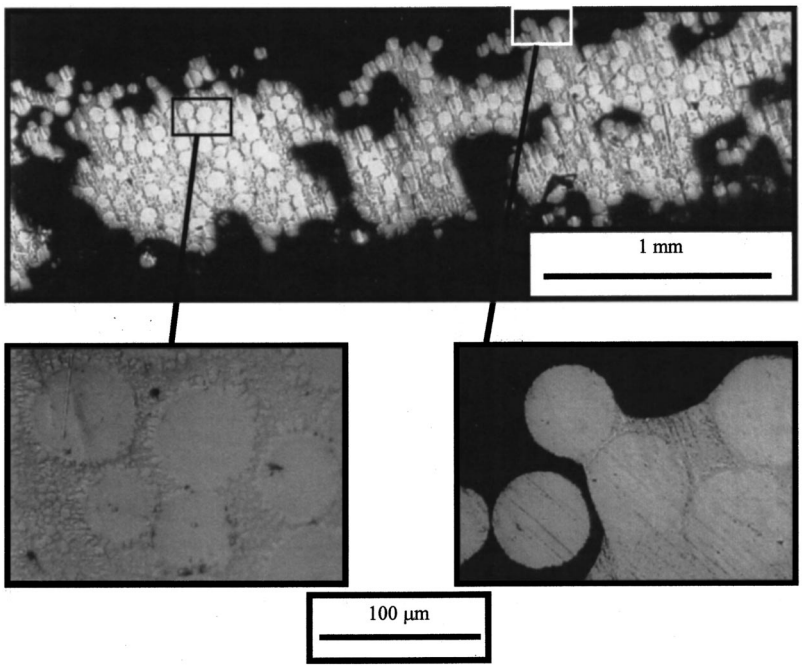

Fig. 2 Micrographs of a cross section of a HAZ. Note the high porosity (dark) regions evident under low magnification (top). Note the unmolten AISI steel with surrounding resolidified nickel braze (bottom left) and the wetting of the solid steel particle by the molten nickel (bottom right).

$$\mathrm{Bi} = P\eta/\pi r k_{\mathrm{eff}}(T_m - T_i) \tag{1}$$

and

$$\mathrm{Pe} = \mathrm{Ur}/\alpha_{\mathrm{eff}}. \tag{2}$$

The theoretical (using $\eta = 0.5$) [12] and experimental results for the onset of melting are shown in Fig. 3. The size ratio ($\mathrm{Sz} = 4r^2/d^2$) is used to distinguish the various experimental results associated with different laser beam radii.

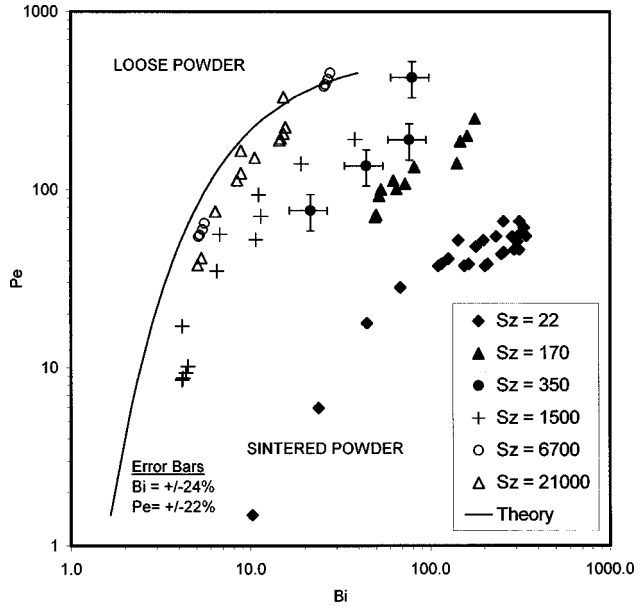

Fig. 3 Predicted and measured onset of melting for the nickel powder

Note that the value of Sz changes modestly as the fraction of nickel is varied since the nickel particles are, on average, slightly smaller than the steel particles. Each Sz value shown corresponds to a different laser beam diameter and actual Sz values are: $18 < \mathrm{Sz} < 25$ for $\mathrm{Sz} = 22$, $139 < \mathrm{Sz} < 192$ for $\mathrm{Sz} = 170$, $336 < \mathrm{Sz} < 393$ for $\mathrm{Sz} = 350$, $1273 < \mathrm{Sz} < 1764$ for $\mathrm{Sz} = 1500$, $5668 < \mathrm{Sz} < 7856$ for $\mathrm{Sz} = 6700$, $17{,}836 < \mathrm{Sz} < 24{,}720$ for $\mathrm{Sz} = 21{,}000$. Although there is considerable uncertainty in the value of η [12] the coupling efficiency should be the same from experiment-to-experiment for a particular Sz value since the data in Fig. 3 are all associated with the same initial and maximum temperature. There may be slight variation in the value of η as X is varied, and the change in the value of η may be responsible for some of the data scatter evident within a particular Sz data set. The uncertainty in the measured data was determined using standard procedures [26]. Estimated uncertainties in the primitive variables are approximately ± 10 percent (with the exception of T_i, T_m, and V, which are approximately ± 1, 2 and 5 percent respectively) resulting in Bi $\approx \pm 24$ percent and Pe $\approx \pm 22$ percent.

As expected, the results indicate that higher temperatures are more readily achieved at higher laser power (large Bi) and slower scanning speeds (small Pe). When Sz is large (6700 and 21,000), the powder layer behaves nearly as a continuum, and the onset of melting may be predicted to within the experimental accuracy using the solution to the energy equation. However, the experimental data reveals very high sensitivity to Sz as the beam diameter approaches that of the particle diameter (small Sz).

The high sensitivity of the results to Sz can be attributed to a variety of factors. At large Sz, the powder may be considered to be a semi-infinite, opaque and rough sheet with, in turn, relatively high coupling efficiency [12]. As Sz becomes smaller, the dimensions of the interstitial regions between particles becomes significant (relative to the laser beam diameter) and the material (when considered to be a continuum) will begin to behave as a semi-transparent medium; requiring higher laser irradiation (Bi) in order to achieve the same maximum temperatures at a particular scanning speed (Pe) [27]. As Sz approaches unity, an irradiated

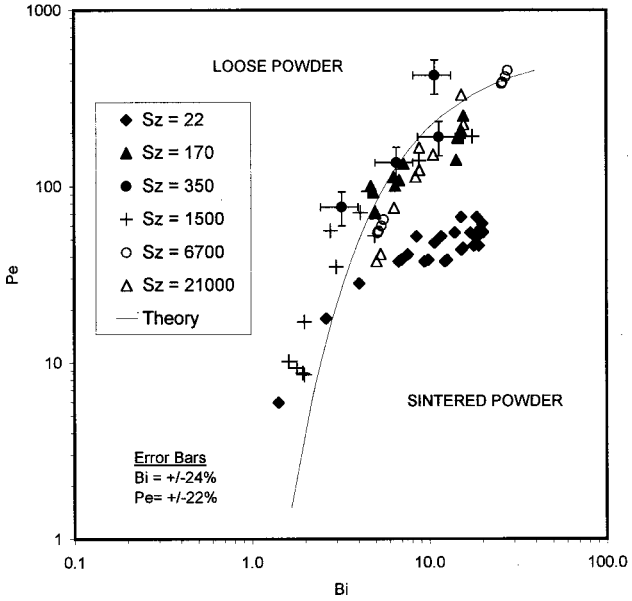

Fig. 4 Predicted and measured onset of melting for the nickel powder with dependence of η with Sz. $\eta = 0.02746 + 0.00012\,Sz$ for $22 < Sz < 4100$.

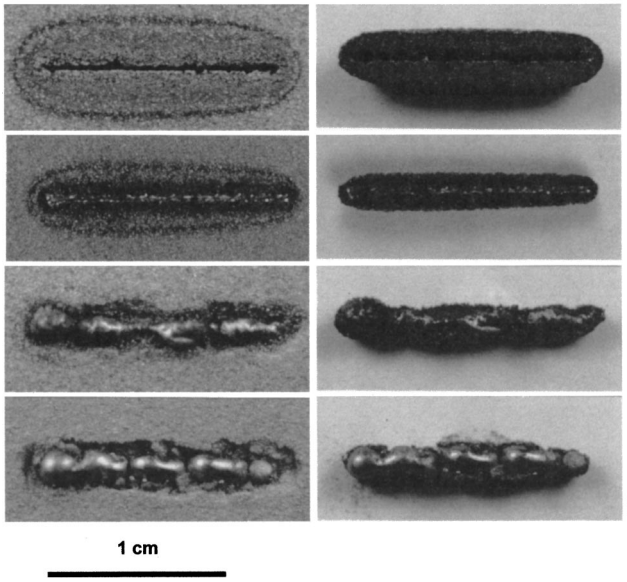

Fig. 5 Observed HAZ morphologies for (top to bottom) $X = 0.3$, 0.5, 0.7, and 1. Bi=19, Pe=1.1, Sz=22.

particle directly beneath the beam will be a poor absorber of laser irradiation due to the extremely low (0.05) absorptivity of nickel (and iron) to 10.6 micron irradiation [13]. Additional effects are discussed in [12]. In addition to the probable high sensitivity of η to Sz, local spatial temperature gradients will increase as Sz becomes smaller. Large temperature gradients will, in turn, produce highly non-uniform differential expansion of individual particles which will affect the particle-to-particle thermal contact resistance and in turn the effective thermal conductivity of the powder bed. As Sz approaches unity, an individually-heated particle will possess considerable exposed surface area and, in turn, large area for heat losses that would require additional laser energy (larger Bi) to increase the particle temperature at a given scanning speed (Pe).

In an attempt to better collapse the experimental data, the issue of laser-material coupling was accounted for in an approximate manner. Specifically, at large $Sz(Sz > (1500+6700)/2 = 4100)$, the material is treated as a continuum and interparticle spacing leads to enhanced absorption of the laser irradiation; the powder layer was assigned a coupling efficiency of $\eta = 0.5$ based upon the measurements reported in [12]. For $Sz = 22$, the material and was assigned a coupling efficiency based upon the measured infrared absorptivity of bulk nickel to irradiation of 10.6 microns ($\alpha \approx 0.05$) [13]. The value of η was varied linearly in the $22 < Sz < 4200$ range. The data of Fig. 3 are re-plotted in Fig. 4.

The results shown in Fig. 4 are in good agreement with the theoretical prediction (except for the $Sz = 22$ results), showing that changes in the laser-material coupling efficiency is a primary reason for the high sensitivity of the thermal response to Sz. Of course, results similar to Fig. 4 might be achieved for processing other materials and may be used in order to determine appropriate processing conditions when formation of a HAZ is desired.

HAZ Morphologies. The results of the preceding section are associated with the onset of the formation of a HAZ (onset of melting of the nickel braze) in a multiple metal powder induced by laser heating. At higher laser heating rates (or slower scanning velocities) significant amounts of nickel are melted and the molten braze infiltrates into the steel matrix by capillary action [11]. Upon cooling, the nickel solidifies and a HAZ is formed. As will become evident, the resulting HAZ morphologies range from the geometrically simple to the extremely complex.

Significant melting rates lead to an increase in the local density beneath the laser beam and a depression of the top surface of the powder (or, as will become evident, a stationary top surface but a highly porous HAZ). For a densified HAZ, advection of the molten nickel can induce motion of the non-molten steel particles by surface tension and viscous forces. As will become evident, this ''entrainment'' effect can lead to the development of significant ''slip planes'' within the porous medium away from the HAZ and, in turn, a decrease in the ability of the medium to conduct thermal energy laterally away from the centerline of the laser scan. As the nickel melts, the laser-material coupling efficiency is expected to decrease dramatically (at large Sz) with high reflectivities associated with the (potentially) smooth liquid metal surface.

Although limited progress in predicting the sensitivity of the metal HAZ morphology (shape) to different processing conditions has been made [11], the simple HAZ geometries that were predicted by Zhang et al. do not correspond particularly well to the richly-textured HAZ morphologies that are observed experimentally. In this section, different HAZ morphologies are presented, the morphologies are categorized by their appearance, and the HAZ morphologies are correlated with dimensionless processing parameters.

Figure 5 includes top views of various HAZ's within the powder bed (left column) as well as the extracted HAZ's (right column) for small Sz. The scanning direction is left-to-right with a laser power of 31 W, a beam radius of 0.13 mm and a scanning velocity of 0.54 mm/s ($Pe = 1.2$, $Bi = 20$ and $Sz = 22$). From top-to-bottom, $X = 0.3$, 0.5, 0.7 and unity.

At $X = 0.3$, a groove that is only several laser beam diameters in width (and depth) is formed within the powder matrix. Material previously within the groove volume has been wicked into the surrounding powder and high temperatures (sufficient to melt the nickel but not the steel) propagate outward from the center of the laser scanning line. The resulting HAZ (right column) is approximately 100 beam diameters wide, is (for the most part) of the same porosity as the initial powder layer (i.e., the top surface of the powder did not slump), and has outer boundaries that are well-defined (a uniform HAZ width exists in the middle 1/3 of the scanning length). The same uniform initial and final porosity of the HAZ is expected, based upon the non-melting behavior of the steel and the results of Dosanjh [1] as well as Mughal and Plumb [3].

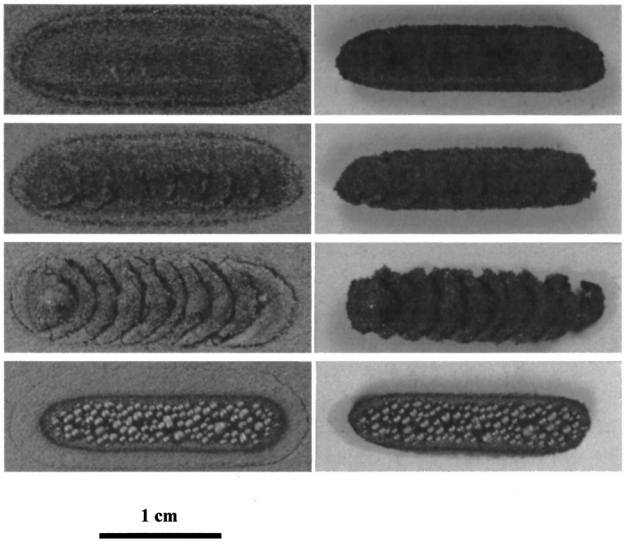

Fig. 6 Observed HAZ morphologies for (top to bottom) $X=0.3$, 0.5, 0.7, and 1. Bi=15, Pe=35, Sz=21,000.

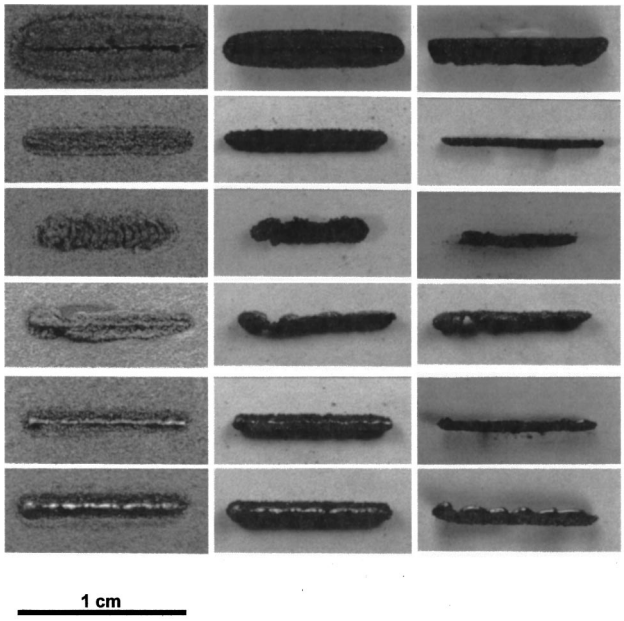

Fig. 7 Classification of 6 major HAZ morphologies. Top to bottom: grooved, sponge, herringbone, tube, pin, balled. The HAZ is shown in top view in the powder (left), top view out of the powder (middle) and side view (right).

As the nickel mass fraction is increased to $X=0.5$ (second row) more material is melted along the laser scan line. However, now the surface tension forces cause the molten metal to form a ''bead'' while advection of the metal to the center of the line scan entrains unmolten steel powder leading to the development of a slip plane between HAZ and the surrounding loose powder. The increased centerline melting and reduced lateral thermal conductance result in a narrower HAZ (right column) with noticeably rougher surface finish. As X is increased further, (0.7 and unity) significant porosity is established in regions adjacent to the HAZ, and the HAZ morphology becomes ''ragged'' as the molten nickel agglomerates into globules which sink into the loose powder. The HAZ's associated with the high nickel content results are undesirable in any net shape manufacturing technology.

During fabrication of objects using laser powder methods, small diameter laser beams (such as those used to produce the results in Fig. 5) might be used to sculpt the edges of the part, while a larger diameter beam could be used to *broadly brush* the interior regions of the object. The results of Fig. 6 are associated with large Sz. Specifically, a laser power of 45 W, a beam radius of 4.1 mm and a scanning velocity of 0.54 mm/s (Pe=35, Bi =15 and Sz=21,000) are used. As in Fig. 4, the nickel mass fractions are $X=0.3$, 0.5, 0.7 and unity.

A comparison of Figs. 5 and 6 shows that, although a larger beam was used in Fig. 6 (30 times larger than in Fig. 5), the resulting HAZ sizes and shapes are remarkably similar for the 0.30 nickel mass fraction cases. Use of the larger beam reduces the peak intensity of the beam, and the thin groove evident in Fig. 5 is not formed. The extracted $X=0.30$ HAZ is highly porous (for all practical purposes it has the same porosity as the loose powder and has a *sponge-like* texture and appearance).

As the mass fraction of the low melting temperature material is increased, more liquid will form due to laser heating and a complex *herringbone* HAZ morphology develops. Visual observation of the powder during laser scanning revealed that as molten nickel is pulled from regions ahead of the laser beam to beneath the beam (by surface tension forces), solid loose steel powder is entrained in the molten nickel flow. The entrainment of solid material induces the formation of crescent-shaped waves in the loose powder layer ahead of the laser beam (see the $X=0.7$ results). The entrainment leads to slip plane development within the powder bed ahead of the beam, which in turn reduces lateral thermal conductance in the powder layer and temporarily cuts off the supply of loose powder that can be entrained to areas beneath the beam. Entrainment of loose powder resumes when the moving laser beam heats and melts additional powder at a downstream scanning location. Finally, for $X=1.0$, the HAZ that is formed consists of small, loose beads of solid nickel formed by surface tension forces. The beads rest in a semi-circular shell of sintered nickel powder particles, leading to a *peapod* morphology so-named since at intermediate Sz values, a single line of uniform diameter, spherical metal droplets form within a rigid semi-circular shell of *sponge-like* material.

Several hundred experiments were performed, HAZ's were extracted and archived, and 6 major HAZ morphologies were identified for the nickel braze, 1018 steel material pair. The *grooved* morphology (Fig. 7 top row) has been discussed in relation to the $X=0.3$ results of Fig. 5. The *sponge* morphology (Fig. 7 second row) is similar to the grooved morphology, but does not have a fully molten region or regions of extremely high local porosity. This morphology is similar to the $X=0.3$ results shown in Fig. 6.

The *herringbone* morphology has been discussed in conjunction with the $X=0.5$ and 0.7 results of Fig. 6 and is shown in the third row of Fig. 7. The periodicity and magnitude of the ripples varies with the processing conditions and the mass fraction of the melting material. In some cases, the magnitude of the rippling becomes so severe that a *fishcale* structure results with the samples breaking into individual, but uniformly-shaped *scales* when extracted from the powder bed. Note that the material preferentially advects to the starting location of the laser scan (LHS) since material is entrained from all directions when initially heated.

The preferential advection of material to locations near the initiation of the laser scan is more evident in the *tube* morphology of the fourth row of Fig. 7 (note the thin bridge of material connecting the starting location with the remainder of the HAZ). The cross section of the tube is circular. The *pin* morphology (fifth row of Fig. 7) is desirable. It consists of a continuous line of solid metal (both resolidified nickel and steel) surrounded by a porous region of resolidified nickel in an unmolten steel matrix. The resulting pin HAZ lies beneath the original surface of the loose powder bed. Finally, the *balled* morphology (last row of Fig. 7) is undesirable, and consists of resolidified nickel regions that are

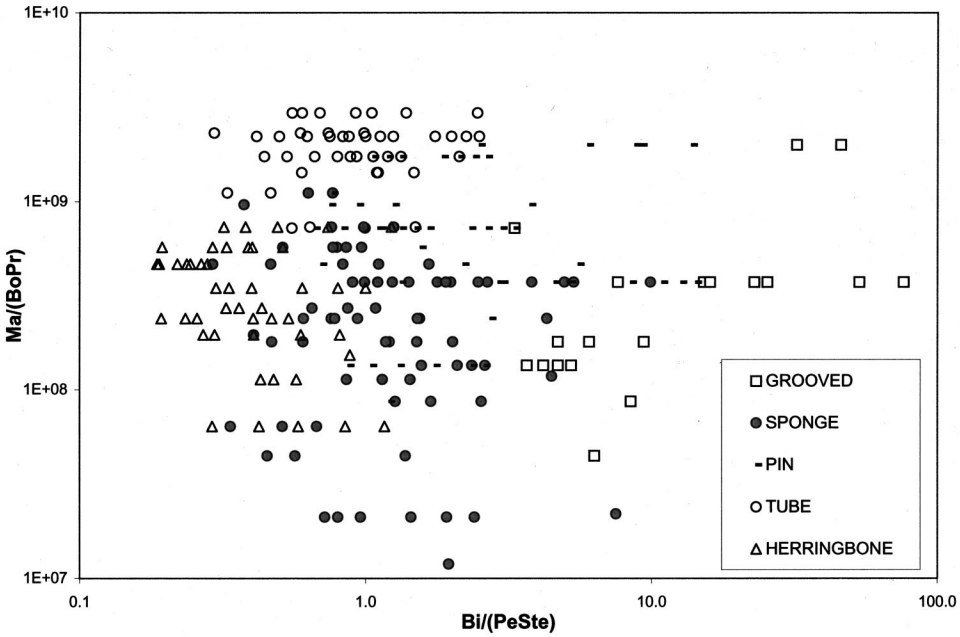

Fig. 8 Process map for $0.3 \leqslant X \leqslant 0.7$

deformed by surface tension forces. The *peapod* morphology of the $X = 1.0$ results of Fig. 6 is a subset of the *balled* morphology.

The 6 major HAZ morphologies, obtained under a very wide variety of processing conditions (for several hundred experiments), were catalogued. Different dimensionless parameters were considered in an attempt to collapse the observed morphology types into a reasonable form. This effort builds upon our previous research where the details of the morphology were not of concern, governing equations could be written to describe the physical processes, the equations were solved and normalized, and the predictions of HAZ size were reported in appropriate dimensionless form [11].

The results shown in Fig. 8 were obtained by a trial-and-error approach. In addition to Bi, Pe, and Sz, four additional parameters were deemed to be significant once the liquid phase is induced. The Stefan and Prandtl numbers include the effects of the latent heat of fusion and molten material motion on the development of temperatures within the system, while the Marangoni and Bond numbers describe the effects of surface tension forces within the liquid phase and the corresponding convective flow within the molten material. These parameters have been used to describe similar physical processes (such as surface rippling) in other systems, such as those that occur during welding or beam processing of metals [28,29]. Different combinations of the dimensionless parameters were formed to investigate which were best at describing the morphological outcome of a laser scan. As shown in Fig. 8, it was observed that Bi/(PeSte) and Ma/(BoPr) collapse the data to a reasonable degree of usefulness. The results of Fig. 8 are applicable in the range $0.3 \leqslant X \leqslant 0.7$. Note that the balled morphology is not included since the results for this morphology are poorly-correlated with the dimensionless parameters used. The lack of correlation is attributed to a high degree of variation in the laser-material coupling efficiency as the material is fully melted into a spherical shape.

Summary and Conclusions

This study was motivated by an evolving manufacturing technology and has been performed in order to provide (a) insight into the rich physical phenomena associated with laser heating of a multiple metal powder matrix, (b) a methodology whereby the onset of the formation of head affected zones (HAZs) may be predicted, and (c) a process map whereby major HAZ morphologies may be correlated with appropriate dimensionless parameters.

The thermal response of the powdered material was investigated by determining the onset of melting of the nickel powder. When the laser beam is of the same order size as the powder diameter (small Sz), the material's thermal response cannot be predicted accurately unless the sensitivity of the laser coupling efficiency (η) to Sz is accounted for. In general, the powder layer cannot be treated as a continuum with respect to the laser beam. When the coupling efficiency's dependence upon Sz is taken into account, the experimental data collapse to a reasonable degree.

The morphologies of HAZ's that are formed by laser heating of the material are extremely complex and varied. In general, a tradeoff exists between forming HAZ's of high density and of high accuracy dimensional accuracy. Six major and distinct HAZ types were identified and the type of HAZ formed was correlated with dimensionless processing parameters. Remarkably different HAZ morphologies develop as both the powder mixture and beam size is varied. The ability to predict the HAZ morphologies is limited since, as the HAZ morphologies change, the effective thermal transport properties within the medium are affected significantly, as is the laser-material coupling efficiency. All of these properties will vary during the process and are coupled to one other.

As in most thermal processing investigations, a wide variety of solid and gas phase chemistries may be considered. The results obtained in this study are limited to the particular materials (and powder size distributions) processed under atmospheric conditions. Although particular results will change as different solids and/or gases are considered, the methodologies used here may serve as a guide for improving the design of processes involving laser heating and melting of metal powders.

Acknowledgments

The authors gratefully acknowledge the support of the National Science Foundation under Grant No. 9796186.

Nomenclature

Bi = Biot number $[= P\eta/(\pi r k_{\text{eff}}(T_m\text{-}T_i))]$
Bo = Bond number $[= \rho_{\text{Ni}} g r^2/\sigma]$

c = specific heat
d = mean particle diameter
g = gravitational acceleration
k = thermal conductivity
Ma = Marangoni number $[=-d\sigma/dT(T_m-T_i)r/(\mu_{\text{eff}}\alpha_{\text{eff}})]$
P = laser power
Pe = Peclet number $[=Ur/\alpha_{\text{eff}}]$
Pr = Prandtl number $[=\mu_{\text{eff}}c_{\text{eff}}/k_{\text{eff}}]$
r = beam radius
Ste = Stefan number $[=\lambda X/c_{\text{eff}}(T_m-T_o)]$
Sz = size ratio $[=4r^2/d^2]$
T = temperature
U = laser scanning speed
V = volume fraction of steel
X = mass fraction of nickel

Greek Symbols

α = thermal diffusivity, material absorptivity
η = laser-material coupling efficiency
λ = latent heat of fusion
μ = dynamic viscosity
ρ = density
σ = surface tension

Subscripts

crit = critical
eff = effective
i = initial
m = melting
Ni = nickel

References

[1] Dosanjh, S. S., 1989, ''Melt Propagation in Porous Media,'' Int. J. Heat Mass Transf., **32**, pp. 1373–1376.
[2] Miller, R. D., 1980, ''Freezing Phenomena in Soils,'' *Applications of Soil Physics*, Academic Press, New York, pp. 254–318.
[3] Mughal, M. P., and Plumb, O. A., 1993, ''Heat Transfer During Melting of Packed Particulate Beds,'' *Heat and Mass Transfer in Materials Processing and Manufacturing*, D. A. Zumbrunnen et al., eds., ASME HTD Vol. 261, pp. 63–72.
[4] Agarwala, M., Bourell, D., Beaman, J., Marcus, H., and Barlow, J., 1995, ''Direct Selective Laser Sintering of Metals,'' Rapid Prototyping Journal, **1**, pp. 26–36.
[5] Weiss, W. L., and Bourell, D. L., 1993, ''Selective Laser Sintering of Intermetallics,'' Metallurgical Transactions A-Physical Metallurgy and Materials Science, **24**, pp. 757–759.
[6] Conley, J. G., and Marcus, H. L., 1997, ''Rapid Prototyping and Solid Freeform Fabrication,'' ASME J. Manuf. Sci. Eng., **119**, pp. 811–816.
[7] Kandis, M., and Bergman, T. L., 1997, ''Observation, Prediction and Correlation of Geometric Shape Evolution Induced by Non-Isothermal Sintering of Polymer Powder,'' ASME J. Heat Transfer, **119**, pp. 824–831.
[8] Kandis, M., Buckley, C. W., and Bergman, T. L., 1999, ''An Engineering Model for Laser-Induced Sintering of Polymer Powders,'' ASME J. Manuf. Sci. Eng., **121**, pp. 360–365.
[9] Kandis, M., and Bergman, T. L., 2000, ''A Simulation-Based Correlation of the Effective Thermal Conductivity and Porosity of Objects Produced by Laser-Induced Sintering of Polymer Powders,'' ASME J. Manuf. Sci. Eng., **122**, pp. 439–444.
[10] Bunnell, D. E., 1995, *Fundamentals of Selective Laser Sintering of Metals*, Ph.D. thesis of the University of Texas at Austin.
[11] Zhang, Y., Faghri, A., Buckley, C. W., and Bergman, T. L., 2000, ''Three-Dimensional Sintering of Two Component Metal Powders with Stationary and Moving Laser Beams,'' ASME J. Heat Transfer **122**, pp. 150–158.
[12] Haag, M., Hugel, H., Algright, C. E., and Ramasamy, S., 1996, ''CO2 Laser Light Absorption Characteristics of Metal Powders,'' J. Appl. Phys., **79**, pp. 3835–3841.
[13] Touloukian, Y. S., and Ho, C. Y., 1972, *Thermophysical Properties of Matter*, **7**, *Thermal Radiative Properties of Metallic Solids*, Plenum Press, New York.
[14] Incropera, F. P., and DeWitt, D. P., 1996, *Fundamentals of Heat and Mass Transfer*, John Wiley & Sons, New York.
[15] Touloukian, Y. S., and Ho, C. Y., 1972, *Thermophysical Properties of Matter*, **2**, *Thermal Conductivity of Metallic Solids*, Plenum Press, New York.
[16] Iida, T., and Guthrie, R. I. L., 1988, *The Physical Properties of Liquid Metals*, Oxford University Press, New York.
[17] Avallone, E. A., and Baumeister, T., 1999, *Mark's Handbook for Mechanical Engineers*, McGraw-Hill, New York.
[18] Nicrobraz® technical data sheet (Wall Colmonoy Corp.)
[19] Duley, W. W., 1983, *Laser Processing and Analysis of Materials*, Plenum Press, New York.
[20] Kaviany, M., 1991, *Principles of Heat Transfer in Porous Media*, Springer-Verlag, New York.
[21] Bala, K., Pradhan, P. R., Saxena, N. S., and Saksena, M. P., 1989, ''Effective Thermal Conductivity of Copper Powders,'' J. Phys. D, **22**, pp. 1068–1072.
[22] German, R. M., 1990, ''Supersolidus Liquid Phase Sintering Part II: Densification Theory,'' Int. J. Powder Metall., **25**, pp. 35–42.
[23] Cline, H. E., and Anthony, T. R., 1977, ''Heat Treating and Melting Material with a Scanning Laser or Electron Beam,'' J. Appl. Phys., **48**, pp. 3895–3900.
[24] Lax, M., 1977, ''Temperature Rise Induced by a Laser Beam,'' J. Appl. Phys., **48**, pp. 3919–3924.
[25] Nissim, Y. I., Lietoila, A., Gold, R. B., and Gibbons, J. F., 1980, ''Temperature Distributions Produced in Semiconductors by a Scanning Elliptical or Circular CW Laser Beam,'' J. Appl. Phys., **51**, pp. 577–583.
[26] Kline, S. J., and McClintock, F. A., 1953, ''Describing Uncertainties in Single-Sample Experiments,'' Mech. Eng. (Am. Soc. Mech. Eng.), **75** pp. 3–8.
[27] Modest, M. F., and Abakians, H., 1986, ''Heat Conduction in a Moving Semi-Infinite Plane Subjected to a Moving Gaussian Heat Source,'' ASME J. Heat Transfer, **108**, pp. 597–601.
[28] Anthony, T. R., and Cline, H. E., 1997, ''Surface Rippling Induced by Surface-Tension Gradients During Laser Surface Melting and Alloying,'' J. Appl. Phys., **48**, pp. 3888, 3894.
[29] Wei, P. S., Chang, C. Y., and Chen, C. T., 1996, ''Surface Ripple in Electron-Beam Welding Solidification,'' ASME J. Heat Transfer, **118**, pp. 960–969.

Using the Concept of Information to Optimally Design Experiments With Uncertain Parameters

A. F. Emery
University of Washington,
Seattle, WA 98195-2600
e-mail: emery@u.washington.edu

When thermal systems are described by models, it is necessary to know the properties and parameters of the model to ensure accurate results. These properties are usually determined from experiments designed to maximize the precision of the estimated properties. Achieving such high precision requires that all of the other properties be known with certainty. This paper describes a method of design and estimation based upon Fisher's concept of information that achieves good precision in estimating thermal properties even when the other parameters are known only approximately. [DOI: 10.1115/1.1370520]

Keywords: Experimental, Heat Transfer, Instrumentation, Measurement Techniques, Modeling

Webster [1] defines an experiment as ''an operation carried out under controlled conditions in order to discover an unknown effect or law, to test or establish a hypothesis, or to illustrate a known law.'' Today, enough is known about most physical processes that we can formulate mathematical models to describe the process with reasonable accuracy *if* the model parameters are known. Thus, most experiments are performed to deduce the properties or parameters of such models either to validate the model or to permit its use in prediction or interpolation. The determination of a model's parameters requires (1) that the experiments be designed to achieve maximum precision; and (2) that the parameter be estimated with as much precision as possible from the data. Because of constraints on the experiment, these two precisions are rarely equal and the latter is often much less than the former. In addition to the sought after parameters, the model will generally involve other parameters which are *presumed to be known* but are in fact uncertain. When the thermal response is highly nonlinear in either the parameters to be estimated or in the uncertain parameters the precisions can differ substantially. In the example presented in this paper, the thermal conductivity will be estimated from an experiment involving convective boundary conditions. Any imprecision in the knowledge of the boundary condition will be reflected in a reduced precision of the estimate of the conductivity. Thus it is necessary to utilize an approach which will minimize the dependence of the precision of the estimation upon the uncertainty of the *presumed to be known* parameters.

Emery et al. [2,3] presented a method, termed the ''Extended Information Method,'' for designing an experiment, by which the effect of uncertainty in the *presumed to be known* parameters was reduced. This method was shown to be very effective when the sensor location and sampling times were chosen appropriately, but to be of reduced effectiveness for non-optimal experiment designs. The reason for its reduced performance was not clear. This paper summarizes the use of Fisher's concept of information in designing experiments and shows that the reduced performance of the ''Extended Information Method'' is caused by the correlation inherently induced by the uncertain parameters.

The experimenter must be careful to distinguish between accuracy and precision. Accuracy refers to how close the estimated parameter is to the true value, while precision refers to how closely grouped different estimates of the parameter will be, i.e., the standard deviation of the estimate. Accuracy is strongly affected by bias errors, inexactness in measurements, etc., and can only be improved by careful attention to all of the details of the experiment and measurement system. Precision, on the other hand, can often be improved by careful design of the experimental protocol by use of statistical techniques. As a simple but nontrivial example, consider the measurement of the length of a bar. The precision of the estimated length, as defined by the standard deviation of the estimated length, can be improved by averaging several readings. Since the standard deviation of the average is given by $\sigma/\sqrt{N}$, where σ is the standard deviation of individual readings and N is the number of readings, extremely high precision can be achieved by basing the average on a large number of readings. Although in principle, N can be chosen large enough to yield nearly a zero standard deviation of the average, the improved precision must be balanced against the cost of the measurements. However, if the measuring device produces an erroneous measurement, nothing about the design for increased precision can eliminate this biased reading. The result of an experiment designed to produce a high level of precision by suitable averaging will be a precise but inaccurate estimate. Accordingly, in the development described in this paper it is assumed that all errors in accuracy have been eliminated.

The precision of the experimental design is measured by the standard deviation of the estimate of the value of the parameter. Given a parameter P, a function of two variables x_1 and x_2, the variance of P is given by the generalized variance equation [4]

$$\sigma_P^2=\left(\frac{\partial P}{\partial x_1}\right)^2\sigma_{11}^2+2\left(\frac{\partial P}{\partial x_1}\right)\left(\frac{\partial P}{\partial x_2}\right)\sigma_{12}^2+\left(\frac{\partial P}{\partial x_2}\right)^2\sigma_{22}^2, \qquad (1)$$

where σ_{ij}^2 represents the covariance of x_i and x_j. Following Fisher's suggestion [5], the inverse of the variance is termed the *Information*, $\mathcal{I}$ (sometimes called the *precision*).

$$\mathcal{I}\equiv 1/\sigma_P^2 \qquad (2)$$

and the aim will be to maximize $\mathcal{I}$ by (1) the choice of the experiment to be performed, the sensor locations, the reading times, and the responses sensed (e.g., temperature or heat flux), and (2) by the choice of the method to estimate the parameter from the data taking into account the uncertainty in other parameters. This approach will be demonstrated by the example of estimating the thermal conductivity of a material from transient temperature readings.

Contributed by the Heat Transfer Division for publication in the JOURNAL OF HEAT TRANSFER. Manuscript received by the Heat Transfer Division January 20, 2000; revision received November 28, 2001. Associate Editor: D. A. Zumbrunnen.

The Example Experiment

Consider a one-dimensional problem with constant properties and time independent boundary conditions. The region is a slab of thickness L, an initial temperature of zero, with convection to a zero temperature at $x=0$ with a convective coefficient of h_0, and at $x=L$ either a prescribed heat flux, Q, or convection from a fixed temperature of unity with a convective coefficient of h_0. The transient temperature histories will be measured at $x=0$ and L and the conductivity will be inferred from these measurements. The measured temperatures will be simulated by adding a zero mean, uncorrelated, gaussian noise with $\sigma_\epsilon/T_{\max}$ of 1 percent to the theoretical values based upon a Biot number of 1 or 10 at both $x=0$ and L, or a flux of $QL/k=1$. There is uncertainty in the convective heat transfer coefficient at $x=0$ but not at $x=L$.

Design of the Experiment

The temperature is a function of geometry, boundary and initial conditions, and properties. All variables that influence the temperature are referred to as ''parameters.''

$$T=F(x,y,z,t,\mathbf{P},\mathbf{B},\mathbf{Q}), \tag{3}$$

where $\mathbf{P}$ represents a vector of the parameters which we wish to estimate, $\mathbf{B}$ represents those which may be uncertain, and $\mathbf{Q}$ represents the fixed parameters whose values are certain. Either $\mathbf{B}$ or $\mathbf{Q}$ may be an empty set. T is assumed to be well behaved in Hadamard's sense, i.e., T is a smooth and well behaved function of all of the parameters and in particular, small changes in any parameter will produce correspondingly small changes in T. The statistics of $\mathbf{P}$ are defined in terms of the probability density distribution $f(\mathbf{P})$ by

$$\overline{\mathbf{P}}=E[\mathbf{P}]=\int \mathbf{P}f(\mathbf{P})d\mathbf{P}$$

$$\sigma_P^2=\int (\mathbf{P}-\overline{\mathbf{P}})^2 f(\mathbf{P})d\mathbf{P} \tag{4}$$

The estimate of $\mathbf{P}$ will be denoted as $\hat{\mathbf{P}}$ and the optimal design will be based upon minimizing the variance of $\hat{\mathbf{P}}$. We need to recognize that the optimal design cannot be developed without considering how $\hat{\mathbf{P}}$ is to be obtained from the data.

In the development that follows, $\mathbf{P}$ and $\mathbf{B}$ will be scalars, P and B, representing the thermal conductivity, k, and the heat transfer coefficient, h_0, respectively. The extension to vectors of parameters is straightforward.

Consider two methods of determining $\hat{P}$, the least squares method and the inverse method. For the usual least squares method the measured temperature is represented by the first term of the Taylor series about $\overline{P}$

$$T=F(\overline{P},\overline{B})+\epsilon$$

$$=\overline{T}+\left.\frac{\partial T}{\partial P}\right|_{\overline{P}}(P-\overline{P})+\epsilon, \tag{5}$$

where ϵ represents a zero mean, random measurement error. $\hat{P}$ is that value of P which minimizes the weighted least squares error

$$LS(P)=(\mathbf{T}-\overline{\mathbf{T}})^T\mathbf{W}^{-1}(\mathbf{T}-\overline{\mathbf{T}}), \tag{6}$$

where $\mathbf{W}$ is the covariance matrix of $\mathbf{T}$ whose elements are given by

$$W_{ij}=\sigma_\epsilon^2\delta_{ij}. \tag{7}$$

The variance of $\hat{P}$ is [6]

$$\Sigma\equiv \mathrm{var}[\hat{P}]=\left[\left(\frac{\partial\mathbf{T}}{\partial P}\right)^T\mathbf{W}^{-1}\left(\frac{\partial\mathbf{T}}{\partial P}\right)\right]^{-1}. \tag{8}$$

While it is clear that the precision is improved by minimizing $\partial P/\partial\mathbf{T}$, the search for the sensor locations and sampling times which would yield this minimum is no easy task. The search, which involves specifying the sensor positions and the sampling times, is complicated because the partial derivatives, $\partial\mathbf{T}/\partial P$ are evaluated at $\overline{P}$ which is unknown. In addition, this approach requires linearizing the temperature and for the highly non-linear relationship between $\mathbf{T}$ and P raises questions about the accuracy of the approach [7], although it can be shown that the weighted least squares method produces an unbiased estimate [8].

There is another way of approaching the problem. Equation (3) can be inverted, at least in principle, to yield the point estimators

$$P_i=G(T_i,\overline{B}). \tag{9}$$

If for each measured temperature, T_i, we solve for the corresponding value, P_i, we may fit these values to a constant, $\hat{P}$, using weighted least squares (this is equivalent to a weighted average). The variance of $\hat{P}$ is identical to that given by Eq. (8.)

If T_i is correlated with T_j because of correlated errors, then P_i will also be correlated with P_j. If there is no correlation, each new data point, T_k, or each new estimation, P_k, will increase the information by $1/\sigma_\epsilon^2$ or $1/\sigma_{P_k}^2$ respectively, and reduce Σ accordingly. However, if a correlation exists, each new data point contributes a reduced amount of information, and as the correlation approaches unity the contribution becomes zero and the precision of $\hat{P}$ is not increased. Although correlated errors can be treated by assuming that they obey some growth law, such as the autoregressive moving average [9], it is better to treat the entire problem as being represented by a stochastic differential Eq. [10,11], but this may lead to a totally intractable problem.

Information

In view of the above noted obstacles in choosing an experimental protocol which will reduce Σ, let us approach the problem by determining how the data contribute to Σ. The Cramér-Rao theorem [6,7,8] for unbiased estimators (which the weighted least squares will be, *only* if iterated to convergence) gives an upper bound to the precision

$$\Sigma^{-1}\leqslant\mathcal{I}\equiv -E\left[\frac{\partial^2}{\partial P^2}\ln f(\mathbf{T}|P)\right] \tag{10a}$$

$$\equiv -E\left[\frac{\partial^2}{\partial P^2}\ln f(\mathbf{T},P)\right], \tag{10b}$$

where $f(\mathbf{T}|P)$ is the marginal conditional probability density for $\mathbf{T}$ given the parameters P and the expectation is taken over all values of P. Eq. (10*a*) applies when P is assumed to be constant, but unknown while Eq. (10*b*) applies when P is assumed to be a random variable. From Bayes' law for conditional probabilities,

$$f(\mathbf{T},P)=f(\mathbf{T}|P)f(P) \tag{10c}$$

and the only difference between Eq. (10*a*) and (10*b*) is $f(P)$, termed the ''prior'' probability of P which represents our knowledge about P before we begin the experiment.

Marginalization

Now consider the case where there is uncertainty about B. The Taylor series in terms of P and B is

$$T=\overline{T}+\left.\frac{\partial T}{\partial P}\right|_{\overline{P}}(P-\overline{P})+\left.\frac{\partial T}{\partial B}\right|_{\overline{B}}(B-\overline{B})+\epsilon. \tag{11}$$

If one has little knowledge about B, then the experiment must be designed to determine both B and P, for instance using the D-optimality approach [12,13].

If the analyst has some idea about the value of B as defined by a prior probability density distribution, then the problem can be approached from a Bayesian point of view. The uncertain param-

eter B clearly affects the solution, yet it is a parameter which we are not seeking. Such parameters are called ''nuisance'' parameters and their effects are accounted for by integrating over all values of B to obtain the marginal probability $f(\mathbf{T}|P)$ which is defined as

$$f(\mathbf{T}|P)=\int_B f(\mathbf{T},B|P)dB. \tag{12a}$$

It is usual to assume that the measurement errors are Gaussian and uncorrelated. On the other hand, $f(B)$ may take a number of forms, e.g., gamma, beta, uniform, laplacian, or gaussian. The power of Eq. (10) is that it permits us to consider a realistic distribution for B. For example; if B represents the emissivity, it is restricted to the range of 0 to 1 and a gamma or beta distribution may be most appropriate.

Lacking specific information about B it is common to assume either that (*a*) B is a constant but unknown for which $f(B)$ = constant (maximal ignorance) or (*b*) that B is a random variable with $f(B)=N(\overline{B},\sigma_B^2)$ [14]. If ϵ and B are gaussian and uncorrelated and if the temperature can be represented by Eq. (11) (i.e., linear in P and B), the joint pdf $f(\mathbf{T},P,B)$ can be factored to yield

$$f(\mathbf{T}|P)=N\left(\overline{\mathbf{T}}+\left.\frac{\partial\mathbf{T}}{\partial P}\right|_{\overline{P}}(P-\overline{P}),\mathbf{W}\right)\times\int_{B_{\min}}^{B_{\max}}N\left(A\left(\frac{\partial\mathbf{T}}{\partial B}\right)^T\sigma_\epsilon^2\left(\mathbf{T}-\overline{\mathbf{T}}-\left.\frac{\partial\mathbf{T}}{\partial P}\right|_{\overline{P}}(P-\overline{P}),A\right)\right)dB, \tag{12b}$$

where

$$W_{ij}=\sigma_\epsilon^2\delta_{ij}+\left(\frac{\partial T_i}{\partial B}\right)\left(\frac{\partial T_j}{\partial B}\right)\sigma_B^2 \tag{12c}$$

and $A^{-1}=\sigma_{pr}[B]^{-2}+(\partial\mathbf{T}/\partial B)^T\sigma_\epsilon^{-2}(\partial\mathbf{T}/\partial B)$. If B is a constant, but unknown, $\sigma_{pr}[B]$ is set to ∞ in A. $f(\mathbf{T}|P)$ is dependent upon P through $\overline{\mathbf{T}}+\partial\mathbf{T}/\partial P|_{\overline{P}}(P-\overline{P})$ in the first term and through the rather complicated argument of the distribution in the integral. If the range of the integration, $B_{\min}$ to $B_{\max}$ is sufficiently wide about the mean value, the integral equals unity and is independent of P. Otherwise, the integral is a function of P and the differentiation required in Eq. (10) to evaluate $\mathcal{I}$ can be exceedingly difficult. As long as the measured temperatures do not differ too much from $\overline{\mathbf{T}}$ and P is close to $\overline{P}$, then if $B_{\min}\leqslant\overline{B}-3\sigma_B$ and $B_{\max}\geqslant\overline{B}+3\sigma_B$ the integral will be unity. This range must be physically realizable. For example, since the convective heat transfer coefficient must be positive, this limits the uncertainty in h to be such that $\overline{h}-3\sigma_h>0$.

Equation (10) also requires a knowledge of $f(P)$. If P is assumed to be constant but unknown and $\mathbf{T}$ and B are gaussian variables, Eq. (10*a*) reduces to an equality [6]

$$\Sigma^{-1}=\mathcal{I}=\left(\frac{\partial\mathbf{T}}{\partial P}\right)^T\mathbf{W}^{-1}\left(\frac{\partial\mathbf{T}}{\partial P}\right), \tag{13}$$

where $\mathbf{W}$ is given by Eq. (12*c*). Eq. (13) provides an upper bound to the precision. In many cases the achievable precision is significantly less. Because of the terms $\partial\mathbf{T}/\partial P$, $\mathcal{I}$ is automatically most sensitive to the dominant parameters of the model. From Eq. (12*c*), we see that there is a correlation and it depends upon σ_B. When there is no uncertainty in B, $\mathbf{W}$ is diagonal and each data point will contribute to the reduction of Σ. But when B is uncertain, the temperatures are correlated through the off-diagonal terms of $\mathbf{W}$ and the precision of the estimate, $\hat{P}$, will be reduced.

The result presented herein are based upon the Cramér-Rao theorem for unbiased estimators. Other estimators exist that have tighter bounds [6]. Biased estimators may also yield better precision [6,8,15]. The question of whether a more precise but biased (i.e., inaccurate) estimator is to be preferred to a less precise but unbiased estimator is a philosophical one and must be examined for each individual case and no general rules can be established. Most experimentalists prefer unbiased estimators based upon eliminating instrument bias, particularly since it is not often possible to uniquely characterize the effect of the bias on the estimated parameter. It must be remembered that using the least squares method for non-linear models introduces bias through the neglect of the higher order terms in the Taylor series expansion and that the maximum likelihood method introduces bias unless the number of readings are large.

Information Results

Figure 1(*a*) depicts the information contributed by each temperature reading as a function of sensor position and sampling time for an applied heat flux at $x=L$ when there is no uncertainty in h for $\mathrm{Bi}_0=10$. The normalized steady state sensitivities at $x=L$ are $k\partial T/\partial k=-1$ and $h\partial T/\partial h=-1/\mathrm{Bi}$ so this experiment is a realistic one for estimating k when Bi is much greater than 1. Because the temperatures are uncorrelated, the total information is simply the sum of the information provided by each sampled temperature. From the figure it is clear that the ideal sensor position is at $x=L$ and that the readings should be taken at long times. In fact, $\mathcal{I}$ is a maximum at steady state and has the value of $(x/L^2)/\sigma_\epsilon^2$.

If instead of applying a constant heat flux, the slab is heated by convection at $x=L$, the information history is as shown on Figure 1(*b*). Here we see that the information content rises very rapidly to a relatively constant value and that the sensors should be placed at $x=L$. However, the information contributed by each reading is

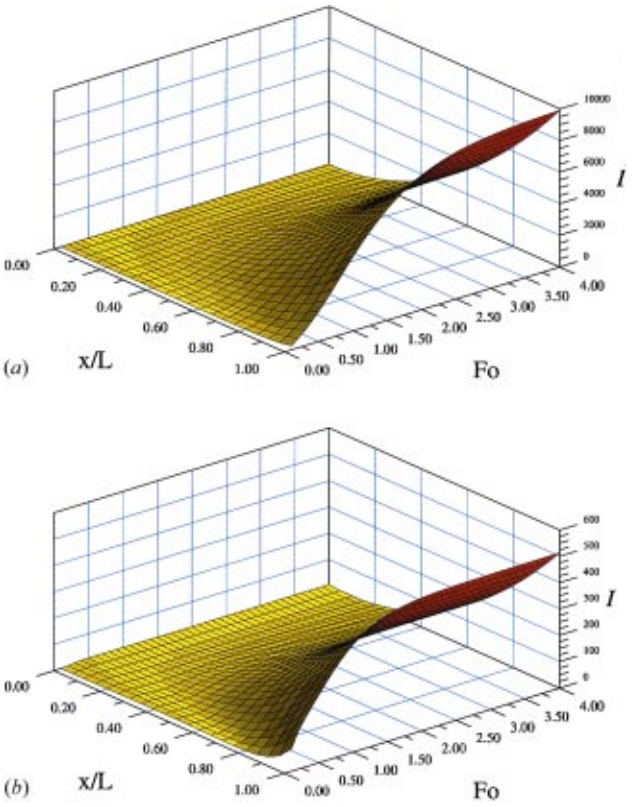

Fig. 1 (*a*) Information contributed by each temperature reading as a function of sensor position and sampling time for a heat flux applied at $x=L$ for $\mathrm{Bi}_0=10$ and $\sigma_h=0$; and (*b*) information contributed by each temperature reading as a function of sensor position and sampling time for convection at $x=L$ for $\mathrm{Bi}_0=\mathrm{Bi}_L=10$ and $\sigma_h=0$.

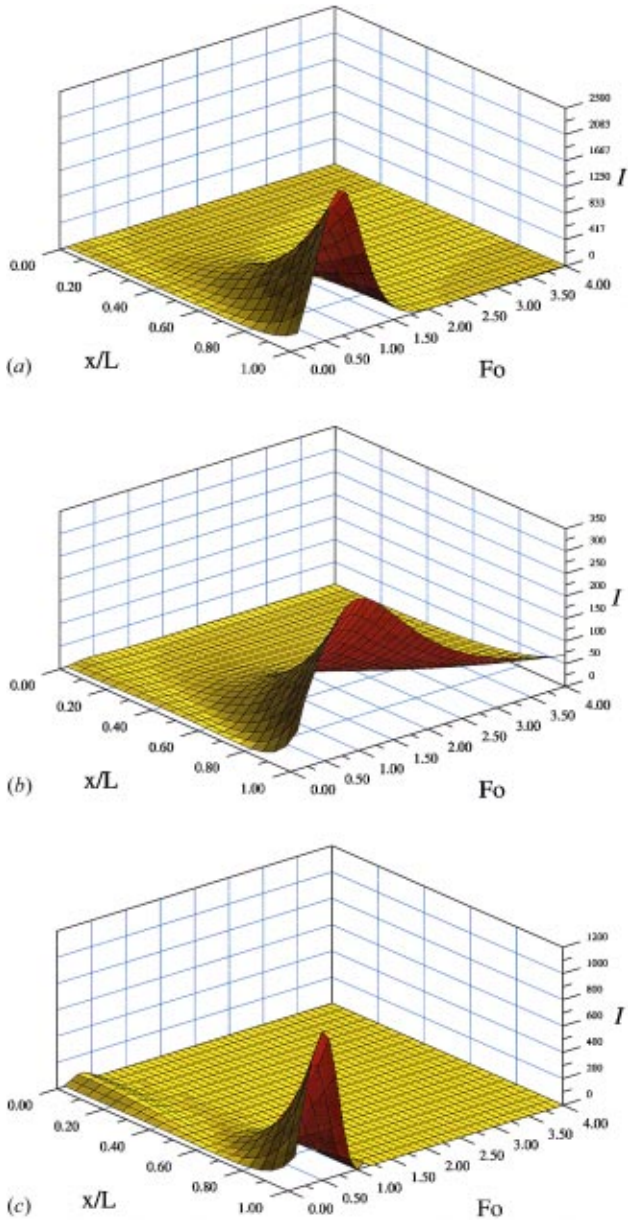

Fig. 2 (*a*) Information contributed by each temperature reading for a heat flux applied at $x=L$ for $Bi_0=10$ and $\sigma_h/\bar{h}_0=0.1$; (*b*) information contributed by each temperature reading for convection at $x=L$ for $Bi_0=Bi_L=10$, and $\sigma_h/\bar{h}_0=0.1$; and (*c*) information contributed by each temperature reading for convection at $x=L$ for $Bi_0=Bi_L=1$, and $\sigma_h/\bar{h}_0=0.1$.

more than an order of magnitude less than for the applied flux case and to achieve equal precision we will need to sample approximately 20 times more temperatures.

If there is uncertainty about the convection coefficient at $x=0$, the situation changes dramatically as shown in Fig. 2. For the prescribed heat flux, a sensor at $x=L$ is still preferable, but the information has been reduced by almost an order of magnitude and, more importantly, now shows a definite peak in time. The rapid reduction in information after the peak at $Fo=0.75$ and the essentially zero information at steady state is due to the correlation caused by σ_B. Clearly the readings should now be concentrated near $Fo=0.75$ where the information is maximum and reading should not be taken at longer times where they contribute little to the precision of the estimate of the conductivity. The convective boundary condition, Fig. 2(*b*), shows a similar peak but a slower reduction and some information can be gained from readings taken at longer times.

In principle one can compensate for the reduced information (and thus poor precision) by increasing the number of sampled temperatures near the peaks shown in Fig. 2. This point will be further discussed in the section on Higher Sampling Rates.

Because of the low sensitivity to h_0 when $Bi_0=10$ the conductivity k can be accurately estimated using either point estimators or the minimum variance approach. However, this low sensitivity does not eliminate the correlation produced by σ_h shown in Fig. 2. When the sensitivity to h_0 is high, e.g., for $Bi_0=1$, then not only is the information reduced, but it proves to be difficult to estimate k. The information for $Bi_0=1$ is illustrated in Fig. 2(*c*) and a comparison with Fig. 2(*a*) shows that (*a*) the information at $x=L$ is reduced and (*b*) there is now a very small amount of information available at $x=0$. The discussion in the rest of the paper is directed towards this case of $Bi_0=1$.

Estimating $\hat{k}$

The conductivity can be estimated in two ways, (*a*) the minimum variance approach and (*b*) point estimators. Minimizing the variance yields the estimator $\hat{P}$ given by

$$\hat{P}=E[P|\mathbf{T})=\int P f(P|\mathbf{T})dP \tag{14a}$$

$$=\int_B\int P f(P,B|\mathbf{T})dPdB \tag{14b}$$

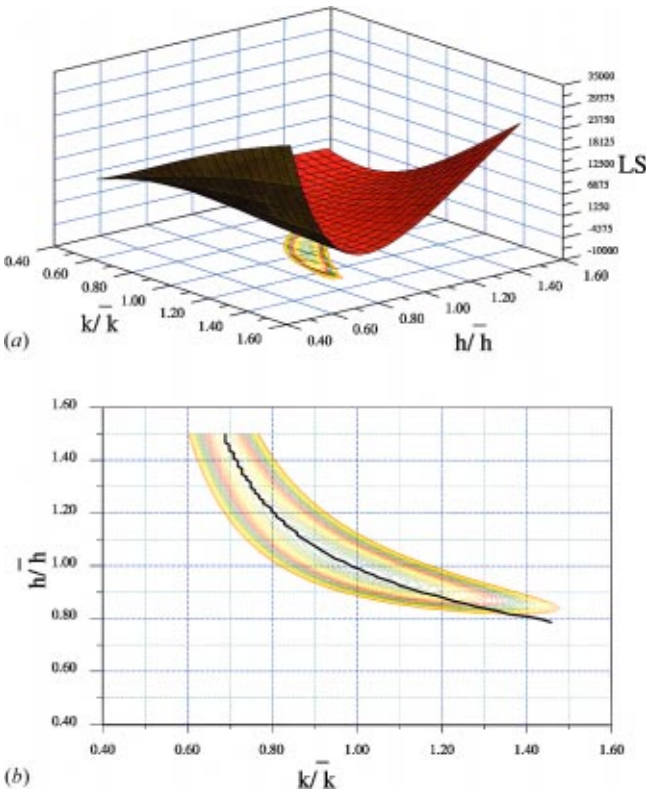

Fig. 3 (a) Values of *LS* as a function of *k* and *h* for a heat flux applied at $x=L$ using 20 temperatures measured at $x=L$ at equal time increments from 0 to $Fo=4.0$ for $Bi_0=1$ and $\sigma_h=0$; and (*b*) locus of minimum values of *LS* for a heat flux applied at $x=L$ as a function of *k* and *h* using 20 temperatures measured at $x=L$ at equal time increments from 0 to $Fo=4.0$ for $Bi_0=1$ and $\sigma_h=0$.

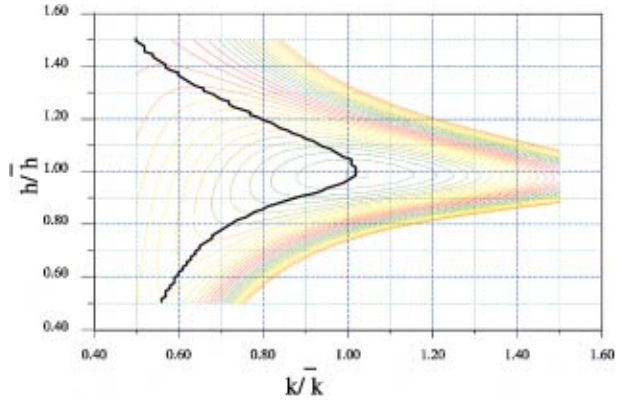

Fig. 4 Locus of minimum values of *LS* for a heat flux applied at $x=L$ as a function k and h using 20 temperatures measured at $x=L$ at equal time increments from 0 to Fo=2.0 for $Bi_0=1$ and $\sigma_h=0$

and the integration is taken over the range of B as described in the section above on marginalization. $f(P|\mathbf{T})$ must be determined from Bayes' rule for conditional probabilities and involves some rather complicated computations, almost always numerical.

If both $\mathbf{T}$ and P are Gaussian then $\hat{P}$ and its precision are given by

$$\hat{P}=\Sigma\left(\frac{\partial\mathbf{T}}{\partial P}\right)^T\mathbf{W}^{-1}\mathbf{T} \tag{14c}$$

$$\Sigma^{-1}=\sigma_{\mathrm{pr}}^{-2}[P]+\left(\frac{\partial\mathbf{T}}{\partial P}\right)^T\mathbf{W}\left(\frac{\partial\mathbf{T}}{\partial P}\right)$$

(if P is a constant, not a random variable, set $\sigma_{pr}[P]=\infty$). In more general situations, because of the difficulty in evaluating $f(P|\mathbf{T})$, it is common to have recourse to the maximum likelihood method in which $\hat{P}$ is found by minimizing

$$L(P)=\ln f(\mathbf{T}|P) \tag{15a}$$

$$=-\frac{1}{2}\ln(|\mathbf{W}|)-\frac{1}{2}(T-\overline{T})^T\mathbf{W}^{-1}(T-\overline{T}), \tag{15b}$$

where in Eq. (15*b*) a gaussian distribution for $\mathbf{T}$ has been assumed. $|\mathbf{W}|$ is the determinant of $\mathbf{W}$ where $\mathbf{W}$ is given by Eq. (12*c*) and the integration has been taken over B. The maximum likelihood method has some undesirable characteristics for small samples, but for reasonably large numbers of samples and when $\mathbf{T}$ and P are gaussian, it gives an unbiased estimation of P and has a precision of $\Sigma=\mathcal{I}^{-1}$

When $|W|$ is a constant, then the first term of Eq. (15*b*) may be ignored. When it is a function of P and B, its effect must be considered. However, in most of our studies its effect has been found to be minimal, but for large uncertainties in B its inclusion in Eq. (15) produces a slightly reduced dependence of $\hat{P}$ on B.

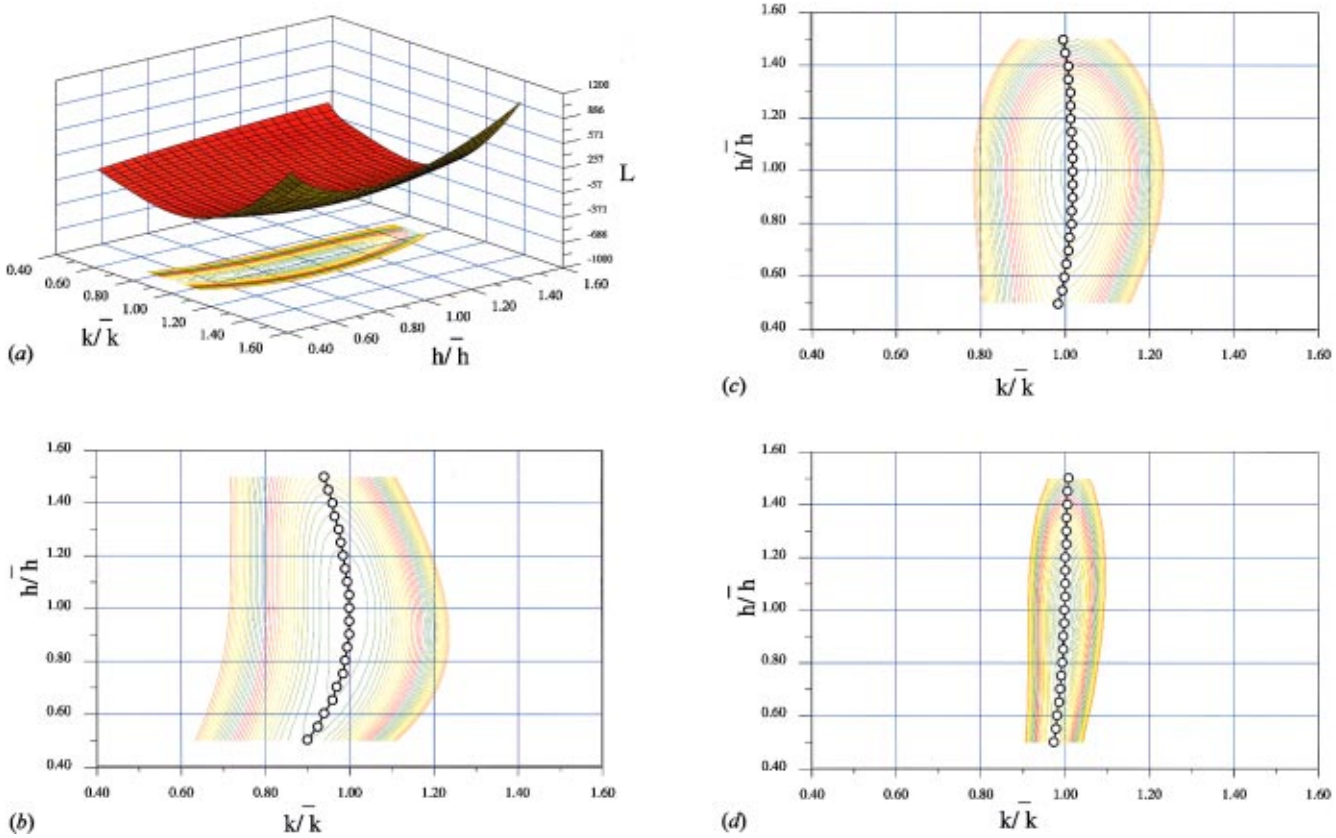

Fig. 5 (*a*) Values of L for a heat flux applied at $x=L$ as a function of k and h using 20 temperatures measured at $x=L$ at equal time increments from 0 to Fo=4.0 for $Bi_0=1$ and $\sigma_h/\bar{h}_0=0.1$; (*b*) locus of minimum values of L for a heat flux applied at $x=L$ as a function of k and h using 20 temperatures measured at $x=L$ at equal time increments from 0 to Fo=4.0 for $Bi_0=1$ and $\sigma_h/\bar{h}_0=0.1$; (*c*) locus of minimum values of L for a heat flux applied at $x=L$ as a function of k and h using 20 temperatures measured at $x=L$ at equal time increments from 0 to Fo=2.0 for $Bi_0=1$ and $\sigma_h/\bar{h}_0=0.1$; and (*d*) locus of minimum values of L for a heat flux applied at $x=L$ as a function of k and h using 20 temperatures measured at $x=0$ at equal time increments from 0 to Fo=4.0 for $Bi_0=1$ and $\sigma_h/\bar{h}_0=0.1$.

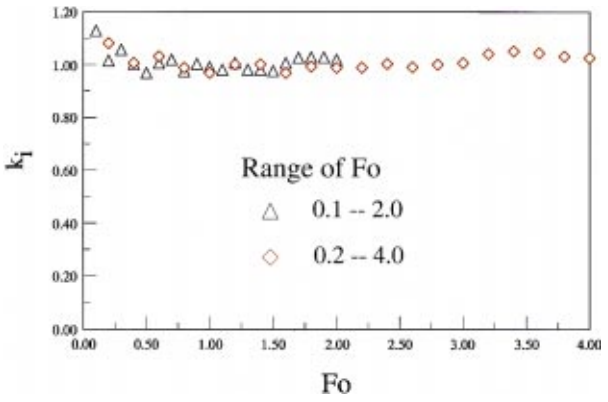

Fig. 6 Values of k_i computed from Eq. (9) for a sensor at $x=L$

The computation of T_i and $\partial T_i/\partial B$ in Eq. (12*c*) must be done for each sampling time and assumed value of *k*. For complex systems, the computation can be very expensive. If *h* is known precisely, then *L* reduces to *LS* whose minimization requires only a line search over the possible values of *k*. Furthermore, since *h* is known, the integration in Eqs. (12*a*) and (14*b*) is not needed. When *h* is uncertain, then we must not only perform the integrations, but must search over both *k* and *h* to find the minimum point. In addition, minimizing *L* involves inverting **W** which, because it is a highly correlated covariance matrix due to the term involving σ_h in Eq. (12*c*), is a very ill-conditioned matrix. Because of the expense of the computations, it is of interest to determine how strongly the value of *h* affects the results. Figure 3(*a*) depicts the variation of *LS* with *k* and *h* when the effect of a variable *h* is ignored (i.e., $\sigma_h=0$). The contours, displayed underneath the surface, are shown in Fig. 3(*b*) with the locus of the minimum values of *LS*, i.e., 10., the values of *k* for each *h*, displayed. It is seen that the estimated value of *k* varies very strongly with *h* and for some values of *h* no solution can be found.

Referring to Fig. 2(*a*), it is seen that very little information was contributed from the temperatures sampled at times greater than a Fourier number of 2.0. Let the 20 points be taken during the time of maximum information. The results are depicted on Fig. 4 and the estimates of *k* are improved for temperatures measured at $x=L$, but are still too dependent upon the choice of *h*.

Let us examine what happens when we minimize *L* where **W** includes the uncertainty in *h*. Figure 5 illustrates this behavior. $\hat{k}$ is now virtually independent of the choice of *h*, although there are small differences in accuracy as a function of sensor position and time. All of the figures depict equal contour levels. Using temperatures measured at long times, Fig. 5(*b*) clearly shows the degrading effect of measurements taken when the information content is low.

A noticeable improvement occurs when sampling is restricted to times of maximal information, Fig. 5(*c*). Since there is some information available at $x=0$ (Fig. 2(*c*)) it is of interest to see whether the conductivity can be estimated using such minimal information. Figure 5(*d*) displays the values of *L* for this case and the value of *k* is estimated well but the lack of information leads to a lower level of precision than that obtained using data from $x=L$.

Table 1 Statistics for estimation of *k* for temperatures measured at *x* for 20 equal time increments using $h=\bar{h}$

x	Fo	$\hat{k}$	$\hat{k}_d$	$\bar{k}$	$\sigma_{\hat{k}}$	$\sigma_{\hat{k}_d}$	$\sigma_{\bar{k}}$
L	0-4	1.009	1.009	1.003	1.09	1.03	0.60
L	0-2	1.003	1.004	1.006	1.05	0.79	0.81
0	0-4	0.964	0.941	1.004	3.43	5.62	3.12
0	0-2	0.988	0.982	0.969	3.84	3.79	4.02

Table 2 Statistics for estimation of *k* for temperatures measured at *x* for 20 equal time increments using $h=1.1\bar{h}$

x	Fo	$\hat{k}$	$\hat{k}_d$	$\bar{k}$	$\sigma_{\hat{k}}$	$\sigma_{\hat{k}_d}$	$\sigma_{\bar{k}}$
L	0-8	1.016	0.972	0.940	1.28	1.35	1.12
L	0-4	1.005	0.979	0.959	1.09	1.03	1.43
L	0-2	1.007	0.998	1.007	1.29	0.95	1.47
0	0-8	1.469	1.216	3.845	3.76	8.72	72.36
0	0-4	0.496	1.213	2.831	3.44	5.62	56.05
0	0-2	0.947	1.120	1.219	3.85	3.79	7.48

The second approach to estimating the conductivity is to determine P_i by solving the inverse equation, Eq. (9). The results are shown on Fig. 6 where the values are tightly grouped about the mean regardless of the sampling period. Both sets of data are weighted least squares fit to determine $\hat{k}$ and the statistics of the fit are listed in Table 1. $\hat{k}$ refers to values fit with **W** given by Eq. (12*c*), $\hat{k}_d$ using only the diagonal terms of **W** and $\bar{k}$ to an unweighted fit.

As expected, estimating k_i using the correct value of *h* yields good results regardless of the fitting method. However, if *h* is incorrectly specified, the results differ substantially as shown in Table 2. When the estimates are based upon temperature readings for which the information content is high, the values obtained using Eq. (12*c*) are good regardless of the period over which the readings were taken. When the off-diagonal terms of **W** dominate the weighting and the assumed value of *h* is in error, the values of k_i tend to diverge with time. A good rule of thumb is to use only those point estimates which show scatter about some mean value and do not show a diverging trend.

The very good results obtained from the maximum likelihood principle using **W** from Eq. (12*c*) and measuring temperatures at times of maximal information, are typical of the different problems that we have examined. These problems involved one- and two-dimensional temperature calculations with uncertainties in convective heat transfer coefficients, ambient temperatures, surface emissivity, applied heat fluxes, specific heat capacities, and sensor locations.

Higher Sampling Rates

It is clear from what has been developed thus far, that the precision is a function both of the design (e.g., boundary conditions, sensor locations, etc.) and the number of readings, *N*. If for a specific design, the precision is not sufficient, then the most obvious tactic is to increase *N*. However, if the information is concentrated in a relatively short time period, increasing *N* means reducing the interval between the readings, i.e., increasing the sampling rate. This increased sampling rate involves two important aspects: (1) the measuring device must be capable of responding accurately to the higher rate, and (2) the use of Eq. (15) requires handling ever larger matrices since **W** is of order $N \times N$. Probably more importantly, the increased sampling rate will generally increase the degree of serial correlation in both ϵ and *B* and thus the ill-conditioning of the covariance matrix. Serially correlated data is fairly extensively treated in the literature where a common approach is to assume that the correlation depends only on $|i-j|$, where *i* and *j* denote the samples, and to assume that the correlation is zero when $|i-j|$ exceeds a certain value specified in an ad-hoc fashion by the experimenter, thus producing a banded covariance matrix. Because of the form of the correlation of Eq. (12*c*), the band is generally so wide that the method is not robust.

In the Extended Information Method of Emery et al. [2,3] the problem was approached by simply ignoring the correlations and treating **W** as a diagonal matrix, that is

$$W_{ij}=\sigma_\epsilon^2\delta_{ij}+\left(\frac{\partial T_i}{\partial B}\right)\left(\frac{\partial T_i}{\partial B}\right)\sigma_B^2. \tag{16}$$

We have found through examining a wide range of problems that Eq. (16) generally gives a reasonably accurate estimate of the

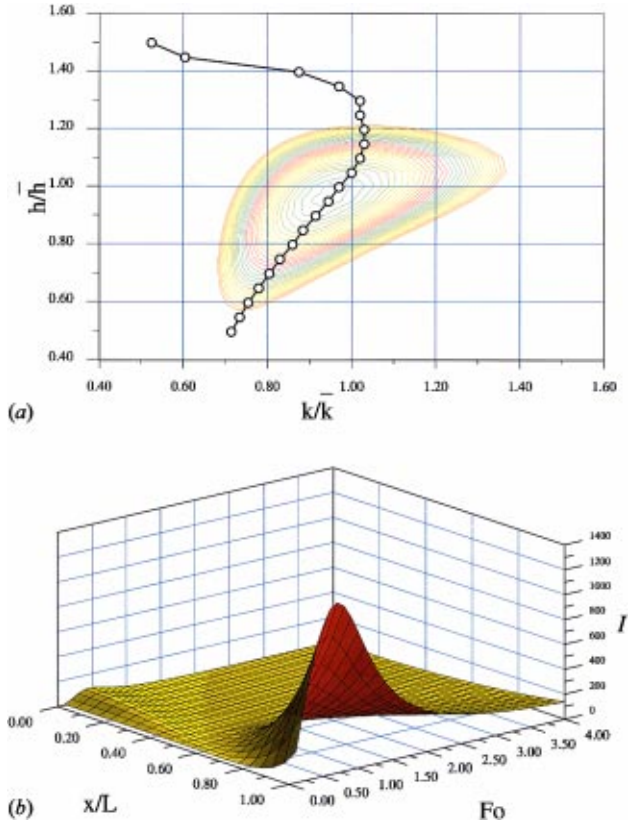

Fig. 7 (*a*) **Locus of minimum values of *L* for a heat flux applied at $x=L$ as a function of *k* and *h* using 20 temperatures measured at $x=L$ at equal time increments from 0 to Fo=2.0 for $Bi_0=1$ and $\sigma_h/\bar{h}_0=0.1$ using Eq. (16); and (*b*) increment of Information provided by a temperature read at Fo for a heat flux applied at *L* for $Bi_0=1$ and $\sigma_h/\bar{h}_0=0.1$ using Eq. (16).**

information and often can be used to obtain a preliminary estimate of the parameter. The question is how to know when Eq. (16) is sufficient. Figure 7(*a*) illustrates the estimation of *k* when this diagonal form of **W** matrix is used.

Comparing Fig. 7(*a*) with Fig. 4(*b*), shows that the sensitivity to the assumed value of *h* is unacceptably high and Eq. (16) offers no improvement over using *LS*. Fortunately, it is easy to determine when Eq. (16) can be used. Since *L* is asymptotically gaussian, if **W** is an accurate representation of the covariance, then $F(=LS(\hat{P})/\sigma_\epsilon^2)$ has a chi-squared distribution with a mean equal to the number of degrees of freedom and a variance of 2N [16]. If **W** is not accurate and there is a high degree of correlation, then *F* will be a much smaller value. Our tests of different problems have demonstrated that whenever the values differ at the 90 percent level of significance, that Eq. (15), with the off-diagonal elements of **W**, must be used for the estimation.

However, even in these cases Eq. (16) does give a sufficiently accurate indication of the information content of each reading, as shown in Fig. 7(*b*) to produce an effective experiment design, compare with Fig. 2(*c*). Schlegel [17] showed that the precision determined using only the diagonal elements is always less than that based upon the full matrix, and thus Eq. (16) gives a conservative estimate of the precision.

Non-Linearities

One point not addressed is the effect of the non-linear nature of the dependence of the parameters on the temperature. Most of the development of parameter estimation assumes that the parameters are linear functions of the data or that a linearized solution is possible. One of the problems caused by the nonlinearity is the existence of multiple minima of *L* and *LS*. The existence of multiple minima affects both the parameter estimation and the experiment design based upon the information content. Because of the highly nonlinear nature of heat transfer, this problem occurs quite often and considerable care must be exercised. Since the global minimum does yield the optimal estimate of the parameter, the more critical question is whether the design is adversely affected by the non-linearities. Emery [2] has examined the case of the convective boundary condition where $\mathcal{I}$ varied strongly with position (Fig. 1(*b*)) and showed that regions of high nonlinearity were also regions of low information and regions of moderate to high amounts of information were quite linear. Since the amount of information is proportional to the sensitivity, i.e., to $\partial T/\partial P$, it is clear from Eq. (5), that this finding is general. Thus we speculate that basing sensor placement and sampling times on designs which yielded maximal values of information would avoid the problem of non-linearities. This has proven true for all of the cases we have studied, but remains in question for more complex problem, particularly when seeking to estimate multiple parameters.

Conclusions

The design of an experiment must consider the process of estimation and must balance two conflicting needs. First, one wishes to use data whose information content has not been seriously degraded by uncertainty in some parameters. Thus, in the example problem a sensor at $x=L$ is preferable to one at $x=0$, Fig. 2(*a*). On the other hand, the estimation should be done with data which is associated with a covariance matrix **W** which contains sufficient information about the effect of the uncertain parameter to result in *L* being insensitive to the uncertain parameter, the sensor at $x=0$ in this case. The recommended procedure is to choose several sets of data which have reasonable amounts of information then to use each set with a simulated noise to determine which provides the best estimates.

The estimation of one or more properties can be done with confidence, even if other required parameters are uncertain, when Eq. (15) is used. The drawback is that the full covariance matrix must be inverted and it is not possible to predict in advance what the contribution from any single temperature reading is because of its serial correlation with the other temperatures. Figure 2(*a*) shows that the information drops and then recovers slightly as time proceeds. We have found that the best design is based upon the initial high information zone with decreasing emphasis on the region of recovered information since that is when the correlation increases to an unsatisfactory level.

When the degree of correlation is sufficiently small, Eq. (16) can be used, at least to design the experiment and often to estimate the parameter. In this case, the temperature readings are independent and the contribution to the total information can be estimated independently of the other readings. This provides one with a computationally acceptable method of designing the experiment, even if Eq. (15) must be used to perform the actual estimation.

When the effect of the uncertain parameter is large, then there is no choice but to design an experiment to estimate both *P* and *B*. This can be done using the *D*-optimality metric as described in [12,13].

Nomenclature

$\mathbf{B}$ = vector of uncertain parameters
Bi_0, Bi_L = Biot number at $x=0$ and *L* respectively
$E[\mathbf{x}]$ = expected value of *x*
$f(P)$ = probability density (pdf) of *P*
F_0 = Fourier number
h = convective heat transfer coefficient
k = thermal Conductivity
$\mathcal{I}$ = information

$\mathbf{N}(\mathbf{a},\mathbf{b})$ = Gaussian distribution with a mean of **a** and a variance of **b**
$\underline{\mathbf{P}}$ = vector of sought after parameters
$\overline{\mathbf{P}}$ = mean value of **P**
$\hat{\mathbf{P}}$ = estimated value of **P**
$\mathbf{Q}$ = vector of certain parameters
T = temperature
$\mathbf{T}$ = vector of temperatures
$\mathbf{T}^T$ = transpose of **T**
$\mathbf{W}$ = covariance matrix of **T**
ϵ = noise
σ_B = standard deviation of B
σ_ϵ = standard deviation of the noise
$\sigma_{pr}[x]$ = standard deviation of the prior distribution of x
$\hat{\boldsymbol{\Sigma}}$ = covariance matrix of $\hat{\mathbf{P}}$

References

[1] Meriam-Webster Online, (dictionary entry), **http://www.webster.com**
[2] Emery, A. F., and Nenarokomov, A. V., 1998, ''Optimal Experiment Design,'' Meas. Sci. Technol., **9**, pp. 864–876.
[3] Emery, A. F., Nenarokomov, A. V., and Fadale, T. D., 1999, ''Uncertainties in Parameter Estimation: The Optimal Experiment Design,'' to be published in Int. J. Heat Mass Transf.
[4] Coleman, H. W., and Steele, W. G., Jr., 1989, *Experimentation and Uncertainty Analysis for Engineers*, J. Wiley and Sons, New York.
[5] Fisher, R. A., 1990, *Statistical Methods, Experimental Design, and Scientific Inference*, J. H. Bennett, ed., Oxford University Press, Oxford.
[6] Sorenson H. W., 1980, *Parameter Estimation: Principles and Problems*, Marcel Dekker, Inc., New York.
[7] Deutsch, R., 1965, *Estimation Theory*, Prentice-Hall, Englewood Cliffs, NJ.
[8] Papoulis, A., 1991, *Probability, Random Variables, and Stochastic Processes*, McGraw-Hill, New York.
[9] Walter, E., and Pronzato, L., 1997, *Identification of Parametric Models From Experimental Data*, Springer Publishing, NY.
[10] Lin, Y. K., and Cai, G. Q., 1995, *Probabilistic Structural Dynamics, Advanced Theory and Applications*, McGraw-Hill Book Co., New York, NY.
[11] Seber, G. A. F., and Wild, C. J., 1989, *NonLinear Regression*, J. Wiley and Sons, New York, NY.
[12] Atkinson, A. C., and Donev, A. N., 1989, *Optimum Experimental Designs*, Oxford University Press, NY.
[13] Emery, A. F., and Fadale, T. D., 1996, ''Design of Experiments Using Uncertainty Information,'' ASME J. Heat Transfer, **118**, pp. 532–538.
[14] Sivia, D. S., 1996, *Data Analysis, A Bayesian Tutorial*, Clarendon Press, Oxford.
[15] Vinod, H. D., and Ullah, A., 1981, *Recent Advances in Regression Methods*, Marcel Dekker, Inc., New York, NY.
[16] Guttman, I., Wilks, S. S., and Hunter, J. S., 1971, *Introductory Engineering Statistics*, J. Wiley and Sons, New York.
[17] Schlegel, L. B., 1963, ''Covariance Matrix Approximations,'' AIAA J., **1**, No. 11, pp. 2672–2673.

Journal of Heat Transfer

Technical Notes

This section contains shorter technical papers. These shorter papers will be subjected to the same review process as that for full papers.

Performance Analysis and Optimization of Annular Fin With a Step Change in Thickness

B. Kundu
Department of Mechanical Engineering, Jalpaiguri Government Engineering College, Jalpaiguri-735102, West Bengal, India

P. K. Das
Department of Mechanical Engineering, Indian Institute of Technology, Kharagpur-721302, India
e-mail: pkd@mech.iitkgp.ernet.in

The temperature distribution in a concentric annular fin with a step change in thickness (AFST) has been obtained analytically. The optimum design of such fins has been performed using Lagrange multiplier technique considering either the fin volume or the rate of heat transfer as the constraint. It has been demonstrated that the optimum AFSTs transfer more heat compared to optimum annular disc fins for a given fin volume as well as for given fin volume and fin length. [DOI: 10.1115/1.1351165]

Keywords: Analytical, Augmentation, Conduction, Finned Surfaces, Heat Transfer, Optimization

Introduction

Concentric annular or radial fins are employed to improve the rate of heat transfer from the external surface of a circular tube. Such fins are commonly used in finned tube cross-flow heat exchangers. The analysis of concentric annular fins with common profile shapes namely, rectangular, triangular, concave and convex parabolic and hyperbolic are available in a number of references [1,2]. Substantial amount of research endeavors have also been made to find out the optimal dimensions of radial fins so that the rate of heat transfer can be maximized for a given fin volume or the fin volume can be minimized for a specified heat duty. Based on calculus of variation, the profile of optimum radial fin has been determined [3–6]. However, the use of fins with optimum profile is restricted due to the associated difficulty of manufacturing. In a parallel effort, optimum dimensions of radial fins have been determined where profile shapes have been specified apriori. Brown [7] has provided the optimum design of radial fins with a rectangular profile. Ulman and Kalman [8] determined optimum dimensions of annular fins with triangular, parabolic as well as hyperbolic profiles using numerical techniques. Kundu and Das [9] have determined the optimum dimensions of eccentric annular disc fins and demonstrated that for a given volume such fins can dissipate more heat compared to concentric annular disc fins when there is a space restriction on one side of the tube. Hollands and Stedman [10] has proposed a design of longitudinal fin with a step reduction in thickness towards the fin tip. For identical efficiency such a fin requires less material compared to a constant thickness fin. A similar profile can also be adopted for radial fins.

In the present work the thermal analysis of concentric annular fins with a step change in thickness (AFST) is presented. The temperature distribution in the fin is obtained as a closed form expression based on one-dimensional conduction. Optimum design of AFSTs have been made both with and without a restriction on fin length. It has further been shown that AFSTs promise material saving when used in lieu of constant thickness annular fins.

Mathematical Analysis

Figure 1 schematically depicts a concentric AFST. The fin has a constant thickness t from the fin base up to radius r_1, beyond that the fin thickness is $pt(0<p\leqslant 1)$ up to the tip. It is assumed that the fin exchanges heat with ambient medium (existing at constant temperature) solely by convection and the coefficient of convective heat transfer is uniform along the fin surface. The nondimensional temperature of the fin is as follows:

$$\theta_1=\frac{T_1-T_a}{T_b-T_a};\quad \theta_2=\frac{T_2-T_a}{T_b-T_a}, \tag{1}$$

where T_a is the ambient temperature, T_b is the fin base temperature, and T_1 and T_2 are the local fin temperature for the intervals $r_i\leqslant r\leqslant r_1$ and $r_1\leqslant r\leqslant r_2$, respectively.

Under steady state operation and for constant conductivity of the fin material, following differential equations in dimensionless form may be obtained for the temperature functions θ_1 and θ_2.

$$\begin{bmatrix} \frac{d}{dR}\left(R\frac{d\theta_1}{dR}\right) \\ \frac{d}{dR}\left(R\frac{d\theta_2}{dR}\right) \end{bmatrix} = \begin{bmatrix} Z_0^2R\theta_1 \\ \frac{Z_0^2R\theta_2}{p} \end{bmatrix} \quad \begin{matrix} 1\leqslant R\leqslant R_1 \\ R_1\leqslant R\leqslant R_2;\quad 0<p\leqslant 1, \end{matrix} \tag{2}$$

where

$$Z_0=\sqrt{\frac{\mathrm{Bi}}{T}},\quad T=\frac{t}{r_i},\quad \mathrm{Bi}=\frac{hr_i}{k},\quad R=\frac{r}{r_i},\quad R_1=\frac{r_1}{r_i}$$

$$\text{and}\quad R_2=\frac{r_2}{r_i}.$$

The above governing differential equation is subjected to the following boundary condition

Contributed by the Heat Transfer Division for publication in the JOURNAL OF HEAT TRANSFER. Manuscript received by the Heat Transfer Division August 10, 1999; revision received October 26, 2000. Associate Editor: D. Zumbrunnen.

$$\text{at} \quad R=1, \quad \theta_1(R)=1 \tag{3}$$

$$\text{at} \quad R=R_1, \quad \theta_1(R)=\theta_2(R) \tag{4}$$

$$\text{and} \quad \frac{d\theta_1}{dR}=p\frac{d\theta_2}{dR}-\mathrm{Bi}_1(1-p)\theta_1 \tag{5}$$

$$\text{at} \quad R=R_2, \quad \frac{d\theta_2}{dR}=-\mathrm{Bi}_2\theta_2, \tag{6}$$

where $Bi_1=h^j r_i/k$, $Bi_2=h^t r_i/k$, and h^j and h^t are the heat transfer coefficients at the junction and tip respectively. Equation (6) can take care of no loss or convective condition at the tip. It may be noted that the boundary conditions Eq. (4) and Eq. (5) indicates the continuity of temperature and heat flux at the intermediate radius R_1, where the step change in thickness occurs.

Solving Eq. (2) along with the boundary conditions, the temperature profile can be written as

$$\theta_1(R)=\frac{D_1(R)[(D_3'(R_1)+\mathrm{Bi}_1)p-D_2'(R_1)-\mathrm{Bi}_1]+pD_1'(R_1)D_2(R)}{pD_3'(R_1)-D_2'(R_1)-\mathrm{Bi}_1+p\mathrm{Bi}_1} \tag{7}$$

$$\theta_2(R)=\frac{D_1'(R_1)D_3(R)}{pD_3'(R_1)-D_2'(R_1)-Bi_1+pBi_1}, \tag{8}$$

where

$$D_1(R)=\frac{I_0(Z_0R)K_0(Z_0R_1)-I_0(Z_0R_1)K_0(Z_0R)}{I_0(Z_0)K_0(Z_0R_1)-I_0(Z_0R_1)K_0(Z_0)} \tag{9}$$

$$D_2(R)=\frac{I_0(Z_0)K_0(Z_0R)-I_0(Z_0R)K_0(Z_0)}{I_0(Z_0)K_0(Z_0R_1)-I_0(Z_0R_1)K_0(Z_0)} \tag{10}$$

$$D_3(R)=\frac{Z_0F_1+\sqrt{p}\mathrm{Bi}_2F_2}{Z_0F_3+\sqrt{p}\mathrm{Bi}_2F_4} \tag{11}$$

$$F_1=I_0\left(\frac{Z_0R}{\sqrt{p}}\right)K_1\left(\frac{Z_0R_2}{\sqrt{p}}\right)+I_1\left(\frac{Z_0R_2}{\sqrt{p}}\right)K_0\left(\frac{Z_0R}{\sqrt{p}}\right) \tag{12}$$

$$F_2=I_0\left(\frac{Z_0R_2}{\sqrt{p}}\right)K_0\left(\frac{Z_0R}{\sqrt{p}}\right)+I_0\left(\frac{Z_0R}{\sqrt{p}}\right)K_0\left(\frac{Z_0R_2}{\sqrt{p}}\right) \tag{13}$$

$$F_3=I_0\left(\frac{Z_0R_1}{\sqrt{p}}\right)K_1\left(\frac{Z_0R_2}{\sqrt{p}}\right)+I_1\left(\frac{Z_0R_2}{\sqrt{p}}\right)K_0\left(\frac{Z_0R_1}{\sqrt{p}}\right) \tag{14}$$

and

$$F_4=I_0\left(\frac{Z_0R_2}{\sqrt{p}}\right)K_0\left(\frac{Z_0R_1}{\sqrt{p}}\right)-I_0\left(\frac{Z_0R_1}{\sqrt{p}}\right)K_0\left(\frac{Z_0R_2}{\sqrt{p}}\right), \tag{15}$$

where I and K are the modified Bessel functions of the first and second kind respectively. The prime means derivative with respect to R.

Heat transfer rate through the fin base q, is given by

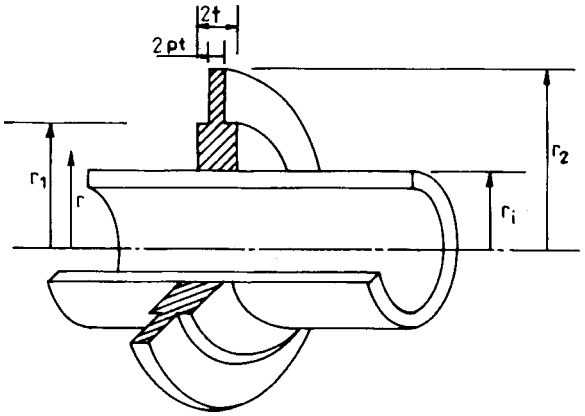

Fig. 1 Annular fin with a step change in thickness

$$Q=\frac{q}{4\pi r_i k(T_b-T_a)}=-T\left.\frac{d\theta_1}{dR}\right|_{R=1}=-T\frac{B_1}{B_2}, \tag{16}$$

where

$$B_1=\begin{vmatrix} D_1'(1) & D_2'(1) & 0 \\ -D_1'(R_1) & -D_2'(R_1)-\mathrm{Bi}_1 & D_3'(R_1)+\mathrm{Bi}_1 \\ 0 & -p & 1 \end{vmatrix} \tag{17}$$

$$B_2=\begin{vmatrix} 1 & -\mathrm{Bi}_1 & -\mathrm{Bi}_1 \\ 0 & p & 1 \\ 1 & D_2'(R_1) & D_3'(R_1) \end{vmatrix} \tag{18}$$

$$D_1'(R)=Z_0\left[\frac{I_1(Z_0R)K_0(Z_0R_1)+I_0(Z_0R_1)K_1(Z_0R)}{I_0(Z_0)K_0(Z_0R_1)-I_0(Z_0R_1)K_0(Z_0)}\right] \tag{19}$$

$$D_2'(R)=-Z_0\left[\frac{I_0(Z_0)K_1(Z_0R)+I_1(Z_0R)K_0(Z_0)}{I_0(Z_0)K_0(Z_0R_1)-I_0(Z_0R_1)K_0(Z_0)}\right] \tag{20}$$

and

$$D_3'(R)=\frac{Z_0}{\sqrt{p}} \times \begin{vmatrix} Z_0 & 0 & \sqrt{p}\mathrm{Bi}_2 \\ I_0(Z_0R_2/\sqrt{p}) & I_1(Z_0R/\sqrt{p}) & I_1(Z_0R_2/\sqrt{p}) \\ -K_0(Z_0R_2/\sqrt{p}) & K_1(Z_0R/\sqrt{p}) & K_1(Z_0R_2/\sqrt{p}) \\ \hline Z_0 & 0 & \sqrt{p}\mathrm{Bi} \\ I_0(Z_0R_2/\sqrt{p}) & I_0(Z_0R_1/\sqrt{p}) & -I_1(Z_0R_2/\sqrt{p}) \\ K_0(Z_0R_2/\sqrt{p}) & K_0(Z_0R_1/\sqrt{p}) & K_1(Z_0R_2/\sqrt{p}) \end{vmatrix}. \tag{21}$$

The rate of heat transfer through the fin becomes maximum if its surface is maintained at its base temperature.

$$Q_i=\frac{q_i}{4\pi r_i k(T_b-T_a)}=\frac{R_2^2+2\mathrm{Bi}_1TR_1(1-p)+2pR_2\mathrm{Bi}_2T-1}{2}. \tag{22}$$

The fin efficiency is defined in a conventional manner as follows:

$$\eta=\frac{Q}{Q_i}. \tag{23}$$

Optimization

Based on the above analysis the optimum design of the fins can be achieved for a better utilization of the fin material.

The fin volume can be expressed in a dimensionless form

$$U=\frac{V}{2\pi r_i^3}=T[R_1+pR_2^2-pR_1^2-1]. \tag{24}$$

If the base radius (r_i), the surface heat transfer coefficients and the thermal conductivity are specified, both the fin volume and the rate heat transfer depend on t, p, r_1, and r_2. This constitutes a four variable one constraint optimization problem treating either the fin volume or the rate of heat transfer as the constraint equation. Following the methodology of Stoecker [11] the condition of optimality can be derived using Lagrange multipliers. Elimination of the multiplier gives the following expressions:

$$\begin{bmatrix} T\frac{\partial B_1}{\partial R_1}+Q\frac{\partial B_2}{\partial R_1} & -2R_1T(1-p) \\ T\frac{\partial B_1}{\partial R_2}+Q\frac{\partial B_2}{\partial R_2} & 2pTR_2 \\ T\frac{\partial B_1}{\partial p}+Q\frac{\partial B_2}{\partial p} & -T(R_1^2-R_2^2) \end{bmatrix} \begin{bmatrix} R_1^2+pR_2^2-pR_1^2-1 \\ T\frac{\partial B_1}{\partial T}+Q\frac{\partial B_2}{\partial T}+B_1 \end{bmatrix} = \begin{bmatrix} 0 \\ 0 \\ 0 \end{bmatrix}. \tag{25}$$

The above equation is a non-homogeneous nonlinear algebraic equation. The optimum fin dimensions can be obtained either by maximizing heat transfer rate for a given fin volume or minimizing fin volume for a given heat transfer duty. Therefore, the real roots of Eq. (25) can be determined by solving either Eq. (16) or Eq. (24) according to the requirement of the designers. This has been done by an iterative technique known as Newton-Raphson method [13]. During computations the initial values of the real roots have been chosen in such a way that at each step of this iteration the convergence criteria [13] is satisfied. Finally, the above solution gives the optimum values of T, p, R_1, and R_2. It may also be mentioned that caution has to be taken for the selection of the initial values of the roots nearer to the optimum values otherwise the solution may be diverged.

Results and Discussion

From the above analysis the thermal performance as well as the optimum dimensions of radial fins with a step change in thickness have been determined for a wide range of parameters. Some typical results are discussed below. All the computations in the present work are based on $Bi_1=Bi_2=Bi$, unless otherwise mentioned.

In Fig. 2 the temperature profile of a typical AFST with a step change in thickness at the midlength of the fin and for a thickness ratio (p) of 0.5 has been depicted. The temperature profile of a constant thickness annular fin with the same volume and Biot number has also been presented beside a comparison. In case of the AFST, an abrupt change in temperature gradient is observed where the step change in thickness occurs. However, at any radial distance the temperature of the AFST is higher than that of the constant thickness fin indicating a higher rate of heat dissipation from the former. It may be mentioned that the Schmidt criteria [12] for an optimum fin is a constant temperature gradient. However, for an annular disc fin the temperature gradient decreases from the base to the tip. On the other hand, Fig. 2 shows that a

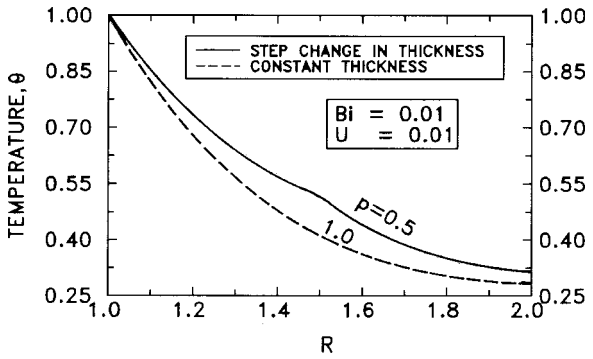

Fig. 2 Temperature distribution of AFST

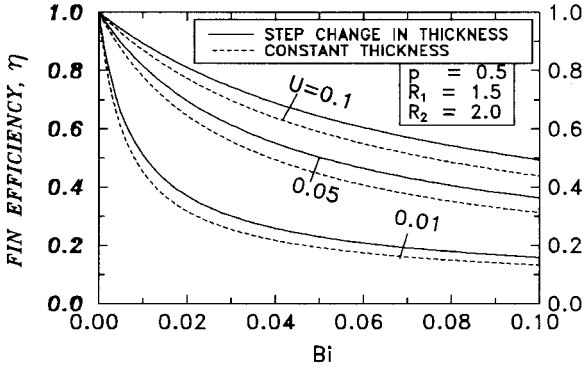

Fig. 3 Comparison between concentric fins and AFSTs with same fin volume and outer radius

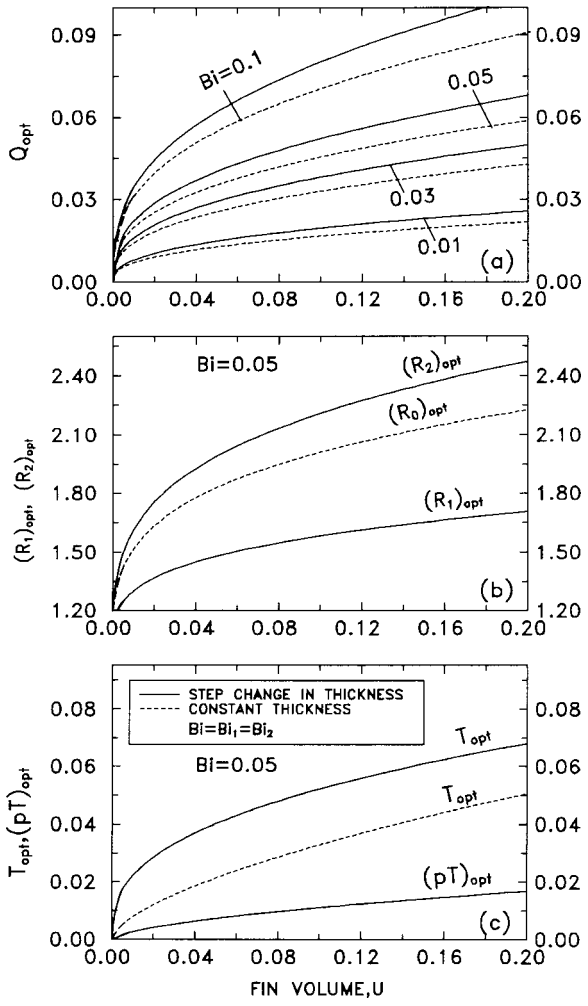

Fig. 4 Variation of optimum design parameters of AFSTs with fin volume: (*a*) maximum heat transfer rate; (*b*) optimum radius ratio; and (*c*) optimum fin thickness

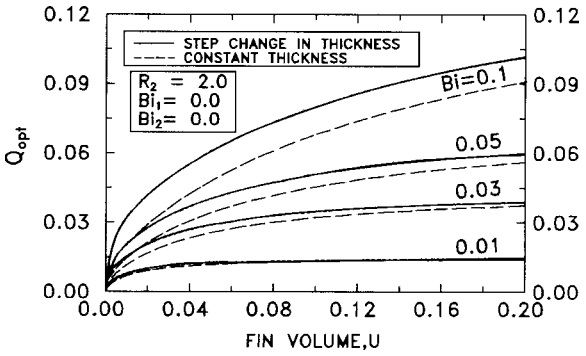

Fig. 5 Variation of the maximum rate of heat dissipation with volume for a restricted fin length

step reduction in thickness improves the temperature gradient towards the fin tip and thereby provides a better design.

In Fig. 3, the thermal efficiency of a radial fin with a step change in thickness has been depicted as a function of Biot number for different fin volumes, while the ratio of thickness (p) and both the intermediate and outer radius have been kept constant. For the sake of comparison the efficiency curves of constant thickness radial fins with identical volume, inner and outer radii have been plotted in the same figure. Efficiency of the fins of both the type decreases with Biot number as expected. Interestingly, for the range of geometrical parameters selected, a step change in thickness results in an increase in efficiency for the same fin volume.

Figure 4 depicts the variation of different optimum parameters of both AFSTs and radial disc fins as a function of fin volume. It may be noted from Fig. 4(a) that the maximum rate of heat dissipation from AFST is more than that of a radial disc fin of identical volume for any given Biot number. Figure 4(b) depicts the variation of the outer radius and intermediate radius of optimum AFSTs as a function of fin volume. The variation of the outer radius $(R_0)_{\text{opt}}$ of radial disc fins is also plotted in the same figure. It is interesting to note that $(R_0)_{\text{opt}}$ will have a value in between $(R_1)_{\text{opt}}$ and $(R_2)_{\text{opt}}$. Finally, Fig. 4(c) indicates that the thickness of an optimum radial fin is higher than the tip thickness but lower than the root thickness of an optimum AFST with identical fin volume.

The above study shows that for a given fin volume, a higher rate of heat transfer is possible from an AFST compared to a radial disc fin. However, an AFST also requires a larger fin length to maximize the rate of heat transfer. This may restrict the use of AFSTs. Therefore, it would be worthwhile to study whether material savings can still be obtained when the outer radii of AFSTs are made fixed. To this end, maximum rate of heat transfer from AFSTs have been determined keeping both the fin volume and the outer radius constant. The condition for optimality can be derived in a similar way as has been done for deriving Eq. (25). The results are shown in Fig. 5. It may be noted that for a given fin volume and outer radius the maximum rate of heat transfer from an AFST is more than that from a radial disc fin. However, the difference decreases with the decrease of Biot number.

Conclusion

In the present work a design modification of concentric annular fins has been suggested in which a step reduction in fin thickness is provided towards the fin tip. Based on one-dimensional conduction an analytical expression has been obtained for the temperature distribution. The temperature distribution is continuous but experiences a change in slope where the step change in thickness occurs.

A scheme for optimizing the design of AFSTs has been presented. It has been shown that an optimum AFST can have a higher rate of heat transfer compared to an optimum annular disc fin of identical volume. However, the length of the former is more. It has subsequently been shown that even for a restricted fin length, AFSTs can be designed to dissipate more heat compared to constant thickness annular fins of same volume.

The performance of a fin can be improved further if the thickness is reduced in several steps in lieu of one. The present methodology can be extended to study a fin with multiple step change in thickness.

References

[1] Mikhailov, M. D., and Ozisik, M. N., 1984, *Unified Analysis and Solutions of Heat and Mass Diffusion*, Dover, New York.
[2] Kern, Q. D., and Kraus, D. A., 1972, *Extended Surface Heat Transfer*, McGraw-Hill, New York.
[3] Duffin, R., 1959, ''A Variational Problem Relating to Cooling Fins,'' J. Math. Mech., **8**, pp. 47–56.
[4] Liu, C. Y., 1962, ''A Variational Problem with Application to Cooling Fins,'' J. Soc. Ind. Appl. Math., **10**, pp. 19–29.
[5] Mikk, I., 1980, ''Convective Fin of Minimum Mass,'' Int. J. Heat Mass Transf., **23**, No. 5, pp. 707–710.
[6] Guceri, S., and Maday, C. J., 1975, ''A Least Weight Circular Cooling Fins,'' ASME J. Ind., **97**, pp. 1190–1193.
[7] Brown, A., 1965, ''Optimum Dimensions of Uniform Annular Fins,'' Int. J. Heat Mass Transf., **8**, pp. 662–665.
[8] Ulman, A., and Kalman, H., 1987, ''Efficiency and Optimized Dimensions of Annular Fins of Different Cross-Section Shapes,'' Int. J. Heat Mass Transf., **32**, pp. 1105–1110.
[9] Kundu, B., and Das, P. K., 1999, ''Performance Analysis and Optimization of Eccentric Annular Disc Fins,'' ASME J. Heat Transfer, **105**, pp. 529–536.
[10] Hollands, K. G. T., and Stedman, B. A., 1992, ''Optimization of an Absorber Plate Fin Having a Step Change in Local Thickness,'' Sol. Energy, **49**, pp. 493–495.
[11] Stoecker, W. F., 1989, *Design of Thermal Systems*, McGraw-Hill, New York.
[12] Schmidt, E., 1926, ''Die Warmenbertrangung Durch Rippen,'' Z. VDI, **70**, pp. 885–951.
[13] Scarborough, J. B., 1966, *Numerical Mathematical Analysis*, Oxford and IBH Publishing Co. Pvt. Ltd., New Delhi, Sixth ed., pp. 215–223.

A Novel Mini Calibrator for Thermochromic Liquid Crystals

Christopher J. Elkins
Physical Science Research Associate, Mechanical Engineering Department, Building 500, Stanford University, Stanford, CA 94305
e-mail: elkins@vk.stanford.edu

John Fessler
Assoc. Mem. ASME, Senior Engineer, Exponent, 149 Commonwealth Drive, Menlo Park, CA 94025
e-mail: jfessler@exponent.com

John K. Eaton
Fellow ASME, Professor, Mechanical Engineering Department, Building 500, Stanford University, Stanford, CA 94305
e-mail: eaton@vk.stanford.edu

A small calibrator has been constructed to facilitate wide-band liquid crystal temperature measurements on complex, curved surfaces. The calibrator's size, 21.3 mm by 20.3 mm by 10.0 mm

Contributed by the Heat Transfer Division for publication in the Journal of Heat Transfer. Manuscript received by the Heat Transfer Division December 14, 1999; revision received November 21, 2000. Associate Editor: A. Majumdar.

thick, makes it ideal for in-situ calibrations at multiple sites on curved surfaces. Its design utilizes the heating/cooling ability of a thermoelectric cooler, and its temperature is quickly and accurately controlled by computer. To test the calibrator's accuracy, a liquid crystal sample was calibrated. Subsequent comparisons to thermistor measurements of a uniform temperature copper block painted with liquid crystals showed the calibration to be accurate to +/−0.1°C between the red start and the approximate blue start temperatures, and the maximum error was less than +/−0.3°C in the dark blue/violet region. [DOI: 10.1115/1.1370505]

Introduction

Thermochromic liquid crystals (TLCs) are liquid substances with special molecular orientations that are sensitive to temperature. As the temperature changes, the optical properties of the crystal change, and the wavelength of reflected light changes. Typically, the color changes from red to violet with increasing temperature. TLCs have been used for temperature measurements for many years, particularly in the narrow band or single color mode [1–6]. Wide band or multi-color utilization of TLCs is more desirable in many cases because it provides a large, continuous temperature field [7–10]. However, the wide band technique can suffer from large uncertainties unless the colors of the TLCs are carefully calibrated with temperature. Typically, the colors, or R, G, and B values, of each pixel in a liquid crystal image, are converted to hue (H), saturation (S), and intensity (I) or value (V). The hue has been found to be a monotonic, though non-linear, function of temperature.

Previous investigators have shown that a hue vs. temperature calibration is highly dependent on lighting and viewing angles [9,11]. They also showed a strong dependence on the ambient lighting conditions and the transparent surfaces through which the crystals are viewed. To reduce the effects of all of these parameters, it is best to calibrate the crystals in-situ using the same experimental set-up for both the calibration and the temperature measurement. If a measurement surface is curved or if the surface is illuminated non-uniformly, multiple calibrations should be performed at multiple positions on the surface. A TLC mini calibrator measuring 21.3 mm by 20.3 mm by 10.0 mm thick has been built for the purpose of making multiple in-situ calibrations in complex geometries.

The mini calibrator is computer controlled and utilizes a Peltier device, a thermoelectric cooler (TEC), to heat and cool a small liquid crystal sample. In addition to the advantages listed above, the mini calibrator can be controlled quickly and accurately. Calibrations require many temperature points to resolve the nonlinear hue vs. temperature curve. A typical calibration for a crystal with a bandwidth of 5°C requires 40–50 points and can be completed in less than 30 minutes. Hysteresis effects may arise from overshooting a desired set temperature for the crystal before setting the temperature. Baughn et al. [12] reported calibration hysteresis error which is strongly dependent on the amount of overshoot. The accurate control of the mini calibrator makes it useful for reducing any possible hysteresis effects in a calibration.

Mini Calibrator Design

An expanded view of the mini calibrator is shown in Fig. 1. The heat exchanger base plate is made from oxygen-free high conductivity (OFHC) copper. Its internal cooling passage is 2.7 mm in diameter. Mini hose barbs are screwed into the plate and sealed with RTV to allow for connection to tubing. In many applications involving temperature measurements at room temperature, the TEC (Melcor, Inc., Trenton, NJ, model FC0.65-65-04-01) can provide sufficient heating/cooling to run the mini calibrator without utilization of the heat exchanger. To run the mini calibrator at temperatures very different from ambient (greater than 30°C), fluid of an appropriate temperature can be circulated through the heat exchanger.

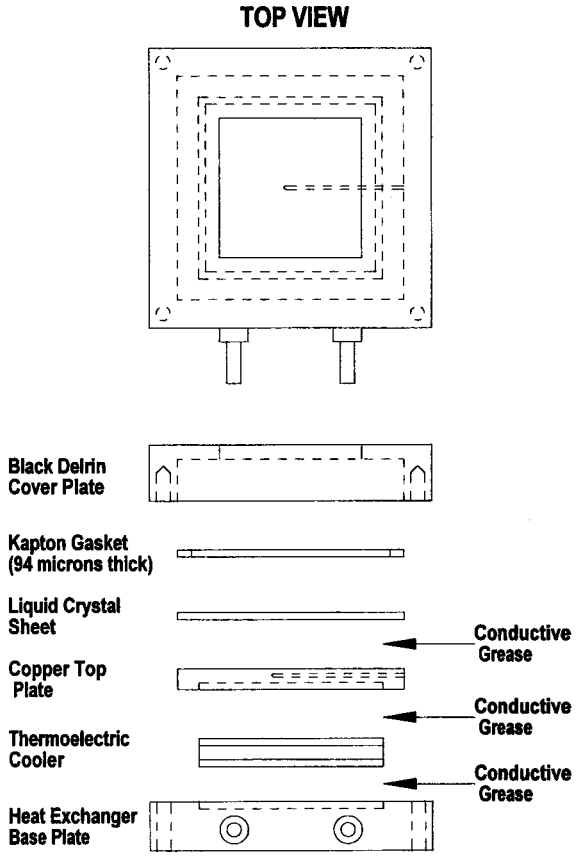

Fig. 1 Illustration showing the assembly of the mini calibrator

A thin layer of silicone heat sink compound (GC Electronics, Backford, IL) is placed between the TEC and the heat exchanger. Similarly, thin layers of this heat sink compound are placed between the TEC and the top plate and the top plate and the sample liquid crystal sheet. The top plate is 2.5 mm thick and made from OFHC copper. It serves as an isothermal surface for the crystal sample. A 1.17 mm diameter hole is drilled into the top plate to accommodate a temperature sensor. Currently, a 0.48 mm diameter thermistor (Cornerstone Sensors, Inc., model T320D103-CA) is used to sense the plate temperature. The liquid crystal sample to be calibrated can be sprayed directly onto the copper plate once a proper black background is applied, or a liquid crystal sheet can be placed on the top plate. Sample liquid crystal sheets from Hallcrest, Inc. and photographic paper (AFGA, MCP310RC) sprayed with encapsulated liquid crystals have worked well.

A black delrin cover plate fits over the liquid crystal sheet and four screws at the corners are used to lightly clamp all of the pieces together. Thin strips of 50 μm thick kapton tape are placed around the inside perimeter of the cover plate to provide a small amount of insulation between the cover and the sample.

Mini Calibrator Control

Computer control of the mini calibrator is achieved with a Dell XPS D233 personal computer, a National Instruments PCI-MIO-16E-4 data acquisition card (National Instruments, Austin, TX), and LabView instrumentation software (National Instruments). The temperature of the top plate is sensed using a thermistor connected to a voltage divider. Two A/D channels are used to sample the excitation and thermistor voltages at 1000 Hz for 0.5 sec. The thermistor resistance is calculated from the average voltages and converted to temperature using calibration charts provided by Cornerstone Sensors, Inc.

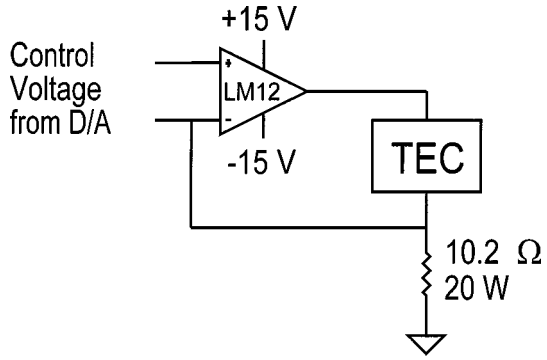

Fig. 2 Mini calibrator power circuit

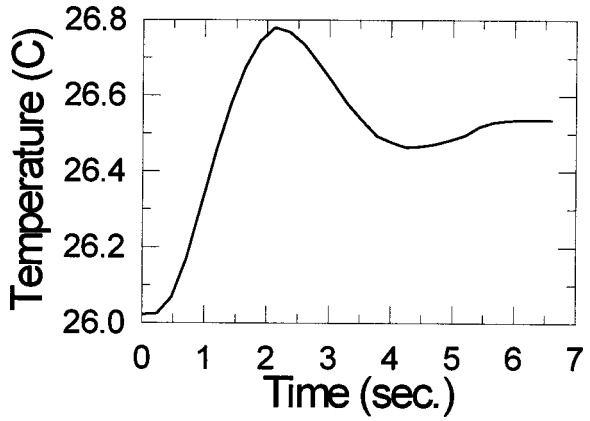

Fig. 3 Time response of the mini calibrator to a 0.5°C step

A proportional, integral, and differential (PID) control algorithm is used to calculate control voltages which are supplied by a *D*/*A* channel to the power circuit shown in Fig. 2. The following control constants worked well for controlling the mini calibrator in the temperature range of 20–60°C when the ambient temperature was approximately 20–30°C: $Kp=0.30$, $Ki=0.003$, $Kd=4.00$.

This system achieved fast, accurate control of the mini calibrator temperature as can be seen in Fig. 3 which shows a time trace of the top plate temperature for a temperature step of 0.5°C. When calibrating liquid crystals for wide band measurements, many temperature points are required to resolve the nonlinear hue vs. temperature curve. For typical calibrations of 5–10°C wide TLCs, steps of 0.2°C are used in the red portion of the temperature range since the slope of the hue vs. temperature is steep. To avoid any possible hysteresis effects, the amount of overshoot if calibrating from low temperatures to high, or undershoot if calibrating from high to low, should be tightly controlled. For calibrations of crystals with 5 or 10°C bandwidth, hysteresis effects were negligible with an overshoot of 0.3°C like that shown in Fig. 3.

Imaging System

A Sony XC-003 CCD camera with a Toyo Optics 12.5–75 mm f/1.8 zoom lens and a Matrox Meteor RGB frame grabber was used to acquire images of the liquid crystal surface of the mini calibrator. The XC-003 CCD camera has several internal parameters that require setting. The most important of these are the gain which is set to 6 dB, the white reference which is set to manual, and the gamma correction which is turned off. The default settings were used for the other parameters. The images were processed using LabView compatible IMAQ Vision software. IMAQ compatible drivers for the Matrox Meteor RGB frame grabber are available from Graftek, Inc. A Fostec AC light source with a 0.5″ fiber optic bundle and spot lens illuminated the mini calibrator. Prinz polarizer filters were used to eliminate stray reflections.

In order to maximize the resolution of the R, G, and B channels, the black and white reference settings for each channel of the Meteor RGB frame grabber are adjusted. The black reference settings of the board are adjusted so the capped camera measures average R, G, and B values less than 10. White reference settings are adjusted while imaging a gray card (Eastman Kodak Company) which should appear to have equal amounts of red, green and blue light. The white reference values are adjusted to give average R, G, and B values slightly less than 250.

The definition for the HSI color space used in this experiment was also used by Farina et al. [11]:

$$\begin{bmatrix} v_1 \\ v_2 \end{bmatrix} = \begin{bmatrix} -1/4 & -1/4 & 1/2 \\ 1/4 & -1/2 & 0 \end{bmatrix} \cdot \begin{bmatrix} R \\ G \\ B \end{bmatrix}$$

$$\text{Hue} \equiv H = \arctan\left(\frac{v_1}{v_2}\right) \cdot \frac{255}{2\pi}$$

$$\text{Saturation} \equiv S = [2 \cdot (v_1^2 + v_2^2)]^{1/2}$$

$$\text{Intensity} \equiv I = \frac{R+G+B}{3}.$$

Here, v_1 and v_2 are intermediate quantities, and R, G, B, H, S, and I have 8-bit resolution. By this definition, hue, saturation, and intensity contain color, color purity, and relative brightness information, respectively.

Experimental Procedure

A copper block and a piece of photographic paper were painted with 25C5W liquid crystals (Hallcrest, Inc.). The photographic paper was placed in the mini calibrator and a calibration curve consisting of hue values at set temperatures was measured. The set temperatures started at 23°C, well below the activation range of the crystal, and increased to 37°C. The data are shown in Fig. 4. Using these data, a look-up table (LUT) was created in which each integral hue value from 0–255 is assigned a temperature value using cubic spline interpolation. The LUT data are shown in Fig. 4. Note that only the monotonic region of the calibration curve can be used.

As a quick check of the calibration repeatability, the temperature of the mini calibrator can be set, and the temperature of the

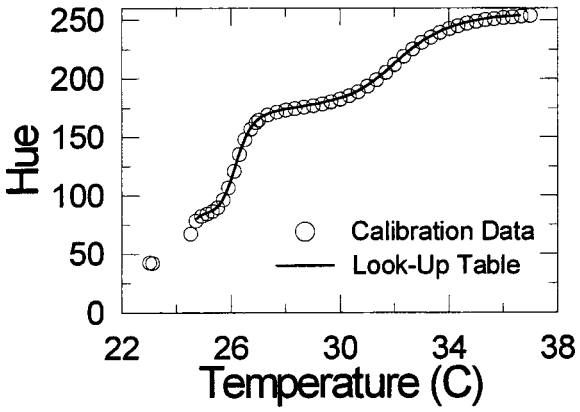

Fig. 4 The calibration data and interpolated look up table values for a 25C5W liquid crystal sample

Table 1 Data showing the accuracy of liquid crystal measurements made using a mini calibrator calibration. Liquid crystal temperature measurements of a uniform temperature copper block are compared to block temperatures measured with a thermistor.

Thermistor Temperature	Liquid Crystal Temperature
25	25.05
26	25.95
27	26.9
28	27.95
29	29.03
30	30
31	31
32	31.9
33	32.85
34	33.8
35	34.75
36	35.7

top plate can be measured using the liquid crystal sheet. The liquid crystal measurements typically agree with the set temperatures to within less than $+/-0.10$°C.

In an alternate test of the accuracy of the liquid crystal calibration, the painted uniform temperature copper block was placed on top of an assembly consisting of a TEC and a copper heat sink. Thermal grease was used between each part to provide good thermal conduction. Here, the copper block surface is an analog to the measurement surface in a heat transfer experiment. The block temperature was set and measured with a thermistor, and the liquid crystal imaging system acquired the surface temperature. Table 1 shows the agreement between the thermistor temperature and the liquid crystal temperature. Agreement is very good (less than 0.1°C) except in the upper blue range where there is a difference of 0.3°C. This is expected, though, since the slope of the calibration is small. At 36°C, a change in hue of 1 corresponds to a change in temperature of 0.4°C.

Conclusion

A liquid crystal mini calibrator has been constructed for use in making wide band liquid crystal temperature measurements. Its small size makes it ideal for in-situ calibrations in complex, curved geometries since calibrations are required at several positions on the measurement surface. Calibrating in-situ improves measurement accuracy by eliminating errors related to differences in viewing angle and lighting between a calibration rig and a test rig. The mini calibrator utilizes the heating and cooling ability of a thermoelectric cooler and computer control to accurately and quickly control its temperature.

A sample of a 25C5W liquid crystal from Hallcrest, Inc. was calibrated. The accuracy of the calibration was tested by viewing the surface of an isothermal copper block of known temperature that was painted with the same crystals. The liquid crystal temperature agreed with the copper block temperature to less than $+/-0.1$°C between the temperatures of 25°C and 32°C corresponding to the red start and the approximate blue start for the 25C5W crystal. At temperatures between 32°C and 36°C, the maximum error was $+/-0.3$°C and is due to the large change in temperature associated with a small change in hue, an artifact of the HSI color space formulation used.

References

[1] Cooper, T. E., Field, R. J., and Meyer, J. F., 1975, ''Liquid Crystal Thermography and Its Application of the Study of Convective Heat Transfer,'' ASME J. Heat Transfer, **97**, pp. 442–405.

[2] Simonich, J. C., and Moffat, R. J., 1982, ''New Technique for Mapping Heat Transfer Coefficient Contours,'' Rev. Sci. Instrum., **53**, pp. 678–683.

[3] Hippensteele, S. A., Russell, L. M., and Torres, F. J., 1986, ''Use of a Liquid-Crystal and Heater-Element Composite for Quantitative, High-Resolution Heat Transfer Coefficients on a Turbine Airfoil Including Turbulence and Surface-Roughness Effects,'' *Pressure and Temperature Measurements*, J. H. Kim and R. J. Moffat, eds., ASME HTD Vol. 58, pp. 105–120.

[4] Jones, T. V., and Hippensteele, S. A., 1987, ''High-Resolution Heat-Transfer-Coefficient Maps Applicable to Compound-Curve Surfaces Using Liquid Crystals in a Transient Wind Tunnel,'' *Developments in Experimental Techniques in Heat Transfer and Combustion*, R. O. Harrington, ed., ASME HTD Vol. 71, pp. 1–9.

[5] Abuaf, N., and Kercher, D. M., 1994, ''Heat Transfer and Turbulence in a Turbulated Blade Cooling Circuit,'' ASME J. Turbomach., **116**, pp. 169–177.

[6] Van Treuren, K. W., Wang, Z., Ireland, P. T., and Jones, T. V., 1994, ''Detailed Measurements of Local Heat Transfer Coefficient and Adiabatic Wall Temperature Beneath and Array of Impinging Jets,'' ASME J. Turbomach., **116**, pp. 369–374.

[7] Hollingsworth, D. K., Boehman, A. L., Smith, E. G., and Moffat, R. J., 1989, ''Measurements of Temperature and Heat Transfer Coefficient Distributions in a Complex Flow Using Liquid Crystal Thermography and True-Color Image Processing,'' *ASME Collected Papers in Heat Transfer*, pp. 35–42.

[8] Dabiri, D., and Gharib, M., 1991, ''Digital Particle Image Thermometry: The Method and Implementation,'' Exp. Fluids, **11**, pp. 77–86.

[9] Camci, C., Kim, K., and Hippensteele, S. A., 1992, ''A New Hue Capturing Technique For The Quantitative Interpretation of Liquid Crystal Images Used In Convective Heat Transfer Studies,'' ASME J. Turbomach., **114**, pp. 765–775.

[10] Wang, Z., Ireland, P. T., Jones, T. V., and Davenport, R., 1994, ''A Color Image Processing System for Transient Liquid Crystal Heat Transfer Experiments,'' ASME Paper No. 94-GT-290.

[11] Farina, D. J., Hacker, J. M., Moffat, R. J., and Eaton, J. K., 1994, ''Illuminant Invariant Calibration of Thermochromic Liquid Crystals,'' Exp. Thermal and Fluid Sci., **9**, pp. 1–12.

[12] Baughn, J. W., Anderson, M. R., Mayhew, J. E., and Wolf, J. D., 1999, ''Hysteresis and Uncertainty of Thermochromic Liquid Crystal Temperature Measurement Based on Hue,'' *Proceedings of the 5th ASME/JSME Joint Thermal Engineering Conference*, March 15–19, 1999, San Diego, CA, paper no. AJTE99/6294.

Acceleration of Anisotropic Scattering Computations Using Coupled Ordinates Method (COMET)

S. R. Mathur
Fluent Inc., Lebanon, NH 03766

J. Y. Murthy
Department of Mechanical Engineering, Carnegie Mellon University, Pittsburgh, PA 15213

Traditional sequential solution procedures for solving coupled heat transfer and radiation problems are known to perform very poorly when the optical thickness is high. This poor performance can be traced to the fact that sequential procedures cannot handle strong inter-equation coupling resulting from large absorption and scattering coefficients. This paper extends the use of the coupled ordinates method (COMET) to problems involving anisotropic scattering, where inter-equation coupling results from the in-scattering terms. A finite volume formulation for arbitrary unstructured meshes is used to discretize the radiative transfer equation. An efficient point-solution procedure is devised which is suit-

Contribued by the Heat Transfer Division for publication in the Journal of Heat Transfer. Manuscript received by the Heat Transfer Division January 4, 2000; revision received November 25, 2000. Associate Editor: R. D. Skocypec.

able for different scattering phase functions, and eliminates the cubic dependence of the operation count on the angular discretization. This solution scheme is used as a relaxation sweep in a multigrid procedure designed to eliminate long-wavelength errors. The method is applied to scattering problems and shown to substantially accelerate convergence for moderate to large optical thicknesses. [DOI: 10.1115/1.1370506]

Keywords: Computational, Heat Transfer, Participating Media, Radiation, Scattering

Introduction

In recent years, the finite volume method [1,2,3,4] and its close counterpart, the discrete ordinates method [5], have emerged as useful techniques for addressing complex radiation problems. However, these methods perform very poorly in the optically thick regime [6,7,8]. It is not unusual for computations to take hundreds of iterations, and oscillation and lack of convergence are common problems. These difficulties can be traced to the sequential solution procedures employed for solving the discretized energy and radiative transfer equation (RTE). When optical thicknesses are large, the strong coupling between these equations makes for poor convergence if the equations are solved sequentially.

In a previous publication, we developed the coupled ordinates method (COMET) for accelerating the convergence of optically thick problems [8]. This method solves the discrete energy equation and the discrete radiative transfer equations (RTE) simultaneously at each grid point to address the coupling problem. By using the point-coupled solution procedure as a relaxation sweep in a multigrid procedure, the method can address the whole range of optical thicknesses. A complete unstructured-mesh formulation using the method was published. Acceleration factors of over 100 were obtained for gray-diffuse enclosures containing optically thick absorbing and emitting media. Unlike previous attempts at acceleration, there was little or no penalty for optically thin cases.

In this paper, we extend the COMET procedure to problems involving both isotropic and anisotropic scattering in complex geometries. When scattering is involved, the RTE in any given ray direction is coupled to the intensities in other directions through the in-scattering term. Unlike absorption and emission, however, application of the COMET procedure to scattering is not straightforward. Conventional LU decomposition and back-substitution, used to solve the algebraic equation set at each cell, involves an $O(L^3)$ operation count, where L is the number of angular directions. Consequently, direct solutions of the algebraic system at each cell become untenably expensive for fine angular discretizations, and accelerations over the sequential procedure may not be obtained except at very high optical thicknesses. In this paper, we devise efficient point-solution procedures which are suitable for the special matrix structures resulting from isotropic, linear-anisotropic and B2 phase functions which do not suffer from this $O(L^3)$ dependence. These solution procedures are coupled to a multigrid scheme suitable for arbitrary unstructured polyhedral meshes. The method is used to solve benchmark problems over a range of optical thicknesses and shown to significantly accelerate convergence for moderate to large optical thicknesses.

For clarity, we consider the temperature field to be given. All boundaries are assumed to be gray-diffuse, though this is not necessary. The primary coupling being considered here is the inter-equation coupling between different ray directions resulting from the in-scattering term. Coupling between the RTE and the energy equation was addressed in a previous paper [8]. The procedures developed here can be combined with those in [8] to compute radiative transfer in general absorbing, emitting and scattering media.

Discretization of RTE

The radiative transfer equation for a gray absorbing, emitting and scattering medium in the direction **s** may be written as [9]:

$$\nabla\cdot(I(\mathbf{s})\mathbf{s}) = -(\kappa+\sigma_s)I(\mathbf{s}) + \kappa I^B + \frac{\sigma_s}{4\pi}\int_{4\pi} I(\mathbf{s}')\Phi(\mathbf{s}',\mathbf{s})d\Omega' \tag{1}$$

Here I^B is the blackbody intensity and Φ is the scattering phase function.

Details of the spatial and angular discretization have been presented elsewhere [4]; we present only a brief summary here. The spatial domain is discretized into N arbitrary unstructured convex polyhedral cells. The angular space 4π at any spatial location is discretized into discrete non-overlapping control angles ω_l, the centroids of which are denoted by the direction vector $\mathbf{s}_l$, and the polar and azimuthal angles θ_l and ϕ_l. Each octant is discretized into $N_\theta \times N_\phi$ solid angles each with a constant angular extent of $\Delta\theta$ and $\Delta\phi$. All unknowns are stored at cell and boundary face centroids.

For each direction l Eq. (1) is integrated over each control volume i and the solid angle ω_l to yield discrete equations of the form [8]

$$\sum_{j=1}^{N} \mu_{ij}^l I_j^l + \alpha_i^l I_i^l = \gamma_i^l \sum_{k=1}^{L} c_{lk} I_i^k + S_i^l + S_i^B . \tag{2}$$

The coefficients μ_{ij}^l in Eq. (2) result from the discretization of the $\nabla\cdot(I\mathbf{s})$ term in Eq. (1). They denote the influence of neighboring cell intensities in the l direction on the intensity in cell i in the same direction. The $\alpha_i^l I_i^l$ term results from absorption and out-scattering, whereas S_i^l results from the emission term. The term S_i^B contains the wall emission and reflection terms. The first term on the RHS results from the discretization of the in-scattering term, and contains the contributions of other directions to the current direction l. The coefficients c_{lk} are given by

$$c_{lk} = \frac{1}{\omega_l}\int_{\omega_l}\int_{\omega_k} \Phi(\mathbf{s}_{l'}\cdot\mathbf{s}_{k'})d\omega_{k'}d\omega_{l'} . \tag{3}$$

COMET Procedure

Equation (2) constitutes a set of coupled linear equations in NL unknowns, viz., the L intensities I_i^l at the N cells. In principle, this set can be solved simultaneously using any linear equation solver. However, the required storage is very large even for relatively coarse angular discretizations and a coupled solution of the entire matrix is rarely used. The most commonly used method is to solve the RTE in each discrete direction sequentially (see [4] for example). In a sequential procedure, only the spatial coupling of intensity in any given direction is treated implicitly. The influence of all other directions is included explicitly via source terms, evaluated using the latest available values.

The rate of convergence of the sequential approach decreases as magnitude of the explicitly-included source terms increases. When a large scattering coefficient is present, the intensities in different directions at a point are coupled more strongly to each other than to the intensities at spatial neighbors. As discussed in [8], in the COMET procedure we addressed this coupling by updating all the directional intensities at a cell together, assuming spatial neighbors fixed. Equation (2) is recast into the following form for a cell i

$$\mathbf{P}_i\mathbf{q}_i + \mathbf{r}_i = 0, \tag{4}$$

where $\mathbf{q}_i$ is the vector of intensities at the cell $[I_i^1, I_i^2, \cdots, I_i^L]^T$ and $\mathbf{P}_i$ is an $L\times L$ matrix given by

$$\begin{bmatrix} M_{ii}^1-\gamma_i^1 c_{11} & -\gamma_i^1 c_{12} & \cdots & -\gamma_i^1 c_{1L} \\ -\gamma_i^2 c_{21} & M_{ii}^2-\gamma_i^2 c_{22} & \cdots & -\gamma_i^2 c_{2L} \\ \vdots & & & \\ -\gamma_i^L c_{L1} & -\gamma_i^L c_{12} & \cdots & M_{ii}^L-\gamma_i^L c_{LL} \end{bmatrix}, \quad (5)$$

where $M_{ii}^l=\mu_{ii}^l+\alpha_i^l$. The vector $\mathbf{r}_i$ is given by

$$\mathbf{r}_i=\begin{bmatrix} \sum_{j=1,i\neq j}^{N} \mu_{ij}^1 I_j^1-S_i^1-S_i^B \\ \vdots \\ \sum_{j=1,i\neq j}^{N} \mu_{ij}^L I_j^L-S_i^L-S_i^B \end{bmatrix}.$$

One relaxation sweep in the COMET procedure consists of a visit to each cell, computing $\mathbf{r}_i$ from prevailing values, and a direct solution of Eq. (4) to obtain the solution vector $\mathbf{q}_i$. Due to the scattering terms, the matrix $\mathbf{P}_i$ is fully populated and is not, in general, diagonally dominant. Therefore the linear equation set has to be solved using expensive direct methods, such as LU decomposition and back-substitution. As a result, the COMET procedure loses its advantage over the traditional sequential solution methods. However, in many applications, the scattering phase function Φ can be expanded in a series of Legendre polynomials [9] as

$$\Phi=1+\sum_{m=1}^{M} A_m P_m(\mathbf{s}\cdot\mathbf{s}'). \quad (6)$$

For such cases the matrix $\mathbf{P}_i$ has a special structure which allows us to obtain a solution in $O(L)$ operations rather than in the $O(L^3)$ operations required by LU decomposition and back substitution. We illustrate the idea for three specific cases below.

Isotropic Scattering

If scattering is isotropic, $\Phi=1$, so that $c_{lk}=\omega_k$. The in-scattering term in Eq. (2) is then of the form $\gamma_i^l I_i^a$ where

$$I_i^a=\sum_{k=1}^{L} I_i^k \omega_k. \quad (7)$$

By introducing I_i^a as an additional independent variable and Eq. (7) as the corresponding additional equation we may write the equation set at cell i as

$$\tilde{\mathbf{P}}_i\tilde{\mathbf{q}}_i+\tilde{\mathbf{r}}_j=0, \quad (8)$$

where $\tilde{\mathbf{q}}$ is the augmented vector $[I_i^1,I_i^2,\cdots,I_i^L,I_i^a]^T$, and $\tilde{\mathbf{P}}_i$ is a $(L+1)\times(L+1)$ matrix given by

$$\begin{bmatrix} M_{ii}^1 & 0 & \cdots & 0 & -\gamma_i^1 \\ 0 & M_{ii}^2 & \cdots & 0 & -\gamma_i^2 \\ \vdots & & & & \\ 0 & 0 & \cdots & M_{ii}^L & -\gamma_i^L \\ \omega_1 & \omega_2 & \cdots & \omega_L & -1 \end{bmatrix}.$$

The advantage of using this form is that the matrix $\tilde{\mathbf{P}}_i$ is easily upper-triangularized in $O(L)$ operations. Inclusion of I_i^a increases the number of unknowns by one; this is independent of the number of angular directions L.

Linear Anisotropic Scattering

If a linear anisotropic phase function is used, $\Phi(\mathbf{s},\mathbf{s}')=a_0+a_1\mathbf{s}\cdot\mathbf{s}'$. With $a_0=1$, from Eq. (3), c_{lk} is found to be

$$c_{lk}=\omega_k+\frac{a_1}{\omega_l}S_l\cdot S_k, \quad (9)$$

where $S_l=\int_{\omega_l}\mathbf{s}d\omega_{l'}$ Defining the vector $\tilde{\mathbf{I}}_i=\Sigma_{k=1}^{L}S_k I_i^k$ the in-scattering term in the direction l for cell i for linear anisotropic scattering may be written as

$$\gamma_i^l\left(I_i^a+\frac{a_1}{\omega_l}S_l\cdot\tilde{\mathbf{I}}_i\right). \quad (10)$$

This form suggests the inclusion of four additional independent variables in the solution vector $\tilde{\mathbf{q}}_i$. These are I_i^a as before, and $\tilde{I}_{xi}$, $\tilde{I}_{yi}$, and $\tilde{I}_{zi}$, the three components of the vector $\tilde{\mathbf{I}}_i$. Thus, $\tilde{\mathbf{P}}_i$ becomes a $(L+4)\times(L+4)$ matrix of the form

$$\begin{bmatrix} M_{ii}^1 & 0 & \cdots & 0 & -\gamma_i^1\frac{a_1}{\omega_1}S_{1x} & -\gamma_i^1\frac{a_1}{\omega_1}S_{1y} & -\gamma_i^1\frac{a_1}{\omega_1}S_{1z} & -\gamma_i^1 \\ 0 & M_{ii}^2 & \cdots & 0 & -\gamma_i^2\frac{a_1}{\omega_2}S_{2x} & -\gamma_i^2\frac{a_1}{\omega_2}S_{2y} & -\gamma_i^2\frac{a_1}{\omega_2}S_{2z} & -\gamma_i^2 \\ \vdots & & & & & & & \\ 0 & 0 & \cdots & M_{ii}^L & -\gamma_i^L\frac{a_1}{\omega_L}S_{Lx} & -\gamma_i^L\frac{a_1}{\omega_L}S_{Ly} & -\gamma_i^L\frac{a_1}{\omega_L}S_{Lz} & -\gamma_i^L \\ S_{1x} & S_{2x} & \cdots & S_{Lx} & -1 & 0 & 0 & 0 \\ S_{1y} & S_{2y} & \cdots & S_{Ly} & 0 & -1 & 0 & 0 \\ S_{1z} & S_{2z} & \cdots & S_{Lz} & 0 & 0 & -1 & 0 \\ \omega_1 & \omega_2 & \cdots & \omega_L & 0 & 0 & 0 & -1 \end{bmatrix}.$$

Once again, $\tilde{\mathbf{P}}_i$ is easily upper-triangularized in $O(L)$ operations. Inclusion of $\tilde{\mathbf{I}}_i$ increases the size of the matrix by three, but this number is invariant with the number of angular directions L, and poses no great penalty.

B2 Phase Function

In addition to the constant and linear parts, the B2 phase function involves a quadratic dependence on $\mathbf{s}\cdot\mathbf{s}'$. Proceeding along the same lines as for the isotropic and linear anisotropic cases, we find that the structure of the matrix $\tilde{\mathbf{P}}_i$ can be simplified by adding a total of 10 new variables so that the solution vector is

$$\tilde{\mathbf{q}}_i=[I_i^1,I_i^2,\cdots,I_i^L,\tilde{I}_{xi},\tilde{I}_{yi},\tilde{I}_{zi},\tilde{I}_i^{xx},\hat{I}_i^{yy},\hat{I}_i^{zz},\hat{I}_i^{xy},\hat{I}_i^{xz},\hat{I}_i^{yz},I_i^a]^T, \quad (11)$$

where $\hat{I}_i^{xx}=\Sigma_{k=1}^{L}\hat{S}_k^{xx}I_i^k$, $\hat{I}_i^{xy}=\Sigma_{k=1}^{L}\hat{S}_k^{xy}I_i^k$ and so on and $\hat{S}^{xx},\hat{S}^{xy}$ etc. are second moments of the ordinate direction

$$\hat{S}_l^{xx}=\int_{\omega_l}(s_x^l)^2 d\omega_{l'} \quad \hat{S}_l^{yy}=\int_{\omega_l}(s_y^l)^2 d\omega_{l'} \quad \hat{S}_l^{zz}=\int_{\omega_l}(s_z^l)^2\, d\omega_{l'}$$

$$\hat{S}_l^{xy}=\int_{\omega_l}\sqrt{2}(s_x^l s_y^l) d\omega_{l'} \quad \hat{S}_l^{xz}=\int_{\omega_l}\sqrt{2}(s_x^l s_z^l) d\omega_{l'}$$

$$\hat{S}_l^{yz}=\int_{\omega_l}\sqrt{2}(s_y^l s_z^l) d\omega_{l'}\,. \tag{12}$$

Now, $\tilde{\mathbf{P}}_i$ is a $(L+10)\times(L+10)$ matrix that is easily upper-triangularized in $O(L)$ operations. The additional variables increase the size of the matrix by six over linear anisotropic scattering, but this number is invariant with the number of angular directions L.

Discussion

The general principle used in the development above is that for scattering phase functions that are expressed as polynomials of $\mathbf{s}\cdot\mathbf{s}'$, the in-scattering term for any direction can be written in terms of variables that are the scalar products of the intensity vector and appropriate moment vectors. This diagonalizes the $L\times L$ matrix resulting from the discretization of the RTE. Although the number of unknowns increases, the increase is independent of the number of directions L. Consequently, the operation count for solving the algebraic system scales linearly in L. This results in a tremendous saving in computational time for even modest angular discretizations over direct solution procedures such as LU decomposition, which scale as $O(L^3)$.

The number of extra variables to be solved increases with the order of the Legendre polynomial being used. Nevertheless, as we will show in the results section, it is worthwhile to use these augmented solution vectors rather than to use the fully populated matrix resulting from the generalized phase function treatment.

Results

Here we apply the point coupled solution procedure to problems involving isotropic and anisotropic scattering and compare the performance to the sequential solution procedure. Since issues of accuracy, spatial and angular discretization as well control-angle overhang have been addressed elsewhere [4], here we focus our attention purely on the convergence characteristics of the two approaches. In the results that follow, the solution is judged to have converged when the scaled residuals for all the equations have reduced to 10^{-6}. At any global iteration, each of the linear equation set is solved to a tolerance of 0.1 reduction in the residual. All the timings reported are obtained on a Sun Ultra Sparcstation 1. $N_\theta\times N_\phi$ is the angular discretization of the octant. All cases are run with 1×10 pixelation [4].

The basic problem we consider is scattering in a quadrilateral cavity. Details of the cavity geometry may be found in [8]. The bottom wall has a temperature T_h, and the other walls are at T_c. The optical thickness $\sigma_s L$ is varied from 0.1 to 100; L is the length of the bottom wall. A baseline unstructured grid of 650 triangles is used; additional finer meshes are constructed by isotropic subdivision as required. We consider different scattering phase functions and different solution approaches.

Isotropic Scattering

We first compute isotropic scattering in the cavity with no emission or absorption for two different sets of boundary conditions. Tables 1 and 2 show a comparison of the sequential and COMET procedures for the case when all walls are black, and $T_c=0$. Table 1 uses a mesh of 650 cells; Table 2 uses a mesh of 2600 cells. Table 3 shows the same comparison using the fine mesh for the case when the lateral walls are assumed to have $\varepsilon=0$. This case corresponds to the boundary conditions used by Fiveland and Jessee [7], and causes the lateral walls to be diffuse reflectors.

Table 1 Isotropic scattering with black walls—comparison of sequential solver and COMET for 650-cell mesh

$\sigma_s L$	Sequential		COMET	
	CPU s	Iter	CPU s	Iter
$N_\theta=N_\phi=2$				
0.1	0.92	7	1.73	4
1.0	1.48	11	1.73	4
10	8.04	75	2.98	5
50	61.87	615	5.7	5
100	143.04	1421	6.88	5
$N_\theta=N_\phi=4$				
0.1	2.91	7	6.02	4
1.0	4.57	11	6.07	4
10	24.24	72	10.61	5
50	183.12	599	20.78	5
100	482.36	1389	25.22	5
$N_\theta=N_\phi=8$				
0.1	10.92	7	30.18	4
1.0	16.96	11	30.33	4
10	91.62	72	53.5	5
50	670.86	595	108.5	5
100	1555.77	1380	126.8	5

We see the from the tables that using COMET results in solution acceleration at moderate to high optical thicknesses for all cases; acceleration factors between 10 and 20 are obtained for $\sigma_s L=50$ or greater. For low optical thicknesses, there may be a performance penalty depending on the boundary conditions used, but the overall solution time in these cases is small, and the penalty is not particularly onerous. The cross-over point at which COMET becomes faster depends on the boundary conditions used. The sequential procedure performs more poorly when gray or reflecting walls are present because the sequential update of the outgoing boundary intensities is done once per global iteration. Since the COMET procedure updates the boundary intensities each sweep of the multigrid procedure, it tends to perform better for gray walls. Both the COMET and sequential procedures are seen to scale approximately linearly with the number of directions.

Table 2 Isotropic scattering with black walls—comparison of sequential solver and COMET for 2600-cell mesh

$\sigma_s L$	Sequential		COMET	
	CPU s	Iter	CPU s	Iter
$N_\theta=N_\phi=2$				
0.1	6.57	6	7.93	4
1.0	7.01	9	8.02	4
10	30.77	72	34.63	6
50	225.46	725	39.66	6
100	559.05	1809	41.75	6
$N_\theta=N_\phi=4$				
0.1	24.06	6	37.43	4
1.0	31.15	10	38.02	4
10	103.08	71	109.4	6
50	738.9	684	124.58	6
100	1832.31	1758	194.06	6
$N_\theta=N_\phi=8$				
0.1	92.06	6	163.19	4
1.0	116.27	10	164.02	4
10	390.03	71	477.58	6
50	2805.81	678	655.74	6
100	7047.15	1745	848.28	6

Table 3 Isotropic scattering with reflecting side walls—comparison of sequential solver and COMET for 2600-cell mesh

$\sigma_s L$	Sequential		COMET	
	CPU s	Iter	CPU s	Iter
$N_\theta = N_\phi = 2$				
0.1	15.1	12	7.5	4
1.0	16.14	19	7.49	4
10	59.52	133	29.85	5
50	424.36	1299	39.79	6
100	1054.74	3255	39.78	5
$N_\theta = N_\phi = 4$				
0.1	54.41	12	46.94	4
1.0	53.79	19	40.62	4
10	188.37	131	159.0	5
50	1295.18	1223	195.83	6
100	3458.91	3147	197.17	6
$N_\theta = N_\phi = 8$				
0.1	236.14	12	156.53	4
1.0	238.98	19	156.53	4
10	708.55	131	870.08	6
50	4915.84	1213	822.2	6
100	13117.35	3123	823.55	5

Linear Anisotropic Scattering

Table 4 shows a comparison of COMET with the sequential solution procedure for the case of linear anisotropic scattering with $\Phi = 1 + 0.5\,\mathbf{s}\cdot\mathbf{s}'$. The bottom wall is at a temperature T_h and the other walls are at T_c. The ratio T_h^4/T_c^4 is chosen to be 16. All walls have $\varepsilon = 0.5$. The 650 cell mesh is used. As with the isotropic case, acceleration factors between 10 and 20 are obtained at moderate to high optical thicknesses. A mild performance penalty is found at low optical thicknesses in some cases. As before, the computational effort scales approximately linearly with the number of angular directions.

Table 4 Linear anisotropic scattering with gray-diffuse walls—comparison of sequential solver and COMET

$\sigma_s L$	Sequential		COMET	
	CPU s	Iter	CPU s	Iter
$N_\theta = N_\phi = 2$				
0.1	2.8	17	3.18	4
1.0	3.8	29	3.16	4
10	14.12	141	4.34	5
50	84.29	141	8.06	5
100	188.74	2001	9.94	5
$N_\theta = N_\phi = 4$				
0.1	9.55	17	10.36	4
1.0	12.09	28	10.35	4
10	44.39	136	14.09	5
50	258.03	871	26.74	5
100	580.0	1959	33.08	5
$N_\theta = N_\phi = 8$				
0.1	36.71	17	49.59	4
1.0	47.26	29	49.61	4
10	165.8	137	67.49	5
50	961.01	866	28.93	5
100	2250.7	1946	154.31	5

Table 5 B2 phase function with gray-diffuse walls—comparison of COMET with optimized and full solvers

$\sigma_s L$	COMET: Optimized		COMET: Full Solve	
	CPU s	Iter	CPU s	Iter
$N_\theta = N_\phi = 2$				
0.1	4.36	4	14.46	4
10	8.61	6	21.56	6
100	19.44	5	47.1	5
$N_\theta = N_\phi = 4$				
0.1	15.4	4	115.64	4
10	30.53	6	230.31	6
100	70.22	5	531.95	5
$N_\theta = N_\phi = 8$				
0.1	67.43	4	5393.89	4
10	135.67	6	10787.53	5
100	317.1	5	24912.64	5

B2 Phase Function

The diagonalization procedure described previously is critical in obtaining acceleration using COMET. Table 5 shows a comparison of COMET performance with and without the procedure for the B2 phase function. A 650 cell mesh is used with all walls at $\varepsilon = 0.5$, and $T_h^4/T_c^4 = 16$. The column labeled ''Optimized'' employs a point-coupled relaxation using the augmented solution vector in Eq. (11). The column labeled ''Full Solve'' employs the general anisotropic scattering formulation, with the solution vector and **P** matrix defined in Eqs. (4) and (5), and an LU decomposition and back-substitution. We see that a substantial penalty is paid for using the full matrix; the computational effort is seen to scale as $O(L^3)$. The optimized procedure, on the other hand, is seen to scale approximately linearly with L. The number of iterations to convergence is of course the same for both procedures. These performance comparisons indicate that the direct solution of the full matrix should be avoided wherever possible.

Combined Absorption, Emission and Linear Anisotropic Scattering

In this final problem, we compute combined absorption, emission and linear anisotropic scattering in the cavity, including the coupled conduction-radiation problem. A description of the COMET procedure for coupling the energy equation and the RTE may be found in [8]. All walls are at $\varepsilon = 0.5$ and $T_h^4/T_c^4 = 16$.

Table 6 Absorption, emission, and linear-anisotropic scattering with gray-diffuse walls—comparison of sequential solver and COMET for 2600-cell mesh

κL	Sequential		COMET	
	CPU s	Iter	CPU s	Iter
$N_\theta = N_\phi = 2$				
0.1	17.73	17	11.36	5
1.0	21.42	32	8.7	5
10	105.78	272	9.61	5
50	661.34	2216	15.8	5
100	1510.42	5061	17.58	5
$N_\theta = N_\phi = 4$				
0.1	64.64	17	48.38	4
1.0	79.31	33	44.33	5
10	350.48	268	48.88	5
50	2398.5	2158	81.43	5
100	5498.74	4947	90.71	5
$N_\theta = N_\phi = 8$				
0.1	233.29	17	252.49	5
1.0	281.64	33	208.2	5
10	1239.46	265	230.5	5
50	8384.18	2143	385.66	5
100	19201.68	4908	430.14	5

The Planck number $(k/4\sigma T_m^3 L)$ is 10^{-3}. Here $T_m^3=(T_h^4-T_c^4)/(4\sigma(T_h-T_c))$. The linear-anisotropic phase function is assumed to be $\Phi=1+0.5\mathbf{s}\cdot\mathbf{s}'$. The single scattering albedo $\sigma_s/(\kappa+\sigma_s)$ is chosen to be 0.5.

A comparison between the sequential procedure and COMET is given in Table 6 for the 2600-cell mesh for different angular discretizations and different optical thicknesses κL. For this case, we see acceleration across the range of optical thickness, with acceleration factors of 50–100 for large optical thicknesses. This increase in acceleration is due to the additional coupling with the energy equation, which is efficiently handled by COMET but not by the sequential procedure. As before, both the sequential procedure and COMET scale linearly with the number of angular directions.

Closure

A point-coupled multigrid procedure has been devised to accelerate the convergence of the finite volume scheme for anisotropic scattering. Care has been taken to devise a formulation which scales approximately linearly with the size of the angular discretization by exploiting the specific structure of the phase function. The formulation is applicable to arbitrary unstructured polyhedra. Acceleration has been found in all pure scattering cases for moderate to high optical thicknesses. There is a penalty at low optical thicknesses in some cases, but it is relatively modest. Even larger gains have been found in the combined conduction-radiation problem involving absorption, emission and scattering.

Our calculations indicate that it is essential to use the diagonalized matrix structure wherever possible in order to obtain acceleration. However, the diagonalization procedure becomes increasingly difficult as the phase function becomes more complicated. As order of the Legendre polynomial expansion increases, the number of extra unknowns to be included increases rapidly, though the method still scales as $O(L)$. For high-order polynomials, these extra variables may result in a performance penalty at coarse angular discretizations. Despite this drawback, the technique shows broad performance gains for many commonly-used phase functions, and holds promise as a general purpose solver for multi-mode heat transfer problems.

Acknowledgments

We wish to acknowledge the use of Fluent Inc.'s solver FLUENT/UNS, and its mesh generators PreBFC and TGrid, in this work.

References

[1] Raithby, G. D., and Chui, E. H., 1990, ''A Finite-Volume Method for Predicting Radiant Heat Transfer in Enclosures With Participating Media,'' J. Heat Transfer, **112**, pp. 415–423.
[2] Chui, E. H., and Raithby, G. D., 1993, ''Computation of Radiant Heat Transfer on a Non-Orthogonal Mesh Using the Finite-Volume Method,'' J. Heat Transfer **23**, pp. 269–288.
[3] Chai, J. C., Parthasarathy, G., Patankar, S. V., and Lee, H. S., 1994 ''A Finite-Volume Radiation Heat Transfer Procedure for Irregular Geometries,'' AIAA Paper 94-2095.
[4] Murthy, J. Y., and Mathur, S. R., 1998, ''Finite Volume Method for Radiative Heat Transfer Using Unstructured Meshes,'' J. Thermophys. Heat Transfer, **12**, No. (3), pp. 313–321.
[5] Fiveland, W. A., and Jessee, J. P., 1994, ''Finite Element Formulation of the Discrete Ordinates Method for Multidimensional Geometries,'' J. Thermophys. Heat Transfer, **8**, No. (3), pp. 426–433.
[6] Chui, E. H., and Raithby, G. D., 1992, ''Implicit Solution Scheme to Improve Convergence Rate in Radiative Transfer Problems,'' Numer. Heat Transfer, **22**, pp. 251–272.
[7] Fiveland, W. A., and Jessee, J. P., 1995, ''Acceleration Schemes for the Discrete Ordinates Method,'' HTD-Vol. 315, 1995 National Heat Transfer Conference, **13**, pp. 11–19.
[8] Mathur, S. R., and Murthy, J. Y., 1999, ''Coupled Ordinates Method for Multigrid Acceleration of Radiation Calculations,'' J. Thermophys. Heat Transfer, **13** No. (4), pp. 467–473.
[9] Modest, M. F., 1993, *Radiative Heat Transfer*. Series in Mechanical Engineering. McGraw Hill, New York.